Particle and light propagation around stellar black holes in alternative theories of gravity and implications to general relativistic tests

MOHSEN FATHI

Supervisor: Dr. José Ricardo Villanueva Lobos (UV)

Internal reviewer: Dr. Víctor Hugo Cárdenas Vera (UV)

External reviewer: Dr. Norman Francisco Cruz Marin (USACH)

External reviewer: Dr. Marco Andrés Olivares Rubilar (UDP)

Tesis para optar al grado de Doctorado en Astrofísica

Instituto de Física y Astronomía

Facultad de Ciencias

Universidad de Valparaíso

ENERO 2023

Valparaíso, Chile.

To *Mona*

This thesis is solely my own composition,
except where specifically indicated in the text.

Mohsen Fathi
Firma:

Enero 2023.
Valparaíso. Chile.

Acknowledgements

First of all, I would like to express especial thanks to my kind-hearted professor, Dr. José Ricardo Villanueva Lobos, without the generous supports of whom from the beginning moments of my presence in Chile, I could not have stepped in this scientific path. I am also rather thankful to him for the knowledge he offered me, and for his flexibility during the hard times that the global pandemic provoked. I am also in debt to Dr. Marco Olivares Rubilar, for all those teaching sessions, during which, he transferred me his experience. I highly appreciate the weekly reunions with José and Marco which followed for two years, and provided this chance for me to learn from them. I am rather thankful to Dr. Víctor Hugo Cárdenas, for his effective contribution in my research progress and for his kind impression I received during my doctorate studies. My special thanks go to Prof. Volker Perlick for the discussions we had through several emails, which helped me obtaining considerable insights on the construction of photon regions in stationary black hole spacetimes. I sincerely thank prof. Georgios V. Kraniotis for his hospitality and collaboration during my visit to the University of Ioannina, where I learned how to implement advanced mathematical tools into various problems in non-linear dynamics. I also take this opportunity to thank the faculty of the Instituto de Física y Astronomía of Universidad de Valparaíso, in particular, Dr. Michel Curé, Dr. Verónica Motta, Dr. Maja Vučković, and Dr. Mónica Zorotovic, from whom I learned a lot. I also appreciate the fast and effective technical supports from Edgar Sanders that helped me maintaining the desirable computational facilities.

Having said all the above, I find it outstanding to thank my wife Mona Kariminezhad, without whom, I would have never been able to go this far. Encouraging me not to stop in non of life's stages, and being there in all those moments that I underwent sever mental pressures, she helped me to survive. So I owe her a life.

This thesis has been supported by a four-year fellowship under the grant number 21190382, from the Agencia Nacional de Investigación y Desarrollo (ANID), owned by the ministry of science, technology, knowledge and innovation of the government of the Republic of Chile.

Overview and the objectives

The equations of motion for particles travelling in the gravitational fields of massive objects, as formulated by the general theory of relativity, have been receiving rigorous attention ever since the advent of the theory. In fact, the approximate solutions to these equations, at the time, could pave the way in figuring out the trajectories of planets and light in the solar system and finally, led to some observational evidences which confirmed general relativity's predictions (as asserted by Eddington in his famous book (Eddington, 1920)). However, the more delicate the experimental tests became, the more they raised the interest in obtaining exact solutions to the equations of motion. This necessitated employing advanced mathematical methods, mainly, because of the resultant differential equations appearing in the equations of motion, which tend to calculate the arc-lengths associated with the particle trajectories. Since the early attempts by Hagihara (Hagihara, 1930) and Darwin (Darwin, 1959, 1961) in obtaining and categorizing the particle orbits in the Schwarzschild spacetime, researchers have been employing different approaches to the computation of the arc-lengths swept by particle trajectories in gravitating systems. These approaches are, in general, based on manipulating elliptic integrals and the resultant elliptic functions, covering the Jacobi and the Weierstraß elliptic functions, as the two most common forms. Ever since, the elliptic and hyper-elliptic functions have received a great deal of interest in analyzing the geodesic structure of massive and mass-less particles in black hole spacetimes (Rauch & Blandford, 1994; Kraniotis & Whitehouse, 2003; Kraniotis, 2004; Beckwith & Done, 2005; Cruz et al., 2005; Kraniotis, 2005; Hackmann & Lämmerzahl, 2008a,b; Bisnovatyi-Kogan & Tsupko, 2008; Kagramanova et al., 2010; Hackmann et al., 2010a,b; Kraniotis, 2011; Enolski et al., 2011; Gibbons & Vyska, 2012; Muñoz, 2014a; Kraniotis, 2014; Muñoz, 2014b; De Falco et al., 2016; Barlow et al., 2017; Vankov, 2017; Chatterjee et al., 2019; Uniyal et al., 2018; Jusufi et al., 2018; Ghaffarnejad et al., 2018; Villanueva et al., 2018; Hsiao et al., 2020; Gralla & Lupsasca, 2020; Kraniotis, 2021).

In this thesis, we investigate the time-like and null geodesics that propagate in the exterior geometry of static and rotating black holes. The first problems that are dealt with, is the derivation of the analytical solutions to the equations of motion, for both the radial and angular types of orbits. To achieve this purpose, we use the standard Lagrangian dynamics and identify the orbits in the context of the corresponding effective potentials. The second objective is to apply the classical general relativistic tests (in particular in the solar system), to examine the relevant mathematical formulations for these tests that are given for each of the black holes spacetimes.

The organization of this thesis is as follows: In chapter 1, we discuss, in detail, the elliptic integrals and their solutions in terms of the Jacobian and Weierstraßian elliptic functions in all of their forms. We also bring several examples to demonstrate their applicability for the relevant problems in classical physics. In chapter 2, we explore the geometrical aspects of the Lagrangian and Hamiltonian on the base manifold. This is followed by the derivation of the geodesic equation from Euler-Lagrange equations. Furthermore, to exemplify this in black hole spacetimes, we calculate the exact solutions to the radial and angular geodesics for the mass-less and massive particles that travel in the exterior geometry of a Schwarzschild black hole, which necessitates the exploitation of the formerly discussed elliptic functions. These trajectories are also plotted for each of the types of orbits. Moreover, we review the derivation of a modified version of the Newman-Janis algorithm to generate the stationary counterparts of static spacetimes. In chapter 3, we begin our studies by investigating the geodesics in a particular spacetime, derived from the fourth order Weyl conformal gravity, under certain circumstances. This static black hole spacetime, is studied in the context of the propagation of mass-less, neutral, and charged massive particles. We also apply several general relativistic tests on this black hole, by means of the derived analytical expressions. Finally, by employing the aforementioned algorithm, a stationary counterpart of this black hole is generated. This black hole is investigated in terms of its ergoregion, photon spheres and shadow. In chapter 4, the propagation of mass-less particles in the exterior geometry of a scale-dependent BTZ black hole is discussed, together with the simulation of the possible orbits. Chapter 5 is devoted to a more complicated case, namely to a Kerr black hole immersed in a non-magnetized plasma, which produces a dielectric medium residing in a curved manifold. We apply an elaboration to all the previously discussed methods, and then, we employ them to the investigation of the light ray trajectories in this medium. The orbits are discussed in both planar and three-dimensional context, by solving, individually, the temporal evolution of the coordinates. In chapter 6, we consider a Schwarzschild black hole associated with quintessence and cloud of strings, which is firstly calibrated in the context of standard general relativistic tests for its parameters. We then continue with the derivation of exact analytical solutions for null and time-like geodesics in this spacetime. We finally switch our study, in chapter 7, to the application of Carathéodory's geometrothermodynamics to a static (Hayward) and a stationary (rotating scale-dependent BTZ) black hole. This discussion, although being different from those done in the previous chapters, is of great interest since it provides a new vision to the black hole thermodynamics and helps for the creation of a boost in the development of this field of study. We construct the perspective of our future studies in chapter 8.

Throughout this thesis, unless in the particular places that is adopted otherwise, we use the geometric units, in which $G = c = \hbar = 1$. Furthermore, in appropriate places where needed, we use the Einstein convention on summing over dummy indices, and the four-dimensional system of coordinates is adopted as $x^\mu = \left(x^0, x^1, x^2, x^3\right)$, in which, the zero component corresponds to the time coordinate, i.e. $x^0 = t$. All the diagrams and simulations have been generated by the software *Mathematica*® 12.0.

Contents

CHAPTER 1

Mathematical preliminaries

In this chapter, we introduce and discuss the elliptic integrals and elliptic functions, based on their well-known varieties. These include their Jacobian and the Weierstraßian forms and we briefly study their applications in classical mechanics which constitute the mathematical foundations of the rest of this thesis.

1.1 Introduction

During its evolution, physics has been confronted several complicated problems, to solve which, a bunch of rather complicated functions were used. These problems, sometimes, have even formed the origins of new mathematical functions that were later developed accordingly. Among the mentioned complicated mathematical tools, the elliptic functions were have been applying widely to solve a great variety of problems in classical mechanics. In fact, in many problems in classical mechanics, one confronts the integral (Taylor, 2005; Gregory, 2006)

$$t(y) = \pm \int_{y_0}^{y} \frac{\mathrm{d}x}{\sqrt{(\frac{2}{m})[E - V(x)]}}, \tag{1.1}$$

giving the spatial dependence of the time coordinate for a moving object of mass m of constant energy E, that has been located in the x-dependent conservative potential $V(x)$. The initial condition y_0 is then chosen in the way that it corresponds to the root of the turning point, given by the equation $E = V(y_0)$. For the latitudinal (polar) motion, we confront the integral

$$\theta(s) = \pm \int_{s_0}^{s} \frac{\mathrm{d}\sigma}{\sqrt{(\frac{2\mu}{\ell^2})[E - V(\sigma^{-1}) - \frac{\ell^2\sigma^2}{2\mu}]}}, \tag{1.2}$$

is inverted as $r(\theta) = \frac{1}{s(\theta)}$ and is used in the central force problems, for an object of the reduced mass μ, constant energy E and the angular momentum ℓ, which has been located in the potential $V(r)$. The initial condition $s(0) = s_0$ is then obtained in terms of the equation $E = V(s_0^{-1}) - \frac{\ell^2 s_0^2}{2\mu}$ for the turning points. To obtain the dependence of the time coordinate with respect to the polar coordinate, we have the integral equation

$$t(\theta) = \pm \int_{\cos\theta_0}^{\cos\theta} \frac{\mathrm{d}u}{\sqrt{(\frac{2}{I_1})(1-u^2)[E - V(u)]}}, \tag{1.3}$$

that corresponds to the $\theta(t)$ solution in the equations of motion. Here, I_1 is the component of the tensor of inertia, for which, the symmetry of the motion id defined[1]. The turning points are then associated with the initial condition $E = V(u_0) = V(\cos\theta_0)$. To obtain the exact analytical solutions to the coordinates (t, x, θ), we then need to do the inversions $t(x) \to x(t)$, $\theta(s) \to s(\theta)$ and $t(\theta) \to \theta(t)$. These solutions are, however, achievable once the above integrals can be expressed in terms of analytical functions. For example, the the time integral in Eq. (1.1) are expressible in terms of trigonometric (or singly periodic) functions, in the case that $V(x)$ is a quadratic polynomial. For the case of the integral (1.2), such solutions can only be achieved when $V(r) = -\frac{k}{r}$ or $V(r) = \frac{kr^2}{2}$. However, in the more general cases, the analytical solutions are not expressed in terms of simple functions. For example, in the case that $V(r) = kr^n$, the integral (1.2) results in elliptic functions for $n = -3, \pm 6, \pm 4, 1$ (Whittaker & McCrae, 1988). Same happens for the integral (1.3), when $V(u) = Mghu$ (a gravitational potential for a particle of mass M, with one fixed point located at distance h from the center of gravity).

1.1.1 The periodicity of elliptic functions

The elliptic functions are thought of as being doubly periodic. These periods, together, form a lattice composed of a parallelogram in the complex plane. To elaborate this, let us consider a function $F(z)$ with the two periods η and η', where z is a complex number. In the case that $F(z + m\eta + n\eta') = F(z)$ for $m, n = 0, \pm 1, \pm 2, \ldots$, and the

[1] In three dimensions, for example, we can let $I_1 = I_2 \neq I_3$.

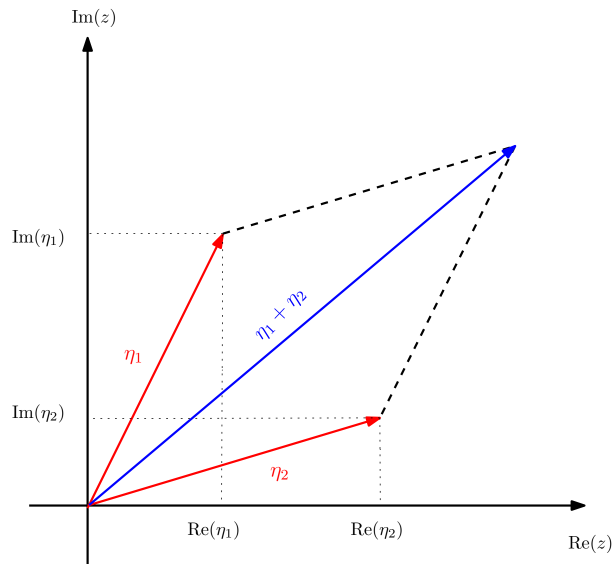

Figure 1.1: The period parallelogram for the double-periodic function $F(z)$.

ratio $\frac{\eta'}{\eta}$ has a positive definite imaginary part, then $F(z)$ is called double-periodic. In the case that $|\eta'| \to \infty$ the function $F(z)$ becomes singly periodic with period η. The mentioned fundamental period-parallelogram of a doubly periodic function is defined by the four points $(0, \eta, \eta', \eta + \eta')$ (see Fig. 1.1). Elliptic functions are indeed defined in this parallelogram and are thought of as double-periodic functions with either two simple zeros or a second order pole ($\wp$-Weierstraß elliptic function), or two first order poles (Jacobi elliptic functions). In fact, an elliptic function $y(x; \boldsymbol{a})$ with $\boldsymbol{a} = (a_0, a_1, a_2, a_3, a_4)$, is defined as the solution to the nonlinear ordinary differential equation

$$\left(\frac{\mathrm{d}y}{\mathrm{d}x}\right)^2 = a_4 y^4 + a_3 y^3 + a_2 y^2 + a_1 y + a_0. \tag{1.4}$$

This equation can be regarded as the inversion of the solution to the integral

$$x(y; \boldsymbol{a}) = x_0 \pm \int_{y_0(\boldsymbol{a})}^{y} \frac{\mathrm{d}s}{\sqrt{a_4 s^4 + a_3 s^3 + a - 2s^2 + a_1 s + a_0}}, \tag{1.5}$$

where $y_0(\boldsymbol{a})$ is a root of the quartic polynomial $a_4 y^4 + a_3 y^3 + a_2 y^2 + a_1 y + a_0$ and $x(y_0; \boldsymbol{a}) = x_0$. The Jacobi elliptic functions are defined in terms of the quartic polynomial $(1 - y^2)(a + by^2)$ with $a, b =$ const., whereas the $\wp$-Weierstraß elliptic functions are defined in terms of the cubic polynomial $4y^3 - g_2 y - g_3$, with g_2 and g_3 known as the Weierstraß invariants (Byrd & Friedman, 1971). These properties will be discussed in more details in the forthcoming sections.

1.2 Jacobi elliptic functions

Let us introduce the three famous Jacobi elliptic functions $(\operatorname{sn} z, \operatorname{cn} z, \operatorname{dn} z)$. First, the Jacobi elliptic function $\operatorname{sn} z \equiv \operatorname{sn}(z|m)$, with modulus $m < 1$, is a solution to the differential equation

$$\left(\frac{\mathrm{d}y}{\mathrm{d}z}\right)^2 = (1-y^2)(1-my^2), \tag{1.6}$$

with the initial condition $y(0) = 0$. The Jacobi elliptic function $\operatorname{cn} z \equiv \operatorname{cn}(z|m)$, with modulus $m < 1$ and the complementary modulus $m' = 1 - m > 0$, is a solution to the differential equation

$$\left(\frac{\mathrm{d}y}{\mathrm{d}z}\right)^2 = (1-y^2)(my^2+m'), \tag{1.7}$$

with the initial condition $y(0) = 1$. Finally, the Jacobi elliptic function $\operatorname{dn} z \equiv \operatorname{dn}(z|m)$, with $m' = 1 - m > 0$, is a solution to the differential equation

$$\left(\frac{\mathrm{d}y}{\mathrm{d}z}\right)^2 = (1-y^2)(y^2-m'), \tag{1.8}$$

with the initial condition $y(0) = 1$. The differential equations (1.6)–(1.7) imply that the Jacobi elliptic functions have the following derivatives with respect to z (Byrd & Friedman, 1971):

$$\operatorname{sn}' z = \operatorname{cn} z \operatorname{dn} z, \tag{1.9a}$$

$$\operatorname{cn}' z = -\operatorname{sn} z \operatorname{dn} z, \tag{1.9b}$$

$$\operatorname{dn}' z = -m \operatorname{cn} z \operatorname{sn} z, \tag{1.9c}$$

where the sign conventions satisfy the identities

$$\operatorname{sn}^2(z|m) + \operatorname{cn}^2(z|m) = 1 = \operatorname{dn}^2(z|m) + m \operatorname{sn}^2(z|m). \tag{1.10}$$

We note that, for the special case $m = 1$, the solutions to the differential equations (1.6)–(1.8) yield

$$\operatorname{sn}(z|1) = \tanh z, \tag{1.11a}$$

$$\operatorname{cn}(z|1) = \operatorname{sech} z, \tag{1.11b}$$

$$\operatorname{dn}(z|1) = \operatorname{sech} z, \tag{1.11c}$$

while for $m = 0$, we get

$$\operatorname{sn}(z|0) = \sin z, \tag{1.12a}$$

$$\operatorname{cn}(z|0) = \cos z, \tag{1.12b}$$

$$\operatorname{dn}(z|0) = 1. \tag{1.12c}$$

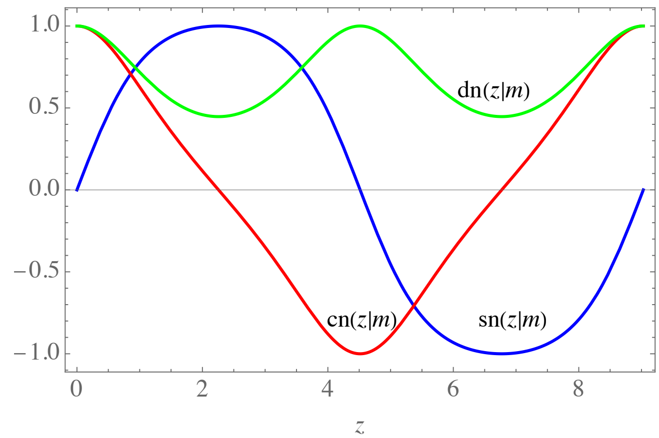

Figure 1.2: Plots of $\mathrm{sn}\,(z|m)$, $\mathrm{cn}\,(z|m)$ and $\mathrm{dn}\,(z|m)$ from $z = 0$ to $4K(m)$ for $m = 0.2$.

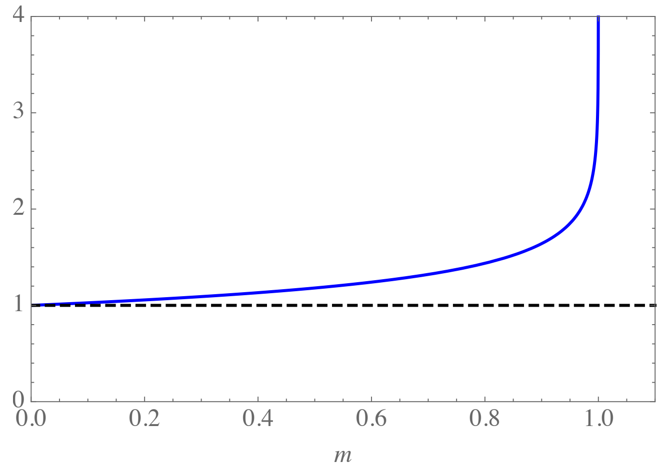

Figure 1.3: The behavior of $\frac{2}{\pi}K(m) = \frac{2}{\pi}K'(1-m)$ with respect to changes in m.

As stated before, the elliptic functions $(\mathrm{sn}\,z, \mathrm{cn}\,z, \mathrm{dn}\,z)$ are doubly periodic functions of z, with real-valued periods that are either $2K$ $(\mathrm{dn}\,z)$ or $4K$ $(\mathrm{sn}\,z$ and $\mathrm{cn}\,z)$ (see Fig. 1.2), with

$$K \equiv K(m) = \int_0^{\frac{\pi}{2}} \frac{\mathrm{d}\theta}{\sqrt{1-m^2\sin^2\theta}} = \frac{\pi}{2}\left(1 + \frac{1}{4}m + \frac{9}{64}m^2 + \ldots\right), \tag{1.13}$$

being the complete elliptic integral of the first kind, and purely imaginary periods that are either $2\mathrm{i}K'$ $(\mathrm{sn}\,z)$ or $4\mathrm{i}K$ $(\mathrm{cn}\,z$ and $\mathrm{dn}\,z)$, where

$$\mathrm{i}K'(m) \equiv \mathrm{i}K(m') = \mathrm{i}\int_0^{\frac{\pi}{2}} \frac{\mathrm{d}\theta}{\sqrt{1-m'\sin^2\theta}}. \tag{1.14}$$

It is apparent from Fig. 1.3 that $K(0) = \frac{\pi}{2} = K'(1)$, whereas $K(m) = K'(1-m) \to \infty$ for $m \to 1$. Furthermore, in Fig. 1.4, we have shown the behaviors of $\mathrm{sn}\,z$ and $-\mathrm{i}\,\mathrm{sn}\,(\mathrm{i}z)$

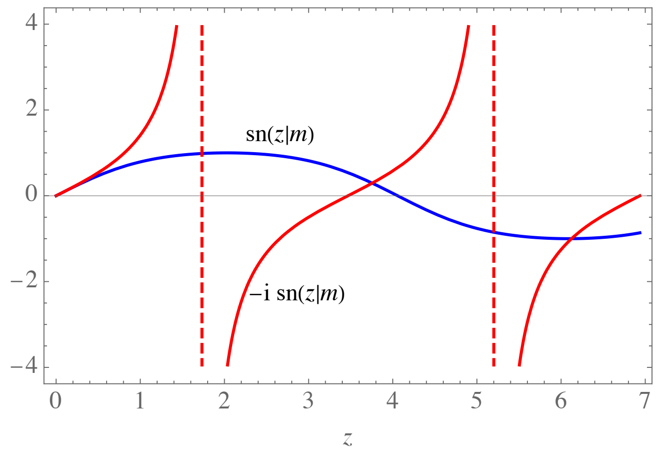

Figure 1.4: Plots of $\mathrm{sn}\,(z|m)$ and $-\mathrm{i}\,\mathrm{sn}\,(\mathrm{i}z|m)$ for $0 \leq z \leq 4K'(m)$ for $m = \frac{2}{3}$.

for $m = \frac{2}{3}$, which exhibit both a real period $(4K)$ and an imaginary period $(2\mathrm{i}K)$. The fundamental period parallelogram for the Jacobi elliptic functions is, therefore, a rectangle with corners at $(0, 4K, 4\mathrm{i}K, 4K + 4\mathrm{i}K')$, where zeros occur for real values of z (at $2K$ and $4K$), while the singularities occur for imaginary values of z (at $\mathrm{i}K'$ and $3\mathrm{i}K'$). The Jacobi elliptic functions for $m > 1$ $(m' < 0)$ are obtained from transformations of the differential equations (1.6)–(1.8) in terms of the new variable $m^{\frac{1}{2}}z$. Accordingly, for $m > 1$ we find

$$\mathrm{sn}\,(z|m) = m^{-\frac{1}{2}}\mathrm{sn}\,(m^{\frac{1}{2}}z|m^{-1}), \tag{1.15a}$$

$$\mathrm{cn}\,(z|m) = \mathrm{dn}\,(m^{\frac{1}{2}}z|m^{-1}), \tag{1.15b}$$

$$\mathrm{dn}\,(z|m) = \mathrm{cn}\,(m^{\frac{1}{2}}z|m^{-1}), \tag{1.15c}$$

that satisfy an identity similar to that in Eq. (1.10).

1.2.1 Seiffert spherical spiral

The periodicity of the Jacobi elliptic functions $\mathrm{sn}\,z$ and $\mathrm{cn}\,z$ can be exemplified in the Seiffert spherical spiral (Whittaker & Watson, 1996; Erdös, 2000). This spiral, defines a periodic curve on the unit sphere which is constructed by means of the cylindrical metric $\mathrm{d}s^2 = \mathrm{d}\rho^2 + \rho^2\mathrm{d}\phi^2 + \mathrm{d}z^2$ where $z = \sqrt{1-\rho^2}$ and $\phi(s) \equiv ks$ is the azimuth angle parametrized by the arc length s (by making this assumption that the initial point of the curve is $(\rho_0, \phi_0, z_0) = (0, 0, 1)$). One can, therefore, obtain the following differential equation:

$$\left(\frac{\mathrm{d}\rho}{\mathrm{d}s}\right)^2 = \left(1-\rho^2\right)\left(1-k^2\rho^2\right), \tag{1.16}$$

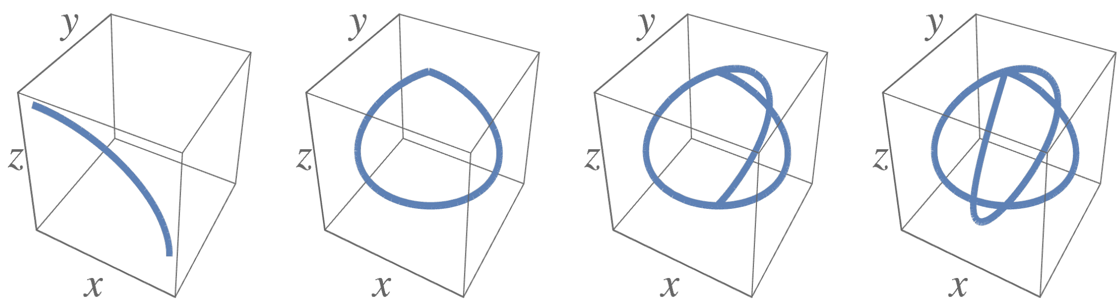

Figure 1.5: Parametric plots of the Seiffert spherical spiral on the surface of the unit sphere for $k = 0.15$ and (from left to right) from $s = 0$ to $s = 2K(k^2)$, $s = 4K(k^2)$, $s = 6K(k^2)$ and $s = 8K(k^2)$.

which is solved in terms of the elliptic functions, giving

$$\rho(s) = \mathrm{sn}\,(s|k^2), \tag{1.17a}$$

$$z(s) = \sqrt{1-\rho^2(s)} = \mathrm{cn}\,(s|k^2), \tag{1.17b}$$

when $0 < m \equiv k^2 < 1$, that satisfies the conditions $\rho(0) = \rho_0$ and $z(0) = z_0$. The Seiffert spiral is then produced by the path of the unit vector

$$\hat{r}(s) = \mathrm{sn}\,(s|k^2)\,[\cos(ks)\hat{x} + \sin(ks)\hat{y}] + \mathrm{cn}\,(s|k^2)\hat{z}, \tag{1.18}$$

on the unit sphere. Furthermore, from the identity $\mathrm{sn}^2 s + \mathrm{cn}^2 s = 1$ we can unsure that $|\hat{r}| = 1\ \forall k$. In Fig. 1.5 we have plotted the Seiffert spherical spiral when s runs up

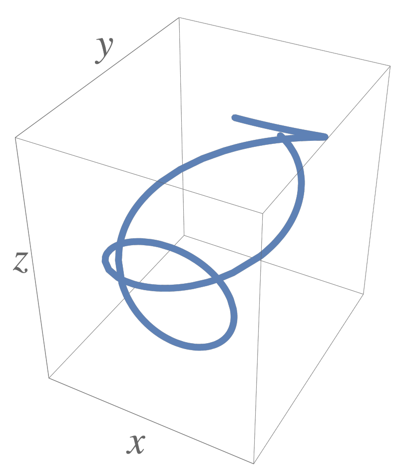

Figure 1.6: Parametric plot of the Seiffert spherical spiral for $k = 0.95$ from $s = 0$ to $s = 4K(k^2)$.

to different values. Note that, at each value $4nK$ with $(n = 1, 2, \dots)$, the orbit returns to the initial point at ρ_0 and z_0. The special case $k = 0$ reproduces the great circle ($\hat{r} = \sin s\hat{x} + \cos s\hat{z}$), which is generated bu the intersection of the (x, z) plane with the unit sphere. In Fig. 1.6 the full complex periodic nature of the Seiffert spiral orbit has been shown.

For the case of $k > 1$, one needs to apply the identities in Eqs. (1.15), yielding

$$\rho(s) = k^{-1}\mathrm{sn}\,(ks|k^{-2}), \tag{1.19a}$$

$$z(s) = \sqrt{1-\rho^2(s)} = \mathrm{dn}\,(ks|k^{-2}), \tag{1.19b}$$

and this means that the period of the Seiffert spiral is $4k^{-1}K(k^{-2})$.

1.2.2 The case of the planar pendulum

The motion of a planar pendulum is described by the differential equation (Whittaker & McCrae, 1988; Landau & Lifshitz, 1976)

$$\left(\frac{\mathrm{d}\phi}{\mathrm{d}\tau}\right)^2 = \frac{\epsilon}{2} - \sin^2\phi, \tag{1.20}$$

where 2ϕ, $\tau \equiv vt$, and $\epsilon \equiv \frac{E}{MgL}$ denote, respectively, the angular deviation of the pendulum from the vertical position, the dimensionless time, and the normalized energy of the pendulum, with M and L being the mass and the length of a pendulum that is subjected to the gravitational field g, and accordingly, its velocity is given by $v = \sqrt{\frac{g}{L}}$. This equation can be transformed to the Jacobi differential equation (1.6), by means of the change of variable $y(\tau) \doteq m^{-\frac{1}{2}}\sin\phi$ (considering $m = \frac{\epsilon}{2}$). This way, the solution to the planar pendulum (for $m < 1$) is obtained as

$$\phi(\tau) = \arcsin\left(m^{\frac{1}{2}}\mathrm{sn}\,(\tau|m)\right). \tag{1.21}$$

For the case of $\epsilon > 2$ (with $m < 1$) one can apply the identities (1.15) that yield

$$\phi(\tau) = \arcsin\left(\mathrm{sn}\,(m^{\frac{1}{2}}\tau|m^{-1})\right). \tag{1.22}$$

Note that, (1.21) corresponds to the *libration* motion, having the period $4m^{-\frac{1}{2}}K(m^{-1})$. When $m = 1$, the identities (1.9) give rise to the solution

$$\phi(\tau) = \arcsin\left(\tanh\tau\right), \tag{1.23}$$

which is given in terms of the singly periodic (hyperbolic) trigonometric functions with an imaginary period, and is known as the *separatrix* solution. The case of $\phi \to \frac{\pi}{2}$

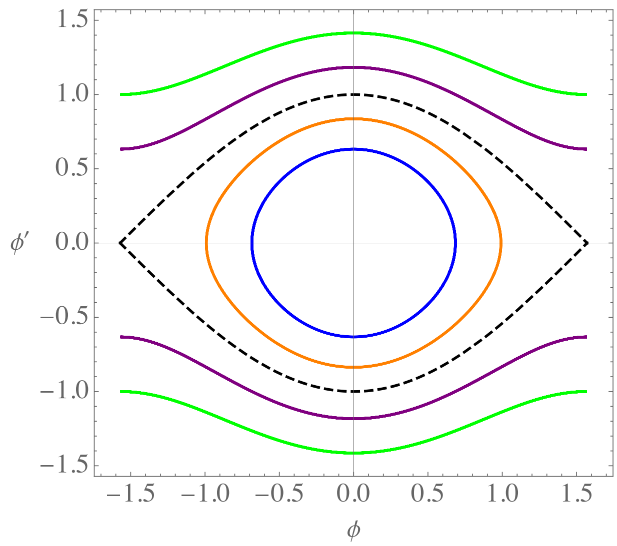

Figure 1.7: The phase portrait (ϕ' versus ϕ) for the planar pendulum. The bounded libration orbits given in Eq. (1.21) for $\epsilon < 2$ (inner curves) and the unbounded rotation orbits (1.22) for $\epsilon > 2$ (outer curves) are separated by the separatrix orbits (1.23) for $\epsilon = 2$ (dashed curves).

for this solution, corresponds $\tau \to \infty$, and therefore, the period of the pendulum on a separatrix motion is infinite. In Fig. 1.7, the phase portrait of pendulum for the above three kinds of orbits has been demonstrated. This portrait, shows the mutual behaviors of the ϕ and the ϕ' coordinates, where for $m < 1$ and applying the identities (1.9) and (1.10), we have

$$\phi' = \frac{m^{\frac{1}{2}}}{\sqrt{1 - m\mathrm{sn}^2\tau}}\mathrm{sn}'\tau = m^{\frac{1}{2}}\mathrm{cn}\,(\tau|m), \tag{1.24}$$

known as the libration angular velocity, whereas for $m > 1$ we get to the rotation angular velocity

$$\phi' = m^{\frac{1}{2}}\mathrm{dn}\,(m^{\frac{1}{2}}\tau|m^{-1}), \tag{1.25}$$

by means of the identities (1.15). As it is observed from Fig. 1.2, the rotational angular velocity (1.25) does not vanish and hence, the rotational orbits in the phase portrait have been generated with the angular velocities of both signs. The identities (1.11) imply that the angular velocity on the separatrix orbit (i.e. with $m = 1$ or $\epsilon = 2$) is $\phi' = \mathrm{sech}\,\tau$, meaning that the pendulum's angular velocity approaches, exponentially, to the zero as $\phi \to \frac{\pi}{2}$. Each orbit in the phase portrait corresponds to the initial conditions $\phi_0 = 0$ and $\phi'_0 = \pm\sqrt{\frac{\epsilon}{2}}$ (only one of the signs is chosen for the libration orbits) and is generated with $-2K\left(\frac{\epsilon}{2}\right) < \tau < 2K\left(\frac{\epsilon}{2}\right)$ (for the libration orbits with $\epsilon < 2$), or $-2\sqrt{\frac{2}{\epsilon}}K\left(\frac{2}{\epsilon}\right) < \tau < 2\sqrt{\frac{2}{\epsilon}}K\left(\frac{2}{\epsilon}\right)$ (for the rotation orbits with $\epsilon > 2$). Note that, the topology of the phase portrait for the planar pendulum is represented as a cylinder, since the condition $\phi = -\frac{\pi}{2}$ is physically equivalent to the case of $\phi = \frac{\pi}{2}$.

1.2.3 Force-free asymmetric top

The Euler equations for a force-free symmetric top can be considered as another physical example, assuming the moments of inertia $I_1 > I_2 > I_3$ (Landau & Lifshitz, 1976). These equations read as

$$I_1\dot{\omega}_1 = (I_2 - I_3)\omega_2\omega_3, \tag{1.26a}$$

$$I_2\dot{\omega}_2 = -(I_1 - I_3)\omega_1\omega_3, \tag{1.26b}$$

$$I_3\dot{\omega}_3 = (I_1 - I_2)\omega_1\omega_2, \tag{1.26c}$$

where the angular velocity $\boldsymbol{\omega} = \omega_1\hat{\mathbf{1}} + \omega_2\hat{\mathbf{2}} + \omega_3\hat{\mathbf{3}}$ can be decomposed in terms of its components along the principal axes of inertia. The conservation laws of the kinetic energy

$$\kappa = \frac{1}{2}\left(I_1\omega_1^2 + I_2\omega_2^2 + I_3\omega_3^2\right) \equiv \frac{1}{2}I_0\Omega_0^2, \tag{1.27}$$

and the squared angular momentum

$$\ell = I_1^2\omega_1^2 + I_2^2\omega_2^2 + I_3^2\omega_3^2 \equiv I_0^2\Omega_0^2, \tag{1.28}$$

are used to define the parameters $I_0 \equiv \frac{\ell^2}{2\kappa}$ and $\Omega_0 \equiv \frac{2\kappa}{\ell}$. These parameters can be used to introduce the definitions

$$\omega_1(\tau) = -\sqrt{\frac{I_0(I_0 - I_3)}{I_1(I_1 - I_3)}}\Omega_0\sqrt{1 - y^2(\tau)} \equiv -\Omega_1(I_0)\sqrt{1 - y^2(\tau)}, \tag{1.29}$$

$$\omega_2(\tau) = -\sqrt{\frac{I_0(I_0 - I_3)}{I_2(I_2 - I_3)}}\Omega_0 y(\tau) \equiv \Omega_2(I_0)y(\tau), \tag{1.30}$$

$$\omega_3(\tau) = -\sqrt{\frac{I_0(I_1 - I_0)}{I_3(I_1 - I_3)}}\Omega_0\sqrt{1 - my^2(\tau)} \equiv \Omega_3(I_0)\sqrt{1 - my^2(\tau)}, \tag{1.31}$$

where $\tau = \left[(I_1 - I_3)\frac{\Omega_1\Omega_3}{I_2\Omega_2}\right] t$ is the dimensionless time used in Eqs. (1.29)–(1.31), and the modulus m is defined as

$$m(I_0) = \frac{(I_0 - I_3)(I_1 - I_2)}{(I_2 - I_3)(I_1 - I_0)}. \tag{1.32}$$

Assuming the condition $m > 0$, the parameter $I_0 = \frac{\ell^2}{2\kappa}$ must satisfy $I_3 < I_0 < I_1$, and hence, we have $0 \le m(I_0) \le 1$ for $I_3 \le I_0 \le I_2$, and $m(I_0) < 1$ for $I_2 < I_0 < I_1$ (with

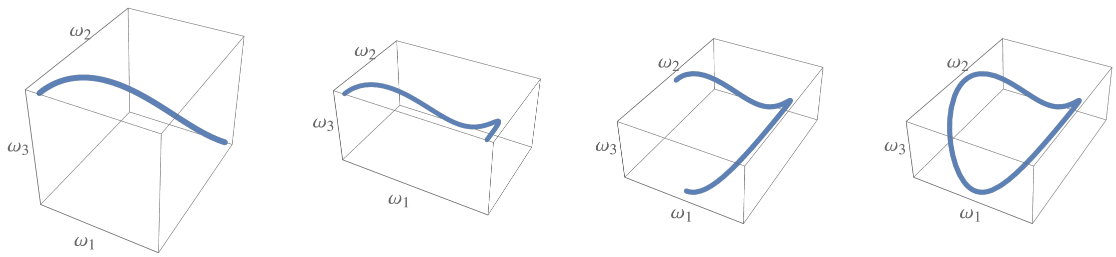

Figure 1.8: Parametric plots of $(\omega_1, \omega_2, \omega_3)$ for the asymmetric free top from $\tau = 0$ to (from left to right) $\tau = K(m), 2K(m), 3K(m), 4K(m)$.

$m \to \infty$ as $I_0 \to I_1$). Substitution of these expression in the Euler equations (1.26), assuming $\omega_2 \equiv \Omega_2 y(\tau)$, yields the dimensionless Jacobi differential equation (1.6), that can be now integrated, accordingly, for the initial conditions $(\omega_1(0), \omega_2(0), \omega_3(0)) = (-\Omega_1, 0, \Omega_3)$, giving (Landau & Lifshitz, 1976)

$$(\omega_1, \omega_2, \omega_3) = (-\Omega_1 \mathrm{cn}\, \tau, \Omega_2 \mathrm{sn}\, \tau, \Omega_3 \mathrm{dn}\, \tau)\,, \tag{1.33}$$

that provide the orbits in Fig. 1.8. This problem can be therefore solved in terms of the Jacobi elliptic functions $(\mathrm{sn}\,, \mathrm{cn}\,, \mathrm{dn}\,)$. Note that, the identity (1.10) can be used to show that the solution (1.33) maintains the constants of the motion (1.27) and (1.28). The case of separatrix solution (i.e. for $m = 1$), we have $I_0 = I_2$ that gives $\Omega_2 \equiv \Omega_0$. Therefore, this type of motion is described by the equations

$$\omega_1(\tau) = -\sqrt{\frac{I_2(I_2 - I_3)}{I_1(I_1 - I_3)}}\Omega_0 \mathrm{sech}\, \tau, \tag{1.34}$$

$$\omega_2(\tau) = \Omega_0 \tanh \tau, \tag{1.35}$$

$$\omega_3(\tau) = -\sqrt{\frac{I_2(I_1 - I_2)}{I_3(I_1 - I_3)}}\Omega_0 \mathrm{sech}\, \tau. \tag{1.36}$$

It is also important to note that the motion of a symmetric top (i.e. for $I_1 = I_2 \neq I_3$) corresponds to the limit $m \equiv 0$ (and $\Omega_2 = \Omega_1$). The Jacobian solution (1.33) for a symmetric top is therefore,

$$(\omega_1, \omega_2, \omega_3) = (-\Omega_1 \cos \tau, \Omega_2 \sin \tau, \Omega_3)\,, \tag{1.37}$$

with $\tau \equiv \left(1 - \frac{I_3}{I_1}\right) \Omega_3 t$ as the dimensionless time.

(g_3, Δ)	e_1	e_2	e_3	ω_1	$\omega_2 \equiv \omega_1 + \omega_3$	ω_3
$(-,-)$	$a - ib$	$a + ib$	$-2a < -1$	$\lvert\Omega'\rvert + \frac{i\Omega}{2}$	$\lvert\Omega'\rvert - \frac{i\Omega}{2}$	$-i\Omega$
$(-,+)$	$d > 0$	$c - d > 0$	$-c < 0$	$\lvert\omega'\rvert$	$-i\omega + \lvert\omega'\rvert$	$-i\omega$
$(+,+)$	$c > 0$	$d - c < 0$	$-d < 0$	ω	$\omega + \omega'$	ω'
$(+,-)$	$2a > 1$	$-a - ib$	$-a + ib$	Ω	$\frac{\Omega}{2} + \Omega'$	$-\frac{\Omega}{2} + \Omega'$

Table 1.1: Cubic roots (e_1, e_2, e_3) and half-periods $(\omega_1, \omega_2, \omega_3)$ for the $\wp$-Weierstraß elliptic function.

1.3 Weierstraß elliptic functions

The $\wp$-Weierstraß elliptic function $\wp(z+\gamma) \equiv \wp(z+\gamma; g_2, g_3)$ is defined as the solution to the differential equation

$$\begin{aligned} \left(\frac{dy}{dz}\right)^2 &= 4y^3 - g_2 y - g_3, \\ &\equiv 4(y-e_1)(y-e_2)(y-e_3), \end{aligned} \tag{1.38}$$

subject to the initial condition $y(0) = \wp(\gamma)$. Here, (e_1, e_2, e_3) denote the roots of the cubic polynomial $4y^3 - g_2 y - g_3$ (such that $e_1 + e_2 + e_3 = 0$), and the invariants g_2 and g_3 are defined in terms of the cubic roots as (Whittaker & Watson, 1996; Abramowitz & Stegun, 1964)

$$g_2 = -4(e_1 e_2 + e_2 e_3 + e_3 e_1) = 2\left(e_1^2 + e_2^2 + e_3^2\right), \tag{1.39a}$$

$$g_3 = 4 e_1 e_2 e_3. \tag{1.39b}$$

The application of $\wp$-Weierstraß elliptic functions are analyzed in terms of four different cases (Table 1.1) based on the signs of $(g_3, \Delta) = [(-,-), (-,+), (+,-), (+,+)]$ where $\Delta = g_2^3 - 27g_3^2$ in the modular discriminant. In Fig. 1.9, the $\wp$-Weierstraß function has been plotted for the case of $\Delta > 0$, demonstrating the two different periods 2ω and $2\omega'$ along the real and the imaginary axes, respectively. The corresponding half-periods are given by

$$\omega(g_2, g_3) = \int_{e_1}^{\infty} \frac{ds}{\sqrt{4s^3 - g_2 s - g_3}}, \tag{1.40a}$$

$$\omega'(g_2, g_3) = i \int_{-\infty}^{e_3} \frac{ds}{\sqrt{|4s^3 - g_2 s - g_3|}}. \tag{1.40b}$$

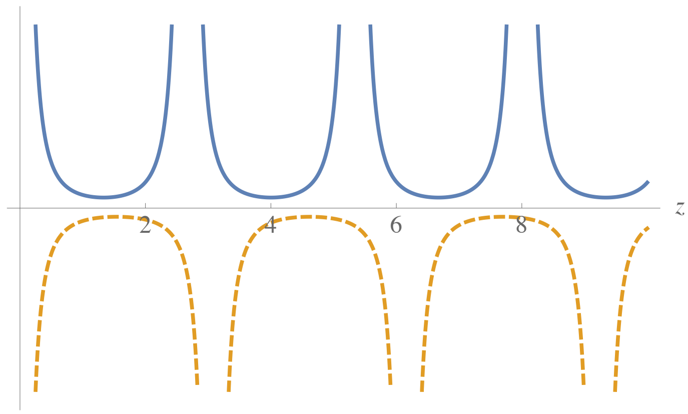

Figure 1.9: Plots of $\wp(z) > 0$ (solid lines) and $\wp(\mathrm{i}z) < 0$ (dashed lines) for $g_2 = 3$ and $g_3 = \frac{1}{2}$ (with $\Delta > 0$) showing the real period 2ω (upper graph) and the imaginary period $2\omega'$ (lower graph) defined, respectively, by Eqs. (1.40).

For the case of $\Delta < 0$, the function $\wp(z)$ has different periods 2Ω and $2\Omega'$ along the real and imaginary axes, respectively, with the half-periods Ω and Ω' defined as

$$\Omega(g_2, g_3) = \int_{e_1}^{\infty} \frac{\mathrm{d}s}{\sqrt{4s^3 - g_2 s - g_3}}, \tag{1.41a}$$

$$\Omega'(g_2, g_3) = \mathrm{i} \int_{-\infty}^{e_1} \frac{\mathrm{d}s}{\sqrt{|4s^3 - g_2 s - g_3|}}. \tag{1.41b}$$

The half-periods $\omega(g_2, g_3)$ and $\omega'(g_2, g_3)$, for the case of $\Delta > 0$, as well as $\Omega(g_2, g_3)$ and $\Omega'(g_2, g_3)$, for the case of $\Delta < 0$, have been plotted for specific cases of the invariants in Fig. 1.10. The cubic roots $e_i = (e_1, e_2, e_3)$ and their corresponding half-periods $\omega_i = (\omega_1, \omega_2, \omega_3)$ have been given in Table 1.1, that satisfy $\wp(\omega_i) \equiv e_i$ and $\wp(z + 2\omega_i) \equiv \wp(z)$, whereas for $i \neq j \neq k$, we have the identity (Whittaker & Watson, 1996)

$$\wp(z + \omega_i) = e_i + \frac{(e_i - e_j)(e_i - e_k)}{\wp(z) - e_i}, \tag{1.42}$$

so that $\wp(\omega_i + \omega_j) = e_k$. In Fig. 1.11, we have plotted the functions $\wp(z + \omega_2)$ and $\wp(z + \omega_3)$ for one complete period, in accordance with the Eq. (1.42). The singular behavior of this relation appears at $z = \omega_i$, which is also apparent in Fig. 1.9 for $i = 1 \neq j, k$. An additional property of the $\wp$-Weierstraß elliptic function is that it is of even parity, i.e. $\wp(-z) = \wp(z)$. Furthermore, under a change of sign $g_3 > 0 \to g_3 = -|g_3| < 0$ (with fixed g_2 and, hence, fixed discriminant Δ), the $\wp$-Weierstraß function satisfies the identity

$$\wp(z; g_2, g_3) \equiv -\wp(\mathrm{i}z; g - 2, |g_3|). \tag{1.43}$$

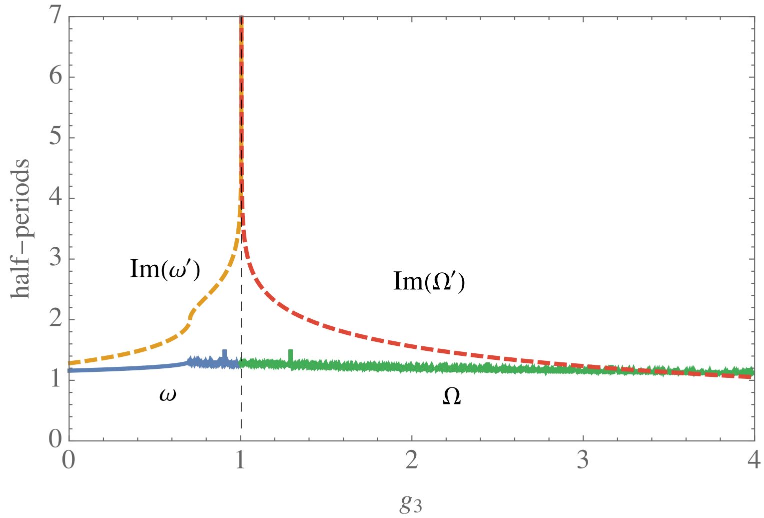

Figure 1.10: The plots of ω and $\mathrm{Im}(\omega')$ for $0 < g_3 < 1$ (Δ¿0), together with the plots of Ω and $\mathrm{Im}(\Omega')$ for $g_3 > 1$ (Δ¡0), considering $g_2 = 3$. The case of $g_3 \to 1$ corresponds to $\Delta \to 0$ and both of $\mathrm{Im}(\omega')$ and $\mathrm{Im}(\Omega')$ diverge, whereas $\Omega(g_2, 1) = \omega(g_2, 1)$. On the other hand, $\omega'(g_2, 0) = \mathrm{i}\omega(g_2, 0)$, and both of Ω and Ω' tend to zero as $g_3 \to \infty$.

The identity (1.43) (termed as the g_3-inversion identity), has been used in Table 1.1 in order to write the transformation

$$\begin{pmatrix} e_1^- \\ e_2^- \\ e_3^- \end{pmatrix} \equiv \begin{pmatrix} \wp\left(\omega_1^-; g_2, g_3\right) \\ \wp\left(\omega_2^-; g_2, g_3\right) \\ \wp\left(\omega_3^-; g_2, g_3\right) \end{pmatrix} \equiv - \begin{pmatrix} \wp\left(\mathrm{i}\omega_1^-; g_2, |g_3|\right) \\ \wp\left(\mathrm{i}\omega_2^-; g_2, |g_3|\right) \\ \wp\left(\mathrm{i}\omega_3^-; g_2, |g_3|\right) \end{pmatrix} \equiv - \begin{pmatrix} \wp\left(\omega_1^+; g_2, |g_3|\right) \\ \wp\left(\omega_2^+; g_2, |g_3|\right) \\ \wp\left(\omega_3^+; g_2, |g_3|\right) \end{pmatrix} \equiv - \begin{pmatrix} e_1^+ \\ e_2^+ \\ e_3^+ \end{pmatrix}, \tag{1.44}$$

abbreviated as $e_i^+(g_3 > 0) \to e_i^-(g_3 < 0)$ for the Weierstraß roots (for fixed g_2 and Δ), which makes use of

$$\left(\omega_1^-, \omega_2^-, \omega_3^-\right) \equiv \mathrm{i}\left(\omega_1^+, \omega_2^+, \omega_3^+\right). \tag{1.45}$$

The transformations (1.44) and (1.45) were previously introduced in order to present a uniform solution of the problem of a moving in a cubic potential in terms of the $\wp$-Weierstraß elliptic function for all values of energy and for all bounded an unbounded orbits. It is worth to note that, in contrast to the simple rectangular form of the fundamental period–parallelogram of the Jacobi elliptic functions, the fundamental period–parallelogram $(0, \omega_1, \omega_2 = \omega_1 + \omega_3)$ of the $\wp$-Weierstraß elliptic function, changes its shape depending on the signs of (g_3, Δ), according to the information in Table 1.1.

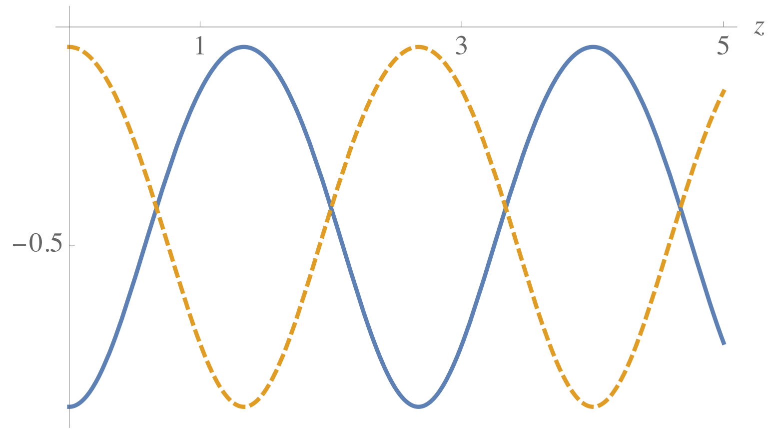

Figure 1.11: The functions $\wp(z+\omega_2)$ (solid curves) and $\wp(z+\omega_3)$ (dashed curves) for $g_2 = 3$ and $g_3 = \frac{1}{2}$ ($\Delta > 0$) plotted in the domain $0 \leq z \leq 2\omega_1$.

1.3.1 Planar pendulum

We reconsider the planar pendulum, as we discussed in Sect. 1.2 for the case of Jacobi elliptic functions. By writing $y = 2\sin^2\phi$ (for which $0 < y < 2$), we transform Eq. (1.20) into the cubic potential equation

$$(y')^2 = 2y(2-y)(\epsilon - y), \tag{1.46}$$

with turning points at $y = 0, 2$ and ϵ. Physical motion is possible only when the right side of Eq. (1.46) is positive. Hence, the motion is periodic between $y = 0$ and $y = \epsilon$ for $\epsilon < 2$, while the motion is periodic between $y = 0$ and $y = 2$ for $\epsilon > 2$. Note that, one can recover the standard $\wp$-Weierstraß differential equation (1.38), by setting

$$y(\tau) = 2\wp(\tau + \gamma) + \mu, \tag{1.47}$$

where $\mu \equiv \frac{1}{3}(\epsilon + 2)$ and the constant γ is determined from the initial condition $y(0)$. The Weierstraß invariants are

$$g_2 = 1 + 3(\mu - 1)^2, \tag{1.48a}$$

$$g_3 = \mu(\mu-1)(\mu-2), \tag{1.48b}$$

and the modular discriminant is $\Delta = \epsilon^2(2-\epsilon)^2 \geq 0$. The Weierstraß solution of the planar pendulum is discussed in terms of the four cases summarized in Table 1.2, where the root $-\frac{\mu}{2}$ corresponds to the turning point $y = 0$, the root $1 - \frac{\mu}{2}$ corresponds to the turning point $y = 2$, and the root $\mu - 1$ corresponds to the turning point $y = \epsilon$.

Case	(g_3,Δ)	ϵ	e_3	e_2	e_1	$\gamma=\omega_3$	Half-period ω_1	κ	m
(a)	$(+,+)$	$0<\epsilon<1$	$-\frac{\mu}{2}$	$\mu-1$	$1-\frac{\mu}{2}$	ω'	ω	1	$\frac{\epsilon}{2}$
(b)	$(-,+)$	$1<\epsilon<2$	$-\frac{\mu}{2}$	$\mu-1$	$1-\frac{\mu}{2}$	$-\mathrm{i}\omega$	$\lvert\omega'\rvert$	1	$\frac{\epsilon}{2}$
(c)	$(-,+)$	$2<\epsilon<4$	$-\frac{\mu}{2}$	$1-\frac{\mu}{2}$	$\mu-1$	$-\mathrm{i}\omega$	$\lvert\omega'\rvert$	$\sqrt{\frac{\epsilon}{2}}$	$\frac{2}{\epsilon}$
(d)	$(+,+)$	$4<\epsilon$	$-\frac{\mu}{2}$	$1-\frac{\mu}{2}$	$\mu-1$	ω'	ω	$\sqrt{\frac{\epsilon}{2}}$	$\frac{2}{\epsilon}$

Table 1.2: Weierstraß roots (e_1,e_2,e_3) and Jacobi parameters $\kappa=\sqrt{e_1-e_3}$, and $m=\frac{(e_2-e_3)}{(e_1-e_3)}$ for the planar pendulum problem.

Using the initial conditions $y(0)=0$ and $y'(0)=0$ (giving $\gamma\equiv\omega_3$ so that $\wp(\gamma)=e_3$), the Weierstraß solutions for cases (a) and (d) are expressed as

$$y(\tau)=2\wp(\tau+\omega')+\mu, \tag{1.49}$$

where $\omega_3=\omega'$ and the period of oscillations is $2\omega_1=2\omega$ (refer to the case of $(g_3,\Delta)=(+,+)$ in Table 1.1). For the cases (b) and (c), the Weierstraß solutions are expressed as

$$y(\tau)=2\wp(\tau-\mathrm{i}\omega)+\mu, \tag{1.50}$$

where $\omega_3=-\mathrm{i}\omega$ and the period of oscillations is $2\omega_1=2\omega$ (refer to the case of $(g_3,\Delta)=(-,+)$ in Table 1.1). As expected, when $\epsilon\to 2$ (i.e. when $\Delta\to 0$), the period $2|\omega'|$ approaches infinity as we approach the pendulum's separatrix (see Fig. 1.10). Each pair of cases (a)–(b) and (c)–(d) in Table 1.2, satisfies the transformations (1.44) and (1.45). For example, considering the case (a), we denote the initial angle as ϕ_0 (with $\phi_0'=0$), where $0<\phi_0<\frac{\pi}{4}$, so that $0<\epsilon=2\sin^2\phi_0<1$, while in case (b), we denote the initial angle as $\bar{\phi}_0$ (with $\bar{\phi}_0'=0$), where $\frac{\pi}{4}<\bar{\phi}_0<\frac{\pi}{2}$, so that $1<\bar{\epsilon}\equiv 2\sin^2\bar{\phi}_0<2$. Introducing the transformation

$$\begin{pmatrix}\phi_0\\ \epsilon\end{pmatrix}\to\begin{pmatrix}\bar{\phi}_0\\ \bar{\epsilon}\end{pmatrix}\equiv\begin{pmatrix}\frac{\pi}{2}-\phi_0\\ 2-\epsilon\end{pmatrix}, \tag{1.51}$$

which generates the g_3-inversion transformation $(g_2,g_3,\Delta)\to(\bar{g}_2,\bar{g}_3,\bar{\Delta})=(g_2,-g_3,\Delta)$ on the Weierstraß invariants for the planar pendulum. From the transformation (1.51) we obtain that $\mu\to\bar{\mu}=2-\mu$, and thus, $(e_1,e_2,e_3)\to(\bar{e}_1,\bar{e}_3,\bar{e}_3)=-(e_3,e_2,e_1)$, and $(\omega_1,\omega_2,\omega_3)\to(\bar{\omega}_1,\bar{\omega}_2,\bar{\omega}_3)=-\mathrm{i}(\omega_3,\omega_2,\omega_1)$, which is also inferred from the transformations (1.44) and (1.45). Furthermore, the solution $\bar{y}(\tau;\bar{\omega}_1)=$

$2\wp(\tau+\bar{\omega}_3;\bar{g}_2,\bar{g}_3)+\bar{\mu}$, having the half-period $\bar{\omega}_1=|\omega'|$, is expressed as

$$\begin{aligned}\bar{y}(\tau;\bar{\omega}_1) &= 2\wp(\tau-\mathrm{i}\omega_1;g_2,-g_3)+(2-\mu)\\ &= 2-[2\wp(\mathrm{i}\tau+\omega_1;g_2,g_3)+\mu]\\ &\equiv 2-y(\mathrm{i}\tau;-\mathrm{i}\omega_3),\end{aligned} \tag{1.52}$$

where the solution $y(\mathrm{i}\tau;-\mathrm{i}\omega_3)$, which has the real half-period $-\mathrm{i}\omega_3=|\omega'|$, is a function of the *imaginary* time $\mathrm{i}\tau$. Because the normalized time $\tau\equiv\left(\frac{g}{L}\right)^{\frac{1}{2}}t$ involves the gravitational acceleration g, we obtain an imaginary time if we invert gravity's direction (i.e. $g\to\bar{g}\equiv -g$), which results in $\tau\to\bar{\tau}\equiv\mathrm{i}\tau$ and $y(\mathrm{i}\tau;-\mathrm{i}\omega_3)\equiv y(\bar{\tau};|\omega'|)$. Therefore, the physical interpretation of the imaginary half-period ω' of the planar pendulum is that its magnitude $|\omega'|$ is the real half-period of the inverted planar pendulum (or pendulum with imaginary time) (Whittaker & McCrae, 1988). Note that, the solution of the planar pendulum in terms of the Jacobi elliptic function $\mathrm{sn}\,(z|m)$ and the $\wp$-Weierstraß elliptic function $\wp(z+\gamma)$, suggests a close connection between them (see appendix A.1). For example, we find the general solution for the planar pendulum for all values of normalized energy ϵ, as

$$2\wp(\tau+\omega_3)+\mu=2m\kappa^2\mathrm{sn}^2(\kappa\tau|m)=\left\{\begin{array}{cc}\epsilon\,\mathrm{sn}^2\left(\tau|\frac{\epsilon}{2}\right) & (\epsilon<2)\\ 2\,\mathrm{sn}^2\left(\sqrt{\frac{\epsilon}{2}}\tau|\frac{2}{\epsilon}\right) & (\epsilon>2)\end{array}\right., \tag{1.53}$$

where $\kappa=\sqrt{e_1-e_3}$ and $m=\frac{e_2-e_3}{e_1-e_3}$ (according to Table 1.2). In appendix A.2, we have shown that the Weierstraß half-periods ω and ω' are related to the Jacobian quarter-periods K and K' as $\omega\equiv K(m)$ and $\omega'\equiv\mathrm{i}K$.

1.3.2 Spherical pendulum

We set the spherical pendulum problem in the cylindrical coordinates (ρ,ϕ,z) (Whittaker & McCrae, 1988). The energy equation for a spherical pendulum of unit mass and unit length is

$$\epsilon v^2=\frac{1}{2}\left(\dot{\rho}^2+\rho^2\dot{\phi}^2+\dot{z}^2\right)+v^2z, \tag{1.54}$$

where, as before, ϵ is the normalized total energy ($v^2\equiv g$). By substituting $\rho(z)=\sqrt{1-z^2}$ (where $-1\le z\le 1$) and the angular momentum conservation law $\ell\equiv\frac{\rho^2\dot{\phi}}{v}$, we obtain the differential equation

$$\begin{aligned}(z')^2 &= 2(\epsilon-z)(1-z^2)-\ell^2\\ &\equiv 2(z-z_1)(z-z_2)(z-z_3),\end{aligned} \tag{1.55}$$

where $z'(\tau) \equiv v^{-1}\dot{z}$ and $z_1 + z_2 + z_3 = \epsilon$. Because the right side of Eq. (1.55) is negative at $z = \pm 1$, the greatest root $z_1 (> 1 < z_2 > z_3 > -1)$ of the cubic polynomial is nonphysical , since it corresponds to an imaginary cylindrical radius ρ. The periodic motion of the spherical pendulum is therefore bounded in the domain $z_3 < z < z_2$. The differential equation (1.55) can be transformed into the standard form (1.38), by setting $z(\tau) = 2\wp(\tau + \gamma) + \mu$, where $\mu = \frac{\epsilon}{3}$, the constant γ determined from the initial condition $z(0)$, and the invariant are $g_2 = 1 + 3\mu^2$ and $g_3 = \frac{\ell^2}{4} + \mu(\mu^2 - 1)$. If we choose the initial condition $z(0) = z_3 > -1$, then $\gamma = \omega_3 = \omega'$ and the solution of the spherical pendulum problem for the z (and ρ) coordinate is

$$z(\tau) = 2\wp(\tau + \omega_3) + \mu \equiv \sqrt{1 - \rho^2(\tau)}. \tag{1.56}$$

The motion is periodic with the half-period $\omega_1 = \omega$, so that, as expected, $z(\omega_1) = 2\wp(\omega_1 + \omega_2) + \mu = 2\wp(\omega_2) + \mu \equiv z_2 < 1$. Note that, the case of the planar pendulum is indeed a special case of the spherical pendulum, by letting $\ell = 0$, and adopting appropriate definitions for (z, ϵ, μ).

The solution for the azimuth angle $\phi(\tau)$ is obtained from the angular-momentum conservation law $\phi'(\tau) = \frac{\ell}{\rho^2(\tau)}$, which yields (Whittaker & McCrae, 1988)

$$\begin{aligned} \phi(\tau) &= \ell \int_0^\tau \frac{\mathrm{d}s}{1 - [2\wp(s + \omega_3) + \mu]^2} \\ &\equiv -\frac{\ell}{4} \int_0^\tau \frac{\mathrm{d}s}{[\wp(s + \omega_3) - \wp(\kappa)][\wp(s + \omega_3) - \wp(\lambda)]}, \end{aligned} \tag{1.57}$$

where we used the initial condition $\phi(0) = 0$ and the imaginary constants κ and λ are defined by the relation $\wp(\kappa) = -\frac{1}{2}(1 + \mu)$ and $\wp(\lambda) = \frac{1}{2}(1 - \mu)$, that correspond, respectively, to $z = -1 < z_3$ and $z = +1 > z_2$. For such constants we have $\wp'(\kappa) = \frac{\mathrm{i}\ell}{2} = \wp'(\lambda)$, which is obtained from the Weierstraß differential equation (1.38) for $z = \kappa$ and λ. These relations allow us to write (1.57) as

$$\phi(\tau) = \frac{\mathrm{i}}{2} \int_0^\tau \mathrm{d}s \left[\frac{\wp'(\lambda)}{\wp(s + \omega_3) - \wp(\lambda)} - \frac{\wp'(\kappa)}{\wp(s + \omega_3) - \wp(\kappa)} \right], \tag{1.58}$$

where we used the identity $\wp(\lambda) - \wp(\kappa) = 1$. Note that, in general, the differentiation of the $\wp$-Weierstraß function is defined as

$$\wp'(x) \equiv \frac{\mathrm{d}}{\mathrm{d}x}\wp(x) = -\sqrt{4\wp^3(x) - g_2\wp(x) - g_3}. \tag{1.59}$$

The integral (1.58) can be solved exactly in terms of the quasi-periodic functions ζ-Weierstraß ($\zeta(\tau)$) and σ-Weierstraß ($\sigma(\tau)$), which are associated with the $\wp$-Weierstraß elliptic function, by $\wp(\tau) = -\zeta'(\tau)$ and $\zeta(\tau) \equiv \frac{\sigma'(\tau)}{\sigma(\tau)}$. Therefore, by means of the relation (Byrd & Friedman, 1971; Whittaker & McCrae, 1988)

$$\begin{aligned}\frac{\wp'(\lambda)}{\wp(s)-\wp(\lambda)} &\equiv \zeta(s-\lambda)-\zeta(s+\lambda)+2\zeta(\lambda)\\ &= \frac{\mathrm{d}}{\mathrm{d}s}\ln\left(\frac{\sigma(s-\lambda)}{\sigma(s+\lambda)}\right)+2\zeta(\lambda),\end{aligned}\tag{1.60}$$

we find the standard solution for the azimuth motion of the pendulum, as

$$e^{2\mathrm{i}\phi(\tau)} = e^{2\tau[\zeta(\kappa)-\zeta(\lambda)]}\left[\left(\frac{\sigma(\tau+\omega_3+\lambda)\sigma(\omega_3-\lambda)}{\sigma(\omega_3+\lambda)\sigma(\tau+\omega_3-\lambda)}\right)\times\left(\frac{\sigma(\tau+\omega_3-\kappa)\sigma(\omega_3+\kappa)}{\sigma(\omega_3-\kappa)\sigma(\tau+\omega_3-\kappa)}\right)\right],\tag{1.61}$$

for which, it is readily verified that $\phi(0)=0$. Note that, Eq. (1.61) can be simplified further by recalling that since the condition $-1<z_3\le\wp(\tau+\omega_3)\le z_2<1$ holds for $\tau\in\mathbb{R}$, there must be the imaginary numbers $\mathrm{i}\alpha$ and $\mathrm{i}\beta$ ($\alpha,\beta\in\mathbb{R}$), such that $\kappa\equiv\omega_3+\mathrm{i}\alpha$ and $\lambda\equiv\omega_3+\mathrm{i}\beta$. Applying the above substitutions, one can recast Eq. (1.61) as

$$e^{2\mathrm{i}\phi(\tau)} = e^{2\tau[\zeta(\kappa)-\zeta(\lambda)]}\left[\left(\frac{\sigma(\tau+2\omega_3+\mathrm{i}\beta)\sigma(-\mathrm{i}\beta)}{\sigma(2\omega_3+\mathrm{i}\beta)\sigma(\tau-\mathrm{i}\beta)}\right)\times\left(\frac{\sigma(\tau-\mathrm{i}\alpha)\sigma(2\omega_3+\mathrm{i}\alpha)}{\sigma(-\mathrm{i}\alpha)\sigma(\tau+2\omega_3+\mathrm{i}\alpha)}\right)\right].\tag{1.62}$$

Making use of the identity $\sigma(\tau+2\omega_3)\equiv-\exp\left[2\eta_3(\tau+\omega_3)\right]\sigma(\tau)$ (Whittaker & Watson, 1996), where $\eta_3\equiv\zeta(\omega_3)$, we find that

$$\frac{\sigma(\tau+2\omega_3+\mathrm{i}\beta)}{\sigma(\tau-\mathrm{i}\beta)} = -e^{2\eta_3(\tau+\mathrm{i}\beta)}\frac{\sigma(\tau+\mathrm{i}\beta)}{\sigma(\tau-\mathrm{i}\beta)},\tag{1.63a}$$

$$\frac{\sigma(-\mathrm{i}\beta)}{\sigma(2\omega_3+\mathrm{i}\beta)} = -e^{-2\mathrm{i}\eta_3\beta}\frac{\sigma(-\mathrm{i}\beta)}{\sigma(\mathrm{i}\beta)} \equiv e^{-2\mathrm{i}\eta_3\beta},\tag{1.63b}$$

obtaining which, we used the fact that $\sigma(\tau)$ is an odd function of τ (i.e. $\sigma(-\mathrm{i}\beta)=-\sigma(\mathrm{i}\beta)$). We therefore obtain

$$e^{2\mathrm{i}\phi(\tau)} \equiv e^{2\tau[\zeta(\kappa)-\zeta(\lambda)]}\left[\frac{\sigma(\tau+\mathrm{i}\beta)\sigma(\tau-\mathrm{i}\alpha)}{\sigma(\tau-\mathrm{i}\beta)\sigma(\tau+\mathrm{i}\alpha)}\right].\tag{1.64}$$

Now since the ratio $\frac{\sigma(\tau+\mathrm{i}\beta)}{\sigma(\tau-\mathrm{i}\beta)}$ has a unit modulus for all $\tau\in\mathbb{R}$, we can then write

$$\begin{aligned}\ln\left(\frac{\sigma(\tau+\mathrm{i}\beta)}{(\sigma(\tau-\mathrm{i}\beta))}\right) &= \mathrm{i}\int_{-\beta}^{\beta}\zeta(\tau+\mathrm{i}s)\mathrm{d}s\\ &= 2\mathrm{i}\int_{0}^{\beta}\mathrm{Re}\left[\zeta(\tau+\mathrm{i}s)\right]\mathrm{d}s.\end{aligned}\tag{1.65}$$

Therefore, the solution (1.62) for the azimuth angle $\phi(\tau)$ can be recast in the form

$$\begin{aligned}\phi(\tau) &= \mathrm{i}\tau\left[\zeta(\omega_3+\mathrm{i}\beta)-\zeta(\omega_3+\mathrm{i}\alpha)\right]+\int_{\alpha}^{\beta}\mathrm{Re}\left[\zeta(\tau+\mathrm{i}s)\right]\mathrm{d}s\\ &\equiv \mathrm{Re}\left[\int_{\alpha}^{\beta}\left[\zeta(\tau+\mathrm{i}s)+\tau\wp(\omega_3+\mathrm{i}s)\right]\mathrm{d}s\right],\end{aligned}\tag{1.66}$$

which is expressed in terms of the quasi-periodic function $\zeta(\tau)$ and $\wp(\tau) = -\zeta'(\tau)$. After a full period $2\omega_1$, when the (ρ, z) coordinates return to their initial values, the azimuth angle is changed by an amount $\Delta\phi \equiv \phi(\tau + 2\omega_1) - \phi(\tau)$, which is expressed as

$$\Delta\phi = 2\omega_1 \int_\alpha^\beta \wp(\omega_3 + \mathrm{i}s)\mathrm{d}s + 2\eta_1(\beta - \alpha), \tag{1.67}$$

to obtain which, we have used the identity $\zeta(\tau + 2\omega_1 + \mathrm{i}s) = \zeta(\tau + \mathrm{i}s) + 2\eta_1$ where $\eta_1 \equiv \zeta(\omega_1)$ (Whittaker & Watson, 1996). The problem of the spherical pendulum in cylindrical coordinates, can be therefore solved by Eqs. (1.56) and (1.66), in terms of the $\wp$-Weierstraß $\wp(\tau + \gamma)$ and the ζ-Weierstraß $\zeta(\tau)$ elliptic functions.

1.3.3 Heavy symmetric top with one fixed point

As the last example, we take care of the motion of a symmetric top $(I_1 = I_2 \neq I_3)$ with one fixed point described in terms of the energy equation

$$E = \frac{1}{2}\left[I_1\dot{\theta}^2 + I_3\varpi_3^2 + \frac{(p_\phi - p_\psi\cos\theta)^2}{I_1\sin^2\theta}\right] + Mgh\cos\theta, \tag{1.68}$$

with E and φ_3 denote, respectively, the total energy of the symmetric top and the constant component of the angular velocity of a mass M with the principal moments of inertia $I_1 = I_2 \neq I_3$. Furthermore, p_ϕ and p_ψ are the angular momenta associated with the negligible Euler angles ϕ and ψ. Defining $\epsilon \doteq \frac{E - \frac{1}{2}\varpi_3^2}{Mgh}$ and $(a, b) \doteq \left(\frac{p_\phi}{I_1 v}, \frac{p_\psi}{I_1 v}\right)$ with $v^2 = \frac{Mgh}{2I_1}$, the differential equation for $u = \cos\theta$ is obtained from Eq. (1.68) as

$$\begin{aligned} \left(u'\right)^2 &= 4\left(1 - u^2\right)(\epsilon - u) - (a - bu)^2 \\ &\equiv 4(u - u_1)(u - u_2)(u - u_3), \end{aligned} \tag{1.69}$$

where prime denotes differentiation with respect to the dimensionless time $\tau = vt$, and $u_3 < u_2 < u_1$ are the roots of the cubic polynomial on the right had side (r.h.s.) of the equation, that because of its negativity at $u = \pm 1$, it is inferred that $-1 < u_3 < u_2 < 1$ and $u_1 > 1$ (which is a nonphysical solution for $u = \cos\theta$). The physical motion is, therefore, periodic in θ and is bounded between $u_3 \equiv \cos\theta_3$ and $u_2 \equiv \cos\theta_2$ (implying $\theta_2 < \theta(\tau) < \theta_3$). Noe applying the change of variable $u \doteq \wp + \mu$ where $\mu = \frac{1}{12}(4\epsilon + b^2)$, the differential equation (1.69) changes its form to the standard differential equation (1.38) for the $\wp$-Weierstraß elliptic function, for which

$$g_2 = 2(2 - ab + 6\mu^2), \tag{1.70a}$$

$$g_3 = (a^2 + b^2) + 2\mu(4\mu^2 - 4 - ab), \tag{1.70b}$$

and $\Delta \equiv \Delta(\epsilon, a, b)$ for this particular problem. The solution is, therefore, expressed in terms of the $\wp$-Weierstraß elliptic function as

$$u(\tau) \equiv \cos\theta(\tau) = \wp(\tau + \gamma) + \mu, \tag{1.71}$$

where γ is determined from the initial condition $\theta(0)$. For the case of $-1 < u_3 = e_3 + \mu < u_2 = e_2 + \mu < 1$, we choose $u(0) = e_3 + \mu = u_3$ (which means that $-1 - \mu < e_3 < 1 - \mu$), so that $\gamma = \omega'$. Accordingly, at the half-period $\tau = \omega$, we find that, as expected, $u(\omega) = \wp(\omega + \omega') + \mu = e_2 + \mu = u_2$. The solution in Eq. (1.71) for $\theta(\tau)$ can be used to integrate the differential equations for the remaining Euler angles. We have

$$\begin{aligned} \phi'(\tau) &= \frac{a - b\cos\theta(\tau)}{1 - \cos^2\theta(\tau)} \\ &\equiv \frac{\mathrm{i}}{2}\left[\frac{\wp'(\kappa)}{\wp(\tau+\omega_3) - \wp(\kappa)} - \frac{\wp'(\lambda)}{\wp(\tau+\omega_3) - \wp(\lambda)}\right], \end{aligned} \tag{1.72}$$

$$\begin{aligned} \chi'(\tau) &= \frac{b - a\cos\theta(\tau)}{1 - \cos^2\theta(\tau)} \\ &\equiv \frac{\mathrm{i}}{2}\left[\frac{\wp'(-\kappa)}{\wp(\tau+\omega_3) - \wp(-\kappa)} - \frac{\wp'(\lambda)}{\wp(\tau+\omega_3) - \wp(\lambda)}\right], \end{aligned} \tag{1.73}$$

to obtain which, we have defined $\psi' \equiv \left(\frac{\omega_3}{v} - b\right) + \chi'$, where $\wp(\kappa) = 1 - \mu$ and $\wp(\lambda) = -(1+\mu)$, with $\wp'(\kappa) = \mathrm{i}(a-b)$ and $\wp'(\lambda) = \mathrm{i}(a+b)$. Note that, the sign of ϕ' in Eq. (1.72) depends on the sign of $a - b\cos\theta_2 < a - b\cos\theta < a - b\cos\theta_3$. If $a > b\cos\theta_2$ (or $a < b\cos\theta_3$), then ϕ' does not change its sign as θ bounces between θ_2 and θ_3 and the motion in ϕ involves monotonic azimuth precession. If $a = b\cos\theta_2$ (or $a = b\cos\theta_3$), ϕ' vanishes at $\theta = \theta_2$ (or $\theta = \theta_3$) and the motion in ϕ exhibits a cusp at that angle (since both θ' and ϕ' vanish). If $a < b\cos\theta_2$, then ϕ' vanishes at an angle $\theta_2 < \theta_0 < \theta_3$ and the motion in ϕ exhibits retrograde motion between $\theta_0 < \theta < \theta_3$. Note that, since the Eqs. (1.72) and (1.58) are the same, the solution to Eq. (1.72) is the same as that of Eq. (1.66) (even if the constants κ and λ are different). This same solution can also be applied to the solution in Eq. (1.73), if the transformation $(a, b) \to (b, a)$ is applied to Eq. (1.72), and also by taking into account that $\wp(\tau)$ is of even parity, whereas $\wp'(\tau)$ is of odd parity.

1.4 Some further physical applications of elliptic functions

Beside the more generalized appellations of elliptic functions in classical Hamiltonian dynamics in the context of Newtonian mechanics, these functions have appeared to be of rigorous applications in the analysis of light and particle trajectories in spacetimes inferred from general relativity and extended theories of gravity. Further in this thesis, this will be dealt with extensively. However, for now, and before closing this chapter, let us discuss as the last example, the exact solutions of the Korteweg–de Vries (KdV) equation (Gratton & Delellis, 1989)

$$\partial_t u + u\partial_x u + \partial_{x,x,x} u = 0, \tag{1.74}$$

which describes the nonlinear evolution of the field $u(x,t)$. This nonlinear equation appears in many areas of physics and is a member of an important class of nonlinear partial differential equations that possesses soliton solutions (Giambó et al., 1984; Gardner et al., 1967; Olver, 1986; Degasperis, 1998). In fact, a travelling-wave solution of the KdV equation (1.74) is a function of the form $u(x,t) = v(\xi)$, where $\xi = \kappa(x - ct)$ denotes the wave phase (with constants κ and c that need to be determined). Substituting this travelling solution into the KdV equation, we obtain an ordinary differential equation for $v(\xi)$ as

$$(v - c)v' + \kappa^2 v''' = 0, \tag{1.75}$$

which can be integrated with respect to ξ to yield

$$\kappa^2 v'' = \alpha + cv - \frac{1}{2}v^2, \tag{1.76}$$

where α is a constant of integration. Multiplying Eq. (1.76) by v' and then, integrating again with respect to ξ, we obtain

$$\frac{\kappa^2}{2}(v')^2 = (\alpha v + \beta) + \frac{c}{2}v^2 - \frac{1}{6}v^3, \tag{1.77}$$

where β is the second constant of integration. One can now see immediately that $v(\xi) \equiv A\wp(\xi) + B$, which can be expressed in terms of the elliptic functions (where $A \equiv -12\kappa^2$ and $B \equiv c$), because the r.h.s. of Eq. (1.77) involves a cubic polynomial in v. The travelling-wave solution of the KdV equation is then

$$u(x,t) = A\wp\left(\kappa(x - ct) + \gamma\right) + B, \tag{1.78}$$

where the constant γ is determined from the initial condition $u(x,0) = u_0(x)$. Using the relation between the Weierstraß and Jacobi elliptic functions (as described on appendix A.1), the travelling-wave solution to the KdV equation may be also expressed as (Olver, 1986; Cervero, 1986)

$$u(x,t) = a\mathrm{cn}^2\left[\kappa(x-ct)+\gamma|m\right]+b \tag{1.79}$$

where $m = \sqrt{\frac{r_3-r_2}{r_3-r_1}}$, $a = r_3 - r_2$, $b = r_2$, and $\kappa = \sqrt{\frac{1}{6}(r_3-r_1)}$. Note that, here $r_1 < r_2 < r_3$ are the roots of the cubic polynomial on the r.h.s. of Eq. (1.77). This second representation is known as the *periodic cnoidal-wave solution* to the KdV equation. Note that, for he special case of $\alpha = 0 = \beta$ in Eq. (1.77), for which $r_3 = 3c$ and $r_1 = 0 = r_2$, we then find $m = 1$, $a = 3c$, $b = 0$ and $\kappa = \sqrt{\frac{c}{2}}$. In this case, the travelling-wave solution becomes

$$u(x,t) = 3c\,\mathrm{sech}^2\left[\sqrt{\frac{c}{2}}(x-ct)\right], \tag{1.80}$$

that describes the well-known localized soliton solution of the KdV equation.

1.5 Summary

The review given in this chapter, highlights some basic properties of the elliptic functions, especially the Weierstraß elliptic functions. The more specific applications of these functions, requires particular treatments of the elliptic integrals of the first, second and third kinds which depending on the physical problem in hand, can be expressed in terms of the elliptic integrals, themselves, or in terms of the Jacobi or Weierstraß elliptic functions. This latter is widely used in this thesis and as we go further into particular relativistic problems that include analytical treatments of particle geodesics in curved spacetimes, appropriate methods of treatments of complicated integrals are presented in details, and the ways they are simplified to known elliptic functions are discussed extensively. We therefore close this chapter at this point, and begin the discoveries of this thesis, after a short chapter on Hamiltonian dynamics and geodesic equations.

CHAPTER 2

The Lagrangian and Hamiltonian dynamics and the calculation of geodesics in black hole spacetimes

In this chapter, some well-known notions on the Hamilton-Jacobi equation, Lagrangian dynamics and Euler-Lagrange equation are restated. This latter is of extensive use in classical mechanics, and therefore, can be regarded as an alternative approach in the derivation of geodesic equations. In the forthcoming sections, we recall some basic methods of variations in the derivation of the Euler-Lagrange equation and we state the mathematical way in the derivation of the geodesic equations as available in the Riemannian geometry. The application of this latter in the Schwarzschild black hole (SBH) spacetime is discussed as well. We close this chapter by discussing the method of separation of variables in the Hamilton-Jacobi equation which leads to the introduction of the Carter's constant. This is of crucial importance in the investigation of geodesics in stationary black hole spacetimes.

2.1 Lagrange's equation of motion

Based on the Hamilton's principle, the motion of a system from time t_1 to time t_2 is such that the action

$$I = \int_{t_1}^{t_2} \mathscr{L} \mathrm{d}t, \tag{2.1}$$

with $\mathscr{L}$ termed as the Lagrangian of the system[1], has a stationary value along the actual path of the motion. This means that, out of all possible paths, by which, the system point could travel from its position at time t_1 to its position at time t_2, it will actually travel along the path, for which, the value of the integral (2.1) is stationary, i.e. the value of I along the given path has the same value to within first-order infinitesimals as that along all neighboring paths. In the mathematical language, this is asserted as the vanishing variation of I, or (Landau & Lifschits, 1975)

$$\delta I = \delta \int_{t_1}^{t_2} \mathscr{L}\left(q_1, \ldots, q_n, \dot{q}_1, \ldots, \dot{q}_n, t\right) = 0, \tag{2.2}$$

where q_i $(i = 1, \ldots, n)$ are the generalized coordinated and $\dot{q}_i \equiv \frac{\mathrm{d}q_i}{\mathrm{d}t}$. In the case that we can can deduce the state of the system by knowing only information about the change of positions of the components of the system over time (i.e. the system constraints are holonomic), the Hamilton's principle is then both a necessary and sufficient condition for the Lagrange's equations. We therefore proceed with deriving the Lagrange's equations of motion, applying the Hamilton's principle.

To elaborate this, let us consider a function $f(y_i, \dot{y}_i)$, where $y_i \equiv y_i(x)$, with x assumed as being the parameter, and $\dot{y}_i \equiv \frac{\mathrm{d}y_i}{\mathrm{d}x}$. Then, a variation of the integral J

$$\delta J = \delta \int_1^2 f\left(y_1(x), \ldots, \dot{y}_1(x), \ldots, x\right) \mathrm{d}x, \tag{2.3}$$

is obtained by expanding each of the curves $y_i(x;\alpha)$ with α being the label of the curves, in the form (Goldstein et al., 2011)

$$\begin{array}{rcccl} y_1(x;\alpha) & = & y_1(x;0) & + & \alpha\eta_1(x), \\ y_2(x;\alpha) & = & y_2(x;0) & + & \alpha\eta_2(x), \\ \vdots & & \vdots & & \vdots \end{array} \tag{2.4}$$

where $y_i(x;0)$ are solutions to the extremum problem, and $\eta_i(x)$ are independent functions of x that vanish at the end points and are continuous through the second deriva-

[1] In Newtonian mechanics, this quantity is defined as $\mathscr{L} = T - V$, where T and V are, respectively, the kinetic and potential energies of a body in a closed dynamical system.

tive, but otherwise are completely arbitrary. Now, varying J in terms of α yields

$$\frac{\partial J}{\partial \alpha}\mathrm{d}\alpha = \int_1^2 \sum_i \left(\frac{\partial f}{\partial y_i}\frac{\partial y_i}{\partial \alpha}\mathrm{d}\alpha + \frac{\partial f}{\partial \dot{y}_i}\frac{\partial \dot{y}_i}{\partial \alpha}\mathrm{d}\alpha \right) \mathrm{d}x. \tag{2.5}$$

Integrating, by parts, the second term in the right hand side (r.h.s.) of Eq. (2.5) yields

$$\int_1^2 \frac{\delta f}{\partial \dot{y}_i}\frac{\partial^2 y_i}{\partial \alpha \partial x}\mathrm{d}x = \frac{\partial f}{\partial \dot{y}_i}\frac{\partial y_i}{\partial \alpha}\bigg|_1^2 - \int_1^2 \frac{\partial y_i}{\partial \alpha}\frac{\mathrm{d}}{\mathrm{d}x}\left(\frac{\partial f}{\partial \dot{y}_i}\right)\mathrm{d}x. \tag{2.6}$$

The first term in the r.h.s. of the above equation vanishes, since all the curves pass through the fixed end points. Now, substituting Eq. (2.6) in Eq. (2.5) results in

$$\delta J = \int_1^2 \sum_i \left(\frac{\partial f}{\partial y_i} - \frac{\mathrm{d}}{\mathrm{d}x}\frac{\partial f}{\partial \dot{y}_i} \right) \delta y_i \mathrm{d}x, \tag{2.7}$$

where once can infer the relation

$$\delta y_i = \left(\frac{\partial y_i}{\partial \alpha} \right)_0 \mathrm{d}\alpha, \tag{2.8}$$

for the variation δy_i, where the subscript 0 indicates infinitesimal departure of the varied path from the correct path. Note that, since the y variables are independent, the variations δy_i will be independent, as well. Once can, therefore, extend the condition $\delta J = 0$ (the Hamilton's principle) to the following condition:

$$\frac{\partial f}{\partial y_i} - \frac{\mathrm{d}}{\mathrm{d}x}\frac{\partial f}{\partial \dot{y}_i} = 0, \tag{2.9}$$

with $i = 1, 2, \ldots, n$, which is known as the Euler-Lagrange differential equation. Solutions to this equation represent the curves, for which, the variation of an integral of the form given in Eq. (2.2) vanishes.

Now, replacing $y_i \to q_i$ and $x \to t$, and consequently, $f(y_i, \dot{y}_i, x) \to \mathscr{L}(q_i, \dot{q}_i, t)$, the Hamilton's principle integral (2.1) can be recast as

$$I = \int_1^2 \mathscr{L}(q_i, \dot{q}_i, t)\mathrm{d}t. \tag{2.10}$$

The Euler-Lagrange equation is therefore transforms to the Lagrange's equation of motion

$$\frac{\mathrm{d}}{\mathrm{d}t}\frac{\partial \mathscr{L}}{\partial \dot{q}_i} - \frac{\partial \mathscr{L}}{\partial q_i} = 0, \tag{2.11}$$

with $i = 1, 2, \ldots, n$.

2.1.1 From Lagrangian to Hamiltonian in the language of differential forms

Here, we bring a brief geometrical description of Hamiltonian dynamics, in the context of manifold theory. In the forthcoming chapters, these notions are approached, once again. This subsection is generally based on the outstanding books by T. Frankel, M. Nakahara, and S. Hassani (Frankel, 2011; Hassani, 2013; Nakahara, 2018).

Hamiltonian mechanics takes place in the phase space of a system. The phase space is derived from the configuration space as follows. The generalized coordinates q_i $(i = 1, \dots, n)$ of a mechanical system, describe an n-dimensional manifold N. The dynamics of the system is described by the time-dependent Lagrangian $\mathscr{L}$, which is a function of $(q^i, \dot{q}^i)$. But $\dot{q}^i \equiv \frac{\mathrm{d}q^i}{\mathrm{d}t}$ are the components of a vector at $(q_1, \dots, q_n)$. Therefore, in the language of manifold theory, a Lagrangian is a function on the tangent bundle of the manifold, $T(N)$. In other words $\mathscr{L} : T(N) \to \mathbb{R}$. On the other hand, the Hamiltonian $\mathscr{H}$ is obtained from the Lagrangian by a Legendre transformation, i.e. $\mathscr{H} = \sum_{i=1}^{n} p_i \dot{q}^i - \mathscr{L}$, where p_i are the components of the momentum covector $(p_1, \dots, p_n)$. The first term can be thought of as the pairing of an element of the tangent space (i.e. $\dot{q}^i$) with its dual (i.e. p_i). In fact, for a point P at the coordinates $(q_1, \dots, q_n)$, we have then $\dot{\boldsymbol{q}} \equiv \dot{q}^i \partial_i \in \mathcal{T}_P(N)$, in which $\mathcal{T}_P(N)$ is the tangent space of manifold N at point P. Hence, if we pair this with the dual vector (covector) $p_j \mathrm{d}x^j \in \mathcal{T}_P^*(N)$, with $\mathcal{T}_P^*(N)$ being the cotangent space of manifold N at point P, we then obtain the first term in the definition of the Hamiltonian. The effect of the Legendre transformation is to replace $\dot{q}^i$ by p_i as the second set of independent variables. This way, we replace $T(N)$ with $T^*(N)$, where $T^*(N)$ is the cotangent bundle of manifold N. Accordingly, the manifold of Hamiltonian dynamics (or the phase space) is $T^*(N)$ with the coordinates (q^i, p_i), on which, the Hamiltonian $\mathscr{H} : T^*(N) \to \mathbb{R}$ is defined.

In fact, $T^*(N)$ is $2n$-dimensional, and is, therefore, a symplectic manifold. Indeed, it can be shown that the 2-form

$$\boldsymbol{\omega} \equiv \sum_{i=1}^{n} \mathrm{d}q^i \wedge \mathrm{d}p_i, \tag{2.12}$$

is non-degenerate, and is therefore, a symplectic 2-form on $T^*(N)$. The phase space, equipped with a symplectic form, turns into a geometric arena, in which, Hamiltonian mechanics unfolds. As described above, a Hamiltonian is a function on the phase space. In general, for the symplectic manifold $(M, \boldsymbol{\omega})$, the Hamiltonian is a real-valued function, i.e. $\mathscr{H} : M \to \mathbb{R}$. Now, given this Hamiltonian, one can define a vector field by taking into account the fact that $\mathrm{d}\mathscr{H} \in T^*(M)$. Since the manifold is symplectic, we can consider a natural isomorphism $\boldsymbol{\omega}^\sharp$ between $T^*(M)$ and $T(M)$. This way, there will be a unique vector field $\boldsymbol{X}_{\mathscr{H}}$ associated with $\mathrm{d}\mathscr{H}$, such that $\boldsymbol{X}_{\mathscr{H}} \equiv \boldsymbol{\omega}^\sharp(\mathrm{d}\mathscr{H}) \equiv (\mathrm{d}\mathscr{H})^\sharp$, that is called the *Hamiltonian vector field with the energy function* $\mathscr{H}$. One can then define a *Hamiltonian system* by the triplet $(M, \boldsymbol{\omega}, \boldsymbol{X}_{\mathscr{H}})$. Note that, the vector field $\boldsymbol{X}_{\mathscr{H}}$ is the generator of the integral curve, which is the evolution path of the system in the phase space. In other words, for $(q^1, \ldots, q^n, p_1, \ldots, p_n)$ as the canonical coordinates for $\boldsymbol{\omega}$, we have that

$$\boldsymbol{X}_{\mathscr{H}} = \frac{\partial \mathscr{H}}{\partial p_i}\frac{\partial}{\partial x^i} - \frac{\partial \mathscr{H}}{\partial q^i}\frac{\partial}{\partial p_i} \equiv \left(\frac{\partial \mathscr{H}}{\partial p_i}, -\frac{\partial \mathscr{H}}{\partial q^i}\right). \tag{2.13}$$

In fact, one can write

$$\mathrm{d}\mathscr{H} = \frac{\partial \mathscr{H}}{\partial q^i}\mathrm{d}q^i + \frac{\partial \mathscr{H}}{\partial p_i}\mathrm{d}p_i. \tag{2.14}$$

For the case of a stationary Hamiltonian (i.e. $\frac{\mathrm{d}\mathscr{H}}{\mathrm{d}t} = 0$), it is then followed that

$$\frac{\partial q^i}{\partial t} = \frac{\partial \mathscr{H}}{\partial p_i}, \tag{2.15a}$$

$$\frac{\partial p_i}{\partial t} = -\frac{\partial \mathscr{H}}{\partial q^i}, \tag{2.15b}$$

for $i = 1, \ldots, n$, which are called the Hamilton's equations. This way, $(q(t), p(t))$ will be an integral curve of $\boldsymbol{X}_{\mathscr{H}}$, if the above equations hold.

2.1.2 Derivation of the geodesic equation from the Lagrange's equation of motion

The geodesic equations, describe the path of a freely-falling object in purely gravitational force field. These equations are intended to give the path, on which, the principle of least action (the less used energy) is respected. In section 2.1, this principle led to the Lagrange's equation (2.11), and here, we argue that this equation reproduces the geodesic equations, as known in the Riemannian geometry.

Considering the Riemannian manifold $(M, \boldsymbol{g})$ with $g_{\mu\nu}$ being its associated metric, we define the Lagrangian

$$\mathscr{L} = \frac{1}{2} g_{\mu\nu}\dot{x}^\mu \dot{x}^\nu, \tag{2.16}$$

for a particle at the coordinates $x^\mu(\tau)$ moving in a vacuum, where $\dot{x}^\mu \equiv \frac{\mathrm{d}x}{\mathrm{d}\tau}$ with τ being the trajectory parametrization, and throughout this thesis, is regarded as the particle's proper time. Now to apply Eq. (2.11), we first consider the second term of its r.h.s., that yields

$$\frac{\partial \mathscr{L}}{\partial x^{\lambda}} = \frac{1}{2} g_{\mu\nu,\lambda} \dot{x}^{\mu} \dot{x}^{\mu}, \tag{2.17}$$

since $x^{\mu} \equiv x^{\mu}(\tau)$ and here we have defined $g_{\mu\nu,\lambda} \equiv \frac{\partial g_{\mu\nu}}{\partial x^{\lambda}}$. The first term of the r.h.s. of Eq. (2.11) includes

$$\frac{\partial \mathscr{L}}{\partial \dot{x}^{\lambda}} = \frac{1}{2} g_{\mu\nu} \left[\delta^{\mu}_{\lambda} \dot{x}^{\nu} + \delta^{\nu}_{\lambda} \dot{x}^{\mu}\right] = \frac{1}{2} g_{\mu\nu} \left[2\delta^{\nu}_{\lambda} \dot{x}^{\mu}\right] = g_{\mu\lambda} \dot{x}^{\mu}, \tag{2.18}$$

since $\boldsymbol{g} \equiv \boldsymbol{g}(\boldsymbol{x}(\tau))$, and δ^{μ}_{λ} is the Kronecker delta. Now, a parametric differentiation of the above equation results in

$$\frac{\mathrm{d}}{\mathrm{d}\tau} \frac{\partial \mathscr{L}}{\partial \dot{x}^{\lambda}} = \frac{\mathrm{d}}{\mathrm{d}\tau} \left[g_{\mu\lambda} \dot{x}^{\mu}\right] = g_{\mu\lambda,\nu} \dot{x}^{\nu} \dot{x}^{\mu} + g_{\mu\lambda} \ddot{x}^{\mu} = \frac{1}{2} g_{\mu\lambda,\nu} \dot{x}^{\nu} \dot{x}^{\mu} + \frac{1}{2} g_{\nu\lambda,\mu} \dot{x}^{\nu} \dot{x}^{\mu} + g_{\mu\lambda} \ddot{x}^{\mu}. \tag{2.19}$$

Now, considering the results in Eqs. (2.17) and (2.19), in the Lagrange's equation (2.11), we get

$$g_{\mu\lambda} \ddot{x}^{\mu} + \Gamma_{\lambda,\mu\nu} \dot{x}^{\mu} \dot{x}^{\nu} = 0, \tag{2.20}$$

where we have used the definition

$$\Gamma_{\lambda\mu\nu} = \frac{1}{2} \left[g_{\mu\lambda,\nu} + g_{\nu\lambda,\mu} - g_{\mu\nu,\lambda}\right], \tag{2.21}$$

for the Christoffel symbol (**?**). Hence, one finally gets the to the geodesic equations

$$\ddot{x}^{\sigma} + \Gamma^{\sigma}{}_{\mu\nu} \dot{x}^{\mu} \dot{x}^{\nu} = 0, \tag{2.22}$$

by applying a $g^{\sigma\lambda}$ multiple. Note that, if the above relation is respected, the integral curves (the geodesics) are said to be *affinely parametrized* in terms of the parameter τ.

2.2 Overview of geodesic motion in Schwarzschild spacetime

The static and stationary spacetimes are good examples of the study of the particle geodesics. In particular, the SBH raises much of interest, because it teaches us a lot about the spacetime causality and the critical motion for mass-less and massive particles. These kinds of critical motion, could be used to locate the photon sphere and the accretion disk around the black hole. In this section, we study the null and time-like geodesics in SBH spacetime. Note that, unless it is supposed otherwise in a particular case, throughout this thesis, a geometric unit is taken into account, according to which $c = G = \hbar = 1$.

The SBH spacetime is described by the line element (Wald, 1984)

$$\mathrm{d}s^2 = g_{\mu\nu}\mathrm{d}x^\mu \mathrm{d}x^\nu = -B(r)\mathrm{d}t^2 + B(r)^{-1}\mathrm{d}r^2 + r^2\mathrm{d}\theta^2 + r^2\sin^2\theta\mathrm{d}\phi^2, \tag{2.23}$$

in the spherical coordinates $x^\mu = (x^0, x^1, x^2, x^3) = (t, r, \theta, \phi)$, where

$$B(r) = \frac{r - r_+}{r}, \tag{2.24}$$

and $r_+ = 2M$ indicates the event horizon hypersurface of a static spherically symmetric black hole of mass M. From now on, and for the sake of convenience, we consider equatorial geodesics by letting $\theta = \frac{\pi}{2}$. Now, applying the definition in Eq. (2.16) to the line element (2.23), one has (Wald, 1984; Chandrasekhar, 1998; Misner et al., 2017)

$$2\mathscr{L} \equiv -\epsilon = -\frac{E^2}{B(r)} + B(r)^{-1}\dot{r}^2 + \frac{L^2}{r^2}, \tag{2.25}$$

in which

$$E \equiv -g_{00}\dot{t} = B(r)\dot{t}, \tag{2.26a}$$

$$L \equiv g_{33}\dot{\phi} = r^2\dot{\phi}, \tag{2.26b}$$

are, respectively, the energy and the angular momentum of the test particles, and correspond to the Killing symmetries of the spacetime. Accordingly, these quantities are regarded as the constants of motion. Furthermore, the parameter ϵ, characterizes the types of the test particles, in the sense that $\epsilon = 1$ defines the time-like geodesics (for massive test particles), whereas $\epsilon = 0$ defines the null geodesics (for mass-less particles). One can recast Eq. (2.25) as

$$\dot{r}^2 = E^2 - V(r), \tag{2.27}$$

where

$$V(r) = B(r)\left[\epsilon + \frac{L^2}{r^2}\right], \tag{2.28}$$

is known as the gravitational effective potential. This potential is crucial to the classification of the possible orbits of the moving test particle in the spacetime around the black hole. Bringing together Eqs. (2.26) and (2.27), two extra equations are generated, reading as

$$\left(\frac{\mathrm{d}r}{\mathrm{d}t}\right)^2 = \frac{B(r)^2}{E^2}\left[E^2 - V(r)\right], \tag{2.29}$$

$$\left(\frac{\mathrm{d}r}{\mathrm{d}\phi}\right)^2 = \frac{r^4}{L^2}\left[E^2 - V(r)\right], \tag{2.30}$$

that give the evolution of the radial coordinate in terms of the coordinate time and the azimuth angle. These equations are indeed the first order differential equations of motion for the test particles. Note that, based on the Eqs. (2.29) and (2.30), particle orbits are possible only for the case of $E^2 > V(r)$.

2.2.1 Radial motion

For the case of $L = 0$, the test particle pursue purely radial motion, and from Eqs. (2.27) to (2.29), we get to the integrals

$$\tau = \int \frac{\mathrm{d}r}{\sqrt{E^2 - \epsilon\left(\frac{r-r_+}{r}\right)}}, \tag{2.31}$$

$$t = \int \frac{r\mathrm{d}r}{(r-r_+)\sqrt{1-\epsilon\left(\frac{r-r_+}{E^2 r}\right)}}. \tag{2.32}$$

These integrals lead to the radial behaviors of the proper and coordinates times.

Time-like geodesics

For the case of $\epsilon = 1$ and by applying the change of variable $x \doteq \frac{r_+}{r}$, the integral (2.31) can be recast as

$$\tau = -r_+ \int \frac{\mathrm{d}x}{x^2\sqrt{E^2-(1-x)}}. \tag{2.33}$$

A second change of variable $u \doteq 1 - x$, will then yield

$$\tau = r_+ \int \frac{\mathrm{d}u}{(1-u)^2\sqrt{E^2-u}}, \tag{2.34}$$

which has the solution

$$\tau(u) = \frac{\sqrt{E^2-u}}{(1-u)(1-E^2)} + (1-E^2)^{-\frac{3}{2}} \arctan\left(\sqrt{\frac{E^2-u}{1-E^2}}\right). \tag{2.35}$$

A sequence of the same changes of variables, helps us recasting the integral (2.32) as

$$t = Er_+ \int \frac{\mathrm{d}u}{u(1-u)^2\sqrt{E^2-u}}, \tag{2.36}$$

which has the solution

$$t(u) = \frac{E^2}{1-E^2}\left[\frac{\sqrt{E^2-u}}{E(1-u)} + \frac{3-2E^2}{E\sqrt{1-E^2}} \arctan\left(\sqrt{\frac{E^2-u}{1-E^2}}\right) \right. \\ \left. -2\left(1-\frac{1}{E^2}\right) \operatorname{arctanh}\left(\frac{1}{E}\sqrt{E^2-u}\right)\right]. \tag{2.37}$$

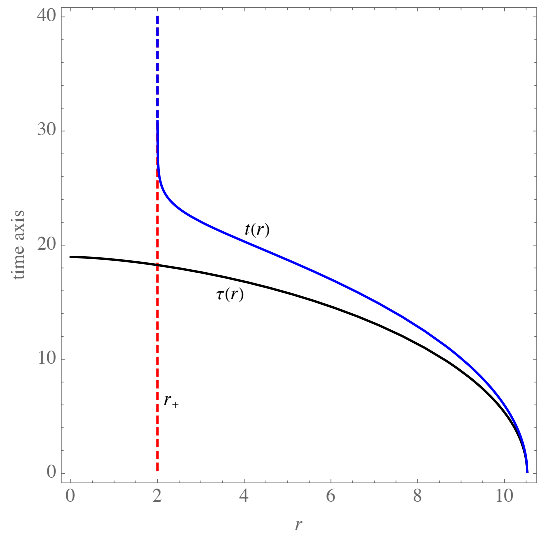

Figure 2.1: The radial behavior of $\tau(r)$ and $t(r)$ for time-like geodesics near a SBH.

Taking into account the applied changes of variables these solutions have been plotted together in Fig. 2.1, indicating the behaviors of $\tau(r)$ and $t(r)$. As it is seen from the figure, a comoving observer sees himself passing the horizon and falling onto the singularity. This is while for a distant observer, the time-like geodesics never passes the horizon and is maintained *frozen*.

Null geodesics

If we pursue the same method for the case of $\epsilon = 0$, we obtain the solutions

$$\tau(r) = \frac{r}{E}, \tag{2.38}$$

$$t(r) = \frac{r}{r_+} + \ln\left(\frac{r - r_+}{r_+}\right). \tag{2.39}$$

These solutions have been plotted in Fig. 2.2, and as we expected the distant observers do not detect any horizon crossing.

2.2.2 Angular motion

For a non-zero angular momentum for the test particles ($L = 0$), the evolution of the ϕ-coordinate needs to be taken into account. From Eq. (2.30), we have

$$\phi = \int_{r_t}^{r} \frac{\mathrm{d}r}{r^2\sqrt{\frac{1}{b^2} - \left(1 - \frac{r_+}{r}\right)\left(\frac{\epsilon}{E^2 b^2} + \frac{1}{r^2}\right)}}, \tag{2.40}$$

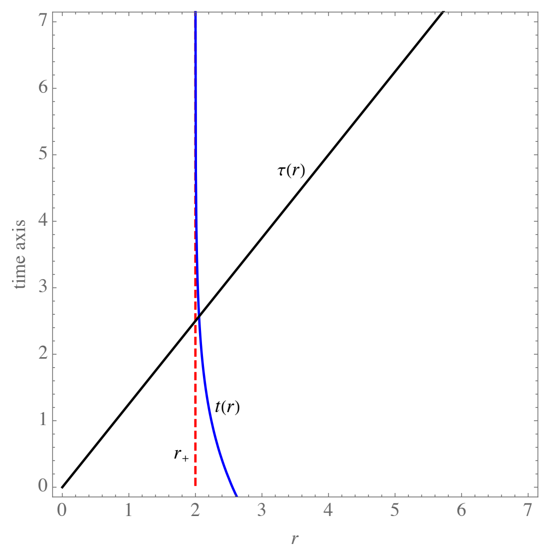

Figure 2.2: The radial behavior of $\tau(r)$ and $t(r)$ for null geodesics near a SBH.

in which, r_t is the turning point of the trajectories and $b = \frac{L}{E}$ is known as the impact parameter. It is, however, important to note that the motions have to be classified regarding the effective potential $V(r)$, according to which, the turning point of the particles' motion is determined by means of the equation $E_t^2 = V(r_t)$ (or $\frac{\mathrm{d}r}{\mathrm{d}\phi} = 0$). These turning points, together with the possible extremums of $V(r)$ (where $V'(r) = 0$), characterize the particle orbits.

Time-like geodesics

For the case of $\epsilon = 1$ in Eq. (2.28), a typical effective potential has been plotted in Fig. 2.3 for a definite value of the angular momentum. This effective potential has a maximum at r_M and a minimum at r_m. We can therefore expect *critical orbits* and *stable circular orbits* for the test particles. The former refers to those trajectories that are unstable and will either fall into the black hole or escape to infinity, and the latter, are completely stable at a definite distance r_m from the singularity. These particular orbits, correspond to the *innermost stable circular orbits* (ISCO) that correspond to the possibility of the formation of accretion disks around the black holes. On the other hand, the critical orbits determine a furthest near-horizon boundary around the black hole, from which, one can receive particles. For the case of null geodesics, this boundary introduces a *photon ring* that confines the *black hole shadow*. In Fig. 2.3, the particle energies that correspond to these radial distances have been notated by E_m and E_M, and accordingly, the orbits of the approaching particles are classified. There are, how-

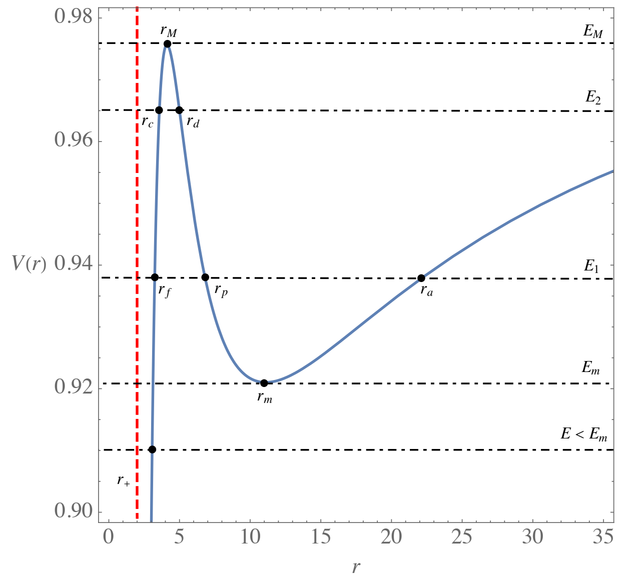

Figure 2.3: The gravitational effective potential for time-like geodesics approaching a SBH, plotted for $L = 3.9$. The unit along the axes has been taken to be M.

ever, two other energy levels E_1 and E_2 correspond to several more turning points. For the case of $E = E_1$, the particles can approach the black hole at the points r_a, r_p and r_f, that correspond respectively, to the *apoapsis*, the *periapsis*, and the *point of infall*. Hence, there orbits are indeed *bound orbits*. When $E = E_2$, the turning points are r_d and r_c, which indicate the *orbits of the first kind* (OFK) and *orbit of the second kind* (OSK). The former is an *unbound orbit* and results in deflection of the trajectories, or their *scattering*. The latter, however, is again a bound orbits an similar to the case of $r = r_f$, results in *capturing* the trajectories onto the singularity. Note that, for $E > E_M$, the particles coming from infinity fall directly onto the singularity. For $E < E_m$, the particles can approach the black hole at an infall point, and then, will fall onto the singularity.

Now, let us rewrite the integral (2.40) as

$$\phi(r) = \int_{r_t}^{r} \frac{\mathrm{d}r}{\sqrt{p_4(r)}}, \tag{2.41}$$

where $p_4(r) = \alpha r^4 + \beta r^3 - r^2 + r_+ r$, and

$$\alpha = \frac{1}{b^2}\left(1 - \frac{1}{E^2}\right), \tag{2.42a}$$

$$\beta = \frac{r_+}{b^2 E^2}. \tag{2.42b}$$

As mentioned before, the solutions to the equation $p_4(r) = 0$, give the turning points

r_t. Applying the change of variable $u \doteq \frac{r_t}{r}$, then changes the above integral to

$$\phi(u) = -\int_1^u \frac{\mathrm{d}u}{\sqrt{\frac{r_+}{r_t}u^3 - u^2 + r_t\beta u + r_t^2\alpha}}, \tag{2.43}$$

in which we have used the fact that $u(r_t) \equiv u_t = 1$. Now, the second change of variable $u \doteq \frac{4r_t}{r_+}\left(U + \frac{1}{12}\right)$, yields

$$\phi(U) = -\int_{U_t}^{U} \frac{\mathrm{d}U}{\sqrt{4U^3 - g_2U - g_3}}, \tag{2.44}$$

in which $U_t = \frac{r_+}{4r_t} - \frac{1}{12}$, and

$$g_2 = \frac{1}{12}(1 - 3r_+\beta), \tag{2.45a}$$

$$g_3 = \frac{1}{432}(2 - 27r_+^2\alpha - 9r_+\beta). \tag{2.45b}$$

The above integral can be separated in the form

$$\phi(U) = \int_U^\infty \frac{\mathrm{d}U}{\sqrt{4U^3 - g_2U - g_3}} - \int_{U_t}^\infty \frac{\mathrm{d}U}{\sqrt{4U^3 - g_2U - g_3}}. \tag{2.46}$$

According to Eq. (1.41a), the above integrals are indeed have the form of the real period of the $\wp$-Weierstraß function. We, however, write the first integral in the r.h.s. of Eq. (2.46), as the inverse $\wp$-Weierstraß function, $ß(U) \equiv \wp^{-1}(U; g_2, g_3)$, and the second one as $ß(U_t) = \phi_0$, namely, the initial angle. Accordingly, and by performing an inversion, this integral equation results in

$$U(\phi) = \wp\left(\phi + \phi_0\right), \tag{2.47}$$

from which, and by taking into account the applied changes of variables, we get the angular solution

$$r(\phi) = \frac{r_+}{4\wp(\phi + \phi_0) + \frac{1}{3}}. \tag{2.48}$$

The equatorial orbits are therefore given by this solution. However, they have to be classified in terms of the turning point r_t and its corresponding energy. To obtain the turning points, we consider solutions to $p_4(r) = 0$, for which, $r = 0$ is a trivial solution. We are therefore left with the equation $p_3(r) = \alpha r^3 + \beta r^2 - r + r_+$. To solve this equation, we first apply the change of variable $r \doteq \frac{4}{\alpha}\left(s - \frac{\beta}{12}\right)$, that provides the alternative form $4s^3 - \mu_2 s - \mu_3 = 0$, where

$$\mu_2 = \frac{1}{12}(3\alpha + \beta^2), \tag{2.49a}$$

$$\mu_3 = \frac{1}{432}(27r_+\alpha^2 + 9\alpha\beta + 2\beta^3). \tag{2.49b}$$

One should note that, the number of real solutions of this equation, depends on the sign of its discriminant $\Delta = \mu_2^3 - 27\mu_3^2$. This way, for $\Delta > 0$, the equation has three real roots, whereas for $\Delta < 0$, it has two complex conjugate roots and one real roots. For the case of $\Delta = 0$, a multiple root is obtained. In order to obtain the general solutions to this equation, we apply the Cardano's method (Cardano, 1993), by recasting the equation in the form

$$4\lambda z^3 \cos^3\theta - \lambda\mu_2 z\cos\theta - \lambda\mu_3 = 0, \tag{2.50}$$

to obtain which, we have used the definition $s \doteq z\cos\theta$, and λ is a Legendre multiply. Now, by doing a comparison with the available trigonometric identity

$$4\cos^3\theta - 3\cos\theta - \cos(3\theta) = 0, \tag{2.51}$$

we get

$$\lambda = \frac{1}{z^3}, \tag{2.52a}$$

$$z = \sqrt{\frac{\mu_2}{3}}, \tag{2.52b}$$

$$\cos(3\theta) = \lambda\mu_3, \tag{2.52c}$$

that provide the angle

$$\theta_n = \frac{1}{3}\arccos\left(\left[\frac{3}{\mu_2}\right]^{\frac{3}{2}}\mu_3\right) + \frac{2\pi n}{3}, \tag{2.53}$$

for $n = 0, 1, 2$. According to the definition for s in terms of θ, this now results in

$$s_n = \sqrt{\frac{\mu_2}{3}}\cos\left(\frac{1}{3}\arccos\left(\left[\frac{3}{\mu_2}\right]^{\frac{3}{2}}\mu_3\right) + \frac{2\pi n}{3}\right), \tag{2.54}$$

and finally, this yields the solution

$$r_n = \frac{4}{\alpha}\left[\sqrt{\frac{\mu_2}{3}}\cos\left(\frac{1}{3}\arccos\left(\left[\frac{3}{\mu_2}\right]^{\frac{3}{2}}\mu_3\right) + \frac{2\pi n}{3}\right) - \frac{\beta}{12}\right]. \tag{2.55}$$

The values of r_t are therefore given in terms of the above solutions, which at most, can be of three real values.

Note that, for the case of critical orbits and the ISCO, one can calculate directly the radial distances by solving $V'(r) = 0$, which give the radial distances

$$r_m = \frac{L^2}{r_+}\left(1 + \sqrt{1 - \frac{3r_+^2}{L^2}}\right), \tag{2.56a}$$

$$r_M = \frac{L^2}{r_+}\left(1 - \sqrt{1 - \frac{3r_+^2}{L^2}}\right), \tag{2.56b}$$

that correspond to the energies

$$E_m^2 = \left[1 + \frac{r_+^2}{L^2\left(1+\sqrt{1-\frac{3r_+^2}{L^2}}\right)^2}\right]\left[1 - \frac{r_+^2}{L^2\left(1+\sqrt{1-\frac{3r_+^2}{L^2}}\right)}\right], \tag{2.57a}$$

$$E_M^2 = \left[1 - \frac{r_+^2}{L^2\left(1-\sqrt{1-\frac{3r_+^2}{L^2}}\right)^2}\right]\left[1 - \frac{r_+^2}{L^2\left(1-\sqrt{1-\frac{3r_+^2}{L^2}}\right)}\right]. \tag{2.57b}$$

Applying the above information to the angular solution given in Eq. (2.48), some possible time-like orbits have been shown in Fig. 2.4.

Null geodesics

The same procedure as applied in the previous subsection, if applied to the case of $\epsilon = 0$, results in the angular solution

$$r(\phi) = \frac{r_+}{4\wp(\phi+\tilde{\phi}_0)+\frac{1}{3}}, \tag{2.58}$$

where $\tilde{\phi}_0 = ß\left(\frac{1}{12}\left[\frac{3r_+}{r_t}-1\right]\right)$, and the corresponding Weierstraß invariants are

$$\tilde{g}_2 = \frac{1}{12}, \tag{2.59a}$$

$$\tilde{g}_3 = \frac{r_+^2}{16r_t^2}\left(\frac{2r_+^2}{27r_t^2} - \frac{r_t^2E^2}{L^2}\right), \tag{2.59b}$$

with r_t being the appropriate turning point for the null trajectories. A typical effective potential for the null trajectories (by letting $\epsilon = 0$ in Eq. (2.28)) has been shown in Fig. 2.5. As inferred from this effective potential, no planetary bound orbits can be available. The only possible orbits are then, critical orbits at $r_M = 3M$ for the energy $E_M^2 = \frac{4}{27}\frac{L^2}{r_+^2}$, OFK at $r = r_d$ and OSK at $r = r_f$, for the energy E_1. These last radial distances are given as

$$r_d = \sqrt{\frac{\xi_2}{3}}\sin\left(\frac{1}{3}\arcsin\left(\xi_3\left[\frac{3}{\xi_2}\right]^{\frac{3}{2}}\right)+\frac{2\pi}{3}\right), \tag{2.60a}$$

$$r_f = \sqrt{\frac{\xi_2}{3}}\sin\left(\frac{1}{3}\arcsin\left(\xi_3\left[\frac{3}{\xi_2}\right]^{\frac{3}{2}}\right)\right), \tag{2.60b}$$

where $\xi_2 = 4b^2$ and $\xi_3 = 4r_+b^2$. In Fig. 2.6, some possible null orbits have been plotted in accordance with the above certain distances and energies.

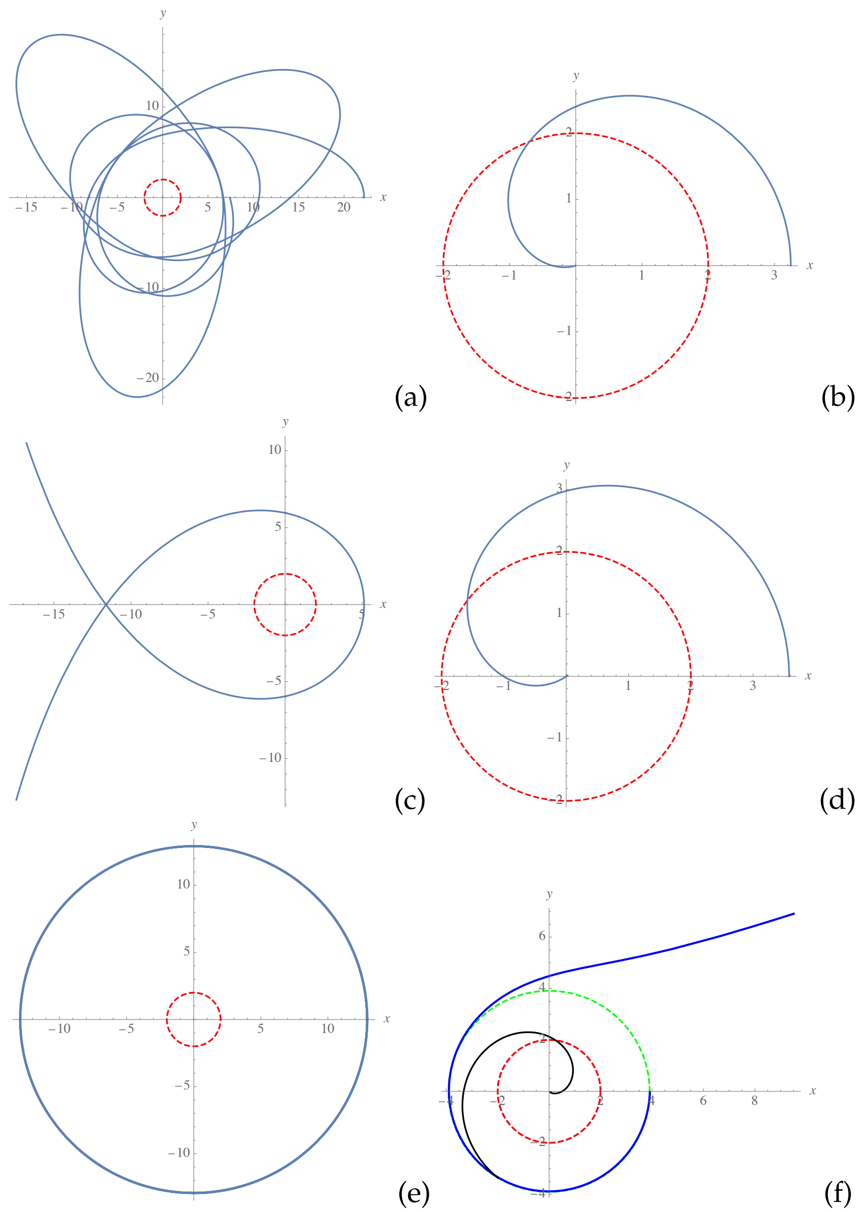

Figure 2.4: Some possible time-like orbits on a SBH, plotted for $M = 1$ and $L = 3.9$, in accordance to the radii and energies in Fig. 2.3. The diagrams correspond to (a) planetary orbits oscillating between r_p and r_a, (b) terminating bound orbit from r_f, (c) OFK from r_d (the particle approaches from r_d, but after passing r_m in goes to infinity), (d) OSK from r_c, (e) ISCO at r_m, and (f) critical orbits at r_M. The dashed red circle indicates the event horizon.

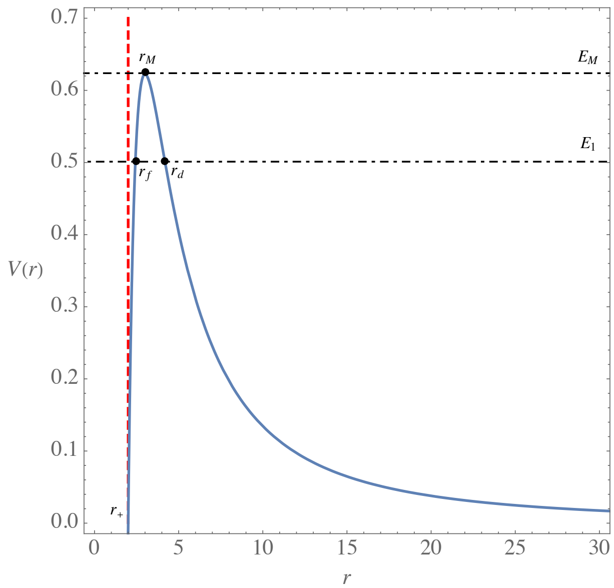

Figure 2.5: The gravitational effective potential for null geodesics approaching a SBH, plotted for $L = 4.1$. The unit along the axes has been taken to be M.

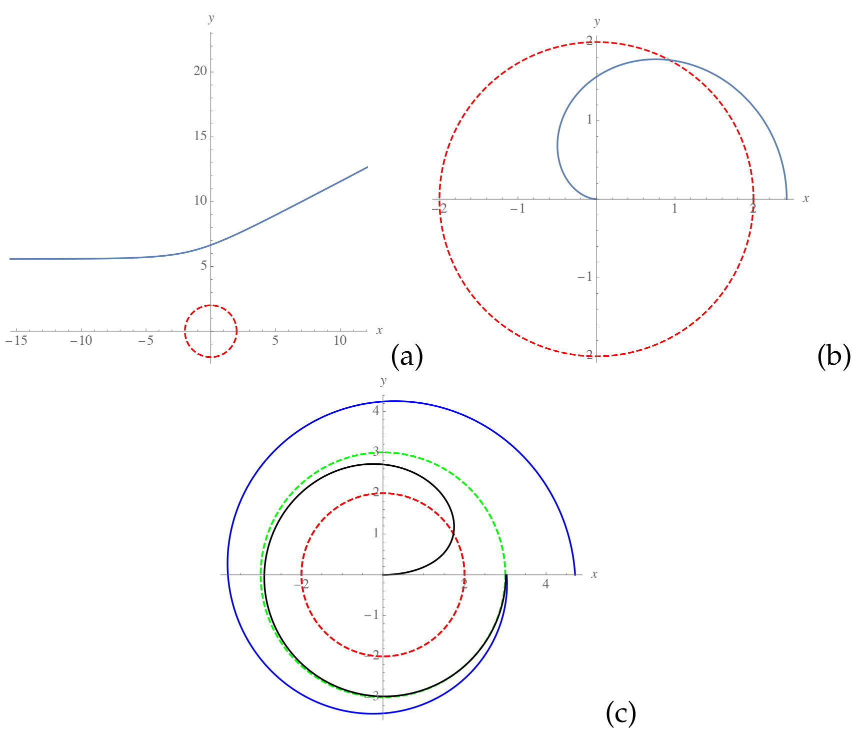

Figure 2.6: Some possible null orbits on a SBH, plotted for $M = 1$ and $L = 4.1$, in accordance to the radii and energies in Fig. 2.5. The diagrams correspond to (a) OFK from r_d, (b) OSK from r_f, and (c) critical orbits at r_M. The dashed red circle indicates the event horizon.

2.3 The modified Newman-Janis algorithm to obtain the Kerr solution

The famous Newman-Janis algorithm (NJA) (Newman & Janis, 1965), has been used for several decades in obtaining the rotating counterparts of static spacetimes. For the SBH spacetime, this leads naturally to the Kerr solution. This method has been also generalized for static spherically symmetric spacetimes with different metric components (Shaikh, 2019). However in this section, we review an alternative algorithm proposed by Azreg-Aïnou (Azreg-Aïnou, 2014; Azreg-Aïnou, 2014).

Let us consider the spacetime metric

$$\mathrm{d}s^2 = -f(r)\mathrm{d}t^2 + \frac{\mathrm{d}r^2}{f(r)} + r^2\left(\mathrm{d}\theta^2 + \sin^2\theta \mathrm{d}\phi^2\right), \tag{2.61}$$

in the spherical coordinates. Now, moving to the Eddington–Finkelstein coordinates (EFC) (u, r, θ, ϕ) by applying to the transformation

$$\mathrm{d}u \doteq \mathrm{d}t - \frac{\mathrm{d}r}{f(r)}, \tag{2.62}$$

leaves us with the line element

$$\mathrm{d}s^2 = -f(r)\mathrm{d}u^2 - 2\mathrm{d}u\mathrm{d}r + r^2\left(\mathrm{d}\theta^2 + \sin^2\theta \mathrm{d}\phi^2\right). \tag{2.63}$$

In fact, to follow with the procedure, we need to apply the Newman-Penrose (NP) formalism, to obtain the null tetrad $Z^\mu_\alpha = (\ell^\mu, n^\mu, m^\mu, \bar{m}^\mu)$, such that (Chandrasekhar, 1998; Misner et al., 2017)

$$g^{\mu\nu} = -\ell^\mu n^\nu - \ell^\nu n^\mu + m^\mu \bar{m}^\nu + m^\nu \bar{m}^\mu, \tag{2.64}$$

with

$$\ell_\mu \ell^\mu = n_\mu n^\mu = m_\mu m^\mu = \ell_\mu m^\mu = n_\mu m^\mu = 0, \tag{2.65a}$$

$$\ell_\mu n^\mu = -m_\mu \bar{m}^\mu = -1, \tag{2.65b}$$

and $\bar{\boldsymbol{m}}$ is the complex conjugate of $\boldsymbol{m}$. Applying the line element (2.63), one gets the corresponding null tetrad as

$$\ell^\mu = \delta^\mu_r, \tag{2.66a}$$

$$n^\mu = \delta^\mu_u - \frac{f(r)}{2}\delta^\mu_r, \tag{2.66b}$$

$$m^\mu = \frac{1}{\sqrt{2}\, r}\left(\delta^\mu_\theta + \frac{\mathrm{i}}{\sin\theta}\delta^\mu_\phi\right). \tag{2.66c}$$

Now to proceed with the modified version of the NJA (MNJA), we do the complex transformations

$$\delta^\mu_r \longrightarrow \delta^\mu_r, \tag{2.67a}$$

$$\delta^\mu_u \longrightarrow \delta^\mu_u, \tag{2.67b}$$

$$\delta^\mu_\theta \longrightarrow \delta^\mu_\theta + \mathrm{i}a\sin\theta\left(\delta^\mu_u - \delta^\mu_r\right), \tag{2.67c}$$

$$\delta^\mu_\phi \longrightarrow \delta^\mu_\phi. \tag{2.67d}$$

The relation in Eq. (2.67a) indicates that the MNJA does not require complexification of the r-coordinate. This way, we will have the transformations $f(r) \longrightarrow F(r,a,\theta)$ and $r^2 \longrightarrow H(r,a,\theta)$. Hence, the null tetrad (2.66) changes to

$$\ell'^\mu = \delta^\mu_r, \tag{2.68a}$$

$$n'^\mu = \delta^\mu_u - \frac{F(r,a,\theta)}{2}\delta^\mu_r, \tag{2.68b}$$

$$m'^\mu = \frac{1}{\sqrt{2H(r,a,\theta)}}\left(\delta^\mu_\theta + \mathrm{i}a\sin\theta\left(\delta^\mu_u - \delta^\mu_r\right) + \frac{\mathrm{i}}{\sin\theta}\delta^\mu_\phi\right), \tag{2.68c}$$

and accordingly,

$$\tilde{g}^{\mu\nu} = -\ell'^\mu n'^\nu - \ell'^\nu n'^\mu + m'^\mu \bar{m}'^\nu + m'^\nu \bar{m}'^\mu. \tag{2.69}$$

Therefore, the following line element is obtained in the EFC:

$$\begin{aligned}\mathrm{d}\tilde{s}^2 = &-F(r,a,\theta)\mathrm{d}u^2 - 2\mathrm{d}u\mathrm{d}r + 2a\sin^2\theta\left[F(r,a,\theta)-1\right]\mathrm{d}u\mathrm{d}\phi + 2a\sin^2\theta\mathrm{d}r\mathrm{d}\phi\\ &+ H(r,a,\theta)\mathrm{d}\theta^2 + \sin^2\theta\left[H(r,a,\theta) - a^2\sin^2\theta\left(F(r,a,\theta)-2\right)\right]\mathrm{d}\phi^2.\end{aligned} \tag{2.70}$$

Now we just need to do a global transformation to go to the Boyer–Lindquist coordinates (BLC). In fact, because of the existence of the cross terms $\mathrm{d}u\mathrm{d}\,r$ and $\mathrm{d}r\mathrm{d}\phi$, we will be in need of transforming the two coordinates u and ϕ. We then apply the definitions

$$\mathrm{d}u \doteq \mathrm{d}t' + \lambda(r)\mathrm{d}r, \tag{2.71a}$$

$$\mathrm{d}\phi \doteq \mathrm{d}\phi' + \chi(r)\mathrm{d}r, \tag{2.71b}$$

that do the transformations form the EFC (unprimed) to the BLC (primed). We assign the expressions (Azreg-Aïnou, 2014)

$$\lambda(r) = -\frac{r^2+a^2}{f(r)r^2+a^2}, \tag{2.72a}$$

$$\chi(r) = -\frac{a}{f(r)r^2+a^2}. \tag{2.72b}$$

The important step here is that we need to get rid of the $\mathrm{d}t\mathrm{d}r$ and $\mathrm{d}\phi\mathrm{d}r$ terms, which appear after doing the transformations. In fact, applying the transformations (2.71) in the line element (2.70), we get

$$\begin{aligned}\mathrm{d}\tilde{s}^2_{\mathrm{BL}} = &-F(r,a,\theta)\left[\mathrm{d}t+\lambda(r)\mathrm{d}r\right]^2+2a\left[F(r,a,\theta)-1\right]\sin^2\theta\left[\mathrm{d}t+\lambda(r)\mathrm{d}r\right]\left[\mathrm{d}\phi+\chi(r)\mathrm{d}r\right]\\ &-\sin^2\theta\left[-H(r,a,\theta)+a^2\sin^2\theta\left(F(r,a,\theta)-2\right)\right]\left[\mathrm{d}\phi+\chi(r)\mathrm{d}r\right]^2\\ &+\left[-2\left(\mathrm{d}t+\lambda(r)\mathrm{d}r\right)+2a\sin^2\theta\left(\mathrm{d}\phi+\chi(r)\mathrm{d}r\right)\right]\mathrm{d}r+H(r,a,\theta)\mathrm{d}\theta^2,\end{aligned} \tag{2.73}$$

in the BLC. Now, by eliminating the cross-term $\mathrm{d}r\mathrm{d}t$, we obtain the equation

$$-2-2\lambda(r)F(r,a,\theta)-2a\chi(r)\sin^2\theta+2a\chi(r)\sin^2\theta F(r,a,\theta)=0, \tag{2.74}$$

which by applying the definitions (2.72), yields

$$F(r,a,\theta)=\frac{r^2f(r)+a^2\cos^2\theta}{r^2+a^2\cos^2\theta}. \tag{2.75}$$

Furthermore, by eliminating $\mathrm{d}r\mathrm{d}\phi$ in Eq. (2.73), we get to the equation

$$\begin{aligned}&2a\sin^2\theta+2a\lambda(r)\sin^2\theta F(r,a,\theta)-2a\lambda(r)\sin^2\theta-2a^2\chi(r)\sin^4\theta F(r,a,\theta)\\ &\qquad+4a^2\chi(r)\sin^4\theta+2\chi(r)\sin^2\theta H(r,a,\theta)=0,\end{aligned} \tag{2.76}$$

which in the same way, results in the expression

$$H(r,a,\theta)=r^2+2a^2\cos^2\theta+r^2f(r)-\left(r^2+a^2\cos^2\theta\right)F(r,a,\theta). \tag{2.77}$$

Now, using Eq. (2.75) together with Eq. (2.77), we get

$$H(r,a,\theta)=r^2+a^2\cos^2\theta. \tag{2.78}$$

Considering the above results in the line element (2.73), we come up with the form

$$\begin{aligned}\mathrm{d}\tilde{s}^2_{\mathrm{BL}} = &-\left(\frac{\Delta-a^2\sin^2\theta}{\Sigma}\right)\mathrm{d}t^2+\frac{\Sigma}{\Delta}\mathrm{d}r^2-2a\sin^2\theta\left(1-\frac{\Delta-a^2\sin^2\theta}{\Sigma}\right)\mathrm{d}t\mathrm{d}\phi\\ &+\Sigma\mathrm{d}\theta^2+\sin^2\theta\left[\Sigma+a^2\sin^2\theta\left(2-\frac{\Delta-a^2\sin^2\theta}{\Sigma}\right)\right]\mathrm{d}\phi^2\end{aligned} \tag{2.79}$$

where we have defined $\Delta=a^2+r^2f(r)$ and $\Sigma=r^2+a^2\cos^2\theta$. It is straightforward to verify that for the case of $f(r)=1-\frac{2M}{r}$, the above line element provides

$$\begin{aligned}\mathrm{d}\tilde{s}^2_{\mathrm{BL}} = &-\left(1-\frac{2Mr}{\Sigma}\right)\mathrm{d}t^2+\frac{\Sigma}{\Delta}\mathrm{d}r^2+\Sigma\mathrm{d}\theta^2+\sin^2\theta\left(r^2+a^2+\frac{2Mra^2\sin^2\theta}{\Sigma}\right)\mathrm{d}\phi^2\\ &-\frac{4Mra\sin^2\theta}{\Sigma}\mathrm{d}t\mathrm{d}\phi,\end{aligned} \tag{2.80}$$

which is the Kerr solution, and here, has been obtained as the stationary (rotating) counterpart of the SBH spacetime, by means of the MNJA.

2.4 Summary

In this chapter, we provided instructive reviews on several concepts, including the Hamiltonian approach to the calculation of particle geodesics and as an example, we applied them to the simplest case, i.e. to the SBH spacetime. Accordingly, we also made use of the previously learnt algebraic notions on elliptic integrals that we discussed in chapter 1. Furthermore, for the future purposes, we introduced and reviewed the MNJA in obtaining the stationary counterparts of static spherically symmetric spacetimes, which will be used in the next chapter.

Chapter 3

The case of a charged Weyl black hole

In this chapter, a charged static spherically symmetric solution, derived from the Weyl conformal theory of gravity (WCG), is taken into account. This charged Weyl black hole (CWBH) will be then discussed in detail, in terms of the particle geodesics. After a brief introduction to the method of derivation of this solution, we proceed with analyzing the trajectories of mass-less and massive particles while moving in this spacetime, by applying the Lagrangian dynamics discussed in the previous chapter. These studies, also include several general relativistic tests which will be applied to CWBH spacetime (Fathi et al., 2020). Furthermore, the scattering of neutral and charged particles is also studied (Fathi et al., 2020, 2021c). We continue with the calculation of the gravitational lensing caused by the CWBH inside an electronic plasma (Fathi & Villanueva, 2021). We finally apply the MNJA this spacetime, in order to obtain its rotating counterpart, and accordingly, the shadow of this stationary black hole is also investigated (Fathi et al., 2021b).

3.1 The spacetime and its derivation

Ever since the late 1990's, the dark matter (DM) and dark energy (DE) scenarios has undergone vigorous efforts to be decoded. The observation of the flat galactic rotation curves (Rubin et al., 1980), the unexpected gravitational lensing (Massey et al., 2010), and the anti-lensing (Bolejko et al., 2013) effects are all related to impacts of an unknown source of mass around the galaxies, the so-called DM halo. This is much more complicated when a highly functioning energy source, i.e. the DE, is assumed to be causing the universe's global geometry to expand rapidly. (Riess et al., 1998; Perlmutter et al., 1999; Astier, 2012). These scenarios taken together constitute the most mysterious problems of contemporary cosmology and astrophysics. On the other hand, some believe that these scenarios stem from our lack of knowledge about the behavior of the gravitational field, as a glue to attach each segment of the universe. This opinion has led to a huge number of proposals for extended theories of gravity, mostly including alternatives to Einstein's general relativity (GR). These vary from the most natural ones, i.e., the $f(R)$ theories, to more complicated ones like scalar-tensor, vector-tensor and (non)metric-theories.

In recent decades, these proposed gravitational theories have been applied to cosmological models (see Ref. (Clifton et al., 2012) for a review), avoiding the need to include DM and DE. In the late 1980's, providing a spherically symmetric vacuum solution to the field equations of the fourth order WCG, which had been introduced in 1918 by H. Weyl (Weyl, 1918) and had been revived by R.J. Riegert in 1984 (Riegert, 1984), P.D. Mannheim and D. Kazanas showed that the controversial problem of flat galactic rotation curves could be explained by relating it to a specific term included in their solution (Mannheim & Kazanas, 1989). Their solution could also regenerate the usual Schwarzschild-de Sitter (SdS) spacetime. This theory is a natural extension of GR and proposed as an alternative to the DM/DE scenarios (Mannheim, 2006), and since then, it has been studied from several points of view (Knox & Kosowsky, 1993; Edery & Paranjape, 1998; Klemm, 1998; Edery et al., 2001; Pireaux, 2004b,a; Diaferio & Ostorero, 2009; Sultana & Kazanas, 2010; Diaferio et al., 2011; Mannheim, 2012; Tanhayi et al., 2011; Said et al., 2012; Lu et al., 2012; Villanueva & Olivares, 2013; Mohseni & Fathi, 2016; Horne, 2016; Lim & Wang, 2017). This theory was also considered a possibility for understanding the quantum cosmology related to the fluctuations of the early universe (Varieschi, 2010; 't Hooft, 2010b,a; 't Hooft, 2011; Varieschi & Burstein, 2013; Varieschi, 2014b; de Vega & Sanchez, 2013; Varieschi, 2014a; Hooft, 2014).

Although it may or may not be the proper alternative theory to general relativity, the WCG exhibits interesting properties. Most importantly, because of its conformal invariance, it has more conformity with the quantum association of the gravitational field, namely, the graviton.

In this chapter, this theory is taken into account while a particular choice for an analytic solution of the extra DM-related term in the solution is considered. This choice, was proposed by Payandeh and Fathi in 2012 (Payandeh & Fathi, 2012), and in this chapter, it is investigated regarding the motion of mass-less and massive particle in the exterior geometry of a charged black hole, which described by this solution (i.e. the CWBH).

The WCG is a theory of fourth order in the metric and is given by the action

$$I_W = -\mathcal{K}\int \mathrm{d}^4x\sqrt{-g}\; C_{\mu\nu\rho\lambda}C^{\mu\nu\rho\lambda}, \tag{3.1}$$

where $g=\det(g_{\mu\nu})$,

$$C_{\mu\nu\lambda\rho} = R_{\mu\nu\lambda\rho} - \frac{1}{2}\left(g_{\mu\lambda}R_{\nu\rho} - g_{\mu\rho}R_{\nu\lambda} - g_{\nu\lambda}R_{\mu\rho} + g_{\nu\rho}R_{\mu\lambda}\right) + \frac{R}{6}\left(g_{\mu\lambda}g_{\nu\rho} - g_{\mu\rho}g_{\nu\lambda}\right) \tag{3.2}$$

is the Weyl conformal tensor and $\mathcal{K}$ is a coupling constant. The conformal invariance of the Weyl tensor causes I_W to remain unchanged under the conformal transformation $g_{\mu\nu}(x) = e^{2\alpha(x)}g_{\mu\nu}(x)$, in which the exponential coefficient indicates local spacetime stretching. The action in Eq. (3.1) can be rewritten as

$$I_W = -\mathcal{K}\int \mathrm{d}^4x\sqrt{-g}\left(R^{\mu\nu\rho\lambda}R_{\mu\nu\rho\lambda} - 2R^{\mu\nu}R_{\mu\nu} + \frac{1}{3}R^2\right). \tag{3.3}$$

Since the Gauss-Bonnet term $\sqrt{-g}\,(R^{\mu\nu\rho\lambda}R_{\mu\nu\rho\lambda} - 4R^{\mu\nu}R_{\mu\nu} + R^2)$ is a total divergence, it does not contribute to the equation of motion. We can therefore simplify the action as (Mannheim & Kazanas, 1989; Kazanas & Mannheim, 1991)

$$I_W = -2\mathcal{K}\int \mathrm{d}^4x\sqrt{-g}\left(R^{\alpha\beta}R_{\alpha\beta} - \frac{1}{3}R^2\right). \tag{3.4}$$

Applying the principle of least action in the form $\frac{\delta I_W}{\delta g_{\alpha\beta}}=0$, leads to the vacuum Bach equation $W_{\alpha\beta}=0$, in which the Bach tensor is defined as

$$W_{\alpha\beta} = \nabla^\sigma\nabla_\alpha R_{\beta\sigma} + \nabla^\sigma\nabla_\beta R_{\alpha\sigma} - \Box R_{\alpha\beta} - g_{\alpha\beta}\nabla_\sigma\nabla_\gamma R^{\sigma\gamma} - 2R_{\sigma\beta}R^{\sigma}{}_{\alpha} + \frac{1}{2}g_{\alpha\beta}R_{\sigma\gamma}R^{\sigma\gamma} - \frac{1}{3}\Big(2\nabla_\alpha\nabla_\beta R - 2g^{\alpha\beta}\Box R - 2RR_{\alpha\beta} + \frac{1}{2}g_{\alpha\beta}R^2\Big). \tag{3.5}$$

The general spherically symmetric solution to the Bach equation has been obtained and discussed (Mannheim & Kazanas, 1989), where Mannheim and Kazanas, in addition to recovering all spherically symmetric solutions to Einstein field equations, including the Schwarzschild and Schwarzschild-(Anti-)de Sitter (SAdS) solutions, proposed the possibility of explaining the flat galactic rotation curves, which is claimed to be a significant feature of the DM scenario.

Now to obtain the analytical solution of the CWBH, let us consider the general spherically symmetric line element (by retrieving the Newton's constant G)

$$\mathrm{d}s^2 = -\left(1 - \frac{2GM}{r} - \frac{1}{3}f(r)\right)\mathrm{d}t^2 + \frac{\mathrm{d}r^2}{1 - \frac{2GM}{r} - \frac{1}{3}f(r)} + r^2\left(\mathrm{d}\theta^2 + \sin^2\theta\mathrm{d}\phi^2\right), \quad (3.6)$$

in which, $f(r)$ is an arbitrary r-dependent function, and has to be determined. The Ricci tensor components of this metric will be then

$$\begin{aligned}
R_{00} &= \left(-r^2 + 2GMr + \frac{1}{3}fr^2\right) \times \left[\frac{1}{12}\frac{\left(f'r^2 + 2fr\right)^2}{f} + \frac{1}{3}\sqrt{3fr^2}\left(-\frac{1}{12}\frac{\sqrt{3}\left(f'r^2 + 2fr\right)^2}{\left(fr^2\right)^{\frac{3}{2}}}\right.\right. \\
&\quad \left.\left. + \frac{1}{6}\frac{\sqrt{3}\left(f''r^2 + 4f'r + 2f\right)}{\sqrt{fr^2}}\right) r^2 - \frac{1}{3}\left(f'r^2 + 2fr\right)r + \frac{1}{3}fr^2\right] r^{-6}, \qquad (3.7) \\
R_{11} &= -\left[\frac{1}{12}\frac{\left(f'r^2 + 2fr\right)^2}{f} + \frac{1}{3}\sqrt{3fr^2}\left(-\frac{1}{12}\frac{\sqrt{3}\left(f'r^2 + 2fr\right)^2}{\left(fr^2\right)^{\frac{3}{2}}}\right.\right. \\
&\quad \left.\left. + \frac{1}{6}\frac{\sqrt{3}\left(f''r^2 + 4f'r + 2f\right)}{\sqrt{fr^2}}\right) r^2 - \frac{1}{3}\left(f'r^2 + 2fr\right)r + \frac{1}{3}fr^2\right] r^{-2} \\
&\quad \times \left(-r^2 + 2GMr + \frac{1}{3}fr^2\right)^{-1}, \qquad (3.8) \\
R_{22} &= -\frac{1}{3}\sqrt{3fr^2}\left(-\frac{1}{3}\frac{\sqrt{3}\left(f'r^2 + 2fr\right)r}{\sqrt{fr^2}} + \frac{1}{3}\sqrt{3}\sqrt{fr^2}\right) r^{-2}, \qquad (3.9) \\
R_{33} &= R_{22}\sin^2\theta, \qquad (3.10)
\end{aligned}$$

where the primes indicate differentiation with respect to the the variable r. Accordingly, the Ricci scalar $R = g^{\alpha\beta}R_{\alpha\beta} = R^{\alpha}{}_{\alpha}$ becomes

$$R = \frac{1}{3}\frac{f''r^2 + 4f'r + 2f}{r^2}. \quad (3.11)$$

Now, employing these values in the components of the Bach tensor (3.5), results in the components

$$
\begin{aligned}
W_{00} &= \frac{r^{-5}}{324}\Big[72f'r^2 - 72fr - 24GMf'^2r^2 + 288GMf''r^2 - 6GMf''^2r^4 - 432rG^2m^2f'' \\
&\quad -360GMf'r + 360r^2G^2M^2f''' - 12f'^2r^3 + 4f^3r + 36f''r^3 - 36r^5f'''' - 108r^4f''' \\
&\quad -3f''^2r^5 - 120GMf'rf - 12r^4GMf'f''' - 132r^3fGMf''' + 96GMff''r^2 \\
&\quad -48r^4GMff'''' - 24GMf'r^3f'' - 2r^5ff'''f' + 396r^3f'''GM - 144r^3G^2M^2f'''' \\
&\quad +144r^4f''''GM - 4fr^4f'f'' + 12f'r^4f'' + 24r^5f''''f + 72r^4ff''' - 4r^5f^2f'''' \\
&\quad -12r^4f^2f''' + 24GMf^2 + 4fr^3f'^2 - 8f^2r^2f' + 48f'r^2f - 144GMf + 6f'r^5f''' \\
&\quad -24r^3ff'' + fr^5f''^2 - 432G^2M^2f'\Big], \qquad (3.12) \\
W_{11} &= -\frac{1}{36}\frac{1}{r^3(-3r+6GM+fr)}\Big[-4r^3f'''f + 24f + 12f''r^2 - 24f'r \\
&\quad -4f'^2r^2 - 4f^2 + 8f'rf + 2f'r^4f''' - 72rf''GM + 4r^3f'f'' - 4ff''r^2 \\
&\quad -36r^2f'''GM - f''^2r^4 + 72GMf'\Big], \qquad (3.13) \\
W_{22} &= -\frac{1}{108r^2}\Big[-24f'r - 4f^2 + 8f'rf + 72GMf' \\
&\quad -4ff''r^2 + 2r^4(f)f'''' + 4r^3f'''f + 4r^3f'f'' \\
&\quad +2f'r^4f''' + 12f''r^2 - 4f'^2r^2 - f''^2r^4 - 6r^4f'''' \\
&\quad -12r^3f''' - 72rf''GM + 12r^3f''''GM + 24f\Big] \qquad (3.14) \\
W_{33} &= W_{22}\sin^2\theta. \qquad (3.15)
\end{aligned}
$$

As it is expected $W^{\alpha}{}_{\alpha} = 0$. Applying the above components to the vacuum Bach equation, we obtain the solution

$$
f(r) = -c_1r^2 - c_2r - \frac{6GM}{r}, \qquad (3.16)
$$

substitution of which in Eq. (3.6), yields

$$
ds^2 = -\left(1 + \frac{1}{3}c_2r + \frac{1}{3}c_1r^2\right)dt^2 + \frac{dr^2}{1 + \frac{1}{3}c_2r + \frac{1}{3}c_1r^2} + r^2\left(d\theta^2 + \sin^2\theta d\phi^2\right). \qquad (3.17)
$$

Now, in order to determine the intergation constants c_1 and c_2 in Eq. (3.16), we use the background field method in the weak field limit. The 00 component of the metric (3.6) can be rewritten as $g_{00} = \eta_{00} + h_{00}$, for small fluctuations $h_{00} = \frac{2GM}{r} + \frac{1}{3}f(r)$, with $\eta_{\alpha\beta}$ being the Minkowski metric in the spherical coordinates. The r-component of the Poisson's equation implies that

$$
\nabla^2 h_{00} \equiv \left(\frac{d^2}{dr^2} + \frac{2}{r}\frac{d}{dr}\right)h_{00} = 8\pi\left(T_{00} + E_{00}\right), \qquad (3.18)
$$

in which, T_{00} is the scalar component of the energy-momentum tensor related to the mass of the source, which in accordance with the spherical symmetry, becomes

$$T_{00} = \rho_0 = \frac{M_0}{\frac{4}{3}\pi r_0^3}, \tag{3.19}$$

where ρ_0 is the mass density of a source of mass M_0 and radius r_0. Furthermore, in Eq. (3.18), the E_{00} term is the scalar component of the electromagnetic energy-momentum tensor, associated with the total charge amount Q_0 of the massive object. Here, since the source is assumed to be static, we consider the vector potential $A_\mu = (\Phi(r), 0, 0, 0)$, where $\Phi(r)$ is the electric potential at point r in the exterior geometry of the total charge Q_0, distributed in a certain volume (i.e. $\Phi(r) = \frac{Q_0}{r}$). We have (Jackson, 1999):

$$E_{00} = \frac{1}{8\pi}\left(\frac{Q_0}{r^2}\right)^2 + \frac{1}{4\pi}\frac{\partial}{\partial r}\left(\Phi(r) \times \frac{Q_0}{r^2}\right) = \frac{1}{8\pi}\frac{Q_0^2}{r^4}. \tag{3.20}$$

Considering Eqs. (3.16), (3.19) and (3.20) in Eq. (3.18), and solving for c_1 or c_2, one obtains the expressions

$$c_1 = -3\frac{M_0}{{r_0}^3} - \frac{1}{2}\frac{(Q_0)^2}{r^4} - \frac{1}{3}\frac{c_2}{r}. \tag{3.21a}$$

$$c_2 = -9\frac{rM_0}{{r_0}^3} - \frac{3}{2}\frac{(Q_0)^2}{r^3} - 3c_1 r. \tag{3.21b}$$

In this study, we only take into account the expression for constant c_2 given Eq. (2). This way, the tt component of line element (3.17) takes the form

$$g_{00} = -\left(1 - \frac{3r^2 M_0}{{r_0}^3} - \frac{1}{2}\frac{Q_0^2}{r^2} - \frac{2}{3}c_1 r^2\right). \tag{3.22}$$

Defining

$$\frac{1}{\lambda^2} = \frac{3M_0}{r_0^3} + \frac{2c_1}{3}, \tag{3.23a}$$

$$Q = \sqrt{2}Q_0, \tag{3.23b}$$

we end up with a line element of the form

$$ds^2 = -B(r)dt^2 + \frac{dr^2}{B(r)} + r^2\left(d\theta^2 + r^2\sin^2\theta d\phi^2\right), \tag{3.24}$$

with the lapse function

$$B(r) = 1 - \frac{r^2}{\lambda^2} - \frac{Q^2}{4r^2}, \tag{3.25}$$

that describes the exterior geometry of the CWBH. If the condition $Q < \lambda$ is satisfied, this spacetime allows for two horizons; the event horizon r_+ and the cosmological horizon r_{++}, located at

$$r_+ = \frac{\lambda}{\sqrt{2}}\sqrt{1-\sqrt{1-\left(\frac{Q}{\lambda}\right)^2}}, \tag{3.26}$$

$$r_{++} = \frac{\lambda}{\sqrt{2}}\sqrt{1+\sqrt{1-\left(\frac{Q}{\lambda}\right)^2}}. \tag{3.27}$$

Obviously, the extremal black hole is obtained when $\lambda = Q$, possessing a unique horizon at $r_{ex} = r_+ = r_{++} = \frac{\lambda}{\sqrt{2}}$, whereas the naked singularity appears when $\lambda < Q$.

It is worth making some clarifications regarding the relevance of the solution given in Eq. (3.25) and the well-known static solutions of general relativity. In the absence of electric charge, when the vacuum case in considered, the known radius r_0 changes to the free radial distance r. Then, by substituting $3M_0 \to 2M$ and $c_1 \to 0$, we re-obtain the SBH spacetime, whereas the SAdS spacetime is regained by letting $2c_1 \to \pm\Lambda$ (with Λ as the cosmological constant). The corresponding horizons can be then regenerated by solving $B(r) = 0$. The relation to the Reissner-Nordström-(Anti-)de Sitter spacetime (RNAdS), however, requires the imaginary transformation $Q \to 2\mathrm{i}Q_0$. Based on the above types of transformation, it is apparent that the transition from the CWBH to the known spherically symmetric spacetimes offered by GR, is not trivial. This stems from the mathematical method applied in the derivation of the charged Weyl black hole solution. Let us now continue our discussion on the infalling geodesics on this black hole.

3.2 Motion of mass-less particles on the CWBH

Based on the discussions given in section 2.2 on the Lagrangian methods, which were exemplified for the case of the SBH, the equatorial geodesic equations can be recast as

$$\left(\frac{\mathrm{d}r}{\mathrm{d}\tau}\right)^2 = E^2 - V(r), \tag{3.28}$$

$$\left(\frac{\mathrm{d}r}{\mathrm{d}t}\right)^2 = B^2(r)\left(1-\frac{V(r)}{E^2}\right), \tag{3.29}$$

$$\left(\frac{\mathrm{d}r}{\mathrm{d}\phi}\right)^2 = \frac{r^4}{b^2}\left(1-\frac{V(r)}{E^2}\right), \tag{3.30}$$

in which

$$V(r) = L^2 \frac{B(r)}{r^2}, \tag{3.31}$$

corresponds to the null geodesics, and has been depicted in Fig. 3.1. This essentially shows same features as that of the de Sitter spacetime in the sense of the existence of two horizons, r_+ and r_{++}. In the forthcoming subsections, we will discuss this potential in more detail.

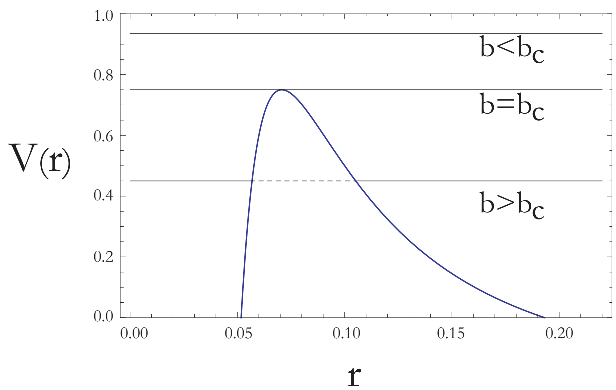

Figure 3.1: Plot of the effective potential $V(r)$ versus the radial coordinate r, for fixed parameter $L = 10^{-1}$, $\lambda = 2 \times 10^{-1}$ and $Q = 10^{-1}$ (in arbitrary units).

3.2.1 Radial geodesics

Mass-less particles (e.g. photons) with zero impact parameter (i.e. $L = 0$), perform a radial motion either towards the event horizon or the cosmological horizon. In this case clearly, the effective potential vanishes, such that Eqs. (3.28) and (6.51) become

$$\frac{\mathrm{d}r}{\mathrm{d}\tau} = \pm E, \quad \text{and} \quad \frac{\mathrm{d}r}{\mathrm{d}t} = \pm B(r). \tag{3.32}$$

Note that, the sign $+$ $(-)$ corresponds to photons falling onto the cosmological (event) horizon. Choosing the initial condition $r = r_i$ when $t = \tau = 0$ for the photons, a straightforward integration of the first in Eq. (3.32) yields

$$\tau(r) = \pm \frac{r - r_i}{E}, \tag{3.33}$$

which in the proper frame of the photons, indicates that they arrive at the event (cosmological) horizon within a finite proper time. On the other hand, to integrate the second relation in Eq. (3.32), let us rewrite the lapse function (3.25) as

$$B(r) = \frac{(r^2 - r_+^2)(r_{++}^2 - r^2)}{\lambda^2 r^2}. \tag{3.34}$$

This way, the second relation of Eq. (3.25) becomes

$$\pm \mathrm{d}t = \frac{\lambda^2 r^2}{(r^2 - r_+^2)(r_{++}^2 - r^2)} \mathrm{d}r. \tag{3.35}$$

One can decompose the r.h.s. of the above equation as

$$\frac{1}{(r^2 - r_+^2)(r_{++}^2 - r^2)} = \frac{A}{r^2 - r_+^2} + \frac{B}{r_{++}^2 - r^2} = \frac{A r_{++}^2 - B r_+^2 + (B - A) r^2}{(r^2 - r_+^2)(r_{++}^2 - r^2)}, \tag{3.36}$$

which results in $A = B = (r_{++}^2 - r_+^2)^{-1}$. This way, Eq. (3.35) yields the integral equation

$$t(r) = \pm \int_0^t \mathrm{d}t = \frac{\lambda^2}{(r_{++}^2 - r_+^2)} \left[\int_{r_i}^r \frac{r^2 \mathrm{d}r}{r^2 - r_+^2} + \int_{r_i}^r \frac{r^2 \mathrm{d}r}{r_{++}^2 - r^2} \right]. \tag{3.37}$$

To do integrations by part for each of the integrals, let us consider the first integral by applying the changes of variables $u \doteq r$ (or $\mathrm{d}u = \mathrm{d}r$), and $\mathrm{d}v \doteq \frac{r \mathrm{d}r}{r^2 - r_+^2}$ (or $v = \frac{1}{2} \ln(r^2 - r_+^2)$). This way, the first integral results in

$$I_1 \equiv \int_{r_i}^r \frac{r^2 \mathrm{d}r}{r^2 - r_+^2} \doteq uv - \int v \mathrm{d}u = \frac{r}{2} \ln\left(r^2 - r_+^2\right)\Big|_{r_i}^r - \int_{r_i}^r \ln\left(r^2 - r_+^2\right) \mathrm{d}r. \tag{3.38}$$

Now, taking into account he formula $\int_{r_i}^r \ln(r^2 - r_+^2) \mathrm{d}r = r \ln(r^2 - r_+^2) - 2r + r_+ \ln\left(\frac{r + r_+}{r - r_+}\right)$, we obtain

$$\begin{aligned} I_1 &= \frac{r}{2} \ln\left(r^2 - r_+^2\right) - \frac{r}{2} \ln\left(r^2 - r_+^2\right) + r - \frac{r_+}{2} \ln\left(\frac{r + r_+}{r - r_+}\right)\Bigg|_{r_i}^r \\ &= r - \frac{r_+}{2} \ln\left(\frac{r + r_+}{r - r_+}\right)\Bigg|_{r_i}^r \\ &= -(r - r_i) \frac{r_+}{2} \ln\left(\left[\frac{r + r_+}{r - r_+}\right]\left[\frac{r_i - r_+}{r_i + r_+}\right]\right). \end{aligned} \tag{3.39}$$

Pursuing the same procedure, the second integral in Eq. (3.37) provides the value

$$\begin{aligned} I_2 &\equiv \int_{r_i}^r \frac{r^2 \mathrm{d}r}{r_{++}^2 - r^2} = -\int_{r_i}^r \frac{r^2 \mathrm{d}r}{r^2 - r_{++}^2} \\ &= -\left[(r - r_i) - \frac{r_{++}}{2} \ln\left(\left|\frac{r + r_{++}}{r_{++} - r}\right| \left|\frac{r_{++} - r_i}{r_{++} + r_i}\right|\right)\right]. \end{aligned} \tag{3.40}$$

Getting together the derived expressions for I_1 and I_2 in Eq. (3.37), we obtain the result

$$t(r) = \pm \left[t_+(r) + t_{++}(r)\right], \tag{3.41}$$

where

$$t_+(r) = \frac{\lambda^2 r_+}{2(r_{++}^2 - r_+^2)} \ln\left|\frac{r - r_+}{r_i - r_+}, \frac{r_i + r_+}{r + r_+}\right|, \tag{3.42a}$$

$$t_{++}(r) = \frac{\lambda^2 r_{++}}{2(r_{++}^2 - r_+^2)} \ln\left|\frac{r_{++} - r_i}{r_{++} - r} \frac{r_{++} + r}{r_{++} + r_i}\right|. \tag{3.42b}$$

Note from Eqs. (3.42) that the coordinate time in Eq. (3.41) diverges for $r \to r_+$ or $r \to r_{++}$. Thus, an observer at $r = r_i$ essentially notes the same behavior for photons crossing either of the horizons in a similar manner as in the spherically symmetric spacetimes in the context of general relativity (Chandrasekhar, 1998; Cruz et al., 2005). The same holds for uncharged Weyl black holes (Villanueva & Olivares, 2013) (see Fig. 3.2). Horizon-crossing, however, can be done in more complex ways once the angular momentum plays its role. This is addressed in the next subsection.

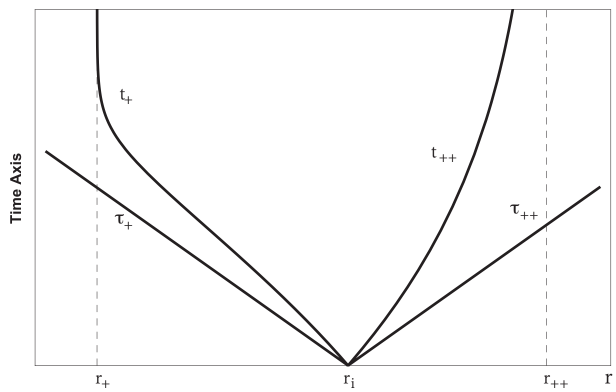

Figure 3.2: Temporal behavior for radial null geodesics on the CWBH. In the proper system, photons can cross the horizons in a finite time (in accordance with Eq. (3.33)), whereas regarding Eq. (3.41), an observer at r_i measures an infinite time for $r \to r_+$ or $r \to r_{++}$. The same behavior is seen in the study of photon motion in static spherically symmetric spacetimes in the context of GR.

3.2.2 Angular geodesics

The angular motion of mass-less particles, whose constants of motion are different from zero is well described by the effective potential (3.108). As can be seen in Fig. 3.1, the effective potential possesses a maximum at $r_c = \frac{Q}{\sqrt{2}}$ (obtained by solving $V'(r) = 0$), which is independent of λ. In order to obtain the critical value of the impact parameter, b_c, let us reconsider Eq. (3.28) at the point r_c. This yields

$$\begin{aligned} \left(\frac{\mathrm{d}r}{\mathrm{d}\tau}\right)^2_{r_c} = 0 &= E_c^2 - V(r_c) \\ &= E_c^2 - B(r_c)\frac{L^2}{r_c^2}. \end{aligned} \tag{3.43}$$

Multiplying both sides by a factor of $\frac{1}{E_c^2}$, we get

$$0 = 1 - \frac{B(r_c)}{r_c^2} b_c^2, \tag{3.44}$$

that results in

$$b_c = \sqrt{\frac{r_c^2}{B(r_c)}}. \tag{3.45}$$

This way, and taking into account the lapse function (3.25), we obtain

$$b_c = \frac{\lambda Q}{\sqrt{\lambda^2 - Q^2}}. \tag{3.46}$$

Comparing the impact parameter of the test particles to this value, we can obtain qualitative descriptions of the angular motions for photons allowed in the exterior spacetime of a charged Weyl black hole. In what follows, we bring detailed discussions about each of these possibilities:

1. ***Critical Trajectories***: If $b = b_c$, an unstable circular orbit of radius r_c is allowed as a subset of the null geodesics family. To obtain the proper period in such orbits, let us once again, consider Eq. (3.28) at the radial distance r_c, but for now, we do not let it to be zero. We therefore have

$$\begin{aligned}
\left(\frac{\mathrm{d}r}{\mathrm{d}\tau}\right)^2_{r_c} = E_c^2 - V(r_c) &= \left[\left(\frac{\mathrm{d}r}{\mathrm{d}\phi}\right)\left(\frac{\mathrm{d}\phi}{\mathrm{d}\tau}\right)\right]^2_{r_c} \\
&= \left[\frac{r^2}{b_c}\left(\frac{E_c^2 - V(r_c)}{E_c^2}\right)^{\frac{1}{2}} \frac{\mathrm{d}\phi}{\mathrm{d}\tau}\right]^2 \\
&= \frac{r^4}{b_c^2}\frac{E_c^2 - V(r_c)}{E_c^2}\left(\frac{\mathrm{d}\phi}{\mathrm{d}\tau}\right)^2.
\end{aligned} \tag{3.47}$$

in which, we have used the relation in Eq. (6.52) in the second line. Now the factor $E_c^2 - V(r_c)$ is eliminated between the l.h.s. and the r.h.s. of the above equation, and we are left with

$$\frac{r^4}{b_c^2}\frac{1}{E_c^2}\left(\frac{\mathrm{d}\phi}{\mathrm{d}\tau}\right)^2 = 1. \tag{3.48}$$

Now, one can infer from Eq. (2.26b) that, for one stable period (i.e. $\Delta\phi = 2\pi$) at r_c, we have $\frac{2\pi}{\Delta\tau} = \frac{L}{r_c^2}$. This way, and renaming $\Delta\tau \equiv T_\tau$ (i.e. the proper period of the unstable orbits), we can write $T_\tau = \frac{2\pi}{L} r_c^2$, or taking into account the value of r_c,

$$T_\tau = \pi \frac{Q^2}{L}, \tag{3.49}$$

which is independent of λ. To obtain the coordinate period, let us decompose

$$\left(\frac{\mathrm{d}\phi}{\mathrm{d}\tau}\right)_{r_c} = \frac{L}{r_c^2} = \frac{\mathrm{d}\phi}{\mathrm{d}t}\frac{\mathrm{d}t}{\mathrm{d}\tau} = \frac{\mathrm{d}\phi}{\mathrm{d}t}\frac{E_c}{B(r_c)} \tag{3.50}$$

to obtain which, we have used the relation (2.26a). This way, the above equation yields

$$\left(\frac{\mathrm{d}\phi}{\mathrm{d}t}\right)_{r_c} = \frac{b_c}{r_c^2}B(r_c) = \frac{1}{b_c}, \tag{3.51}$$

for which, we have used Eq. (3.45) in the last step. Now, once again, for a complete period we get $\frac{2\pi}{\Delta t} = \frac{1}{b_c}$. Renaming $\Delta t = T_t$ (i.e. the coordinate period of the unstable orbits), we finally get

$$T_t = 2\pi\, b_c = 2\pi\,\frac{\lambda\, Q}{\sqrt{\lambda^2 - Q^2}}. \tag{3.52}$$

which depends on both λ and Q. It is straightforward to check that

$$T_t = \frac{L}{Q\sqrt{1-\left(\frac{2Q}{\lambda}\right)^2}}T_\tau, \tag{3.53}$$

which implies $T_t > T_\tau$.

To obtain the analytical solution of the unstable orbits, we return to the angular equation of motion (6.52), which by means of the relations in Eqs. (3.108) and (3.25), yields

$$\begin{aligned}\left(\frac{\mathrm{d}r}{\mathrm{d}\phi}\right)^2 &= \frac{r^4}{b^2}\left(1-\frac{b^2}{r^2}+\frac{b^2}{\lambda^2}+\frac{b^2Q^2}{r^4}\right)\\ &= r^4\left(\frac{1}{b^2}+\frac{1}{\lambda^2}\right)-r^2+Q^2.\end{aligned} \tag{3.54}$$

Note that, using the value of b_c in Eq. (3.411), one can recast

$$\frac{1}{b_c^2}+\frac{1}{\lambda^2} = \frac{\lambda^2-Q^2}{Q^2\lambda^2}+\frac{1}{\lambda^2} = \frac{1}{Q^2}. \tag{3.55}$$

Hence, to obtain the equation of motion for the case of critical (unstable) orbits, by letting $b = b_c$ in Eq. (3.54) and using the relation in Eq. (3.55), we obtain the differential equation

$$\left(\frac{\mathrm{d}r}{\mathrm{d}\phi}\right)^2 = \frac{P_4^c(r)}{Q^2}, \tag{3.56}$$

where

$$\begin{aligned}P_4^c(r) = r^4 - Q^2r^2 + \frac{Q^4}{4} &= \left(r^2-\frac{Q^2}{2}\right)^2\\ &= \left[(r+r_c)(r-r_c)\right]^2.\end{aligned} \tag{3.57}$$

So, combining Eqs. (3.56) and (3.57), we get

$$\frac{\mathrm{d}r}{\mathrm{d}\phi} = \pm\frac{1}{\sqrt{2}}\frac{(r+r_c)|r-r_c|}{r_c}. \tag{3.58}$$

For those photons initiating from outside of r_c (i.e. $r_c < r_i < r_{++}$), we can then recast Eq. (3.58) as

$$\frac{\mathrm{d}r}{\mathrm{d}\phi} = \pm\frac{r^2 - r_c^2}{\sqrt{2}\,r_c}, \tag{3.59}$$

which explains the critical trajectories of the first kind, while the relation

$$\frac{\mathrm{d}r}{\mathrm{d}\phi} = \pm\frac{r_c^2 - r^2}{\sqrt{2}\,r_c}, \tag{3.60}$$

describes those of the second kind for photons initiating their motion from inside of r_c (i.e. $r_+ < r_i < r_c$). Solutions to these equations can be obtained by direct integration. For the case of Eq. (3.59), let us apply the change of variable $\varphi \doteq \frac{\phi}{\sqrt{2}}$, we get to the differential equation $\frac{\mathrm{d}r}{\mathrm{d}\varphi} = \pm\frac{r^2-r_c^2}{r_c}$. Now a second change of variable $x \doteq \frac{r}{r_c}$ provides

$$\frac{\mathrm{d}x}{\mathrm{d}\varphi} = \pm\left(x^2 - 1\right), \tag{3.61}$$

which, by adopting the positive part, has the solution $\varphi(x) = \coth x$. Taking into account the applied changes of variables, we obtain the solution to the first kind motion as

$$r(\phi) = r_c \coth\left(\frac{\phi}{\sqrt{2}}\right). \tag{3.62}$$

Pursuing the same procedure for Eq. (3.60), the second kind solution becomes

$$r(\phi) = r_c \tanh\left(\frac{\phi}{\sqrt{2}}\right). \tag{3.63}$$

In Fig. 7.6, the critical trajectories (3.177) and (3.178) have been plotted.

2. ***Deflection Zone***. Light deflection in WCG, in the context of the Mannheim-Kazanas solution, has been discussed (Sultana & Kazanas, 2010; Cattani et al., 2013; Sultana, 2013). Here, address the same problem, for the CWBH under study. When photons attain the impact parameter $b_c < b < \infty$, they are deflected due to the effective potential barrier. Thus, and as in the previous case, they encounter orbits of the first and second kind (OFK and OSK). Photons coming from a finite distance r_i ($r_+ < r_i < r_c$ or $r_c < r_i < r_{++}$) to the distance $r = r_f$ or $r = r_d$ (which are obtained from the relation $V(r_f) = V(r_d) = E^2$) are then

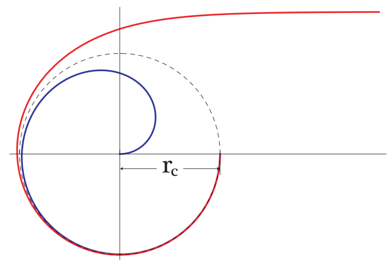

Figure 3.3: Critical trajectories of photons with $b = b_c$. Orbits of the first and the second kinds are allowed for test particles that approach by spiraling to the unstable circular orbit at $r = r_c$.

pulled back to either of the two horizons and are, in fact, deflected. To calculate the turning points, we therefore take care of the equation

$$E^2 - \frac{L^2 B(r)}{r^2} = 0 \tag{3.64}$$

in which, $\frac{B(r)}{r^2} = \frac{1}{r^2} - \frac{1}{\lambda^2} - \frac{Q^2}{r^4}$. Dividing by a factor E^2, the above equation yields

$$\frac{1}{\beta^2} = \frac{1}{r^2} - \frac{Q^2}{r^4}, \tag{3.65}$$

where the *anomalous impact parameter* is defined as

$$\frac{1}{\beta^2} = \frac{1}{b^2} + \frac{1}{\lambda^2}. \tag{3.66}$$

To obtain the roots of Eq. (3.65), we apply the change of variable $x \doteq \frac{1}{r^2}$, which then leads to the equation $\frac{1}{\beta^2} = x - Q^2 x^2$. This equation, after reconsideration of the applied change of variable, result sin the turning points

$$r_f = \frac{\beta}{\sqrt{2}} \sqrt{1 - \sqrt{1 - \left(\frac{Q}{\beta}\right)^2}}, \tag{3.67}$$

$$r_d = \frac{\beta}{\sqrt{2}} \sqrt{1 + \sqrt{1 - \left(\frac{Q}{\beta}\right)^2}}. \tag{3.68}$$

Note that in the limit $b \to \infty$, the anomalous impact parameter becomes $\beta = \lambda$ and we obtain the identities $r_f(b = \infty) = r_+$ and $r_d(b = \infty) = r_{++}$ (see Eqs. (3.26), (3.142) and Eqs. (3.27), (3.143)). The equations of motion are once again obtained by integrating the general radial relation in Eq. (6.52) for both kinds of orbits. To do this, we perform the change of variable $r = \beta\sqrt{u + 1/3}$, which generates the equation

$$\pm \frac{\mathrm{d}u}{\mathrm{d}\phi} = \sqrt{4u^3 - g_2 u - g_3}. \tag{3.69}$$

This leads to the integrals

$$\phi = \int_{u_d}^{u} \frac{\mathrm{d}u'}{\sqrt{4u'^3 - g_2 u' - g_3}} \quad (\text{with } u_d < u), \tag{3.70a}$$

$$\phi = \int_{u}^{u_f} \frac{\mathrm{d}u'}{\sqrt{4u'^3 - g_2 u' - g_3}} \quad (\text{with } u_f > u), \tag{3.70b}$$

for OFK and OSK, respectively. The above integrals yield

$$r(\phi) = \beta \sqrt{\frac{1}{3} + \wp(\omega_d - \phi)} \tag{3.71}$$

for OFK, and

$$r(\phi) = \beta \sqrt{\frac{1}{3} + \wp(\omega_f + \phi)}, \tag{3.72}$$

for OSK, were the Weierstraß invariants are

$$g_2 = \frac{4}{3} - \frac{Q^2}{\beta^2}, \tag{3.73a}$$

$$g_3 = \frac{8}{27} - \frac{Q^2}{3\beta^2}. \tag{3.73b}$$

Furthermore, the phase parameters are given by

$$\omega_d = ß\left(\frac{r_d^2}{\beta^2} - \frac{1}{3}\right), \tag{3.74a}$$

$$\omega_f = ß\left(\frac{r_f^2}{\beta^2} - \frac{1}{3}\right), \tag{3.74b}$$

The qualitative behavior of OFK and OSK is shown in Fig. 7.7. We should note here that the signature of the above coefficients affects the polynomial on the right hand side of Eq. (3.69). Letting $\beta_c = \beta|_{b=b_c}$ we get $\beta_c = Q$ and based on Eqs. (3.73) we have:

- For $g_2 > 0$ we have $\bar{\beta}_2 < \beta < \beta_c$,
- For $g_3 > 0$ we have $\beta > \bar{\beta}_3 > \beta_c$, in which $\bar{\beta}_2 = \frac{3\beta_c}{2\sqrt{3}} = \sqrt{\frac{2}{3}}\bar{\beta}_3$.

Since we are interested in the region inside the effective potential, we disregard the first case above. We can therefore categorize the following conditions on the coefficients:

Condition 1) for $\beta > \bar{\beta}_3$ we have $g_2 > 0$ and $g_3 > 0$.

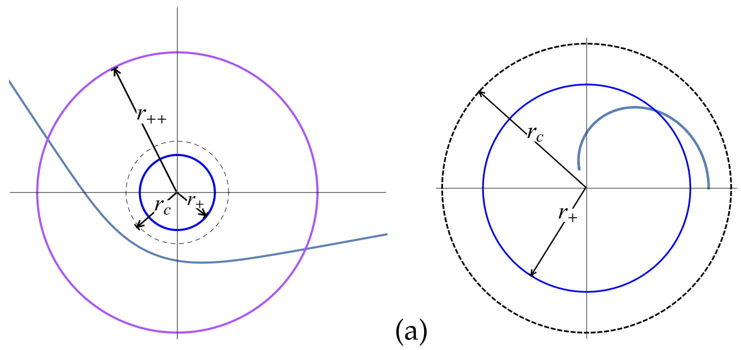

Figure 3.4: The deflecting trajectories governed by equations of motion given in Eqs. (3.154) and (3.72). The plots demonstrate (a) OFK and (b) OSK. As we can see, the hyperbolic form of OFK allows incoming trajectories to enter the cosmological horizon before their escape to infinity. On the other hand, those that follow OSK, will rapidly enter the event horizon and fall onto the singularity.

Condition 2) for $\beta_c < \beta < \bar{\beta}_3$ we have $g_2 > 0$ and $|g_3| > 0$.

It is worth mentioning that, as appears in the decreasing segment of Fig. 3.1, the effective potential can change its type of curvature in an inflection point. This appears at the point r_0, for which $V''(r_0) = 0$, giving $r_0 = \pm\sqrt{\frac{5}{6}}Q$, where

$$V_0 \equiv V(r_0) = L^2 \left(\frac{21}{25Q^2} - \frac{1}{\lambda^2} \right). \tag{3.75}$$

Moreover, applying the definition in Eq. (3.66) to the turning points (where $V(r) = E^2$), we get

$$\frac{1}{\beta^2} = \frac{1}{r_t^2} \left(1 - \frac{2\bar{\beta}_3^2}{9r_t^2} \right), \tag{3.76}$$

where r_t indicates the turning points, implying that the above relation is valid only on the curve given by the effective potential. From Eq. (3.76) we infer that

$$\beta_0 = \frac{10\sqrt{2}}{3\sqrt{21}}\bar{\beta}_3, \tag{3.77}$$

in which $\beta_0 \equiv \beta|_{r=r_0}$. This provides $\beta_0 \approx 1.03\ \bar{\beta}_3$. Therefore, the effective potential's value corresponding to $\bar{\beta}_3$ is larger than V_0. However, regarding the small difference between $\bar{\beta}_3$ and β_0, geodesics following the OFK described by Eq. (3.72) are more likely to fall to bound orbits, as the potential changes from being concave to being convex at r_0.

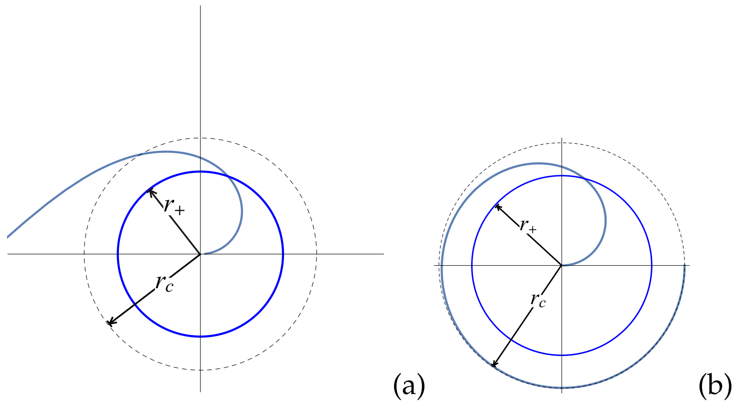

Figure 3.5: The capturing process for particles possessing $b \leq b_c$. The figures indicate approaching particles with (a) $b < b_c$ and (b) $b = b_c$.

3. ***Capture Zone***: Particles with the impact parameter $0 < b = b_a < b_c$ will experience an inevitable infall onto black hole horizons. Obviously, the above depends on the initial conditions, specifically on the direction of the velocity at the moment of starting the description of the trajectory. In both cases, the cross-section is given by (**?**)

$$\sigma = \pi\, b_c^2 = \frac{\pi\lambda^2 Q^2}{\lambda^2 - Q^2}. \tag{3.78}$$

In a similar way as discussed before, we integrate Eq. (6.52) to obtain the equation of motion, which reads

$$r(\phi) = \beta\sqrt{\frac{1}{3} + \wp(\omega_a + \phi)}, \tag{3.79}$$

where $\omega_a = ß(\frac{r_a^2}{\beta^2} - \frac{1}{3})$ is the phase parameter corresponding to the point of approach r_a. Note that, depending on the impact parameter, capturing can happen in different ways. As we can see in Fig. 3.19, for $b < b_c$, the trajectories coming from infinity are captured directly on the event horizon. This is while those with $b = b_c$ follow a spiral-formed trajectory toward the horizon.

Now that the angular motions have been discussed, we can make use of them to relate the features of a CWBH to the classical test of GR. We start from gravitational lensing.

3.2.3 Bending of light and the lens equation

Regarding the deflection of light in the OFK, gravitational lenses can form. Gravitational lensing of spherically symmetric black holes has been widely studied in the

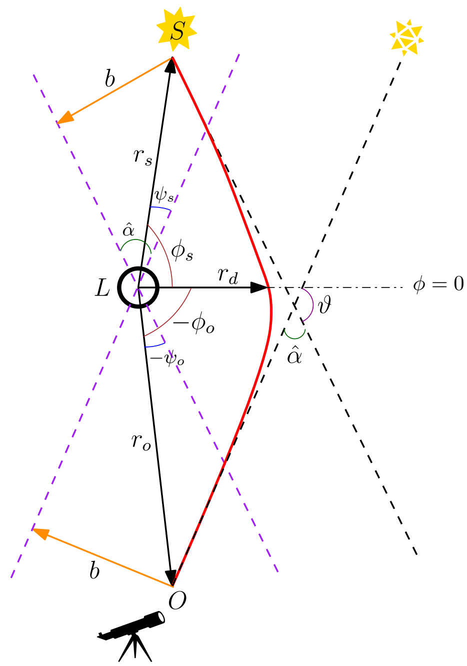

Figure 3.6: A schematic illustration of the lensing phenomena. The shortest distance r_d to the lens L, has been taken to be the turning point in the OFK, lying on the $\phi = 0$ line. The source and the observer are located at $S(r_s, \phi_s, b)$ and $O(r_o, \phi_o, b)$.

literature, for example for the case of the SBH (Virbhadra & Ellis, 2000) and for more general cases where theoretical aspects of this phenomenon have been developed to compare the predicted higher order images with those of realistic observations (Bozza, 2010). In particular, for charged black holes in the context of RN geometry, this effect has been applied to study the intrinsic characteristics of the background spacetime (Zhao et al., 2016). There are also some interesting discussions using which, one can obtain greater insight into the various types of lensing and their applications in astrophysics and cosmology (Treu & Ellis, 2015).

Now let us construct the geometry of the problem and apply it to the spacetime under study. Consider the diagram in Fig. 3.6. The source and the observer, characterized by their position, angle and the impact parameter of the light passing them, are respectively located at $S(r_s, \phi_s, b)$ and $O(r_o, -\phi_o, b)$. The shortest distance r_d to the lens is the turning point given in Eq. (3.143) and $r = r_d$ indicates $\phi = 0$. Regarding the figure, we can infer that:

$$\vartheta = \phi_s - \psi_s + |\phi_o| - |\psi_o|, \tag{3.80}$$

and $\vartheta + \hat{\alpha} = \pi$ relates the deflection angle $\hat{\alpha}$ to the position angles ϕ_o and ϕ_s. It is straightforward to calculate:

$$\psi_s = \hat{\alpha} - \arcsin(\frac{b}{r_s}), \tag{3.81}$$

$$|\psi_o| = \hat{\alpha} - \arcsin(\frac{b}{r_o}). \tag{3.82}$$

Once again, applying appropriately Eqs. (6.52) and (3.69), we obtain the angles ϕ_s and ϕ_o and therefore the lens equation is obtained as:

$$\begin{aligned}\hat{\alpha} = \arcsin\left(\frac{b}{r_o\, r_s}\left[\sqrt{r_o^2 - b^2} + \sqrt{r_s^2 - b^2}\right]\right) + 2\omega_d \\ - \left[ß\left(\frac{r_s^2}{\beta^2} - \frac{1}{3}\right) + \left|ß\left(\frac{r_o^2}{\beta^2} - \frac{1}{3}\right)\right|\right] - \pi,\end{aligned} \tag{3.83}$$

where ω_d is the same as that in Eq. (3.74a). The above relation, gives the lens equation for light rays passing a CWBH. During the lensing process, as light deflects from the black hole, it experiences a temporal dilation. This causes another important effect which is discussed as the second test in the next section.

3.2.4 Gravitational time delay

One interesting relativistic effect associated with the propagation of photons, is the apparent delay in the time of propagation for a light signal passing the Sun's proximity. Known as the Shapiro time delay (**?**), this effect is a relevant correction for astronomical observations. The time delay of radar echoes corresponds to the determination of the time delay of radar signals which are transmitted from the Earth through a region near the Sun to another planet or to a spacecraft, and are then reflected back to Earth (see Fig. 3.7). The time interval between emission and return of a pulse as measured by a clock on Earth is given by

$$t_{12} = 2\left[t(r_1, \rho_0) + t(r_2, \rho_0)\right], \tag{3.84}$$

where ρ_0 corresponds to the closest proximity to the Sun. Returning to Eq. (6.51):

$$\dot{r} = \dot{t}\,\frac{\mathrm{d}r}{\mathrm{d}t} = \frac{E}{B(r)}\frac{\mathrm{d}r}{\mathrm{d}t} = \sqrt{E^2 - \frac{L^2}{r^2}B(r)}\,. \tag{3.85}$$

Taking into account the fact that at ρ_0 the radial velocity $\frac{\mathrm{d}r}{\mathrm{d}t}$ vanishes, the following relation is obtained:

$$\frac{L^2}{E^2} \equiv b^2 = \frac{\rho_0^2}{B(\rho_0)}. \tag{3.86}$$

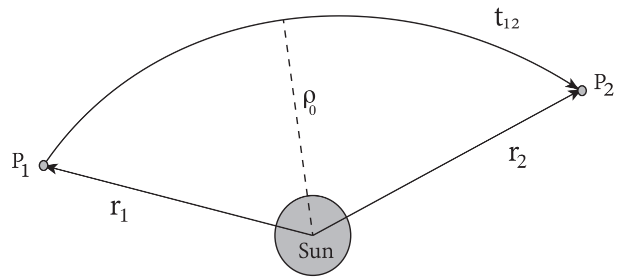

Figure 3.7: Scheme for the gravitational time delay effect. A light signal is emitted from P_1 at r_1 to P_2 at r_2 and returns to P_1. Here, ρ_0 is the closet approach to the Sun, and t_{12} is the time interval between emission and return of the pulse as measured by a clock on Earth.

Now, using Eq. (3.86) in Eq. (6.49), the coordinate time which the light requires to go from ρ_0 to r is

$$t(r,\rho_0) = \int_{\rho_0}^{r} \frac{dr}{B(r)\sqrt{1-\frac{\rho_0^2}{B(\rho_0)}\frac{B(r)}{r^2}}}. \tag{3.87}$$

So, in the first order of corrections, we get

$$t(r,\rho_0) \approx \sqrt{r^2-\rho_0^2} + t_Q + t_\lambda, \tag{3.88}$$

where

$$t_Q = \frac{3\,Q^2}{2\,\rho_0}\text{arcsec}\left(\frac{r}{\rho_0}\right), \tag{3.89a}$$

$$t_\lambda = \frac{1}{3\lambda^2}\sqrt{r^2-\rho_0^2}\left[r^2+\frac{\rho_0^2}{2}\right]. \tag{3.89b}$$

In the non-relativistic context, light travels in Euclidean space and we can calculate the time interval between emission and reception of the pulse as

$$t_{12}^E = 2\left(\sqrt{r_1^2-\rho_0^2}+\sqrt{r_2^2-\rho_0^2}\right). \tag{3.90}$$

Therefore, the expected relativistic time dilation in the journey $1 \longrightarrow 2 \longrightarrow 1$ can be defined as:

$$\Delta t := t_{12} - t_{12}^E\,, \tag{3.91}$$

which, by exploiting Eqs. (3.84) and (3.88) to (3.90), yields

$$\Delta t = \Delta t_Q + \Delta t_\lambda\,, \tag{3.92}$$

where

$$\Delta t_Q = \frac{3\,Q^2}{\rho_0}\left[\operatorname{arcsec}\left(\frac{r_1}{\rho_0}\right)+\operatorname{arcsec}\left(\frac{r_2}{\rho_0}\right)\right], \tag{3.93a}$$

$$\begin{aligned}\Delta t_\lambda = \frac{2}{3\lambda^2}\Bigg[&\sqrt{r_1^2-\rho_0^2}\left(r_1^2+\frac{\rho_0^2}{2}\right)\\ &+\sqrt{r_2^2-\rho_0^2}\left(r_2^2+\frac{\rho_0^2}{2}\right)\Bigg].\end{aligned} \tag{3.93b}$$

For a round trip in the solar system, we have ($\rho_0 \ll r_1, r_2$)

$$\begin{aligned}\Delta t_\odot \approx\ & \frac{3\,Q^2}{\rho_0}\left[\operatorname{arcsec}\left(\frac{r_1}{\rho_0}\right)+\operatorname{arcsec}\left(\frac{r_2}{\rho_0}\right)\right]\\ &+\frac{2}{3\lambda^2}\left(r_1^3+r_2^3\right).\end{aligned} \tag{3.94}$$

The above time dilation depends separately on terms relevant to the electric charge and the cosmological constant. However, the closest approach (ρ_0) only contributes to the charge-relevant terms, confirming that the electric charge has only short-distance effects, whereas the cosmological term is effective in long distance.

The time delay in propagating beams is a completely relativistic effect. In the next section and as the third test, we discuss another specific experiment, relevant to this effect.

3.2.5 The Sagnac effect

The Sagnac effect (Sagnac, 1913) is one of the most fascinating classical tests to prove the geometrical nature of gravitation, although it was firstly proposed as a disapproval of the special theory of relativity (SR). In the current era, however, the study of this phenomena is favored because of numerous interesting phenomenon, to which, it can be related. For example, it can be treated as a formal analogy of the Aharonov-Bohm effect (Sakurai, 1980; Rizzi & Ruggiero, 2003b,a; Ruggiero, 2005; Ruggiero & Tartaglia, 2014), in the sense that the standard dynamics which raise the natural splitting developed by Cattaneo (Cattaneo, 1958, 1959a,c,b; Cattaneo et al., 1963), is described in terms of analogue gravito-electromagnetic potentials. Thus, the dynamics of test particles (massive or mass-less), relative to a given time-like congruence Γ of the rotating frame of an ideal interferometer, can be written in terms of gravito-electromagnetic fields. Therefore, in a rotating frame fixed to the rotating interferometer, the contravariant and covariant components of the unit tangent vector $\gamma(\boldsymbol{x})$ to the time-like congruence Γ are given by

$$\gamma^t = 1/\sqrt{-g_{tt}}, \quad \gamma^i = 0, \tag{3.95a}$$
$$\gamma_t = -\sqrt{-g_{tt}}, \quad \gamma_i = g_{it}\gamma^t, \tag{3.95b}$$

where the index i indicates the spatial coordinates. Here $g_{\mu\nu}$ corresponds to the metric components of the (pseudo-)Riemannian manifold $\mathcal{M}$ in the rotating frame. In this way, the gravito-electromagnetic potentials are defined by (Rizzi & Ruggiero, 2004)

$$\Phi^G = -c^2\gamma^t, \tag{3.96}$$
$$A_i^G = c^2\,\frac{\gamma_i}{\gamma_t}, \tag{3.97}$$

which make it possible to calculate the gravito-magnetic Aharonov-Bohm time difference between the counter-propagating matter or light beams detected by a comoving observer, by means of the relation

$$\Delta\tau = \frac{2\gamma_t}{c^3}\int_{\mathcal{C}} \vec{A}^G \cdot \mathrm{d}\vec{\ell} = \frac{2\gamma_t}{c^3}\int_{\mathcal{S}} \vec{B}^G \cdot \mathrm{d}\vec{a}. \tag{3.98}$$

In what follows, we calculate the Sagnac effect using the above expression for the exterior spacetime of a charged Weyl black hole, considering counter-propagating beams on an equatorial plane ($\theta = \frac{\pi}{2}$) along fixed circular trajectories ($r = R$).

In order to apply this formalism, let us rewrite the CWBH metric by retrieving c in the non-rotating coordinates $x^{\alpha'} = (ct', r', \theta', \phi')$:

$$\mathrm{d}s^2 = -\left(1 - \frac{r'^2}{\lambda^2} - \frac{Q^2}{4r'^2}\right) c^2\mathrm{d}t'^2 + \frac{\mathrm{d}r'^2}{1 - \frac{r'^2}{\lambda^2} - \frac{Q^2}{4r'^2}} + +r'^2(\mathrm{d}\theta'^2 + \sin^2\theta'\,\mathrm{d}\phi'^2). \tag{3.99}$$

The transformation to the local frame of the rotating interferometer (described in $x^\alpha = (ct, r, \theta, \phi)$) is written as $x^\alpha = e^\alpha{}_{\alpha'}x^{\alpha'}$, in which

$$e^\alpha{}_{\alpha'} \equiv \frac{\partial x^\alpha}{\partial x^{\alpha'}} = \begin{pmatrix} 1 & 0 & 0 & 0 \\ 0 & 1 & 0 & 0 \\ 0 & 0 & 1 & 0 \\ -\Omega & 0 & 0 & 1 \end{pmatrix} \tag{3.100}$$

is the frame transformation Jacobian, and Ω represents the constant angular velocity of the physical system. Thus, we get

$$ct = ct', \; r = r', \; \theta = \theta', \; \phi = \phi' - \Omega t'. \tag{3.101}$$

Applying this, and letting $r = R$ and $\theta = \frac{\pi}{2}$, the line element (3.99) can be recast in x^α as

$$\mathrm{d}s^2 = -\left(1 - \frac{R^2}{\lambda^2} - \frac{Q^2}{4R^2} - \frac{R^2\Omega^2}{c^2}\right) c^2\mathrm{d}t^2 + 2\Omega R^2\mathrm{d}\phi\mathrm{d}t + R^2\mathrm{d}\phi^2. \tag{3.102}$$

Therefore, the components of the vector field $\boldsymbol{\gamma}(\boldsymbol{x})$, in the rotating frame, are given by

$$\gamma^t = \gamma_J, \quad \gamma_t = -\gamma_J^{-1}, \quad \gamma_\phi = \frac{\Omega}{\Omega_R} R\,\gamma_J, \tag{3.103}$$

with

$$\gamma_J = \frac{\Omega_R}{\sqrt{\Omega_0^2 - \Omega^2}}, \tag{3.104}$$

where Ω_0 is given by

$$\Omega_0 \equiv \sqrt{\Omega_R^2 - \Omega_\lambda^2 - \Omega_Q^2}, \tag{3.105}$$

and

$$\Omega_R \equiv \frac{c}{R}, \quad \Omega_\lambda \equiv \frac{c}{\lambda}, \quad \Omega_Q \equiv \frac{c\,Q}{2R^2}. \tag{3.106}$$

So, using the above results in Eq. (3.97), we obtain that the only non-zero component of the gravito-magnetic potential is $A_\phi^G = -c\Omega R^2\gamma_J^2$, and the proper time delay between the counter-propagating beams relative to a comoving observer on the rotating frame is given by

$$\Delta\tau = \frac{4\pi}{\Omega_R}\frac{\Omega}{\sqrt{\Omega_0^2 - \Omega^2}}. \tag{3.107}$$

The variations of this time difference in terms of Ω have been compared for three different constant spatial separations between the source and the interferometer in Fig. 3.8. As we can see, the most intense increase in $\Delta\tau$ can happen for smaller Ω for larger separations. Hence, the same time difference values can be measured in slower rotating interferometers at larger distances from the black hole, as in those with faster rotation at shorter distances. Note that, since $\Delta\tau$ must be positive, an interferometer at a specific distance from the black hole can possess only a definite range of Ω to work properly. This kind of confinement for the same range of separations and angular velocities used in Fig. 3.8 has been demonstrated in Fig. 3.9. Essentially, the functional relationship between $\Delta\tau$ and Ω is the same as that found by Hu and Wang (Hu & Wang, 2006). However, there is a natural shift in the value of the constant Ω_0 compared to the RN case. Clearly, this difference comes from the positivity of the term associated with the electric charge (given by substituting $\Omega_{\mathrm{RN}} \to \mathrm{i}\Omega_0$), and also the specific relations to R, as the radius of the circular orbits of counter-propagating beams (see Eq. (19) of the above paper). One important implication of Eq. (3.107) is that, putting aside the

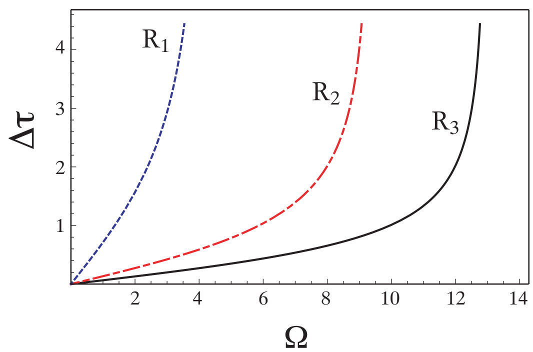

Figure 3.8: Time difference $\Delta\tau$ between the counter-propagating beams detected by a comoving observer as a function of the angular velocity Ω, for various separation distances between the source and an ideal rotating interferometer. The plots are for $R_1 = 7 \times 10^7$, $R_2 = 3 \times 10^7$ and $R_3 = 2 \times 10^7$ considering $\lambda = 2 \times 10^{10}$ and $Q = 2 \times 10^7$ (all values are in arbitrary length units).

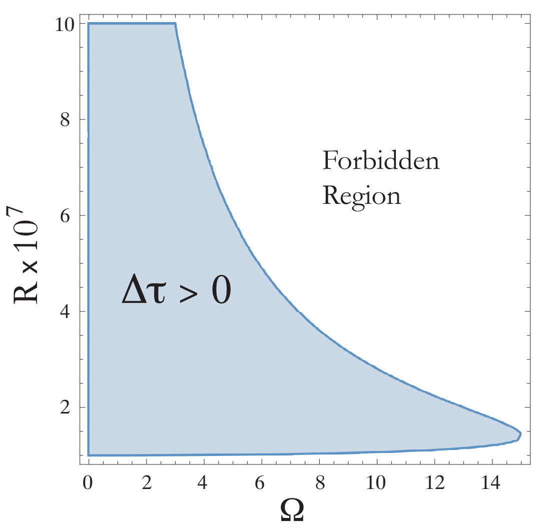

Figure 3.9: Region plot for the condition $\Delta\tau > 0$ for the separation distances between the source and the interferometer, R and the angular velocity of the comoving observer, Ω, for $\lambda = 2 \times 10^{10}$ and $Q = 2 \times 10^7$ (all values are in arbitrary length units).

Schwarzschild and the electric-charge-associated terms which are common between the RN black hole (RNBH) and the CWBH, the cosmological contribution included in Ω_λ^2 results in larger values of $\Delta\tau$ compared to the RNBH case. This indicates that, unlike the RN case, the CWBH can provide means of measuring the Sagnac effect at large distances.

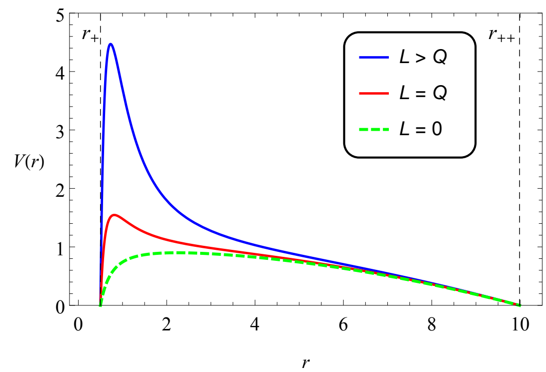

Figure 3.10: The effective potential of the CWBH, plotted for with $\lambda = 10$ and $Q = 1$, specified for particles with different designations of angular momentum. The larger the angular momentum, the more unstable is the potential's apex. The values of the horizons correspond to $r_+ \simeq 0.5$ and $r_{++} \simeq 10$.

3.3 Motion of massive particles

Considering Eqs. (3.28), (6.51) and (6.52), and taking into account $\epsilon = 1$, the effective potential for time-like geodesics is given by

$$V(r) = B(r)\left(1 + \frac{L^2}{r^2}\right), \tag{3.108}$$

which has been plotted in Fig. 3.10. As we can see, the intensity of the potentials' maximum is rather sensitive to L. The radial and angular motions of the test particles in this potential, are described by the following equations:

$$\left(\frac{\mathrm{d}r}{\mathrm{d}t}\right)^2 = \frac{B^2(r)}{E^2}\left[E^2 - V(r)\right], \tag{3.109}$$

$$\left(\frac{\mathrm{d}r}{\mathrm{d}\phi}\right)^2 = \frac{r^4}{L^2}\left[E^2 - V(r)\right]. \tag{3.110}$$

The effective potential in Eq. (3.108) is responsible for the determination of possible orbits around the black hole. In the next subsection, we will discuss the possible orbits in this potential, by presenting direct analytical solutions of the angular equations of motion.

3.3.1 Angular Motion

In general, the most common trajectories followed by particles as they approach the black hole, are angular trajectories ($L \neq 0$). Once again, we drag the reader's attention

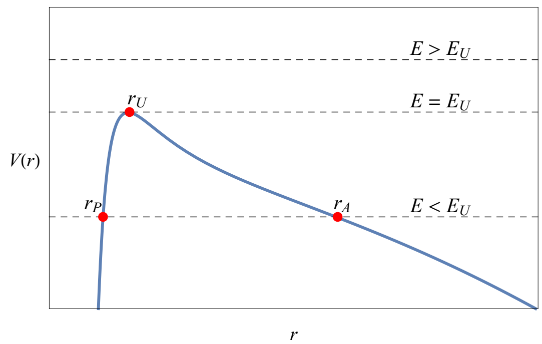

Figure 3.11: The effective potential for test particles with angular momentum. Based on the values of E, several turning points (approaches) are available. These include the radius of unstable circular orbits r_U, and two other points, r_P and r_A. At these turning points, we have $E^2 = V(r_t)$.

to the radial behavior of the effective potential, as illustrated in Fig. 3.24. Corresponding to the values of E, the turning points r_t relate to different kinds of orbits and they satisfy $E^2 = V(r_t)$. To determine these points, we should take care of their relevant orbital conditions. In fact, according to Fig. 3.24, three turning points are denoted; $r_t = r_U$ (for unstable circular orbits), $r_t = r_P$ (the smallest orbital separation) and $r_t = r_A$ (the largest orbital separation). In the forthcoming subsections, we ramify the relevant orbital conditions of approaching test particles and determine the mentioned turning points in accordance with each particular type of motion. We begin with discussing the potential's maximum and its relevant quantities. Afterwards, other kinds of orbits are studied.

Unstable circular orbits

According to Fig. 3.24, the effective potential offers instability at its maximum, where $V'(r) = 0$. Form Eq. (3.108), this generates

$$L^2Q^2 - \left(2L^2 - \frac{Q^2}{2}\right) r^2 - \frac{2}{\lambda^2} r^6 = 0, \tag{3.111}$$

which is an equation of sixth order. Applying the Cardano's method, we can obtain three different radii for the unstable circular orbits, by solving Eq. (3.236). Let us explain the method.

Equation (3.236) can be reduced into an equation of the third order, by applying the change of variable $X \doteq r^2$. Accordingly, the reduced equation becomes

$$4X^3 + a_1 X - a_2 = 0, \tag{3.112}$$

in which we have used

$$a_1 = 4\lambda^2\left(L^2 - \frac{Q^2}{4}\right), \tag{3.113}$$

$$a_2 = 2\lambda^2 L^2 Q^2. \tag{3.114}$$

For $a_1 = 0$ (i.e. $L = \frac{Q}{2}$), the equation is easily solved as $X^3 = a_2/4$. Since always $a_2 > 0$, the general form of the equation only varies depending on the sign of a_1. Accordingly, we compare Eq. (3.112) by two hyperbolic identities

$$4\sinh^3\vartheta + 3\sinh\vartheta - \sinh(3\vartheta) = 0, \tag{3.115}$$

$$4\cosh^3\vartheta - 3\cosh\vartheta - \cosh(3\vartheta) = 0. \tag{3.116}$$

The following two cases are available:

- For $L > \frac{Q}{2}$: Since $(a_1, a_2) > 0$, then defining $X \doteq \Xi_0 \sinh\vartheta$, we recast Eq. (3.112) as

$$\ell\,\Xi_0^3\sinh^3\vartheta + a_1\ell\,\Xi_0\sinh\vartheta - a_2\,\ell = 0, \tag{3.117}$$

  in which, ℓ is a Legendre coefficient. Comparing Eqs. (3.117) and (3.115), we get

$$\ell = \frac{4}{\Xi_0^3}, \tag{3.118a}$$

$$\Xi_0 = \sqrt{\frac{4a_1}{3}}, \tag{3.118b}$$

$$\sinh(3\vartheta) = \sqrt{\frac{27a_2^2}{4a_1^3}} \doteq \Xi_1. \tag{3.118c}$$

  It is therefore inferred that $\vartheta = \frac{1}{3}\text{arcsinh}\,\Xi_1$, resulting in

$$X = \Xi_0\sinh\left(\frac{1}{3}\arcsin\,\Xi_1\right). \tag{3.119}$$

- For $L < \frac{Q}{2}$: This time, since $a_1 < 0$ and $a_2 > 0$, the comparison is made to Eq. (3.116), by means of the definition $X \doteq \Xi_0\cosh\vartheta$. Pursuing the same procedure as the previous case, we obtain

$$X = \Xi_0\cosh\left(\frac{1}{3}\text{arccosh}(\Xi_1)\right). \tag{3.120}$$

Applying the above method and by appropriate substitutions, we obtain the three solutions

$$r_U = \left(\Xi_0 \sinh\left[\frac{1}{3}\text{arcsinh}(\Xi_1)\right]\right)^{\frac{1}{2}}, \qquad L > \frac{Q}{2} \tag{3.121}$$

$$r_U = \left(\frac{Q^4\lambda^2}{8}\right)^{\frac{1}{6}}, \qquad L = \frac{Q}{2} \tag{3.122}$$

$$r_U = \left(\Xi_0 \cosh\left[\frac{1}{3}\text{arccosh}(\Xi_1)\right]\right)^{\frac{1}{2}}, \qquad L < \frac{Q}{2} \tag{3.123}$$

to Eq. (3.236), where

$$\Xi_0 = 4\lambda\sqrt{\frac{|L^2 - Q^2/4|}{3}}, \tag{3.124}$$

$$\Xi_1 = \frac{3Q^2L^2}{8\lambda}\sqrt{\frac{3}{|L^2 - Q^2/4|^3}}. \tag{3.125}$$

One can also calculate the period of the above orbits, measured by the test particles (proper period) and a distant observer (coordinate period) (Chandrasekhar, 1998). In the same way as we pursued in subsection 3.2.2, one can obtain the following relations for a long term circular orbit:

$$\Delta\tau_U = \frac{r_U^2}{L_U}\,\Delta\phi_U, \tag{3.126}$$

$$\Delta t_U = \frac{E_U}{L_U}\,\frac{r_U^2}{B(r_U)}\,\Delta\phi_U. \tag{3.127}$$

For one complete orbit, we have $\Delta\phi_U = 2\pi$, and we define the proper and coordinate periods as

$$T_\tau = \frac{2\pi\, r_U^2}{L_U}, \tag{3.128}$$

$$T_t = \frac{2\pi\, r_U^2 E_U}{B(r_U)L_U}. \tag{3.129}$$

The expression for L_U is calculated by solving Eq. (3.236) for the angular momentum at the fixed circular radius r_U. We have

$$L_U = \frac{1}{\sqrt{2}}\sqrt{\frac{4r_U^4 - Q^2\lambda^2}{\frac{Q^2\lambda^2}{r_U^2} - 2\lambda^2}}. \tag{3.130}$$

This, together with the condition $E_U^2 = V(r_U)$ at the distance r_U, provides

$$T_\tau = 2\pi\lambda\, r_U\sqrt{\frac{4r_U^2 - 2Q^2}{Q^2\lambda^2 - 4r_U^4}}, \tag{3.131}$$

$$T_t = \frac{4\pi\lambda\, r_U^2}{\sqrt{\lambda^2 Q^2 - 4r_U^4}}. \tag{3.132}$$

Further in this section, we will discuss the critical trajectories corresponding to the above radii of unstable orbits. However for now, let us continue our discussion by studying the hyperbolic motions around the black hole.

Orbits of the first kind and the scattering zone

In the case that, for orbiting test particles, the condition $E < E_U$ is satisfied, they can approach the black hole at two distinct points. Referring to Fig. 3.24, these points are determined by $r_t = r_P$ and $r_t = r_A$, at which $\frac{\mathrm{d}r}{\mathrm{d}\phi}|_{r_t} = 0$ or $E^2 = V(r_t)$. The angular equation of motion in Eq. (3.110) can be recast as

$$\left(\frac{\mathrm{d}r}{\mathrm{d}\phi}\right)^2 = \frac{r^6 - \alpha\, r^4 - \beta\, r^2 + \gamma}{L^2\lambda^2} \equiv \frac{\mathfrak{P}(r)}{L^2\lambda^2}, \tag{3.133}$$

where

$$\alpha = \lambda^2(1 - E^2) - L^2, \tag{3.134a}$$

$$\beta = \lambda^2(L^2 - Q^2), \tag{3.134b}$$

$$\gamma = \lambda^2 L^2 Q^2. \tag{3.134c}$$

The determination of the turning points r_P and r_A can be done by solving $\mathfrak{P}(r_t) = 0$ which is again an equation of sixth order and can be solved by means of the Cardano's method. The equation $\mathfrak{P}(r) = 0$ produces

$$X^3 - \alpha X^2 - \beta X + \gamma = 0, \tag{3.135}$$

where $X \doteq r^2$. Now performing the Tschirnhaus transformation $S = X - \frac{\alpha}{3}$, we get

$$S^3 - \bar{a}_1 S - \bar{a}_2 = 0, \tag{3.136}$$

in which

$$\bar{a}_1 = \frac{4}{3}\left(\alpha^2 + 3\beta\right), \tag{3.137a}$$

$$\bar{a}_2 = 4\left(\frac{2\alpha^3}{27} + \frac{\alpha\beta}{3} - \gamma\right). \tag{3.137b}$$

Considering the trigonometric identity

$$4\cos^3\vartheta - 3\cos\vartheta - \cos(3\vartheta) = 0, \tag{3.138}$$

we define $S = \xi_0 \cos\vartheta$ and recast Eq. (3.136) as

$$\ell\,\xi_0^3 \cos^3\vartheta - \ell\,\bar{a}_1 \xi_0 \cos\vartheta - \ell\,\bar{a}_2 = 0. \tag{3.139}$$

As in the previous cases, comparing the above equations we obtain

$$\xi_0 = 2\sqrt{\frac{\beta}{3} + \frac{\alpha^2}{9}}, \tag{3.140a}$$

$$\xi_1 = \left(\frac{8\alpha^3}{9} + 4\alpha\beta - 12\gamma\right)\sqrt{\frac{3}{(4\beta + \frac{4\alpha^2}{3})^3}}, \tag{3.140b}$$

where $2n\pi$ indicates the periodic symmetry of the cosine function. Accordingly, and using the reverse transformations, the solutions to $\mathfrak{P}(r)$ can be given as

$$r_n = \left[\xi_0 \cos\left(\frac{1}{3}\arccos\xi_1 + \frac{2n\pi}{3}\right) + \frac{\alpha}{3}\right]^{\frac{1}{2}}. \tag{3.141}$$

The above solution results in positive values for $n = 0, 2$ and is periodically repeated as $n \to n+3$. We can therefore take two different values as physically meaningful solutions to our equation, by designating $r_A = r_{n=0}$ and $r_P = r_{n=2}$ which is in agreement with $r_A > r_P$. This procedure results in

$$r_A = \left(\xi_0 \cos\left[\frac{1}{3}\arccos\xi_1\right] + \frac{\alpha}{3}\right)^{1/2}, \tag{3.142}$$

$$r_P = \left(\xi_0 \cos\left[\frac{1}{3}\arccos\xi_1 + \frac{4\pi}{3}\right] + \frac{\alpha}{3}\right)^{1/2}. \tag{3.143}$$

Particles reaching r_A can experience a hyperbolic OFK which has the significance of scattering. To find the explicit angular equation of motion for this process, we directly integrate Eq. (3.244). In fact, the change of variables applied in solving $\mathfrak{P}(r) = 0$ can not make a simple reduction of order to solve the differential equation in Eq. (3.244). This kind of definition provides a fourth order elliptic integral equation which, although doable, is hard to solve. We therefore propose a more efficient method for this particular case. Since the scattering happens at r_A, we instead, define the following non-linear change of variable:

$$x \doteq \left(\frac{r_A}{r}\right)^2, \tag{3.144}$$

producing $\mathrm{d}r = -r_A\left(\frac{\mathrm{d}x}{2x^{\frac{3}{2}}}\right)$, which reduces Eq. (3.244) to

$$\mathrm{d}\phi = \pm L\lambda \frac{-r_A\,\mathrm{d}x}{2\sqrt{\gamma\,\tilde{\mathfrak{P}}(x)}}, \tag{3.145}$$

in which

$$\gamma\,\tilde{\mathfrak{P}}(x) \equiv x^3\mathfrak{P}(x) = \gamma\left(x^3 - \tilde{\alpha}x^2 - \tilde{\beta}x + \tilde{\gamma}\right), \tag{3.146}$$

where

$$\tilde{\alpha} = \frac{\beta\, r_A^2}{\gamma}, \tag{3.147a}$$

$$\tilde{\beta} = \frac{\alpha\, r_A^4}{\gamma}, \tag{3.147b}$$

$$\tilde{\gamma} = \frac{r_A}{\gamma}. \tag{3.147c}$$

A further change of variable

$$u \doteq \frac{1}{4}\left(x - \frac{\tilde{\alpha}}{3}\right), \tag{3.148}$$

leads to the following reduced integral form of Eq. (3.145):

$$\int_{\phi_0}^{\phi} \mathrm{d}\phi' = \pm\frac{2\sqrt{\gamma}}{L\lambda\, r_A}\int_{u_A}^{u} \frac{-\mathrm{d}u'}{\sqrt{\mathfrak{P}(u')}}, \tag{3.149}$$

in which $u_A = \frac{1}{4}(1 - \frac{\beta\, r_A^2}{3\gamma})$, and

$$\mathfrak{P}(u) = 4u^3 - g_2 u - g_3, \tag{3.150}$$

where

$$g_2 = \frac{1}{4}\left(\frac{\tilde{\alpha}}{3} + \tilde{\beta}\right), \tag{3.151a}$$

$$g_3 = \frac{1}{16}\left(\frac{2\tilde{\alpha}^3}{27} + \frac{\tilde{\alpha}\,\tilde{\beta}}{3} - \tilde{\gamma}\right), \tag{3.151b}$$

are the Weierstraß coefficients, associated with the third order polynomial $\mathfrak{P}(u)$. Recasting Eq. (3.149), we have

$$\pm\frac{2\sqrt{\gamma}}{L\lambda\, r_A}(\phi - \phi_0) = -\left\{\int_{u_A}^{\infty} \frac{\mathrm{d}u'}{\sqrt{\mathfrak{P}(u')}} - \int_{u}^{\infty} \frac{\mathrm{d}u'}{\sqrt{\mathfrak{P}(u')}}\right\} = -\left\{ß(u_A) - ß(u)\right\}. \tag{3.152}$$

Accordingly, using the values of $\tilde{\gamma}$ and γ, and defining $\varphi_A = ß(u_A)$, from Eq. (3.152) we deduce

$$u(\phi) = \frac{1}{4}\left(\frac{r_A^2}{r^2(\phi)} - \frac{\beta\, r_A^2}{3\gamma}\right) = \wp\left(\pm\frac{2\sqrt{\gamma}}{L\lambda\, r_A}(\phi_0 - \phi) + \varphi_A\right), \tag{3.153}$$

which for $\phi_0 = 0$ results in the solution

$$r(\phi) = \frac{r_A}{\sqrt{4\wp(\varphi_A - \kappa_A\,\phi) + \frac{\beta r_A^2}{3\gamma}}}, \tag{3.154}$$

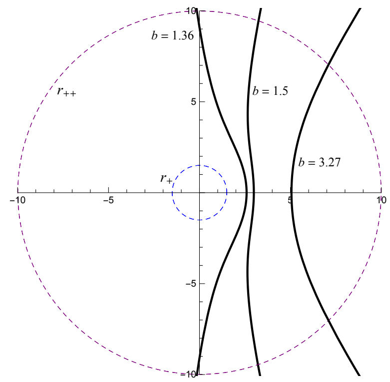

Figure 3.12: Scattering of particles for different impact parameters $b = 1.36, 1.5$ and 3.27. It is observed that the scattering process can be attractive or repulsive, depending on the impact parameter. The plots have been done for $Q = 1$ and $\lambda = 10$.

where

$$\kappa_A = \frac{2Q}{r_A}, \tag{3.155a}$$

$$\varphi_A = ß\left(\frac{1}{4} - \frac{\beta r_A^2}{12\gamma}\right). \tag{3.155b}$$

The OFK for particles around the CWBH has been plotted in Fig. 3.25, which has been classified in terms of the impact parameter b, associated with the trajectories. we can see that the lower b is, the more the trajectories are inclined to the black hole during their scattering.

The scattering angle

During the scattering process, the particles experience an escape to the infinity. Let us consider the scheme in Fig. 3.13. The particles commence their approach to the black hole at point e and the scattered particles recede to infinity at point s, which are characterized respectively by $e(r_e, \phi_e, b)$ and $s(r_s, \phi_s, b)$. Letting $r(\phi)|_{\phi=0} = r_A$, the shortest distance to the black hole is taken to be r_A, at which the scattering happens. According to the figure, and in the same way we obtained the lens equation in subsection 3.2.3, we have

$$\delta = \pi - \Theta = \phi_e - \psi_e + |\phi_s| - |\psi_s|. \tag{3.156}$$

Any angle $\phi(r)$ observed by the moving particles in this kind of motion, is obtained by reversing Eq. (3.154), giving

$$\phi(r) = \frac{1}{\kappa_A}\left[ß\left(\frac{1}{4} - \frac{\beta r_A^2}{3\gamma}\right) - ß\left(\frac{r_A^2}{4r^2} - \frac{\beta r_A^2}{12\gamma}\right)\right]. \tag{3.157}$$

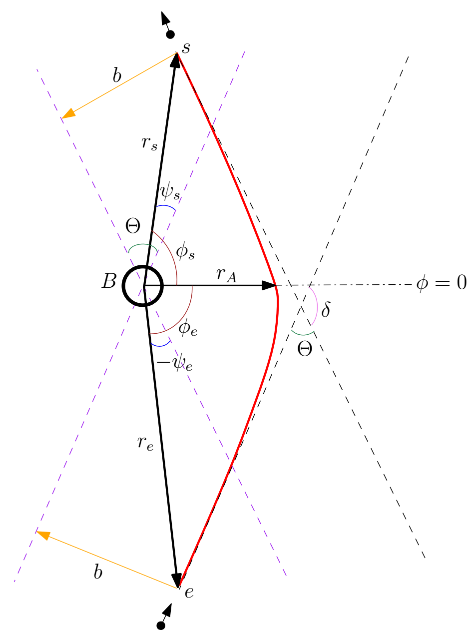

Figure 3.13: A schematic illustration of the scattering phenomena. The shortest distance to the black hole B, has been taken to be r_A, lying on the $\phi = 0$ line. The incident and the scattered particles are located respectively at $e(r_e, \phi_e, b)$ and $s(r_s, \phi_s, b)$.

Furthermore, according to the figure, it is easily inferred that

$$\psi_e = \Theta - \arcsin\left(\frac{b}{r_e}\right), \tag{3.158}$$

$$|\psi_s| = \Theta - \arcsin\left(\frac{b}{r_s}\right). \tag{3.159}$$

Assuming that the incident particles are coming from infinity and escaping to infinity, we have $\psi_e = |\psi_s| = \Theta$ and $\phi_e = |\phi_s| = \phi(\infty) \equiv \phi_\infty$. At this limit we can recast Eq. (3.156) as $\Theta = 2\phi_\infty - \pi$, for which, applying Eq. (3.157), we obtain the scattering angle as

$$\Theta = \frac{2}{\kappa_A}\left[ß\left(\frac{1}{4} - \frac{\beta\, r_A^2}{12\gamma}\right) - ß\left(-\frac{\beta\, r_A^2}{12\gamma}\right)\right] - \pi. \tag{3.160}$$

The evolution of the scattering angle has been plotted in Fig. 3.14 which has an asymptotic behavior as $E \to E_U$.

The differential cross section

Regarding the spherical symmetry of our problem, the angle Θ obtained above, indeed measures the deflection angle between the incident and the scattered beams, that together with the azimuth angle ϕ, can construct the solid angle element $\mathrm{d}\Omega =$

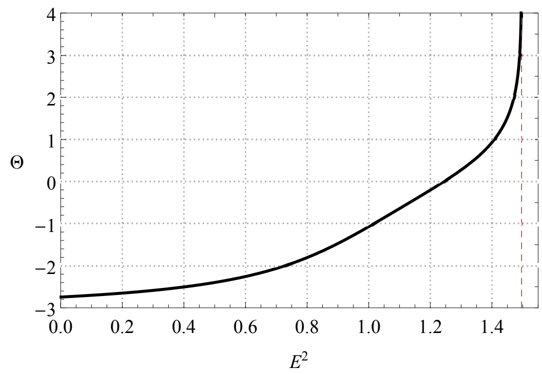

Figure 3.14: The behavior of Θ in terms of E^2, demonstrated for $L = 2$, $Q = 1$ and $\lambda = 10$. As it is expected, the scattering angle reaches its limit as E tends to E_U which in this case is around 1.496.

$\sin\Theta\,\mathrm{d}\Theta\,\mathrm{d}\phi$ as the differential angular range of the scattered particles at angle Θ. Furthermore, since the impact parameter b is perpendicular to the incoming and scattered trajectories, one can define the scattering cross section σ as the area covered by the scattered particles in the plane of b. This way, σ has the differential size $\mathrm{d}\sigma = b\,\mathrm{d}\phi\,\mathrm{d}b$. The differential cross section can be then expressed as

$$\sigma(\Theta) \doteq \frac{\mathrm{d}\sigma}{\mathrm{d}\Omega} = \frac{b}{\sin\Theta}\left|\frac{\partial b}{\partial\Theta}\right|. \tag{3.161}$$

In fact, from Eq. (3.160) we have

$$\frac{\kappa_A}{2}(\Theta+\pi) = \varphi_{A_0} + \varphi_{A_1}, \tag{3.162}$$

in which

$$\varphi_{A_0} \doteq \text{ß}\left(\frac{1}{4} - \frac{\beta\, r_A^2}{12\gamma}\right), \tag{3.163a}$$

$$\varphi_{A_1} \doteq -\text{ß}\left(-\frac{\beta\, r_A^2}{12\gamma}\right). \tag{3.163b}$$

We define

$$\Psi(L) \doteq \wp\left(\frac{\kappa_A}{2}(\Theta+\pi)\right) = \wp\left(\varphi_{A_0} + \varphi_{A_1}\right), \tag{3.164}$$

where (Byrd & Friedman, 1971)

$$\Psi(L) = \frac{1}{4}\left[\frac{\wp'(\varphi_{A_0}) - \wp'(\varphi_{A_1})}{\wp(\varphi_{A_0}) - \wp(\varphi_{A_1})}\right]^2 - \wp(\varphi_{A_0}) - \wp(\varphi_{A_1}). \tag{3.165}$$

Note that, using the definition in Eq. (3.260), we can recast Eq. (3.161) as

$$\sigma(\Theta) = b\csc\Theta\left|\frac{\partial\Psi}{\partial\Theta}\right|\left|\frac{\partial b}{\partial\Psi}\right| = \frac{\kappa_A}{4}\csc\Theta\left|\wp'\left(\frac{\kappa_A}{2}(\theta+\pi)\right)\right|\left|\frac{\partial b^2}{\partial\Psi}\right|, \tag{3.166}$$

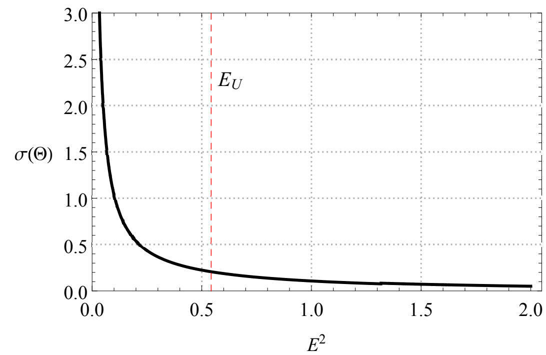

Figure 3.15: The evolution of $\sigma(\Theta)$ in terms of E^2, plotted for $L = 0.8$, $Q = 0.5$ and $\lambda = 0.6$. For these values, $E_U^2 \approx 0.54$.

for which, considering $\frac{\partial b^2}{\partial \Psi} = \frac{\partial b^2/\partial L}{\partial \Psi/\partial L}$, we finally obtain

$$\sigma(\Theta) = \frac{\kappa_A L}{2E^2} \csc\Theta \left|\wp'\left(\frac{\kappa_A}{2}(\theta+\pi)\right)\right| \left|\frac{\partial \Psi}{\partial L}\right|^{-1}. \tag{3.167}$$

The complexity of the relation of $\Psi(L)$, makes the resultant expression of $\sigma(\Theta)$ rather large and complicated. We however, have demonstrated the behavior of this function in Fig. 3.15, in terms of the quantity E^2. We have considered smaller values for the constants to be able to generate a more perceptible plot. Note that, there is an asymptotic behavior as $E \to 0$, and $\sigma(\Theta)$ tends to zero, soon after E passes E_U.

Radial acceleration

The equation of motion for the radial coordinate in Eq. (3.28), beside demonstrating the way through which the particles approach the black hole, can also provide information on the Newtonian centripetal effective force acting on the particles. This force is indeed indicated by the radial acceleration a_r which is defined as $a_r \equiv \ddot{r}$ in terms of the radial coordinate. Using Eq. (3.28) for the effective potential (3.108), we have

$$a_r = -\frac{1}{2}V'(r) = -\frac{L^2Q^2}{2r^5} + \frac{L^2 - \frac{Q^2}{4}}{r^3} + \frac{r}{\lambda^2}. \tag{3.168}$$

Introducing $r_{\max}$ and $r_{\min}$, respectively as the turning points where a_r reaches its maximum and minimum (by satisfying $\partial_r a_r = 0$), we obtain

$$r_{\max} = \left(\eta_0 \cos\left[\frac{1}{3}\arccos\eta_1\right]\right)^{1/2}, \tag{3.169}$$

$$r_{\min} = \left(\eta_0 \cos\left[\frac{1}{3}\arccos(\eta_1) + \frac{4\pi}{3}\right]\right)^{1/2}, \tag{3.170}$$

where

$$\eta_0 = 2\lambda\sqrt{L^2 - \frac{Q^2}{4}}, \tag{3.171a}$$

$$\eta_1 = -\frac{5L^2Q^2}{4\lambda}\left(L^2 - \frac{Q^2}{4}\right)^{-\frac{3}{2}}, \tag{3.171b}$$

and are valid only for $Q < 2L$. These distances have the identical value r_L (corresponding to $\eta_1 = \pm 1$), when the angular momentum approaches the value L_0 given by

$$L_0 = \sqrt{\chi_1 + \chi_2 \cosh\left[\frac{1}{3}\text{arccosh}\left[\frac{\chi_3}{\chi_2^3}\right]\right]}, \tag{3.172}$$

where

$$\chi_1 = \frac{9Q^2}{4}, \tag{3.173a}$$

$$\chi_2 = \frac{20Q}{8\sqrt{3}\,\lambda}, \tag{3.173b}$$

$$\chi_3 = \frac{25Q^4}{1024\lambda^2}. \tag{3.173c}$$

The equality $r_{\text{max}} \equiv r_{\text{min}} = r_L$ has been shown in Fig. 7.5, where we have plotted a_r for three different values of L. In accordance with the values chosen in the figure, the $L = 0.14$ curve has only one extremum corresponding to $r_L \approx 0.31$. In this case, the test particles will experience a constant effective force towards the black hole while traveling on their trajectories.

So far, we have scrutinized the OFK for particles approaching from r_A. However, altering this point the OSK happens as we will discuss next.

Orbits of the second kind

Once the approaching point to the black hole coincides with the turning point r_P in Eq. (3.143) ($r_+ < r_P < r_U$), the OSK occurs. Pursuing the same method, applied in deriving the equation of motion for the OFK, we obtain

$$r(\phi) = \frac{r_P}{\sqrt{4\wp(\varphi_P + \kappa_P\phi) + \frac{\beta r_P^2}{3\gamma}}}, \tag{3.174}$$

with the corresponding Weierstraß coefficients

$$g_{22} = \frac{r_P^4}{4}\left[\frac{\beta^2}{3\gamma^2} + \frac{\alpha}{\gamma}\right], \tag{3.175a}$$

$$g_{33} = \frac{r_P^6}{16}\left[\frac{2\beta^3}{27\gamma^3} + \frac{\alpha\beta}{3\gamma^2} - \frac{1}{\gamma}\right], \tag{3.175b}$$

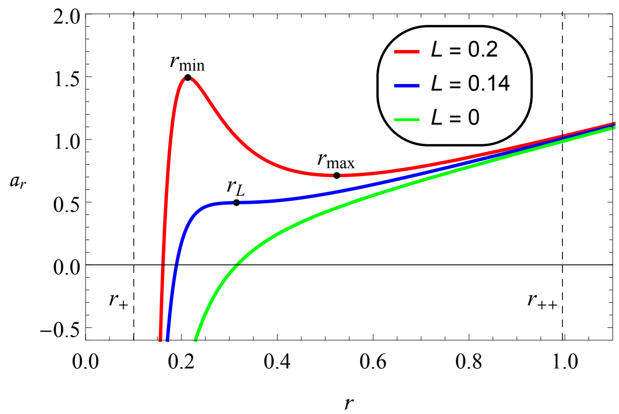

Figure 3.16: The evolution of the radial acceleration $a_r \equiv \ddot{r}$ inside the casual region $r_+ < r < r_{++}$ plotted for $Q = 0.2$, $\lambda = 1$ and three different values of L. The case of $L = 0.2$ has two extremums at $r_{\min} \approx 0.21$ and $r_{\max} \approx 0.52$. The case of $r_{\min} = r_{\max} = r_L$ happens for $L = 0.14$ where $r_L \approx 0.31$.

and

$$\kappa_P = \frac{2Q}{r_P}, \tag{3.176a}$$

$$\varphi_P = ß\left(\frac{1}{4} - \frac{\beta r_P^2}{12\gamma}\right). \tag{3.176b}$$

In Fig. 7.7 we have demonstrated the OSK for particles with three different impact parameters. The larger the impact parameter is, the more the trajectories need to curve in their final segment, before their in-fall to the black hole.

Now that the deflecting trajectories have been discussed, we will pay attention to the case that the particles' impact parameter raise to that of unstable circular orbits.

Critical trajectories

In the case of $E = E_U$, the particles can be confined on unstable circular orbits of the radius r_U. This kind of motion is indeed ramified into two cases; critical trajectories of the first kind (CFK) in which the particles come from a distant position $\tilde{R}$ to r_U and those of the second kind (CSK) where the particles start from an initial point $\tilde{R}_0$ at the vicinity of r_U and then tend to this radius by spiraling. Applying the angular equation of motion and pursuing the same methods as in the case of deflecting trajectories, we obtain the following equations of motion for the aforementioned trajectories:

$$r_I(\phi) = \frac{\tilde{R}}{\sqrt{(1 + \frac{\tilde{R}^2}{r_U^2}) \tanh^2(\varphi_{C_1} + \kappa_C \phi) - 1}} \tag{3.177}$$

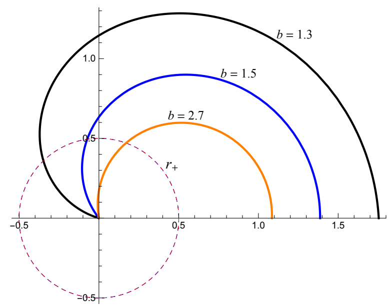

Figure 3.17: Orbits of the second kind for particles approaching the black hole at $r = r_P$, for three different impact parameters, $b = 1.3, 1.5$ and 2.7. As we can see, smaller impact parameters in this kind of orbit result in larger paths for the orbiting particles before their fall into the event horizon, and therefore, a more intense change in the shape of orbit in the final segment. The plots have been done for $Q = 1$ and $\lambda = 10$.

for the CFK, and

$$r_{II}(\phi) = \frac{\tilde{R}_0}{\sqrt{(1+\frac{\tilde{R}_0^2}{r_U^2})\tanh^2(\varphi_{C_2}+\kappa_C\phi)-1}} \tag{3.178}$$

for the CSK. Here,

$$\kappa_C = \frac{r_U\sqrt{\tilde{R}^2+r_U^2}}{\lambda L}, \tag{3.179a}$$

$$\varphi_{C_1} = \operatorname{arctanh}\left(\frac{r_U}{\sqrt{\tilde{R}^2+r_U^2}}\right), \tag{3.179b}$$

$$\varphi_{C_2} = \operatorname{arctanh}\left(\frac{r_U\sqrt{\tilde{R}^2+\tilde{R}_0^2}}{\tilde{R}_0\sqrt{\tilde{R}^2+r_U^2}}\right). \tag{3.179c}$$

In Fig. 3.18, the CFK and CSK have been demonstrated in a single figure to indicate their difference in approach to the region of the circular orbits.

Capture zone

In addition to the OSK, terminating orbits can also occur when the value of E for the approaching particles exceeds that of unstable circular orbits; i.e. $E > E_U$. If we consider approaching particles with the same angular momentum, this corresponds to particles with $b < b_U$, where $b_U = \frac{L_U}{E_U}$ is the critical impact parameter possessed by particles traveling on the unstable circular orbits. The equation of captured trajectories is similar to that for the deflecting trajectories and is obtained by replacing r_A or r_P by a

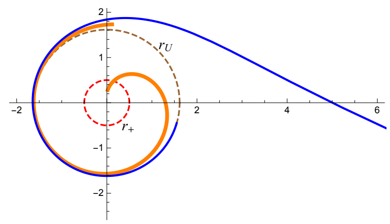

Figure 3.18: The critical trajectories $r_I(\phi)$ (blue) and $r_{II}(\phi)$ (orange) plotted for $Q = 1$, $\lambda = 10$ and $L = 2$. For this values, $E_U \approx 1.5$ and $r_U \approx 1.6$ and the trajectories have been plotted for $\tilde{R} \approx 7.67$ and $\tilde{R}_0 = 1.3$.

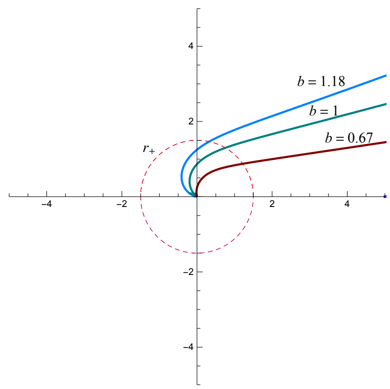

Figure 3.19: The captured trajectories for particles approaching from $r_0 = 5$, plotted for $Q = 1$, $\lambda = 10$ and $L = 2$. Accordingly, the critical impact parameter is $b_U \approx 2$ and the trajectories plotted here correspond to $b = 1.18, 1$ and 0.67.

constant initial distance, say r_0, as an arbitrary starting point. This kind of motion, has been plotted in Fig. 3.19 for three different impact parameters in the allowed range.

3.3.2 Radial Trajectories

In this subsection, a similar phenomenon, as studied in subsection 3.2.1 will be studied for radially moving massive particles in the exterior geometry of the CWBH.

The radial motion of particles is characterized by the condition $L = 0$, for which the effective potential reduces to

$$V_r(r) = 1 - \frac{r^2}{\lambda^2} - \frac{Q^2}{4r^2}. \tag{3.180}$$

which allows a maximum at $r_u = \sqrt{\frac{Q\lambda}{2}}$, having the value

$$V_r(r_u) \equiv E_u^2 = 1 - \frac{Q}{\lambda}. \tag{3.181}$$

Before going any further, let us ramify the types of possible radial motions, based on the value of E^2 compared with the above E_u^2.

- *Frontal scattering*: When $E < E_u$, particles approaching the black hole from a finite distance, are diverted at r_a (or r_p) towards the black hole's horizons. Since no angular motion is considered for the particles, this kind of scattering is completely frontal.

- *Critical radial motion*: For $E = E_u$, particles can stay on an unstable radial distance of radius $r = r_u$. Therefore, particles coming from an initial distance r_i or d_i ($r_u < r_i < r_{++}$ and $r_+ < d_i < r_u$) will ultimately fall on r_u.

- *Radial capture*: If $E > E_u$, particles coming from a finite distance ρ_0 ($r_+ < \rho_0 < r_{++}$), are pulled towards the horizons from the same distance.

We will study these types of radial trajectories which are classified in terms of E. For now, let us rewrite the radial velocity relations given in Eqs. (3.28) and (3.109) as

$$\left(\frac{\mathrm{d}r}{\mathrm{d}\tau}\right)^2 = \frac{r^4 + (E^2-1)\lambda^2 r^2 + \frac{Q^2\lambda^2}{4}}{\lambda^2 r^2} \equiv \frac{\mathfrak{p}(r)}{r^2}, \tag{3.182}$$

$$\left(\frac{\mathrm{d}r}{\mathrm{d}t}\right)^2 = \frac{(r^2-r_+^2)^2(r_{++}^2-r^2)^2\,\mathfrak{p}(r)}{E^2\lambda^4 r^6}. \tag{3.183}$$

These are the key relations in scrutinizing the radial trajectories of different kinds. As before, the possible motions are studied regarding the time measurements done by observers comoving with the trajectories (τ) and distant observers (t).

Frontal scattering

Two turning points are available at either sides of r_u, namely $r_p < r_u < r_a$ (see Fig. 7.4). Since they are turning points, these distances are identified by solving $\mathfrak{p}(r) = 0$, from which we obtain

$$r_p = \lambda\sqrt{1-E^2}\,\sin\left(\frac{1}{2}\arcsin\left(\frac{1-E_u^2}{1-E^2}\right)\right), \tag{3.184}$$

$$r_a = \sqrt{1-E^2}\,\cos\left(\frac{1}{2}\arcsin\left(\frac{1-E_u^2}{1-E^2}\right)\right). \tag{3.185}$$

In the case of $E = 0$, the above radial distances tend to the event and cosmological horizons. In Fig. 7.4, the effective potential $V_r(r)$ has been plotted, where the extremum r_u and the turning points r_p and r_a are indicated. Since these turning points are solutions

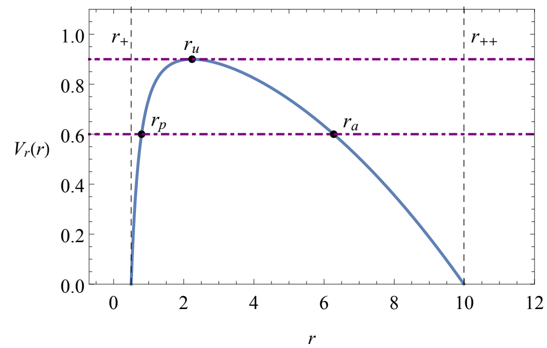

Figure 3.20: The effective potential for radial trajectories plotted for $Q = 1$ and $\lambda = 10$. The radial distances r_u, r_p and r_a have been indicated.

to $\mathfrak{p}(r) = 0$, we can therefore rewrite Eq. (6.58) as

$$\left(\frac{\mathrm{d}r}{\mathrm{d}\tau}\right)^2 = \frac{(r^2 - r_a^2)(r^2 - r_p^2)}{r^2} \equiv \frac{\mathfrak{p}_s(r)}{\lambda^2 r^2}, \tag{3.186}$$

which implies $\mathfrak{p}(r) = \frac{\mathfrak{p}_s(r)}{\lambda^2}$. The first kind of scattering, happens when the particles approach at r_a. Let us assume that for comoving and distant observers, the particles are at $r = r_a$, when $\tau = t = 0$. Accordingly, exploiting Eqs. (3.186) and (6.59), we obtain the following radial dependencies for the time parameters:

$$\tau(r) = \frac{\lambda}{2} \ln\left|\frac{2\left(\sqrt{\mathfrak{p}_s(r)} + r^2\right) - (1 - E^2)}{2r_a^2 - (1 - E^2)}\right| \tag{3.187}$$

for the comoving, and

$$t(r) = \frac{\lambda^3 E}{2(r_{++}^2 - r_+^2)}\left[\frac{r_{++}^2 \ln|F_1(r)|}{\sqrt{\mathfrak{p}_s(r_{++})}} - \frac{r_+^2 \ln|F_2(r)|}{\sqrt{\mathfrak{p}_s(r_+)}}\right] \tag{3.188}$$

for the distant observers, where

$$F_1(r) = \frac{(r_{++}^2 - r_a^2)}{(r_{++}^2 - r^2)}\frac{F_{++}(r)}{F_{++}(r_a)}, \tag{3.189a}$$

$$F_2(r) = \frac{(r_a^2 - r_+^2)}{(r^2 - r_+^2)}\frac{F_+(r)}{F_+(r_a)}, \tag{3.189b}$$

in which,

$$F_{++}(r) = 2\mathfrak{p}_s(r_{++}) + (1 - E^2 - 2r_{++}^2)(r_{++}^2 - r^2) + 2\sqrt{\mathfrak{p}_s(r_{++})\,P_{++}(r)}, \tag{3.190a}$$

$$F_+(r) = 2\mathfrak{p}_s(r_+) - (1 - E^2 - 2r_+^2)(r^2 - r_+^2) + 2\sqrt{\mathfrak{p}_s(r_+)\,P_+(r)}, \tag{3.190b}$$

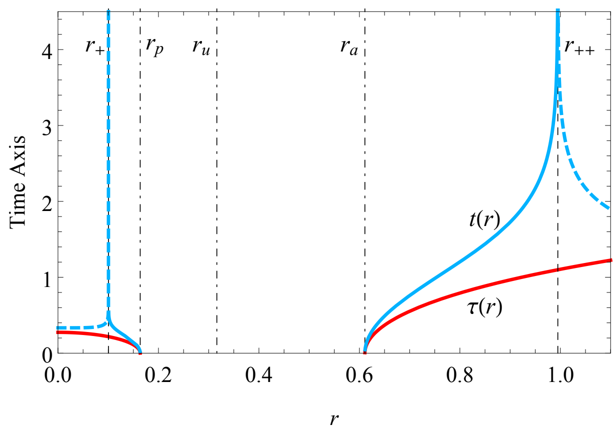

Figure 3.21: The radial behavior of the proper and coordinate times in the two kinds of frontal scattering, plotted for $Q = 0.2$, $\lambda = 1$ and $E^2 = 0.6$. After being scattered from r_a (or r_p), the comoving observers see a horizon crossing. This is while a distant observer never observe this (frozen falling particles).

and

$$P_{++}(r) = \mathfrak{p}_s(r_{++}) + (1 - E^2 - 2r_{++}^2)(r_{++}^2 - r^2) + (r_{++}^2 - r^2)^2, \tag{3.191a}$$

$$P_{+}(r) = \mathfrak{p}_s(r_{+}) - (1 - E^2 - 2r_{+}^2)(r^2 - r_{+}^2) + (r^2 - r_{+}^2)^2. \tag{3.191b}$$

To obtain the radial behavior of the time parameters in the second kind scattering (scattering from r_p), it suffices to change $r_a \to r_p$ in the above relations and reverse the evolution. In Fig. 3.21, the radial behaviors of $t(r)$ and $\tau(r)$ have been plotted for a specific value of E for the two kinds of scattering. As we can see, the comoving observers see particles crossing the horizons, whereas, according to the distant observers, the particles will never cross the horizons. In this regard, at the vicinity of the horizons, the particles appear frozen to the distant observers.

Critical radial motion

Motion of particles with $E = E_u$, coming from $r_i > r_u$ or $d_i < r_u$ (respectively, regions (I) and (II) in Fig. 3.29), depends on the initial conditions at these points. According to Fig. 3.29, the discontinuity of $\frac{d\tau}{dr}$ and $\frac{dt}{dr}$, at r_i and d_i, tell us about the final fate of the approaching particles. In this regard, they can either fall on $r = r_u$ or be pulled towards the horizons. Both fates can be obtained by integrating the equations of motion for the time parameters. For particles coming from r_i, we derive the following

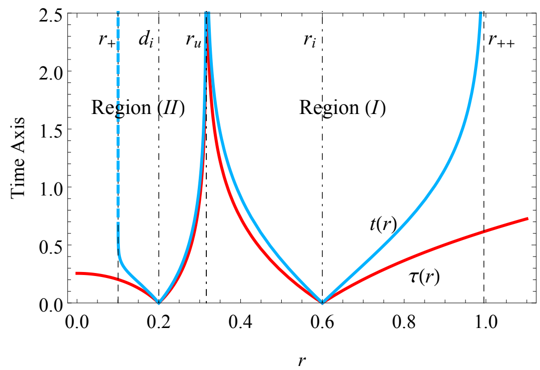

Figure 3.22: Plot of the critical radial motion in regions (I) and (II), plotted for $Q = 0.2$, $\lambda = 1$ and $E^2 = 0.8$. It is assumed $r_i = 0.6$ and $d_i = 0.2$. In both cases, the comoving and distant observers see that the particles approach r_u asymptotically, whereas once again, the horizon crossing is seen only for comoving observers.

temporal relations in accordance with the comoving and distant observers:

$$\tau_I(r) = \pm\frac{\lambda}{2}\ln\left|\frac{r^2 - r_u^2}{r_i^2 - r_u^2}\right|, \tag{3.192}$$

$$t_I(r) = \pm\frac{\lambda^3 E}{2}\left[t_u(r) - t_{++}(r) - t_+(r)\right], \tag{3.193}$$

where

$$t_{++}(r) = \frac{r_{++}^2}{(r_{++}^2 - r_+^2)(r_{++}^2 - r_u^2)}\ln\left|\frac{r_{++}^2 - r^2}{r_{++}^2 - r_i^2}\right|, \tag{3.194a}$$

$$t_+(r) = \frac{r_+^2}{(r_{++}^2 - r_+^2)(r_u^2 - r_+^2)}\ln\left|\frac{r^2 - r_+^2}{r_i^2 - r_+^2}\right|, \tag{3.194b}$$

$$t_u(r) = \frac{r_u^2}{(r_{++}^2 - r_u^2)(r_u^2 - r_+^2)}\ln\left|\frac{r^2 - r_u^2}{r_i^2 - r_u^2}\right|. \tag{3.194c}$$

The corresponding evolution of these coordinates has been demonstrated in Region (I) of Fig. 3.29. The temporal equations of motion for particles coming from d_i are similar to the last ones and are given by considering the exchanges $\tau_{II}(r) = -\tau_I(r)$, $t_{II}(r) = -t_I(r)$ and $r_i \to d_i$. Region (II) of Fig. 3.29, indicates their radial evolution.

Radial capture

In the case that $E > E_u$, the particle trajectories are inevitably pulled towards the horizons; the particles are captured. To solve Eq. (6.58) for the comoving time parameter, we consider a reference value $E = 1 + \frac{Q}{\lambda}$ which is in general, larger than E_u. If we assume that at $\tau = 0$, the particles are at a finite distance ρ_0 (i.e. $\tau(\rho_0) = 0$), then the solutions are classified as

- For $E_u^2 < E^2 < 1 + \frac{Q}{\lambda}$:

$$\tau(r) = \pm\frac{\lambda}{2}\left[\operatorname{arcsinh}\left(\frac{2r^2 + E^2 - 1}{\eta_E}\right) - k_0\right]. \tag{3.195}$$

- For $E^2 = 1 + \frac{Q}{\lambda}$:

$$\tau(r) = \pm\frac{\lambda}{2}\ln\left|\frac{2r^2 + Q}{2\rho_0^2 + Q}\right|. \tag{3.196}$$

- For $E^2 > 1 + \frac{Q}{\lambda}$:

$$\tau(r) = \pm\frac{\lambda}{2}\ln\left|\frac{2\sqrt{\mathfrak{p}(r)} + 2r^2 + E^2 - 1}{2\sqrt{\mathfrak{p}(r)} + 2\rho_0^2 + E^2 - 1}\right|. \tag{3.197}$$

In above, we have defined

$$\eta_E = \sqrt{(E^2 - E_u^2)(1 + \frac{Q}{\lambda} - E^2)}, \tag{3.198a}$$

$$k_0 = \operatorname{arcsinh}\left(\frac{2\rho_0^2 + E^2 - 1}{\eta_E}\right). \tag{3.198b}$$

The relation of the time parameter for the distant observers can be considered the same as that in Eq. (6.67), and we just need to replace $r_a \to \rho_0$. In Fig. 3.23 we have plotted the behavior of the above coordinates in the radial capture process. The behavior is more or less like the radial scattering, except the fact that in both kinds of trajectories (towards r_{++} or r_+), the trajectories are being captured from the initial distance ρ_0.

3.3.3 Geodetic precession

In 1916, de Sitter imposed a relativistic correction to the gyroscopic precession of the Earth-Moon system in its orbiting motion in the curved spacetime around the sun (de Sitter, 1916). This correction, known as geodetic effect (or geodetic precession, de Sitter precession or de Sitter effect), does not take into account the rotation of the central mass. The inclusion of this latter for rotating objects, results in a more general effect, called the dragging of inertial frames (or the Lense-Thirring effect) (Lense & Thirring, 1918). The geodetic precession effect has had a great influence in astrophysical observations and in fact constitutes one of the significant tests of general relativity. From a theoretical viewpoint, however, there are several methods in the derivation of

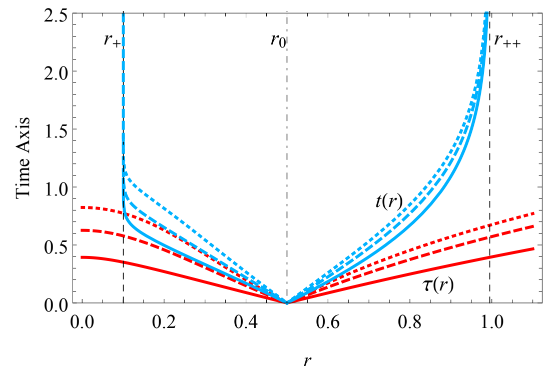

Figure 3.23: Plot of the radial capture for particles. With $Q = 0.2$, $\lambda = 1$ and $\rho_0 = 0.5$. The way of the behavior of the time parameters are similar to those in the radial scattering. The plots have been done for three different values of $E > E_u$ and are classified as **dotted**: $E^2 = 1 < 1 + \frac{Q}{\lambda}$, **dashed**: $E^2 = 1.2 = 1 + \frac{Q}{\lambda}$ and **solid**: $E^2 = 2 > 1 + \frac{Q}{\lambda}$.

geodetic precession and frame dragging (Schiff, 1960; Ashby & Shahid-Saless, 1990; Krisher, 1997; Jonsson, 2007; Wohlfarth & Pfeifer, 2013; Lämmerzahl et al., 2001; Will, 2014). Here, we pursue a well-known method, consisting of a transformation to the local frame of an orbiting gyroscope in the curved spacetime generated by metric potential (3.25). Same method has been employed to calculate the geodetic precession in the Mannheim-Kazanas solution of the WCG (Said et al., 2013). Other methods, including the parameterized post-Newtonian (PPN) formalism can be found extensively in the available literature (Misner et al., 2017).

Now we calculate the geodetic precession of the spin vector $\bar{\boldsymbol{S}}$ of a gyroscope angular motion which is orbiting with the angular velocity ω. To proceed with this, let us identify the local frame of the gyroscope, by introducing the rotating coordinate system, characterized by the new angular coordinate

$$\mathrm{d}\varphi = \mathrm{d}\phi - \omega\,\mathrm{d}t. \tag{3.199}$$

This changes the non-rotating metric of the CWBH to that in rotating coordinates, which for $\theta = \frac{\pi}{2}$ reads as

$$\mathrm{d}s^2 = -\left[B(r) - r^2\omega^2\right]\left(\mathrm{d}t - \frac{r^2\omega}{B(r) - r^2\omega^2}\,\mathrm{d}\varphi\right)^2 + \frac{\mathrm{d}r^2}{B(r)} + \frac{r^2 B(r)}{B(r) - r^2\omega^2}\,\mathrm{d}\varphi^2. \tag{3.200}$$

Comparing to the canonical form (Rindler, 2006)

$$\mathrm{d}s^2 = -e^{2\Phi}(\mathrm{d}t - \bar{S}_i\mathrm{d}x^i)^2 + h_{ij}\mathrm{d}x^i\mathrm{d}x^j, \tag{3.201}$$

where $x^i = (r, \varphi)$, we infer

$$\Phi = \frac{1}{2}\ln\left(B(r) - r^2\omega^2\right), \tag{3.202}$$

$$\bar{S}_1 = 0, \tag{3.203}$$

$$\bar{S}_2 = \frac{r^2\omega}{B(r) - r^2\omega^2}, \tag{3.204}$$

$$h_{11} = \frac{1}{B(r)}, \tag{3.205}$$

$$h_{22} = \frac{r^2 B(r)}{B(r) - r^2\omega^2}. \tag{3.206}$$

We assume that all the possible non-gravitational forces acting on the gyroscope are applied at its center of mass, so no torques are available in its rotating rest frame. In this regard, the spin vector $\bar{\boldsymbol{S}}$ is Fermi-Walker transported along the gyroscope's world-line. Furthermore, if we consider the orbits are on a circle of constant radius r_g, then it is inferred that

$$\left.\frac{\partial\Phi}{\partial r}\right|_{r=r_g} = 0 \implies \omega_g^2 = \frac{Q^2}{4r_g^4} - \frac{1}{\lambda^2}. \tag{3.207}$$

This also indicates that the curve $r = r_g$ is a geodesic and the gyroscope is indeed free falling. The above angular velocity is essentially the Kepler frequency of the orbits. The corresponding rotational rate of the gyroscope in its rest frame is given by (Schiff, 1960; Misner et al., 2017)

$$\Omega^2 = \frac{e^{2\Phi}}{8} h^{ik} h^{jl} \left[\left(\frac{\partial\bar{S}_i}{\partial x^j} - \frac{\partial\bar{S}_j}{\partial x^i}\right)\left(\frac{\partial\bar{S}_k}{\partial x^l} - \frac{\partial\bar{S}_l}{\partial x^k}\right)\right], \tag{3.208}$$

which is calculated at $r = r_g$. Therefore, applying Eqs. (3.202)–(3.206) in Eq. (3.208), we obtain

$$\Omega_g = \omega_g, \tag{3.209}$$

as the rotational rate of a gyroscope orbiting in the gravitational field of a CWBH. The gyroscope is at rest in its proper frame, however, a distant observer will detect a time dilation, which according to Eq. (3.200) is characterized by

$$\Delta\tau = \sqrt{B(r_g) - r_g^2\omega_g^2}\,\Delta t = \sqrt{1 - \frac{Q^2}{2r_g^2}}\,\Delta t. \tag{3.210}$$

After a complete revolution, the orientation of the gyroscope's spin vector, relative to its rest frame, is changed by the angle

$$\hat{\alpha}_{\rm rev} = \Omega_g \Delta\tau_{\rm rev} = \Omega_g\sqrt{1 - \frac{Q^2}{2r_g^2}}\,\Delta t_{\rm rev}, \tag{3.211}$$

where $\Delta t_{\rm rev} = \frac{2\pi}{\omega_g}$ is the coordinate time measured in one revolution. Hence, the observed precession in the course of one orbit is calculated as $\hat{\alpha}'_{\rm rev} = 2\pi - \hat{\alpha}_{\rm rev}$, that by exploiting Eqs. (3.209) and (3.211) yields

$$\hat{\alpha}'_{\rm rev} = 2\pi\left[1 - \sqrt{1 - \frac{Q^2}{2r_g^2}}\right]. \tag{3.212}$$

In the case that $r_g \gg Q$, to the first order of approximation, the precession in Eq. (3.212) becomes

$$\hat{\alpha}'_{\rm rev} \approx \frac{\pi Q^2}{2r_g^2} \quad \left(\frac{\rm rad}{\rm rev}\right), \tag{3.213}$$

where "rad" and "rev" stand for "radians" and "revolution". The above relation has been obtained in geometric units. The value of $\hat{\alpha}'_{\rm rev}$ is however dimensionless and can be used to compare with the general relativistic results within proper conditions.

The general relativistic precession for a gyroscope rotating a mass $\tilde{m}$ in a circular orbit of radius r_g, is given by (Rindler, 2006)

$$\hat{\alpha}'_{\rm rev(gen)} \approx \frac{3\pi\tilde{m}}{r_g} \quad \left(\frac{\rm rad}{\rm rev}\right) \tag{3.214}$$

in geometric units (for a guide to the change of units see appendix B.1). The period of the gyroscope's orbit is easily obtained as

$$\tilde{T}_{\rm rev(gen)} = 2\pi\sqrt{\frac{r_g^3}{\tilde{m}}} \quad \left(\frac{\rm m}{\rm rev}\right). \tag{3.215}$$

Hence, using Eq. (3.214) and (3.215) we have

$$\hat{\alpha}'_{\rm rev(gen)} \approx \frac{3\tilde{m}^{\frac{3}{2}}}{2r_g^{\frac{5}{2}}} \quad \left(\frac{\rm rad}{\rm m}\right). \tag{3.216}$$

For the Earth of mass $\tilde{m}_e \approx 4.43 \times 10^{-3}$ m, and radius $R_e = 6371 \times 10^3$ m (Luzum et al., 2011), if we let $r_g = R_e$, then $\tilde{T}_{\rm rev(gen)} \approx 1.52 \times 10^{12}$ m, and the gyroscope will have approximately 6.22×10^3 orbits around the Earth in one year. Using the above values in Eq. (3.216) gives $\hat{\alpha}'_{\rm rev(gen)} \approx 4.32 \times 10^{21}\,\frac{\rm rad}{\rm m} \approx 8.41\,\frac{\rm arcsec}{\rm yr}$[1] (see appendix B.1). In the Gravity Probe B (GP-B) mission, a satellite containing four gyroscopes, was set to orbit around the Earth at the altitude $r_h = 642$ km. The general relativistic prediction of the geodetic precession in the gyroscopic spin is therefore obtained by considering this altitude, giving

$$\hat{\alpha}'_{\rm rev(gen)} \approx 8.41\left[\frac{R_e}{R_e + r_h}\right]^{\frac{5}{2}} \approx 6.62 \quad \left(\frac{\rm arcsec}{\rm yr}\right), \tag{3.217}$$

[1] 1 rad = 206265 arcsec.

which is equal 6620 $\frac{\text{mas}}{\text{yr}}$[2]. This value is confirmed by the reported value, $6602 \pm 18\ \frac{\text{mas}}{\text{yr}}$, from the GP-B mission in 2011 (Everitt et al., 2011, 2015).

Turning back to the problem of an orbiting gyroscope around a charged source in WCG, it is plausible to adopt $r_g \equiv r_U$, where r_U is the radius of circular orbits, discussed in sub-subsection 3.3.1 and derived in Eqs. (3.121)–(3.123). Accordingly, the period of the orbits, measured by a distant observer, is that given in Eq. (3.239). If we apply these to the precession in Eq. (3.213), and re-scale the result, we get

$$\hat{\alpha}'_{\text{rev}} \approx \left(1.95 \times 10^{24}\right) \frac{Q^2 b_U}{4 r_U^4} |B(r_U)| \quad \left(\frac{\text{mas}}{\text{yr}}\right), \tag{3.218}$$

in which the numerical factor is inferred from the earlier notes in the general relativistic case and the explanations given in appendix B.1. In this relation, as introduced before, b_U is the impact parameter associated with the circular trajectories. Exploiting Eq. (3.130) and the fact that $E_U^2 = V(r_U)$, yields

$$b_U \equiv \frac{L_U}{E_U} = \left| \frac{\omega_U}{\omega_U^2 + \frac{2}{\lambda^2} - \frac{1}{r_U^2}} \right| \quad (\text{m}), \tag{3.219}$$

where we have defined

$$\omega_U^2 = \frac{Q^2}{4 r_U^4} - \frac{1}{\lambda^2} \quad \left(\frac{1}{\text{m}^2}\right). \tag{3.220}$$

To apply a numerical assessment of $\hat{\alpha}'_{\text{rev}}$, we need a spherically symmetric gravitating system with positive net charge. For this reason, we use the presented data for the case that the stability of charged white dwarfs with masses comparable to that of the sun ($M_\odot$) (Carvalho et al., 2018). To elaborate this, let us consider the gyroscope is rotating such a white dwarf in a circular orbit of radius r_U, given in Eq. (3.123). In Table 3.1, the physical properties of the massive sources have been given. There, we have also presented the calculated values of the precession in Eq. (3.218) for each case. Note that, the central density $\tilde{\rho}_w$ has been considered in identifying the parameter λ of the spacetime lapse function and the value of c_1 has been specified in accordance to the original article where the solution of the CWBH has been presented (Payandeh & Fathi, 2012) (see appendix B.1 for more details). As it is expected from Eq. (3.218), the precession vanishes for $Q = Q_w = 0$. Adopting a very small angular momentum (of order $\sim 10^{-8}$ m), we can see rather large precessions when $Q_w \neq 0$.

It is of worth to, once again, discuss the general relativistic approach. To do that however, we need to consider static charged sources whose exterior geometry is given

[2]"mas" is an abbreviation for milliarcsec, and 1 mas = $4.848 \times 10^{-9}\ \frac{\text{rad}}{\text{yr}}$.

$M_w/M_\odot$	R_w $(\times 10^3\ \mathrm{m})$	$\tilde{\rho}_w$ $(\times 10^{-14}\ \mathrm{m}^{-2})$	Q_w (m)	$\hat{\alpha}'_{\mathrm{rev}}$ (mas/yr)	$\hat{\alpha}'_{\mathrm{rev(RN)}}$ (mas/yr)
1.416	1021	1.71316	0	0	7.86833×10^{13}
1.532	1299	2.25971	349.676	1.02422×10^{13}	5.48841×10^{13}
1.698	1539	2.5664	699.267	2.32618×10^{13}	4.49524×10^{13}
1.928	1336	4.91076	1053.77	6.70766×10^{13}	6.69618×10^{13}
2.203	1166	14.4211	1411.64	2.63875×10^{14}	1.01421×10^{14}
2.203	916.8	29.7037	1774.68	6.83293×10^{14}	1.79096×10^{14}

Table 3.1: The properties of the charged white dwarfs (Carvalho et al., 2018) (given in geometric units), and the values of precessions inferred from Eqs. (3.218) and (3.222). For the case of precession in the CWBH geometry, we have let $L = 10^{-7.6}$ m, and the radius of orbits for the gyroscopes in the RN geometry has been put $r_g = R_w + r_h$ for each of the cases.

by the RN metric with the lapse function (Ryder, 2009)

$$B_{\mathrm{RN}}(r) = 1 - \frac{2\tilde{m}}{r} + \frac{Q_0^2}{r^2}, \tag{3.221}$$

describing spherically symmetric sources with charge Q_0. As mentioned before, the transition between the charged Weyl and the general relativistic geometries is not trivial. Hence, we pursue the same method as introduced earlier, to obtain the general relativistic precession in the context of charged sources. Accordingly, one obtains

$$\hat{\alpha}'_{\mathrm{rev(RN)}} \approx \left(1.95 \times 10^{24}\right) \left[\frac{\sqrt{\tilde{m}}\left(3\tilde{m}r_g - Q_0^2\right)}{2r_g^{\frac{7}{2}}}\right] \left(\frac{\mathrm{mas}}{\mathrm{yr}}\right), \tag{3.222}$$

assuming that $r_g \gg \tilde{m}$ and $r_g \gg Q_0$. Supposing that the gyroscope is orbiting at the altitude $r_h = 642$ km around the same white dwarfs of the previous case, then $r_g = R_w + r_h$. Taking into account $\tilde{m} = M_w$, $Q_0 = Q_w$ and $M_\odot = 1.48 \times 10^3$ m, the calculated general relativistic precessions have been given in the last column of Table 3.1. One can observe a remarkable conformity with the results inferred from WCG for the case of $Q_w \neq 0$.

3.4 Motion of charged particles

The scattering of charged particles in electric fields is indeed one of the most re-known phenomena in physics and has had numerous applications in small and large scale observations. Regarding the former, and without loss of generality, the famous Rutherford scattering experiment that led to the discovery of the atomic nucleus, is described in terms of elastic deflecting trajectories of charged particles from a heavy charged central mass. Such particle trajectories, beside being well-known in small atomic scales, have been also investigated widely in black hole spacetimes. In fact, the study of motion of test particles in the gravitational field of black holes, dates back to the early days of general relativity and ever since, it has found its way in classic textbooks (Misner et al., 2017; Futterman et al., 1988; Chandrasekhar, 1998) and reviews (Poisson et al., 2011; Blanchet et al., 2011). The interest in performing such studies, beside their applicability in testing general relativity and modified theories of gravity, stems mostly in the opportunity that they provide to correctly analyze the dynamics of extremely warped regions around black holes. In these regions, based on the effective gravitational potential that affects the particles, they can lie on different types of orbits, among which, and in particular, the deflecting trajectories relate tightly to the scattering phenomena. It is well-known that the charge parameter of charged black hole spacetimes (like the RN and Kerr-Newman (KN) geometries), contributes in the gravitational potential of the black hole and therefore, can affect the motion of neutral particles. In the case of charged test particles moving around such black holes, the additional electromagnetic potential changes the nature of deflecting trajectories to a special form of the Rutherford scattering. The importance of this kind of motion is such that it has received a large number of performed studies in analyzing, numerically and analytically, the respected equations of motion and the scattering cross-sections. These studies have been done in the contexts of GR and alternative gravity (Bicak et al., 1989; Karas & Vokrouhlicky, 1990; Aliev & Özdemir, 2002; Pugliese et al., 2011; Olivares et al., 2011; Fathi, 2013; Hackmann & Xu, 2013; Lim, 2015; García et al., 2015; Pugliese et al., 2017; Das et al., 2017; Iftikhar, Sehrish, 2018; Vrba et al., 2020; Khan & Ren, 2020; Yi & Wu, 2020; Abdujabbarov et al., 2020; Javlon et al., 2020; Anacleto et al., 2020; Villanueva & Olivares, 2015; Sarkar et al., 2018; Zhao et al., 2018; González et al., 2018; Shaymatov et al., 2020; Narzilloev et al., 2020). Moreover, regarding the chaotic nature of particle scattering (Stuchlík, Zdenek & Kolos, Martin, 2016), realistic astrophysical situations can be found that also demonstrate the creation of ultra-high energy particles (Stuchlík et al., 2020; Tursunov et al., 2020).

Although black holes with net electric charge are still remained as purely theoretical objects, however, studying them can pave the way in understanding physical phenomena like radiation reaction of particles (Gal'tsov, 1982; Tursunov et al., 2018) and black hole evaporation (Chen & Huang, 2019). Hence, the interest in investigating particle motion around charged black holes becomes more justified and, as well as in general relativity, it has found its way into alternative theories of gravity.

Along the same effort, in this section, we investigate the motion and the scattering of charged test particles, as they travel in the exterior of the CWBH, and as before, we study different types of orbits, for the both cases of angular and radial motion. Additionally, assuming the congruence deviation of a bundle of infalling world-lines, we discuss the internal interactions between the particles and point out their effects on the kinematical congruence expansion.

3.4.1 The Lagrangian dynamics of charged test particles

The Hamilton-Jacobi method of describing the motion of particles of mass m and charge q in an electromagnetic field, is based on the superhamiltonian (Misner et al., 2017)

$$\mathcal{H} = \frac{1}{2} g^{\mu\nu} p_\mu p_\nu, \tag{3.223}$$

in which the 4-momentum $\boldsymbol{p}$ satisfies $p_\mu p^\mu = -m^2$ and is defined as

$$p_\mu = g_{\mu\nu} \frac{\mathrm{d}x^\nu}{\mathrm{d}\tau} = \left(\pi_\mu + q A_\mu\right), \tag{3.224}$$

in terms of the affine parameter τ, the vector potential $\boldsymbol{A}$ and the generalized momentum $\boldsymbol{\pi}$, which is given according to the canonical Hamilton equation

$$\frac{\mathrm{d}\pi_\mu}{\mathrm{d}\tau} = -\frac{\partial \mathcal{H}}{\partial x^\mu}. \tag{3.225}$$

Recasting $\mathcal{H}$ in terms of the *characteristic Hamilton function* (i.e. the Jacobi action)

$$\mathcal{H} = -\frac{\partial S}{\partial \tau}, \tag{3.226}$$

we have $\pi_\mu = \frac{\partial S}{\partial x^\mu}$ and the Hamilton-Jacobi equation of the wave crests can be written as

$$\frac{1}{2} g^{\mu\nu} \left(\frac{\partial S}{\partial x^\mu} + q A_\mu\right) \left(\frac{\partial S}{\partial x^\nu} + q A_\nu\right) + \frac{\partial S}{\partial \tau} = 0. \tag{3.227}$$

The generalized momentum $\boldsymbol{\pi}$ is indeed responsible for the possible constants of motion. For stationary spherically symmetric spacetimes, such as that of the CWBH, these constants are

$$\pi_t \doteq -E = g_{tt} \frac{\mathrm{d}t}{\mathrm{d}\tau} - q A_t, \tag{3.228a}$$

$$\pi_\phi \doteq L = g_{\phi\phi} \frac{\mathrm{d}\phi}{\mathrm{d}\tau} - q A_\phi. \tag{3.228b}$$

As stated in section 3.1, the only non-zero term of the vector potential for the CWBH is $A_t = \frac{\tilde{q}}{r} = \frac{Q}{\sqrt{2}r}$. One can therefore specify Eq. (3.227) for the equatorial orbits as

$$\frac{-1}{B(r)}\left(\frac{\partial S}{\partial t}+\frac{qQ}{\sqrt{2}r}\right)^2+B(r)\left(\frac{\partial S}{\partial r}\right)^2+\frac{1}{r^2}\left(\frac{\partial S}{\partial \phi}\right)^2+2\frac{\partial S}{\partial \tau}=0. \tag{3.229}$$

Based on the method of separation of variables of the Jacobi action, Eq. (3.229) can be solved by defining (Carter, 1968)

$$S=-Et+S_0(r)+L\phi+\frac{1}{2}m^2\tau, \tag{3.230}$$

for which, interpolation in Eq. (3.229) results in

$$S_0(r)=\pm\int\frac{\mathrm{d}r}{B(r)}\sqrt{(E-V_-)(E-V_+)}, \tag{3.231}$$

where the radial potentials are given by

$$V_{\pm}(r)=V_q(r)\pm\sqrt{B(r)\left(m^2+\frac{L^2}{r^2}\right)}, \tag{3.232a}$$

$$V_q(r)\doteq\frac{qQ}{\sqrt{2}r}. \tag{3.232b}$$

Note that, both of the $\pm$ branches of $V_{\pm}(r)$ converge to the value $E_+ = \frac{qQ}{\sqrt{2}r_+}$ at $r = r_+$, which can be either positive or negative, depending on the sign of the electric charges, q and Q. Here we adopt the condition $qQ > 0$, so that the V_- branch is always negative (in the causal region $r_+ < r < r_{++}$), and we can consider the positive branch as the effective potential, i.e. $V_{eff} \doteq V_+ \equiv V$. Furthermore, applying Eqs. (3.230) and (3.231), it is possible to obtain the following three velocities:

$$u(r)\equiv\frac{\mathrm{d}r}{\mathrm{d}\tau}=\pm\sqrt{(E-V_-)(E-V)}, \tag{3.233}$$

$$v_t(r)\equiv\frac{\mathrm{d}r}{\mathrm{d}t}=\pm\frac{B(r)u(r)}{E-V_q(r)}, \tag{3.234}$$

$$v_\phi(r)=\frac{\mathrm{d}r}{\mathrm{d}\phi}=\pm\frac{r^2u(r)}{L}. \tag{3.235}$$

The zeros of the above velocities do correspond to the so-called turning points, r_t, which are specified by the condition $V(r_t) = E_t$. Additionally, these equations lead to the quadratures that determine the evolution of the trajectories. This is dealt with in the forthcoming subsections and the corresponding analytical solutions are obtained.

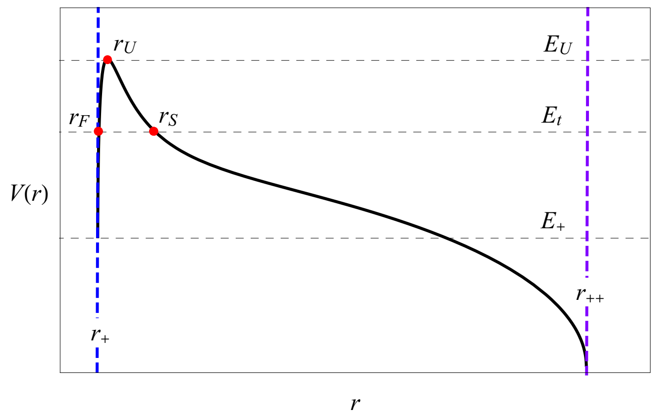

Figure 3.24: The effective potential for test particles with angular momentum, plotted for $m = 1$, $L = 1$, $Q = 1$, $q = 0.5$ and $\lambda = 10$. The turning points are determined by the intersection of E and the effective potential (i.e. $E_t = V(r_t)$). These include the radius of unstable circular orbits r_U, and two other points, r_S and r_F.

3.4.2 Angular Motion

Here we focus on analyzing the trajectories followed by charged particles with non-zero angular momentum ($L \neq 0$). The effective potential in Eq. (3.232) has been plotted in Fig. 3.24, in which the turning points r_t correspond to the values of $E = E_t$ that satisfy $E_t = V(r_t)$. The significance of these points is that they do reveal the possible orbits of the test particles. In fact, according to Fig. 3.24, three turning points are highlighted; $r_t = r_U$ (the radius of unstable circular orbits), $r_t = r_S$ (the distance from the point of scattering) and $r_t = r_F$ (the point of no return, or the capturing distance).

Unstable circular orbits

As observed from the effective potential in Fig. 3.24, the orbits become unstable at the a maximum, whose corresponding radius is limited from above to a circle of radius r_U, where the gravitational attraction caused by the mass of the source, is completely replaced by the cosmological repulsion caused by the term $\tilde{\varepsilon}$. This radius of unstable circular orbits, or the *static radius* (Stuchlík, 1983; Stuchlík & Hledík, 1999), is given by the condition $V'(r) \equiv \left.\frac{\partial V(r)}{\partial r}\right|_{r_U} = 0$. Hence, from Eq. (3.232) we get

$$\left.\left(\sqrt{\frac{G(r;L)}{B(r)}}\,\frac{B'(r)}{2} - \sqrt{\frac{B(r)}{G(r;L)}}\,\frac{L^2}{r^3} - \frac{qQ}{\sqrt{2}r^2}\right)\right|_{r_U} = 0, \tag{3.236}$$

in which the function $G(r;L)$ is defined as

$$G(r;L) = m^2 + \frac{L^2}{r^2}. \tag{3.237}$$

In fact, the left hand side of Eq. (3.236) leads to an incomplete polynomial of twelfth degree in r, and hence, it can be solved only numerically. It is however still possible to calculate the proper (T_τ) and the coordinate (T_t) periods of these orbits. Combining Eqs. (3.233), (3.234) and (3.235), and the fact that for a complete orbit $\Delta\phi_U = 2\pi$, we have

$$T_\tau \equiv \Delta\tau = \frac{2\pi r_U^2}{L_U}, \tag{3.238}$$

$$T_t \equiv \Delta t = \frac{2\pi r_U^2}{L_U}\frac{E_U - V_q(r_U)}{B(r_U)} = T_\tau\sqrt{\frac{G_U}{B_U}}, \tag{3.239}$$

where $G_U \equiv G(r_U;L_U)$ and $B_U \equiv B(r_U)$. Solving Eq. (3.236), we then obtain an expression for L_U as (appendix B.2)

$$L_U = \sqrt{\frac{\mathfrak{b} - \sqrt{\mathfrak{b}^2 - 4\mathfrak{a}\mathfrak{c}}}{2\mathfrak{a}}}, \tag{3.240}$$

as the angular momentum for the circular orbits, where

$$\mathfrak{a} = \frac{(Q^2 - 2r_U^2)^2}{r_U^6}, \tag{3.241a}$$

$$\mathfrak{b} = \frac{2Q^2(1+q^2)}{r_U^2} - \frac{Q^4(2+q^2)}{2r_U^4} - \frac{8r_U^2 - 2Q^2(1-q^2)}{\lambda^4}, \tag{3.241b}$$

$$\mathfrak{c} = \frac{Q^4(1+2q^2)}{4r_U^2} - 2q^2Q^2 + \frac{4r_U^6}{\lambda^4} - \frac{2Q^2r_U^2(1-q^2)}{\lambda^2}. \tag{3.241c}$$

Accordingly, one can obtain the proper frequency

$$\omega_\tau = \frac{2\pi}{T_\tau} = \sqrt{\frac{\mathfrak{b} - \sqrt{\mathfrak{b}^2 - 4\mathfrak{a}\mathfrak{c}}}{2\mathfrak{a}r_U^4}}, \tag{3.242}$$

straightly from Eqs. (3.238) and (3.240). The coordinate frequency can then be given by the ratio

$$\frac{\omega_\tau}{\omega_t} = \sqrt{\frac{G_U}{B_U}}. \tag{3.243}$$

These values correspond to the velocity of particles on a surface, where they can maintain a circular orbit before falling into the event horizon or escape from it. In the study of particle trajectories, the critical orbits can locate the innermost possible stable orbits around black holes and therefore are of great importance. The test particles, however, can also be scattered at the turning point r_S, pursue a hyperbolic motion and escape the black hole. For electrically charged particles, this corresponds to the so-called Rutherford scattering. We continue our discussion by analyzing this kind of orbit.

Orbits of the first kind and the gravitational Rutherford scattering

The particle deflection by the CWBH happens when the condition $E_+ < E < E_U$ is satisfied. This indeed results in two points of approach, $r_t = r_S$ and $r_t = r_F$, at which, $\frac{\mathrm{d}r}{\mathrm{d}\phi}|_{r_t} = 0$ or $E_t = V(r_t)$ (see Fig. 3.24). The relevant equation of motion can be derived from Eqs. (3.233) and (3.235), giving

$$\left(\frac{\mathrm{d}r}{\mathrm{d}\phi}\right)^2 = \frac{\mathcal{P}(r)}{v^2}, \tag{3.244}$$

where

$$\mathcal{P}(r) \equiv r^6 + \mathcal{A}r^4 + \mathcal{B}r^3 + \mathcal{C}r^2 + \mathcal{D}, \tag{3.245a}$$

$$v = \frac{L\lambda}{m}, \tag{3.245b}$$

with

$$\mathcal{A} = v^2\left(\frac{E^2 - m^2}{L^2} + \frac{1}{\lambda^2}\right), \tag{3.246a}$$

$$\mathcal{B} = -2Ev^2\left(\frac{qQ}{\sqrt{2}L^2}\right), \tag{3.246b}$$

$$\mathcal{C} = \frac{\mathcal{D}}{L^2} - \frac{\mathcal{B}}{2E} - v^2, \tag{3.246c}$$

$$\mathcal{D} = v^2\left(\frac{mQ}{2}\right)^2. \tag{3.246d}$$

To determine the turning points r_S and r_F, one therefore needs to solve $\mathcal{P}(r_t) = 0$, which is an incomplete equation of sixth degree in r, and values of $r(\phi)$ can therefore be obtained through numerical methods. To deal with this problem, we pursue the inverse process and find an analytical expression for $\phi(r)$. The behavior of $r(\phi)$ can then be demonstrated by means of numerical interpolations.

To proceed with this method, let us consider that $\mathcal{P}(r)$ has two distinct real roots, corresponding to the turning points $r_1 = r_S$ and $r_2 = r_F$, two equal and negative real roots, say $r_3 = r_4 < 0$, and finally, a complex conjugate pair r_5 and $r_6 = r_5^*$.

Accordingly, we can recast $\mathcal{P}(r)$ as

$$
\begin{aligned}
\mathcal{P}(r) &= \prod_{j=1}^{6}(r-r_j) \\
&= (r-r_S)(r-r_F)(r-r_5)(r-r_3)^2(r-r_5^*).
\end{aligned} \tag{3.247}
$$

Taking into account the outgoing trajectories, the equation of motion (3.244) can then be written as

$$
\phi(r) = v\int_{r_S}^{r}\frac{\mathrm{d}r}{\sqrt{\mathcal{P}(r)}}. \tag{3.248}
$$

Particles reaching r_S, experience an OFK that has the significance of gravitational Rutherford scattering when the test particles are electrically charged. Considering the change of variable

$$
u_j \doteq \frac{1}{\frac{r_j}{r_S}-1}, \quad j=\{2,3,5,6\}, \tag{3.249}
$$

the above integral results in (appendix B.3)

$$
\phi(r) = \kappa_0\left[\text{ß}(U) - \frac{u_3}{4}\mathfrak{F}(U)\right], \tag{3.250}
$$

where

$$
\mathfrak{F}(U) = \frac{1}{\wp'(\Omega_S)}\left[2\zeta(\Omega_S)\text{ß}(U) + \ln\left|\frac{\sigma\left(\text{ß}(U)-\Omega_S\right)}{\sigma\left(\text{ß}(U)+\Omega_S\right)}\right|\right], \tag{3.251}
$$

for which, the Weierstraß invariants are

$$
\mathbf{g}_2 = \frac{\mathbf{a}^2}{12} - \frac{\mathbf{b}}{4}, \tag{3.252a}
$$

$$
\mathbf{g}_3 = \frac{1}{16}\left(\frac{\mathbf{ab}}{3} - \frac{2\mathbf{a}^3}{27} - \mathbf{c}\right). \tag{3.252b}
$$

Here, we have defined

$$
U \equiv U(r) = \frac{1}{4\left(\frac{r}{r_S}-1\right)} + \frac{\mathbf{a}}{12}, \tag{3.253a}
$$

$$
\Omega_S = \text{ß}\left(\frac{\mathbf{a}}{12} - \frac{1}{4\left[\frac{r_3}{r_S}-1\right]}\right), \tag{3.253b}
$$

with

$$
\mathbf{a} = u_2 + u_5 + u_6, \tag{3.254a}
$$

$$
\mathbf{b} = u_2(u_5+u_6) + u_5u_6, \tag{3.254b}
$$

$$
\mathbf{c} = u_2u_5u_6. \tag{3.254c}
$$

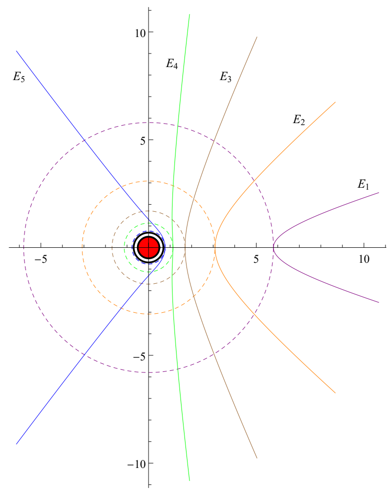

Figure 3.25: The Rutherford scattering plotted for $m = 1$, $Q = 1$, $q = 0.5$, $\lambda = 10$ and $L = 1$. For these values, $r_+ = 0.50$, $r_U = 0.69$ and $E_U = 1.72$. The trajectories have been plotted for $E_1 = 0.88$, $E_2 = 1.1$, $E_3 = 1.3$, $E_4 = 1.5$ and $E_5 = 1.7$, while their corresponding scattering distance (r_S) have been indicated by dashed circles. As it is observed, the condition $E_5 \approx E_U$ has made the corresponding shape of the scattering to be of a convex form, showing an appeal to the critical orbits.

The *scattering angle* in Eq. (3.250) gives the change in the particles' orientation as they approach and recede the black hole at the scattering point r_S. To illustrate their corresponding trajectories, we make a list of points $(r_t, \phi(r_t))$ and then find the numerical interpolating function of $r(\phi)$. The resultant OFK trajectories have been illustrated in Fig. 3.25 for particles of different values for E. As it is observed, the scattering can be formed convexly (approaching) or concavely (receding). For particles coming from infinity, the scattering angle can be written as (Villanueva & Olivares, 2015)

$$\vartheta = 2\phi_\infty - \pi, \tag{3.255}$$

in which $\phi_\infty \equiv \phi(\infty)$. Accordingly, from Eq. (3.250) we have

$$\begin{aligned}\vartheta = -\pi + 2\kappa_0 \Bigg[\text{ß}\left(\frac{\mathbf{a}}{12}\right) + \frac{u_3}{4} \Bigg\{ & \frac{1}{\sqrt{\frac{1}{432}\left(4\mathbf{a}^3 - 18\mathbf{ab} + 27u_3\left(\mathbf{b} - \mathbf{a}u_3 + u_3^2\right)\right)}} \\ & \times \left[2\zeta(\Omega_S)\text{ß}\left(\frac{\mathbf{a}}{12}\right) + \ln\left|\frac{\sigma\left(\text{ß}\left(\frac{\mathbf{a}}{12}\right) - \Omega_S\right)}{\sigma\left(\text{ß}\left(\frac{\mathbf{a}}{12}\right) + \Omega_S\right)}\right| \right] \Bigg\} \Bigg].\end{aligned} \tag{3.256}$$

The value of ϑ is specified directly by the initial E and the corresponding particular solutions r_j, which are determined by the equation $E = V(r)$. These values therefore, cannot be considered to evolve in terms of a single variable. However, one can calculate the scattering angle for each particular trajectory, by applying Eq. (3.256). Additionally, the differential cross section (3.161) can be calculated for the charged particles. To proceed with this, from Eqs. (3.250) and (3.255) we have

$$\frac{1}{2\kappa_0}(\vartheta+\pi)=\varphi_1+\varphi_2, \tag{3.257}$$

in which

$$\varphi_1 \equiv \text{ß}\left(\frac{\mathbf{a}}{12}\right), \tag{3.258a}$$

$$\varphi_2 \equiv -\frac{u_3}{4}\mathfrak{F}\left(\frac{\mathbf{a}}{12}\right). \tag{3.258b}$$

We define

$$\Psi(L) \doteq \wp\left(\frac{\vartheta+\pi}{2\kappa_0}\right)=\wp\left(\varphi_1+\varphi_2\right), \tag{3.259}$$

or (Byrd & Friedman, 1971)

$$\Psi(L)=\frac{1}{4}\left[\frac{\wp'(\varphi_1)-\wp'(\varphi_2)}{\wp(\varphi_1)-\wp(\varphi_2)}\right]^2-\wp(\varphi_1)-\wp(\varphi_2). \tag{3.260}$$

Now, applying the definition in Eq. (3.260), we can recast Eq. (3.161) as

$$\sigma(\vartheta)=b\csc\vartheta\left|\frac{\partial\Psi}{\partial\vartheta}\right|\left|\frac{\partial b}{\partial\Psi}\right|=\frac{1}{4\kappa_0}\csc\vartheta\left|\wp'\left(\frac{\vartheta+\pi}{2\kappa_0}\right)\right|\left|\frac{\partial b^2}{\partial\Psi}\right|, \tag{3.261}$$

for which, the identity $\frac{\partial b^2}{\partial\Psi}=\frac{\partial b^2/\partial L}{\partial\Psi/\partial L}$ yields

$$\sigma(\vartheta)=\frac{L}{2\kappa_0 E^2}\csc\vartheta\left|\wp'\left(\frac{\vartheta+\pi}{2\kappa_0}\right)\right|\left|\frac{\partial\Psi}{\partial L}\right|^{-1}. \tag{3.262}$$

The expression of Ψ is analytically complicated. However, as before, the value of Eq. (3.262) can be numerically calculated regarding definite initial values for distinct scattered trajectories.

3.4.3 Radial Trajectories

The vanishing angular momentum of the radially moving particles, reduces the effective potential in Eq. (3.232) to

$$V_r(r)=V_q(r)+m\sqrt{B(r)}, \tag{3.263}$$

whose behavior has been plotted in Fig. 7.4. Accordingly, the motion becomes unstable where $V_r'(r)=0$, solving which, leads to the maximum distance of the unstable motion, reading as

$$r_u=\left[\tilde{\alpha}-\sqrt{\tilde{\alpha}^2-\tilde{\beta}}\right]^{1/2}, \tag{3.264}$$

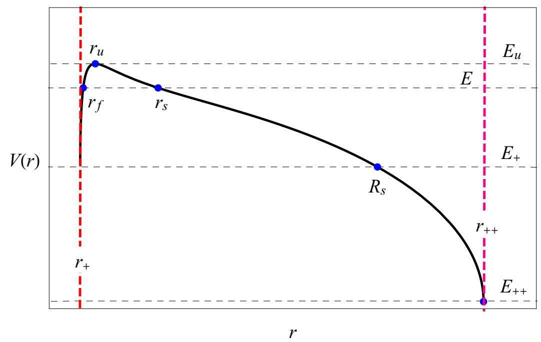

Figure 3.26: The effective potential for radially moving particles plotted for $m = 1$, $Q = 1$, $q = 0.5$ and $\lambda = 10$. The maximum distance of unstable motion, r_u, and the two turning points r_s and r_f have been indicated in accordance with their corresponding values of E. In particular, the point R_s is related to the distance at which the particles of the constant of motion E_+, experience their Rutherford scattering.

where (see appendix B.4)

$$\tilde{\alpha} = \sqrt{\tilde{U} - \frac{\tilde{a}}{6}}, \tag{3.265a}$$

$$\tilde{\beta} = 2\tilde{\alpha}^2 + \frac{\tilde{a}}{2} + \frac{\tilde{b}}{4\tilde{\alpha}}, \tag{3.265b}$$

given that

$$\tilde{U} = 2\sqrt{\frac{\tilde{\eta}_2}{3}} \cosh\left(\frac{1}{3}\text{arccosh}\left(\frac{3}{2}\tilde{\eta}_3\sqrt{\frac{3}{\tilde{\eta}_2^3}}\right)\right), \tag{3.266}$$

with

$$\tilde{a} = -\frac{Q^2\lambda^2}{2}\left(1 - \frac{q^2}{m^2}\right), \tag{3.267a}$$

$$\tilde{b} = -\frac{q^2Q^2\lambda^4}{2m^2}, \tag{3.267b}$$

$$\tilde{c} = \frac{Q^4\lambda^4}{16}\left(1 + \frac{2q^2}{m^2}\right), \tag{3.267c}$$

$$\tilde{\eta}_2 = \frac{\tilde{a}^2}{48} + \frac{\tilde{c}}{4}, \tag{3.267d}$$

$$\tilde{\eta}_3 = \frac{\tilde{a}^3}{864} + \frac{\tilde{b}^2}{64} - \frac{\tilde{a}\tilde{c}}{24}. \tag{3.267e}$$

Taking into account $E_u \equiv V_r(r_u)$, as in the angular case, possible motions are categorized based on the value of E compared with its critical value, E_u:

- *Frontal Rutherford scattering of the first and the second kinds (RSFK and RSSK)*: For $E_{++} < E < E_u$, the potential allows for a turning point r_s ($r_u < r_s < r_{++}$) which corresponds to the scattering distance (RSFK). In the case that $E_+ < E < E_u$, there is also another turning point r_f ($r_+ < r_f < r_u$), from which, the trajectories are captured into the event horizon (RSSK).

- *Critical radial motion*: For $E = E_u$, the particles can stay on an unstable radial distance of radius $r = r_u$. Therefore, those coming from the initial distances r_i or d_i ($r_u < r_i < r_{++}$ and $r_+ < d_i < r_u$ respectively), will ultimately fall on r_u, or cross the horizons.

Now, let us rewrite the radial velocity relations, given in Eqs. (3.233) and (3.234), as

$$\left(\frac{\mathrm{d}r}{\mathrm{d}\tau}\right)^2 = \frac{m^2\mathfrak{p}(r)}{\lambda^2 r^2}, \tag{3.268}$$

$$\left(\frac{\mathrm{d}r}{\mathrm{d}t}\right)^2 = \frac{m^2(r^2-r_+^2)^2(r_{++}^2-r^2)^2\mathfrak{p}(r)}{E^2\lambda^6 r^4(r-\frac{\sqrt{2}qQ}{E})^2}, \tag{3.269}$$

with

$$\mathfrak{p}(r) \equiv r^4 + \bar{a}r^2 + \bar{b}r + \bar{c}, \tag{3.270}$$

where

$$\bar{a} = \frac{(E^2-m^2)\lambda^2}{m^2}, \tag{3.271a}$$

$$\bar{b} = -\frac{\sqrt{2}qQE\lambda^2}{m^2}, \tag{3.271b}$$

$$\bar{c} = \frac{Q^2(m^2+2q^2)\lambda^2}{4\,m^2}. \tag{3.271c}$$

Frontal scattering

As it is inferred from the effective potential in Fig. 7.4, particles can encounter two turning points r_s and r_f which are located at either sides of the critical distance ($r_f < r_u < r_s$). These turning points do lead the trajectories to different fates. Particles with $E_{++} < E < E_+$, however, can only escape the black hole by being scattered at the only possible turning point r_s. Same as discussed in Sec. 6.2.3, the turning points are where the particles' coordinate velocity vanishes, which for the radial trajectories requires $\mathfrak{p}(r) = 0$ in Eq. (6.71), giving

$$r_s = \bar{\alpha} + \sqrt{\bar{\alpha}^2 - \bar{\beta}}, \tag{3.272}$$

$$r_f = \bar{\alpha} - \sqrt{\bar{\alpha}^2 - \bar{\beta}}. \tag{3.273}$$

These radii are basically based on the same components as in Eqs. (3.265)–(3.267), and we only need to replace $\tilde{a} \to \bar{a}$, $\tilde{b} \to \bar{b}$ and $\tilde{c} \to \bar{c}$, according to the values given in

Eqs. (3.271). Having determined the turning points, the polynomial $\mathfrak{p}(r)$ can be decomposed accordingly. As described above, the first kind scattering (RSFK) happens when the particles approach at r_s, which is now considered as their initial position. Therefore Eq. (6.58) can be solved as (appendix B.5)

$$\tau(r) = \frac{-\lambda}{m\sqrt{\gamma_0}}\left[\text{ß}(\mathrm{U}) + \frac{1}{4}\mathrm{F}(\mathrm{U})\right], \tag{3.274}$$

where

$$\mathrm{F}(\mathrm{U}) = \frac{1}{\wp'(\Omega_s)}\left[2\zeta(\Omega_s)\text{ß}(\mathrm{U}) + \ln\left|\frac{\sigma\left(\text{ß}(\mathrm{U}) - \Omega_s\right)}{\sigma\left(\text{ß}(\mathrm{U}) + \Omega_s\right)}\right|\right], \tag{3.275}$$

and the function $\mathrm{U}(r)$ and the Weierstraß coefficients are given as

$$\mathrm{U}(r) = \frac{r_s}{4(r - r_s)} + \frac{\gamma_1}{12\gamma_0}, \tag{3.276a}$$

$$\Omega_s = \text{ß}\left(\frac{\gamma_1}{12\gamma_0}\right), \tag{3.276b}$$

$$\bar{g}_2 = \frac{\gamma_1^2}{12\gamma_0^2} - \frac{1}{\gamma_0}, \tag{3.276c}$$

$$\bar{g}_3 = \frac{1}{16}\left(\frac{4\gamma_1}{3\gamma_0^2} - \frac{2\gamma_1^3}{27\gamma_0^3} - \frac{1}{\gamma_0}\right), \tag{3.276d}$$

with

$$\gamma_1 = 6 + \frac{\bar{a}}{r_s^2}, \tag{3.277a}$$

$$\gamma_0 = 4 + \frac{2\bar{a}}{r_s^2} + \frac{\bar{b}}{r_s^3}. \tag{3.277b}$$

The relation in Eq. (6.63) measures the radial change of the time parameter for observers comoving with the particles. For distant observers, such measurement is done on the coordinate time, whose evolution can be obtained by exploiting the velocity in Eq. (6.59). Applying the same method as before, we obtain

$$t(r) = -\delta_0\left[\text{ß}(\mathrm{U}) + \frac{1}{4}\sum_{k=1}^{4}\delta_k\mathrm{F}_k(\mathrm{U})\right], \tag{3.278}$$

where

$$\mathrm{F}_k(\mathrm{U}) = \frac{1}{\wp'(\Omega_k)}\left[2\zeta(\Omega_k)\text{ß}(\mathrm{U}) + \ln\left|\frac{\sigma\left(\text{ß}(\mathrm{U}) - \Omega_k\right)}{\sigma\left(\text{ß}(\mathrm{U}) + \Omega_k\right)}\right|\right], \tag{3.279}$$

and

$$\Omega_k = \text{ß}\left(\frac{\gamma_1}{12\,\gamma_0} + \frac{z_k}{4}\right), \tag{3.280}$$

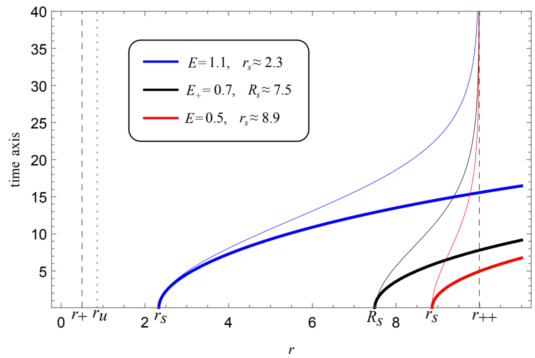

Figure 3.27: The radial behavior of the proper and coordinate times in the RSFK, for three scattering points and their corresponding values of E. After the scattering, the comoving observers (thick line) see a horizon crossing. This is while a distant observer (thin line) never observes this (frozen falling particles). The plots have been done for $m = 1$, $Q = 1$, $q = 0.5$ and $\lambda = 10$.

in which $z_k \doteq \frac{1}{(r_k/r_s)-1}$, with $r_1 \equiv r_+$, $r_2 \equiv -r_+$, $r_3 \equiv r_{++}$ and $r_4 \equiv -r_{++}$, and the coefficients are expressed as

$$\delta_0 = \frac{\lambda^2 E}{m\sqrt{\gamma_0}} \frac{z_1 z_2 z_3 z_4}{z_5 r_s^2}, \tag{3.281a}$$

$$\delta_1 = \frac{(z_1+1)^2 z_1 (z_1 - z_5)}{(z_1-z_2)(z_1-z_3)(z_1-z_4)}, \tag{3.281b}$$

$$\delta_2 = \frac{(z_2+1)^2 z_2 (z_2 - z_5)}{(z_2-z_1)(z_2-z_3)(z_2-z_4)}, \tag{3.281c}$$

$$\delta_3 = \frac{(z_3+1)^2 z_3 (z_3 - z_5)}{(z_3-z_1)(z_3-z_2)(z_3-z_4)}, \tag{3.281d}$$

$$\delta_4 = \frac{(z_4+1)^2 z_4 (z_4 - z_5)}{(z_4-z_1)(z_4-z_2)(z_4-z_3)}. \tag{3.281e}$$

Since these trajectories escape the black hole, they will eventually confront the cosmological horizon. In Fig. 3.27, the temporal relations in Eqs. (6.63) and (6.67) have been used to demonstrate the RSFK, as observed by comoving and distant observers, for three different scattering distances.

Frontal scattering of the second kind

By switching the scattering distance to r_f, the particles experience the RSSK and they confront the event horizon. The corresponding equations of motion are the same as those in the case of RSFK and are given by exchanging $r_s \leftrightarrow r_f$ in the relations. The corresponding temporal parameters have been demonstrated in Fig. 3.28. Same as be-

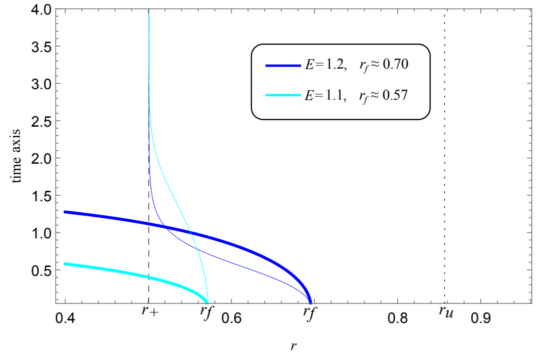

Figure 3.28: The RSSK for two different scattering points and their corresponding values of E, plotted for $m = 1$, $Q = 1$, $q = 0.5$ and $\lambda = 10$.

fore, the comoving and distance observers see different fates for the infalling particles, but here, regarding the capture process by the event horizon.

Critical radial motion

In the case that $E = E_u$, the unstable (critical) motion of particles depends on whether they approach from $r_i > r_u$ or from $d_i < r_u$. According to the discontinuity of $\frac{\mathrm{d}\tau}{\mathrm{d}r}$ and $\frac{\mathrm{d}t}{\mathrm{d}r}$ at r_i and d_i, we can expect two different behaviors for the approaching particles, in the sense that they either fall on $r = r_u$ (fate I) or be pulled towards the horizons (fate II). These are revealed by integrating the equations of motion for the time parameters. For particles coming from r_i, we obtain

$$\tau_I(r) = \pm\frac{\lambda}{m}\left[\tau_A(r) - \tau_B(r) - \tau_A(r_i) + \tau_B(r_i)\right], \tag{3.282}$$

$$\tau_{II}(r) = \mp\frac{\lambda}{m}\left[\tau_A(r) - \tau_B(r) - \tau_A(d_i) + \tau_B(d_i)\right], \tag{3.283}$$

for the comoving observers, where

$$\tau_A(r) = \operatorname{arcsinh}\left(\frac{r + r_u}{\sqrt{\bar{a} + 2r_u^2}}\right), \tag{3.284a}$$

$$\tau_B(r) = \frac{r_u}{\sqrt{6r_u^2 + \bar{a}}}\operatorname{arcsinh}\left(\frac{6r_u^2 + \bar{a} + 2r_u(r - r_u)}{|r - r_u|\sqrt{\bar{a} + 2r_u^2}}\right). \tag{3.284b}$$

For the distant observers, we get

$$t_I(r) = \pm\frac{\lambda^3 E}{m r_u^2}\sum_{n=0}^{4}\varpi_n\left[t_n(r) - t_n(r_i)\right], \tag{3.285}$$

$$t_{II}(r) = \mp\frac{\lambda^3 E}{m r_u^2}\sum_{n=0}^{4}\varpi_n\left[t_n(r) - t_n(d_i)\right], \tag{3.286}$$

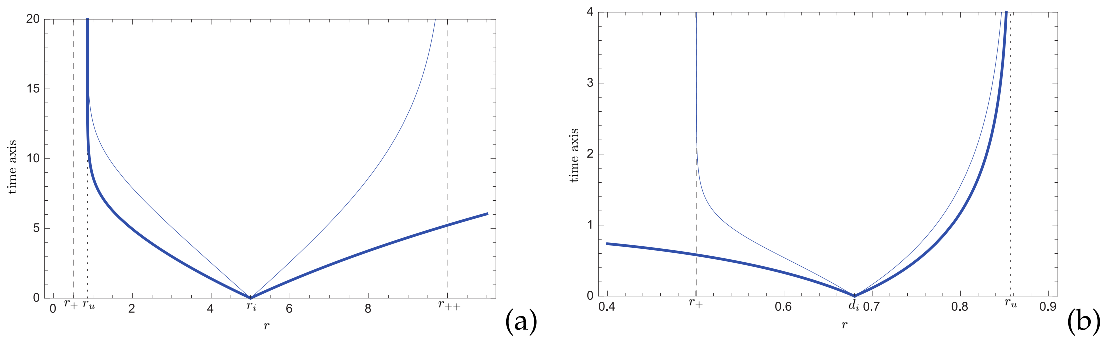

Figure 3.29: The critical radial motion for fates I and II, plotted for comoving (thick line) and distant (thin line) observers, by letting $m = 1$, $Q = 1$, $q = 0.5$ and $\lambda = 10$. The trajectories have been specified for particles approaching from (**a**) $r = r_i = 5$ and (**b**) $r = d_i = 0.68$.

where

$$t_n(r) = \frac{r_u}{\sqrt{R_n^2}} \operatorname{arcsinh}\left(\frac{R_n^2 + (r_u + r_n)(r - r_n)}{|r - r_u|\sqrt{\bar{a} + 2r_u^2}}\right), \tag{3.287a}$$

$$R_n^2 = 3r_u^2 + \bar{a} + 2r_u r_n + r_n^2, \tag{3.287b}$$

and the coefficients are given as

$$\varpi_0 = \frac{r_u^3(r_u - r_5)}{(r_1 - r_u)(r_2 - r_u)(r_3 - r_u)(r_4 - r_u)}, \tag{3.288a}$$

$$\varpi_1 = \frac{r_u r_1^2(r_1 - r_5)}{(r_1 - r_u)(r_1 - r_2)(r_1 - r_3)(r_1 - r_4)}, \tag{3.288b}$$

$$\varpi_2 = \frac{r_u r_2^2(r_2 - r_5)}{(r_2 - r_u)(r_2 - r_1)(r_2 - r_3)(r_2 - r_4)}, \tag{3.288c}$$

$$\varpi_3 = \frac{r_u r_3^2(r_3 - r_5)}{(r_3 - r_u)(r_3 - r_1)(r_3 - r_2)(r_3 - r_4)}, \tag{3.288d}$$

$$\varpi_4 = \frac{r_u r_4^2(r_4 - r_5)}{(r_4 - r_u)(r_4 - r_1)(r_4 - r_2)(r_4 - r_3)}, \tag{3.288e}$$

in which $r_0 \equiv r_u$, $r_1 \equiv r_+$, $r_2 \equiv -r_+$, $r_3 \equiv r_{++}$ and $r_4 \equiv -r_{++}$. The critical radial behavior of temporal parameters, as measured by the comoving and the distant observers, have been plotted in Fig. 3.29, separately for the initial points r_i and d_i. In each of the diagrams, the cases I and II have been demonstrated and the horizon crossing is shown accordingly.

So far, both the angular and the radial trajectories of charged particles were studied and possible analytical solutions to the equations of motion were given. It is however worth mentioning that the study of the physical properties of moving particles is not summarized to the evolution of a single particle's trajectory. In the case that a bundle of trajectories is taken into account, definite kinematical parameters will play important roles in the characterization of a *flow* of particle trajectories. Accordingly, and in the next subsection, we consider such a flow of particles and study how it reacts to the internal and external forces acting on the world-lines.

3.4.4 A congruence of infalling charged particles

We consider a bundle of particle trajectories, which together, constitute a congruence of world-lines that fall onto the CWBH. Essentially, the congruence kinematics is a tool to inspect the Penrose–Hawking singularity theorems (Penrose, 1965; Hawking, 1965, 1966; Penrose, 2002) and is accurately formulated by the well-known Raychaudhuri equation (Raychaudhuri, 1955). This equation formulates the way the congruences would evolve their cross-sectional (transverse) area (Kar & SenGupta, 2007).

Here, we switch our discussion to the possibility of applying some geometrical methods in order to demonstrate the deviation of a congruence of time-like trajectories while they pass the black hole. For particles passing a RN black hole, this deviation has been studied in detail (Balakin et al., 2000; Heydari-Fard et al., 2019).

In the geometric sense, the congruence deviation gives the relative acceleration between the curves that are generated by the tangential vector $\boldsymbol{u}$, in terms of the Jacobi (deviation) vector field $\boldsymbol{\xi}$. This vector field resides on the curves that connect points of equal τ on smooth planes of world-lines. These vectors satisfy (Wald, 1984; Poisson, 2009)

$$\mathfrak{L}_{\boldsymbol{u}}\boldsymbol{\xi} = \mathfrak{L}_{\boldsymbol{\xi}}\boldsymbol{u}, \tag{3.289}$$

where $\mathfrak{L}_{\boldsymbol{X}}$ indicates the Lie differentiation with respect to a vector field $\boldsymbol{X}$. The above equation therefore can be recast as

$$\xi^{\mu}{}_{;\nu}u^{\nu} = u^{\mu}{}_{;\nu}\xi^{\nu}. \tag{3.290}$$

In above, the semicolons correspond to covariant differentiation. Note that, the quantity $\boldsymbol{\xi}\cdot\boldsymbol{u}$[3] varies along the congruence as (?)

$$\begin{aligned}\frac{D}{d\tau}\left(\boldsymbol{\xi}\cdot\boldsymbol{u}\right) &\equiv \left(\boldsymbol{\xi}\cdot\boldsymbol{u}\right)_{;\nu}u^{\nu}\\ &= \frac{1}{2}\left(\boldsymbol{u}\cdot\boldsymbol{u}\right)_{;\nu}\xi^{\nu} + a_{\mu;\nu}\xi^{\mu}u^{\nu},\end{aligned} \tag{3.291}$$

where

$$a^{\mu} = u^{\mu}{}_{;\nu}u^{\nu}, \tag{3.292}$$

[3]Throughout this thesis, we notate $\boldsymbol{x}\cdot\boldsymbol{y} = g_{\mu\nu}x^{\mu}y^{\nu}$ for two vectors $\boldsymbol{x}$ and $\boldsymbol{y}$.

is the four-acceleration of the non-inertial frames, according to non-gravitational effects. In this regard, a non-zero $\boldsymbol{a}$ corresponds to a vector field which is not parallel-transported along the world-lines. Accordingly, the congruence deviation equation can then be written as

$$\begin{aligned}\mathfrak{A}^{\mu} \doteq \frac{D^2\xi^{\mu}}{\mathrm{d}\tau^2} &\equiv \left(\xi^{\mu}{}_{;\nu}u^{\nu}\right)_{;\gamma}u^{\gamma} \\ &= a^{\mu}{}_{;\nu}\xi^{\nu} - R^{\mu}{}_{\nu\alpha\beta}u^{\nu}\xi^{\alpha}u^{\beta}. \qquad (3.293)\end{aligned}$$

This vector, measures the *relative acceleration* between two world-lines, as measured by the change in $\boldsymbol{\xi}$, and connects it to the spacetime curvature (Pirani, 1956; Bażański, 1989).

According to the Eqs. (3.233), (3.234) and (3.235), we know that a congruence of charged particles with angular motion, that fall onto the charged black hole, is generated by the following four-velocity:

$$u^{\mu} = \left(\frac{E - V_q(r)}{B(r)}, \sqrt{(E-V_-)(E-V)}, 0, \frac{L}{r^2}\right), \qquad (3.294)$$

which satisfies $\boldsymbol{u}\cdot\boldsymbol{u} = -m^2$ (we let $m = 1$). The congruence deviation (Jacobi) field, related to the vector field (3.294), can then take the generic form

$$\xi^{\mu} = \left(\xi^0(r), \xi^1(r), 0, \xi^3(r)\right), \qquad (3.295)$$

for which, the consideration of the Lie transportation condition (i.e. $\mathfrak{L}_{\boldsymbol{u}}\boldsymbol{\xi} = \boldsymbol{0}$), provides

$$\xi^0(r) = 2^{11/4}\lambda^2\left(\frac{E - rV_q(r)}{4 - 4\lambda^2 + Q^2\lambda^2} - \frac{E - V_q(r)}{r^2\left(4 - 4\lambda^2 + \frac{Q^2\lambda^2}{r^2}\right)}\right), \qquad (3.296)$$

$$\xi^1(r) = 2^{3/4}\sqrt{(E-V)(E-V_-)}, \qquad (3.297)$$

$$\xi^3(r) = -2^{5/4}L\left(1 - \frac{1}{r^2}\right). \qquad (3.298)$$

The above vector field results in a non-zero rate of change of $\boldsymbol{\xi}\cdot\boldsymbol{u}$, indicating that the Jacobi field $\boldsymbol{\xi}$ is nowhere orthogonal to the congruence.

The four-acceleration of the infalling charged particles in electromagnetic fields, obey the following relation (Misner et al., 2017):

$$a^{\mu} = -\frac{q}{m}g^{\mu\nu}F_{\nu\alpha}u^{\alpha}, \qquad (3.299)$$

which is given in terms of the field strength tensor

$$F_{\mu\nu} = A_{\nu;\mu} - A_{\mu;\nu}. \qquad (3.300)$$

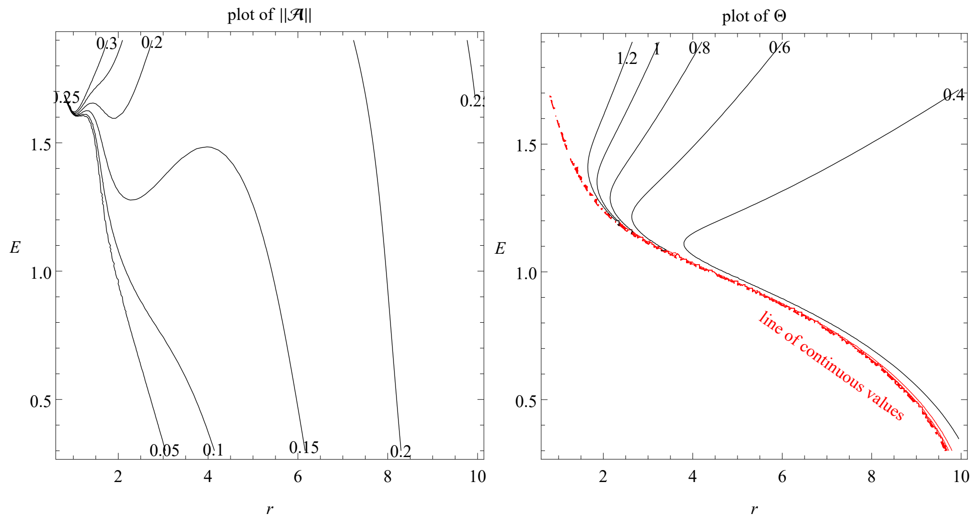

Figure 3.30: The behaviors of $\|\mathfrak{A}\|$ and Θ for $0.3 < E < 1.9$, considering $Q = 1$, $q = 0.5$, $\lambda = 10$ and $L = 1$. The corresponding event and cosmological horizons are located respectively at 0.5 and 9.98. The contours indicate discrete values for the parameters for specific ranges of r and E. In particular, the parameter Θ, beside discrete ones, can have very close values that reside on a line tangent to the contours.

Accordingly, the congruence deviation equation (3.293) can be recast as (Balakin et al., 2000; Heydari-Fard et al., 2019)

$$\mathfrak{A}^\mu = -R^\mu{}_{\nu\alpha\beta} u^\nu \xi^\alpha u^\beta - \frac{q}{m} g^{\mu\alpha} \left(F_{\alpha\beta;\nu} u^\beta \xi^\nu + F_{\alpha\beta} u^\beta{}_{;\nu} \xi^\nu \right). \tag{3.301}$$

Since, this acceleration is related to the internal interaction of the world-lines, it naturally affects the expansion of the congruence. This expansion is defined as the fractional rate of change of the transverse subspace of the congruence, and in our case is defined as (**?**)

$$\Theta = u^\mu{}_{;\mu}. \tag{3.302}$$

Accordingly, we can compare the behavior of $\mathfrak{A}$ with that of the congruence expansion as the particle world-lines approach the black hole. For this, we consider the norm of the aforementioned vector field, i.e. $\|\mathfrak{A}\|$[4], and plot it for a definite range of E, inside the causal region. Same is done for the congruence expansion (see Fig. 3.30). As it is seen in the figures, the approaching congruence is of positive expansion, so that its transverse cross-section increases in area and the world-lines recede from each other. This is in agreement with the positive acceleration between the world-lines, as it is shown in the diagram of $\|\mathfrak{A}\|$. As the particles approach the event horizon, the

[4]The norm of a vector $\boldsymbol{X}$ is defined as $\|\boldsymbol{X}\| \doteq \sqrt{\boldsymbol{X}\cdot\boldsymbol{X}}$.

congruence's internal acceleration merges to a single value at a specific E, which indicates that only distinct particles can reach that region and there they will maintain a constant mutual force. In other regions, distant from the event horizon, the particle deflection (and scattering) can happen under positive congruence expansion and positive internal acceleration. According to the figures, for some fixed values of E, the internal interactions between the world-lines remain repulsive at all distances, however, this repulsion is smaller at regions near the event horizon. This is while the congruence expansion reaches its maximum values for the same initial conditions. This is therefore a signature of scattering, where the expansion of the scattered congruence is a result of interactions with the source. On the other hand, for higher E, the relative acceleration and the congruence expansion take their maximum values near the black hole. The expansion in this case is naturally a result of internal interactions between the world-lines. We can therefore infer that the dynamical characteristics of a bundle of infalling world-lines on the CWBH, can indicate the effect of such interactions on the way the particles approach and recede the source, through their specific type of orbit.

3.5 Gravitational lensing inside a plasma

This section is dedicated to the application of elliptic integrals in calculating the gravitational lensing of light rays passing the CWBH spacetime when it is immersed in an inhomogeneous plasma, described by a coordinate-dependent refractive index. In fact, the usage of elliptic integrals in studying the light deflection in black hole spacetimes filled with plasma, has been dealt with for some regular black holes (Bisnovatyi-Kogan & Tsupko, 2017b). We try to get more insights to the abilities of the elliptic integrals in the calculation of the deflection angles of light ray trajectories, by choosing specific refractive ansatzes that are complicated enough, to be able to include a wide range of dependencies of the black hole surroundings on the horizon distances. This is done by considering two ansatzes for the plasmic refractive indices that are expressed as functions of the black hole horizons. Beside calculating the deflection angle, we also relate the aforementioned ansatzes to the black hole's photon sphere and shadow. The role of the elliptic integrals becomes more apparent in this regard, since without knowing the ability of the black hole in bending of light, one cannot talk about related features.

3.5.1 Light propagation in plasmic medium

Some backgrounds

Light propagation in medium is indeed described in the phase space, whose Hamiltonian dynamics gives the structure of the manifold's cotangent bundle. Given the manifold $(\mathcal{M}, g_{\alpha\beta})$ expressed in the chart x^α, the cotangent bundle $T^*\mathcal{M}$ provides the means to define the Hamiltonian $H \equiv H(x^\alpha, p_\alpha)$ where p_α is the momentum (wave) covector associated with the cotangent bundle. The Hamilton-Jacobi equation is therefore given in the form

$$H(x^\alpha, p_\alpha) = \frac{1}{2}\, \mathfrak{g}^{\alpha\beta} p_\alpha p_\beta = 0, \tag{3.303}$$

in which $\mathfrak{g}^{\alpha\beta}(x^\alpha)$ is the metric describing $T^*\mathcal{M}$, and is called the *optical metric*. In this sense, the wave (co)vector p_α is considered parallel to the tangential velocity 4-vector $u^\alpha \equiv \dot{x}^\alpha$[5] of the light congruence, i.e. $p_\alpha = \mathfrak{g}_{\alpha\beta} u^\beta$ and according to Eq. (3.303), the light propagates on null congruences with respect to the cotangent bundle. This however is not what an observer on $\mathcal{M}$ would measure, because $p_\alpha \neq g_{\alpha\beta} u^\alpha$ and $g^{\alpha\beta} p_\alpha p_\beta \neq 0$. This means that light behaves like massive particles during its propagation in a medium. In general, such media are given the properties of dielectrics. In fact, the connection between the light propagation in dielectric media and that in the gravitational systems, was recognized in the early days of the advent of general relativity. According to Eddington, relativistic forms of light propagation near a massive object, can be emulated in an appropriate refractive medium (Eddington, 1920). In reverse, Gordon pointed out that light propagation in a medium with specific refractive properties, can be emulated in a curved spacetime background endowed with an optical metric inferred from the optical properties of that medium (Gordon, 1923). This connection was elaborated further in terms of the effect permittivity (ε) and permeability (μ) of an arbitrary spacetime metric by Plebanski (Plebanski, 1960) and for the first time, the Gordon's optical metric was used by de Felice to construct (mathematically) a dielectric medium which could mimic a SBH (de Felice, 1971). The Gordon's optical metric is written as (Synge, 1960)

$$\mathfrak{g}^{\alpha\beta} = g^{\alpha\beta} + \left(1 - n^2\right) v^\alpha v^\beta, \tag{3.304}$$

where $n(x^\alpha) \equiv \sqrt{\varepsilon\mu}$ and v^α are respectively the scalar refractive index and the tangential velocity 4-vector of the dielectric in the comoving frame[6]. In order to include

[5] Here, over-dots indicate ∂_τ where τ is the congruence affine parameter.

[6] In fact, since the observer moves on a time-like curve on $\mathcal{M}$, then in the $(-+++)$ sign convention, $g_{\alpha\beta} v^\alpha v^\beta = -1$. In the same sense, the contraction $v^\alpha p_\alpha$ should be normalized to a real value, which here

anisotropy, birefringence and magnetoelectric couplings, the notion of the optical metric has been given efforts to be generalized (Ehlers, 1968; Chen & Kantowski, 2009b,a; Thompson, 2018). In the most covariant form, this metric is pseudo-Finslerian, according to the relation

$$\mathfrak{g}^{\alpha\beta} = \frac{\partial^2 H}{\partial p_\alpha \partial p_\beta}. \tag{3.305}$$

So far, we have presented some general information for light propagation inside non-magnetized plasma. More technical and mathematical information will be given in section 5.1.

In what follows, we consider that a spherically symmetric region (the exterior geometry of the CWBH) is filled with a dielectric material, in the form of an inhomogeneous cold plasma with a scalar refractive index. We can therefore assume that the light follows the trajectories on the background described by Gordon's optical metric (3.304).

Light propagation in a spherically symmetric plasmic medium surrounding a static black hole

The index of refraction of an inhomogeneous non-magnetized, optically-thin plasmic shell is given by the relation

$$n^2(r) = 1 - \frac{\omega_p^2(r)}{\omega^2(r)}, \tag{3.306}$$

where ω_p is the electron plasma frequency given by

$$\omega_p^2(r) = K_e\, N(r), \quad K_e = \frac{e^2}{\epsilon_0\, m_e} = 3182.6\,[\mathrm{m}^3/\mathrm{s}^2]. \tag{3.307}$$

Here $N(r)$ is the electron concentration in plasma, e is the electric charge of the electron and m_e is the electron mass.

For the sake of simplicity, in what follows, we restrict our analysis to the equatorial plane, hence, $p_\vartheta = 0$. Under such condition, applying the optical metric (3.304) to the Hamiltonian in Eq. (3.303) we get

$$\begin{aligned} H &= \frac{1}{2}\left[g^{\alpha\beta} p_\alpha p_\beta + \hbar^2 \omega_p^2(r)\right] \\ &= \frac{1}{2}\left(-\frac{p_t^2}{B(r)} + B(r) p_r^2 + \frac{p_\phi^2}{r^2} + \hbar^2\omega_p^2(r)\right), \end{aligned} \tag{3.308}$$

is the energy of a photon of frequency ω ($\mathcal{E} = \hbar\omega$), evaluated by an observer, comoving with the plasma.

in a spherically symmetric spacetime as in Eq. (3.24). Accordingly, the canonical Hamilton's equations

$$\dot{p}_\alpha = -\frac{\partial H}{\partial x^\alpha}, \qquad \dot{x}^\alpha = \frac{\partial H}{\partial p_\alpha}, \tag{3.309}$$

in the cyclic coordinates (t, ϕ) yield

$$\dot{p}_t = -\frac{\partial H}{\partial t} = 0 \quad \Rightarrow p_t = -\hbar\omega_0 = \text{cte.}, \tag{3.310}$$

$$\dot{p}_\phi = -\frac{\partial H}{\partial \phi} = 0 \quad \Rightarrow p_\phi = \ell = \text{cte.}, \tag{3.311}$$

regarding which, we can infer that $\hbar\omega_0 \equiv \mathcal{E}_0$ and ℓ are constants of motion, associated with its temporal and rotational invariance. The remaining equations read

$$\begin{aligned} \dot{p}_r &= -\frac{\partial H}{\partial r} = \\ &= \frac{\ell^2}{r^3} - \frac{\mathrm{d}}{\mathrm{d}r}\left[\frac{\hbar^2\omega_p^2(r)}{2}\right] - \frac{1}{2}\frac{\mathrm{d}B(r)}{\mathrm{d}r}\left[p_r^2 + \frac{\hbar^2\omega_0^2}{B^2(r)}\right], \end{aligned} \tag{3.312}$$

$$\dot{t} = \frac{\partial H}{\partial p_t} = -\frac{p_t}{B(r)} = \frac{\hbar\omega_0}{B(r)}, \tag{3.313}$$

$$\dot{\phi} = \frac{\partial H}{\partial p_\phi} = \frac{p_\phi}{r^2} = \frac{\ell}{r^2}, \tag{3.314}$$

$$\dot{r} = \frac{\partial H}{\partial p_r} = B(r)\, p_r. \tag{3.315}$$

There is also one extra condition

$$0 = \frac{\ell^2}{r^2} + B(r)\, p_r^2 - \left[\left(\frac{\hbar\omega_0}{\sqrt{B(r)}}\right)^2 - \hbar^2\omega_p^2(r)\right], \tag{3.316}$$

inferred from the Hamilton-Jacobi equation. Note that, the radial dependence of the photon's frequency, measured by the comoving observer, is obtained by the redshift formula

$$\omega(r) = \frac{\omega_0}{\sqrt{B(r)}}. \tag{3.317}$$

Therefore, it is no hard to see from Eqs. (3.316) and (3.317) that, in a given position r, the photon frequency $\omega(r)$ is bigger than the plasma frequency $\omega_p(r)$, i.e.

$$\omega(r) > \omega_p(r), \tag{3.318}$$

which is an empirical constraint for light propagation in plasma (**?**).

Now, turning to the subject in hand, we commence studying the light propagation in the above system. Using Eqs. (3.314) and (3.315), the general orbits are governed by

$$\left(\frac{\mathrm{d}r}{\mathrm{d}\phi}\right)^2 = \frac{\dot{r}^2}{\dot{\phi}^2} = \mathfrak{F}(r), \tag{3.319}$$

with

$$\mathfrak{F}(r) = r^2 B(r)\left[\frac{h^2(r)}{h^2(\mathcal{R})} - 1\right], \tag{3.320}$$

where

$$h^2(r) = \frac{r^2\, n^2(r)}{B(r)} = \frac{r^2}{B(r)}\left(1 - \frac{\omega_p^2(r)}{\omega^2(r)}\right), \tag{3.321a}$$

$$h^2(\mathcal{R}) = \frac{\ell^2}{\hbar^2\omega_0^2} = b^2. \tag{3.321b}$$

Equation (3.321b) relates the closest approach to the source, $\mathcal{R}$, to the impact parameter b (another constant of motion). Therefore, for the case of the CWBH and exploiting Eqs. (3.319) to (3.321b), the deflection angle for a light ray that travels from r_{++} to $\mathcal{R}$ and returns again to r_{++}, can be calculated as

$$\begin{aligned}\widehat{\alpha} &= 2b\int_{\mathcal{R}}^{r_{++}} \frac{\mathrm{d}r}{\sqrt{r^2B(r)h^2(r) - b^2r^2B(r)}} - \pi \\ &= 2b\int_{\mathcal{R}}^{r_{++}} \frac{\mathrm{d}r}{\sqrt{r^4n^2(r) - b^2r^2B(r)}} - \pi.\end{aligned} \tag{3.322}$$

The above deflection, relates to the lensing effect caused by massive sources. This shows that how outermost objects can change their apparent position. The above deflection angle however could be determined specifically, once $n(r)$ is given an appropriate algebraic expression, regarding the causality conditions.

3.5.2 Specific cases of $n(r)$ for the CWBH

The casual connection in the spacetime constructed by the CWBH, suggests that an observer inside the cosmological horizon cannot be aware of the events from the region covered by $r > r_{++}$ (see Fig. 3.31). For this reason, any algebraic assignment for the refractive index $n(r)$ should respect this kind of causality. This means that the refraction is well-defined only inside the boarders of the casual connection. Accordingly, we propose relevant algebraic forms, regarding the boundaries of the causality.

First ansatz

Taking into account a case in which $n(r_{++}) = n(r_+) = 0$, we propose the following ansatz:

$$n^2(r) = B(r)\left[\frac{r_{++}^2}{r^2} + 1\right], \tag{3.323}$$

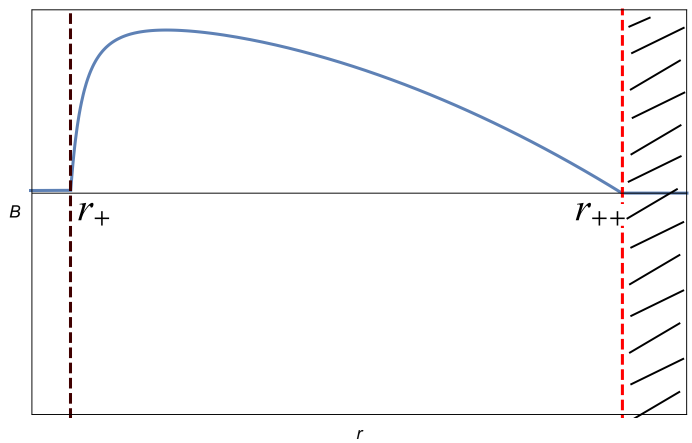

Figure 3.31: The causal structure offered by a charged Weyl black hole. Events outside r_{++} does not have casual connections with the observers residing inside it.

which of course, has its maximum at $r_+ < r_{\max} < r_{++}$. By means of Eq. (3.34), this can be rewritten as

$$n^2(r) = \frac{(r_{++}^4 - r^4)(r^2 - r_+^2)}{\lambda^2 r^4}. \tag{3.324}$$

The integrand in Eq. (4.49) is $\frac{1}{\sqrt{\mathfrak{P}(r)}}$, in which, according to the above definition, we have

$$\mathfrak{P}(r) = \frac{(r_{++}^2 - r^2)(r^2 - r_+^2)}{\lambda^2}(r^2 - \mathcal{R}^2). \tag{3.325}$$

Here, $\mathcal{R} = \sqrt{b^2 - r_{++}^2}$ is the closest approach as appeared in Eq. (3.321b). This implies that $b > r_{++}$. Now, recasting

$$\mathfrak{P}(r) = \frac{r^6 r_{++}^2 r_+^2 \mathcal{R}^2}{\lambda^2}\left(\frac{1}{r^2} - \frac{1}{r_{++}^2}\right)\left(\frac{1}{r_+^2} - \frac{1}{r^2}\right)\left(\frac{1}{\mathcal{R}^2} - \frac{1}{r^2}\right), \tag{3.326}$$

we can rewrite the deflection angle in Eq. (4.49) as

$$\begin{aligned} \delta &\equiv \hat{\alpha} + \pi \\ &= \frac{b\lambda}{r_{++} r_+ \mathcal{R}} \int_0^{\xi_{++}} \frac{\mathrm{d}\xi}{\sqrt{\xi(\xi_{++} - \xi)(\xi_+ + \xi)}}, \end{aligned} \tag{3.327}$$

for which, we have used the change of variable

$$\xi(r) \doteq \frac{1}{\mathcal{R}^2} - \frac{1}{r^2}, \tag{3.328}$$

and have defined

$$\xi_{++} = \xi(r_{++}), \tag{3.329a}$$

$$\xi_+ = \frac{1}{r_+^2} - \frac{1}{\mathcal{R}^2}. \tag{3.329b}$$

The integral in Eq. (3.327) is in fact an elliptic integral of the first kind. We therefore get

$$\delta = \frac{b\lambda}{r_{++}r_{+}\mathcal{R}}\,\bar{\bar{g}}\,K(k) \tag{3.330}$$

in which (Byrd & Friedman, 1971)

$$\bar{\bar{g}} = \frac{2}{\sqrt{\xi_{++}+\xi_{+}}} = \frac{2r_{++}r_{+}}{\sqrt{r_{++}^2-r_{+}^2}}, \tag{3.331a}$$

$$K(k) \equiv F\left(\varphi(\xi_{++}),k\right) = \int_0^{\frac{\pi}{2}} \frac{\mathrm{d}\eta}{\sqrt{1-k^2\sin^2\eta}}, \tag{3.331b}$$

where the latter is the complete elliptic integral of the first kind, given

$$\varphi(y) = \arcsin\left(\sqrt{\frac{\xi_{++}+\xi_{+}}{\xi_{++}}\,\frac{y}{y+\xi_{+}}}\right), \tag{3.332a}$$

$$k = \sqrt{\frac{\xi_{++}}{\xi_{++}+\xi_{+}}} = \frac{r_{+}}{\mathcal{R}}\sqrt{\frac{r_{++}^2-\mathcal{R}^2}{r_{++}^2-r_{+}^2}}. \tag{3.332b}$$

Regarding the relation between b and $\mathcal{R}$, the deflection could be rewritten in terms of either of the above parameters as

$$\delta(\lambda,b) = \frac{2b\lambda}{\sqrt{(b^2-r_{++}^2)(r_{++}^2-r_{+}^2)}}\,K\left(k(b)\right), \tag{3.333a}$$

$$\delta(\lambda,\mathcal{R}) = \frac{2\lambda}{\mathcal{R}}\sqrt{\frac{\mathcal{R}^2+r_{++}^2}{r_{++}^2-r_{+}^2}}\,K\left(k(\mathcal{R})\right). \tag{3.333b}$$

Note that, not all values of b are allowed for the light ray trajectories. Since $b > r_{++}$ and $k > 0$, regarding Eq. (3.332b), we have either $\sqrt{\frac{3}{2}}\,r_{++} \leq b < \sqrt{2}\,r_{++}$ or $r_{++} < b \leq \sqrt{\frac{3}{2}}\,r_{++}$. This has been shown in Fig. 3.32. Also, the behavior of δ has been demonstrated in Fig. 3.33, distinctly for the above two categories. The plots show that the second kind of confinement for b, results in more fast varying deflections.

Second ansatz

As the second guess, we consider a more complicated algebraic form, reading

$$n^2(r) = \frac{B(r)}{r^2}\left[b^2+(r^2+\sigma^2)^2\left(r^2-r_{++}^2\left(1-\frac{\sigma^2}{r_{+}^2}\right)\right)\right], \tag{3.334}$$

in which $\sigma \equiv \sigma(r_{+},r_{++})$ is a function whose value satisfies the condition $0 < \sigma < r_{+}$. Exploiting this in the integrand, we get

$$\mathfrak{P}(r) = \frac{1}{\lambda^2}\left[(r^2-r_{+}^2)(r_{++}^2-r^2)(r^2+\sigma^2)^2(r^2-\mathcal{R}^2)\right], \tag{3.335}$$

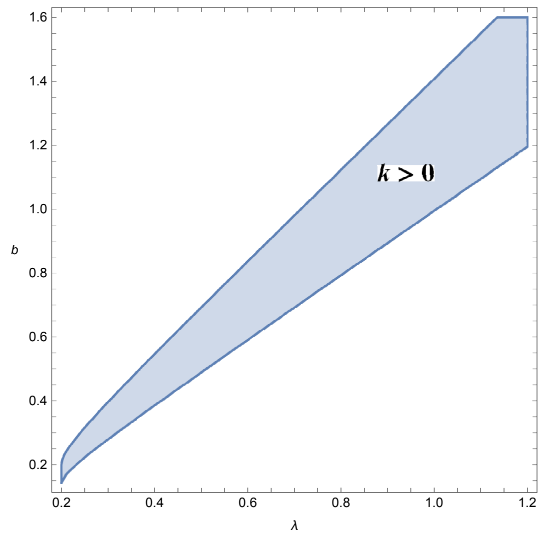

Figure 3.32: The region of allowed values for b for which the condition $k>0$ is satisfied. The plot has been done for $Q=0.1$. The considered range for b is from $1.02\,r_{++}$ to $1.4\,r_{++}$ for the given λ and Q, so that it can cover the allowed values.

where the newly defined closest approach is $\mathcal{R}=\sqrt{r_{++}^2\left(1-\frac{\sigma^2}{r_+^2}\right)}$. Upon recasting, the above polynomial becomes

$$\mathfrak{P}(r)=\left(\frac{r^5 r_+ r_{++}\sigma^2\mathcal{R}^2}{\lambda}\right)^2\left(\frac{1}{r_+^2}-\frac{1}{r^2}\right)\left(\frac{1}{r^2}-\frac{1}{r_{++}^2}\right)\\ \times\left(\frac{1}{r^2}+\frac{1}{\sigma^2}\right)^2\left(\frac{1}{\mathcal{R}^2}-\frac{1}{r^2}\right). \tag{3.336}$$

Applying the same change of variable as in Eq. (3.328), we get

$$\delta=\frac{b\lambda}{r_+ r_{++}\mathcal{R}\sigma}\mathcal{I}_1, \tag{3.337}$$

where

$$\mathcal{I}_1=\int_0^{\xi_{++}}\frac{\left(\xi-\frac{1}{\mathcal{R}^2}\right)\,\mathrm{d}\xi}{(\xi-\bar{\xi})\sqrt{\xi(\xi_++\xi)(\xi_{++}-\xi)}}. \tag{3.338}$$

Here we have defined

$$\bar{\xi}\doteq\frac{1}{\mathcal{R}^2}+\frac{1}{\sigma^2}, \tag{3.339}$$

and other definitions remain the same as in the previous case. The integral in Eq. (3.338) has an elliptic counterpart so that we can rewrite it as (Byrd & Friedman, 1971)

$$\mathcal{I}_1=\frac{\bar{\bar{g}}}{\mathcal{R}^2\bar{\xi}}\int_0^{K(k)}\frac{1-\beta_1^2\,\mathrm{sn}^2(\eta)}{1-\beta^2\mathrm{sn}^2(\eta)}\mathrm{d}\eta, \tag{3.340}$$

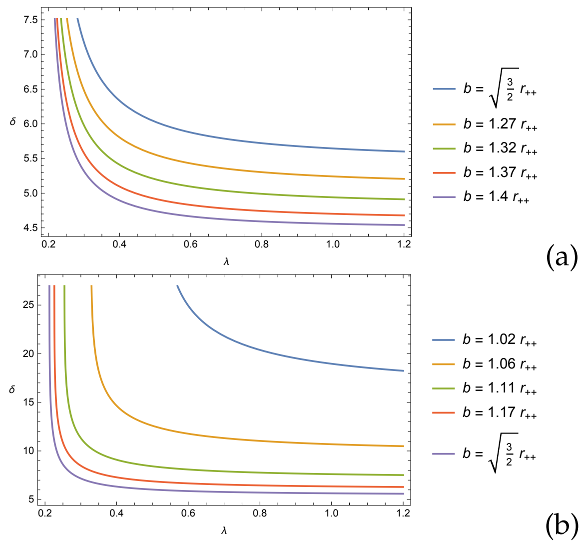

Figure 3.33: The range for the deflection angles obtained from the refractive index of the first kind, for five given values for the impact parameter, within the allowed range for each case. We have taken $Q = 0.1$ and the plots have been done for (a) $\sqrt{\frac{3}{2}}\, r_{++} \leq b < \sqrt{2}\, r_{++}$ and (b) $r_{++} < b \leq \sqrt{\frac{3}{2}}\, r_{++}$. As it is seen, the second condition makes the deflection to change more rapidly toward the stable value.

in which

$$\beta^2 = \frac{\frac{1}{\mathcal{R}^2}(\xi_+ + \bar{\bar{\xi}})}{\bar{\bar{\xi}}(\xi_+ + \frac{1}{\mathcal{R}^2})}\, \beta_1^2 = \frac{\xi_{++}(\xi_+ + \bar{\bar{\xi}})}{\bar{\bar{\xi}}(\xi_{++} + \xi_+)}, \tag{3.341}$$

and $\mathrm{sn}(\eta)$ is a Jacobi elliptic function, doubly periodic in η, and is defined as (Byrd & Friedman, 1971)

$$\mathrm{sn}(\eta) = \sin(\varphi), \tag{3.342}$$

with φ given in Eq. (3.332). Considering the above elliptic counterpart, we get

$$\mathcal{I}_1 = \frac{\bar{\bar{g}}}{\mathcal{R}^2 \beta^2 \bar{\mu}} \left[\beta_1^2 K(k) + (\beta^2 - \beta_1^2)\Pi(\beta^2, k)\right], \tag{3.343}$$

where

$$\Pi(\beta^2, k) = \int_0^{\frac{\pi}{2}} \frac{\mathrm{d}\eta}{(1 - \beta^2 \sin^2\eta)\sqrt{1 - k^2 \sin^2\eta}} \tag{3.344}$$

is the complete elliptic integral of the third kind. With this in mind, and taking into account the definition in Eq. (3.331), we finally get

$$\delta = \frac{2b\lambda}{\mathcal{R}\sigma\left(1 + \frac{\mathcal{R}^2}{\sigma^2}\right)\sqrt{r_{++}^2 - r_+^2}} \left(\frac{r_+^2 + \sigma^2}{\mathcal{R}^2 + \sigma^2} K(k) + \frac{\mathcal{R}^2 - r_+^2}{\mathcal{R}^2 + \sigma^2} \Pi(\beta^2, k)\right), \tag{3.345}$$

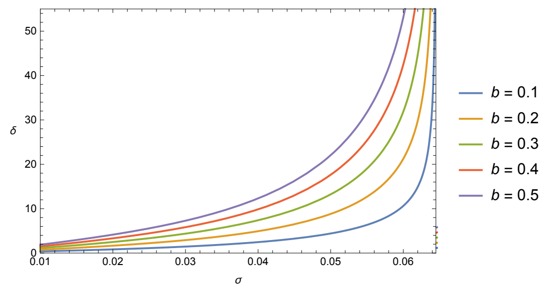

Figure 3.34: The behavior of the deflection angle obtained from the refractive index of the second kind, for five different impact parameters. The smaller the impact parameter is, the faster δ increases. The asymptotic behavior however stems in the presence of elliptic integrals in the description of δ. In this figure, we can see that for a certain value of σ, the light rays escape from the black hole. The plots have been done for $Q = 0.1$ and $\lambda = 0.25$ (in arbitrary length units).

which is compatible with

$$\beta^2 = \frac{\mathcal{R}^2 + \sigma^2}{r_+^2 + \sigma^2}\beta_1^2 = \frac{(r_{++}^2 - \mathcal{R}^2)(r_+^2 + \sigma^2)}{(r_{++}^2 - r_+^2)(\mathcal{R}^2 + \sigma^2)}, \tag{3.346}$$

and $k = (r_+/\mathcal{R})\beta_1$. Note that, since b does not have any contribution in the parameter $\mathcal{R}$, this angle does not put any restrictions on the impact parameter and the condition $k > 0$ is always satisfied. The behavior of the deflection in Eq. (3.345) has been plotted in Fig. 3.34 for some different impact parameter. The asymptotic behavior of the plots, stems in the elliptic functions included in the description of δ. Similar behavior was observed in Fig. 3.33. Physically, this means that light rays with definite impact parameters, can only contribute to the lensing process of black holes with definite physical properties (namely λ and Q). So, for certain black holes, not all rays can provide imaging through gravitational lensing. In the plots of Fig. 3.34, light ray deflections are given in terms of changes of the parameter σ.

3.5.3 The photon sphere

Photon spheres are those hypersurfaces, on which light rays can stay on a stable circular path. The innermost photon sphere has the radius $\mathcal{R}$ introduced above. The photon surfaces however can be determined by analyzing purely angular light orbits. This condition requires $\dot{r} = \ddot{r} = 0$, that from Eq. (3.315) it follows that $p_r = 0$. We therefore can rewrite the Hamilton-Jacobi equation as

$$\ell^2 = \hbar^2 r^2 \left[\frac{\omega_0^2}{B(r)} - \omega_p^2(r) \right]. \tag{3.347}$$

Furthermore, differentiating Eq. (3.315) with respect to the affine parameter, results in

$$\dot{p}_r = \frac{1}{B(r)}\left(\ddot{r} - \frac{\mathrm{d}B(r)}{\mathrm{d}r}\dot{r}\,p_r\right), \tag{3.348}$$

according to which, the zero radial velocity condition implies $\dot{p}_r = 0$. Hence, Eq. (3.312) can be recast as

$$\ell^2 = \frac{\hbar r^3}{2}\left[\frac{\mathrm{d}\omega_p^2(r)}{\mathrm{d}r} + \frac{\mathrm{d}B(r)}{\mathrm{d}r}\left(\frac{\omega_0^2}{B^2(r)}\right)\right]. \tag{3.349}$$

Subtracting the above equations and after some manipulations, we get the equation governing the radius of the circular light orbits

$$\frac{\mathrm{d}}{\mathrm{d}r}h^2(r) = 0. \tag{3.350}$$

Solutions to this equation determine the radius of photon spheres. Satisfaction of Eq. (3.350) is done by letting $h^2(r) = \mathfrak{c} = \text{const}$. Applying this in Eq. (3.321a) and taking into account the redshift in Eq. (3.317) we get

$$\omega_p^2(r) = \frac{\omega_0^2}{B(r)}\left(1 - \frac{\mathfrak{c}\,B(r)}{r^2}\right). \tag{3.351}$$

This demands the following condition for $r > r_+$:

$$\frac{r^2}{B(r)} > \mathfrak{c}. \tag{3.352}$$

Furthermore, considering Eq. (3.306) in Eq. (3.350) we get

$$\begin{aligned} 0 = &\left(2B(r) - r\left(\frac{\mathrm{d}}{\mathrm{d}r}B(r)\right)\right)\left(1 - B(r)\frac{\omega_p^2(r)}{\omega_0^2}\right) \\ &- r\,B(r)\left[\left(\frac{\mathrm{d}}{\mathrm{d}r}B(r)\right)\frac{\omega_p^2(r)}{\omega_0^2} + \frac{2B(r)\omega_p(r)}{\omega_0^2}\left(\frac{\mathrm{d}}{\mathrm{d}r}\omega_p(r)\right)\right]. \end{aligned} \tag{3.353}$$

In the case of no plasmic surroundings, we have $\omega_p(r) = 0$, yielding the following photon sphere radius in vacuum:

$$r_{\mathrm{ph}}^{(\mathrm{vac})} = \frac{\sqrt{2}\,r_+\,r_{++}}{\sqrt{r_+^2 + r_{++}^2}}. \tag{3.354}$$

From the values in Eqs. (3.26) and (3.27), this gives $r_{\mathrm{ph}}^{(\mathrm{vac})} = \frac{Q}{\sqrt{2}}$, which is the same as the radius of the critical orbits, r_c obtained before for the CWBH in vacuum (Fathi et al., 2020)[7].

[7]Note that, the radius in Eq. (3.354) will never regain the famous Schwarzschild $r = 3M$ photon sphere, by letting $r_+ = r_{++} = 2M$. This is because the metric potential in Eq. (3.25) is totally different in structure, regarding the presence and the definition of the λ parameter.

However, in the presence of plasma, this photon sphere is characterized by solving Eq. (3.353), which yields

$$\omega_p^2(r) = \frac{\lambda^2\omega_0^2\left(r^2(r_+^2 + r_{++}^2) - r_+^2 r_{++}^2\right)}{r^2(r^2 - r_+^2)(r_{++}^2 - r^2)}. \tag{3.355}$$

Note that, as long as the condition $\lambda > Q$ is satisfied, the positivity of the right hand side of the above relation is guaranteed.

Given the frequency in Eq. (3.355), the radius $r_{\rm ph}$ now depends on one other characteristic of the plasmic medium, namely the refractive index. This can be seen through Eq. (3.306), providing $\omega_p^2(r) = \frac{\omega_0^2[1-n^2(r)]}{B(r)}$. This, together with Eq. (3.355), results in the following alternative for the refractive index:

$$n^2(r) = 1 - \frac{(r_+^2 + r_{++}^2)}{r^2} + \left(\frac{r_+ r_{++}}{r^2}\right)^2. \tag{3.356}$$

The determination of $r_{\rm ph}$, however, requires other definitions for $n^2(r)$. To deal with this, we therefore recall the specific cases discussed previously.

- For the first ansatz in Eq. (3.324) (plasma of the first kind (PFK)), Eq. (3.356) provides $r_{\rm ph} = r_+$. This means that the corresponding hypersurface, formed as the 3-dimensional (3D) closure of the 2D circles characterized by $r = r_+$, is indeed a null surface. Although this result could seem unexpected, we here refer the reader to the fact that this photon surface is observed through a dispersive medium (plasma) that based on the geometric structure of the respected refractive index, could affect the photon surface to be located differently from that in the vacuum.

- For the case in Eq. (3.334) (plasma of the second kind (PSK)), we get

$$\begin{aligned} r_{\rm ph} = \frac{\mathcal{A}^{-\frac{1}{6}}}{\sqrt{6}\,r_+}\Big[&2^{\frac{4}{3}}(r_+r_{++})^4 + 2(r_+r_{++})^2\mathcal{A}^{\frac{1}{3}} + (-2\mathcal{A})^{\frac{2}{3}} \\ &+\sigma^2\left(2^{\frac{7}{3}}\,(r_+r_{++})^2\left(r_+^2 - r_{++}^2\right) - 2\left(2r_+^2 + r_{++}^2\right)\mathcal{A}^{\frac{1}{3}}\right) \\ &+\sigma^4\left(2^{\frac{4}{3}}(r_+^4 + r_{++}^4) - 2^{\frac{7}{3}}(r_+r_{++})^2\right)\Big]^{\frac{1}{2}}, \end{aligned} \tag{3.357}$$

  with

$$\mathcal{A} = \sqrt{\mathcal{B}^2 - 4\left((\sigma\, r_{++})^2 + r_+^2(r_{++}^2 + \sigma^2)\right)^6} - \mathcal{B}, \tag{3.358}$$

  where

$$\begin{aligned} \mathcal{B} = 27b^2r_+^6 + 2(\sigma r_{++})^6 + 6\,\sigma^4\left(r_{++}^2 + \sigma^2\right)(r_+r_{++})^2\left[\left(r_{++}^2 + \sigma^2\right)\,r_+^2 - r_{++}^2\right] \\ - r_+^6\left(2r_{++}^6 - 27\lambda^2 + 6\,\sigma^2 r_{++}^2(r_{++}^2 + \sigma^2) + 2\sigma^6\right). \end{aligned} \tag{3.359}$$

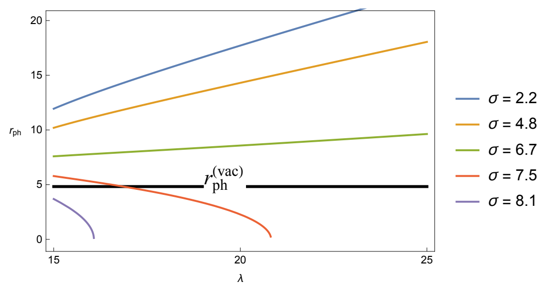

Figure 3.35: Confronting the radii of vacuum and plasmic photon spheres. The plots have been done for $b = 10$, $Q = 7$ and five different values of σ which have been selected according to $\sigma < r_+$. Changes in b do not have any effects on the form of the curves. Obviously, the value of $r_{\rm ph}^{\rm (vac)}$ does not depend on λ and is therefore a constant in this regard. This is while the plasmic $r_{\rm ph}$ raises constantly for smaller values of σ, whereas it drops fast for larger ones.

In Fig. 3.35, we have confronted the above radius for different values of σ, with the radius of the photon sphere in the vacuum case. We have considered a fixed b, because the curves with different values of b will coincide. The vacuum photon sphere exhibits a constant size, whereas the plasmic one can change its radius, depending on the value of σ. It is observed that, increase in λ has different effects on $r_{\rm ph}$, depending on the corresponding σ. This means that, the small–σ photon spheres expand as λ increases, whereas the large–σ ones would shrink.

3.5.4 The implications for $N(r)$

Even though the spacetime effects are imposed on the description of the refractive index, nevertheless, the physical interpretation of the particle distribution inside the spacetime is given by the concentration function $N(r)$. Applying the definition given in Eqs. (3.306) and (3.307), we get

$$N(r) = \frac{\omega_0^2}{K_e B(r)}\left[1 - n^2(r)\right]. \tag{3.360}$$

In this subsection, by paying attention to this quantity, we go deeper into the physical implications of both kind plasmas.

The PFK generates

$$N_1(r) = \frac{\omega_0^2\left[r^4\lambda^2 - \left(r^2 - r_+^2\right)\left(r_{++}^4 - r^4\right)\right]}{r^2\left(r^2 - r_+^2\right)\left(r_{++}^2 - r^2\right)}, \tag{3.361}$$

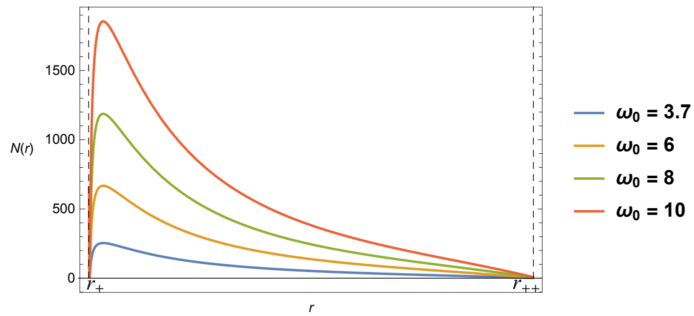

Figure 3.36: The behavior of particle concentration $N_1(r)$ for four values of ω_0, in the region between the horizons. All four concentrations have a maximum at the same radial distance and at the horizons, N_1 is indefinite. It however tends to zero at the vicinity of both horizons. The plots have been done for $Q = 7$, $\lambda = 19.4$, $b = 9$ and we have absorbed K_e into ω_0 (all values are in arbitrary length units).

the behavior of which has been illustrated in Fig. 3.36 inside the causal region. For the PSK, the concentration becomes

$$N_2(r) = \frac{\omega_0^2}{K_e r^2}\left[\frac{r^4\lambda^2}{(r^2-r_+^2)(r_{++}^2-r^2)} - b^2 - (r^2+\sigma^2)^2\left(r^2 - r_{++}^2\left(1-\frac{\sigma^2}{r_+^2}\right)\right)\right], \quad (3.362)$$

which evolves as plotted in Fig. 3.37 for five different values of σ, in the region $r_+ < r < r_{++}$. As it is expected, the concentration drops from its highest values at the vicinity of r_+, by moving toward r_{++}. As we can see from the plots of $N_1(r)$ and $N_2(r)$ (for definite values of σ), the electron concentration can tend to zero long before reaching the cosmological horizon (where the concentration should be indefinite). One important implication of this property, is that the effect of the plasma can be seen in regions outside its presence, because the refraction $n(r)$ is available in all the region $r_+ < r < r_{++}$. This can be interpreted as a combination of electromagnetic effects and optical gravity, manifesting themselves through the refractive index. For the second kind plasma, the fall in the value of $N_2(r)$ happens faster for smaller σ. However we should bear in mind that, through their relation to the horizons, every pair (λ, Q) is related to a range for σ, which has to satisfy $0 < \sigma < r_+$.

As a matter of interest, let us think of the PSK as a spherically symmetric halo, filling the region $r_+ < r < r_{++}$. Although electrons are not usually considered as dark matter candidates, however, it may be of interest to revisit their plasmic distribution in the cold dark matter realm. In this regard, we therefore compare the total masses

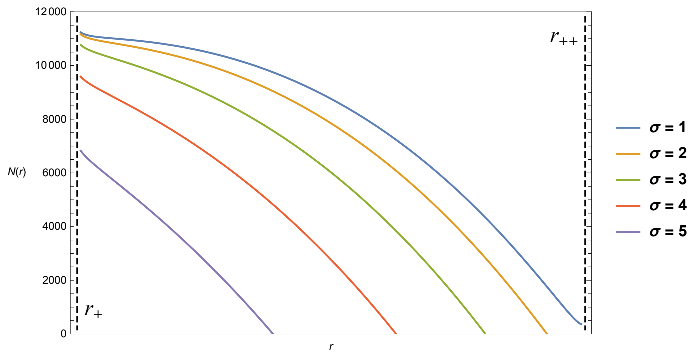

Figure 3.37: The evolution of particle concentration $N_2(r)$ for five values of σ, in the region between the horizons. The concentration drops by moving toward r_{++}. Significantly, larger σ results in a less steep decrease in the concentration. The plots have been done for $Q = 7$, $\lambda = 15$, $b = 10$ and $\omega_0 = 1.37$ (we have absorbed K_e into ω_0 and all values are in arbitrary length units). The above values have been chosen to obtain a good scale of observation and alternations in these values will just change the scale of the plots, not their form of behavior.

obtained from the above particle concentration, and that given by the Navarro-Frenk-White (NFW) density profile. The NFW profile for a cold dark matter distribution is (Navarro et al., 1995, 1996)

$$\rho(r) = \frac{\rho_0}{\frac{r}{\mathfrak{r}_s}\left(1+\frac{r}{\mathfrak{r}_s}\right)^2}, \tag{3.363}$$

in which the initial density ρ_0 and the scale radius $\mathfrak{r}_s$ depend on the characteristics of the halos. The integrated mass of the halo is obtained by integrating the above profile within the total volume. Considering a spherically symmetric halo, we obtain

$$\begin{aligned} M_{\mathrm{NFW}} &= \int_0^{\mathfrak{r}_{\max}} \rho(r)\, 4\pi r^2 \mathrm{d}r \\ &= 4\pi\rho_0\mathfrak{r}_s^3\left[\ln\left(\frac{\mathfrak{r}_s+\mathfrak{r}_{\max}}{\mathfrak{r}_s}\right) - \frac{\mathfrak{r}_{\max}}{\mathfrak{r}_s+\mathfrak{r}_{\max}}\right], \end{aligned} \tag{3.364}$$

up to a maximum radius $\mathfrak{r}_{\max}$. On the other hand, the total electron mass encompassed in a spherically symmetric plasmic halo, characterized by the number density $N_2(r)$ in Eq. (3.362), can be obtained by doing an integration over the volume in the region $r_+ < r < r_{++}$. This yields

$$\begin{aligned} M_P &= m_e \int_{r_+}^{r_{++}} N_2(r)\, 4\pi r^2 \mathrm{d}r \\ &= \frac{4\pi m_e\omega_0^2}{105 r_+^2}\Big[\, 3r_+^2\left(5r_+^7 - 35(b^2+\lambda^2)(r_{++}-r_+) - 7r_+^5 r_{++}^2\right. \\ &\quad \left. +2r_{++}^7\right) + 7(6r_+^7 - 7r_+^5 r_{++}^2 + 4r_+^2 r_{++}^5 - 3r_{++}^7)\,\sigma^2 \\ &\quad -35(r_{++}^2 - r_+^2)(r_+^3 + 2r_{++}^3)\sigma^4 + 105(r_{++}-r_+)r_{++}^2\sigma^6\Big]. \end{aligned} \tag{3.365}$$

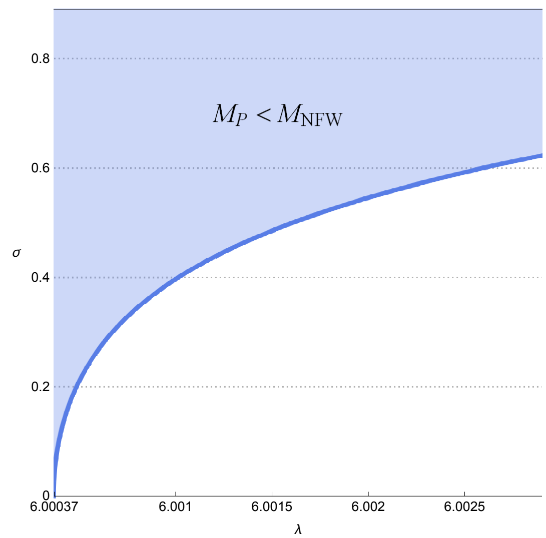

Figure 3.38: The numerical evaluation of the $M_P \leq N_{\rm NFW}$ condition. The plot has been done for $b = 5.2$, $Q = 3$, $\omega_0 = 2$, $\rho_0 = 1$, $\mathfrak{r}_s = 0.6$ and $\mathfrak{r}_{\rm max} = 10$. The solid blue line shows the possibility of having a plasmic electron distribution, which obeys the NFW cold dark matter density profile.

Solving the equation $M_P = N_{\rm NFW}$ for either of σ or λ, one can get an estimation criteria, in which the plasmic surrounding can behave as a cold dark matter halo in the context of NFW description. Solutions to this equation however, although achievable, are rather complicated and do not have algebraic values. We instead, demonstrate the above criteria in a plot as in Fig. 3.38. The figure indicates more possible similarity between the electron plasma and the NFW cold dark matter, for the lower limits of σ and λ.

3.5.5 Shadow of the black hole

As we know, the deflecting trajectories governed by the angular equation of motion in Eq. (3.319), can provide OFK and OSK. While the OFK is responsible for the gravitational lensing, the OSK, on the other hand, results in the darkness of the sky for an observer who is observing the black hole. Hence, this observer encounters a dark disk which is the black hole's shadow. This shadow is surrounded by the photon trajectories following OFK. For this reason, it can be noticed by the observer. In this regard, the photon sphere is, in fact, the boundary of the shadow because it is the final possible limit, at which the photons can lie. It is, therefore, unstable with respect to

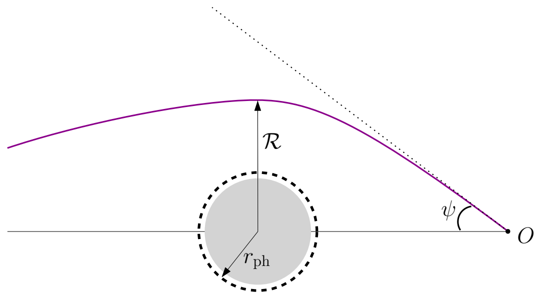

Figure 3.39: For an observer located at O, the angular diameter (ψ) of the black hole depends on the closest approach to the black hole. When $\mathcal{R} \to r_{\rm ph}$, then ψ indicates the angular diameter of the shadow (here $\psi_{\rm sh}$).

perturbations. This is essential to the determination of the shadow.

To proceed, we calculate the angular diameter of the shadow, by considering an observer located outside the outermost photon sphere. Pursuing the method given in Ref. (**?**), let us consider the scheme in Fig. 3.39. The observer, located at the distance r_O, sends a light ray into the past at an angle ψ, which according to the line element (3.24), is given by

$$\psi = \operatorname{arccot}\left(\sqrt{\frac{1}{r^2 B(r)}}\,\frac{\mathrm{d}r}{\mathrm{d}\phi}\right)\Big|_{r=r_O}, \tag{3.366}$$

which by means of Eqs. (3.319) and (3.320), becomes

$$\psi = \operatorname{arccot}\left(\sqrt{\frac{h^2(r)}{h^2(\mathcal{R})}-1}\right)\Big|_{r=r_O}. \tag{3.367}$$

This can be recast as

$$\sin^2\psi = \frac{h^2(\mathcal{R})}{h^2(r_O)}. \tag{3.368}$$

Once the light rays have reached their final possible stable orbits at $r_{\rm ph}$, they indicate the outermost boundary of the black hole. Hence, the shadow can be determined by letting $\mathcal{R} \to r_{\rm ph}$ (see Fig. 3.39). Accordingly, the corresponding angular diameter of the shadow is obtained as

$$\sin^2\psi_{\rm sh} = \frac{h^2(r_{\rm ph})}{h^2(r_O)}. \tag{3.369}$$

Applying Eq. (3.321a) we can calculate the above angle for the shadow. In the absence of plasma (i.e. for $h^2(r) = \frac{r^2}{B(r)}$), applying the radius in Eq. (3.354), this angle becomes

$$\sin^2\psi_{\rm sh}^{(\rm vac)} = \frac{4r_+^2 r_{++}^2\left(r_O^2 - r_+^2\right)\left(r_{++}^2 - r_O^2\right)}{r_O^4\left(r_{++}^2 - r_+^2\right)^2}. \tag{3.370}$$

For the PFK and PSK, discussed and analyzed in the previous subsections, we get the following results:

- From Eq. (3.323) we get

$$\sin^2\psi_{\mathrm{sh}} = \frac{r_+^2 + r_{++}}{r_O^2 + r_{++}}, \tag{3.371}$$

for $r_{\mathrm{ph}} = r_+$ ($b = \sqrt{r_+^2 + r_{++}^2}$).

- From Eq. (3.334), the angle in Eq. (3.368) becomes

$$\sin^2\psi = \frac{b^2 r_+^2 + \left(\sigma^2 + \mathcal{R}^2\right)^2 \left(r_{++}^2\sigma^2 - r_+^2\left(r_{++}^2 - \mathcal{R}^2\right)\right)}{b^2 r_+^2 + \left(r_O^2 + \sigma^2\right)^2 \left(r_{++}^2\sigma^2 - r_+^2\left(r_{++}^2 - r_O^2\right)\right)}. \tag{3.372}$$

Applying the condition in Eq. (3.369) and the radius in Eq. (3.357), the angular diameter of the shadow is obtain as

$$\sin^2\psi_{\mathrm{sh}} = \frac{\lambda^2 r_+^2}{\left(r_O^2 + \sigma^2\right)^2 \left(r_{++}^2\left(r_+^2 - \sigma^2\right) - r_O^2 r_+^2\right) - b^2 r_+^2}. \tag{3.373}$$

Note that, not all values of b are permitted to be possessed by the photons. This means that only certain photons with allowed impact parameters can identify the shadow. Such photons are those which could escape the black hole by passing the nearest possible distance (the critical distance) from it. According to the above relation, the condition $0 < \sin^2\psi_{\mathrm{sh}} < 1$ implies

$$b^2 < b_{\max}^2 - \lambda^2, \tag{3.374}$$

in which

$$b_{\max}^2 = \frac{\left(r_O^2 + \sigma^2\right)^2 \left(r_{++}^2\left(r_+^2 - \sigma^2\right) - r_O^2 r_+^2\right)}{r_+^2}. \tag{3.375}$$

This means that for every triplet (λ, Q, σ), only photons satisfying the condition in Eq. (3.374) can identify the shadow. In Fig. 3.40, a region has been plotted in which, the values of b satisfy the above condition. Accordingly, and in Fig. 3.41, the angular diameters of the shadow have been plotted respectively for the vacuum, the PFK and the PSK. For all cases, no extremal black holes are observable. However, shadow of the black hole surrounded by the PFK, achieves its maximum angular diameter for the lower values of λ. This is while for the one corresponding to the PSK, ψ_{sh} tends to zero for same range of λ. This means that, this model of plasmic surrounding prohibits the shadow to appear to the observer, when the cosmological term in Eq. (3.25) is dominant.

The discussion in this section, dealt with the way though which a charged Weyl black hole manifests itself to an observer residing in $r_+ < r < r_{++}$. To demonstrate the

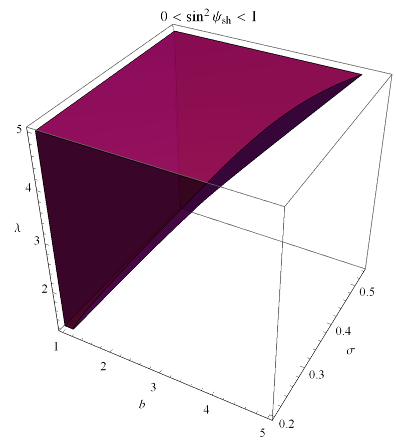

Figure 3.40: The allowed values of b which satisfy the condition $0 < \sin^2\psi_{\rm sh} < 1$. The region has been plotted for $Q = 0.6$ and $r_O = 0.8$.

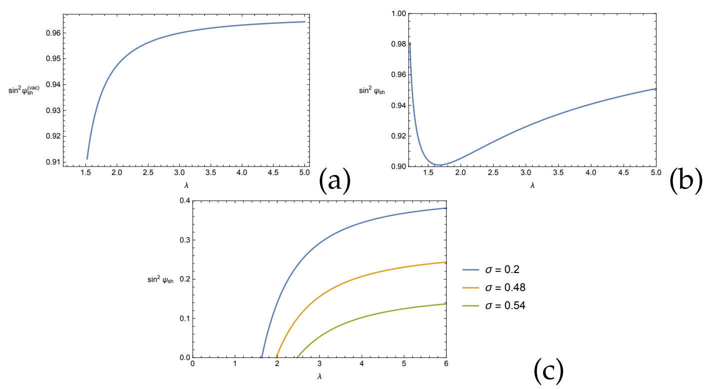

Figure 3.41: The radial diameter given in terms of $\sin^2\psi_{\rm sh}$, for (a) vacuum, (b) PFK and (c) PSK. The plots have been done for $Q = 0.6$, $r_O = 0.78$ and the impact parameter for the plots (b) and (c) has been taken as $b = 0.8$ (arbitrary length units have been considered).

shadow, it is usual to define some celestial coordinates which are obtained by doing a frame transformation from the curved background spacetime to the frame of a local observer in vacuum (Chandrasekhar, 1998; Tsukamoto, 2018) or in the presence of plasma (Perlick & Tsupko, 2017). The latter is also applicable to the spacetimes which are not asymptotically flat. The case of static vacuum spacetime has also been investigated (Singh & Ghosh, 2018). The shadow of the CWBH is completely symmetric and does not give more information other than those we have obtained so far. We therefore leave the discussion here and in the next section, we proceed with the calculation of the shadow of a rotating counterpart of the CWBH, which is more informative.

3.6 A rotating counterpart and its shadow

In fact, the light propagation around black holes is of remarkable importance in astrophysics, specially because of the evidences that can be achieved by advancements in the field of observational astronomy. For example, the recent black hole imaging of the shadow of M87*, done by the Event Horizon Telescope (EHT) (Akiyama et al., 2019a), was another significant affirmation of general relativity. Technically speaking, and as discussed in the previous section, photons that lie on unstable orbits in the gravitational field of the black holes, will either fall onto the event horizon or escape to infinity. To the observer, these latter ones constitute a bright photon ring which confines the black hole shadow (Synge, 1966; Cunningham & Bardeen, 1972; Bardeen, 1973; Luminet, 1979). In particular, the Luminet's optical simulation of a SBH and its accretion in 1979 (Luminet, 1979), gave more insights about the photon rings that result from the extremely warped geometry around the black holes. The formulations obtained in this way, then helped scientists to confine the shadow of rotating black holes inside their respected photon rings. Accordingly, the mathematical methods to calculate the form and size of a Kerr black hole's shadow were then developed by Bardeen (Bardeen et al., 1972; Bardeen, 1973; Cunningham & Bardeen, 1973), and the same methods were reused by Chandrasekhar (Chandrasekhar, 1998). These methods were later developed and generalized widely (Bray, 1986; Vázquez & Esteban, 2004; Grenzebach et al., 2014; Grenzebach, 2016; Perlick et al., 2018; Bisnovatyi-Kogan & Tsupko, 2018). Having these methods in hand, a large number of black hole spacetimes, including those with cosmological components, were given rigorous analytical calculations, simulations, numerical, and observational studies (de Vries, 1999; Shen et al., 2005; Amarilla et al., 2010; Amarilla & Eiroa, 2012; Yumoto et al., 2012; Amarilla & Eiroa, 2013; Atamurotov et al., 2013; Abdujabbarov et al., 2015, 2016; Amir et al., 2018; Tsukamoto, 2018; Cunha & Herdeiro, 2018; Mizuno et al., 2018; Mishra et al., 2019; Kumar et al., 2020). The black hole shadow is of great importance as it provides information about the light propagation in near-horizon regions. Recently, several investigations have been devoted to establish relations between the shadow and black hole parameters (Zhang & Guo, 2020; Belhaj et al., 2020; Kramer et al., 2004; Psaltis, 2008; Harko et al., 2009; Psaltis et al., 2015; Johannsen et al., 2016; Psaltis, 2019; Dymnikova & Kraav, 2019; Kumar & Ghosh, 2020).

In this section we apply the algorithm introduced in section 2.3, in order to construct the stationary counterpart of the CWBH solution. We use the first order light-like geodesic equations, to proceed with studying the optical appearance of the black hole to distant observers, by means of calculating the photon spheres and the black hole shadow. Furthermore, a particular geometric method is then used to indicate the conformity between the deformation and the angular size of the shadow.

3.6.1 The stationary solution

In order to apply the MNJA to the CWBH spacetime, we substitute the line element (3.24) in Eq. (2.79), which results in

$$\begin{aligned} \mathrm{d}s^2 = -\frac{\Xi}{\Sigma}\mathrm{d}t^2 + \frac{\Sigma}{\Delta}\,\mathrm{d}r^2 + \Sigma\,\mathrm{d}\theta^2 - 2a\sin^2\theta\left(1-\frac{\Xi}{\Sigma}\right)\mathrm{d}t\,\mathrm{d}\phi \\ + \sin^2\theta\left[\Sigma + a^2\sin^2\theta\left(2-\frac{\Xi}{\Sigma}\right)\right]\mathrm{d}\phi^2, \end{aligned} \tag{3.376}$$

as the solution to the rotating charged Weyl black hole (RCWBH), where

$$\Xi = \Delta - a^2\sin^2\theta, \tag{3.377a}$$

$$\Delta = a^2 + r^2 B(r), \tag{3.377b}$$

$$\Sigma = r^2 + a^2\cos^2\theta. \tag{3.377c}$$

Note that, the black hole's spin parameter a has the dimension of m in our geometric units. Also, the black hole's angular velocity is $\omega = -\frac{g_{t\phi}}{g_{\phi\phi}}$ (Poisson, 2009). In fact, if the reference lapse function (3.6) is applied to Eq. (5.61a), the components of the Bach tensor $W_{\alpha\beta}$, are vanished for the same expression of $f(r)$ as that in Eq. (3.16). We must however note that, this process can only be done by substitution of this lapse function in the components of the Bach tensor, applying a computer software[8]. Hence, the line element (3.376) is a vacuum rotating solution to Weyl gravity, if a lapse function of the general form (3.22) is taken into account. Accordingly, for a massive charged spherical source, like the one assumed for the CWBH, the same constants can be obtained if the same method is pursued. The only difference is that, the associated vector potential generated by the source, changes its form to (Misner et al., 2017)

$$\tilde{A}_\alpha = \frac{qr}{\Sigma}\left(1, 0, 0, -a\sin^2\theta\right). \tag{3.378}$$

The exterior geometry of the RCWBH is therefore specified by applying the lapse function (3.25), that provides

$$\Delta = a^2 + r^2 - \frac{r^4}{\lambda^2} - \frac{Q^2}{4}. \tag{3.379}$$

[8]The calculation of the components of the Bach tensor has been done by the software Maple™ 2018.

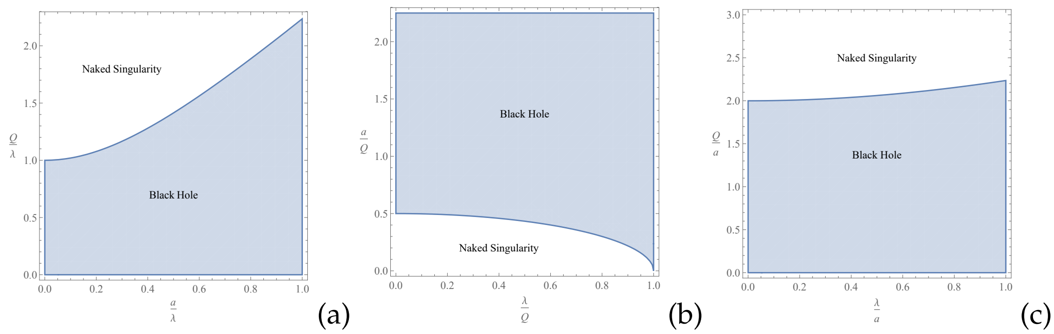

Figure 3.42: The mutual sensitivity of the possibility of horizon formation to the pairs (a) (Q, a), (b) (a, λ), and (c) (Q, λ). In the diagrams, the border between the regions of black hole and naked singularity, indicates the extremal black hole limit.

As for the spherically symmetric stationary spacetimes, the RCWBH admits two Killing vectors $\boldsymbol{\xi}_{(t)}$ and $\boldsymbol{\xi}_{(\phi)}$, satisfying

$$\xi^{\alpha}_{(t)}\xi_{\alpha(t)} = g_{tt}, \tag{3.380}$$

$$\xi^{\alpha}_{(\phi)}\xi_{\alpha(\phi)} = g_{\phi\phi}, \tag{3.381}$$

that correspond to the translational and rotational symmetries, and the relevant invariants of motion. The black hole's event and cosmological horizons, are now obtained by solving $g^{rr} = 0$, which results in (see appendix B.6)

$$r_+ = \lambda \sin\left(\frac{1}{2}\arcsin\left(\frac{2}{\lambda}\sqrt{\frac{Q^2}{4} - a^2}\right)\right), \tag{3.382}$$

$$r_{++} = \lambda \cos\left(\frac{1}{2}\arcsin\left(\frac{2}{\lambda}\sqrt{\frac{Q^2}{4} - a^2}\right)\right), \tag{3.383}$$

for which, the extremal black hole horizon $r_{\rm ex} = \frac{\lambda}{\sqrt{2}}$ is obtained for $Q_{\rm ex} = \pm\sqrt{4a^2 + \lambda^2}$, and a naked singularity appears for $Q > \sqrt{4a^2 + \lambda^2}$ (for $Q > 0$). As shown in Fig. 3.42, not all values of Q, λ and a are allowed to construct a black hole (censored region). Also, as shown in Fig. 3.43, for fixed λ and a, increase in Q increases the size of r_+ and decreases that of r_{++}, until they coincide on $r_+ = r_{++} = r_{\rm ex}$ at $Q = Q_{\rm ex}$. Same happens for decrease in λ for fixed Q and a, that leads to $\lambda = \lambda_{\rm ex}$, and decrease in a for fixed λ and Q, leading to $a = a_{\rm ex}$. It is also easy to show that the hypersurfaces corresponding to r_+ and r_{++}, are null. We continue analyzing the RCWBH in the next subsection, regarding the stationary and static observers.

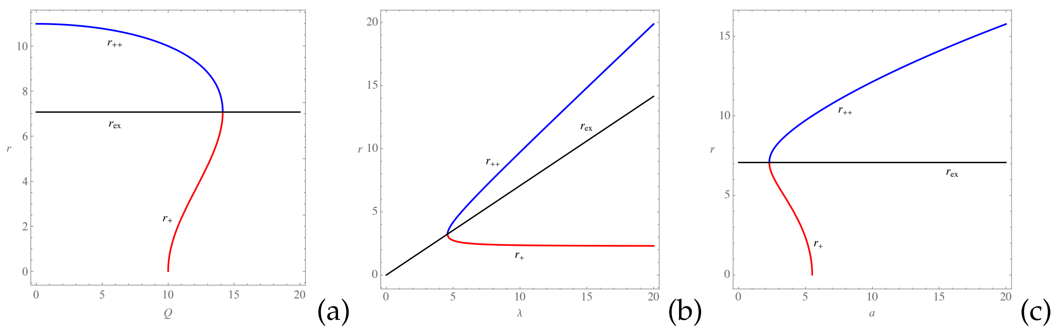

Figure 3.43: The behavior of the horizons of the RCWBH, plotted for (a) $\lambda = 10$ and $a = 5$, (b) $Q = 11$ and $a = 5$, and (c) $\lambda = 10$ and $Q = 11$.

3.6.2 The Ergosphere

Beside being encompassed by the event horizon, the rotating black holes are also characterized by another hypersurface, which is formed as a result of the black hole's spin and limits the existence of static observers. This surface is therefore identified with the event horizon, only in the limit of the vanishing spin parameter (Bardeen et al., 1972; Bardeen, 1973; Chandrasekhar, 1998). In this subsection, we determine this surface and discuss it analytically as well as illustratively. However, let us firstly consider an important feature of rotating spacetimes, by considering the zero angular momentum observers (ZAMOs), with the vanishing angular momentum defined as (Poisson, 2009)

$$\begin{aligned} \tilde{L} &\equiv g_{\phi\alpha}\frac{\mathrm{d}x^{\alpha}}{\mathrm{d}\tau} \\ &= g_{\phi t}\frac{\mathrm{d}t}{\mathrm{d}\tau} + g_{\phi\phi}\frac{\mathrm{d}\phi}{\mathrm{d}\tau} = 0. \end{aligned} \tag{3.384}$$

Accordingly, the observer's angular velocity is obtained from Eqs. (3.376) and (3.377), reading as

$$\Omega = \frac{\mathrm{d}\phi}{\mathrm{d}t} = -\frac{g_{t\phi}}{g_{\phi\phi}} = \frac{a\left(r^2 + a^2 - \Delta\right)}{\left(r^2 + a^2\right)^2 - \Delta a^2 \sin^2\theta}, \tag{3.385}$$

which is the same as the angular velocity of the rotating black hole and increases as r decreases, until it reaches its maximum value

$$\Omega_{\max} = \Omega|_{r=r_+} \equiv \Omega_H = \frac{a}{r_+^2 + a^2} = \omega_+, \tag{3.386}$$

where $\omega_+ \equiv \omega(r_+)$ is the black hole's angular velocity at its event horizon. For a slowly rotating black hole (small a), Ω_H reduces to

$$\Omega_H \approx \frac{a}{\lambda^2 \sin^2\left(\frac{1}{2}\arcsin\left(\frac{Q}{\lambda}\right)\right)}. \tag{3.387}$$

Therefore, on the event horizon, ZAMOs move in the same direction as the black hole's own rotation (also called *corotation*), as a result of dragging of their inertial frames. Aside from the ZAMOs, now to deal with the static observers, let us consider their velocity four-vector as

$$u^\alpha = \mathfrak{n}\,\xi^\alpha_{(t)}, \tag{3.388}$$

with the normalization factor $\mathfrak{n} = (-g_{\alpha\beta}\xi^\alpha_{(t)}\xi^\beta_{(t)})^{-\frac{1}{2}} = \frac{1}{\sqrt{-g_{tt}}}$, according to Eq. (3.380). Such observers cannot exist everywhere in the spacetime, and they are indeed confined to a limit defined in terms of the validity of Eq. (3.388). In fact, for $\mathfrak{n}^{-2} = -g_{tt} = 0$, this equation breaks down and $\boldsymbol{\xi}_{(t)}$ becomes null. This way, a *static limit*[9] is obtained, whose radius, r_{SL}, is calculated by solving the equation $g_{tt} = 0$. This equation yields the two positive solutions

$$r_{SL1} = \lambda \sin\left(\frac{1}{2}\arcsin\left(\frac{2}{\lambda}\sqrt{\frac{Q^2}{4} - a^2\cos^2\theta}\right)\right), \tag{3.389}$$

$$r_{SL2} = \lambda \cos\left(\frac{1}{2}\arcsin\left(\frac{2}{\lambda}\sqrt{\frac{Q^2}{4} - a^2\cos^2\theta}\right)\right), \tag{3.390}$$

that satisfy the condition of causality $r_+ < r_{SL1} < r_{SL2} < r_{++}$. The domain $r < r_{SL1}$, corresponds to a region, in which, the static observers can no longer remain static[10], and the so-called *frame-dragging* effect forces them to rotate with the black hole. In Fig. 3.44, the behavior of the above two solutions has been plotted for a definite value of a. As the angular parameter increases, the static limit surface (corresponding to r_{SL1}) recedes from the event horizon. On the other hand, r_{SL2} shrinks under the same conditions. Note that, in the case of an extremal black hole ($Q^2 = 4a^2 + \lambda^2$), the above surfaces coincide at

$$r_{SL(\mathrm{ex})} = \lambda \cos\left(\frac{\pi}{4} - \frac{1}{4}\arccos\left(\frac{8a^2\sin^2\theta + \lambda^2}{\lambda^2}\right)\right). \tag{3.391}$$

Comparing Eqs. (3.382) and (3.389), we can notice that for $\theta \neq n\pi$ $(n = 0, \pm1, \pm2, ...)$, the surface of static limit does not coincide with that of the event horizon, and these surfaces, together, form an *ergosphere* (or *ergoregion*). To demonstrate the ergosphere of

[9]The surface corresponding to the static limit, is also called the surface of infinite redshift (Ryder, 2009).

[10]In other words, they will no longer exist.

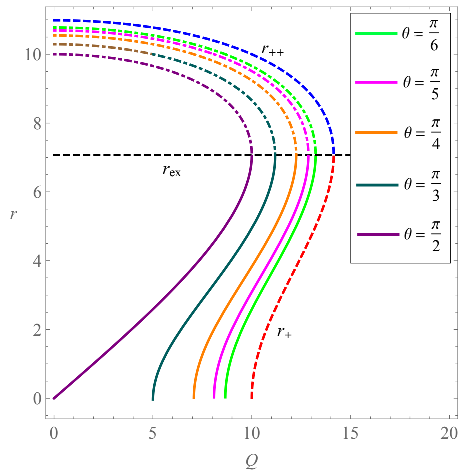

Figure 3.44: The behavior of r_{SL}, with respect to changes in Q. The plots have been done for $\lambda = 10$ and $a = 5$ and five different values of θ. The solid and dot-dashed curves correspond respectively to r_{SL1} and r_{SL2}, and the black hole horizons have been shown with dashed lines.

the black hole, let us introduce the Cartesian coordinates (Boyer & Lindquist, 1967)

$$x = \sqrt{r^2 + a^2} \sin\theta \cos\phi, \tag{3.392a}$$

$$y = \sqrt{r^2 + a^2} \sin\theta \sin\phi, \tag{3.392b}$$

$$z = r \cos\theta, \tag{3.392c}$$

which are defined in terms of the Boyer-Lindquist coordinates of the line element (3.376). Accordingly, the horizon hypersurfaces can be plotted, as being observed either from the coordinate of axial symmetry (i.e. in the x-y plane), or from the y (or x) coordinate (i.e. in the z-x (or z-y) plane). In Fig. 3.45, the horizons and the static limit surfaces have been plotted for several values of a and Q within the allowed values of Fig. 3.42, and therefore, the ergosphere for each of these cases has been demonstrated. As it is seen in the figures, increase in a for each fixed value of Q, stretches the event horizon's cross-section and acts in favor of dividing the ergosphere into separate regions at each side of the event horizon. In the special cases of $Q > \lambda$, r_{SL1} and r_{SL2} match in certain regions outside the event horizon and form ergospheres of peculiar shapes. For the extremal black hole, it is naturally $Q > \lambda$ and the spacetime encounters one horizon and one static limit, and its ergosphere increases in size as the distance between the values of Q and a increases. In fact, stationary observers of

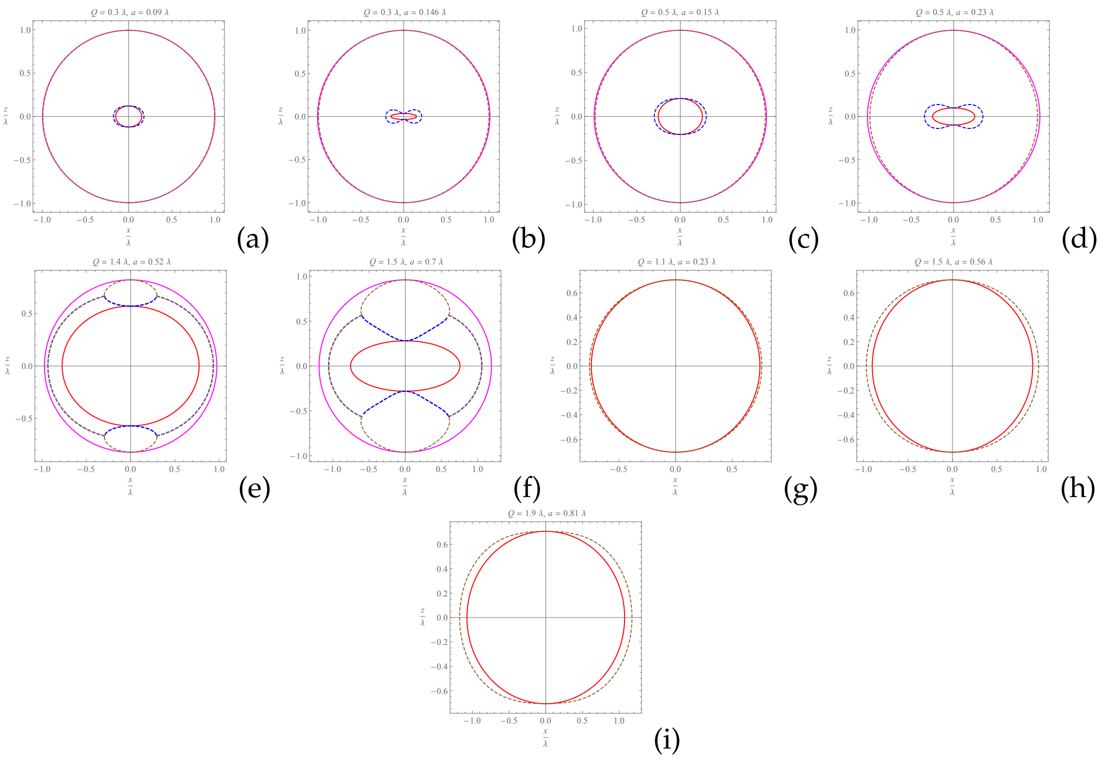

Figure 3.45: The hypersurfaces corresponding to the horizons and the static limit, plotted for $\lambda = 10$ and several fixed values of Q and a, as viewed from the y axis. The axes have been given in terms of dimension-less values $\frac{z}{\lambda}$ and $\frac{x}{\lambda}$. In the (a)-(f) diagrams, the smaller and the larger solid contours correspond respectively to r_+ and r_{++}, whereas the smaller and the larger dashed ones relate to r_{SL1} (the static limit) and r_{SL2}. The region $r_+ < r < r_{SL1}$ indicates the ergosphere in each of the cases. The figures have been scaled in a way that the r_{++} surface appears as a complete circle. The (g)-(i) diagrams demonstrate the ergoregion in the case of the extremal black hole. The solid and the dashed contours correspond respectively to r_{ex} and $r_{SL(\mathrm{ex})}$.

angular velocity Ω and the four-velocity $u_s^\alpha = \mathfrak{n}_s \xi_s^\alpha$, with

$$\xi_s^\alpha = \xi_{(t)}^\alpha + \Omega \xi_{(\phi)}^a, \tag{3.393}$$

$$\mathfrak{n}_s^{-2} = -g_{\alpha\beta}\xi_s^\alpha \xi_s^\beta = -g_{\phi\phi}\left(\Omega^2 - 2\omega\Omega + \frac{g_{tt}}{g_{\phi\phi}}\right), \tag{3.394}$$

can exist in the ergosphere, as long as the Killing vector $\boldsymbol{\xi}_s$ remains time-like. This corresponds to $\mathfrak{n}_s^{-2} > 0$, or $\Omega_- < \Omega < \Omega_+$, with

$$\Omega_\pm = \omega \pm \frac{\sqrt{\Delta}\sin\theta}{g_{\phi\phi}}. \tag{3.395}$$

Accordingly, this vector becomes null on the event horizon[11]. Therefore, by approaching the event horizon, $\Omega \to \Omega_H \equiv \Omega_+$, and the particles will be in the state of corotation with the black hole. Such particles encounter the surface gravity (Poisson, 2009)

$$\kappa = \left.\frac{\Delta'(r)}{2(r^2+a^2)}\right|_{r=r_+}, \tag{3.396}$$

at the vicinity of the event horizon. Applying Eqs. (5.61a) and (3.382), and after a little algebra, this gives

$$\kappa = \frac{r_+}{a^2+r_+^2}\sqrt{\lambda^2 - Q^2 + 4a^2}. \tag{3.397}$$

For the extremal black hole ($r_+ \to r_{\rm ex}$), we have from Eq. (3.396) that $\kappa_{\rm ex} = 0$. Note that, for asymptotically flat spacetimes, where the energy can be defined relative to an observer located at infinity, the ergosphere is highlighted also by a theoretical scenario, termed as the *Penrose process*, through which, particles of negative energy created in the ergosphere can extract positive rotational energy from a rotating black hole (Penrose, 2002).

Note that, the optical appearance of a black hole to distant observers, does not rely on the positioning of its ergosphere, since this latter, affects only the time-like particles. The conceived image of a black hole is, in fact, a shadow that is confined by particular photons on unstable (critical) orbits. Such photons construct a photon surface around the black hole. For the case of the RCWBH, this will be given a detailed discussion in the next subsection.

3.6.3 Shadow of the black hole

Here, we apply the method of separation of variables in the Hamilton–Jacobi equation (Carter, 1968; Chandrasekhar, 1998). Accordingly, we write the Hamilton-Jacobi equation as

$$\mathcal{H} = -\frac{\partial \mathcal{S}}{\partial \tau} = \frac{1}{2} g^{\alpha\beta} \frac{\partial \mathcal{S}}{\partial x^\alpha}\frac{\partial \mathcal{S}}{\partial x^\beta} = -\frac{1}{2}\mu^2, \tag{3.398}$$

where $\mathcal{H}$, $\mathcal{S}$ and μ, are respectively the canonical Hamiltonian, the Jacobi action and the rest mass of particles. Defining the four-momentum $p_\alpha = \frac{\partial \mathcal{S}}{\partial x^\alpha}$ ($p_\alpha p^\alpha = \mu^2$), the action can be separated by the Carter's method, as

$$\mathcal{S} = \frac{1}{2}\mu^2\tau - \tilde{\mathcal{E}} t + \tilde{\mathcal{L}}\phi + \mathcal{S}_r(r) + \mathcal{S}_\theta(\theta), \tag{3.399}$$

[11] This also proves that the event horizon is a Killing horizon.

in which $\mathcal{S}_r(r) \equiv p_r$, $\mathcal{S}_\theta(\theta) \equiv p_\theta$, and

$$\tilde{\mathcal{E}} = -p_t = -\left(g_{tt}\frac{\mathrm{d}t}{\mathrm{d}\tau} + g_{t\phi}\frac{\mathrm{d}\phi}{\mathrm{d}\tau}\right), \tag{3.400}$$

$$\tilde{\mathcal{L}} = p_\phi = g_{\phi t}\frac{\mathrm{d}t}{\mathrm{d}\tau} + g_{\phi\phi}\frac{\mathrm{d}\phi}{\mathrm{d}\tau}, \tag{3.401}$$

are the constants of motion. Physically, $\tilde{\mathcal{L}}$ is associated with the particles' angular momentum around the axis of symmetry. On the other hand, $\tilde{\mathcal{E}}$ cannot be regarded as the energy of particles, because the spacetime under consideration is not asymptotically flat. Using Eqs. (3.399)-(3.401) in the Hamilton-Jacobi equation (3.398), and applying the method of separation of variables for the case of mass-less particles (photons with $\mu = 0$), the equations of motion are then given in terms of the four differential equations (Chandrasekhar, 1998)

$$\Sigma\frac{\mathrm{d}t}{\mathrm{d}\tau} = \frac{r^2+a^2}{\Delta}\left(\tilde{\mathcal{E}}\left(r^2+a^2\right) - a\tilde{\mathcal{L}}\right) - a\left(a\tilde{\mathcal{E}}\sin^2\theta - \tilde{\mathcal{L}}\right), \tag{3.402}$$

$$\Sigma\frac{\mathrm{d}r}{\mathrm{d}\tau} = \pm\sqrt{\mathcal{R}(r)}, \tag{3.403}$$

$$\Sigma\frac{\mathrm{d}\theta}{\mathrm{d}\tau} = \pm\sqrt{\Theta(\theta)}, \tag{3.404}$$

$$\Sigma\frac{\mathrm{d}\phi}{\mathrm{d}\tau} = \frac{a}{\Delta}\left(\tilde{\mathcal{E}}\left(r^2+a^2\right) - a\tilde{\mathcal{L}}\right) - \left(a\tilde{\mathcal{E}} - \frac{\tilde{\mathcal{L}}}{\sin^2\theta}\right), \tag{3.405}$$

defining

$$\mathcal{R}(r) = \left(\left(r^2+a^2\right)\tilde{\mathcal{E}} - a\tilde{\mathcal{L}}\right)^2 - \Delta\left(\mathcal{D} + \left(a\tilde{\mathcal{E}} - \tilde{\mathcal{L}}\right)^2\right), \tag{3.406a}$$

$$\Theta(\theta) = \mathcal{D} - \left(\frac{\tilde{\mathcal{L}}^2}{\sin^2\theta} - a^2\tilde{\mathcal{E}}^2\right)\cos^2\theta, \tag{3.406b}$$

in which, $\mathcal{D}$ is the Carter's separation constant. The photon trajectories are therefore characterized by two dimension-less impact parameters

$$\tilde{b} = \frac{\tilde{\mathcal{L}}}{\tilde{\mathcal{E}}}, \tag{3.407}$$

$$\tilde{\eta} = \frac{\mathcal{D}}{\tilde{\mathcal{E}}^2}. \tag{3.408}$$

It is also common to use the generalized Carter's constant of motion $\mathcal{K} = \mathcal{D} + (a\tilde{\mathcal{E}} - \tilde{\mathcal{L}})^2$ (Chandrasekhar, 1998). As stated before, photon surfaces are those regions around the black hole, in which, the photons travel on unstable (critical) orbits. In this situation, the radial effective potential associated with the photon trajectories reaches its extremum at the corresponding critical distance r_p. Accordingly, Eq. (6.49) provides the conditions

$$\mathcal{R}(r_p) = 0, \tag{3.409a}$$

$$\left.\frac{\partial \mathcal{R}(r)}{\partial r}\right|_{r=r_p} = 0, \tag{3.409b}$$

$$\left.\frac{\partial^2 \mathcal{R}(r)}{\partial r^2}\right|_{r=r_p} > 0. \tag{3.409c}$$

The importance of the impact parameters $\tilde{b}$ and $\tilde{\eta}$ is their relevance to the fate of approaching photons to the black hole. In this regard, photons can either fall on unstable orbits, escape from, or captured by the black hole, respectively, if their associated impact parameters are equal, smaller, or larger than a critical value. In fact, Eqs. (3.409a) and (3.409b) result in the two equations

$$\left(a^2 + r_p^2 - a\,\tilde{b}_c\right)^2 - \left(\tilde{\eta}_c + \left(a - \tilde{b}_c\right)^2\right)\Delta(r_p) = 0, \tag{3.410a}$$

$$4r_p^3 + r_p\left(4a^2 - 4a\,\tilde{b}_c\right) - \left(\tilde{\eta}_c + \left(a - \tilde{b}_c\right)^2\right)\Delta'(r_p) = 0, \tag{3.410b}$$

in which, $\tilde{b}_c$ and $\tilde{\eta}_c$ are the critical values of these impact parameters, corresponding to the photons on unstable orbits at r_p. The above equations provide two pairs of $(\tilde{b}_c, \tilde{\eta}_c)$, that only the pair

$$\tilde{b}_c(r_p) = \frac{\left(a^2 + r_p^2\right)\Delta'(r_p) - 4r_p\Delta(r_p)}{a\Delta'(r_p)}, \tag{3.411}$$

$$\tilde{\eta}_c(r_p) = \frac{r_p^2\left[8\Delta(r_p)\left(2a^2 - 2\Delta(r_p) + r_p\Delta'(r_p)\right) - r_p^2\Delta'(r_p)^2\right]}{a^2\Delta'(r_p)^2}, \tag{3.412}$$

satisfies the condition (3.409c). Accordingly, the photons on unstable orbits are identified by $\tilde{\eta}_c = 0$, resulting in the two real positive values

$$r_{p-} = \frac{Q}{\sqrt{1 + \frac{4a^2}{\lambda^2}}}\sin\left(\frac{1}{2}\arcsin\left(\sqrt{\left(1 - \frac{4a^2}{Q^2}\right)\left(1 + \frac{4a^2}{\lambda^2}\right)}\right)\right), \tag{3.413}$$

$$r_{p+} = \frac{Q}{\sqrt{1 + \frac{4a^2}{\lambda^2}}}\cos\left(\frac{1}{2}\arcsin\left(\sqrt{\left(1 - \frac{4a^2}{Q^2}\right)\left(1 + \frac{4a^2}{\lambda^2}\right)}\right)\right), \tag{3.414}$$

that implies $Q > 2a$ for r_{p-} to exist. In general, these solutions satisfy $r_+ < r_{p_-} < r_{p+} < r_{++}$. However, to ensure the important condition $r_{p-} > \tilde{r}$, the cosmological component of the spacetime metric should satisfy $\tilde{\varepsilon} < \tilde{\varepsilon}_0$, where

$$\tilde{\varepsilon}_0 = \frac{3\left(4a^2 + 4\tilde{r}(\tilde{r} - 3\tilde{m}) - Q^2\right)}{8\tilde{r}^4}, \tag{3.415}$$

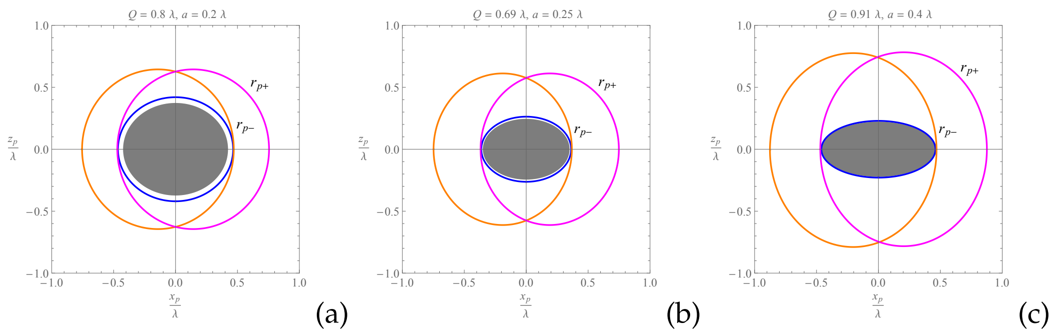

Figure 3.46: The shape of the photon regions ($r_{p-} < r < r_{p+}$), as viewed from the y axis, plotted for $\lambda = 10$, and different values of Q and a. The event horizon r_+ occupies the central shaded region, and is encompassed by the rings r_{p-} and r_{p+}. The blue contour corresponds to the boundary of the inner ring r_{p-}, that coincides with the event horizon, only for the extremal black hole with $Q = Q_{\text{ex}}$ and $r_{p-} = r_+ = r_{\text{ex}}$.

to obtain which, we have used Eq. (3.413) and the expression in Eq. (3.23a). Note that, Eqs. (3.382) and (3.413) imply that the inner photon ring is identified with the event horizon under the critical condition $Q = Q_{\text{ex}}$, that corresponds to the extremal black hole, for which $r_{p-} = r_+ = r_{\text{ex}}$. Furthermore, the photon ring radii should also respect the condition $\Theta(\theta) \geq 0$ (Chandrasekhar, 1998), for which, Eq. (5.103) yields $\tilde{\eta}_c \geq \tilde{b}_c^2 \cot^2\theta - a^2\cos^2\theta$ on the photon surface, or by using Eqs. (3.411) and (3.412),

$$4r_p^2\Delta(r_p)\left(\frac{\Delta(r_p)}{\sin^2\theta} - 9\right) \leq \left(9 + 2r_p^2 + 9\cos(2\theta)\right)\frac{\Delta'(r_p)}{\sin^2\theta}\left(r_p\Delta(r_p) - \frac{\Delta'(r_p)}{16}\right). \quad (3.416)$$

Applying the Cartesian coordinates in Eq. (5.141), r_{p-} and r_{p+} and the corresponding photon regions ($r_{p-} < r < r_{p+}$), have been plotted in Fig. 3.46, together with the event horizon, for some definite values of the black hole parameters. As it is observed from the figures, faster spinning RCWBH can produce larger photon regions. In fact, the shape of the photon regions informs about that of the black hole shadow, since the shadow is confined to the photon surfaces. Those photons on unstable orbits that can reach the distant observers, can create an image of the outer regions of the event horizon. Such photons are therefore responsible, for example, for the image obtained from M87* (Akiyama et al., 2019a).

To proceed with the determination of the shadow of the RCWBH, we should bear in mind that this spacetime is not asymptotically flat. We therefore cannot consider an observer at infinity, as is traditionally done (Bardeen, 1973; Cunningham & Bardeen, 1973; Vázquez & Esteban, 2004). Therefore, instead of using the celestial coordinates in the sky of an observer at infinity, we locate an observer at the coordinate position

(r_o, θ_o), which is characterized by the orthonormal tetrad $\boldsymbol{e}_{\{A\}}$, selected as

$$\boldsymbol{e}_0 = \left.\frac{\left(\Sigma + a^2\sin^2\theta\right)\partial_t + a\,\partial_\phi}{\sqrt{\Sigma\,\Delta}}\right|_{(r_o,\theta_o)}, \tag{3.417}$$

$$\boldsymbol{e}_1 = \left.\sqrt{\frac{1}{\Sigma}}\,\partial\theta\right|_{(r_o,\theta_o)}, \tag{3.418}$$

$$\boldsymbol{e}_2 = -\left.\frac{\left(\partial_\phi + a\sin^2\theta\,\partial_t\right)}{\sqrt{\Sigma}\sin\theta}\right|_{(r_o,\theta_o)}, \tag{3.419}$$

$$\boldsymbol{e}_3 = -\left.\sqrt{\frac{\Delta}{\Sigma}}\,\partial r\right|_{(r_o,\theta_o)}, \tag{3.420}$$

that satisfy ${e_A}^\alpha {e^B}_\alpha = \delta^B_A$. This method makes it possible to calculate the celestial coordinates in general spacetimes with cosmological constituents (Grenzebach et al., 2014; Grenzebach, 2016) . In the above set of tetrads, the time-like vector $\boldsymbol{e}_0$ is supposed to be the velocity four-vector of the selected observer. Furthermore, $\boldsymbol{e}_3$ is set to point towards the black hole and $\boldsymbol{e}_0 \pm \boldsymbol{e}_3$ is the generator of the principal null congruence. This way, a linear combination of $\boldsymbol{e}_{\{A\}}$ is tangent to the light ray $\boldsymbol{\ell}(\tau) = (t(\tau), r(\tau), \theta(\tau), \phi(\tau))$, which is sent from the black hole to the past. The tangent to this light ray can be parameterized in two ways as

$$\frac{\mathrm{d}\boldsymbol{\ell}}{\mathrm{d}\tau} = \frac{\mathrm{d}t}{\mathrm{d}\tau}\partial_t + \frac{\mathrm{d}r}{\mathrm{d}\tau}\partial_r + \frac{\mathrm{d}\theta}{\mathrm{d}\tau}\partial_\theta + \frac{\mathrm{d}\phi}{\mathrm{d}\tau}\partial_\phi, \tag{3.421}$$

$$\frac{\mathrm{d}\boldsymbol{\ell}}{\mathrm{d}\tau} = \mathfrak{c}\left(-\boldsymbol{e}_0 + \sin\vartheta\cos\psi\,\boldsymbol{e}_1 + \sin\vartheta\sin\psi\,\boldsymbol{e}_2 + \cos\vartheta\,\boldsymbol{e}_3\right), \tag{3.422}$$

in which, ϑ and ψ are newly defined celestial coordinates in the observer's sky and

$$\mathfrak{c} = \boldsymbol{g}\left(\boldsymbol{\ell}, \boldsymbol{e}_0\right) = \frac{a\tilde{\mathcal{L}} - \left(\Sigma + a^2\sin^2\theta\right)\tilde{\mathcal{E}}}{\sqrt{\Sigma\,\Delta}}. \tag{3.423}$$

It can be easily noticed that $\vartheta = 0$ points, directly, to the black hole. Since the boundary curve of the shadow is generated by those light rays that come onto the critical (unstable) null geodesics at the radial distance r_p, this region therefore corresponds to the critical impact parameters $\tilde{b}_c$ and $\tilde{\eta}_c$, given in Eqs. (3.411) and (3.412). The corresponding celestial coordinates (ψ_p, ϑ_p) at this distance, for the observer located at (r_o, θ_o), have been derived as (Grenzebach et al., 2014)

$$\mathcal{P}(r_p, \theta_o) := \sin\psi_p = \frac{\tilde{b}_c(r_p) + a\cos^2\theta_o - a}{\sqrt{\tilde{\eta}_c(r_p)}\,\sin\theta_o}, \tag{3.424}$$

$$\mathcal{T}(r_p, r_o) := \sin\vartheta_p = \frac{\sqrt{\Delta(r_o)\,\tilde{\eta}_c(r_p)}}{r_o^2 - a(\tilde{b}_c(r_p) - a)}. \tag{3.425}$$

Accordingly, the ϑ coordinate has its maximum and minimum values, respectively, for $\psi_p = -\frac{\pi}{2}$ and $\psi_p = \frac{\pi}{2}$. This helps us obtaining the corresponding values of r_p for each of the cases. Applying Eq. (3.424), these conditions result in the equation

$$\Sigma(r_p,\theta_o)\Delta'(r_p) - 4r_p\Delta(r_p) \\ = \mp r_p \sin\theta_o \sqrt{16\left(a^2-\Delta(r_p)\right)\Delta(r_p) + 8r_p\Delta(r_p)\Delta'(r_p) - r_p^2\Delta'(r_p)^2}, \quad (3.426)$$

where $\Sigma(r_p,\theta_o) = r_p^2 + a^2\cos^2\theta_o$. This equation is of fourth order in r_p, and has the positive solutions

$$r_{p\min} = \sqrt{\frac{\bar{c}_2}{\bar{c}_1}}\sin\left(\frac{1}{2}\arcsin\left(\frac{2\sqrt{\bar{c}_3/\bar{c}_1}}{\bar{c}_2/\bar{c}_1}\right)\right), \quad (3.427)$$

$$r_{p\max} = \sqrt{\frac{\bar{c}_2}{\bar{c}_1}}\cos\left(\frac{1}{2}\arcsin\left(\frac{2\sqrt{\bar{c}_3/\bar{c}_1}}{\bar{c}_2/\bar{c}_1}\right)\right), \quad (3.428)$$

in which

$$\bar{c}_1 = 4\left[4a^2\cot^2\theta_o\left(a^2\cos^2\theta_o+\lambda^2\right) - \lambda^2\left(4a^2+\lambda^2\right) + \lambda^4\csc^2\theta_o\right], \quad (3.429a)$$

$$\bar{c}_2 = 2\lambda^4\csc^2\theta_o\left[-8a^2+Q^2\cos(2\theta_o)+Q^2\right] \\ + 8a^2\lambda^2\cot^2\theta_o\left[a^2\cos(2\theta_o)-3a^2+\lambda^2+Q^2\right], \quad (3.429b)$$

$$\bar{c}_3 = \frac{1}{2}\lambda^4\csc^2\theta_o\left[a^4\cos(4\theta_o) + \left(Q^4-12a^4\right)\cos(2\theta_o) \\ + 19a^4 - 8a^2Q^2 + Q^4\right]. \quad (3.429c)$$

The values in Eqs. (3.427) and (3.428) are indeed those radii where the boundary of the photon region intersects with the cone $\theta = \theta_o$. When $a = 0$, we have $r_{p\max} = r_{p\min} = \frac{Q}{\sqrt{2}}$, which is the radius of the unstable photon orbits around a static CWBH, and it does not depend on λ (Fathi et al., 2020). This unique value corresponds to the constant value of $\vartheta_p = \frac{\pi}{2}$ for $a = 0$. The shadow of the static black hole is therefore circular.

Now, getting back to the case of $a \neq 0$, the two-dimensional Cartesian coordinates for the chosen observer of the velocity four-vector $\boldsymbol{e}_0$, are now obtained by applying the stereographic projection of the celestial sphere (ψ_p, ϑ_p), onto a plane. This provides the coordinates (Grenzebach et al., 2014)

$$X_p = -2\tan\left(\frac{\vartheta_p}{2}\right)\sin\psi_p, \quad (3.430)$$

$$Y_p = -2\tan\left(\frac{\vartheta_p}{2}\right)\cos\psi_p. \quad (3.431)$$

The case of $\theta_o = \frac{\pi}{2}$ corresponds to the equatorial plane of view for the observer. Taking this into account, in Fig. 3.47, we have used the above coordinates to obtain the shadow of the RCWBH, for different values of electric charge and spin parameter. The curves use r_p as their parameter. In general, and for a given spin parameter, the size of the shadow increases by increasing the electric charge, and as it is inferred from the figures, by raising the black hole's spin, the shadow shrinks and tends to the positive part of the coordinate plane. It can also be noted that the shadow becomes oblate toward the $X_p = 0$ axis from the negative sector of the coordinate plane, whereas it is sharp toward that, from the positive sector. However, the amount of such deformations cannot be inferred directly from the $\frac{Q}{a}$ fraction, and is indeed a consequence of the spacetime's response to the changes in the electric charge. In fact, the size and the deformation of the shadow casts of black holes have been used to estimate their dynamical properties. In the forthcoming subsection, using a specific geometric method, we relate the angular size of a deformed shadow to the physical characteristics of the black hole. However, before proceeding with that, it is of worth to make a comparison between the formation and the evolution of the shadows of the Kerr-Newman-de Sitter black hole (KNdSBH) and the RCWBH. This way, we will be able to gain some visualizations for the differences between the general relativistic spacetimes and that of the RCWBH. The line element associated with the KNdSBH is given by (Griffiths & Podolský, 2009)

$$\begin{aligned} \mathrm{d}s^2_{\mathrm{kn}} = &-\frac{\Delta_r - a^2\Delta_\theta \sin^2\theta}{\Sigma}\,\mathrm{d}t^2 + \frac{\Sigma}{\Delta_r}\,\mathrm{d}r^2 + \frac{\Sigma}{\Delta_\theta}\,\mathrm{d}\theta^2 \\ &+ \frac{2}{\Sigma}\left[\Delta_r a\sin^2\theta - a\Delta_\theta \sin^2\theta\left(\Sigma + a^2\sin^2\theta\right)\right]\mathrm{d}t\,\mathrm{d}\phi \\ &+ \frac{1}{\Sigma}\left[\left(\Sigma + a^2\sin^2\theta\right)^2\Delta_\theta\sin^2\theta - \Delta_r a^2\sin^4\theta\right]\mathrm{d}\phi^2, \end{aligned} \tag{3.432}$$

in which, the new functions

$$\Delta_r = r^2 - 2M_0 r + a^2 + Q_0^2 + \frac{R_0 r^2}{12}\left(a^2 + r^2\right), \tag{3.433a}$$

$$\Delta_\theta = 1 + \frac{R_0 a^2\cos^2\theta}{12}, \tag{3.433b}$$

with $R_0 \equiv 4\Lambda$, associate with a massive object of mass M_0 and charge Q_0. The shadow of the KNdSBH is calculated using the celestial coordinates (Grenzebach et al., 2014)

$$\sin\psi_p^{\mathrm{kn}} = \frac{1}{\sqrt{\Delta_\theta(\theta_o)}}\sin\psi, \tag{3.434}$$

$$\sin\vartheta_p^{\mathrm{kn}} = \sin\vartheta_p, \tag{3.435}$$

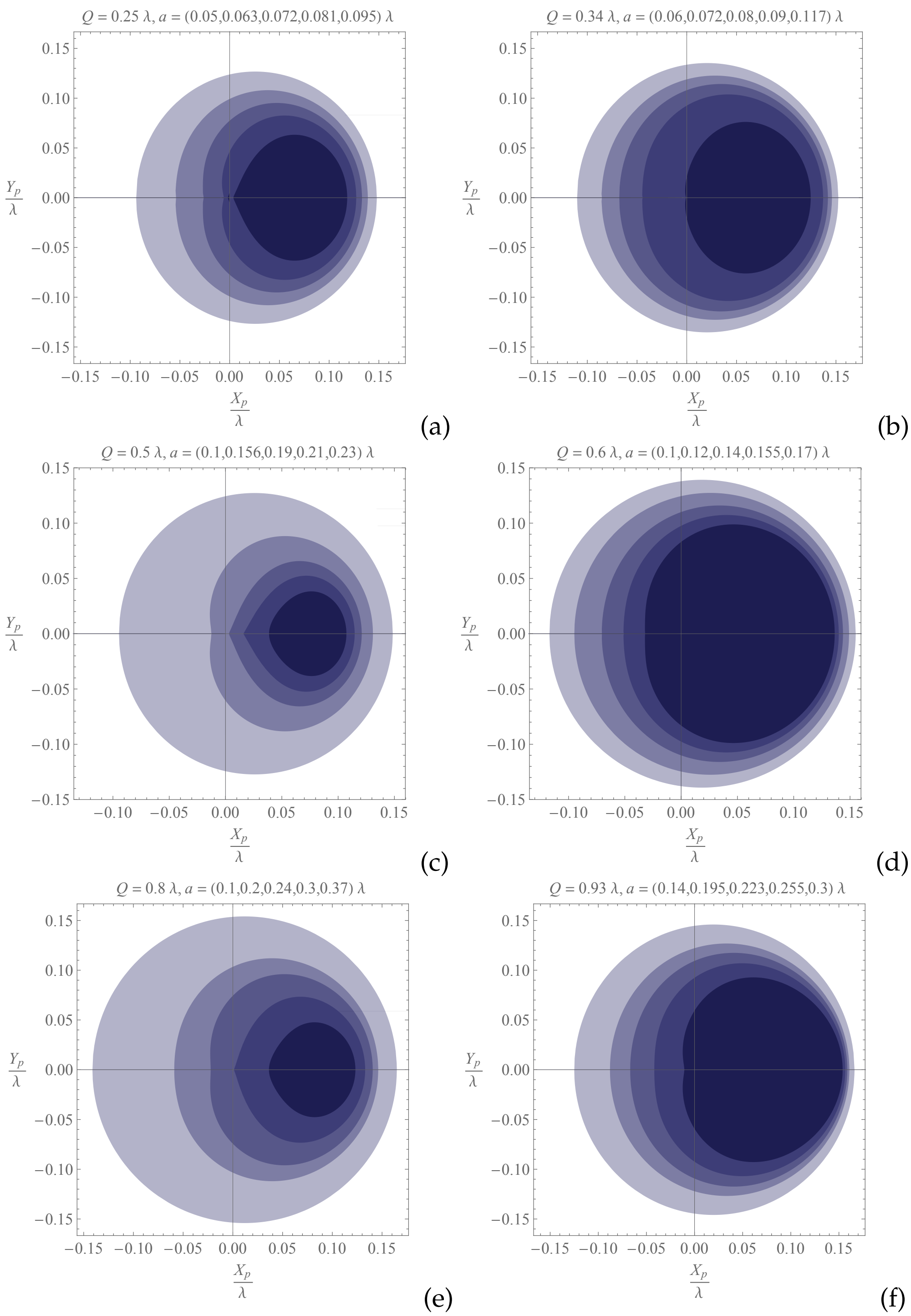

Figure 3.47: The shadow of the RCWBH for $a \neq 0$, plotted for $\lambda = 10$ and $r_o = 5\lambda$. Each diagram corresponds to a fixed value of Q and five values of a, which are sorted from the largest to the smallest parametric curve. The figures have been scaled in order to have an approximate circular shape for the smallest a in each of the diagrams.

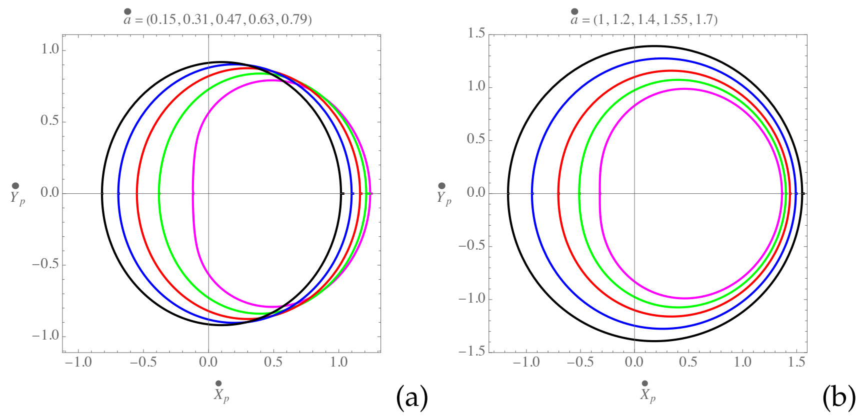

Figure 3.48: Shadows of (a) the KNdSBH and (b) the RCWBH plotted for $\dot{Q} = 6$, $\dot{r}_o = 5$ and $\theta_o = \frac{\pi}{2}$, for both of the black holes. The cosmological terms have been considered as $\dot{R}_0 = \dot{c}_1 = 10^{-3}$. For the case of RCWBH, this value corresponds to $\lambda = 10$, if $\dot{r}_0 \approx 6.93$. The values of the re-scaled spin parameter $\dot{a}$, have been sorted from the less oblate to the most oblate parametric curves. As it is observed, respecting the corresponding black hole masses, the shadow of the RCWBH is greater in size.

which are here given in terms of those in Eqs. (3.424) and (3.425), and the same impact parameters in Eqs. (3.411) and (3.412). Defining $\dot{\mathfrak{q}}$, as the dimension-less version of a black hole quantity $\mathfrak{q}$, re-scaled by the corresponding black hole mass parameters[12], in Fig. 3.48, we have applied the Cartesian coordinates (3.430) and (3.431), to compare the shadows of the KNdSBH and the RCWBH, for definite values of the black hole parameters, and several values of the spin parameter. Having in mind the re-scaling of the coordinates, it is seen from the diagrams that the RCWBH has larger shadows than the KNdSBH, respecting their black hole masses. Additionally, the increase in the spin parameter, makes the shadow of the KNdSBH to shrink outside the larger ones, whereas for the RCWBH, this happens inside of those.

The angular size of the shadow

The celestial coordinates defined in Eqs. (3.424) and (3.425) can be used in order to calculate the angular diameters of the shadow. As shown in the left panel of Fig. 3.49, these angular diameters are expressed in terms of the celestial coordinates (ψ_p, ϑ_p). We replace these angular diameters by (Grenzebach et al., 2015)

[12]For example, letting M_0 to be the black hole's mass for both of the RCWBH and KNdSBH, then $\dot{a}$ means $\frac{a}{M_0}$, and etc. In particular, $\dot{c}_1 = \frac{c_1}{M_0^2}$ and $\dot{R}_0 = \frac{R_0}{M_0^2}$.

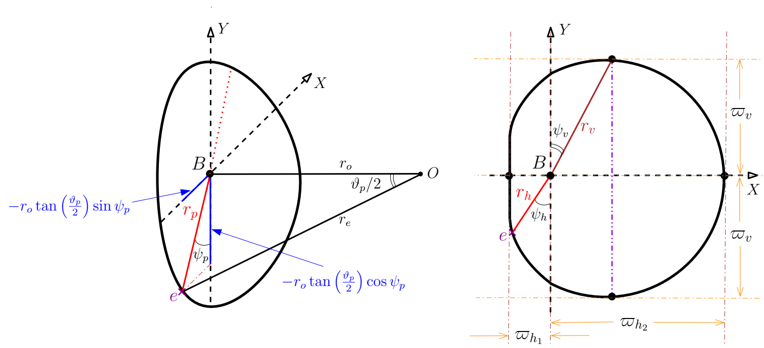

Figure 3.49: Characterization of an oblate shadow in terms of the angular diameters. The celestial coordinates (ψ_p, ϑ_p) are transformed to the Cartesian coordinates (X, Y), as indicated in the left panel. The black hole at point B is located at the center of the Cartesian coordinates. The observer at point O and at the distance r_o from the black hole, observes the event e on the shadow. In the right panel, the angular diameters corresponding to the mentioned celestial coordinates, are now expressed in terms of three angular radii ϖ_{h_1}, ϖ_{h_2} and ϖ_v, according to the symmetry with respect to the X-coordinate.

$$\delta_h = \varpi_{h_1} + \varpi_{h_2}, \tag{3.436}$$

$$\delta_v = 2\varpi_v, \tag{3.437}$$

which are defined in terms of the three angular radii ϖ_{h_1}, ϖ_{h_2} and ϖ_v, that obey the properties (see the right panel of Fig. 3.49)

$$\sin\varpi_{h_i} = \sin\vartheta_{h_i}\sin\psi_{h_i}, \quad (i = 1, 2), \tag{3.438}$$

$$\sin\varpi_v = \sin\vartheta_v\cos\psi_v, \tag{3.439}$$

or from Eqs. (3.424) and (3.425),

$$\sin\varpi_{h_i} = \mathcal{T}(r_{h_i}, r_o)\mathcal{P}(r_{h_i}, \theta_o), \tag{3.440}$$

$$\sin\varpi_v = \mathcal{T}(r_v, r_o)\sqrt{1 - \mathcal{P}^2(r_v, \theta_o)}. \tag{3.441}$$

Once again we restrict ourselves to the equatorial plane by letting $\theta_o = \frac{\pi}{2}$, so that the horizontal angular diameter corresponds to $\psi_h = \pm\frac{\pi}{2}$, and we need to solve $\mathcal{P}^2(r_h, \frac{\pi}{2}) = 1$ for this case. Using Eq. (3.424) together with Eqs. (3.411) and (3.412), this condition provides an equation of fourth order in r_h, which has the positive solutions

$$r_{h_1} = \sqrt{\bar{C}_1}\sin\left(\frac{1}{2}\arcsin\left(\frac{2\sqrt{\bar{C}_2}}{\bar{C}_1}\right)\right), \tag{3.442}$$

$$r_{h_2} = \sqrt{\bar{C}_1}\cos\left(\frac{1}{2}\arcsin\left(\frac{2\sqrt{\bar{C}_2}}{\bar{C}_1}\right)\right), \tag{3.443}$$

where

$$\bar{C}_1 = \frac{Q^2 - 2a^2}{2\left(\frac{a^2}{\lambda^2}\right) + 1}, \tag{3.444a}$$

$$\bar{C}_2 = \frac{2a^4 - \frac{3}{2}a^2\left(a^2 + \frac{1}{4}\right)}{\left(\frac{a^2}{\lambda^2}\right) + 1}. \tag{3.444b}$$

The horizontal angular radii are then calculated by evaluating the product $\mathcal{T}(r_{h_{1,2}}, r_o)\mathcal{P}(r_{h_{1,2}}, \frac{\pi}{2})$, and from there, δ_h can be evaluated using Eq. (3.436). To calculate the vertical angular radius, we take into account the fact that this radius corresponds to those points on the shadow's boundary, where the tangent to the curve $\mathcal{C}(r_v, r_o, \theta_o) \equiv \sin^2 \varpi_v$ vanishes. Accordingly, we encounter the equation $\partial_{r_v}\mathcal{C}(r_v, r_o, \frac{\pi}{2}) = 0$. Considering this condition and applying Eq. (3.441) together with Eqs. (3.424) and (3.425), we obtain the unique positive value

$$r_v = r_o\sqrt{\frac{Q^2 - 2a^2}{2\left(a^2 + r_o^2\right)}}, \tag{3.445}$$

which evaluates the vertical angular radii as

$$\sin^2 \varpi_v = \frac{\left(Q^2 - 2a^2\right)\left(\lambda^2\left(4a^2 - Q^2 + 4r_o^2\right) - 4r_o^4\right)}{8a^4\lambda^2 + a^2\left(8r_o^2\left(\lambda^2 + r_o^2\right) - 2\lambda^2 Q^2\right) + 4r_o^4\left(\lambda^2 - Q^2\right)}. \tag{3.446}$$

The vertical angular diameter δ_v, can be therefore calculated using Eq. (3.437). In Fig. 3.50, the behaviors of δ_h and δ_v have been plotted in terms of changes in Q and a. As observed from the diagrams, each of the horizontal diameter curves has a maximum, which is more significant for smaller a. Furthermore, the horizontal size is larger for smaller a, and all the curves tend to a same value as Q increases. On the other hand, the curves corresponding to the vertical diameter, expose a smooth decrease in value with respect to increase in Q, for each of the cases. Also, increase in the spin parameter only increases the vertical size of the shadow, and in contrast with the previous case, the vertical size is smaller for smaller a. These can be inferred, as well, from the density plots in the right panel diagrams. Moreover, as seen in Eqs. (3.440) and (3.441), the other effective factor in the angular sizes of the shadow, is the observer's distance r_o. As shown in the bottom panels of Fig. 3.50, by increase in r_o outside r_{p+}, the shadow increases in size until its angular diameters reach a constant maximum value, within a finite distance inside the causal region. In fact, for the vertical diameter, the radial distance r_o could encounter a minimum and a maximum, that can be obtained from Eq. (3.446) as

$$r^2_{o_{\min}^{\max}} = \frac{1}{2}\left(\lambda^2 \pm \sqrt{\lambda^2\left(4a^2 - Q^2 + \lambda^2\right)}\right), \tag{3.447}$$

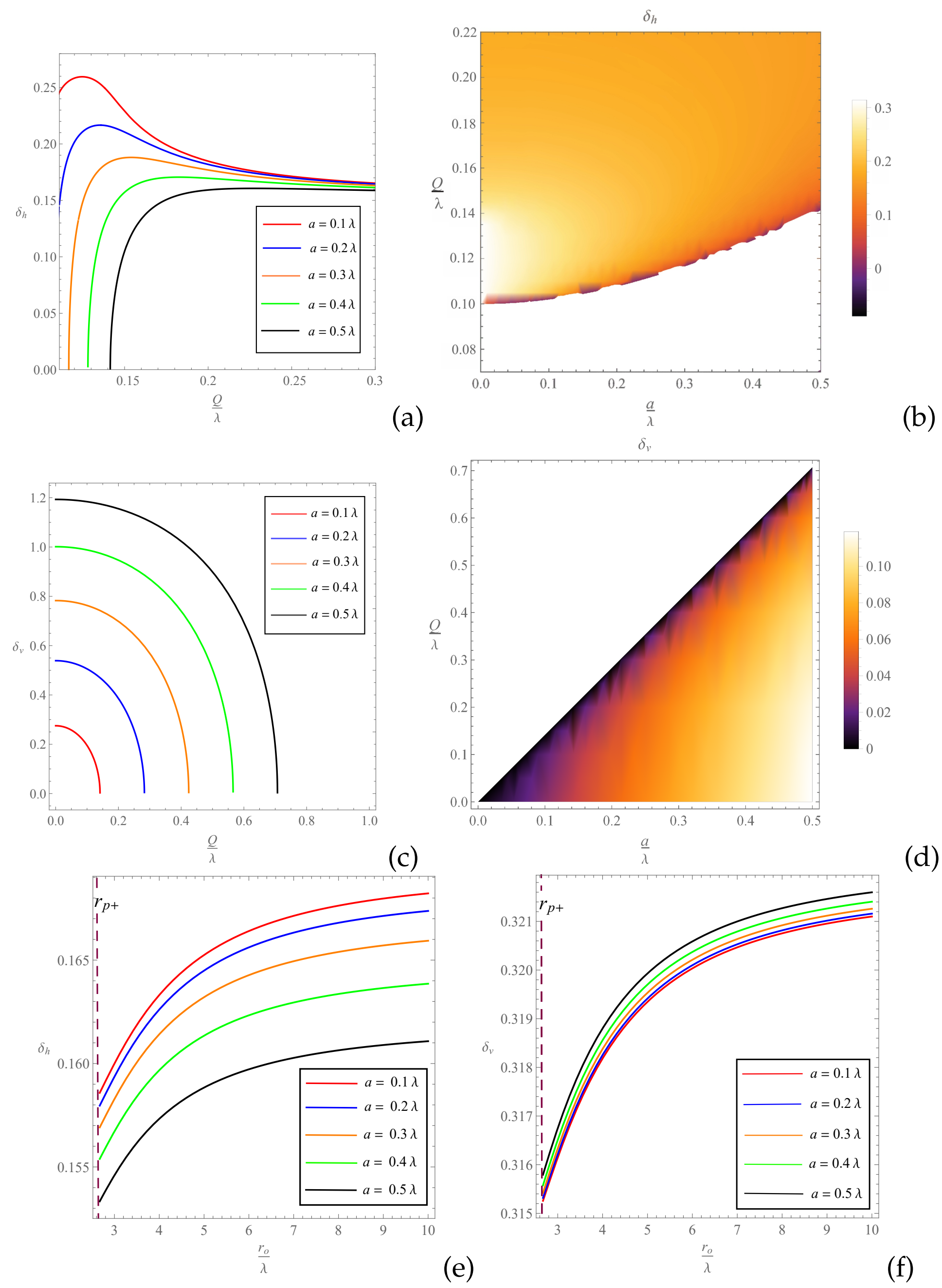

Figure 3.50: The variations of the horizontal (diagrams (a), (b)) and the vertical (diagrams (c), (d)) angular diameters of the RCWBH as functions of Q and a, plotted for $\lambda = 10$ and $r_o = 5\lambda$. In the left panels, the changes of angular diameters in terms of Q, have been plotted distinctly for five values of a. In the right panels, Q and a have been let to change freely. The bottom panel diagrams ((e), (f)), correspond respectively to the dependence of the angular diameters on the variations of the observer's location r_o, which have been plotted for $Q = 0.3\lambda$.

where, $r_{o\,\mathrm{min}}$ exists only for $Q > 2a$, for which, r_{p-} also exists. It is important to note that, the increase in size of the shadow by distance, is a consequence of the peculiar contribution of the cosmological term λ for the RCWBH. This term becomes more dominant as r_o increases.

It is of worth comparing the above vertical diameter, with the angular diameter assigned to the shadow of M87*. This way, we can obtain an estimation for the charge component of the RCWBH, if it has the same angular diameter. For M87*, located at the distance $r_{o*} \approx 5.18 \times 10^{23}$m from earth, the values associated with the lapse function components in Eqs. (3.23) are $M_{0*} \approx 6.4 \times 10^9 M_\odot$ and $r_{0*} \approx 1.82 \times 10^{13}$m (Akiyama et al., 2015). The angular diameter of the shadow has been observed as $\tilde{d}_* = (42 \pm 3)\ \mu$as[13] (Akiyama et al., 2019a). To do the comparison, we fix the cosmological component of the spacetime to the current value of the cosmological constant, by letting $c_{1*} = \Lambda_0 \approx 1.11 \times 10^{-52}\ \mathrm{m}^{-2}$ (Planck Collaboration, et al., 2016). Furthermore, the recent evaluation of the spin parameter of M87* is $a_* = 0.9 \pm 0.05$ (Tamburini et al., 2019). Assuming these values together with the equivalence $\tilde{d}_* = \delta_v$, and by taking into account the expression in Eq. (3.446), we get $Q_* \approx 1.8\,\mathrm{m}$. This value is approximately equivalent to 2.1×10^{17}C, which is nearly the charge of 10^{36} protons[14]. This value corresponds to a charge density of $\tilde{\rho}_{Q*} \approx 8.32 \times 10^{-24}\ \frac{\mathrm{C}}{\mathrm{m}^3}$ for the black hole.

3.7 Summary

In this chapter, we introduced a particular static charged black hole inferred from the WCG. We applied the standard Lagrangian method to calculate analytical solutions to the equations of motion for mass-less and massive test particles. In order to do so, we applied several elliptic intergation methods which enabled us to construct a firm mathematical foundations for our solutions and made it possible to simulate the orbits for all possible cases. Furthermore, we considered the gravitational Rutherford scattering for this black hole, studying which, we confronted a particular case of a hyper-elliptic integral which was treated by means of decomposition of the character-

[13] $1\ \mu\mathrm{as} \approx 4.85 \times 10^{-12}$ rad.

[14] The change from SI to geometric units for the electric charge is $Q_{(\mathrm{Coulomb})} = \sqrt{\frac{4\pi\epsilon_0 c^4}{G}}\, Q_{(\mathrm{meters})} = 1.15964 \times 10^{17} Q_{(\mathrm{meters})}$, and the proton's electric charge is $q_p = 1.602 \times 10^{-19}$C. For the mass, $M_{0(\mathrm{meters})} = M_{0(\mathrm{kg})} \times \frac{G}{c^2}$, and we have considered $M_\odot = 1.989 \times 10^{30}$kg (Phillips, 1995).

istic function into its possible real and imaginary solutions. This way, the scattering of charged test particles was simulated accordingly. Additionally, the gravitational lensing of this black hole when it is immersed in a plasmic medium was analyzed by exploiting rigorous elliptic integration methods. We finally applied the MNJA to obtain a stationary counterpart of this black hole, for which, the fundamental hypersurfaces, including the ergosphere and the photon regions were studied in detail. We also analyzed the shadow of the black hole applying an alternative method of calculating the celestial coordinates.

CHAPTER 4

The case of a scale-dependent BTZ black hole

In this chapter we study the motion of mass-less particles on a static Bañados-Teitelboim-Zanelli (BTZ) black hole background in the context of scale-dependent (SD) gravity, which is characterized by the running parameter ϵ. Thus, by using standard methods we obtain the equation of motions and then analytic solutions are found. The relevant non-trivial differences appear when we compare our solution against the classical counterpart (Fathi et al., 2020).

4.1 Introduction

Given that black holes combine classical and quantum effects, the research of this kind of objects might help us to improve our understanding of how gravity and quantum mechanics work together. In particular, jut after the seminal work of Deser, Jackiw, ’t Hooft and Witten (Deser et al., 1984; Deser & Jackiw, 1988; ’t Hooft, 1988; Witten, 1988), gravitation in (2+1) dimensions was considered as an ideal scenario to investigate conceptual issues such as the nature of observables and the “problem of time” (Carlip, 1995). Thus, in order to check the effects beyond GR, the BTZ black hole (the first black hole obtained with negative cosmological constant in that dimension), serves as a toy model to try to understand quantum gravity.

Originally, general relativity in (2+1) dimensions was not considered seriously. One of the main reasons is that it does not have a Newtonian limit (Barrow et al., 1986), however, the pioneer BTZ solution showed that it is indeed a black hole and it is interesting to learn about it since, firstly, it has an event horizon, and secondly, it appears as the final state of a collapsing matter, and finally, it has thermodynamic properties quiet similar to a (3+1)-dimensional black hole (Carlip, 1995).

Thus, after the discovery of the BTZ black hole solution (Bañados et al., 1992, 1993) the idea of gravity in (2+1) dimensions gained the attention of adepts to analyze several interesting properties that are usually treated in the (3+1)-dimensional counterpart. For example, its geodesic structure (Cruz et al., 1994), thermodynamic properties (Carlip, 1995; Bañados, 1999; Cruz & Lepe, 2004), quasinormal modes (QNM) (Cardoso & Lemos, 2001; Crisostomo et al., 2004; Panotopoulos, 2018), stable and regular interior solutions that matches with a BTZ background (Cruz & Zanelli, 1995; García & Campuzano, 2003; Cruz et al., 2005; Cataldo & Cruz, 2006) SD solutions (Koch et al., 2016; Rincón et al., 2018), among others. In the light of this, in this chapter we will investigate the gravitational effects on light produced in the spacetime of the SD version of the classical BTZ black hole. The importance of this study is twofold, firstly, because the motion of light provides a way to classify an arbitrary spacetime (in order to reveal its structure) and secondly, because the quantum features of this SD black hole could modify the classical trajectories of light.

4.2 The SD theory

The so-called SD scenario has received considerable attention in the context of black holes, wormholes, QNM as well as other applications. Given that the philosophy beyond this method is novel, we will briefly summarize the main points regarding how this idea is applied.

The crucial point is that in the SD scenario, the couplings of a certain theory are not constant any more. Inspired by the asymptotic safety program we allow that the coupling evolve with certain energy scale. This assumption allows to extend the classical well–defined solutions to include quantum corrections which, by definition, are taken to be small. In our particular problem, we only have two coupling: i) the Newton's coupling G_k and ii) the cosmological coupling Λ_k. One should note that the Newton's coupling is related to the gravitational coupling by mean of the simple relation $\kappa_k \equiv 8\pi G_k$. The problem have two independent fields: i) the arbitrary energy scale k

and ii) the metric field $g_{\mu\nu}$. The effective action is then written as

$$\Gamma[g_{\mu\nu}, k] \equiv \int \mathrm{d}^3x \sqrt{-g} \left[\frac{1}{2\kappa_k} \Big(R - 2\Lambda_k \Big) + \mathcal{L}_M \right], \tag{4.1}$$

where $\mathcal{L}_M$ is the Lagrangian density of the matter fields, and after varying the effective action with respect to the metric field, the effective Einstein field equations are obtained as follows:

$$G_{\mu\nu} + \Lambda_k g_{\mu\nu} \equiv \kappa_k T^{\text{effec}}_{\mu\nu}, \tag{4.2}$$

where the effective energy-momentum tensor is defined according to

$$\kappa_k T^{\text{effec}}_{\mu\nu} = \kappa_k T^{M}_{\mu\nu} - \Delta t_{\mu\nu}. \tag{4.3}$$

The object $T^{\text{effec}}_{\mu\nu}$ now includes two contributions, i.e. in addition to the usual matter content, we now have the non-matter source provided by the running of the gravitational coupling. This new tensor is then defined as:

$$\Delta t_{\mu\nu} \equiv G_k \Big(g_{\mu\nu} \Box - \nabla_\mu \nabla_\nu \Big) G_k^{-1}. \tag{4.4}$$

Even though matter source is always an interesting ingredient in gravitational theories, we will focus on the simplest case in which $T^{M}_{\mu\nu} = 0$, to investigate the effect of the SD couplings into a the well-known BTZ black hole solution. Note that, under some circumstances, the cosmological coupling is taken as a source term giving rise to $T^{M}_{\mu\nu} \neq 0$. This, however, is just a reinterpretation of the cosmological constant and does not provide a real source.

The additional field $k(x)$ gives us an auxiliary equation to complete the set. Thus, the relation is obtained from the condition

$$\frac{\delta \Gamma[g_{\mu\nu}, k]}{\delta k} = 0. \tag{4.5}$$

This restriction can be seen as *posteriori* regarding background independence (Stevenson, 1981; Reuter & Weyer, 2004; Becker & Reuter, 2014; Dietz & Morris, 2015; Labus et al., 2016; Morris, 2016; Ohta, 2017) The Eq. (4.5) provides us a restriction between G_k and Λ_k, which reveals that the cosmological parameter needs to be considered in order to obtain self-consistent SD solutions. Notice that if we consider an additional contribution i.e., if $\mathcal{L}_M \neq 0$, then the cosmological coupling is not mandatory. As we commented before, the above equation closes the system, but the implementation of this, is a difficult task.

To elicit the physical information from these equations, one has to set the renormalization scale $k(x)$ in terms of the physical variables of the system under consideration $k \rightarrow k(x, \dots)$. This choice, however, breaks the re-parametrization symmetry. In order to recover the aforementioned symmetry, and to circumvent the use of Eq. (4.5), we can supplement the field equations by assuming some energy constraint. Usually we have four standard energy conditions which play important roles in GR. Despite the existence of numerous occasions where these conditions are violated, in general, a well-defined model (solution) maintains the validity of, at least, one of the energy conditions. In general, among the four energy conditions, the so-called null energy condition (NEC) is the least restrictive one. We take advantage of the extreme NEC condition to get

$$T^{\text{effec}}_{\mu\nu}\ell^\mu\ell^\nu = -\Delta t_{\mu\nu}\ell^\mu\ell^\nu \stackrel{!}{=} 0, \tag{4.6}$$

where ℓ^μ is a null vector (Rincón & Koch, 2018a). A clever choice of this vector allows us to get the differential equation

$$G(r)\frac{\mathrm{d}^2G(r)}{\mathrm{d}r^2} - 2\left(\frac{\mathrm{d}G(r)}{\mathrm{d}r}\right)^2 = 0. \tag{4.7}$$

for the gravitational coupling. Solving the above differential equation, we decrease a degree of freedom of the problem. After replacing $G(r)$ into the effective Einstein field equations, we are able to obtain the functions involved. It is remarkable to note that, for the case of coordinate transformations we have

$$\nabla^\mu G_{\mu\nu} = 0. \tag{4.8}$$

In the next section we will briefly discuss a new black hole solution in the context of SD couplings, inspired by quantum gravity (Koch et al., 2016).

4.3 The background: static circularly symmetric black hole solutions

The metric, in the absence of charge, adopts circular symmetry whereas the functions involved only have radial dependence. With this in mind, the line element defined in terms of the usual Schwarzschild coordinates (ct, r, ϕ), is as follow

$$\mathrm{d}s^2 = -f(r)\,\mathrm{d}(ct)^2 + f(r)^{-1}\,\mathrm{d}r^2 + r^2\mathrm{d}\phi^2, \tag{4.9}$$

for which, we need to find the metric function $f(r)$ and the cosmological coupling $\Lambda(r)$. Solving first the Eq. (4.7) and then the set of $\{f(r), \Lambda(r)\}$, we obtain

$$
\begin{aligned}
G(r) =& \frac{G_0}{1+\epsilon r}, && (4.10)\\
f(r) =& -\frac{8G_0M_0}{c^2}Y(r) + \frac{r^2}{\ell_0^2}, && (4.11)\\
\Lambda(r) =& -\frac{1}{\ell_0^2}\left(\frac{1+3\epsilon r}{1+\epsilon r}\right) + \frac{8M_0G(r)}{c^2r^2}Y(r)\left[r\epsilon + \frac{1}{2}(1+2r\epsilon)\left(\frac{\mathrm{d}\ln Y(r)}{\mathrm{d}\ln r}\right)\right], && (4.12)
\end{aligned}
$$

where $Y(r)$ is an auxiliary function defined as follow

$$
Y(r) \equiv 1 - 2x + 2x^2 \ln\left(1+\frac{1}{x}\right), \quad x \equiv r\epsilon. \tag{4.13}
$$

The set of constants $(\cdots)_0$ are defined as the classical values, and ϵ is the parameter which encodes the SD corrections. We then have four integration constants: i) the gravitational coupling G_0, ii) the cosmological coupling $\Lambda_0 \equiv -\ell_0^{-2}$, iii) the classical mass M_0, and finally, iv) the running parameter ϵ. On the other hand, the non-rotating classical solution (Bañados et al., 1992, 1993), should be obtained when ϵ is turned off, i.e.

$$
\begin{aligned}
&\lim_{\epsilon\to 0} G(r) = G_0, && (4.14)\\
&\lim_{\epsilon\to 0} f(r) = f_0(r) \equiv -\frac{8M_0G_0}{c^2} + \frac{r^2}{\ell_0^2}, && (4.15)\\
&\lim_{\epsilon\to 0} \Lambda(r) = \Lambda_0. && (4.16)
\end{aligned}
$$

According to the fact that the exact solution for the SD problem is complicated, it is plausible to take into account small quantum corrections. Hence, we expand the full solution up to the first order in ϵr. Such a consideration, in fact, corresponds to taking $Y(r) \approx 1-2x$ which merely confines x to the domain of small positive values. Such an adoption enables us to recover fully analytical descriptions of radial-angular world-lines and to compare them with classical results in a desirable transparency. Consideration of the higher order terms in the running parameter however, will rely totally on a numerical investigation which does not lie within the scope of this paper. At this level, it is essential to highlight the range of the SD parameter ϵ. Firstly, note that the combination $x = \epsilon r$ should be small in order to maintain the validity of our approximation. In this sense, given that r should be large, then the corresponding inverse parameter ϵ should be small, to keep $x \ll 1$. Secondly, we should keep in mind that the SD scenario is supposed to include quantum features. The latter means that the allowed corrections are supposed to be small. In the light of the above two arguments, we are looking for solutions when the SD parameter is, for instance, $10^{-2} \lesssim \epsilon \lesssim 10^{-1}$; values which are quite smaller than unity. Now, returning to the mentioned kind of expansion for $Y(r)$, the solutions are reduced to

$$G(r) \approx G_0 \, (1 - \epsilon r), \tag{4.17}$$

$$f(r) \approx \frac{r^2}{\ell_0^2} + 16M\epsilon r - 8M, \tag{4.18}$$

$$\Lambda(r) \approx \Lambda_0 (1 + 2r\epsilon), \tag{4.19}$$

where $M \equiv \frac{M_0}{m_p}$ is the dimensionless mass, and m_p is the Planck mass in the (2+1)-gravity given by (Cruz & Lepe, 2004)

$$m_p = \frac{c^2}{G_0}. \tag{4.20}$$

The event horizon can be obtained demanding that $f(r) = 0$. Thus, from Eq. (4.18) we have the two solutions

$$r_{\pm} = \pm \, R_0 \left[\sqrt{1 + (\epsilon R_0)^2} \mp (\epsilon R_0) \right], \tag{4.21}$$

where only the positive root has physical meaning. Furthermore, the parameter $R_0 \equiv \sqrt{8M}\ell_0$ is the classical horizon (i.e. the event horizon when ϵ goes to zero). Again, taking a Taylor series for small ϵ we observe how the classical horizon is corrected by taking into account quantum effects

$$r_+ \approx R_0 \left[1 - \epsilon R_0 + \frac{1}{2}(\epsilon R_0)^2 + \mathcal{O}(\epsilon^3) \right]. \tag{4.22}$$

Notice that an important relation is obtained from Eq. (4.21)

$$8M = \frac{r_+^2}{\ell_0^2} + 16M\epsilon r_+, \tag{4.23}$$

and also, the lapse function can be written as

$$f(r) \quad = \quad \frac{1}{\ell_0^2}(r - r_+)(r - r_-). \tag{4.24}$$

4.4 Null geodesics

In order to apply the standard Lagrangian procedure discussed in chapter 2, to investigate the motion of mass-less test particles on a static SDBTZ black hole background, we write the Lagrangian associated to the line element (7.31) as (Chandrasekhar, 1998; Cruz et al., 2005; Villanueva et al., 2018)

$$2\mathcal{L} = -f(r)\,c^2\dot{t}^2 + \dot{r}^2 f(r)^{-1} + r^2\,\dot{\phi}^2 = 0. \tag{4.25}$$

The corresponding conjugate momenta are

$$\Pi_t = -f(r)c^2\dot{t} = -\mathcal{E}, \quad \Pi_\phi = r^2\dot{\phi} = L. \tag{4.26}$$

Here, $\mathcal{E}$ is cannot be associated with the energy (per unit of mass) since the spacetime is not asymptotically flat. Applying Eqs. (4.26) into Eq. (4.25), and defining $E \equiv \frac{\mathcal{E}}{c^2}$, we obtain

$$\left(\frac{\mathrm{d}r}{\mathrm{d}\tau}\right)^2 = E^2 - V_{\text{eff}}(r), \tag{4.27}$$

where

$$V_{\text{eff}}(r) = L^2\frac{f(r)}{r^2}. \tag{4.28}$$

This potential presents a maximum at $r_m = \epsilon^{-1}$ and has the value

$$V_{\text{eff}}(r)\bigg|_{r=r_m} = \left(\frac{L}{\ell_0}\right)^2\left[1+(\epsilon R_0)^2\right]. \tag{4.29}$$

In Fig. 4.1 this effective potential has been plotted for different values of the parameters. It is remarkable that the classical solution does not depend on the horizon radius, however, the quantum counterpart depends on the combination ϵR_0 which means that the maximum will be shifted when ϵ increases. Using the second relation of Eq. (4.26) and the chain rule, we obtain the radial-angular equation of motion, which is given by

$$L^2\left(\frac{1}{r^2}\frac{\mathrm{d}r}{\mathrm{d}\phi}\right)^2 = E^2 - V_{\text{eff}}(r). \tag{4.30}$$

Additionally, Eq. (4.28) together with Eqs. (6.51) and (4.30), allow us to obtain explicitly the equations of motion, which read

$$\left(\frac{\mathrm{d}r}{\mathrm{d}\tau}\right)^2 = \left[E^2 - \left(\frac{L}{\ell_0}\right)^2\right] - \frac{16M\epsilon L^2}{r} + \frac{8ML^2}{r^2}, \tag{4.31}$$

and, with the change of variable $u \doteq \frac{1}{r}$,

$$\left(-\frac{\mathrm{d}u}{\mathrm{d}\phi}\right)^2 = \left(\frac{1}{b^2} - \frac{1}{b_c^2}\right) + 8M(u-u_m)^2 \equiv g(u), \tag{4.32}$$

where $u_m = \epsilon$, $b = \frac{L}{E}$ is the impact parameter and b_c is a critical impact parameter, which corresponds to the value of the impact parameter for photons whose constant of motion $E^2 = V_{\text{eff}}(r_m)$, given by

$$b_c = \frac{\ell_0}{\sqrt{1+(\epsilon R_0)^2}}. \tag{4.33}$$

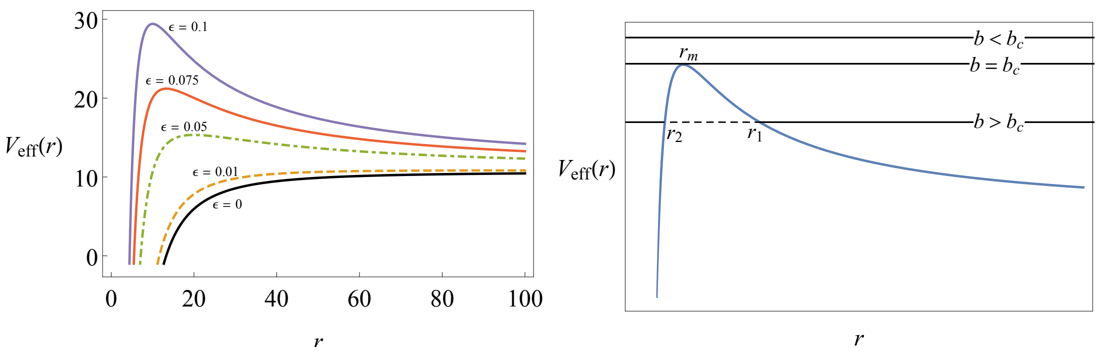

Figure 4.1: Plots for the effective potential V_{eff} as a function of the radial coordinate r, which presents a maximum equal to $V_{\text{eff}} = \frac{L^2}{b_c^2}$, where b_c is the critical impact parameter given by Eq. (4.33), at $r_m = \epsilon^{-1}$. LEFT: Evolution of the effective potential for different values of the running parameter: $\epsilon = 10^{-1}$, $\epsilon = 7.5 \times 10^{-2}$, $\epsilon = 5 \times 10^{-2}$, $\epsilon = 10^{-2}$ and $\epsilon = 0$, in arbitrary reciprocal length units. RIGHT: Depending on the value of the impact parameter, different trajectories are obtained. Thus, if $b > b_c$ there are two turning points, r_1 and r_2, which correspond to the periastron and apastron distance for orbits of the first and second kind, respectively; geodesics with impact parameter $b = b_c$ allows an unstable circular orbit so photons arriving from infinity asymptotically approaches to the circle of radius r_m by spiralling. Also, from the opposite side, photons approach the same circle by spiralling around it; finally, if $b < b_c$ the motion is unbounded and photons coming from infinite goes to the event horizon and vice versa.

We observe that the critical value is, in this case, smaller than the classical counterpart (or more precisely, than the usual non-rotating BTZ black hole).

4.4.1 Radial motion

Photons with vanished angular momentum $L = 0$ have a zero effective potential, and then follow a radial motion. By imposing this condition in Eq. (4.31), it is straightforward to see that

$$r(\tau) = r_0 \pm E\tau, \tag{4.34}$$

where r_0 is the location of the photon at $\tau = 0$, and the plus (minus) sign indicates that the movement is made towards the spatial infinity (event horizon). For the coordinate time, we use together Eqs. (4.26)-(4.31) to obtain the following quadrature

$$\frac{\mathrm{d}r}{\mathrm{d}t} = \frac{c}{\ell_0^2}(r - r_+)(r - r_-), \tag{4.35}$$

so, an elementary integration yields

$$r(t) = \frac{r_+ - \kappa_o r_- \, e^{\pm \frac{t}{t_c}}}{1 - \kappa_o \, e^{\pm \frac{t}{t_c}}}, \tag{4.36}$$

where

$$\kappa_0 = \frac{r_0 - r_+}{r_0 - r_-}, \quad t_c = \frac{\ell_0^2}{c(r_+ - r_-)}. \tag{4.37}$$

Notice from Eq. (4.36) and Fig. 7.39 that for a non-comoving observer, photons take

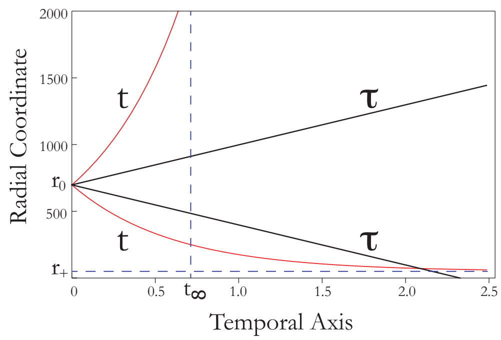

Figure 4.2: Plot for the radial coordinate as a function of the proper time τ and coordinate time t, described by Eqs. (4.34) and (4.36), respectively.

an infinite time to reach the horizon r_+, and a finite time

$$t_\infty = t_c \, \ln \kappa_0^{-1} \tag{4.38}$$

to escape to infinity. This behaviour was reported before by Villanueva & Vásquez in the context of asymptotically Lifshitz spacetimes (Villanueva & Vásquez, 2013).

4.4.2 The critical motion

Returning to the general equation (4.32), we must distinguish the different possible cases based on the disposition of the roots of the polynomial $g(u) = 0$. In order to obtain a qualitative analysis of the allowed motion we refers to the Fig. 4.1. Clearly in terms of the impact parameter b, there are three different allowed types of motion. The first one corresponds to the case $b = b_c$, so we have $g(u) = 8M(u - u_m)^2 = 0$ and the motion corresponds to an asymptotic (unstable)circular orbit at $r = r_m$. Thus, considering $\phi = 0$ when $r = r_0$, an integration of Eq. (4.32) leads to

$$r(\phi) = \frac{r_0}{\frac{r_0}{r_m} + \left(1 - \frac{r_0}{r_m}\right) e^{\pm\sqrt{8M}\phi}}, \tag{4.39}$$

where the plus (minus) sign corresponds to the motion for which $r_0 > r_m$ ($r_0 < r_m$), and the corresponding polar plot are showed in Fig. 4.3. In the plots, we have also shown the classical case ($\epsilon = 0$ or $r_m \to \infty$) for the same values of the impact parameter and the starting point. However, as it can be seen in the left panel of Fig. 4.1, the

$\epsilon = 0$ case does not possess any maximums in its corresponding effective potential. It therefore can not offer critical motions. Hence, Fig. 4.3 shows together, the critical motion in SDBTZ spacetime with a non-critical motion in BTZ spacetime. By comparison, we can see that for the same values of the physical parameters, spiral infall on the black hole event horizon appears in the classical case. There is also one more

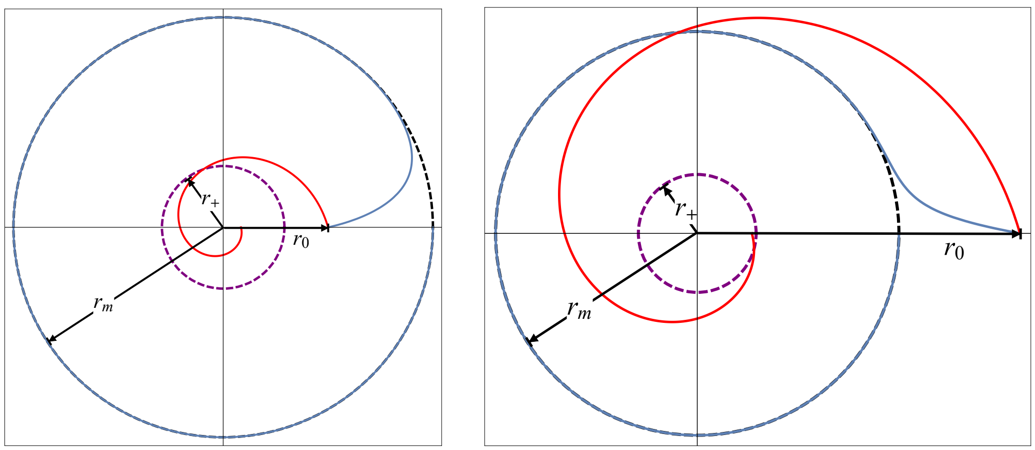

Figure 4.3: Polar plots for the motion of photons whose impact parameter is set to $b = b_c$. The red trajectories indicate non-critical motions corresponding to the case of $\epsilon = 0$ (the usual non-rotating BTZ black hole), whereas the blue ones show critical motion in the SDBTZ spacetime, characterized as follows: LEFT: Photons start from the distance $r_0 < r_m$ and approach asymptotically to the unstable circular orbit at r_m. RIGHT: Photons come from $r_0 > r_m$ and approach asymptotically to the unstable circular orbit at r_m. Both graphs were made using $\epsilon = 10^{-2}$, $M = 10$ and $\ell_0 = 100$, so that $r_m = 100$, $b_c = 11.11$ (all values are in arbitrary length units). In the classical case in both plots, photons start from r_0 and fall onto the event horizon by spiraling.

interesting concept which is worth bringing up. As seen above, the motion of photons in black hole spacetimes is rather peculiar and their ability to escape the from being trapped, is restricted to some specific rules. Formerly, Synge had figured out that photons moving in the Schwarzschild spacetime can escape to infinity if they move on directions constructing a escape cone (Synge, 1966), which was later called the *cone of avoidance* by Chandrasekhar (Chandrasekhar, 1998). This constructs the foundations of the study of the so-called *black hole shadow* (Perlick, 2004; Grenzebach et al., 2014, 2015; Perlick et al., 2015; Abdujabbarov et al., 2016; Contreras et al., 2019). Such a shadow has recently been observed for the M87 central black hole (Akiyama et al., 2019a,b).

Returning to the critical orbits obtained above, we can define a cone of avoidance exploiting its null geodesic generators. Denoting Ψ as the half angle of the cone, then (Chandrasekhar, 1998; Cruz et al., 2005; Kuniyal et al., 2016)

$$\cot\Psi = \frac{1}{r}\frac{\mathrm{d}\tilde{r}}{\mathrm{d}\phi}, \tag{4.40}$$

where $\tilde{r}$ is the proper length along the generators of the cone

$$\mathrm{d}\tilde{r} = \frac{\mathrm{d}r}{\sqrt{f(r)}} = \frac{\ell_0\,\mathrm{d}r}{\sqrt{(r-r_+)(r-r_-)}}. \tag{4.41}$$

Combining Eqs. (4.41) and (4.30) with Eq. (4.40) one obtains that

$$\tan\Psi = \left(\frac{r_+}{R_0}\frac{r_-}{R_0}\right)^{\frac{1}{2}} \frac{\left(\frac{r}{r_+}-1\right)^{\frac{1}{2}}\left(\frac{r}{r_-}-1\right)^{\frac{1}{2}}}{\frac{r}{r_m}-1}. \tag{4.42}$$

From this last equation it follows that

$$\Psi \to \begin{cases} \sim \frac{r_m}{R_0} & \text{if} \qquad r \to \infty \\ = \frac{1}{2}\pi & \text{if} \qquad r = r_m \\ = 0 & \text{if} \qquad r = r_+ \end{cases} \tag{4.43}$$

An important remark from the first of Eqs. (4.43) is that the angle Ψ goes to a constant (non-zero) value as $r \to \infty$. The same happens for Schwarzschild-anti-de Sitter black holes (Cruz et al., 2005; Stuchlík & Hledík, 1999) in the context of (3+1)-gravity. In the same context however, we encounter $\Psi \sim \frac{1}{r}$ as $r \to \infty$ for Schwarzschild and Schwarzschild-de Sitter black holes (Chandrasekhar, 1998; Stuchlík & Hledík, 1999).

4.4.3 The deflecting trajectories

As shown in Fig. 4.1, in the case when $b_c < b < b_0$ (with $b_0 = \lim_{\epsilon\to 0} b_c = \ell_0$) there are two kinds of allowed orbits: the OFK for $r > r_1$, and the OSK for $r < r_2$. The values of the turning points $r_{1,2}$ are obtained from the condition $E^2 = V_{\text{eff}}$, and are given by

$$r_1 = \frac{r_m}{1-\varepsilon}, \quad r_2 = \frac{r_m}{1+\varepsilon}, \tag{4.44}$$

where ε is the eccentricity given by

$$\varepsilon = \frac{r_m}{\sqrt{8M\mathcal{D}}}, \tag{4.45}$$

and $\mathcal{D}$ is the anomalous impact parameter given by the relation

$$\frac{1}{\mathcal{D}^2} = \frac{1}{b_c^2} - \frac{1}{b^2}. \tag{4.46}$$

Therefore, for the OFK kind with $\phi = 0$ at $r = r_1$, a quick integration of Eq. (4.32) yields

$$r(\phi) = \frac{r_m}{1 - \varepsilon \cosh\left(\sqrt{8M}\phi\right)}, \tag{4.47}$$

which is depicted in Fig. 4.4. Note that, the test particles reach the infinity for an angle

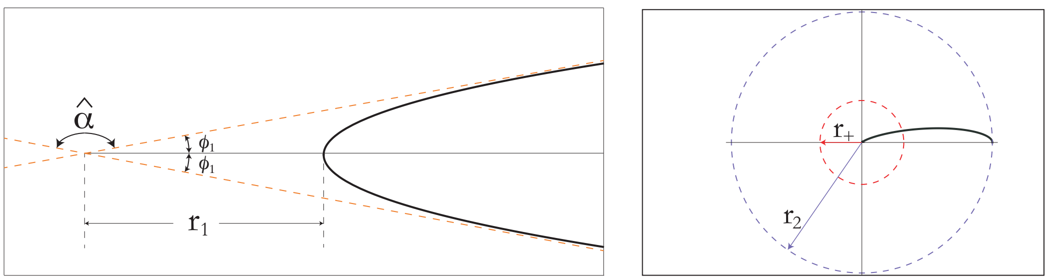

Figure 4.4: Polar plot for the (un-)bound and motion of photons whose impact parameter is $b > b_c$. LEFT: OFK for photons whose radial coordinate is always greater than the periastron distance r_1, and the motion is symmetric with respect to r_1 so the deflection angle results to be $\widehat{\alpha} = \pi - 2\phi_1$. RIGHT: OSK for photons whose radial coordinate is always smaller than the apastron distance r_2. Both graphs were made using $\epsilon = 10^{-2}$, $M = 10$ and $\ell_0 = 100$, so that $r_m = 100$, $b_c = 11.11$ (all values are in arbitrary length units). For the case of $\epsilon = 0$, only this kind of orbit is obtained, according to the relation in Eq. (4.51).

$\phi = \pm\phi_1$, given by

$$\phi_1 = \frac{1}{\sqrt{8M}} \operatorname{arccosh}\left(\frac{1}{\varepsilon}\right), \tag{4.48}$$

so the deflection angle $\widehat{\alpha} = \pi - 2\phi_1$ becomes

$$\widehat{\alpha}(b) = \pi - \frac{1}{\sqrt{2M}} \operatorname{arccosh}\left(\frac{\sqrt{8M}b_c}{r_m} \frac{1}{\sqrt{1 - \left(\frac{b_c}{b}\right)^2}}\right). \tag{4.49}$$

In Fig. 4.5 the the eccentricity (4.45) and deflection angle (4.49) are plotted as a function of the impact parameter b. On the other hand, the OSK for which $\phi = 0$ at $r = r_2$, are described by the following relation:

$$r(\phi) = \frac{r_m}{1 + \varepsilon \cosh\left(\sqrt{8M}\phi\right)}. \tag{4.50}$$

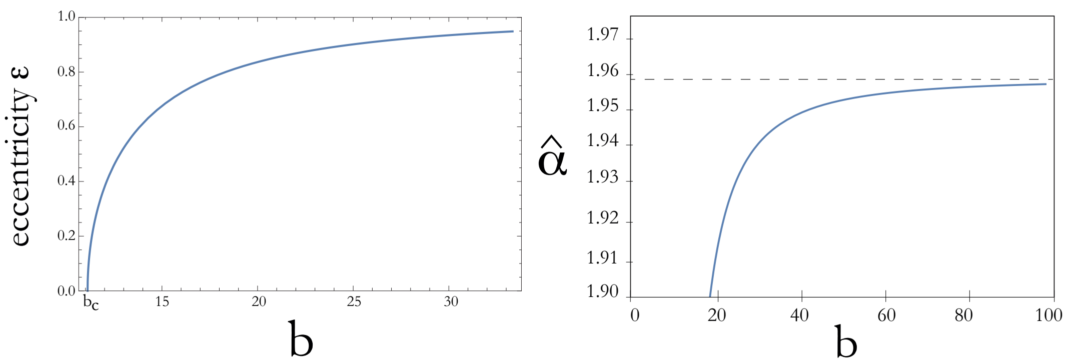

Figure 4.5: LEFT: Eccentricity parameter ε as a function of the impact parameter b. Note that the critical impact parameter corresponds the vanishing eccentricity. RIGHT: The deflection angle $\widehat{\alpha}$ as a function of the impact parameter b. Both graphs were made using $\epsilon = 10^{-2}$ (in arbitrary reciprocal length units), $M = 10$ and $\ell_0 = 100$ (in arbitrary length units), so that $r_m = 100$, $b_c = 11.11$ (in arbitrary length units).

This kind of orbit is depicted in the right panel of Fig. 4.4 and, obviously, depends on the same parameter as for the OFK. In the case of $\epsilon = 0$, the equation of motion will be

$$r(\phi)|_{\epsilon=0} = \pm\sqrt{8M}\,\mathcal{D}\,\mathrm{sech}(\sqrt{8M}\,\phi), \tag{4.51}$$

which only results in OSK, completely the same as that in the right panel of Fig. 4.4. The only difference, is the value of the apastron distance which in this case is given by

$$r_2|_{\epsilon=0} = \sqrt{8M}\,\mathcal{D}. \tag{4.52}$$

This is, in fact, an expected behavior since the relevant effective potential for the case of $\epsilon = 0$ does not propose a maximum within finite distances. Hence, no deflection to infinity (or OFK) can be anticipated (see Fig. 4.1).

4.4.4 The captured trajectories

When $0 < b < b_c$, the polynomial $g(u)$ possesses a complex conjugate pair, so that the motion is a terminating bound orbit. This means that photons fall to the event horizon (or, depending on the initial conditions, to the spatial infinity) from a finite distance r_0. Therefore, for test particles coming from $r_0 > r_m$ where $\phi = 0$, the trajectory is described by

$$r(\phi) = \frac{r_m}{1 + \bar{\varepsilon}\,\sinh(\sqrt{8M}\phi - \varphi)}. \tag{4.53}$$

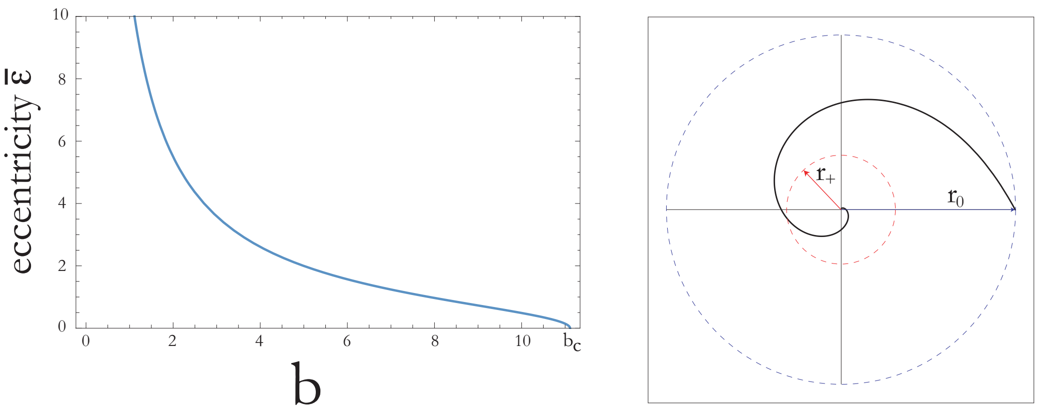

Figure 4.6: LEFT: Eccentricity parameter $\bar{\varepsilon}$ as a function of the impact parameter b for the terminating bound orbit. The critical impact parameter corresponds the zero value of the eccentricity and its tends to infinity as $b \to 0$. RIGHT: The trajectory followed by photons in a terminating bound orbit, in which, $\phi = 0$ at $r = r_0$. Both graphs were made using $\epsilon = 10^{-2}$ (in arbitrary reciprocal length units), $M = 10$ and $\ell_0 = 100$ (in arbitrary length units), so that $r_m = 100$, $b_c = 11.11$ (in arbitrary length units).

Here $\bar{\varepsilon}$ is the eccentricity associated to the capturing trajectories, and is given by

$$\bar{\varepsilon} = \frac{r_m}{\sqrt{8M}\bar{\mathcal{D}}}, \tag{4.54}$$

with

$$\frac{1}{\bar{\mathcal{D}}^2} = \frac{1}{b^2} - \frac{1}{b_c^2}, \tag{4.55}$$

and φ depends on the initial position according to

$$\varphi = \text{arcsinh}\left[\bar{\varepsilon}^{-1}\left(1 - \frac{r_m}{r_0}\right)\right]. \tag{4.56}$$

Note from Eq. (4.54) that the range of the eccentricity is now $0 < \bar{\varepsilon} < \infty$, as shown in the left panel of Fig. 4.6. Also, in the right panel of the same graph the terminating bound trajectory has been plotted. Once again, the classical BTZ case can be obtained by letting $\epsilon = 0$, giving

$$r(\phi)|_{\epsilon=0} = \sqrt{8M}\,\bar{\mathcal{D}}\,\text{csch}\left[\sqrt{8M}\,\phi + \text{arcsinh}\left(\frac{\sqrt{8M}\bar{\mathcal{D}}}{r_0}\right)\right], \tag{4.57}$$

which turns out to obey the same capturing behavior as in the SD case.

4.5 Summary

In this chapter we studied some relevant aspects of the geodesic structure of a SD non-rotating BTZ black hole. Since the value of the running parameter ϵ is small, we can justify its first-order expansion and this way, the analytical study of different possible trajectories of mass-less particles becomes possible.

The radial motion presents some similar feature as for the standard (or SD) black holes, as we saw in the previous chapters.

The angular motion, on the other hand, is completely different to the standard non-rotating BTZ black hole, due to the existence of the extra term $16M\epsilon r$ in Eq. (4.18). Precisely speaking, the SDBTZ black hole provides more complex physical situations which are absent in its classical counterpart. The linear term proportional to ϵr plays a crucial role. Thus, given the structure of the lapse function, the effective potential has a maximum (located at $r_m = \epsilon^{-1}$), and therefore, three well-defined regions are generated, according to which, bound and unbound orbits become available.

The obtained results indicate that, relying on the availability of the running parameter, the SDBTZ theory can offer more types of orbits, including escape to infinity. This latter, is of great importance because it enables us to talk about the gravitational lensing effect. We therefore can conclude that the SD theory is more capable of enveloping relativistic effects, proposed as well by GR, and seems worth of studying further in the context of other observational features of gravity.

Chapter 5

The case of a Kerr black hole inside plasma

During the last decade, numerous investigations have been published which follow the discussions given by Synge (Synge, 1960), that apply modern mathematical methods to make possible the determination and confinement of light propagation in the spacetimes of theoretical (non-)static black holes that are surrounded by plasmic or dark fluid media (Bisnovatyi-Kogan & Tsupko, 2009, 2010; Tsupko & Bisnovatyi-Kogan, 2013; Morozova et al., 2013; Bisnovatyi-Kogan & Tsupko, 2015; Perlick et al., 2015; Atamurotov et al., 2015; Abdujabbarov et al., 2016; Bisnovatyi-Kogan & Tsupko, 2017a; Perlick & Tsupko, 2017; Schulze-Koops et al., 2017; Abdujabbarov et al., 2017; Liu et al., 2017; Haroon et al., 2019; Kimpson et al., 2019; Babar et al., 2020; Junior et al., 2020; Badía & Eiroa, 2021). Despite this, the analytical treatment of light ray trajectories in non-vacuum black hole surroundings is seemed to be overlooked. In fact, such analysis can help classifying the other possible orbits in such conditions, that are not usually considered to determine the black holes' photon spheres and shadows. Hence, in this chapter, we apply the mathematical methods introduced and used in the previous chapters, to calculate the light ray paths while they travel in a non-vacuum non-static spacetime. Accordingly, we investigate the optical nature of the exterior spacetime of a Kerr black hole, considering that it is immersed in an inhomogeneous anisotropic plasmic medium whose structural functions are constant (Fathi et al., 2021a).

5.1 An overview of light propagation in non-magnetized plasma

In this section, a simple plasma model is considered as a medium for the propagation of electromagnetic waves, and by taking into account the respective dispersion, the ray optics is studied. The most simple plasmic model, namely a two-fluid model with vanishing pressure. This way, the dynamics of the system is governed by the equations (all indices are four-dimensional) (Breuer et al., 1980, 1981)

$$F_{[\beta\gamma,\alpha]} = \mathbf{0}, \tag{5.1}$$

$$F^{\alpha\beta}{}_{;\beta} = J^{\alpha} + enU^{\alpha}, \tag{5.2}$$

$$mU^{\beta}U^{\alpha}{}_{;\beta} = eF^{\alpha}{}_{\beta}U^{\beta}, \tag{5.3}$$

$$(nU^{\alpha})_{;\alpha} = 0, \tag{5.4}$$

$$\boldsymbol{U}\cdot\boldsymbol{U} = -1. \tag{5.5}$$

where the subscript comma indicates partial differentiation, $F_{\alpha\beta}$ is the field strength tensor, J^{α} is the ionic current, e is the electron charge, m is the electron mass, n is the electron number density, and U^{α} is the electron four-vector. The Eq. (5.3) is the equation of motion for the electron fluid (Euler equations plus Lorentz force). Note that, as long as the plasma is sufficiently cold, one can ignore the pressure of the electron fluid, which we assume here as a valid approximation. The Eq. (5.4) is the equation of charge conservation of the electron component. Note that, although the total charge is already guaranteed by Eq. (5.2), it is not solely for the electron component. It has been shown that the above system of evolution equations admits a locally well-posed initial value problem, and therefore, Eqs. (5.1)–(5.5) are linearization stable (Breuer et al., 1980). This property guarantees that the solutions of the linearized equations are close to solutions of the full equations, i.e., that the linearization gives a meaningful approximation. So, we can linearize the above set of equations around some background solution. For simplicity, we restrict ourselves to the case of a background solution with vanishing electromagnetic field. In other words, our background solution is given bu a non-negative scalar function $\mathring{n}$ and a vector field $\mathring{\boldsymbol{U}}$, that satisfy

$$\mathbf{0} = J^{\alpha} + e\mathring{n}\mathring{U}^{\alpha}, \tag{5.6}$$

$$\mathring{U}^{\beta}\mathring{U}^{\alpha}{}_{;\beta} = \mathbf{0}, \tag{5.7}$$

$$\left(\mathring{n}\mathring{U}^{\alpha}\right)_{;\alpha} = 0, \tag{5.8}$$

$$\mathring{\boldsymbol{U}} \cdot \mathring{\boldsymbol{U}} = -1. \tag{5.9}$$

Now, having in hand this background solution, one can linearize Eqs. (5.1)–(5.5), by perturbing (up to the first order) its corresponding fields as

$$F_{\alpha\beta} = \mathbf{0} + \hat{F}_{\alpha\beta}, \tag{5.10}$$

$$n = \mathring{n} + \hat{n}, \tag{5.11}$$

$$U^{\alpha} = \mathring{U}^{\alpha} + \hat{U}^{\alpha}, \tag{5.12}$$

where the hatted parameters are the first order perturbations on the selected background defined in Eqs. (5.6)–(5.9). The resulting equations govern the dynamics of sufficiently weak electromagnetic waves $\hat{\boldsymbol{F}}$ in our plasma which, according to $\mathring{\boldsymbol{F}} = \mathbf{0}$, is assumed non-magnetized. We shall presuppose that the metric $\boldsymbol{g}$ and the and the ionic current $\boldsymbol{J}$ are unperturbed. The first assumption is in agreement with our general stipulation to work on a fixed metric background i.e., to disregard the back-reaction, governed by Einstein field equations, of matter and electromagnetic fields on the metric. The second assumption means that the effect of the electromagnetic wave on the ions is ignored. This is a reasonable approximation since the inertia of the ions is much bigger than that of the electrons. On these assumptions, the linearized system of equations for the perturbations takes the form

$$\hat{F}_{[\beta\gamma,\alpha]} = \mathbf{0}, \tag{5.13}$$

$$\hat{F}^{\alpha\beta}{}_{;\beta} = e\mathring{n}\hat{U}^{\alpha} + e\hat{n}\mathring{U}^{\alpha}, \tag{5.14}$$

$$m\mathring{U}^{\beta}\hat{U}^{\alpha}{}_{;\beta} + m\hat{U}^{\beta}\mathring{U}^{\alpha}{}_{;\beta} = e\hat{F}^{\alpha}{}_{\beta}\mathring{U}^{\beta}, \tag{5.15}$$

$$\left(\mathring{n}\hat{U}^{\alpha} + \hat{n}\mathring{U}^{\alpha}\right)_{;\alpha} = 0, \tag{5.16}$$

$$\mathring{\boldsymbol{U}} \cdot \hat{\boldsymbol{U}} = 0. \tag{5.17}$$

With $\boldsymbol{g}$, $\mathring{n}$ and $\mathring{\boldsymbol{U}}$ known, Eqs. (5.13)–(5.17) is a system of first order linear differential equations for $\hat{\boldsymbol{F}}$, $\hat{n}$ and $\hat{\boldsymbol{U}}$. It is our goal to find dynamical equations for $\hat{\boldsymbol{F}}$ alone, i.e., to eliminate $\hat{n}$ and $\hat{\boldsymbol{U}}$. This is indeed possible provided that the background density $\mathring{n}$ has no zeros, i.e.

$$\mathring{n} > 0, \tag{5.18}$$

in the spacetime region considered. If this condition is satisfied, we can proceed as follows.

From Eq. (5.14) we find, with the help of Eqs. (5.9) and (5.17), that

$$e\hat{n} = -\mathring{U}_\alpha \hat{F}^{\alpha\beta}{}_{;\beta}, , \tag{5.19}$$

$$e\mathring{n}\hat{U}^\alpha = \hat{F}^{\alpha\beta}{}_{;\beta}\left(\delta^\alpha_\gamma + \mathring{U}^\alpha \mathring{U}_\gamma\right). \tag{5.20}$$

Since we can divide by $\mathring{n}$, Eq. (5.20) can be used to eliminate $\hat{U}$ from Eq. (5.15). This results in the following linear second order differential equation for $\hat{\boldsymbol{F}}$:

$$\mathring{U}^\beta\left(\delta^\alpha_\gamma + \mathring{U}^\alpha \mathring{U}_\gamma\right)\hat{F}^{\gamma\delta}{}_{;\beta\delta} + \left[\mathring{U}^\beta{}_{;\beta}\left(\delta^\alpha_\gamma + \mathring{U}^\alpha \mathring{U}_\gamma\right) + \mathring{U}^\alpha{}_{;\gamma}\right]\hat{F}^{\gamma\delta}{}_{;\delta} - \frac{e^2}{m}\mathring{n}\mathring{U}^\beta \hat{F}^\alpha{}_\beta = \mathbf{0}. \tag{5.21}$$

If we have a solution $\hat{\boldsymbol{F}}$ of Eqs. (5.13) and (5.21), we can define $\hat{n}$ and $\hat{\boldsymbol{U}}$ by Eqs. (5.19) and (5.20), respectively. It is easy to check that then the full system of Eqs. (5.13)–(5.17) is satisfied. In other words, we have reduced this system to dynamical equations for $\hat{\boldsymbol{F}}$ alone, given by Eqs. (5.13)–(5.21).

To rewrite Eqs. (5.13) and (5.21) in a more convenient form, we express $\hat{\boldsymbol{F}}$ in terms of a potential $\hat{\boldsymbol{A}}$, defined in terms of the relation

$$\hat{F}_{\alpha\beta} = \hat{A}_{[\beta,\alpha]} = \hat{A}_{[\beta;\alpha]}, \tag{5.22}$$

and we assume that $\hat{\boldsymbol{A}}$ satisfies the *Landau gauge condition*

$$\hat{\boldsymbol{A}} \cdot \mathring{\boldsymbol{U}} = 0, \tag{5.23}$$

in the rest system of the background electron fluid. In fact, $\hat{\boldsymbol{A}}$ is locally and uniquely determined by $\hat{\boldsymbol{F}}$ up to the gauge transformations

$$\hat{\boldsymbol{A}} \longmapsto \hat{\boldsymbol{A}} + \boldsymbol{\partial} h, \tag{5.24}$$

where h is any spacetime function that is constant along the flow lines of $\mathring{\boldsymbol{U}}$. In other words, h can be freely prescribed on a hypersurface transverse to those flow lines. Using Eq. (5.22), Eq. (5.13) is automatically satisfied and (5.21) takes the form

$$\mathcal{D}^{\alpha\zeta}\hat{A}_\zeta = \mathbf{0}, \tag{5.25}$$

where the differential operator $\mathcal{D}^{\alpha\zeta}$ is defined by

$$\begin{aligned}\mathcal{D}^{\alpha\zeta}\hat{A}_\zeta = \mathring{U}^\beta &\left(\delta^\alpha_\gamma + \mathring{U}^\alpha \mathring{U}_\gamma\right)\left[\hat{A}_\zeta{}^{;\zeta\gamma}{}_{;\beta} - g^{\zeta\gamma}\Box\hat{A}_{\zeta;\beta}\right] \\ &+ \left[\mathring{U}^\beta{}_{;\beta}\left(\delta^\alpha_\gamma + \mathring{U}^\alpha \mathring{U}_\gamma\right) + \mathring{U}^\alpha{}_{;\gamma}\right]\left[\hat{A}_\zeta{}^{;\zeta\gamma} - g^{\zeta\gamma}\Box\hat{A}_\zeta\right] \\ &\qquad + \frac{e^2}{m}\mathring{n}\left[\mathring{U}^\zeta \hat{A}_\zeta{}^{;\alpha} - g^{\alpha\zeta}\mathring{U}^\beta \hat{A}_{\zeta;\beta}\right],\end{aligned} \tag{5.26}$$

where $\Box \hat{A}_\zeta \equiv \hat{A}_\zeta{}^{;\delta}{}_{;\delta}$. In fact, Eq. (5.25) determines the dynamics of electromagnetic waves in our plasma, and consists of four component equations, but only three of them are independent since the equation

$$\mathring{\boldsymbol{U}} \cdot \boldsymbol{\mathcal{D}} \cdot \hat{\boldsymbol{A}} = 0, \tag{5.27}$$

is identically satisfied for any $\hat{\boldsymbol{A}}$. By the Landau gauge condition (5.23), $\hat{\boldsymbol{A}}$ has three independent components. Hence, we have as many equations as unknown functions. In this sense, Eq. (5.25) gives a determined system of linear third order differential equations for the electromagnetic potential. To make this explicit, one can choose, on an appropriate open subset of spacetime, an orthonormal tetrad field $\mathbf{e}_a$ ($a = 0, 1, 2, 3$), with $\mathbf{e}_0 = \mathring{\boldsymbol{U}}$. By Eq. (5.23), $\hat{\boldsymbol{A}}$ is of the component form $\hat{A}_\zeta = g_{\zeta\kappa} \hat{A}^m \mathrm{e}_m^\kappa$, with some scalar functions $\hat{A}^1$, $\hat{A}^2$ and $\hat{A}^3$ on that domain. Multiplication of Eq. (5.25) with $g_{\alpha\gamma} \mathrm{e}_m^\gamma$ gives us three equations for the three functions $\hat{A}^1$, $\hat{A}^2$ and $\hat{A}^3$. It is shown by Breuer and Ehlers (Breuer et al., 1980, 1981) that this system of linear differential equations admits a local existence and uniqueness theorem for any data $\hat{A}^m, \mathring{U}^\alpha \partial_\alpha \hat{A}^m$, and $\mathring{U}^\alpha \mathring{U}^\beta \partial_\alpha \partial_\beta \hat{A}^m$, prescribed on a space-like hypersurface. In this sense, Eq. (5.25) is the system of evolution equations for electromagnetic waves in our plasma. Those evolution equations are of second order in the field strengths, and they are not supplemented by constraints.

With the dynamical law (5.25) at hand, we can now perform the passage to the ray optics. As mentioned at the beginning of this section, it will be crucial to consider one-parameter families of background fields rather than fixed background fields. The background fields that enter into the differential operator $\boldsymbol{\mathcal{D}}$, are the metric $\boldsymbol{g}$, the electron number density $\mathring{n}$, and the electron four-velocity $\mathring{\boldsymbol{U}}$. Let us fix such a set of background fields which have to satisfy Eqs. (5.6)–(5.9) and (5.18). Furthermore, let us fix a spacetime point and a coordinate system around this point. We assume that the chosen point is represented by the coordinates $\boldsymbol{x}_0 = \left(x_0^0, x_0^1, x_0^2, x_0^3\right)$. Referring to this fixed coordinate system, we define new background fields, depending on a real parameter $\mathscr{B}$, by

$$g_{\alpha\beta}(\mathscr{B}, x) = g_{\alpha\beta}\left(x_0 + \mathscr{B}(x - x_0)\right), \tag{5.28}$$

$$\mathring{n}(\mathscr{B}, x) = \mathring{n}\left(x_0 + \mathscr{B}(x - x_0)\right), \tag{5.29}$$

$$\mathring{U}^\alpha(\mathscr{B}, x) = \mathring{U}^\alpha\left(x_0 + \mathscr{B}(x - x_0)\right). \tag{5.30}$$

For $0 \leq \mathscr{B} \leq 1$, the new background fields $\boldsymbol{g}(\mathscr{B}, \cdot)$, $\mathring{n}(\mathscr{B}, \cdot)$, and $\mathring{\boldsymbol{U}}(\mathscr{B}, \cdot)$ are well defined on the domain considered, and they satisfy again equations (5.6)–(5.9) as well as the condition (5.18) Note that, this observation does not carry over if an electromagnetic background field $\mathring{\boldsymbol{F}} \neq \mathbf{0}$ is to be taken into account. For a magnetized plasma, one cannot assume the same, $\mathscr{B}$-dependence for all fields $\boldsymbol{g}, \mathring{n}, \mathring{\boldsymbol{U}}$ and $\mathring{\boldsymbol{F}} = \mathbf{0}$. For $\mathscr{B} \to 0$, the components of the background fields become constant in the coordinate system under consideration. In this sense, $\boldsymbol{g}(0,\cdot), \mathring{n}(0,\cdot)$ and $\mathring{\boldsymbol{U}}(0,\cdot)$ are homogeneous fields. In particular, $\boldsymbol{g}(0,\cdot)$ is a flat metric and $\mathring{\boldsymbol{U}}(0,\cdot)$ is covariantly constant, i.e., an inertial system, with respect to this metric. For this reason, we shall refer to this limit as to the *homogeneous background limit*.

If we replace in Eq. (5.2) the original background fields $\boldsymbol{g}$, $\mathring{n}$ and $\mathring{\boldsymbol{U}}$ by $\boldsymbol{g}(\mathscr{B},\cdot), \mathring{n}(\mathscr{B},\cdot)$ and $\mathring{\boldsymbol{U}}(\mathscr{B},\cdot)$, respectively, we get a one-parameter family of differential operators $\boldsymbol{\mathcal{D}}(\mathscr{B},\cdot)$. It is our plan to enter into the differential equation $\boldsymbol{\mathcal{D}}(\mathscr{B},\cdot) \cdot \hat{\boldsymbol{A}} = \mathbf{0}$ with an approximate-plane-wave ansatz for the potential $\hat{\boldsymbol{A}}(\mathscr{B},\cdot)$. Hence, we consider two-parameter families of the form

$$\hat{A}_\zeta(\mathscr{A},\mathscr{B},x) = \frac{\mathscr{A}}{\mathscr{B}} \mathrm{Re}\left\{\exp\left[\frac{\mathrm{i}}{\mathscr{A}} S(x_0 + \mathscr{B}(x-x_0))\right] \hat{a}_\zeta\left(\mathscr{A}, x_0 + \mathscr{B}(x-x_0)\right)\right\}, \quad (5.31)$$

where S is a real-valued function whose gradient has no zeros, and is referred to as the *eikonal function* of the approximate-plane-wave family. This equation satisfy the Landau gauge condition

$$\mathring{\boldsymbol{U}}(\mathscr{B},x) \cdot \hat{\boldsymbol{A}}(\mathscr{A},\mathscr{B},x) = 0. \quad (5.32)$$

We assume that the complex amplitudes are of the form

$$\hat{a}_\zeta(\mathscr{A},\cdot) = \sum_{N=0}^{N_0+1} \hat{a}_\zeta^N(\cdot)\mathscr{A}^N + \mathcal{O}(\mathscr{A}^{N_0+2}), \qquad \forall\ N_0 \geq -1, \quad (5.33)$$

and that

$$\begin{aligned}\hat{F}_{\alpha\beta} &= \hat{A}_{[\beta,\alpha]}(\mathscr{A},\mathscr{B},x) \\ &= \mathrm{Re}\left\{\exp\left[\frac{\mathrm{i}}{\mathscr{A}} S(x_0+\mathscr{B}(x-x_0))\right] \mathrm{i}\left(S\hat{a}^0_{[\beta}\right)_{,\alpha]}(x_0+\mathscr{B}(x-x_0)) + \mathcal{O}(\mathscr{A})\right\}, \quad (5.34)\end{aligned}$$

is an approximate-plane-wave family, for any fixed $\mathscr{B}$ with $0 < \mathscr{B} \leq 1$. For an approximate plane wave in this family, the frequency function with respect to the background electron rest system (5.30), is then given by

$$\omega(\mathscr{A},\mathscr{B},x) = \frac{\mathscr{B}}{\mathscr{A}} \mathring{U}^\alpha\left(x_0+\mathscr{B}(x-x_0)\right) S_{,\alpha}\left(x_0+\mathscr{B}(x-x_0)\right). \quad (5.35)$$

To perform the passage to ray optics, we have to assume that our approximate-plane-wave family satisfies the dynamical equations asymptotically. Since we have two parameters $\mathscr{A}$ and $\mathscr{B}$ at our disposal, we can consider asymptotic behavior with respect to different kinds of limits.

The first possibility is to keep $\mathscr{B}$ fixed and to consider the condition

$$\lim_{\mathscr{A}\to 0}\left[\frac{1}{\mathscr{A}^N}\mathcal{D}^{\alpha\zeta}(\mathscr{B},\cdot)\hat{A}_\zeta(\mathscr{A},\mathscr{B},\cdot)\right]=0,\qquad N\in\mathbb{Z}. \tag{5.36}$$

It can be characterized as the high frequency limit on a fixed background. In the case at hand, the lowest non-trivial order is $N=-3$. This results in an eikonal equation equal to the vacuum eikonal equation in the background metric $\boldsymbol{g}(\mathscr{B},\cdot)$, i.e. that the corresponding rays are exactly the null geodesics of this background metric. In other words, if the high-frequency limit is taken on a fixed background, the plasma has no influence on the rays. In particular, there is no dispersion. Note that, this corresponds to the case of $\mathscr{B}=1$ which makes it of no particular effects. Now we want to consider a different kind of limit, namely to let $\mathscr{B}$ and $\mathscr{A}$ go to zero, simultaneously, with the quotient $\frac{\mathscr{A}}{\mathscr{B}}$ kept fixed. We can then simply put $\mathscr{A}=\mathscr{B}$, and consider the condition

$$\lim_{\mathscr{A}\to 0}\left[\frac{1}{\mathscr{A}^N}\mathcal{D}^{\alpha\zeta}(\mathscr{A},\cdot)\hat{A}_\zeta(\mathscr{A},\mathscr{A},\cdot)\right]=0,\qquad N\in\mathbb{Z}. \tag{5.37}$$

Keeping $\frac{\mathscr{A}}{\mathscr{B}}$ fixed implies that the frequency function Eq. (5.35) is kept fixed at the point x_0. Therefore, this kind of limit can be characterized as the homogeneous background limit with fixed frequency at x_0. We shall now prove that this limit gives, indeed, a different eikonal equation. To that end, we have to assume that Eq. (5.37) holds in lowest non-trivial order which is now given by $N=0$. This is true if and only if the equation

$$Q_\alpha{}^\zeta\hat{a}^0_\zeta=0, \tag{5.38}$$

holds at x_0, where

$$Q_\alpha{}^\zeta=\mathring{U}^\beta S_{,\beta}\left(-S_{,\alpha}S^{,\zeta}-\mathring{U}_\alpha\mathring{U}^\gamma S_{,\gamma}S^{,\zeta}+\delta^\zeta_\alpha S^{,\delta}S_{,\delta}+\delta^\zeta_\alpha\frac{e^2}{m}\mathring{n}\right). \tag{5.39}$$

Here we have used the equation

$$\mathring{\boldsymbol{U}}(x_0)\cdot\hat{\boldsymbol{a}}^0(x_0)=0, \tag{5.40}$$

which follows from the Landau gauge condition (5.32). Since Eq. (5.34) is supposed to be an approximate-plane-wave family, $\hat{\boldsymbol{a}}$ must be non-zero and linearly independent of $S_{,\zeta}$. The condition that Eq. (5.38) admits a solution $\hat{\boldsymbol{a}}^0$ of this kind at x_0, gives the desired eikonal equation at x_0 for S. We have, thus, to solve the eigenvalue problem of $Q_\alpha{}^\zeta$ restricted to the orthocomplement of $\mathring{\boldsymbol{U}}$. We find that there are three real eigenvalues

$$\lambda_1 = \mathring{U}^\beta S_{,\beta} \left(- \left[\mathring{U}^\gamma S_{,\gamma} \right]^2 + \frac{e^2}{m} \mathring{n} \right), \tag{5.41a}$$

$$\lambda_2 = \lambda_3 = \mathring{U}^\beta S_{,\beta} \left(S^{,\delta} S_{,\delta} + \frac{e^2}{m} \mathring{n} \right). \tag{5.41b}$$

If either $\mathring{U}^\beta S_{,\beta} = 0$ or $S_{,\alpha} = \pm\sqrt{\frac{e^2}{m}\mathring{n}}\,\mathring{U}_\alpha$, all three eigenvalues coincide and Eq. (5.38) is satisfied by any $\hat{\boldsymbol{a}}^0$. Otherwise, we find $\lambda_1 \neq \lambda_2 = \lambda_3$ .In the latter case, the eigenspace pertaining to λ_1 is one-dimensional and spanned by $S_{,\zeta} + \mathring{U}_\zeta \mathring{U}^\beta S$, whereas the eigenspace pertaining to $\lambda_2 = \lambda_3$ is two- dimensional and consists of all X_ζ with $\mathring{U}^\zeta X_\zeta = S^{,\zeta} X_\zeta = 0$.

Equation (5.38) admits a non-trivial solution $\hat{\boldsymbol{a}}^0$ which is perpendicular to $\mathring{\boldsymbol{U}}$ if and only if one of the eigenvalues $\lambda_{1,2,3}$ is zero. From the form of the eigenspaces we see that in any such case $\hat{\boldsymbol{a}}^0$ can be chosen linearly independent of $S_{,\zeta}$. Hence, the eikonal equation takes the form $\lambda_1\lambda_2\lambda_3 = 0$ which is equivalent to

$$\mathring{U}^\beta S_{,\beta} \left(- \left[\mathring{U}^\gamma S_{,\gamma} \right]^2 + \frac{e^2}{m} \mathring{n} \right) \left(S^{,\delta} S_{,\delta} + \frac{e^2}{m} \mathring{n} \right) = 0. \tag{5.42}$$

Let us be precise about this result. Our assumption that the asymptotic condition (5.37) holds in lowest non-trivial order requires that S satisfies Eq. (5.42) at the point x_0 around which the construction was done. Although we have used a fixed coordinate system around the chosen spacetime point to perform the homogeneous background limit, the eikonal equation is a covariant equation (i.e., independent of this coordinate system). If S satisfies this covariant equation on an open spacetime domain $\mathcal{U}$, it is associated with an asymptotic solution of lowest non-trivial order, in the homogeneous-background sense, around any point of $\mathcal{U}$. That is to say, to any such S we can find a non-trivial amplitude $\hat{\boldsymbol{a}}(\mathscr{A}, \cdot)$ on $\mathcal{U}$ such that the following holds. If we choose any coordinate system around any point of $\mathcal{U}$, thereby defining the one-parameter family of operators $\boldsymbol{D}(\mathscr{B}, \cdot)$ and the two-parameter family (5.31) of electromagnetic fields, the asymptotic condition (5.37) is satisfied for $N = 0$. As a matter of fact, a similar statement is true for any N.

Owing to the terms proportional to $\mathring{n}$, the eikonal equation is not homogeneous with respect to ∂S, which indicates dispersion.

The product structure of the eikonal equation (5.42) suggests to introduce three partial Hamiltonians

$$\mathcal{H}_1(x,\boldsymbol{p}) = \overset{\circ}{\boldsymbol{U}}(x)\cdot\boldsymbol{p}, \tag{5.43}$$

$$\mathcal{H}_2(x,\boldsymbol{p}) = \frac{1}{2}\left[-\left(\overset{\circ}{\boldsymbol{U}}(x)\cdot\boldsymbol{p}\right)^2 + \frac{e^2}{m}\overset{\circ}{n}(x)\right], \tag{5.44}$$

$$\mathcal{H}_3(x,\boldsymbol{p}) = \frac{1}{2}\left[\boldsymbol{p}\cdot\boldsymbol{p} + \frac{e^2}{m}\overset{\circ}{n}(x)\right], \tag{5.45}$$

where P_α is the momentum covector, and $\boldsymbol{p}\cdot\boldsymbol{p} \equiv g^{\alpha\beta}(x)p_\alpha p_\beta$. The three partial Hamiltonians determine three branches of the dispersion relation. The branches defined by $\mathcal{H}_2$ and $\mathcal{H}_3$ have an intersection given by the equation $p_\alpha = \pm\sqrt{\frac{e^2}{m}\overset{\circ}{n}(x)}\,\overset{\circ}{U}_\alpha(x)$. At all points of phase space where this equation does not hold, at most one of the three partial dispersion relations can be satisfied (This is true as long as our assumption (5.18) is valid).

Now let us assign to each solution S of the partial eikonal equation

$$\mathcal{H}_i\left(x,\partial S(x)\right) = 0, \qquad i = 1,2,3, \tag{5.46}$$

a (partial) transport vector field K^α defined by

$$K^\alpha(x) = \frac{\partial \mathcal{H}_i}{\partial p_\alpha}\left(x,\partial S(x)\right). \tag{5.47}$$

The integral curves of $\boldsymbol{K}$ are called the (i-)rays associated with S. The totality of all i-rays, associated with any solution of Eq. (5.46), is found by solving Hamilton's equations (2.15) for $i = 1,2,3$, respectively.

It is worth mentioning that this definition associates a unique congruence of rays to each solution S of the full eikonal equation (5.42). This can be verified in the following way. In almost all cases, a solution of the full eikonal equation satisfies exactly one of the three partial eikonal equations (5.46). The only exception occurs if, at some point x, the equation $S_{,\alpha}(x) = \pm\sqrt{\frac{e^2}{m}\overset{\circ}{n}(x)}\,\overset{\circ}{U}_\alpha(x)$ holds such that Eq. (5.46) is satisfied for $i = 2$ and $i = 3$, simultaneously. At such points we have two partial transport vectors, given by Eq. (5.47) with $i = 2$ and with $i = 3$, respectively. Luckily enough, we find from Eqs. (5.44) and (5.45), that these two partial transport vectors coincide.

Let us consider the three partial Hamiltonians one by one. Solutions of the partial eikonal equation (5.46) with $i = 1$ are pathological insofar as they have vanishing frequency in the background rest system of the electron fluid, $\overset{\circ}{U}^\alpha(x)S_{,\alpha}(x) = 0$. Hence, $\overset{\circ}{\boldsymbol{U}}$ is not an "admissible reference system" for the approximate-plane-wave interpretation. The transport vector field (5.47) associated with such a solution is given by

$$\boldsymbol{K}(x) = \overset{\circ}{\boldsymbol{U}}(x), \tag{5.48}$$

which means that the rays are the integral curves of $\mathring{\boldsymbol{U}}$. Note that, $\mathcal{H}_1(\cdot, \partial S(\odot)) = 0$ implies that the eigenvalues (5.41a) and (5.41b) coincide, $\lambda_1 = \lambda_2 = \lambda_3 = 0$, and that Eq. (5.38) is identically satisfied for all $\hat{\boldsymbol{a}}^0$. In other words, the amplitude $\hat{F}^0_{\alpha\beta} = \mathrm{i}\hat{a}^0_{[\alpha}S_{,\beta]}$ is not restricted by any polarization condition.

For a solution of the second partial eikonal equation $\mathcal{H}_2(x, \partial S(x)) = 0$, the frequency function with respect to the background rest system of the electron fluid is determined by the equation

$$\mathring{U}^\alpha(x) S_{,\alpha}(x) = \pm\omega_p(x), \tag{5.49}$$

where ω_p denotes the plasma frequency defined by

$$\omega_p^2(x) = \frac{e^2}{m}\mathring{n}(x). \tag{5.50}$$

For the transport vector field (5.47) associated with such a solution S we find

$$\boldsymbol{K}(x) = \pm\omega_p(x)\mathring{\boldsymbol{U}}(x), \tag{5.51}$$

such that the rays coincide, again, with the integral curves of $\mathring{\boldsymbol{U}}$ (recalling that the parametrization of the rays is arbitrary). The case $S^{,\alpha} = \pm\omega_p \mathring{U}^\alpha$ plays a special role, since in this case S satisfies the partial eikonal equation (5.46) not only for $i = 2$ but also for $i = 3$. For this special solution we have again $\lambda_1 = \lambda_2 = \lambda_3$ and, thus, no polarization condition of zeroth order. For all other solutions of $\mathcal{H}_2(x, \partial S(x)) = 0$, Eq. (5.38) requires that $\hat{\boldsymbol{a}}^0$ is in the eigenspace pertaining to the eigenvalue λ_1 given by Eq. (5.41a), i.e., that $\hat{\boldsymbol{a}}^0$ is a multiple of $S_{,\zeta} + \mathring{U}_{,\zeta}\mathring{U}^\gamma S_{,\gamma}$. This condition implies that the electric component of $\hat{f}^0_{\alpha\beta} = \mathrm{i}\hat{a}^0_{[\alpha}S_{,\beta]}$ with respect to $\mathring{U}^\beta$ is a linear combination of $\mathring{U}_\alpha$ and $S_{,\alpha}$ and that the corresponding magnetic component vanishes. This is tantamount to a longitudinal polarization condition in the sense that the electric field strength is parallel to the spatial wave covector, i.e., $\hat{f}^0_{\alpha\beta}\mathring{U}^\beta = \mathfrak{c}\left(S_{,\alpha} + \mathring{U}^\beta S_{,\beta}\mathring{U}_\alpha\right)$ with some real-valued function $\mathfrak{c}$. Those longitudinal modes described by the partial Hamiltonian $\mathcal{H}_2$ are known as *plasma oscillations*.

Now let us turn to the third partial Hamiltonian $\mathcal{H}_3$. For $i = 3$, formula (5.47) yields the same expression for the transport vector field as in vacuum. In other words

$$K^\alpha(x) = g^{\alpha\beta}(x) S_{,\beta}(x). \tag{5.52}$$

Using our assumption that $\mathring{n}$ has no zeros, we find that the three-rays (i.e., the rays determined by the partial Hamiltonian $\mathcal{H}_3$) are exactly the time-like geodesics of the metric $\omega_p^2 g_{\alpha\beta}$ which is conformally equivalent to $g_{\alpha\beta}$. The easiest way to verify this result is by changing $\mathcal{H}_3$ according to

$$\mathcal{H}_3(x,\boldsymbol{p}) = \frac{1}{2}\left[\boldsymbol{p}\cdot\boldsymbol{p} + \omega_p^2(x)\right] \longmapsto \tilde{\mathcal{H}}_3(x,\boldsymbol{p}) = \frac{1}{\omega_p^2(x)}\mathcal{H}_3(x,\boldsymbol{p}) = \frac{1}{2}\left[\frac{\boldsymbol{p}\cdot\boldsymbol{p}}{\omega_p^2(x)} + 1\right]. \tag{5.53}$$

This transformation leaves the rays unchanged up to reparametrization, i.e., we can use $\tilde{\mathcal{H}}_3$ instead of $\mathcal{H}_3$ for the determination of the three-rays. Solving Hamilton's equations (2.15) with this transformed Hamiltonian gives, of course, the time-like geodesics of the conformally resealed metric $\tilde{g}_{\alpha\beta} = \omega_p^2 g_{\alpha\beta}$ parametrized by $\tilde{g}_{\alpha\beta}$-proper time. To go further in analyzing this Hamiltonian, and to relate it to the derivation of the light trajectories, we relate (Bisnovatyi-Kogan & Tsupko, 2017a)

$$\omega_p(x) = \frac{4\pi e^2}{m} N_p(x), \tag{5.54}$$

where N_p in the electron number density. Defining the plasmic refractive index (Atamurotov et al., 2015)

$$n^2 = 1 + \frac{\boldsymbol{p}\cdot\boldsymbol{p}}{(\boldsymbol{p}\cdot\boldsymbol{u})^2} = 1 - \frac{\omega_p^2}{\omega^2}, \tag{5.55}$$

with $\boldsymbol{u}$ as the observer's four-velocity, we can recast the Hamiltonian as

$$\mathcal{H}(x,\boldsymbol{p}) \equiv \mathcal{H}_3(x,\boldsymbol{p}) = \frac{1}{2}\left[\boldsymbol{p}\cdot\boldsymbol{p} - (n^2-1)(\boldsymbol{p}\cdot\boldsymbol{u})^2\right]. \tag{5.56}$$

Here, the quantity $\boldsymbol{p}\cdot\boldsymbol{u} = -\omega$ gives the effective energy of the photons of frequency ω, as measured by the observer.

As discussed in chapter 2, the Hamilton-Jacobi approach, requires the contribution of the Jacobi action $\mathcal{S}$, given by

$$p_\alpha = \frac{\partial \mathcal{S}}{\partial x^\alpha}, \tag{5.57a}$$

$$\mathcal{H} = -\frac{\partial \mathcal{S}}{\partial \tau}, \tag{5.57b}$$

with τ as the curve parametrization. Now, if the observer is located on the x^0 curves, it has the four-velocity $u^\alpha = \frac{\delta_0^\mu}{\sqrt{-g_{00}}}$, which, employing Eqs. (5.57), yields the Hamilton-Jacobi equation as (Atamurotov et al., 2015; Perlick & Tsupko, 2017)

$$\begin{aligned}\frac{\partial \mathcal{S}}{\partial \tau} &= -\frac{1}{2}\left[g^{\alpha\beta}\frac{\partial \mathcal{S}}{\partial x^\alpha}\frac{\partial \mathcal{S}}{\partial x^\beta} + \omega_p^2\right]\\ &= -\frac{1}{2}\left[g^{\alpha\beta}\frac{\partial \mathcal{S}}{\partial x^\alpha}\frac{\partial \mathcal{S}}{\partial x^\beta} - \left(n^2-1\right)\omega^2\right],\end{aligned} \tag{5.58}$$

in which, we have used the identity $\boldsymbol{p}\cdot\boldsymbol{u} = \frac{p_0}{\sqrt{g_{00}}} = -\omega$. Therefore, the general equations governing the light ray trajectories are

$$\frac{\partial\mathcal{H}}{\partial p_\alpha} = \frac{\mathrm{d}x^\alpha}{\mathrm{d}\tau}, \tag{5.59a}$$

$$\frac{\partial\mathcal{H}}{\partial x^\alpha} = -\frac{\mathrm{d}p_\alpha}{\mathrm{d}\tau}, \tag{5.59b}$$

$$\mathcal{H} = 0. \tag{5.59c}$$

5.2 Light propagating in Kerr spacetime within non-magnetized plasma

Let us rewrite the Kerr line element in Eq. (2.80) as

$$\mathrm{d}s^2 = -\left(1-\frac{2Mr}{\rho^2}\right)\mathrm{d}t^2 + \frac{\rho^2}{\Delta}\mathrm{d}r^2 + \rho^2\mathrm{d}\theta^2 + \sin^2\theta\left(r^2+a^2+\frac{2Mra^2\sin^2\theta}{\rho^2}\right)\mathrm{d}\phi^2 - \frac{4Mra\sin^2\theta}{\rho^2}\,\mathrm{d}t\mathrm{d}\phi, \tag{5.60}$$

with

$$\Delta = r^2 + a^2 - 2Mr, \tag{5.61a}$$

$$\rho^2 = r^2 + a^2\cos^2\theta, \tag{5.61b}$$

and $a = \frac{J}{M}$, where J is the black hole's angular momentum. The Kerr black hole spacetime admits for a Cauchy and an event horizon (notated respectively by r_- and r_+), whose surfaces are determined by solving $\Delta = 0$, and are given by

$$r_\mp = M \mp \sqrt{M^2 - a^2}. \tag{5.62}$$

Also, as discussed in subsection 3.6.2, the state of corotation and the static limit are determined by the equation $g_{tt} = 0$, that provides the radial distances

$$r_{\mathrm{SL}\pm}(\theta) = M \pm \sqrt{M^2 - a^2\cos^2\theta}, \tag{5.63}$$

which together with the horizons $r_\mp$, form the black hole's interior and exterior ergospheres in the regions $r_{\mathrm{SL}-} < r < r_-$ and $r_+ < r < r_{\mathrm{SL}+}$. Throughout this section, we restrict our study to the domain of outer communications, i.e., the domain outside the event horizon ($r > r_+$), and we consider the case of $a^2 \leq M^2$, that corresponds to a black hole rather than a naked singularity. The famous method of separation of the Jacobi action, is based on the definition (Carter, 1968; Chandrasekhar, 1998)

$$\mathcal{S} = -Et + L\phi + \mathcal{S}_r(r) + \mathcal{S}_\theta(\theta) + \frac{1}{2}m^2\tau, \tag{5.64}$$

in which E, L and m are, respectively, the energy, angular momentum, and the mass associated with the test particles (here, $m = 0$). Along with the method of separation of the Hamilton-Jacobi equation introduced by Perlick and Tsupko (Perlick & Tsupko, 2017), we recast the Hamiltonian (5.56) in the Kerr spacetime as

$$\begin{aligned}\mathcal{H}(x, \boldsymbol{p}) = \frac{1}{2\rho^2}\bigg[\Delta\, p_r^2 + p_\theta^2 + \left(a p_t \sin\theta + \frac{p_\phi}{\sin\theta}\right)^2 \\ - \frac{1}{\Delta}\left(p_t(r^2+a^2) + a p_\phi\right)^2 + \rho^2\omega_p^2\bigg].\end{aligned} \tag{5.65}$$

Assuming $\omega_p \equiv \omega_p(r,\theta)$, it is then straightforward to see that $\frac{\partial\mathcal{H}}{\partial t} = 0 = \frac{\partial\mathcal{H}}{\partial\phi} = 0$. Therefore, taking into account Eqs. (5.57a) and (5.64), we can specify the constants of motion as

$$E = -\frac{\partial\mathcal{S}}{\partial t} = -p_t = \omega_0, \tag{5.66a}$$

$$L = \frac{\partial\mathcal{S}}{\partial\phi} = p_\phi. \tag{5.66b}$$

Physically, the angular momentum component p_ϕ corresponds, to the axial symmetry of the spacetime. The nature of ω_0, on the other hand, becomes clear if we specify the light rays' frequency. In fact, the special case of $\omega_p(r,\theta)$ corresponds to the three constants of motion, $\mathcal{H} = 0$, ω_0 and L. Accordingly, we can apply the Carter's method of separation of the Hamilton-Jacobi equation, through which, the light ray trajectories are given in terms of integrable equations (Carter, 1968; Chandrasekhar, 1998). Using Eqs. (5.65) and (5.66), the Hamilton-Jacobi equation, $\mathcal{H}(x,\boldsymbol{p}) = 0$, yields

$$0 = \Delta\, p_r^2 + p_\theta^2 + \left(\omega_0\, a\sin\theta - \frac{L}{\sin\theta}\right)^2 - \frac{1}{\Delta}\left[\omega_0(r^2+a^2) - aL\right]^2 + \rho^2\omega_p^2. \tag{5.67}$$

The separability property of the Hamilton-Jacobi equation, demands that Eq. (5.67) can be divided into separated r-dependent and θ-dependent segments. This has been made possible by defining (Perlick & Tsupko, 2017)

$$\omega_p(r,\theta)^2 = \frac{f_r(r) + f_\theta(\theta)}{r^2 + a^2\cos^2\theta}, \tag{5.68}$$

for some functions $f_r(r)$ and $f_\theta(\theta)$. Now, the identity

$$\left(\omega_0\, a\sin\theta - \frac{L}{\sin\theta}\right)^2 = (L^2\csc^2\theta - a^2\omega_0^2)\cos^2\theta + (L - a\omega_0)^2, \tag{5.69}$$

together with Eqs. (5.67) and (5.68), separates the Hamilton-Jacobi equation as

$$\begin{aligned} \mathcal{Q} &= p_\theta^2 + (L^2 \csc^2\theta - a^2\omega_0^2)\cos^2\theta + f_\theta(\theta) \\ &= -\Delta\, p_r^2 + \frac{1}{\Delta}\left[\omega_0(r^2+a^2) - aL\right]^2 - (L - a\omega_0)^2 - f_r(r), \end{aligned} \tag{5.70}$$

in which, $\mathcal{Q}$ is the so-called *Carter's constant*. Recasting the above equations, yields

$$p_\theta^2 = \mathcal{Q} - (L^2\csc^2\theta - a^2\omega_0^2)\cos^2\theta - f_\theta(\theta), \tag{5.71}$$

$$\Delta\, p_r^2 = \frac{1}{\Delta}\left[\omega_0(r^2+a^2) - aL\right]^2 - \mathcal{Q} - (L - a\omega_0)^2 - f_r(r). \tag{5.72}$$

Insertion of Eqs. (5.71) and (5.72) into the Hamiltonian (5.65), and then using Eq. (5.59a), provides the first order differential equations of motion as

$$\rho^2\frac{\mathrm{d}r}{\mathrm{d}\tau} = \sqrt{\mathcal{R}(r)}, \tag{5.73}$$

$$\rho^2\frac{\mathrm{d}\theta}{\mathrm{d}\tau} = \sqrt{\Theta(\theta)}, \tag{5.74}$$

$$\rho^2\frac{\mathrm{d}\phi}{\mathrm{d}\tau} = \frac{L(\rho^2 - 2Mr)\csc^2\theta + 2Ma\omega_0 r}{\Delta}, \tag{5.75}$$

$$\rho^2\frac{\mathrm{d}t}{\mathrm{d}\tau} = \frac{\omega_0\Sigma^2 - 2MaLr}{\Delta}, \tag{5.76}$$

where

$$\mathcal{R}(r) = \left[\omega_0(r^2+a^2) - aL\right]^2 - \Delta\left[\mathcal{Q} + f_r(r) + (L - a\omega_0)^2\right], \tag{5.77a}$$

$$\Theta(\theta) = \mathcal{Q} - f_\theta(\theta) - \cos^2\theta\left(L^2\csc^2\theta - a^2\omega_0^2\right), \tag{5.77b}$$

$$\Sigma^2 = \rho^2\left(r^2+a^2\right) + 2Mra^2\sin^2\theta. \tag{5.77c}$$

Finally, defining the dimension-less *Mino time*[1], γ, as $\rho^2\mathrm{d}\gamma = M\mathrm{d}\tau$ (Mino, 2003), the equations of motion are now rewritten as

$$M\frac{\mathrm{d}r}{\mathrm{d}\gamma} = \sqrt{\mathcal{R}(r)}, \tag{5.78}$$

$$M\frac{\mathrm{d}\theta}{\mathrm{d}\gamma} = \sqrt{\Theta(\theta)}, \tag{5.79}$$

$$M\frac{\mathrm{d}\phi}{\mathrm{d}\gamma} = \frac{L(\rho^2 - 2Mr)\csc^2\theta + 2Ma\omega_0 r}{\Delta}, \tag{5.80}$$

$$M\frac{\mathrm{d}t}{\mathrm{d}\gamma} = \frac{\omega_0\Sigma^2 - 2MaLr}{\Delta}. \tag{5.81}$$

In the what follows, we continue our discussion by analyzing the above equations of motion, in order to find analytically exact solutions to the light ray trajectories travelling in (non-magnetized) inhomogeneous anisotropic plasma around the black hole.

[1]Note that, in the geometric units we use, the parameter time has the dimensions of length. Same holds for the curve parameter τ.

5.2.1 Analytical study of null geodesics

The separation condition in Eq. (5.68) characterizes the plasma, regarding its geometric distribution in the spacetime surrounding the black hole. Therefore, the characteristic functions $f_r(r)$ and $f_\theta(\theta)$, play important roles in defining the plasma's configuration. In this subsection, we confine the light rays to an inhomogeneous anisotropic plasma, by adopting the particular choices

$$f_r(r) \equiv f_r = \Omega_0^2 R^2 = \text{constant}, \tag{5.82}$$

$$f_\theta(\theta) \equiv f_\theta = \Omega_0^2 a^2 = \text{constant}. \tag{5.83}$$

This way, Eq. (5.68) can be recast as

$$\omega_p(r,\theta)^2 = \Omega_0^2 \left(\frac{R^2 + a^2}{r^2 + a^2\cos^2\theta}\right), \tag{5.84}$$

where R is the mean radius of the gravitating object, and Ω_0 is a positive constant. Within the text, we use, frequently, the conventions

$$\xi = \frac{L}{\omega_0}, \tag{5.85}$$

$$\eta = \frac{\mathscr{Q}}{\omega_0^2}, \tag{5.86}$$

in order to simplify the analysis.

The evolution of the radial distance (the r-motion)

In the study of particle trajectories in curved spacetimes, it is of crucial importance to know how the particles approach and recede from the source of gravity. Based on the nature of the interactions, this study is traditionally done by calculating the radial, effective gravitational potential, that acts on the particles (Misner et al., 2017). Hence, to scrutinize the r-motion for the light ray trajectories in the context under consideration, we focus on the radial equation of motion (5.78), and rewrite the expression in Eq. (5.77a) as

$$\mathcal{R}(r) = \mathscr{P}(r)\left[\omega_0 - V_-(r)\right]\left[\omega_0 - V_+(r)\right], \tag{5.87}$$

where $\mathscr{P}(r) = r^4 + a^2r^2 + 2Ma^2r$, and the radial gravitational potentials are given by

$$V_\mp(r) = \frac{1}{\mathscr{P}(r)}\left\{2MaLr \mp \left[\Delta\mathscr{P}(r)\left(\mathscr{Q} + f_r + L^2 - \frac{a^2L^2}{\Delta}\right) + 4a^2L^2M^2r^2\right]^{\frac{1}{2}}\right\}, \tag{5.88}$$

taking into account the condition (5.82). The negative branch is not of our interest, since it has no classical interpretations[2]. We therefore, choose the positive branch of

[2] In the context of quantum theory of fields, negative energies are related to antiparticles that move backwards in time (Lancaster & Blundell, 2014).

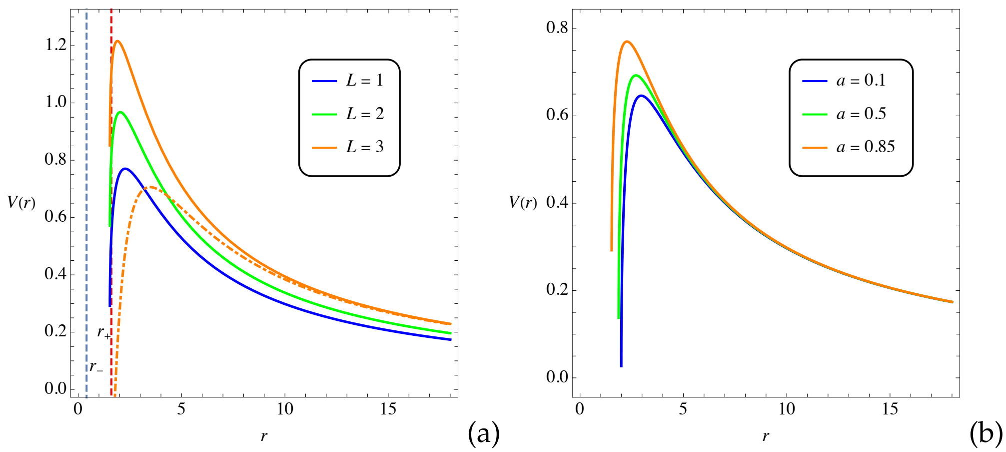

Figure 5.1: The radial effective potential in an inhomogeneous anisotropic plasma in the region $r > r_+$, plotted for $\mathscr{Q} = 9M^2$ and $f_r = 1M^2$. The diagrams have been generated for (a) $a = 0.85M$ and three different values of L (the solid lines), and (b) $L = 1M$ and three different values of a. The dot-dashed curve in the diagram (a), corresponds to the retrograde motion, which has been plotted for $a = -0.85M$ and $L = 3M$ (For these diagrams and for all the forthcoming ones, the unit along the axes is considered to be M).

Eq. (5.88) as the effective potential, i.e. $V_{\text{eff}} = V_+(r) \equiv V(r)$, noting that $V(r \to \infty) = 0$. In Fig. 5.1, this effective potential has been demonstrated for different values of a and L. According to the diagrams, no stable orbits are expected since the effective potentials do not possess any minimums. Note that, the photons can also pursue a motion along the opposite direction of the black hole's spin, which is the significance of the retrograde motion. As seen in the left panel of Fig. 5.1, the effective potential corresponding to the retrograde motion (plotted for $a < 0$), exhibits a lower maximum energy for the the same angular momentum. Therefore, photons on the retrograde motion encounter a remarkably smoother gravitational potential.

The possible trajectories are then categorized based on the turning points. However, before proceeding with the determination of the turning points, let us rewrite Eq. (5.78) as

$$M\frac{\mathrm{d}r}{\mathrm{d}\gamma} = \omega_0\sqrt{\mathcal{P}(r)}, \tag{5.89}$$

in terms of the characteristic polynomial

$$\mathcal{P}(r) = r^4 + \mathcal{A}r^2 + \mathcal{B}r + \mathcal{C}, \tag{5.90}$$

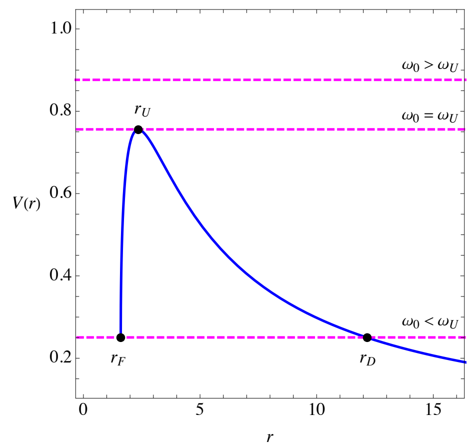

Figure 5.2: A typical effective potential, plotted for $a = 0.8M$, $L = 1M$, and $\mathscr{Q} + f_r = 10M^2$ (which are the values that will be taken into account for all the forthcoming diagrams). The categorization of orbits is done by comparing the photon energy ω_0 with that for photons on the UCO, i.e. ω_U (for the above values, $\omega_U \approx 0.755232$). Photons with the energy $\omega_0 > \omega_U$, will experience an inevitable fall onto the black hole's event horizon. For the special case of $\omega_0 < \omega_U$, the photons encounter two turning points r_D and r_F.

where

$$\mathcal{A} = a^2 - \xi^2 - \eta - \eta_r, \tag{5.91a}$$

$$\mathcal{B} = 2M\left[\eta + \eta_r + (\xi - a)^2\right], \tag{5.91b}$$

$$\mathcal{C} = -a^2(\eta + \eta_r), \tag{5.91c}$$

and $\eta_r = \frac{f_r}{\omega_0^2}$.

The turning points

Let us consider a typical effective potential as demonstrated in Fig. 5.2. The possible types of motion are categorized regarding the photon frequency (energy) ω_0, compared with its value ω_U, for photons on the unstable circular orbits (UCO). When $\omega_0 > \omega_U$, the characteristic polynomial $\mathcal{P}(r)$ has four complex roots, which for $\omega_0 = \omega_U$, reduces to two complex roots and a (degenerate) positive real root. This latter corresponds to the UCO at the orbital radius r_U. For the case of $\omega_0 < \omega_U$, the polynomial has two complex and two positive reals roots, r_D and r_F, that correspond to the turning points of the photon orbits. In fact, Eqs. (5.78) and (5.81) also inform about the characteristics of the turning points. Defining the coordinate velocity $v_c(r) = \frac{\mathrm{d}r}{\mathrm{d}t}$, then the turning points, r_t, are where $v_c(r_t) = 0$. Based on the definition given in Eq. (5.89), this condition is equivalent to $\mathcal{P}(r_t) = 0$, which together with Eq. (5.90), results in the two radii (see appendix B.4)

$$r_D = \tilde{R} + \sqrt{\tilde{R}^2 - \tilde{Z}}, \tag{5.92}$$

$$r_F = \tilde{R} - \sqrt{\tilde{R}^2 - \tilde{Z}}, \tag{5.93}$$

where

$$\tilde{R} = \sqrt{\Xi - \frac{\mathcal{A}}{6}}, \tag{5.94a}$$

$$\tilde{Z} = 2\tilde{R}^2 + \frac{\mathcal{A}}{2} + \frac{\mathcal{B}}{4\tilde{R}}, \tag{5.94b}$$

and

$$\Xi = 2\sqrt{\frac{\chi_2}{3}}\cosh\left(\frac{1}{3}\operatorname{arccosh}\left(\frac{3}{2}\chi_3\sqrt{\frac{3}{\chi_2^3}}\right)\right), \tag{5.95}$$

in which,

$$\chi_2 = \frac{\mathcal{A}^2}{48} + \frac{\mathcal{C}}{4}, \tag{5.96a}$$

$$\chi_3 = \frac{\mathcal{A}^3}{864} + \frac{\mathcal{B}^2}{64} - \frac{\mathcal{A}\,\mathcal{C}}{24}. \tag{5.96b}$$

The turning points r_D and r_F correspond to different fates for the trajectories. Respecting Fig. 5.2, photons that approach the black hole at r_D, will deflect to infinity by pursuing an OFK. The equation of motion (5.89), if solved at the vicinity of the deflection point r_D, yields the OFK as (appendix C.1)

$$r_d(\gamma) = \frac{[1 + u_d(\gamma)]\, r_D}{u_d(\gamma)}, \tag{5.97}$$

in which

$$u_d(\gamma) = 4\wp\left(\frac{\omega_0\sqrt{C_3}\,\gamma}{M r_D}\right) - \frac{\alpha_1}{3}, \tag{5.98}$$

with the Weierstraß invariants

$$\tilde{g}_2 = \frac{1}{4}\left(\frac{\alpha_1^2}{3} - \alpha_2\right), \tag{5.99a}$$

$$\tilde{g}_3 = \frac{1}{16}\left(\frac{\alpha_1\alpha_2}{3} - \frac{2\alpha_1^3}{27} - \alpha_3\right), \tag{5.99b}$$

given that $\alpha_1 = \frac{C_2}{C_3}$, $\alpha_2 = \frac{C_1}{C_3}$ and $\alpha_3 = \frac{C_0}{C_3}$, and the respected coefficients defined as

$$C_0 = r_D^4, \tag{5.100a}$$

$$C_1 = 4r_D^4, \tag{5.100b}$$

$$C_2 = r_D^2\left(6r_D^2 + \mathcal{A}\right), \tag{5.100c}$$

$$C_3 = r_D\left(4r_D^3 + 2\mathcal{A}r_D + \mathcal{B}\right). \tag{5.100d}$$

On the other hand, r_F is the point of no return, corresponding to the OSK. Applying the same method we pursued to calculate the OFK, at the approaching point r_F, the OSK is found to obey the equation

$$r_f(\gamma) = \frac{\left[1 + u_f(\gamma)\right] r_F}{u_f(\gamma)}, \tag{5.101}$$

where

$$u_f(\gamma) = 4\wp\left(-\frac{\omega_0\sqrt{\tilde{C}_3}\,\gamma}{Mr_F}\right) - \frac{\tilde{\alpha}_1}{3}, \tag{5.102}$$

with the Weierstraß coefficients having the same form of expressions as those in Eqs. (5.99), and $\tilde{\alpha}_1 = \frac{\tilde{C}_2}{\tilde{C}_3}$, $\tilde{\alpha}_2 = \frac{\tilde{C}_1}{\tilde{C}_3}$ and $\tilde{\alpha}_3 = \frac{\tilde{C}_0}{\tilde{C}_3}$, that relate respectively to the same coefficients in Eqs. (5.100), by doing the exchange $r_D \to r_F$. In Fig. 5.3, the OFK and

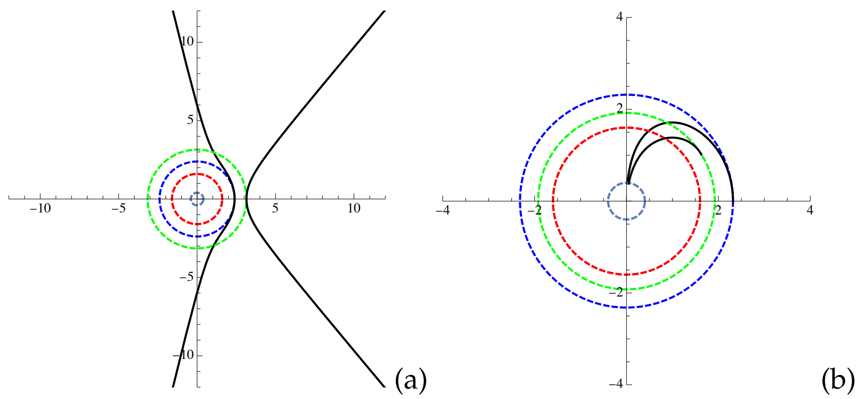

Figure 5.3: The polar plots of $r(\gamma)$, respecting (a) OFKs and (b) OSKs, plotted for $\omega_0 = 0.755$ (blue circles), and $\omega_0 = 0.70$ (green circles). The two inner circles indicate r_+ and r_-.

OSK have been plotted for the light rays approaching the black hole, for definite dynamical parameters. As it is expected, the OFK initiates from the turning point r_D and escape to infinity, and can therefore, reach a distant observer. This concept, if treated for the trajectories with angular components, has the significance of bending of light in curved spacetimes.

It is worth notifying the difference between the two types of the OFK, as indicated in panel (a) of the figure. As it is expected, the more ω_0 increases toward its critical value ω_U, the more the trajectories are inclined towards the black hole. In order to find a switching value for ω_0, at which the OFK change their deflecting character, let us recall that $r_D \equiv r_D(\omega_0)$ and $r_F \equiv r_F(\omega_0)$, whose behaviors have been plotted in Fig. 5.4. As it is observed in the figure, there is a region of the steepest declination

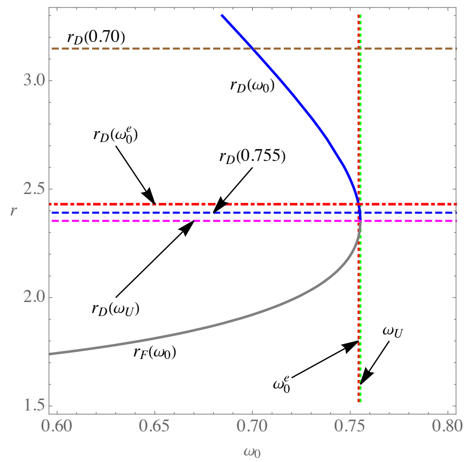

Figure 5.4: The plot of $r_D(\omega_0)$ and $r_F(\omega_0)$, in accordance to the values given in Fig. 5.3. The dashed lines indicate $r_D(0.70)$, $r_D(0.755)$ and $r_D(\omega_U)$, and the switching radius $r_D(\omega_0^{\rm e})$, shown by the dot-dashed line, corresponds to the starting point of a region, where the trajectories begin to change their deflecting character. In this case, $\omega_0^{\rm e} \approx 0.7543$.

of r_D, located at the vicinity of ω_U. This region starts in accordance with a switching value $\omega_0^{\rm e}$, from which, the trajectories start to change their deflecting character.

On the other hand, the OSK starts from r_F and ends in falling onto the singularity. Hence, light rays that are engaged in this process, will never go beyond the distance r_F from the black hole and cannot reach an observer at infinity. Note that, in the case of $\omega_0 = \omega_U$, the light rays will approach at the point $r_F < r_U < r_D$, that satisfy the equation $V'(r_U) = 0$. As mentioned above, this corresponds to the UCO. In Fig. 5.5,

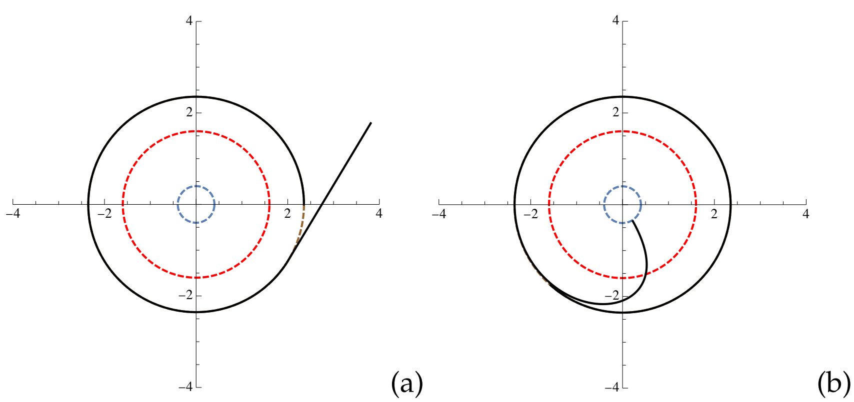

Figure 5.5: The polar plots of (a) the UCOFK and (b) the UCOSK, plotted for $\omega_0 \approx \omega_U$. The outer circle, indicates $r_U \approx 2.166051$.

this kind of orbit has been plotted, regarding its first and the second kinds (UCOFK and UCOSK), by exploiting the equations of motion obtained above, applied for the radial distance r_U. The UCOFK, in particular, is responsible for the formation of the black hole shadow.

The capture zone

In addition to the photons with $\omega_0 < \omega_U$ that approach the black hole from the radial distance r_F, those incident photons with $\omega_0 > \omega_U$, also become completely unstable in the region dominant by the effective potential, and are captured by the black hole (see Fig. 5.2). The form of the equation of motion for such photons, is the same as those in Eqs. (5.97) and (5.101), but the point of approach can be any point $r_I > r_+$. In Fig. 5.6, an example of this kind of orbit has been plotted.

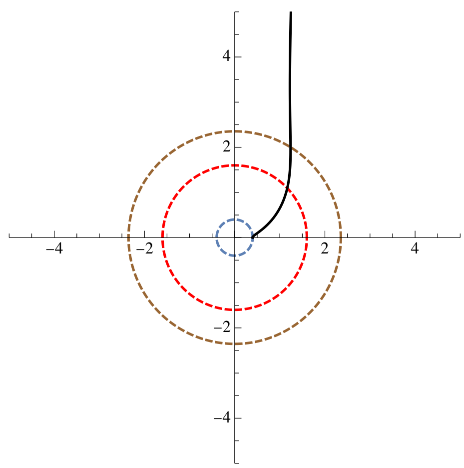

Figure 5.6: The radial capture. The outer circle corresponds to r_U.

The evolution of the polar angle (the θ-motion)

The θ-motion is governed by Eqs. (5.79) and (5.77b), for which, the condition (5.83) implies

$$\Theta(\theta) = \mathscr{Q} - f_\theta - \cos^2\theta\left(L^2\csc^2\theta - a^2\omega_0^2\right) \geq 0. \tag{5.103}$$

that can be recast as

$$\Theta(\theta) = a^2\cos^2\theta\Big[\left(\omega_0 - \sqrt{W(\theta)}\,\right)\left(\omega_0 + \sqrt{W(\theta)}\,\right)\Big], \tag{5.104}$$

where

$$W(\theta) = \left(\frac{L\csc\theta}{a}\right)^2 - (\mathscr{Q} - f_\theta)\left(\frac{\sec\theta}{a}\right)^2, \tag{5.105}$$

is the angular gravitational potential felt by the light rays in the plasma. Essentially, this potential has a general form which can be defined for the case of null geodesics (Schee & Stuchlík, 2009), and here, is recovered by letting $f_\theta = 0$ in Eq. (5.105). We define

$$\tilde{\eta} = \eta - \frac{f_\theta}{\omega_0^2} \equiv \frac{\mathscr{Q} - f_\theta}{\omega_0^2}, \tag{5.106}$$

for more convenience. Now, performing the change of variable $z = \cos\theta$, Eq. (5.79) can be recast as

$$-\frac{M}{\omega_0}\frac{\mathrm{d}z}{\mathrm{d}\gamma} = \sqrt{\Theta_z}, \tag{5.107}$$

where

$$\Theta_z = \tilde{\eta} - (\tilde{\eta} + \xi^2 - a^2)z^2 - a^2 z^4, \tag{5.108}$$

and the condition $\Theta_z > 0$ is required. Clearly, the characteristics of the motion depend directly on the nature of Θ_z. Accordingly, we assess the equation of motion (5.107), separately, for the cases $\tilde{\eta} > 0$, $\tilde{\eta} = 0$, and $\tilde{\eta} < 0$. These cases completely categorize the types of the θ-motion.

The case of $\tilde{\eta} > 0$

In this case, the expression in Eq. (5.108) remains unchanged, and the condition $\Theta_z > 0$, confines the z parameter in the domain $-z_{\text{min}} \leq z \leq z_{\text{max}}$, where

$$z_{\text{max}}^2 = \frac{\chi_0}{2\,a^2}\left(\sqrt{1 + \frac{4a^2\,\tilde{\eta}}{\chi_0^2}} - 1\right), \tag{5.109a}$$

$$z_{\text{min}} = -z_{\text{max}}, \tag{5.109b}$$

in which, $\chi_0 = \xi^2 + \tilde{\eta} - a^2 > 0$. The mentioned domain, corresponds to the polar range $\theta_{\text{min}} \leq \theta \leq \theta_{\text{max}}$, given that $\theta_{\text{min}} = \arccos(z_{\text{max}})$ and $\theta_{\text{max}} = \arccos(-z_{\text{max}})$. This range defines a cone, to which, the test particles' motion is confined. Having this in mind, we can solve the equation of motion (5.107) by direct integration, resulting in (see appendix C.2)

$$\theta(\gamma) = \arccos\left(z_{\text{max}} - \frac{3}{12\wp(\kappa_0\gamma) + \psi_0}\right), \tag{5.110}$$

where

$$\kappa_0 = \frac{\omega_0 a\sqrt{2z_{\text{max}}\left(z_0^2 + z_{\text{max}}^2\right)}}{M}, \tag{5.111a}$$

$$\psi_0 = \frac{z_0^2 + 5z_{\text{max}}^2}{2z_{\text{max}}\left(z_0^2 + z_{\text{max}}^2\right)}, \tag{5.111b}$$

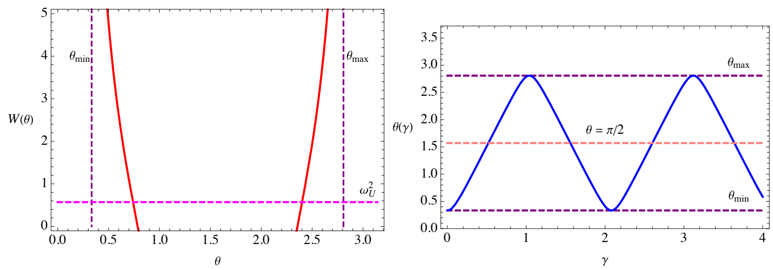

Figure 5.7: The angular effective potential and the temporal evolution of the coordinate θ for the case of $\tilde{\eta} > 0$, plotted for $\mathscr{Q} = 9M^2$ and $f_\theta = 1M^2$. To plot $\theta(\gamma)$, we have considered $\omega_0 = 0.755$.

with

$$z_0^2 = \frac{\chi_0}{2\,a^2}\left(\sqrt{1+\frac{4a^2\,\tilde{\eta}}{\chi_0^2}}+1\right), \tag{5.112}$$

and

$$g_2 = \frac{z_0^4 + z_{\rm max}^4 - 14 z_0^2 z_{\rm max}^2}{48 z_{\rm max}^2\left(z_0^2+z_{\rm max}^2\right)^2}, \tag{5.113a}$$

$$g_3 = \frac{33 z_0^4 z_{\rm max}^2 - 33 z_0^2 z_{\rm max}^4 + z_0^6 - z_{\rm max}^6}{1728 z_{\rm max}^3\left(z_0^2+z_{\rm max}^2\right)^3}, \tag{5.113b}$$

are the respected Weierstraß invariants. Using the analytical solution (5.110), the temporal evolution of $\theta(\gamma)$ for the case of $\tilde{\eta} > 0$ has been shown in Fig. 5.7, together with the behavior of $W(\theta)$. As it can be observed from the behavior of $W(\theta)$, the values of energy that rely in the region $\omega_0 \leq \omega_U$ are allowed. The light rays, therefore, can opt all kinds of possible orbits that were discussed in the previous section. Accordingly, and applying the analytical solutions of the radial coordinate, the cross-sectional behaviors of the above orbits have been plotted in Fig. 5.8, for the case of $\tilde{\eta} > 0$, inside the cone of confinement in the z-x plane (i.e. for $\phi = 0$).

The case of $\tilde{\eta} = 0$

The parameter z, in this case, is confined to the domain $\bar{z}_{\rm min} \leq z \leq \bar{z}_{\rm max}$ with $\bar{z}_{\rm min} = 0$ and $\bar{z}_{\rm max} = \sqrt{1-(\frac{\xi}{a})^2}$. This domain corresponds to the cone $\bar{\theta}_{\rm min} \leq \theta \leq \frac{\pi}{2}$, where $\bar{\theta}_{\rm min} = \arccos\left(\bar{z}_{\rm max}\right)$. In this case, the effective angular potential (5.105) takes the form

$$W(\theta) = \left(\frac{L\csc\theta}{a}\right)^2. \tag{5.114}$$

It is straightforward to see that $W'(\theta) = 0$ gives $\bar{\theta}_0 = \frac{\pi}{2} = \bar{\theta}_{\rm max}$, according to which, the minimum of the angular effective potential, $W_{\rm min} = W(\frac{\pi}{2})$, is obtained. One can

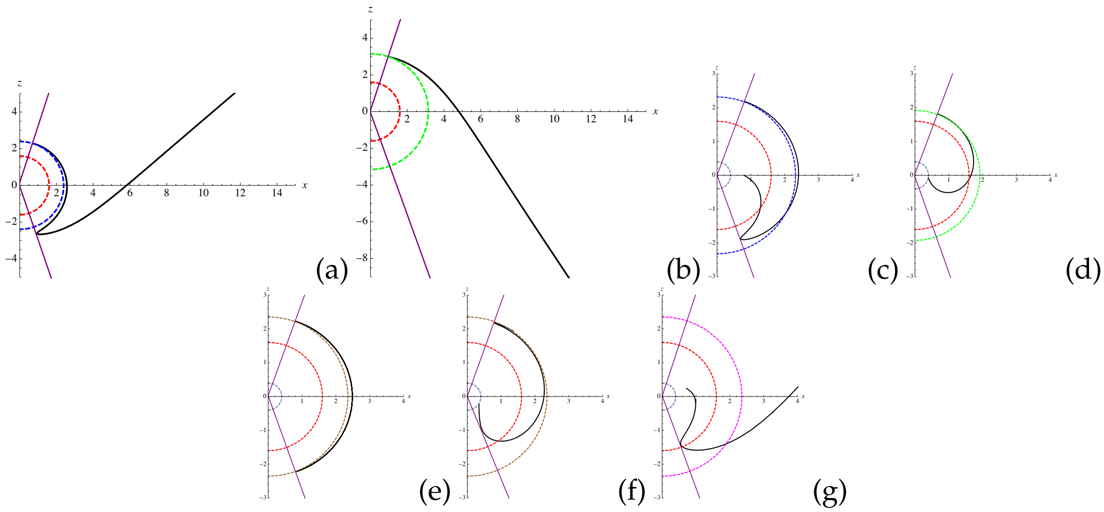

Figure 5.8: The cross-sectional behaviors of the deflecting, critical, and capturing trajectories, for the case of $\tilde{\eta} > 0$, inside the cone of confinement, in the z-x plane. The diagrams indicate (a) OFK for $\omega_0 = 0.755$, (b) OFK for $\omega_0 = 0.70$, (c) OSK for $\omega_0 = 0.755$, (d) OSK for $\omega_0 = 0.70$, (e) UCOFK, (f) UCOSK, and (g) radial capture for $\omega_0 = 1$.

therefore infer that the case of $\tilde{\eta} = 0$ also allows for a stable polar equatorial motion. Taking into account $\theta(0) = \bar{\theta}_{\min}$, the direct integration of Eq. (5.107) yields

$$\theta(\gamma) = \arccos\left(\sqrt{1 - \left(\frac{\xi}{a}\right)^2} \operatorname{sech}\,(\kappa_1 \gamma)\right), \tag{5.115}$$

which implies $a^2 > \xi^2$, and we have defined $\kappa_1 = \frac{\omega_0}{M}\sqrt{a^2 - \xi^2}$. Accordingly, the temporal evolution of $\theta(\gamma)$ and the corresponding angular effective potential have been plotted in Fig. 5.9. As it can be observed, in contrast with the case of $\tilde{\eta} > 0$, the allowed energies for the case of $\tilde{\eta} = 0$ are higher than their critical value (i.e. $W_{\min} > \omega_U^2$), and therefore, only the capturing trajectories are possible, which in Fig. 5.10, has been demonstrated inside the cone of confinement.

The case of $\tilde{\eta} < 0$

Under this condition, the expression in Eq. (5.108) takes the form

$$\Theta_z = -|\tilde{\eta}| + (|\tilde{\eta}| + a^2 - \xi^2)z^2 - a^2 z^4, \tag{5.116}$$

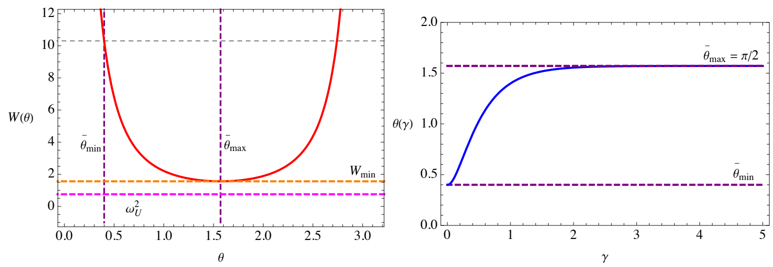

Figure 5.9: The angular effective potential and the temporal evolution of the coordinate θ, for the case of $\tilde{\eta} = 0$ (which here corresponds to $\mathscr{Q} = f_\theta = 9M^2$). To plot $\theta(\gamma)$, we have considered $\omega_0 = \sqrt{10.30}$.

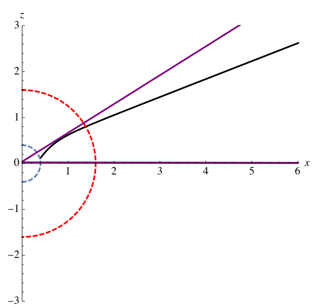

Figure 5.10: The capturing trajectory for the case of $\tilde{\eta} = 0$, inside the cone of confinement, plotted for $\omega_0 = \sqrt{10.30}$. The outer and inner circles indicate, respectively, r_+ and r_-.

and $\Theta_z > 0$ requires $|\tilde{\eta}| + a^2 - \xi^2 > 0$, which is satisfied inside the domain $\bar{\bar{z}}_{\rm min} \leq z \leq \bar{\bar{z}}_{\rm max}$, where

$$\bar{\bar{z}}_{\rm min} = \mu_0 \sin\left(\frac{1}{2}\arcsin\left(\mu_1\right)\right), \tag{5.117a}$$

$$\bar{\bar{z}}_{\rm max} = \mu_0 \cos\left(\frac{1}{2}\arcsin\left(\mu_1\right)\right), \tag{5.117b}$$

with

$$\mu_0 = \frac{\sqrt{|\tilde{\eta}| + a^2 - \xi^2}}{a}, \tag{5.118a}$$

$$\mu_1 = \frac{2a\sqrt{|\tilde{\eta}|}}{|\tilde{\eta}| + a^2 - \xi^2}. \tag{5.118b}$$

The corresponding particle-cone is therefore confined to $\bar{\bar{\theta}}_{\rm min} \leq \theta \leq \bar{\bar{\theta}}_{\rm max}$, where $\bar{\bar{\theta}}_{\rm min} = \arccos\left(\bar{\bar{z}}_{\rm max}\right)$ and $\bar{\bar{\theta}}_{\rm max} = \arccos\left(\bar{\bar{z}}_{\rm min}\right)$, and the respected effective potential is

$$W(\theta) = \left(\frac{L\csc\theta}{a}\right)^2 + |\mathscr{Q} - f_\theta|\left(\frac{\sec\theta}{a}\right)^2. \tag{5.119}$$

Once again, to determine the possible stable polar orbits we solve $W'(\theta) = 0$, which yields

$$\bar{\bar{\theta}}_0 = \arctan\left(|\tilde{\eta}|^{\frac{1}{4}}\sqrt{\frac{\omega_0\left(L+\omega_0|\tilde{\eta}|^{\frac{1}{2}}\right)}{L^2+\omega_0^2|\tilde{\eta}|}}\right). \tag{5.120}$$

This value satisfies $\bar{\bar{\theta}}_{\min} \leq \bar{\bar{\theta}}_0 \leq \bar{\bar{\theta}}_{\max}$, and corresponds to the minimum of the angular effective potential for the case of $\tilde{\eta} < 0$. To find the analytical solution for $\theta(\gamma)$, we pursue the same method as in the case of $\tilde{\eta} > 0$, that provides (see appendix C.3)

$$\theta(\gamma) = \arccos\left(\bar{\bar{z}}_{\max} - \frac{3}{12\wp\left(\kappa_2\gamma\right)+\varphi_0}\right), \tag{5.121}$$

where

$$\kappa_2 = \frac{\omega_0 a\sqrt{2\bar{\bar{z}}_{\max}\left(2\bar{\bar{z}}_{\max}^2-\mu_0^2\right)}}{M}, \tag{5.122a}$$

$$\varphi_0 = \frac{6\bar{\bar{z}}_{\max}^2-\mu_0^2}{2\bar{\bar{z}}_{\max}\left(2\bar{\bar{z}}_{\max}^2-\mu_0^2\right)}, \tag{5.122b}$$

and the corresponding Weierstraß invariants are

$$\bar{\bar{g}}_2 = \frac{\mu_0^4+12\mu_0^2\bar{\bar{z}}_{\max}^2-12\bar{\bar{z}}_{\max}^4}{48\left(\mu_0^2\bar{\bar{z}}_{\max}-2\bar{\bar{z}}_{\max}^3\right)^2}, \tag{5.123a}$$

$$\bar{\bar{g}}_3 = -\frac{\mu_0^2\left(\mu_0^4-36\mu_0^2\bar{\bar{z}}_{\max}^2+36\bar{\bar{z}}_{\max}^4\right)}{1728\left(2\bar{\bar{z}}_{\max}^3-\mu_0^2\bar{\bar{z}}_{\max}\right)^3}. \tag{5.123b}$$

As in the previous cases, we have plotted the respected angular effective potential and the temporal evolution of the θ-coordinate, in Fig. 5.11, for the case of $\tilde{\eta} < 0$, which similar to the case of $\tilde{\eta} = 0$, indicates that $W_{\min} > \omega_U^2$. Hence, only the capturing trajectories are allowed (see Fig. 5.12).

The evolution of the azimuth angle (the ϕ-motion)

A feasible approach to calculate the ϕ-motion, is to divide the integral equation (5.80) into θ-dependent and r-dependent parts, in a way that we get

$$\phi(\gamma) = \Phi_\theta(\gamma) + \Phi_r(\gamma), \tag{5.124}$$

with

$$\Phi_\theta(\gamma) = \int_{\theta_{\min}}^{\theta(\gamma)} \frac{L\mathrm{d}\theta}{\sin^2\theta\sqrt{\Theta(\theta)}}, \tag{5.125a}$$

$$\Phi_r(\gamma) = \int_{r_i}^{r(\gamma)} \frac{\left(a^2L+2Ma\omega_0 r\right)\mathrm{d}r}{\Delta\sqrt{\mathcal{R}(r)}}, \tag{5.125b}$$

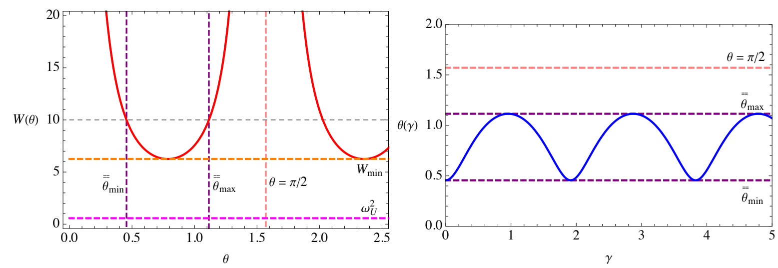

Figure 5.11: The angular effective potential and the temporal evolution of the coordinate θ for the case of $\tilde{\eta} < 0$, plotted for $\mathscr{Q} = 9M^2$ and $f_\theta = 10M^2$. To plot $\theta(\gamma)$, we have considered $\omega_0 = \sqrt{10}$.

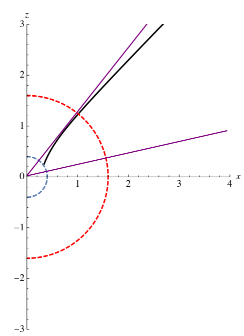

Figure 5.12: The capturing trajectory for the case of $\tilde{\eta} < 0$, plotted for $\omega_0 = \sqrt{10}$.

in which, the minimum value of the θ coordinate has been assumed to coincide with the initial point r_i, which can be set as either of the turning points. According to the fact that the general form of the equation of motion has been considered, this assumption does not affect the final analytical results for the ϕ-motion. Direct integration of the integral (5.125a) results in the following cases:

- For $\tilde{\eta} > 0$ we get (see appendix C.4)

$$\Phi_\theta(\gamma) = \mathcal{K}_0\left[\mathcal{K}_1\mathcal{F}_1(U_\theta) - \mathcal{K}_2\mathcal{F}_2(U_\theta) - \kappa_0\gamma\right], \tag{5.126}$$

in which, κ_0 has been given in Eq. (5.111a), and (with $j = 1, 2$)

$$\mathcal{F}_j(U_\theta) = \frac{1}{\wp'(v_j)}\left[\ln\left(\frac{\sigma\big(ß(U_\theta) - v_j\big)}{\sigma\big(ß(U_\theta) + v_j\big)}\right) + 2ß(U_\theta)\zeta(v_j)\right], \tag{5.127}$$

which here, is given in terms of the corresponding Weierstraß invariants g_2 and

g_3, as in Eqs. (5.113). Furthermore,

$$v_1 = ß\left(-\frac{\psi_0}{12} - \frac{1}{4[1-z_{\max}]}\right), \tag{5.128a}$$

$$v_2 = ß\left(-\frac{\psi_0}{12} + \frac{1}{4[1+z_{\max}]}\right), \tag{5.128b}$$

$$U_\theta = \frac{1}{4(z_{\max} - \cos\theta)} - \frac{\psi_0}{3}, \tag{5.128c}$$

in which, $z_{\max}$ and ψ_0 are given in Eqs. (5.109a) and (5.111b), and

$$\mathcal{K}_0 = \frac{\xi}{a\sqrt{2z_{\max}\left(z_{\max}^2 + z_0^2\right)(1-z_{\max})(1+z_{\max})}}, \tag{5.129a}$$

$$\mathcal{K}_1 = \frac{1+z_{\max}}{8(1-z_{\max})}, \tag{5.129b}$$

$$\mathcal{K}_2 = \frac{1-z_{\max}}{8(1+z_{\max})}. \tag{5.129c}$$

Note that, for the sake of simplicity in the demonstration of the trajectories, we will set $\phi(\theta_{\min}) = 0$ as the initial condition. The complete γ-dependent expression for $\Phi_\theta(\gamma)$ is then obtained by substituting $\theta \to \theta(\gamma)$ in the above relations.

- For $\tilde{\eta} = 0$, pursuing the same mathematical methods, we find

$$\Phi_\theta(\gamma) = \bar{\mathcal{K}}_0\left[\bar{\mathcal{K}}_1\bar{\mathcal{F}}_1(\bar{U}_\theta) - \bar{\mathcal{K}}_2\bar{\mathcal{F}}_2(\bar{U}_\theta) - ß\left(\bar{U}_\theta\right)\right], \tag{5.130}$$

in which, $\bar{\mathcal{F}}_\theta(\theta)$ has the same expression as in Eq. (5.127), considering the exchanges

$$v_1 \to \bar{v}_1 = ß\left(-\frac{5}{24\bar{z}_{\max}} - \frac{1}{4[1-\bar{z}_{\max}]}\right), \tag{5.131a}$$

$$v_2 \to \bar{v}_2 = ß\left(-\frac{5}{24\bar{z}_{\max}} + \frac{1}{4[1+\bar{z}_{\max}]}\right), \tag{5.131b}$$

$$U_\theta \to \bar{U}_\theta = \frac{1}{4(\bar{z}_{\max} - \cos\theta)} - \frac{5}{24\bar{z}_{\max}}, \tag{5.131c}$$

and the corresponding Weierstraß invariants are

$$\bar{g}_2 = \frac{1}{48\bar{z}_{\max}^2}, \tag{5.132a}$$

$$\bar{g}_3 = -\frac{1}{1728\bar{z}_{\max}^3}. \tag{5.132b}$$

Furthermore,

$$\bar{\mathcal{K}}_0 = \frac{\xi}{a\sqrt{2\bar{z}_{\max}^3}\,(1-\bar{z}_{\max})(1+\bar{z}_{\max})}, \tag{5.133a}$$

$$\bar{\mathcal{K}}_1 = \frac{1+\bar{z}_{\max}}{8(1-\bar{z}_{\max})}, \tag{5.133b}$$

$$\bar{\mathcal{K}}_2 = \frac{1-\bar{z}_{\max}}{8(1+\bar{z}_{\max})}. \tag{5.133c}$$

- For $\tilde{\eta} < 0$ we obtain

$$\Phi_\theta(\gamma) = \bar{\bar{\mathcal{K}}}_0 \left[\bar{\bar{\mathcal{K}}}_1 \bar{\bar{\mathcal{F}}}_1(\bar{\bar{U}}_\theta) - \bar{\bar{\mathcal{K}}}_2 \bar{\bar{\mathcal{F}}}_2(\bar{\bar{U}}_\theta) - \kappa_2 \gamma \right], \tag{5.134}$$

with κ_2 given in Eq. (5.122a). To obtain $\bar{\bar{\mathcal{F}}}_j(\bar{\bar{U}}_\theta)$, we need to apply

$$v_1 \to \bar{\bar{v}}_1 = ß\left(-\frac{\varphi_0}{12} - \frac{1}{4[1-\bar{\bar{z}}_{\max}]}\right), \tag{5.135a}$$

$$v_2 \to \bar{\bar{v}}_1 = ß\left(-\frac{\varphi_0}{12} + \frac{1}{4[1+\bar{\bar{z}}_{\max}]}\right), \tag{5.135b}$$

$$U_\theta \to \bar{\bar{U}}_\theta = \frac{1}{4(\bar{\bar{z}}_{\max} - \cos\theta)} - \frac{\varphi_0}{3}, \tag{5.135c}$$

in Eqs. (5.127) and (5.128), with $\bar{\bar{z}}_{\max}$, μ_0 and φ_0, defined, respectively, in Eqs. (5.117b), (5.118a) and (5.122b). The corresponding Weierstraß invariants are the same as $\bar{\bar{g}}_2$ and $\bar{\bar{g}}_3$, given in Eqs. (5.123), and

$$\bar{\bar{\mathcal{K}}}_0 = \frac{\xi}{a\sqrt{2\bar{\bar{z}}_{\max}\left(2\bar{\bar{z}}^2_{\max} - \mu_0^2\right)(1-\bar{\bar{z}}_{\max})(1+\bar{\bar{z}}_{\max})}}, \tag{5.136a}$$

$$\bar{\bar{\mathcal{K}}}_1 = \frac{1+\bar{\bar{z}}_{\max}}{8(1-\bar{\bar{z}}_{\max})}, \tag{5.136b}$$

$$\bar{\bar{\mathcal{K}}}_2 = \frac{1-\bar{\bar{z}}_{\max}}{8(1+\bar{\bar{z}}_{\max})}. \tag{5.136c}$$

The r-dependent integral (5.125b) provides (see appendix C.5)

$$\Phi_r(\gamma) = \mathcal{K}_+ \mathcal{F}_+(U_r) - \mathcal{K}_- \mathcal{F}_-(U_r) - \tilde{B}\, ß(U_r), \tag{5.137}$$

in which

$$\mathcal{F}_\pm(U_r) = \frac{1}{\wp'(\Upsilon_\pm)}\left[\ln\left(\frac{\sigma(\Upsilon_\pm - ß(U_r))}{\sigma(\Upsilon_\pm + ß(U_r))}\right) + 2ß(U_r)\zeta(\Upsilon_\pm)\right], \tag{5.138}$$

given that

$$\mathcal{K}_\pm = \frac{r_i\left(a^2 L + 2Ma\omega_0 r_i\right) + 2Ma\omega_0 r_i(r_i - r_\pm)}{4\omega_0\sqrt{\tilde{\alpha}}(r_i - r_\pm)^2(r_+ - r_-)}, \tag{5.139a}$$

$$\tilde{B} = \frac{\left(a^2 L + 2Ma\omega_0 r_i\right)}{\omega_0\sqrt{\tilde{\alpha}}(r_i - r_+)(r_i - r_-)}, \tag{5.139b}$$

$$U_r \equiv U_r(\gamma) = \frac{\alpha_1}{12} - \frac{r_i}{4\left[r(\gamma) - r_i\right]}, \tag{5.139c}$$

$$\Upsilon_\pm = ß\left(\frac{\alpha_1}{12} - \frac{r_i}{4\left[r_i - r_\pm\right]}\right), \tag{5.139d}$$

where the coefficient α_1 and the Weierstraß invariants, are the same as those given in Eqs. (5.99), considering $r_D \to r_i$. Furthermore

$$\tilde{\alpha} = 2\mathcal{A} + 4r_i^2 + \frac{\mathcal{B}}{r_i}. \tag{5.140}$$

Now, having in hand the analytical expressions for all the spatial coordinates, we are able to simulate the possible orbits, based on the simultaneous evolution of these coordinates. Respecting the allowed values of ω_0, in Fig. 5.13, the orbits that we have previously illustrated in Figs. 5.8, 5.10, and 5.12, are demonstrated in the three-dimensional form, by applying the following Cartesian correspondents of the Boyer-Lindquist coordinates (Boyer & Lindquist, 1967)

$$x(\gamma) = \sqrt{r^2(\gamma) + a^2} \sin\theta(\gamma) \cos\phi(\gamma), \tag{5.141a}$$

$$y(\gamma) = \sqrt{r^2(\gamma) + a^2} \sin\theta(\gamma) \sin\phi(\gamma), \tag{5.141b}$$

$$z(\gamma) = r(\gamma) \cos\theta(\gamma), \tag{5.141c}$$

known as the Kerr-Schild Cartesian coordinates. In presenting the figures, we have also considered the case of the vacuum Kerr spacetime, for which, the characteristic functions $f_r(r)$ and $f_\theta(\theta)$ in Eq. (5.68), vanish identically. In fact, in the three-dimensional treatment of the trajectories, a fixed positive Carter's constant $\mathscr{Q}$, does not allow for the construction of the cases $\tilde{\eta} = 0$ and $\tilde{\eta} < 0$ in the vacuum Kerr spacetime. Hence, the possible comparison between the light propagation in the plasmic and vacuum Kerr spacetimes can only be done in the context of $\tilde{\eta} > 0$ which corresponds to the first six diagrams of Fig. 5.13. As indicated in these diagrams, the sensible differences between these media, are seen in the OFKs. While the light ray trajectories in plasma (black curves) occupy a wider spatial range around the black hole, those in the vacuum (blue curves) are more close to the event horizon. Passing the plasma, will therefore, change the amount of light deflection and this can be inspected through the process of gravitational lensing (see below). The other types of trajectories do not show any sensible differences. Hence, in what follows we continue with the equatorial lens equation for the black hole.

Gravitational lensing

Let us, for now, confine ourselves to the equatorial plan (with $\theta = \frac{\pi}{2}$), on which we have $\mathscr{Q} = f_\theta$. Therefore, by means of Eqs. (5.78) and (5.80), the differential equation that governs the gravitational lensing is

$$\left.\frac{\mathrm{d}\phi}{\mathrm{d}r}\right|_{\theta=\frac{\pi}{2}} = \frac{L\left(r^2 - 2Mr\right) - 2Ma\omega_0 r}{\Delta\sqrt{\left[\omega_0(r^2+a^2) - aL\right]^2 - \Delta\left[f_\theta + f_r + (L - a\omega_0)^2\right]}} = \mathfrak{F}^{-1}(r), \tag{5.142}$$

according to which, the lens equation is written as

$$\hat{\vartheta} = 2\int_{r_D}^{\infty} \frac{\mathrm{d}r}{\mathfrak{F}(r)} - \pi, \tag{5.143}$$

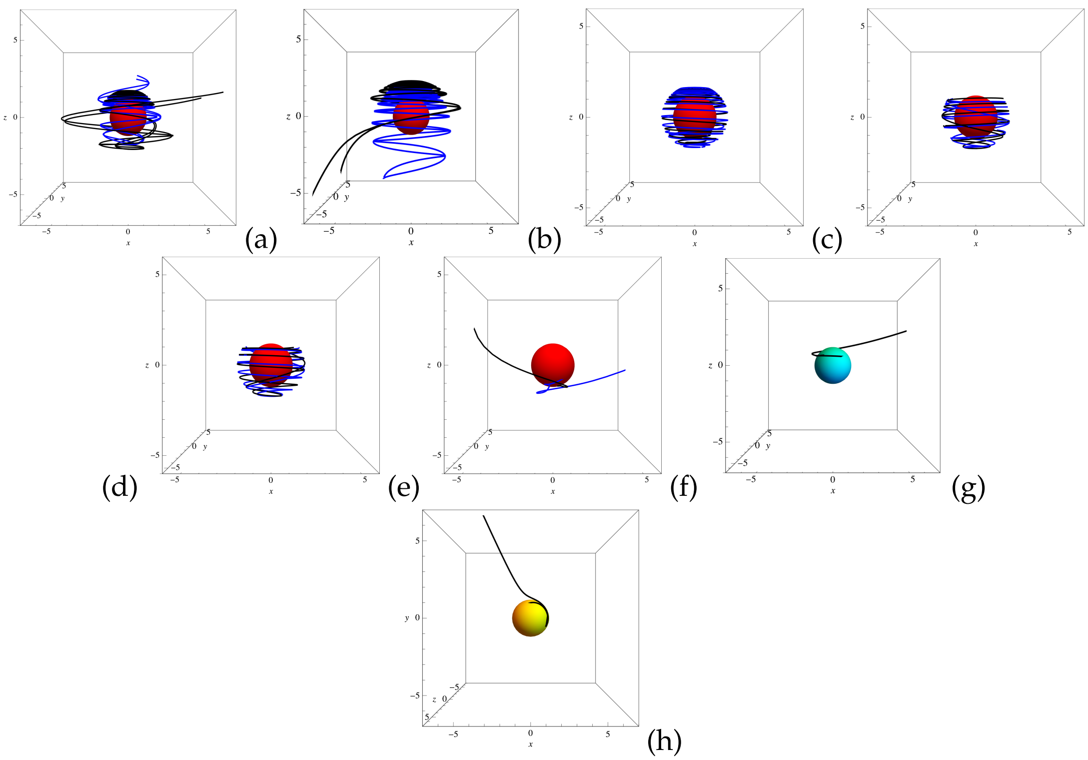

Figure 5.13: The three-dimensional simulations of the possible orbits plotted for $\mathscr{Q} = 9M^2$, corresponding to the three cases of $\tilde{\eta} > 0$ (a-f) where the black trajectories have been calculated for $f_r = f_\theta = 1M^2$ and the blue ones indicate the null trajectories in the vacuum Kerr spacetime (i.e. for $f_r = f_\theta = 0$), $\tilde{\eta} = 0$ (g), and $\tilde{\eta} < 0$ (h). The sphere in the middle indicates the event horizon. The diagrams correspond to (a) OFK for $\omega_0 = 0.755$, (b) OFK for $\omega_0 = 0.70$, (c) OSK for $\omega_0 = 0.755$, (d) UCOFK, (e) UCOSK, (f) capture for $\omega_0 = 1$, (g) capture for $\omega_0 = \sqrt{10.30}$, (h) capture for $\omega_0 = \sqrt{10}$. Theses last two trajectories do not have a vacuum counterpart, for the above chosen Carter's constant.

where $\hat{\vartheta}$ is the deflection angle and r_D is that in Eq. (6.99). This provides (see appendix C.6)

$$\hat{\vartheta} = 2\tilde{\mathcal{K}}_+\mathcal{F}_+\left(\frac{\alpha_1}{12}\right) - 2\tilde{\mathcal{K}}_-\mathcal{F}_-\left(\frac{\alpha_1}{12}\right) - 2\tilde{B}\,ß\left(\frac{\alpha_1}{12}\right) - \pi, \tag{5.144}$$

in which, $\mathcal{F}_\pm$ are given in Eq. (5.138),

$$\tilde{\mathcal{K}}_\pm = \frac{r_D}{4\omega_0\sqrt{\tilde{\alpha}}(r_D - r_\pm)^2(r_+ - r_-)}\Big[Lr_D\left(-2aM\omega_0(r_D - r_\pm)^2 - r_D + 2r_\pm\right) \\ - 2aMr_\pm\omega_0 + L^2r_D(r_D - 2M)(r_D - r_\pm)^2 - 2LMr_\pm\Big], \tag{5.145a}$$

$$\tilde{B} = \frac{r_D[L(r_D - 2M) - 2aM\omega_0]}{4\omega_0\sqrt{\tilde{\alpha}}(r_D - r_-)(r_D - r_+)}, \tag{5.145b}$$

and $\Upsilon_\pm$ are the same as those in Eq. (5.139d) with $r_i \to r_D$. Applying the data given in Fig. 5.13, one obtains $\hat{\vartheta} = 47.137°$ and $\hat{\vartheta} = 110.869°$, respectively, for $\omega_0 = 0.755$ and $\omega_0 = 0.70$. This is while for a vacuum background (i.e. $f_r = f_\theta = 0$), these values change to $\hat{\vartheta} = 27.276°$ and $\hat{\vartheta} = 52.997°$, for the same initial frequencies.

The evolution of the coordinate time (the t-motion)

We exploit the same methods of integration, as we had for the case of the ϕ-motion. Accordingly, considering Eq. (5.81), together with Eqs. (5.78) and (5.79), we can write the integral equation for the t-motion as

$$t(\gamma) = t_\theta(\gamma) + t_r(\gamma), \tag{5.146}$$

with

$$t_\theta(\gamma) = -\int_{\theta_{\min}}^{\theta(\gamma)} \frac{\omega_0 a^2 \sin^2\theta \, \mathrm{d}\theta}{\sqrt{\Theta(\theta)}}, \tag{5.147a}$$

$$t_r(\gamma) = \int_{r_i}^{r(\gamma)} \frac{\left[\omega_0(r^2+a^2)^2 - 2MaLr\right] \mathrm{d}r}{\Delta\sqrt{\mathcal{R}(r)}}. \tag{5.147b}$$

Recalling the functions that we have defined formerly, the θ-dependent integral above gives these three cases:

- For $\tilde{\eta} > 0$:

$$t_\theta(\gamma) = 2a\Big\{\zeta\Big(\text{ß}\big(U_\theta(\theta_{\min})\big)\Big) - \zeta\Big(\text{ß}\big(U_\theta(\theta)\big)\Big) + \left(\frac{1}{4} + \frac{\chi_0^2}{12a^2}\right)\Big[\text{ß}\big(U_\theta(\theta_{\min})\big) - \text{ß}\big(U_\theta(\theta)\big)\Big]\Big\}. \tag{5.148}$$

- For $\tilde{\eta} = 0$:

$$t_\theta(\gamma) = 2a\Big\{\zeta\Big(\text{ß}\big(\bar{U}_\theta(\theta_{\min})\big)\Big) - \zeta\Big(\text{ß}\big(\bar{U}_\theta(\theta)\big)\Big) + \left(\frac{1}{6} + \frac{\xi^2}{12a^2}\right)\Big[\text{ß}\big(\bar{U}_\theta(\theta_{\min})\big) - \text{ß}\big(\bar{U}_\theta(\theta)\big)\Big]\Big\}. \tag{5.149}$$

- For $\tilde{\eta} < 0$:

$$t_\theta(\gamma) = 2a\Big\{\zeta\Big(\text{ß}\big(\bar{\bar{U}}_\theta(\theta_{\min})\big)\Big) - \zeta\Big(\text{ß}\big(\bar{\bar{U}}_\theta(\theta)\big)\Big) + \left(\frac{1}{4} - \frac{\mu_0^2}{12}\right)\Big[\text{ß}\big(\bar{\bar{U}}_\theta(\theta_{\min})\big) - \text{ß}\big(\bar{\bar{U}}_\theta(\theta)\big)\Big]\Big\}. \tag{5.150}$$

The r-dependent integral (5.147b) provides the solution

$$t_r(\gamma) = \tau_0 \sum_{j=1}^{5} \tau_j \Big[\mathcal{T}_j\big(r(\gamma)\big) - \mathcal{T}_j(r_i)\Big], \tag{5.151}$$

in which (letting $\mathcal{T}_j \equiv \mathcal{T}_j\big(r(\gamma)\big)$) (see appendix C.7)

$$\mathcal{T}_1 = ß(U_r), \tag{5.152a}$$

$$\begin{aligned}\mathcal{T}_2 = &\frac{\wp''\left(\frac{\tilde{\beta}}{12}\right)}{\wp'^3\left(\frac{\tilde{\beta}}{12}\right)} \ln\left(\frac{\sigma\left(ß(U_r)+\frac{\tilde{\beta}}{12}\right)}{\sigma\left(ß(U_r)-\frac{\tilde{\beta}}{12}\right)}\right) - \frac{1}{\wp'^2\left(\frac{\tilde{\beta}}{12}\right)}\left[\zeta\left(ß(U_r)+\frac{\tilde{\beta}}{12}\right)\right.\\ &\left.+\zeta\left(ß(U_r)-\frac{\tilde{\beta}}{12}\right)\right] - 2ß(U_r)\left[\frac{\wp\left(\frac{\tilde{\beta}}{12}\right)}{\wp'^2\left(\frac{\tilde{\beta}}{12}\right)} + \frac{\wp''\left(\frac{\tilde{\beta}}{12}\right)\zeta\left(\frac{\tilde{\beta}}{12}\right)}{\wp'^3\left(\frac{\tilde{\beta}}{12}\right)}\right],\end{aligned} \tag{5.152b}$$

$$\mathcal{T}_3 = \frac{1}{\wp'\left(\frac{\tilde{\beta}}{12}\right)}\left[\ln\left(\frac{\sigma\left(\frac{\tilde{\beta}}{12}-ß(U_r)\right)}{\sigma\left(\frac{\tilde{\beta}}{12}+ß(U_r)\right)}\right) + 2ß(U_r)\zeta\left(\frac{\tilde{\beta}}{12}\right)\right], \tag{5.152c}$$

$$\mathcal{T}_4 = \mathcal{F}_+(U_r), \tag{5.152d}$$

$$\mathcal{T}_5 = \mathcal{F}_-(U_r), \tag{5.152e}$$

recalling the expressions defined previously, and

$$\tau_0 = \frac{r_i}{\omega_0\sqrt{C_3}(r_i - r_+)(r_i - r_-)}, \tag{5.153a}$$

$$\tau_1 = \omega_0(r_i^2 + a^2)^2 - 2MaLr_i, \tag{5.153b}$$

$$\tau_2 = \frac{\omega_0}{16}\, r_i^2 (r_i - r_+)(r_i - r_-), \tag{5.153c}$$

$$\tau_3 = \omega_0\, r_i^4 \left[\frac{4u_+u_- - (u_+ + u_-)}{4u_+^2 u_-^2}\right], \tag{5.153d}$$

$$\tau_4 = \frac{\omega_0\left[r_i^2\,(u_+ - 1)^2 + a^2u_+^2\right]^2}{4u_+^2(u_- - u_+)} - \frac{MaLr_i\,(u_+ - 1)\,u_+}{2(u_- - u_+)}, \tag{5.153e}$$

$$\tau_5 = -\frac{\omega_0\left[r_i^2\,(u_- - 1)^2 + a^2u_-^2\right]^2}{4u_-^2\,(u_- - u_+)} + \frac{MaLr_i\,(u_- - 1)\,u_-}{2(u_- - u_+)}, \tag{5.153f}$$

where $u_\pm = \left[\frac{r_\pm}{r_i} - 1\right]^{-1}$, the relevant Weierstraß invariant are given in Eqs. (5.99), and the constant C_3 has been taken from Eq. (5.100d), considering $r_D \to r_i$.

Note that, to simulate the angular trajectories, the Mino time γ is used as the curve parameter. The above derivations for the time coordinate t are, therefore, of pure mathematical significance and are presented only to have in hand the complete evolution of the spacetime coordinates.

5.3 Photon spheres (regions)

In this section, the important notion of the photon regions in stationary black hole spacetimes is discussed, which is related directly to the formation of the black hole shadow. For the particular case of the Kerr black hole in plasmic medium, the photon regions and the shadow of the black hole has been discussed by Perlick and Tsupko (Perlick & Tsupko, 2017), where they introduced the geometric decomposition given in Eq. (5.68). In this section however, beside calculating the photon regions for an anisotropic inhomogeneous plasma, we also include more photon surfaces that characterize the black hole and its image.

In fact, photon regions are regions in the spacetime that are filled by *spherical light rays*, i.e., with solutions to the ray equation (5.78), that stay on a sphere $r = \text{const.}$ Hence, although the term *photon sphere* is commonly used in the literature, but it is relatively incorrect. Each of these spherical light rays stays on a sphere with the θ-coordinate varying between two turning points, and exists for radius values in a certain interval. In this sense, only the innermost and the outermost ones are circular (depending only on the physical properties of the black hole), and unstable spherical light rays (i.e. UCOs) can serve as the limit curves for the light rays that approach them in a spiral motion. All the other spherical light rays are non-planar. So, the photon region is the closure of all points, through which, such spherical light rays exist. To determine the photon region, one has to consider the r-component and the θ-component of the equations for the light rays and respect the conditions $\frac{\mathrm{d}r}{\mathrm{d}\gamma} = 0$, $\frac{\mathrm{d}^2 r}{\mathrm{d}\gamma^2} = 0$ (or equivalently, $\mathcal{R}(r) = 0$, $\mathcal{R}'(r) = 0$), and $\Theta(\theta) \geq 0$, in accordance to the equations (5.78) and (5.79). After doing appropriate manipulations, these conditions result in the following relations

$$\mathcal{R} = 0 \;\;\Rightarrow\;\; \left[(r^2 + a^2) - a\xi\right]^2 - \Delta\left[\eta + \eta_r + (\xi - a)^2\right] = 0, \tag{5.154a}$$

$$\mathcal{R}'(r) = 0 \;\;\Rightarrow\;\; 4r\left[(r^2 + a^2) - a\xi\right] - 2(r - M)\left[\eta + (\xi - a)^2 + \eta_r\right] = 0, \tag{5.154b}$$

$$\tilde{\eta}\sin^2\theta \geq \cos^2\theta\left(\xi^2 - a^2\sin^2\theta\right). \tag{5.154c}$$

From Eqs. (5.154a) and (5.154b), one can derive the critical locus (ξ_p, η_p), given as

$$\xi_p = \frac{M(r^2 - a^2) - r\Delta}{a(r - M)}, \tag{5.155a}$$

$$\eta_p = \frac{r^3}{a^2(r - M)^2}\left[4a^2 M - r(r - 3M)^2\right] - \eta_r, \tag{5.155b}$$

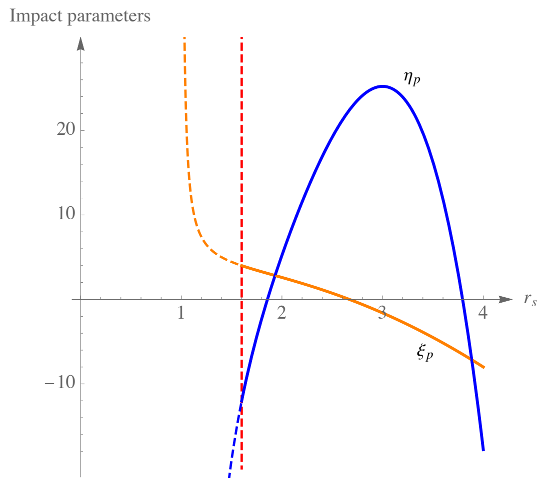

Figure 5.14: The locus (ξ_p, η_p), determining the constants of motion for the spherical photon orbits, which has been plotted for $f_r = f_\theta = 1M^2$, $\omega_0 = 0.75$, and $a = 0.8M$.

substitution of which in Eq. (5.154c), provides the condition

$$\tan^2\theta \left\{ \frac{r^3\left[4a^2M - r(r-3M)^2\right]}{a^2(r-M)^2} - \frac{f_r + f_\theta}{\omega_0^2} \right\} \geq \left[\frac{M(r^2-a^2) - r\Delta}{a(r-M)}\right]^2 - a^2\sin^2\theta, \tag{5.156}$$

that governs the formation of the photon region. Note that, the critical locus is important in the determination of the spherical photon orbits orbits. In Fig. 5.14, the behavior of these critical parameters has been plotted. On the other hand, as we have established before, the orbits are characterized, crucially, depending on the sign of the impact parameter η. In particular, the case of $\eta \to 0$ corresponds to either $\mathscr{Q} \to 0$ or $E \to \infty$. This latter has the significance of UCO, which can be also regarded in terms of the condition $R''(r) < 0$.

For the case of vacuum Kerr spacetime ($\eta_r = 0$), one can consider the above condition together with Eq. (5.155b) that yields

$$4a^2M - r_p(r_p - 3M)^2 = 0 \quad \Rightarrow \quad \pm 2a\sqrt{M} = r_p^{\frac{3}{2}} - 3Mr_p^{\frac{1}{2}}, \tag{5.157}$$

which has the solutions

$$r_{p\pm} = 2\left[1 + \cos\left(\frac{2}{3}\arccos(\mp a)\right)\right], \tag{5.158}$$

that correspond, respectively, to the outer (with retrograde motion) and inner (with prograde motion) planar circular photon orbits. Furthermore, by solving directly $4a^2M - r_p(r_p - 3M)^2 = 0$, which has the particular solution

$$r_{p0} = 2M\left[1 - \cos\left(\frac{\pi}{3} - \frac{1}{3}\arccos\left(\frac{2a^2}{M^2} - 1\right)\right)\right]. \tag{5.159}$$

This radius, corresponds to the circular photon orbit that are visible to the observers located at $\theta_o = 0$ (face-on observers).

One should note that, by coming to the equatorial plane which relates to a θ-constant condition (i.e. $\theta = \frac{\pi}{2}$ or $\theta_o = 0$), we rely on the symmetry of the spacetime, which instead of a spherical symmetry, is an axial symmetry (here, around the z-axis). This way, as it is pretty simple to be inferred from the equation of motion for the ϕ-coordinate (5.80), and also from the expressions we have for $r_{p\pm}$ and $r_{\mathrm{SL}\pm}$ in Eqs. (5.158) and (5.63), that these latter radii are just circles in the equatorial plane (in our case, ellipses in the Kerr-Schild Cartesian coordinates). For the case of the ergosurfaces, the radius $r_{\mathrm{SL}-}$ vanishes on the equatorial plane and we are left with $r_{\mathrm{SL}+} = 2M$. For the case of spherical photon orbits, all the others have combined prograde and retrograde motions, and become unobservable in the equatorial plane, as it can be inferred easily from their dependence on the θ-coordinate[3]

To proceed with the demonstration of the photon surfaces, we once again apply the Kerr-Schild coordinates (5.141) for the case of $y = 0$, to obtain the cross-section of the photon region in the polar plane (i.e. the z-x plane). Accordingly, one can write $x = \sqrt{r^2 + a^2}\sin\theta$ and $z = r\cos\theta$, which can be solved for r and θ, giving

$$r = \frac{1}{\sqrt{2}}\sqrt{(x^2 + z^2) - a^2 + \sqrt{4a^2z^2 + (x^2 + z^2 - a^2)^2}}\,, \tag{5.160a}$$

$$\theta = \arcsin\left(\frac{\sqrt{2}x}{\sqrt{x^2 + z^2 + a^2 + \sqrt{4a^2z^2 + (x^2 + z^2 - a^2)^2}}}\right). \tag{5.160b}$$

These values are then replaced inside the expressions for $r_{p\pm}$, r_{p0}, $r_{\mathrm{SL}\pm}$ and etc., in order to do the appropriate `RegionPlot` and `ContourPlot` in *Mathematica*®. In Fig. 5.15, the photon surfaces of a Kerr black hole located in vacuum, have been shown for several values of the spin parameter. These surfaces confine the photon regions, ergoregions and etc., and are rather informative in the perception of the spacetime's causal structure. For the case that the plasma is available, applying the condition (5.156), we consider the same values for the plasma parameters, as were taken for the case of $\tilde{\eta} > 0$ in the panels (a-f) of Fig. 5.13, to show the corresponding photon regions in Fig. 5.16. Several further examples can be generated by altering a and hence, the corresponding ω_0.

[3] In fact, it can be inferred from Eq. (5.156) that these orbits depend directly on the θ-coordinate and cannot exist for $\theta = \frac{\pi}{2}$.

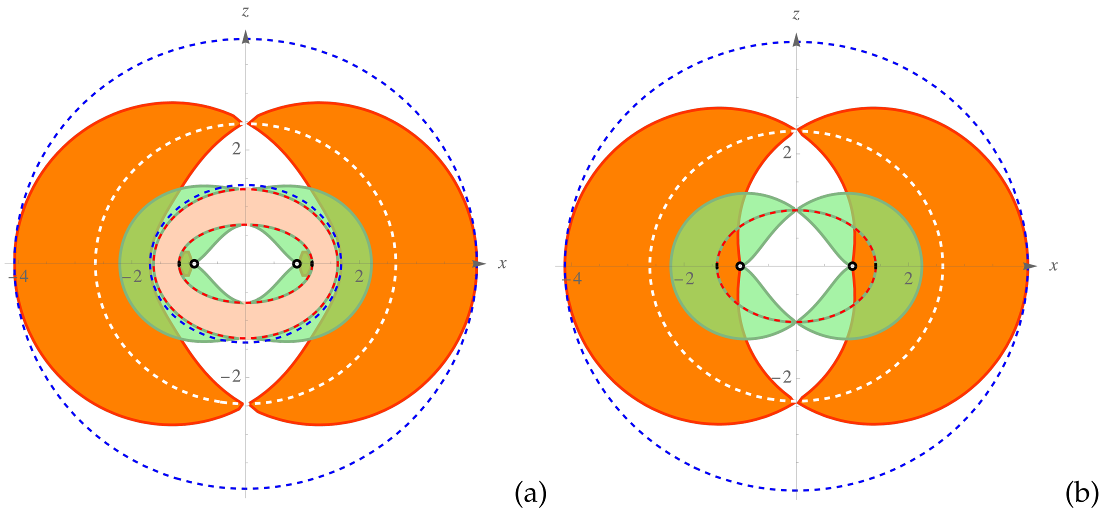

Figure 5.15: The photon surfaces in the polar (z-x) plane, for a Kerr black hole located in vacuum, plotted for (a) $a = 0.95M$, and (b) $a = M$, shown by regions in orange. The larger and smaller dashed curves in blue indicate respectively r_{p+} and r_{p-}. Same holds for the red dashed ones that indicate r_+ and r_-, with their separation filled with light color in panel (a). Furthermore, the white dashed curve is r_{p0}. The photon region which has entered the domain $0 < r < r_-$, corresponds to the causality violation. The green regions correspond to the interior and exterior ergoregions. Finally, the circles ∘ indicate the ring singularity at $z = 0$ and $x = a^2$.

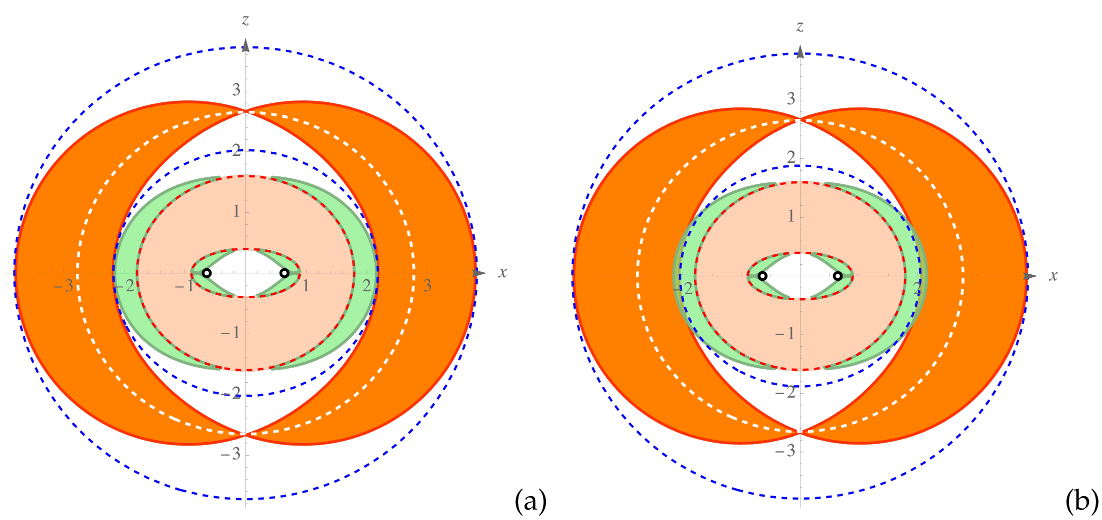

Figure 5.16: The photon surfaces in the polar (z-x) plane, for a Kerr black hole located in a plasma with $f_r = f_\theta = 1M^2$, plotted for $a = 0.8M$, and (a) $\omega_0 = 0.50$, and (b) $\omega_0 = \omega_U$. The color coding is the same as that of Fig. 5.15. No causality violating regions can be observed.

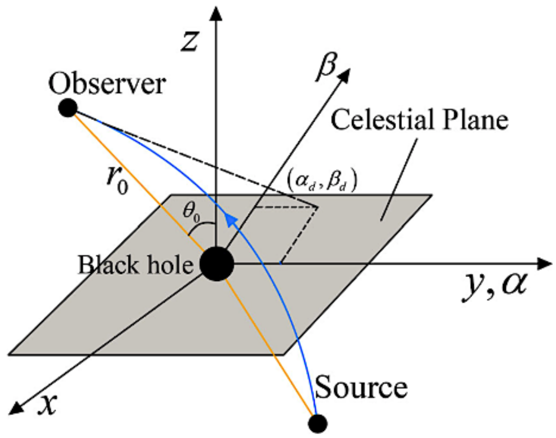

Figure 5.17: The celestial plane for an observer at (r_o, θ_o).

5.4 Shadow of the black hole

In this section, we apply the traditional approach to the parametrization of the shadow of the stationary asymptotically flat spacetimes, and in particular, the Kerr spacetime (Cunningham & Bardeen, 1973; Chandrasekhar, 1998; Vázquez & Esteban, 2004), to calculate the shadow of the Kerr black hole in the plasmic medium. We first present a review on the mathematical methods which have been developed so far.

Let us consider the two-dimensional celestial plane with the coordinates (α, β), as indicated in Fig. 5.17, for an observer who is located at (r_o, θ_o), and is supposed to reside on a line perpendicular to the celestial plane. The local frame of the observer is supposed to be defined in the Cartesian coordinates (x, y, z), and for simplicity, we assume that the y-coordinate coincides with the α-coordinate. In this sense, the observer is in the x-z plane, for which, $\phi_o = 0$. Similar to what we discussed in section 3.6.3, the light rays can be thought of as travelling on the parametric curve $\ell(r) = (x(r), y(r), z(r))$, which now, the radial coordinate r is considered as the curve parametrization, where $r^2 = x^2 + y^2 + z^2$. In fact, the tangent to this curve at the point of the observer is given by

$$\left(\frac{\mathrm{d}x}{\mathrm{d}r}\right)_{r_o} \hat{x} + \left(\frac{\mathrm{d}y}{\mathrm{d}r}\right)_{r_o} \hat{y} + \left(\frac{\mathrm{d}z}{\mathrm{d}r}\right)_{r_o} \hat{z}, \tag{5.161}$$

which represents a straight line, connecting the observer to the point (α_d, β_d) on the celestial plane (see Fig. 5.17). This latter point is given by

$$x_d = -\beta_d \cos\theta_o, \tag{5.162a}$$

$$y_d = \alpha_d, \tag{5.162b}$$

$$z_d = \beta_d \cos\left(\frac{\pi}{2} - \theta_o\right) = \beta_d \sin\theta_o, \tag{5.162c}$$

Therefore, to summarize, we have the point $(-\beta_d \cos\theta_o, \alpha_d, \beta_d \sin\theta_o)$ in the Cartesian coordinates, through which, the tangent vector $\vec{V} = \left(\frac{\mathrm{d}x}{\mathrm{d}r}, \frac{\mathrm{d}y}{\mathrm{d}r}, \frac{\mathrm{d}z}{\mathrm{d}r}\right) \equiv (a, b, c)$ passes. In general, any position vector can be written as $\vec{R} = (x, y, z) = (x_o + ar, y_o + br, z_o + cr)$. On the other hand, in the spherical coordinates we have $x = r\sin\theta\cos\phi$, $y = r\sin\theta\sin\phi$ and $z = r\cos\theta$, which result in the infinitesimal displacements

$$\mathrm{d}x = \sin\theta\cos\phi\mathrm{d}r + r\cos\phi\cos\theta\mathrm{d}\theta - r\sin\theta\sin\phi\mathrm{d}\phi, \tag{5.163a}$$

$$\mathrm{d}y = \sin\theta\sin\phi\mathrm{d}r + r\sin\phi\cos\theta\mathrm{d}\theta + r\sin\theta\cos\phi\mathrm{d}\phi, \tag{5.163b}$$

$$\mathrm{d}z = \cos\theta\mathrm{d}r - r\sin\theta\mathrm{d}\phi. \tag{5.163c}$$

Hence, at the point of the observer, we have the following relations

$$z_o = z_o + r_o \frac{\mathrm{d}z}{\mathrm{d}r}\bigg|_{r_o} \Rightarrow r_o\cos\theta_o - r_o^2\sin\theta_o \frac{\mathrm{d}\theta}{\mathrm{d}r}\bigg|_{r_o} = 0 \overset{z_o=\beta_d\sin\theta_o}{\Longrightarrow} \beta_d = r_o^2 \frac{\mathrm{d}\theta}{\mathrm{d}r}\bigg|_{r_o}, \tag{5.164}$$

$$\begin{aligned} y_o = y_o + r_o \frac{\mathrm{d}y}{\mathrm{d}r}\bigg|_{(r_o,\theta_o,\phi_o)} &\Rightarrow r_o\sin\theta_o\sin\phi_o + r_o^2\sin\phi_o\cos\theta_o \frac{\mathrm{d}\theta}{\mathrm{d}r}\bigg|_{r_o} + r_o^2\sin\theta_o\cos\phi_o \frac{\mathrm{d}\phi}{\mathrm{d}r}\bigg|_{r_o} \\ &= 0 \overset{y_o=\alpha_d,\ \phi_o=0}{\Longrightarrow} \alpha_d = -r_o^2\sin\theta_o \frac{\mathrm{d}\phi}{\mathrm{d}r}\bigg|_{r_o}, \end{aligned} \tag{5.165}$$

which describe a point on the celestial plane. Now to obtain the specific relations for (α, β), we reconsider the equations of motion (5.78)–(5.80), that yield

$$\frac{\mathrm{d}\theta}{\mathrm{d}r}\bigg|_{r_o,\theta_o} = \sqrt{\frac{\Theta(\theta_o)}{\mathcal{R}(r_o)}}, \tag{5.166a}$$

$$\frac{\mathrm{d}\phi}{\mathrm{d}r}\bigg|_{r_o,\theta_o} = \frac{L\left(\rho_0^2 - 2Mr_o\right)\csc^2\theta_o - 2Ma\omega_0 r_o}{\Delta_o\sqrt{\mathcal{R}(r_o)}}, \tag{5.166b}$$

where $\Delta_o \equiv \Delta(r_o)$. For the case of an observer at the infinity (where the spacetime is essentially flat) and by means of the Eqs. (5.77a) and (5.77b), the above relations result in

$$\begin{aligned} \alpha &= \lim_{r_o\to\infty}\left[\frac{\left\{\frac{L_p}{\sin^2\theta_o}\left(r_o^2 + a\cos^2\theta_o - 2Mr_o\right) - 2Ma\omega_0 r_o\right\}\left(-r_o^2\sin\theta_o\right)}{\left(r_o^2 + a^2 - 2Mr_o\right)\sqrt{\omega_0^2\left[\left(r_o^2+a^2\right) - a\xi_p\right]^2 - \Delta_o\omega_0^2\left[\eta_p + \frac{f_r(r_o)}{\omega_0^2} + (\xi_p - a)^2\right]}}\right] \\ &= \lim_{r_o\to\infty}\frac{\sim -\left(\frac{L_p}{\sin\theta_o}r_o^4\right)}{\sim\ \omega_0 r_o^4} = -\frac{\xi_p}{\sin\theta_o}, \end{aligned} \tag{5.167}$$

$$\begin{aligned}\beta &= \lim_{r_o\to\infty}\sqrt{\frac{\left[\mathscr{Q}_p - f_\theta(\theta_o) - \cos^2\theta_o\left(L_p^2\csc^2\theta_o - a^2\omega_0^2\right)\right]r_o^4}{\omega_0^2\left[(r_o^2+a^2)-a\xi_p\right]^2 - \Delta_o\omega_0^2\left[\eta_p + \frac{f_r(r_o)}{\omega_0^2} + (\xi_p - a)^2\right]}}\\
&= \lim_{r_o\to\infty}\sqrt{\frac{\sim\left[\mathscr{Q}_p - f_\theta(\theta_o) - \cos^2\theta_o\left(L_p^2\csc^2\theta_o - a^2\omega_0^2\right)\right]r_o^4}{\sim\ \omega_0^2 r_o^4}}\\
&= \sqrt{\eta_p - \frac{f_\theta(\theta_o)}{\omega_0^2} - \cos^2\theta_o\left(\xi_p^2\csc^2\theta_o - a^2\right)}\\
&= \sqrt{\eta_p - \xi_p^2\cot^2\theta_o + a^2\cos^2\theta_o - \frac{f_\theta(\theta_o)}{\omega_0^2}},\end{aligned}\tag{5.168}$$

where L_p is the angular momentum relevant to the unstable circular orbits, as introduced in section 5.3, and ξ_p and η_p have been defined in Eqs. (5.155). For the case of $\theta_o = \frac{\pi}{2}$, the above expressions are simplified significantly.

Note that, there is also an alternative (even though older) method, which is based on the transformations of the momentum covector $\boldsymbol{p}$, to the observer's local frame. In this method, the celestial coordinates are given the relations (Cunningham & Bardeen, 1973; Chandrasekhar, 1998)

$$\alpha = \lim_{r_o\to\infty}\left(-\frac{r_o p^{(\phi)}}{p^{(t)}}\right)_{r_o,\theta_o},\tag{5.169}$$

$$\beta = \lim_{r_o\to\infty}\left(\frac{r_o p^{(\theta)}}{p^{(t)}}\right)_{r_o,\theta_o},\tag{5.170}$$

where $p^{(j)} = e^{(j)}{}_\mu p^\mu = \eta^{jj} e_{(j)}{}^\nu g_{\nu\mu} g^{\mu\sigma} p_\sigma$, with η_{jj} being the spatial part of the Minkowski metric in the spherical coordinates, and the

$$e_{(t)} = \partial_t,\tag{5.171a}$$

$$e_{(r)} = \partial_r,\tag{5.171b}$$

$$e_{(\theta)} = \frac{1}{r}\partial_\theta,\tag{5.171c}$$

$$e_{(\phi)} = \frac{1}{r\sin\theta}\partial_\phi,\tag{5.171d}$$

are the tetrad transformations from the Kerr spacetime to the observer's local frame in the Cartesian spherical coordinates. It is straightforward to check that, by applying the above tetrad to the celestial coordinates in Eqs. (5.169) and (5.170), one will get the same expressions as those given in Eqs. (5.167) and (5.168).

In Fig. 5.18, we have applied these expressions to do the parametric plots of the black hole shadows, with r taken as the parameter. Note that, a general study of the

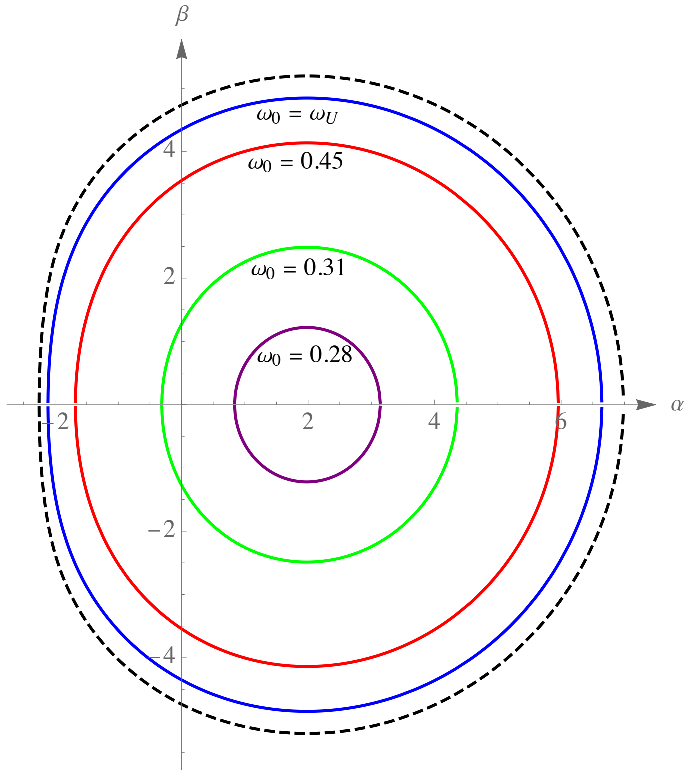

Figure 5.18: The parametric curves indicating the boundaries of the black hole shadows, plotted for a Kerr black hole with $a = 0.99M$, located in a plasmic medium with $f_r = f_\theta = 1M^2$. The curves correspond to different initial frequencies and the dashed curve corresponds to a Kerr black hole in a vacuum. Obviously, the change in the initial frequency does not have any effect on the vacuum shadow.

shadow casts of axisymmetric black holes in plasmic media, has been given recently by Badía and Eiroa (Badía & Eiroa, 2021).

5.5 Summary

There is no doubt that physical systems offer different criteria for them to be describable efficiently and completely. In this chapter, we have considered such criteria for monochromatic light rays of peculiar frequency ω_0, that travel in the exterior spacetime geometry of a Kerr black hole which is filled by an inhomogeneous anisotropic electronic plasma. Following the mathematical formulations founded by Synge, it is well-known that light rays will no longer travel on null geodesics inside dispersive media. We therefore, applied a proper Hamilton-Jacobi formalism which enabled us generating the differential equations of motion. Accordingly, the effective gravitational potential provides different conditions corresponding to different types of orbits for the light rays that travel on time-like trajectories with respect to the background spacetime manifold. In fact, we have tried to carry out an ambitious study on the optical conditions that govern the light propagation in plasmic medium, mostly because such studies are usually restricted to the visible limit of the black holes' exterior and their shadow. We, however, paid attention to the other types of orbits offered by the effective potential and obtained the exact analytical solutions to their respective equations of motion. We characterized the plasmic medium with the two structural functions f_r and f_θ, that enabled us conceiving the property of anisotropy. The resultant equations of motion were in the form of elliptic integrals, to solve which, we adopted specific algebraic methods that gave rise to Weierstraßian functions as the analytical solutions. Furthermore, the dimension-less Mino time was chosen as the curve parameter, so that we could have more well-expressed coordinate evolution. This parameter was then exploited in the parametric plots to perform three-dimensional simulations of the light ray trajectories. Note that, the effective potential does not offer any planetary orbits, so that the light rays, beside being able to form photon rings on the UCO, can only escape from or be captured by the black hole. These kinds of trajectories, as demonstrated within the text, are bounded to cones of definite vertex angles. Based on the specific frequency (energy) of the light rays, ω_0, the intensity of the deflection in the escaping trajectories can vary, and the rays may travel on more fast-changing hyperbolic curves as ω_0 approaches its critical value, ω_U. Note that, since we express the plasma frequency ω_p in terms of the black hole's physical characteristics in Eq. (5.84), the impacts of plasma are then included, indirectly, through the variations of the effective potential and the consequent types of orbit. In the presented analytical solutions, this was done by introducing the effective impact parameter $\tilde{\eta}$ and its dependent constants. Although the temporal evolution of the coordinates have appeared to be of rather complicated mathematical expressions, they however, can establish the basement of further studies, specified to certain models of plasma that are in connection with black holes' parameters. Such studies can offer astrophysical applications and are left for the future.

Chapter 6

Schwarzschild black hole with quintessence and cloud of strings

In this chapter, we concern about applying general relativistic tests on the spacetime produced by a static black hole associated with cloud of strings, in a universe filled with quintessence. The four tests we apply are precession of the perihelion in the planetary orbits, gravitational redshift, deflection of light, and the Shapiro time delay. Through this process, we constrain the spacetime's parameters in the context of the observational data, which results in about $\sim 10^{-9}$ for the cloud of strings parameter, and $\sim 10^{-20}\ \mathrm{m}^{-1}$ for that of quintessence. The response of the black hole to the gravitational perturbations is also discussed. Moreover, a complete study of the null and time-like geodesics is presented (Cárdenas et al., 2021; Fathi et al., 2022).

6.1 Probing the parameters

The dark side of the universe has found its way into the physical observations, regarding the flat galactic rotation curves, anti-lensing, and the accelerated expansion of the universe (Rubin et al., 1980; Massey et al., 2010; Bolejko et al., 2013; Riess et al., 1998; Perlmutter et al., 1999; Astier, 2012). This, in fact, has affected the way we look at the astrophysical phenomena. Among these, and since the end of the last century, two main observational discoveries have appeared as the keys to obtain a better understating of our universe. First, the confirmation of the highly isotropic black body radiation, of the order 10^{-5} of the temperature fluctuations, observed for the cosmic microwave background radiation (CMBR) (Bennett et al., 1994), and second, the discovery of the accelerated expansion of the universe (in the context of the Friedmann-Lamaître-Robertson-Walker (FLRW) metric), using the type Ia supernovae observations (Riess et al., 1998; Perlmutter et al., 1999). In this context, a concordance model emerges from the observations, which is the so-called Lambda-Cold Dark Matter (ΛCDM) model.

Despite being simple, this model has been able to give a fairly good description of a wealth amount of the observational data, although its deep theoretical origin is still a mystery, and no clue has been given so far, for the origin and the value of the included cosmological constant. One of the main issues here is the *coincidence problem*, or why we live in the exact epoch where the contribution of this constant is of the same order of magnitude as that of matter? In fact, in the extended versions of the model that assume a dynamical source, even no fundamental idea has been put forward to understand this component.

Nevertheless, there is an approach that has been able to successfully ameliorate the coincidence problem, by replacing the cosmological constant with a quintessence field, in which, the case of an inflaton field during the inflationary epoch, is used as a guide. In order to study the astrophysical phenomena, therefore, it seems logical to consider this model as a conservative approach, since no better explanation exists. Such phenomena may include supernovae, galaxy clusters, or quasars, in addition to which, black hole astrophysics can be named. Black holes, in particular, have appeared among the most interesting astrophysical objects, and the recent imaging of the M87* (Akiyama et al., 2019a) has shown that black holes, beside stemming in theoretical concepts, are potentially observable.

On the other hand, taking into account the cosmological dynamics, the evolution of black holes can also be affected by the dark side of the universe, in which they reside. This process has been discussed extensively in the context of general relativity and alternative theories of gravity (Jimenez Madrid & Gonzalez-Diaz, 2008; Jamil, 2009; Li et al., 2020; Roy & Yajnik, 2020). Geometrically, such calculations would add a dark component to the black hole spacetime under consideration, which is inferred from the cosmological energy-momentum constituents. Such calculations may include the consideration of a dark matter halo (Xu et al., 2018; Das et al., 2021), or the coupling of the spacetime with a quintessential field (Kiselev, 2003; Saadati & Shojai, 2019; Ali Khan et al., 2020). Furthermore, it has been argued that the cosmological perfect fluid can be regarded as a relativistic dust cloud, consisting of one-dimensional strings (instead of point particles), and this viewpoint led to a specific form of spacetime generalization (Stachel, 1977), which associates the black hole to the so-called cloud of strings.

This spacetime was generalized further to a gauge-invariant version (Letelier, 1979) and its geodesic structure has been also investigated recently (Batool & Hussain, 2017).

In this chapter, we take into account a static black hole spacetime which is associated with both the quintessential field and the cloud of strings (Toledo & Bezerra, 2018; Dias e Costa et al., 2019; Toledo & Bezerra, 2019), for which, the geodesic structure regarding the radial and circular orbits has been also investigated (Mustafa & Hussain, 2021). Furthermore, a rotating version of the black was generated together with discussing its thermodynamics (Toledo & Bezerra, 2020). One interesting feature of this black hole spacetime, is that it can include both the effects of dark matter and dark energy, in the sense that the included quintessential component, as well as stemming from the accelerated expansion of the universe, can act as an extra potential granted to the spacetime, to recover the unseen galactic matter. As it will be represented in what follows, such contribution can be found in the Mannheim-Kazanas solution to the fourth order WCG, that is proposed to recover the flat galactic rotation curves (Mannheim & Kazanas, 1989). The cloud of strings is, however, related to a cosmological model, in which the extended (string-like) objects play role as the sources of gravity, and construct the universe (Letelier, 1979). On the other hand, the respected parameters of the mentioned components are supposed to be appropriately calibrated in the context of standard observations, which is the aim of this section.

6.1.1 The black hole solution in the dark background

The static, spherically symmetric black hole solution in the quintessential background, which is surrounded by a cloud of strings, is described by the following metric in the $x^\mu = (t, r, \theta, \phi)$ coordinates:

$$\mathrm{d}s^2 = g_{\mu\nu}\mathrm{d}x^\mu \mathrm{d}x^\nu = -B(r)\mathrm{d}t^2 + B^{-1}(r)\mathrm{d}r^2 + r^2\mathrm{d}\theta^2 + r^2 \sin^2\theta \mathrm{d}\phi^2, \tag{6.1}$$

with the lapse function defined as (Toledo & Bezerra, 2018; Dias e Costa et al., 2019; Toledo & Bezerra, 2019)

$$B(r) = 1 - \alpha - \frac{2M}{r} - \frac{\gamma}{r^{3w_q+1}}, \tag{6.2}$$

in which, α, M, γ and w_q, represent, respectively, the dimensionless string cloud parameter ($0 < \alpha < 1$), the black hole mass, the quintessence parameter and the equation of state (EoS) parameter. For a perfect fluid distribution of matter/energy, this latter is defined by $P_q = w_q \rho_q$, with P_q and ρ_q as the quintessential energy pressure and density, and lies within the range $-1 < w_q < -\frac{1}{3}$. This parameter is set to be responsible for the cosmological acceleration and the special case of $w_q = -1$ recovers the cosmological constant.

To proceed further with our study, we will consider the case of $w_q = -\frac{2}{3}$ which corresponds to the black hole spacetime with the lapse function

$$B(r) = 1 - \alpha - \frac{2M}{r} - \gamma r, \tag{6.3}$$

located in a matter dominated universe (Wei & Cai, 2008). Note that, the last term resembles the dark matter-related term included in the Mannheim-Kazanas static spherically symmetric solution to the vacuum Bach equations, which is proposed to recover the flat galactic rotation curves (Mannheim & Kazanas, 1989). In this sense, the parameter γ can be related to both the dark matter/energy constituents of the spacetime, based on its value (for smaller values, it is mostly related to dark matter).

This spacetime is not asymptotically flat, however, its three-dimensional subspace has an asymptotic deficit of angle (Matos et al., 2002). Such effect is also intensified by the presence of the cloud of strings. Note that, for this particular choice for the w_q, the dimension of γ is m^{-1}.

Defining (Toshmatov et al., 2017; Toledo & Bezerra, 2020)

$$\rho(r) = M + \frac{\alpha r}{2} + \frac{\gamma r^2}{2}, \tag{6.4}$$

for a quintessential energy tensor $T_{\mu\nu} = (\varepsilon, P_r, P_\theta, P_\phi)$ with a constituent of cloud of strings, one can confirm that (Toledo & Bezerra, 2020)

$$\varepsilon = \frac{2\rho'}{8\pi} = -P_r, \tag{6.5a}$$

$$P_\theta = P_r - \frac{\rho'' r + 2\rho'}{8\pi r} = P_\phi, \tag{6.5b}$$

with primes denoting differentiation with respect to the r-coordinate, hold in the context of general relativity $G_{\mu\nu} = 8\pi T_{\mu\nu}$, where $G_{\mu\nu}$ is the Einstein tensor. Hence, the solution (6.3) can be regarded as a static black hole spacetime surrounded by a cloud of strings, that is located in a universe filled with quintessential dark energy. Note that, for a comoving time-like observer with a velocity four-vector field $u^\mu = (1,0,0,0)$, the values in Eq. (6.5) provide

$$T_{\mu\nu}u^\mu u^\nu = \frac{\alpha + 2\gamma r}{8\pi r^2}. \tag{6.6}$$

It is straightforward to verify that for the specific choice of $w_q = -\frac{2}{3}$, we have $0 < \gamma < \frac{(1-\alpha)^2}{8M} \equiv \gamma_c$, and hence, $T_{\mu\nu}u^\mu u^\nu > 0$. One can therefore infer that the weak energy condition (WEC) is respected. Note that $\gamma_c \to 0$ for $\alpha \to 1$, and $\gamma_c = \frac{1}{8M}$ for $\alpha \to 0$.

This black hole spacetime admits two horizons located at the real roots of the equation $B(r) = 0$, which are

$$r_{++} = \frac{1-\alpha}{\gamma}\cos^2\left[\frac{1}{2}\arcsin\left(\frac{2\sqrt{2M\gamma}}{1-\alpha}\right)\right], \tag{6.7}$$

$$r_{+} = \frac{1-\alpha}{\gamma}\sin^2\left[\frac{1}{2}\arcsin\left(\frac{2\sqrt{2M\gamma}}{1-\alpha}\right)\right], \tag{6.8}$$

denoting, respectively, the (quintessential) cosmological, and the event horizons, which will merge to $r_+ = r_{++} = r_s = 2M$ at the limits $\alpha \to 0$ and $\gamma \to 0$. Accordingly, one can re-express the lapse function as

$$B(r) = \frac{\gamma}{r}(r - r_+)(r_{++} - r). \tag{6.9}$$

Note that, for every specific choice of α within its allowed range, an extremal black hole is obtained for the case of $\gamma = \gamma_c$, with the only horizon located at $r_e = \frac{4M}{1-\alpha}$, whereas $\gamma > \gamma_c$ corresponds to a naked singularity.

6.1.2 Astrophysical implications

We now proceed with comparing the theoretical inferences of doing standard tests on the black hole, with the relevant observational data. Through this process, one can establish reliable bounds on the parameters of the spacetime. In what follows, we apply four distinct tests on the black hole, and infer appropriate numerical values of the parameters α and γ, according to which, the observational and experimental results can be recovered. Note that, since these tests are standard, their explanations can be therefore found in any textbook on general relativity. Hence, we skip the introductory notes and proceed directly to the calculations. We begin with calculating the precession in the perihelion of planetary orbits in the solar system.

The advance of the perihelion

An elementary method to study this effect was presented by Cornbleet (Cornbleet, 1993), which was later applied to other spacetimes (Cruz et al., 2005; Olivares & Villanueva, 2013). The general idea is to compare the Keplerian elliptic orbits in the Minkowski spacetime (presented in a Lorentzian coordinate system), with those given in the Schwarzschild coordinates. This way, the desired general relativistic corrections are emerged. Let us consider the unperturbed Lorentzian metric

$$ds^2 = -dt^2 + dr^2 + r^2 d\theta^2 + r^2 \sin^2\theta d\phi^2, \tag{6.10}$$

in the (t, r, θ, ϕ) coordinates, together with metric (6.1), which we now assume to be in the (t', r', θ, ϕ) coordinates. Accordingly, the relation between (t, r) and (t', r') can be given in the binomial approximations

$$dt' = \left(1 - \frac{\alpha}{2} - \frac{M}{r} - \frac{\gamma}{2} r\right) dt, \tag{6.11a}$$

$$dr' = \left(1 + \frac{\alpha}{2} + \frac{M}{r} + \frac{\gamma}{2} r\right) dr. \tag{6.11b}$$

Therefore, in the invariant plane $\theta = \frac{\pi}{2}$, the element of area in the Lorentzian system is $dA = \int_0^R r dr d\phi = \frac{1}{2} R^2 d\phi$, where R is the areal distance from the planet to the source. This way, the Kepler's second law can be cast as

$$\frac{dA}{dt} = \frac{1}{2} R^2 \frac{d\phi}{dt}. \tag{6.12}$$

On the other hand, in the Schwarzschild coordinates we have

$$\begin{aligned} dA' &= \int_0^R r dr' d\phi = \int_0^R \left(r + \frac{\alpha}{2} r + M + \frac{\gamma}{2} r^2\right) dr d\phi \\ &= \frac{R^2}{2}\left(1 + \frac{\alpha}{2} + \frac{2M}{R} + \frac{\gamma}{3} R\right) d\phi. \end{aligned} \tag{6.13}$$

Therefore, by means of the transformations (6.11), the Kepler's second law is written as

$$\begin{aligned} \frac{dA'}{dt'} &= \frac{1}{2} R^2 \left(1 + \frac{\alpha}{2} + \frac{2M}{R} + \frac{\gamma}{3} R\right) \frac{d\phi}{dt'} \\ &= \frac{1}{2} R^2 \left(1 + \frac{\alpha}{2} + \frac{2M}{R} + \frac{\gamma}{3} R\right) \left(1 + \frac{\alpha}{2} + \frac{M}{R} + \frac{\gamma}{2} R\right) \frac{d\phi}{dt} \\ &\simeq \frac{1}{2} R^2 \left(1 + \alpha + \frac{3M}{R} + \frac{4M\gamma}{3}\right) \frac{d\phi}{dt}. \end{aligned} \tag{6.14}$$

In fact, since the law must be held covariant in all coordinate systems, one can infer from Eqs. (6.12) and (6.14), that $d\phi' = (1 + \alpha + \frac{3M}{R} + \frac{4M\gamma}{3}) d\phi$. Accordingly, for an angular increment $\Delta\phi'$, one gets

$$\int_0^{\Delta\phi'} \mathrm{d}\phi' = \int_0^{\Delta\phi=2\pi} \left(1+\alpha+\frac{3M}{R}+\frac{4M\gamma}{3}\right)\mathrm{d}\phi, \tag{6.15}$$

for a single orbit. Knowing that $R = \frac{l}{(1+\varepsilon\cos\phi)}$, for an ellipse with the eccentricity ε and the semi-latus rectum l, one gets

$$\begin{aligned}\Delta\phi' &= 2\pi\left(1+\alpha+\frac{4M\gamma}{3}\right)+\frac{3M}{l}\int_0^{2\pi}(1+\varepsilon\cos\phi)\mathrm{d}\phi\\ &= 2\pi+\Delta\phi_{gr}+\Delta\phi_{cs}+\Delta\phi_{q},\end{aligned} \tag{6.16}$$

where

$$\Delta\phi_M = \frac{6\pi M}{l}, \tag{6.17a}$$

$$\Delta\phi_\alpha = 2\pi\alpha, \tag{6.17b}$$

$$\Delta\phi_\gamma = \frac{8\pi M\gamma}{3}, \tag{6.17c}$$

correspond, respectively, to the corrections due to general relativity, cloud of strings and quintessence.

To test the above relation in the solar system, we let $M = M_\odot = 1476.1$ m, and therefore, the advance of perihelion in arcseconds per century, is obtained as

$$\delta \equiv \Delta\phi' - 2\pi = 573.912\frac{v}{l} + 1.296v\alpha + 2.55072v\gamma, \tag{6.18}$$

in which, v corresponds to the number of orbits per year, l is given in 10^9 m, α is of order of 10^{-8}, and γ of $10^{-11}\ \mathrm{m}^{-1}$, in accordance with the observed planetary precession in the perihelion in the solar system (see Fig. 6.1).

Gravitational redshift

The famous frequency shift for photons passing a static source, can be inferred from the famous relation (Ryder, 2009)

$$\frac{\nu}{\nu_i} = \sqrt{\frac{B(r)}{B(r_i)}}. \tag{6.19}$$

which is a result of the existence of a time-like Killing vector associated with the spacetime. Here, (r_i, ν_i) and (r, ν) are, respectively, the initial and the observed values of the radial distance to the source and frequency. For the near-earth experiments, however, we have $\alpha \ll 1$ and $\gamma r \ll \frac{2M}{r}$. One can therefore approximate Eq. (6.19) as

$$\frac{\nu}{\nu_i} \simeq \left(\frac{\nu}{\nu_i}\right)_{\mathrm{gr}} + \left(\frac{r-r_i}{r_i r}\right)M\alpha - \frac{(r-r_i)}{2}\gamma, \tag{6.20}$$

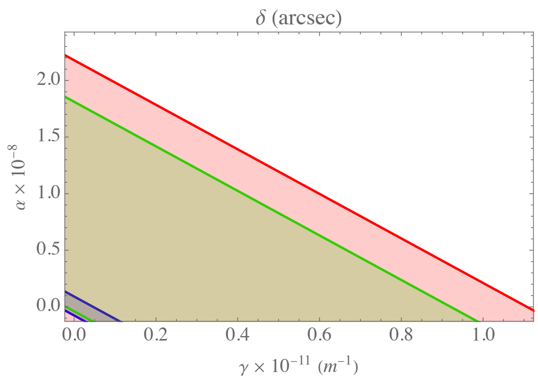

Figure 6.1: Constraining the parameters α and γ, based on the values for the precession in the perihelion of Mercury (blue lines), Venus (green lines), and Earth (red lines) (the respected values are given in the paper by Cornbleet (Cornbleet, 1993).

where

$$\left(\frac{\nu}{\nu_i}\right)_{\text{gr}} \equiv 1 - \frac{M}{r} + \frac{M}{r_i}, \tag{6.21}$$

is the general relativistic value due to the massive source, which has been tested with the hydrogen maser in the Gravity Probe A (GP-A) redshift experiment, with an accuracy of the order of 10^{-14} (Vessot et al., 1980). Accordingly, the following constraint is obtained:

$$\left|\left(\frac{r - r_i}{r_i r}\right) M\alpha - \frac{(r - r_i)}{2}\gamma\right| \lesssim 10^{-14}. \tag{6.22}$$

Comparing the initial position $r_i = r_\oplus$ on the Earth of mass $M = M_\oplus = 4.453 \times 10^{-3}$ m, and the observer on a satellite at a height of 15000 km above the Earth, the above relation yields

$$|4.877\alpha - 7.5\gamma| \lesssim 1, \tag{6.23}$$

which constrains $\alpha \sim 10^{-4}$ and $\gamma \sim 10^{-20}\text{m}^{-1}$ (see Fig. 6.2).

Deflection of light

The process of light deflection, or the so-called gravitational lensig, can be approached, theoretically, by means of the geodesic equations for the light rays (null geodesics). Indicating $\dot{x}^\mu \equiv \frac{\mathrm{d}x^\mu}{\mathrm{d}s}$, one can get from the line element (6.1) that

$$\epsilon = -\frac{E^2}{B(r)}\dot{t}^2 + \frac{\dot{r}^2}{B(r)} + \frac{L^2}{r^2}, \tag{6.24}$$

where $E \equiv B(r)\dot{t}$ and $L \equiv r^2\dot{\phi}$ are the constants of motion, and as in the previous subsections, we have considered the equatorial trajectories corresponding to $\theta = \frac{\pi}{2}$.

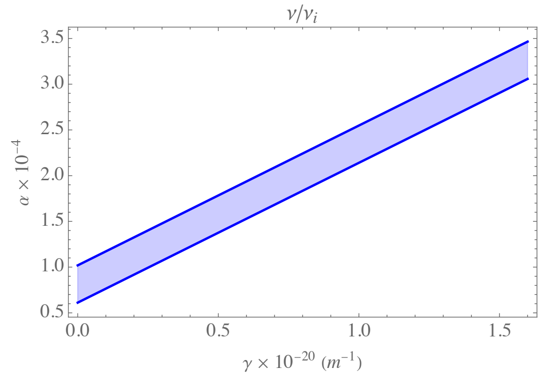

Figure 6.2: The confidence range for α and γ, in accordance with the redshift observed in the GP-A (Vessot et al., 1980).

The parameter ϵ indicates the nature of the geodesics, in the sense that the null and the time-like trajectories are identified, respectively, by $\epsilon = 0$, and $\epsilon = -1$. Accordingly, the first order, angular, equation of motion for the light rays (i.e. photons as the test particles) passing the black hole, is given by

$$\left(\frac{\dot{r}}{\dot{\phi}}\right)^2 = \left(\frac{\mathrm{d}r}{\mathrm{d}\phi}\right)^2 = \frac{r^4}{b^2} - (1-\alpha)r^2 + 2Mr + \gamma r^3, \tag{6.25}$$

with b as the impact parameter. Performing the change of variable $r \doteq \frac{1}{u}$, the above equation yields

$$\left(\frac{\mathrm{d}u}{\mathrm{d}\phi}\right)^2 = \frac{1}{b^2} - (1-\alpha)u^2 + 2Mu^3 + \gamma u, \tag{6.26}$$

that reduces to the standard Schwarzschild equation of light deflection in the limit of $\alpha \to 0$ and $\gamma \to 0$. Differentiating Eq. (6.26) with respect to ϕ, gives

$$u'' + u = 3Mu^2 + \alpha u + \frac{\gamma}{2}, \tag{6.27}$$

where the primes denote differentiations with respect to ϕ. Following the procedure established by Straumann (Straumann, 2013), we obtain

$$u = \frac{1}{b}\sin\phi + \frac{3M}{2b^2} + \frac{\alpha\sqrt{2}}{2b} + \frac{\gamma}{2} + \left(\frac{M}{2b^2} + \frac{\alpha\sqrt{2}}{12b}\right)\cos(2\phi). \tag{6.28}$$

Note that, $u \to 0$ results in $\phi \to \phi_\infty$, with

$$-\phi_\infty = \frac{2M}{b} + \frac{7\alpha\sqrt{2}}{12} + \frac{\gamma b}{2}. \tag{6.29}$$

The deflection angle of the light rays passing the black hole is, therefore, obtained as

$$\hat{\vartheta} = 2\left|-\phi_\infty\right| = \frac{4M}{b} + \frac{7\alpha\sqrt{2}}{6} + \gamma b, \tag{6.30}$$

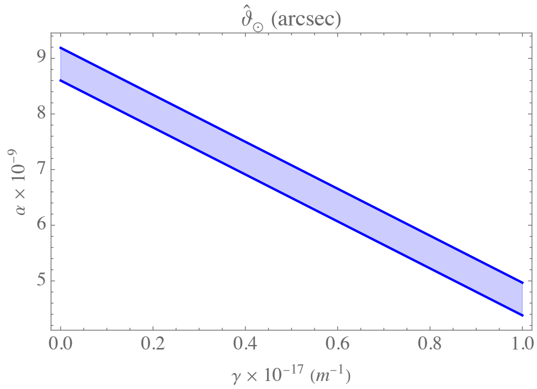

Figure 6.3: The constraints on α and γ for the deflection angle of the Sun.

which recovers the famous form of $\hat{\vartheta}_{\mathrm{Sch}} = \frac{4M}{b}$ for the SBH in the limits $\alpha \to 0$ and $\gamma \to 0$. This latter, if applied for the Sun as the massive source, provides $\hat{\vartheta}_{\mathrm{Sch}} = \frac{4M_{\odot}}{R_{\odot}} = 1.75092$ arcsec. Note that, the observed deflection angle by the Sun has been measured as $\hat{\vartheta}_{\odot} = 1.7520$ arcsec for the prograde position, and $\hat{\vartheta}_{\odot} = 1.7519$ arcsec for the retrograde one (Roy & Sen, 2019), which produces an error of about 0.0001 arcsec. This error constrains the parameters as $\alpha \sim 10^{-9}$ and $\gamma \sim 10^{-17}\mathrm{m}^{-1}$ (see Fig. 6.3).

Gravitational time delay

Claimed as the fourth test of general relativity, the Shapiro time delay has appeared as an interesting effect which is of observational significance. This effect, which refers to the delay in the radar echos of the electromagnetic signals passing massive objects, was proved experimentally by, approximately, the same time of its proposition (Shapiro, 1964; Shapiro et al., 1968). Furthermore, as inferred from recent astrophysical observations, this effect can be seen for two other mass-less energy propagators, namely the neutrinos and the gravitational waves, which act in favor of the existence of dark matter (Boran et al., 2018). Here, we proceed with the determination of the resultant Shapiro effect for photons that pass the black hole, by calculating the time difference between the emission and the observation of a light ray, which is sent from the point $P_1 = (t_1, r_1)$, travels to $P_2 = (t_2, r_2)$, and returns back to P_1. Accordingly, we are concerned with the time interval

$$t_{12} = 2\,t(r_1, \rho_0) + 2\,t(r_2, \rho_0), \tag{6.31}$$

with ρ_0 as closest approach to the black hole. Taking into account the definitions given in the previous subsection, we have

$$\dot{r} = \dot{t}\frac{\mathrm{d}r}{\mathrm{d}t} = \frac{E}{B(r)}\frac{\mathrm{d}r}{\mathrm{d}t}, \tag{6.32}$$

from which, one can recast Eq. (6.24) as

$$\frac{E}{B(r)}\frac{\mathrm{d}r}{\mathrm{d}t} = \sqrt{E^2 - \frac{L^2}{r^2}B(r)}, \tag{6.33}$$

for mass-less particles. According to the fact that at $r = \rho_0$, the radial velocity of the test particle is vanished, it is straightforward to infer $b^{-2} = \frac{B(\rho_0)}{\rho_0^2}$. This way, the coordinate time is found to vary as

$$t(r,\rho_0) = \int_{\rho_0}^{r} \frac{\mathrm{d}r}{B(r)\sqrt{1 - \frac{\rho_0^2}{B(\rho_0)}\frac{B(r)}{r^2}}}, \tag{6.34}$$

during its journey from ρ_0 to r. So, to the first order of corrections we obtain

$$t(r,\rho_0) \approx \sqrt{r^2 - \rho_0^2} + t_M(r,\rho_0) + t_\alpha(r,\rho_0) + t_\gamma(r,\rho_0), \tag{6.35}$$

where

$$t_M(r,\rho_0) = M\left[\sqrt{\frac{r-\rho_0}{r+\rho_0}} + 2\ln\left(\frac{r+\sqrt{r^2-\rho_0^2}}{\rho_0}\right)\right], \tag{6.36a}$$

$$t_\alpha(r,\rho_0) = \alpha\sqrt{r^2-\rho_0^2}, \tag{6.36b}$$

$$\begin{aligned} t_\gamma(r,\rho_0) = \gamma\rho_0^2&\left[\sqrt{\frac{r-\rho_0}{r+\rho_0}} - \ln\left(\frac{r+\sqrt{r^2-\rho_0^2}}{\rho_0}\right)\right] \\ &+ \frac{\gamma}{2}\left[r\sqrt{r^2-\rho_0^2} + \rho_0^2\ln\left(\frac{r+\sqrt{r^2-\rho_0^2}}{\rho_0}\right)\right]. \end{aligned} \tag{6.36c}$$

Defining the time difference $\Delta t := t_{12} - t_{12}^E$ as the delay for the journey $P_1 \to P_2 \to P_1$, with $t_{12}^E = 2\left(\sqrt{r_1^2-\rho_0^2} + \sqrt{r_2^2-\rho_0^2}\right)$ being the travel time interval between the same points in the Euclidean space, one obtains

$$\Delta t = \Delta t_M + \Delta t_\alpha + \Delta t_\gamma, \tag{6.37}$$

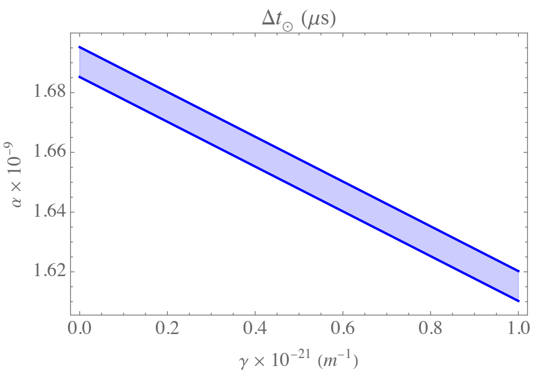

Figure 6.4: The constraints of α and γ regarding the time delay in the solar system.

in which

$$\Delta t_M = 2M\left[\sqrt{\frac{r_1-\rho_0}{r_1+\rho_0}}+\sqrt{\frac{r_2-\rho_0}{r_2+\rho_0}}+2\ln\left(\frac{\tilde{\mathfrak{t}}^E_{12}}{\rho_0^2}\right)\right], \tag{6.38a}$$

$$\Delta t_\alpha = \alpha t^E_{12}, \tag{6.38b}$$

$$\Delta t_\gamma = 2\gamma\,\rho_0^2\left[\sqrt{\frac{r_1-\rho_0}{r_1+\rho_0}}+\sqrt{\frac{r_2-\rho_0}{r_2+\rho_0}}-\ln\left(\frac{\tilde{\mathfrak{t}}^E_{12}}{\rho_0^2}\right)\right] + \gamma\left[r_1\sqrt{r_1^2-\rho_0^2}+r_2\sqrt{r_2^2-\rho_0^2}+\rho_0^2\,\ln\left(\frac{\tilde{\mathfrak{t}}^E_{12}}{\rho_0^2}\right)\right], \tag{6.38c}$$

and $\tilde{\mathfrak{t}}^E_{12} = \left(r_1+\sqrt{r_1^2-\rho_0^2}\right)\left(r_2+\sqrt{r_2^2-\rho_0^2}\right)$. The expression in Eq. (6.37) is, therefore, the time delay in the echo of light rays passing the black hole. In order to achieve a sensible value for this delay, let us confine ourselves to the solar system, which demands $\rho_0 \ll r_1, r_2$. This way, the above difference is approximated as

$$\Delta t_\odot \approx 4M\left[1+\ln\left(\frac{4r_1r_2}{\rho_0^2}\right)\right]+2\alpha(r_1+r_2)+\gamma\left[r_1^2+r_2^2-\rho_0^2\ln\left(\frac{4r_1r_2}{\rho_0^2}\right)\right]. \tag{6.39}$$

Hence, by letting $M \to M_\odot$, $\alpha \to 0$, and $\gamma \to 0$, we recover $\Delta t_{\text{Sch}} = 4M_\odot\left[1+\ln\left(\frac{4r_1r_2}{\rho_0^2}\right)\right]$, as the Schwarzschild limit of the Shapiro time delay in the solar system. Considering r_1 and r_2 to be, respectively, the Earth-Sun and the Sun-Mars distances, and $\rho_0 \approx R_\odot + (5\times 10^6)$ m, as the approximate radial distance from the Sun's center to its corona, one calculates $\Delta t_{\text{Sch}} \approx 246$ ¯s. Note that, the measured error in the observed time difference for the round trip during the Viking mission was about 10 ns (Reasenberg et al., 1979). This is related to the confidence values $\alpha \sim 10^{-9}$ and $\gamma \sim 10^{-21}\text{m}^{-1}$ (see Fig. 6.4).

6.1.3 Black hole's response to gravitational perturbations and the quasi-normal modes

The damping oscillations of the field perturbations in the black hole spacetimes, or the black holes' quasi-normal modes (QNMs), have been of interest among astrophysicists, because of their direct relation to the propagation of the gravitational waves. In fact, the late-time wave form of the black hole ringing is typically identified by a QN frequency (Vishveshwara, 1970; Press, 1971; Goebel, 1972), which has raised in importance ever since the recent detection of the gravitational waves (Abbott et al., 2016b,a). The QNMs are therefore absorbing a great deal of attention from the scientific community, since they are also applicable in the gravitational wave astronomy (Schutz, 1987; Kokkotas & Schmidt, 1999; Marranghello, 2007; Ferrari & Gualtieri, 2008; Paschalidis & Stergioulas, 2017). In a more general view, the QNMs are responses of the black holes (or stars) to perturbations. For the SBH surrounded by a cloud of strings, the QNMs have been recently calculated (Graça et al., 2017; Cai & Miao, 2020). For scalar perturbations, the scalar QNMs for a RN black hole associated with quintessence and cloud of strings have been given by Toledo and Bezerra (Toledo & Bezerra, 2019). In this subsection, we continue with calculating the QNMs for the Schwarzschild case, however, we take into account the gravitational perturbations, and confine ourselves to the parameter values that have been determined in the previous subsection. For the black hole under consideration, the metric can be perturbed as

$$\mathfrak{g}_{\mu\nu} = g_{\mu\nu} + h_{\mu\nu}, \tag{6.40}$$

according to which, the Einstein equation varies as $\delta G_{\mu\nu} = 8\pi\delta T_{\mu\nu}$. This perturbation problem can be reduced to a single wave equation, by decomposing it into tensorial spherical harmonics, in the following manner (Kokkotas & Schmidt, 1999):

$$\chi(x^\mu) = \sum_{\ell,m} \frac{X_{\ell,m}(t,r)}{r} Y_{\ell,m}(\theta,\phi), \tag{6.41}$$

where the function $X_{\ell,m}(t,r)$ is, in fact, a combination of the all ten independent components of $h_{\mu\nu}$. Note that, since the spacetime under consideration is spherically symmetric, one can omit the index m in the spherical harmonics. Accordingly, we consider the Schrödinger-like wave equation

$$\frac{\partial^2 X_\ell}{\partial t^2} - \left(\frac{\partial^2}{\partial r_*^2} - V_\ell(r)\right) X_\ell = 0, \tag{6.42}$$

to govern the radial perturbations outside the event horizon, in which

$$r_* = \frac{r_+ \ln(r - r_+) - r_{++} \ln(r_{++} - r)}{\gamma(r_{++} - r_+)}, \tag{6.43}$$

is the corresponding "tortoise" radial coordinates obeying $\mathrm{d}r_* = \frac{\mathrm{d}r}{B(r)}$, and $V_\ell(r)$ is the Regge-Wheeler effective potential (Regge & Wheeler, 1957). The above equation admits two kinds of perturbations, each of which, has an appropriate parity of the effective potential:

- For the odd-parity (axial) perturbations, that transform as $(-1)^{\ell+1}$ under the parity transformation, we have

  $$V_\ell^-(r) = B(r)\left[\frac{\ell(\ell+1)}{r^2} + \frac{\sigma}{r}B'(r)\right], \tag{6.44}$$

  where $\sigma = 0, 1$ and -3, correspond, respectively, to the electromagnetic, scalar, and gravitational perturbations.

- For the even-parity (polar) perturbations, that transform as $(-1)^\ell$ under the parity transformation, we have

  $$V_\ell^+(r) = \frac{2B(r)}{r^3}\left[\frac{9M^3 + 9kM^2 r + 3k^2 M r^2 + k^2(k+1)r^3 - 9Mr(\alpha + \gamma r)}{(3M + kr)^2}\right], \tag{6.45}$$

  where $2k = (\ell - 1)(\ell + 2)$. For the case of $\alpha = \gamma = 0$, the above relation reduces to the Zerilli effective potential for the perturbations on SBH (Zerilli, 1970).

The potentials have a peak near $r = r_+$, and clearly, they both vanish at the horizons. Considering this, and among several methods in the calculation of the QNMs (Kokkotas & Schmidt, 1999), we apply the Schutz-Will semi-analytic formula (Schutz & Will, 1985)

$$\begin{aligned}(M\omega_n)^2 &= V_\ell(r_0) - i\left(n + \frac{1}{2}\right)\sqrt{-2\frac{\mathrm{d}^2 V_\ell(r_0)}{\mathrm{d}r_*^2}} \\ &= V_\ell(r_0) - i\left(n + \frac{1}{2}\right)\sqrt{-2B(r_0)\frac{\mathrm{d}}{\mathrm{d}r}\left[B(r_0)\frac{\mathrm{d}V_\ell(r_0)}{\mathrm{d}r}\right]},\end{aligned} \tag{6.46}$$

which originates from the WKB method of solving the wave scattering problem. Here, ω_n is the complex QNM frequency, and r_0 is the aforementioned potential peak at the vicinity of the event horizon.

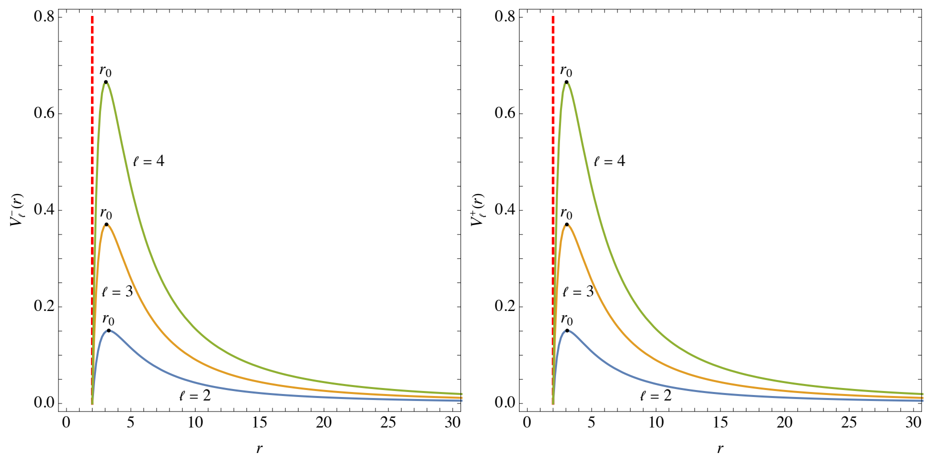

Figure 6.5: The Regge-Wheeler effective potentials, plotted for $\alpha = 2 \times 10^{-8}$, $\gamma = 2 \times 10^{-20} \frac{1}{M}$, and the three cases of $\ell = 2, 3$ and 4. The red dashed line indicates the event horizon, and for each of the cases, the potential peak has been indicated by r_0. The behavior of the potentials are the same up to 5.54% of difference. The unit of length along the axes is M, and the gravitational perturbations have been taken into account.

Let us consider the fundamental mode, that corresponds to $\ell = 2$ and $n = 0$. Accordingly, and applying the potential (6.44) with $\sigma = -3$, we get

$$M\omega_0 = \frac{1}{r_0^2}\Big[-ir_0\sqrt{-120M^2 - 36(\alpha - 3)Mr_0 + 3r_0^2\left[\alpha(\gamma r_0 + 6) + \gamma r_0 - 6\right]} \\ + 12M^2 + 6(\alpha - 3)Mr_0 - 3r_0^2(\gamma r_0 + 2)(\alpha + \gamma r_0 - 1)\Big]^{\frac{1}{2}}. \quad (6.47)$$

The determination of the modes however depends explicitly on the values of α and γ, which also identify r_0 for each of the cases. To elaborate this, we consider Fig. 6.5, where we have plotted the potentials given in Eqs. (6.45) and (6.44), based on definite values of the metric parameters which have been constrained in the previous subsection in accordance with the observational data, for $\ell = 2, 3$, and 4, and for the case of gravitational perturbations ($\sigma = -3$). Based on the small difference revealed from the potentials $V_\ell^{\mp}(r)$, we take into account the critical distance r_0, which is inferred from V_ℓ^-, reading as $r_0 \approx 3.28M$. This way, the fundamental mode is calculated as $M\omega_0 \approx 0.44 - 0.21\mathrm{i}$. To infer the corresponding value in kHz, one needs to multiply it by $2\pi(5142\,\mathrm{Hz}) \times (\frac{M_\odot}{M})$, which provides the frequency of approximately 1.4 kHz with the damping time 0.66 ms, for a black hole of $M = 10M_\odot$. The first four QNMs of the black hole have been given in Table 6.1, for $\ell = 2, 3$ and 4. Furthermore, in Fig. 6.6, more modes have been shown in the complex plane, whose number for each value of the harmonic index ℓ, can be infinite (Bachelot & Motet-Bachelot, 1993; Ferrari &

n	$\ell = 2$	$\ell = 3$	$\ell = 4$
0	0.43973 − 0.205123i	0.65644 − 0.243493i	0.857432 − 0.260443i
1	0.597172 − 0.453131i	0.836703 − 0.573103i	1.04025 − 0.644016i
2	0.730026 − 0.617779i	1.00316 − 0.79668i	1.22435 − 0.911962i
3	0.843535 − 0.748508i	1.14892 − 0.97385i	1.38999 − 1.1246i

Table 6.1: The first four QNMs of the black hole for $\ell = 2, 3$, and 4, regarding the parameters given in Fig. 6.5.

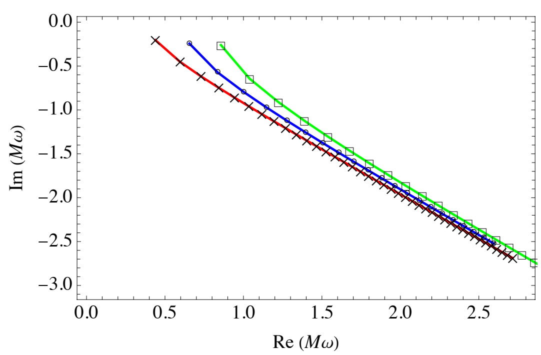

Figure 6.6: The spectrum of the QNMs for $\ell = 2$ (red), $\ell = 3$ (blue), and $\ell = 4$ (green).

Mashhoon, 1984). Also, as it can be seen from the diagrams, the absolute values of the imaginary parts of the frequencies grow rapidly, which implies that the higher modes do not contribute significantly in the emitted gravitational wave signals. This can been seen, as well, in a single mode by growing ℓ.

Taking into account the astrophysical constraints we made on the spacetime's parameters, the above QNMs are the most reliable ones for the black hole, since they relate to the confidence level of the aforementioned parameters.

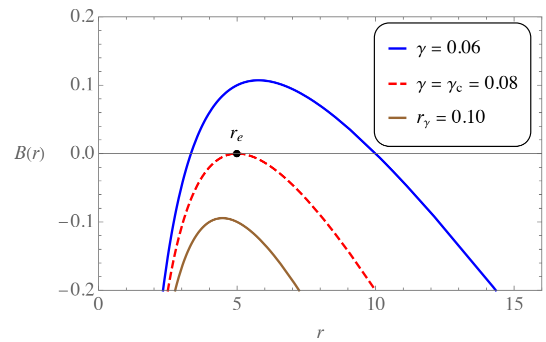

Figure 6.7: Plot of the lapse function for different values of the γ parameter. For this diagram and all the forthcoming ones, we have considered $\alpha = 0.2$, and the unit of length along the axes is M. This way, the extremal horizon will be located at $r_e = 5$.

6.2 Study of time-like and null geodesics

In this section, in addition to the cases of radial and circular orbits studied by Mustafa and Hussain (Mustafa & Hussain, 2021) for the black hole under study in this chapter, we also present an analytical investigation of general angular orbits for both of the null and time-like geodesics, that include deflecting trajectories, critical and planetary orbits. Furthermore, for the aforementioned radial and circular orbits, we apply special elliptic integration methods that enable us expressing the solutions in the more compact and aesthetic Weierstraßian forms. In order to complete the work done in the above reference, we go deeper into these kind of orbits by classifying them in accordance with their corresponding effective potentials. In particular, to provide more perception, the radial orbits are plotted for each of these cases.

However, before proceeding with this, let us turn our attention to the behavior of the lapse function (6.3) which has been shown in Fig. 6.7 for different values of γ. The infinite redshift happens when the curves pass the $B(r) = 0$ line for the first time (at the event horizon), whereas, the infinite blueshift happens when they pass this line for the second time (at the cosmological horizon). The corresponding extremal horizon r_e, has been also indicated in this diagram.

6.2.1 Particle dynamics

Following the Lagrangian method exploited in the previous chapters, we define

$$\mathcal{L} = \frac{1}{2} g_{\mu\nu} \dot{x}^{\mu} = -\frac{1}{2}\epsilon, \tag{6.48}$$

that provides the radial evolution equation

$$\dot{r}^2 = E^2 - V_{\text{eff}}(r), \tag{6.49}$$

with

$$V_{\text{eff}}(r) = B(r)\left[\epsilon + \frac{L^2}{r^2}\right], \tag{6.50}$$

and the two other equations

$$\left(\frac{\mathrm{d}r}{\mathrm{d}t}\right)^2 = B^2(r)\left[1 - \frac{V_{\text{eff}}(r)}{E^2}\right], \tag{6.51}$$

$$\left(\frac{\mathrm{d}r}{\mathrm{d}\phi}\right)^2 = \frac{r^4}{L^2}\left[E^2 - V_{\text{eff}}(r)\right]. \tag{6.52}$$

6.2.2 Radial motion

The test particles with $L = 0$ are of great importance, since in the case of null geodesics they can construct the casual structure of the spacetime, and in the case of time-like geodesics, the difference between the perception of comoving and distant observers of infalling objects onto the black hole, is revealed. We begin with the null radial geodesics and continue with the time-like ones.

Null geodesics

Letting $\epsilon = 0$, one can then see from Eq. (6.50) that for the radially moving massless particles (e.g. photons), we have $V_{\text{eff}}(r) = 0$. Accordingly, Eqs. (6.49) and (6.51) become

$$\dot{r} = \pm E, \tag{6.53}$$

$$\frac{\mathrm{d}r}{\mathrm{d}t} = \pm B(r). \tag{6.54}$$

Note that, the sign $+$ $(-)$ corresponds to the photons falling onto the cosmological (event) horizon. Choosing the initial radial distance $r = r_i$ for $t = \tau = 0$, and regarding the expression in Eq. (6.9), the above two equations provide the solutions

$$\tau(r) = \pm\frac{r - r_i}{E}, \tag{6.55}$$

$$t(r) = \pm\frac{1}{\gamma(r_{++} - r_+)}\left[r_+ \ln\left|\frac{r - r_+}{r_i - r_+}\right| - r_{++}\ln\left|\frac{r_{++} - r}{r_{++} - r_i}\right|\right]. \tag{6.56}$$

In Fig. 6.8, the above solutions have been demonstrated.

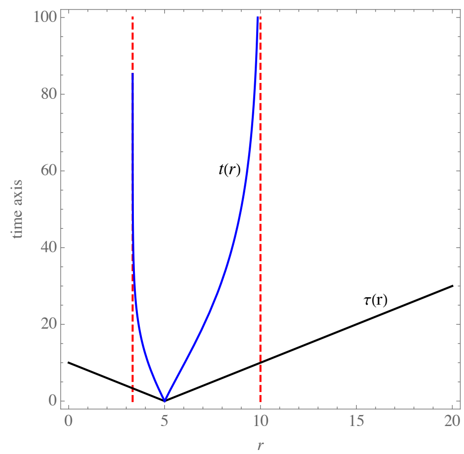

Figure 6.8: The radial null geodesics plotted for $\gamma = 0.06$, $E = 0.5$ and $r_i = 5$. The diagrams indicate the asymptotic behavior of $t(r)$ (blue curves) and horizon crossing of $\tau(r)$ (black lines).

Time-like geodesics

By letting $\epsilon = 1$ and $L = 0$ in Eq. (6.50), the radial effective potential $V_r(r)$ for time-like trajectories is obtained, whose profile has been shown in Fig. 6.9. Accordingly, the motion becomes unstable where $V_r'(r) = 0$, solving which, yields

$$d_u = \sqrt{\frac{2M}{\gamma}}, \tag{6.57}$$

as the maximum distance of the unstable motion. Taking into account $E_u^2 \equiv V_r(d_u) = 1 - \alpha - 2\sqrt{2M\gamma}$, the possible radial orbits are then categorized as follows, based on the value of E compared with its critical value E_u:

- *Frontal scatterings of the first and the second kind (FSFK and FSSK)*: For $0 < E^2 < E_u^2$, the potential allows for the turning point d_s ($d_u < d_s < r_{++}$) corresponding to the scattering distance (FSFK). In the case of $0 < E^2 < E_u^2$, another turning point d_f ($r_+ < d_f < d_u$) occurs for those trajectories that fall onto the event horizon and are captured (RSSK).

- *Critical radial motion*: For $E^2 = E_u^2$, the test particles that come from the initial distance d_i ($d_u < d_i < r_{++}$) fall on the unstable radius d_u, and those that come from d_0 ($r_+ < d_0 < d_u$), cross the horizon.

- *Radial capture*: For $E^2 > E_u^2$, particles approaching a finite distance d_j ($r_+ < d_j < r_{++}$), fall directly onto the event horizon.

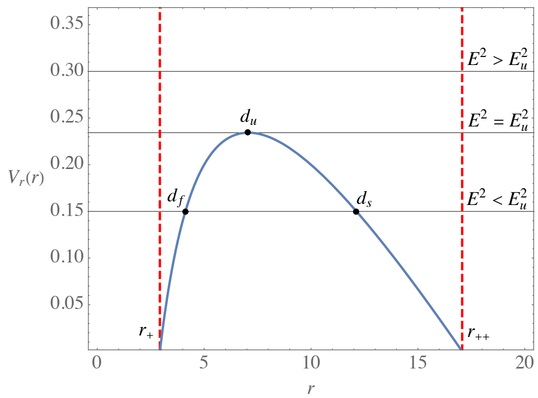

Figure 6.9: The effective potential for radially moving massive particles plotted for $\gamma = 0.04$. In this particular case, the maximum distance of unstable orbit, is $d_u = 7.07$ in accordance with $E^2 = E_u^2 = 0.23$, and the two turning points $d_s = 12.3$ and $d_f = 4.12$ have been indicated in accordance with the corresponding value $E^2 = 0.15$. The point d_s is related to the distance, at which, the particles $0 < E^2 < E_u^2$, experience their frontal scattering.

Now, to formulate the time-like radial orbits, let us recall the radial velocity relations

$$\dot{r}^2 = \frac{\gamma\,\mathfrak{p}(r)}{r}, \tag{6.58}$$

$$\left(\frac{\mathrm{d}r}{\mathrm{d}t}\right)^2 = \frac{\gamma^3(r-r_+)^2(r_{++}-r)^2\mathfrak{p}(r)}{E^2r^3}, \tag{6.59}$$

which are inferred from Eqs. (6.9), (6.49) and (6.51), with

$$\mathfrak{p}(r) \equiv r^2 - \left(\frac{1-\alpha-E^2}{\gamma}\right) r + \frac{2M}{\gamma}. \tag{6.60}$$

In general, the equation $\mathfrak{p}(r) = 0$ is satisfied at any turning point for the radial orbits. We continue by discussing the frontal scatterings.

FSFK and FSSK

The polynomial (6.60) vanishes for the two radii

$$d_s = \frac{1-\alpha-E^2}{\gamma}\cos^2\left(\frac{1}{2}\arcsin\left(\frac{2\sqrt{2M\gamma}}{1-\alpha-E^2}\right)\right), \tag{6.61}$$

$$d_f = \frac{1-\alpha-E^2}{\gamma}\sin^2\left(\frac{1}{2}\arcsin\left(\frac{2\sqrt{2M\gamma}}{1-\alpha-E^2}\right)\right). \tag{6.62}$$

For the case of FSFK that occurs at $r = r_s$, the differential equation (6.58) provides the solution

$$\tau(U) = \frac{d_s}{4\sqrt{\gamma d_f}}\left[F(U_s) - F(U)\right], \tag{6.63}$$

where

$$F(U) = \frac{1}{\wp'(\Omega_s)}\left[\ln\left|\frac{\sigma\left(\text{ß}(U)-\Omega_s\right)}{\sigma\left(\text{ß}(\text{U})+\Omega_s\right)}\right| + 2\zeta(\Omega_s)\text{ß}(U)\right]. \tag{6.64}$$

In Eq. (6.64)

$$U(r) = \frac{d_s}{4r} - \frac{d_s+d_f}{12d_f}, \tag{6.65a}$$

$$U_s = \frac{1}{4} - \frac{d_s+d_f}{12d_f}, \tag{6.65b}$$

$$\Omega_s = \text{ß}\left(-\frac{d_s+d_f}{12d_f}\right), \tag{6.65c}$$

$$\tag{6.65d}$$

and the corresponding Weierstraß invariants are

$$g_2 = \frac{1}{12d_f^2}\left(d_s^2 - d_s d_f + d_f^2\right), \tag{6.66a}$$

$$g_3 = \frac{1}{432d_f^3}(d_s-2d_f)(d_s-d_f)(2d_s-d_f). \tag{6.66b}$$

The solution in Eq. (6.63) corresponds to the radial evolution of the proper time for comoving observers. For the case of distant observers, one can integrate Eq. (6.59), that yields

$$t(U) = \delta_0\sum_{k=1}^{2}\delta_k\left[F_k(U_s) - F_k(U)\right], \tag{6.67}$$

with the same expressions for $U(r)$ and U_s as in Eqs. (6.65a) and (6.65b). In the above solution, we have defined

$$F_k(U) = \frac{1}{\wp'(\Omega_k)}\left[\ln\left|\frac{\sigma\left(\text{ß}(U)-\Omega_k\right)}{\sigma\left(\text{ß}(U)+\Omega_k\right)}\right| + 2\zeta(\Omega_k)\text{ß}(U)\right], \tag{6.68}$$

for which the Weierstraß invariants are those in Eqs. (6.66), and

$$\delta_0 = \frac{Ed_s}{4\gamma\sqrt{\gamma d_f}(r_{++}-r_+)}, \tag{6.69a}$$

$$\delta_1 = 1, \tag{6.69b}$$

$$\delta_2 = -1, \tag{6.69c}$$

$$\Omega_1 = \text{ß}\left(\frac{d_s}{4r_{++}} - \frac{d_s+d_f}{12d_f}\right), \tag{6.69d}$$

$$\Omega_2 = \text{ß}\left(\frac{d_s}{4r_+} - \frac{d_s+d_f}{12d_f}\right). \tag{6.69e}$$

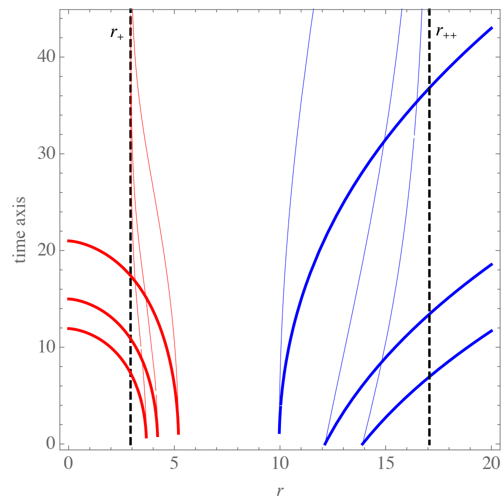

Figure 6.10: The plots of FSFK (blue) and FSSK (red), for $\gamma = 0.04$ and in accordance with three different energies $E^2 = 0.1, 0.15$ and 0.21 (from bottom to top), corresponding to three different initial points for each of the cases (i.e. d_s for FSFK and d_f for FSSK). The thick curves show the radial evolution of the proper time $\tau(r)$, whereas the thin ones demonstrate that of the coordinate time $t(r)$.

The above solutions describe radially moving particles on the FSFK, which are scattered at the distance d_s. Accordingly, to obtain the solutions for the FSSK, it is enough to do the change $d_s \to d_f$ in the above solutions, and reverse the direction of the radial propagation. The frontal scatterings of time-like geodesics have been shown in Fig. 6.10, for both of the FSFK and FSSK.

Critical radial motion

Particles with $E^2 = E_u^2$, can approach from two directions, initiating from either the radial distance d_i ($d_u < d_i < r_{++}$), or from d_0 ($r_+ < d_0 < d_u$), each of which, lead to a different fate. We distinguish these fates, respectively by regions (I) and (II), as indicated in Fig. 6.11. Solving the temporal equation (6.58), and by taking into account the fact that for critical orbits the characteristic polynomial changes its form to $\mathfrak{p}(r) = (r - d_u)^2$, we then obtain

$$\tau_{\mathrm{I}}(r) = \pm \left[\tau_A(r, d_u) - \tau_A(d_i, d_u)\right], \tag{6.70a}$$

$$\tau_{\mathrm{II}}(r) = \mp \left[\tau_A(r, d_u) - \tau_A(d_0, d_u)\right], \tag{6.70b}$$

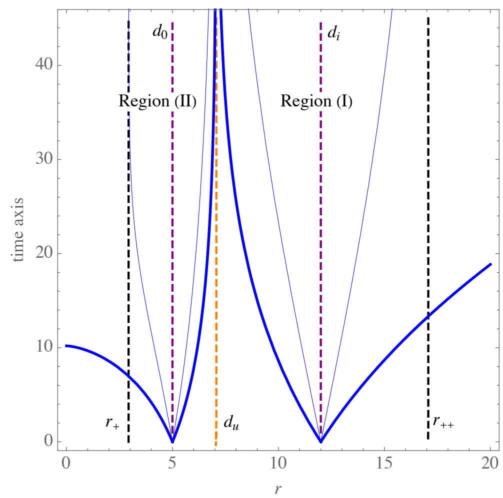

Figure 6.11: The critical radial motion in regions (I) and (II), plotted for comoving (thick curves) and distant (thin curves) observers, for the case of $\gamma = 0.04$. This value provides $d_u = 7.07$ corresponding to $E_u^2 = 0.23$. The trajectories have been specified for particles approaching from $d_0 = 5$ and $d_i = 12$.

where we have defined the function

$$\tau_A(r, y) = 2\sqrt{\frac{r}{\gamma}} - 2\sqrt{\frac{y}{\gamma}}\text{arctanh}\left(\sqrt{\frac{r}{y}}\right). \tag{6.71}$$

For the distant observes and to obtain the evolution of the t-coordinate, we integrate Eq. (6.59), which results in

$$t_{\mathrm{I}}(r) = \pm E_u \sum_{n=1}^{3} \varpi_n \left[t_n(r) - t_n(d_i)\right], \tag{6.72a}$$

$$t_{\mathrm{II}}(r) = \mp E_u \sum_{n=1}^{3} \varpi_n \left[t_n(r) - t_n(d_0)\right], \tag{6.72b}$$

with

$$t_1(r) = \tau_A(r, r_{++}), \tag{6.73a}$$

$$t_2(r) = \tau_A(r, r_{+}), \tag{6.73b}$$

$$t_3(r) = \tau_A(r, d_u), \tag{6.73c}$$

and

$$\varpi_1 = \frac{-r_{++}}{\gamma\,(r_{++} - r_+)(r_{++} - d_u)}, \tag{6.74a}$$

$$\varpi_2 = \frac{-r_+}{\gamma\,(r_{++} - r_+)(d_u - r_+)}, \tag{6.74b}$$

$$\varpi_3 = \frac{d_u}{\gamma\,(r_{++} - d_u)(d_u - r_+)}. \tag{6.74c}$$

The critical radial motion of the temporal coordinates has been plotted in Fig. 6.11, in accordance with the above solutions and for the two different initial distances d_i and d_0, that generate the discussed regions.

6.2.3 Angular motion

Here, we analyze the angular motion of mass-less and massive particles, by solving the angular equation of motion (6.52). As before, we apply the methods of integrating the elliptic integrals that appear in the course of this study. In a spacial occasion, a hyper-elliptic integral is generated for the case of planetary orbits of massive particles. This integral will be dealt with by means of a particular form of the Lauricella hypergeometric function.

Null geodesics

For the case of $\epsilon = 0$ in Eq. (6.50), the effective potential for the angular null geodesics becomes

$$V_n(r) = \frac{\gamma L^2}{r^3}\,(r - r_+)\,(r_{++} - r)\,, \tag{6.75}$$

which has been plotted in Fig. 6.12. It can be checked that raising and lowering L, changes only the scale of the axes, not the shape of the effective potential. So, the one given in Fig. 6.12, can categorize all the possible null orbits. As before, the turning points are where $E^2 = V_n(r_t)$ is satisfied, which for the case of angular geodesics, correspond to the vanishing of the angular equation of motion (6.52). In Fig. 6.12, these turning points have been indicated by r_d and r_f, indicating respectively, the radial distances for the OFK and the OSK. The other turning point r_c, at which the condition $V'(r_c) = 0$ is satisfied, provides the unstable orbits of the first and the second kind, i.e. COFK and COSK.

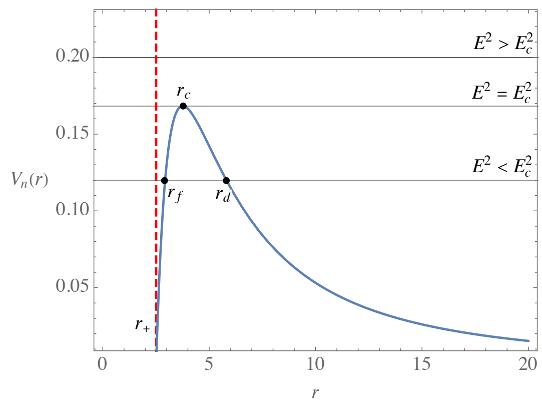

Figure 6.12: The effective potential for angular null geodesics plotted for $\gamma = 0.001$ and $L = 3$. Altering the values of L only affects the scale of the potential and leaves its shape unchanged. For this particular potential, the turning points are located at $r_d = 5.81$ and $r_f = 2.93$ corresponding to $E^2 = 0.12$, and $r_c = 3.76$ corresponding to $E_c^2 = 0.168$.

Period of the unstable circular orbits

The condition $V_n'(r_c) = 0$ results in the radial distance

$$r_c = \frac{2(1-\alpha)}{\gamma} \sin^2\left(\frac{1}{2} \arcsin\left(\frac{\sqrt{6M\gamma}}{1-\alpha}\right)\right). \tag{6.76}$$

To compute the proper and the coordinate periods of orbits at r_c, we know from the discussion in chapter 3 that

$$\Delta\tau_c = \frac{r_c^2}{L}\Delta\phi_c, \tag{6.77}$$

$$\Delta t_c = \frac{E_c}{L}\frac{r_c^2}{B(r_c)}\Delta\phi_c. \tag{6.78}$$

This way, for one complete revolution, one obtains the periods

$$T_\tau \equiv \Delta\tau_c|_{\Delta\phi_c = \frac{\pi}{2}} = \frac{2\pi r_c^2}{L}, \tag{6.79}$$

for comoving observers and

$$T_t \equiv \Delta t_c|_{\Delta\phi_c = \frac{\pi}{2}} = \frac{2\pi r_c}{\sqrt{B(r_c)}}, \tag{6.80}$$

for distant observers.

Deflecting trajectories

The turning points r_d and r_f can be calculated by solving the equation

$$\left(\frac{\mathrm{d}r}{\mathrm{d}\phi}\right)^2 = \frac{\mathcal{P}_4(r)}{L^2} = 0, \tag{6.81}$$

where $\mathcal{P}_4(r) = r\left[E^2 r^3 + L^2\gamma r^2 - L^2(1-\alpha)r + 2ML^2\right]$. Beside the trivial solution $r = 0$, the equation $\mathcal{P}_4(r) = 0$ has the three real roots

$$r_d = \sqrt{\frac{\xi_2}{3}}\cosh\left(\frac{1}{3}\operatorname{arccosh}\left(3\xi_3\sqrt{\frac{3}{\xi_2^3}}\right)\right) - \frac{\gamma b^2}{3}, \tag{6.82}$$

$$r_n = \sqrt{\frac{\xi_2}{3}}\cosh\left(\frac{1}{3}\operatorname{arccosh}\left(3\xi_3\sqrt{\frac{3}{\xi_2^3}}\right) + \frac{2\pi\mathrm{i}}{3}\right) - \frac{\gamma b^2}{3}, \tag{6.83}$$

$$r_f = \sqrt{\frac{\xi_2}{3}}\cosh\left(\frac{1}{3}\operatorname{arccosh}\left(3\xi_3\sqrt{\frac{3}{\xi_2^3}}\right) + \frac{4\pi\mathrm{i}}{3}\right) - \frac{\gamma b^2}{3}, \tag{6.84}$$

in which, as expected, the positive-valued ones are only r_d and r_f, and $b \equiv \frac{L}{E}$ is the impact parameter. Here, we have defined

$$\xi_2 = 4\left[\frac{\gamma b^2}{3} + b^2(1-\alpha)\right], \tag{6.85a}$$

$$\xi_3 = -4\left[\frac{\gamma b^4}{3}(1-\alpha) + \frac{2\gamma^3 b^6}{27} + 2b^2 M\right]. \tag{6.85b}$$

This way, one can recast $\mathcal{P}_4(r) = \frac{E^2}{4} r(r-r_d)(r-r_f)(r-r_n)$, which eases the integation of the equation of motion. To obtain the analytical solution for the deflecting trajectories, we first consider the OFK at r_d. The direct intergation of the relation $L\left(\frac{\mathrm{d}r}{\mathrm{d}\phi}\right) = \sqrt{\mathcal{P}_4(r)}$, results in

$$r(\phi) = \frac{r_f r_n}{r_d\left[\frac{\ell_0}{3r_d^2} - 4\wp\left(\omega_d - \kappa_d\phi\right)\right]}, \tag{6.86}$$

with the Weierstraß invariants

$$\tilde{g}_2 = \frac{\ell_0^2 - 3r_f r_n \ell_1}{12 r_d^4}, \tag{6.87a}$$

$$\tilde{g}_3 = -\frac{27(r_d r_f r_n)^2 + 2\ell_0^3 - 9 r_f r_n \ell_0 \ell_1}{432 r_d^6}, \tag{6.87b}$$

where $\omega_d = ß(U_d)$, in which

$$U_d = \frac{\ell_0 - 3r_f r_n}{12 r_d^2}, \tag{6.88}$$

and we have defined the constants

$$\kappa_d = \frac{r_f r_n}{8 b r_d}, \tag{6.89a}$$

$$\ell_0 = r_d r_f + r_d r_n + r_f r_n, \tag{6.89b}$$

$$\ell_1 = r_d^2 + r_d r_f + r_d r_n. \tag{6.89c}$$

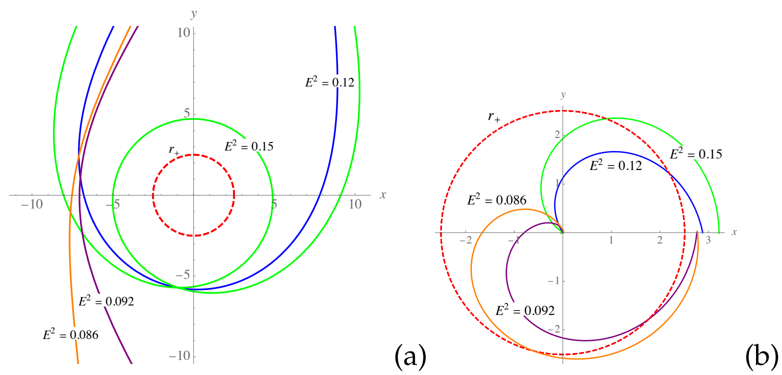

Figure 6.13: The deflecting trajectories for null geodesics corresponding to (a) OFK, and (b) OSK, plotted for different values of E^2 and in accordance with the parameters given in Fig. 6.12.

Pursuing the same procedure for photons approaching from r_f, one obtains the analytical solution

$$r(\phi) = \frac{r_d r_n}{r_f\left[\frac{\ell_0}{3r_f^2} - 4\wp\left(\omega_f + \kappa_f\phi\right)\right]}, \tag{6.90}$$

in which, the Weierstraß invariants and the constants ω_f and κ_f have the same forms as in Eqs. (6.87)–(6.89), assuming the exchange $r_d \leftrightarrow r_f$. In Fig. 6.13, the OFK and OSK have been plotted for several energies.

Note that, the OFK can be used to obtain the lens equation. Accordingly, the angle of deflection due to the gravitational lensing is calculated as (Misner et al., 2017)

$$\hat{\vartheta} = 2\left(\phi_\infty - \phi_d\right) - \pi, \tag{6.91}$$

in which $\phi_\infty \equiv \phi(\infty)$ and $\phi_d = \phi(r_d)$, where the radial behavior of the azimuth angle in the equatorial plane is given as

$$\phi(r) = L\int\frac{\mathrm{d}r}{\sqrt{\mathcal{P}_4(r)}}, \tag{6.92}$$

according to Eq. (6.81). This way, the lens equation is obtained as

$$\hat{\vartheta} = \frac{2}{\kappa_d}\left[ß\left(\frac{1}{4r_d^2}\left[\frac{\ell_0}{3} - r_f r_n\right]\right) - ß\left(\frac{\ell_0}{12r_d^2}\right)\right] - \pi, \tag{6.93}$$

by taking into account the inversion of Eq. (6.86) for an unbound (flyby) orbit.

Critical trajectories

In the case of $E = E_c$, the characteristic polynomial gains the form $\mathcal{P}_4(r) = r(r - r_c)^2(r - r_n)$, according to which, one can do the intergation of the equation of motion,

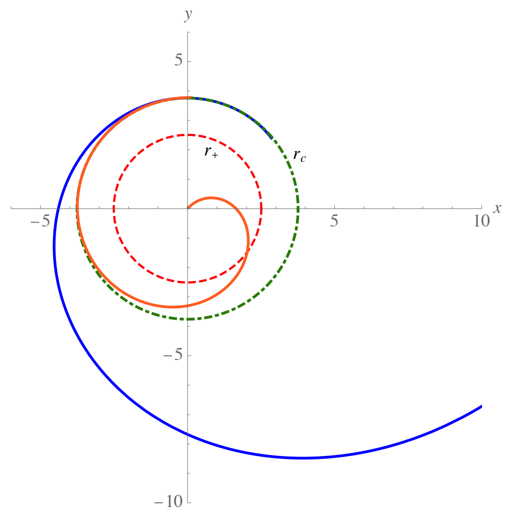

Figure 6.14: The COFK (blue) and the COSK (orange), plotted in accordance with the information given in Fig. 6.12.

based on the approaching points $r_c < r_{i_1} < r_{++}$ and $r_+ < r_{i_2} < r_c$. This way, and taking into account $b = b_c(\equiv \frac{L}{E_c})$, one obtains the two solutions

$$r_{\mathrm{I}}(\phi) = r_c - \frac{r_n}{r_c\left[(r_c - r_n)\tanh\left(\varphi_{i_1} - \kappa_c\phi\right) - r_c\right]}, \tag{6.94}$$

that corresponds to the COFK for particles approaching from r_{i_1}, and

$$r_{\mathrm{II}}(\phi) = r_c + \frac{r_n}{r_c\left[(r_c - r_n)\tanh\left(\varphi_{i_2} - \kappa_c\phi\right) - r_c\right]}, \tag{6.95}$$

corresponding to the COSK for particles that approach from r_{i_2}. In these expressions

$$\kappa_c = \frac{r_c}{2}\sqrt{1 - \frac{r_n}{r_c}}, \tag{6.96a}$$

$$\varphi_{i_{1,2}} = \operatorname{arctanh}\left(\sqrt{\frac{r_c^2 r_{i_{1,2}} - r_n}{r_c(r_c - r_n) r_{i_{1,2}}}}\right). \tag{6.96b}$$

In Fig. 6.14 These orbits have been plotted in accordance with the approaching points, which lead to different fates for the trajectories.

Time-like geodesics

For the case of $\epsilon = 1$, the effective potential (6.50) gains the form

$$V_t(r) = \frac{\gamma}{r}\left(r - r_+\right)\left(r_{++} - r\right)\left(1 + \frac{L^2}{r^2}\right), \tag{6.97}$$

for the angular time-like geodesics. It is however important to note that, unlike the null case, the values of the angular momentum L are crucial in the characterization of the possible orbits for time-like geodesics. In other words, different choices of L can lead to different available orbits, in accordance with the changes in the shape of the effective potential. Therefore, one needs to find the corresponding limiting values of L, that characterize $V_t(r)$.

To elaborate this, we first consider the limit where the points of inflection and extremums coincide. These points are where the equations $V'(r) = 0$ and $V''(r) = 0$ are satisfied, simultaneously (marginally stable orbits). The corresponding angular momentums are then ramified to $L_{\rm IS}$, for which $V_t(r)$ presents a minimum at $r_{\rm IS}$ where the innermost stable circular orbit (ISCO) occurs, and $L_{\rm OS}$, for which $V_t(r)$ has a minimum at $r_{\rm OS}$ where the outermost stable circular orbit (OSCO) happens. Furthermore, for the critical value $L = L_C$, the effective potential represents two maximum of equal energy levels, occurring at the radial distances r_{C_1} and r_{C_2}. Based on the above notions, we can categorize the angular momentums as follows:

- For $0 < L < L_{\rm IS}$ an unstable orbit is available without the presence of stable circular orbits.
- For $L = L_{\rm IS}$ an unstable orbit and ISCO are available.
- For $L_{\rm IS} < L < L_C$ a stable circular orbit and two unstable orbits are available. In this case, the first maximum is smaller than the second one, so the energy of the unstable orbit at the larger radius, is greater than that at the smaller radius.
- For $L = L_C$ there are one stable circular orbit, and two unstable orbits of equal energies.
- For $L_C < L < L_{\rm OS}$ there are one stable circular orbit and two unstable orbits. The energy of the unstable orbit at the smaller radius, is greater than that at the larger radius.
- For $L = L_{\rm OS}$ an unstable orbit and OSCO are available.
- For $L > L_{\rm OS}$ only an unstable orbit is available.

In Fig. 6.15, several branches of $V_t(r)$ have been plotted, by taking into account the above limits and values. In what follows, we confine ourselves to the case of $L = L_C$ and the possible time-like orbits are discussed.

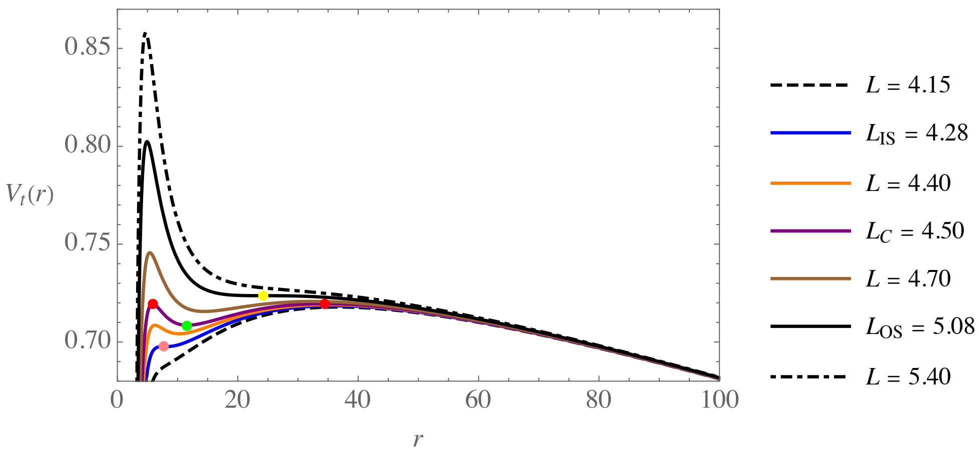

Figure 6.15: The different curves of $V_t(r)$ plotted for $\gamma = 0.001$, and ramified in terms of the limiting values of the angular momentum. The red dots indicate the radii of unstable orbits, r_{C_1} and r_{C_2}, which are with equal energies and correspond to the L_C curve.

Planetary orbits

Planetary orbits are oscillations between two turning points and are, therefore, bounded between two radii. To discuss the planetary orbits, we select the curve corresponding to L_C from the effective potential, as demonstrated in Fig. 6.16. In this diagram, the stable circular orbits and the critical orbits can occur, respectively, at $r = r_S$ and $r_{C_{1,2}}$. The planetary orbits, however, are only available for the energy level $E_U^2 < E^2 < E_C^2$, where the equation

$$\left(\frac{\mathrm{d}r}{\mathrm{d}\phi}\right)^2 = \frac{P_5(r)}{L^2} = 0, \tag{6.98}$$

in addition to the trivial solution $r = 0$, possesses the four real solutions r_D (OFK), r_A (apoapsis), r_P (periapsis), and r_F (OSK). In Eq. (6.98), the characteristic polynomial is inferred from Eq. (6.52) as $P_5(r) = r\big[\gamma r^4 - (1 - \alpha - E^2)r^3 + (2M + L^2\gamma)r^2 - L^2(1 - \alpha)r + 2ML^2\big]$. The equation $P_5(r) = 0$ for this energy level results in the solutions (see appendix D.1)

$$r_D = M\left[\tilde{\rho} + \sqrt{\tilde{\rho}^2 - \tilde{\beta}} - \frac{\tilde{a}}{4}\right], \tag{6.99}$$

$$r_A = M\left[\tilde{\rho} - \sqrt{\tilde{\rho}^2 - \tilde{\beta}} - \frac{\tilde{a}}{4}\right], \tag{6.100}$$

$$r_P = M\left[-\tilde{\rho} + \sqrt{\tilde{\rho}^2 - \tilde{\lambda}} - \frac{\tilde{a}}{4}\right], \tag{6.101}$$

$$r_F = M\left[-\tilde{\rho} + \sqrt{\tilde{\rho}^2 - \tilde{\lambda}} - \frac{\tilde{a}}{4}\right], \tag{6.102}$$

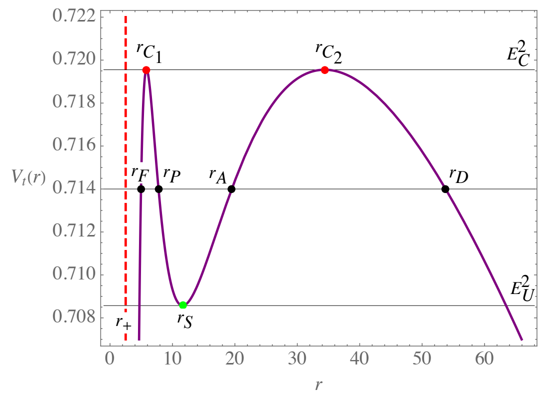

Figure 6.16: The behavior of $V_t(r)$ for $L = L_C$ (in accordance with Fig. 6.15). Here, $r_{C_1} = 5.85$ and $r_{C_2} = 34.37$, corresponding to $E_C^2 = 0.719$, $r_S = 11.63$ corresponding to $E_U^2 = 0.708$, and $r_D = 53.76$, $r_A = 19.51$, $r_P = 7.77$ and $r_F = 4.96$, corresponding to $E^2 = 0.714$.

where

$$\tilde{\rho} = \sqrt{\tilde{U} - \frac{\tilde{A}}{6}}, \tag{6.103a}$$

$$\tilde{\beta} = 2\tilde{\rho}^2 + \frac{\tilde{A}}{2} + \frac{\tilde{B}}{4\tilde{\rho}}, \tag{6.103b}$$

$$\tilde{\lambda} = 2\tilde{\rho}^2 + \frac{\tilde{A}}{2} - \frac{\tilde{B}}{4\tilde{\rho}}, \tag{6.103c}$$

with

$$\tilde{A} = \tilde{b} - \frac{3\tilde{a}^2}{8}, \tag{6.104a}$$

$$\tilde{B} = \tilde{c} + \frac{\tilde{a}^3}{8} - \frac{\tilde{a}\tilde{b}}{2}, \tag{6.104b}$$

$$\tilde{C} = \tilde{d} + \frac{\tilde{a}^2\tilde{b}}{16} - \frac{3\tilde{a}^4}{256} - \frac{\tilde{a}\tilde{c}}{4}, \tag{6.104c}$$

given that

$$\tilde{a} = -\frac{1 - \alpha - E^2}{M\gamma}, \tag{6.105a}$$

$$\tilde{b} = \frac{2M + L^2\gamma}{M^2\gamma}, \tag{6.105b}$$

$$\tilde{c} = -\frac{L^2(1-\alpha)}{M^3\gamma}, \tag{6.105c}$$

$$\tilde{d} = \frac{2L^2}{M^3\gamma}, \tag{6.105d}$$

and we have defined the function

$$\tilde{U} = \sqrt{\frac{\tilde{\eta}_2}{3}} \cosh\left(\frac{1}{3}\operatorname{arccosh}\left(3\tilde{\eta}_3\sqrt{\frac{3}{\tilde{\eta}_2^3}}\right)\right), \tag{6.106}$$

that includes the constant coefficients

$$\tilde{\eta}_2 = \frac{\tilde{A}^2}{12} + \tilde{C}, \tag{6.107a}$$

$$\tilde{\eta}_3 = \frac{\tilde{A}^3}{216} - \frac{\tilde{A}\tilde{C}}{6} + \frac{\tilde{B}^2}{16}. \tag{6.107b}$$

This way, the characteristic polynomial can be recast as $P_5(r) = r(r_D - r)(r_A - r)(r - r_P)(r - r_F)$ for the case that the planetary orbits are present.

For particles reaching at the turning point r_A (or r_P) with the initial azimuth angle $\phi_0 = 0$, the planetary orbits are then characterized by the equation

$$\phi(r) = -L\int_{r_A}^{r} \frac{\mathrm{d}r}{\sqrt{P_5(r)}}, \tag{6.108}$$

which contains a hyper-elliptic integral on its right hand side. After applying specific intergation methods and manipulations, this integral results in the solution (see appendix D.2)

$$\phi(r) = \frac{2L}{\sqrt{l^3\gamma}}\sqrt{1-\frac{r}{r_A}}F_D^{(4)}\left(\frac{1}{2},\frac{1}{2},\frac{1}{2},\frac{1}{2},\frac{1}{2};\frac{3}{2};c_1,c_2,c_3,1-\frac{r}{r_A}\right), \tag{6.109}$$

in which $l^3 = (r_D - r_A)(r_A - r_P)(r_A - r_F)$, and $F_D^{(4)}$ is the incomplete Lauricella hypergeometric function of the fourth order, which is defined in the context of the integral equation (Exton, 1976; Akerblom & Flohr, 2005)

$$\int_0^{1-\frac{r}{r_A}} u^{-\frac{1}{2}}(1-u)^{-\frac{1}{2}}\prod_{i=1}^{3}(1-x_i u)^{-b_i}\,\mathrm{d}u = 2\sqrt{1-\frac{r}{r_A}}F_D^{(4)}\left(\frac{1}{2},b_1,b_2,b_3,\frac{1}{2};\frac{3}{2};c_1,c_2,c_3,1-\frac{r}{r_A}\right), \tag{6.110}$$

where $b_1 = b_2 = b_3 = \frac{1}{2}$, and

$$c_1 = -\frac{r_A}{(r_D - r_A)}, \tag{6.111a}$$

$$c_2 = \frac{r_A}{(r_A - r_P)}, \tag{6.111b}$$

$$c_3 = \frac{r_A}{(r_A - r_F)}. \tag{6.111c}$$

In order to simulate the planetary orbits, we use the solution (6.109) to make a list of points $(\phi(r_t), r_t)$ in the domain $r_P < r_t < r_A$, and then we do the inversion by means

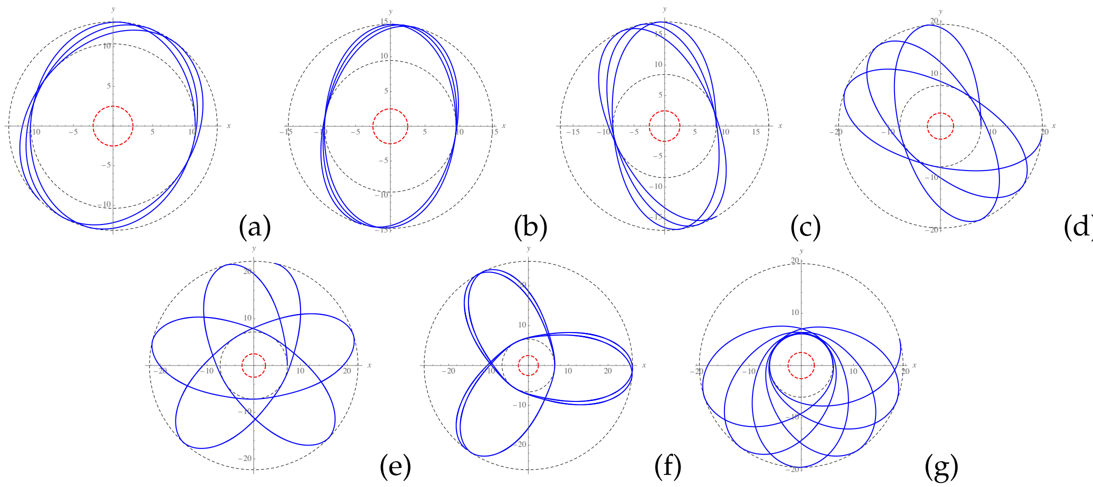

Figure 6.17: Some examples of time-like planetary orbits, plotted in accordance with the effective potential in Fig. 6.16, for the energies (a) $E^2 = 0.709$, (b) $E^2 = 0.710$, (c) $E^2 = 0.712$, (d) $E^2 = 0.714$, (e) $E^2 = 0.716$, (f) $E^2 = 0.718$ and (g) $E^2 = 0.7194$. The inner and outer dashed circles indicate, respectively, r_P and r_A for each energy level and the small red circle is r_+.

of numerical interpolations. In Fig. 6.17, some examples of planetary orbits have been plotted for some different ranges of energy $E_S^2 < E^2 < E_C^2$.

Furthermore, the solution (6.109) allows for the determination of the precession of the periapsis in planetary orbits. This precession is given by $\Phi_{\rm pl} = 2\phi_{AP} - 2\pi$, where ϕ_{AP} is the azimuth angle swiped between r_A and r_P during the bound orbit. This way, one obtains

$$\Phi_{\rm pl} = \frac{4L}{\sqrt{l^3\gamma}}\sqrt{1-\frac{r_P}{r_A}}F_D^{(4)}\left(\frac{1}{2},\frac{1}{2},\frac{1}{2},\frac{1}{2},\frac{1}{2};\frac{3}{2};c_1,c_2,c_3,1-\frac{r_P}{r_A}\right) - 2\pi, \tag{6.112}$$

as the exact expression for the precession in the planetary orbits.

OFK and OSK

The same effective potential in Fig. 6.16, offers the OFK and OSK for particles approaching at r_D and r_F. So the same solution in Eq. (6.109) holds for these kinds of orbits, and the only thing that changes is the point of approach. Therefore, following the same numerical method as applied for the planetary orbits, in Fig. 6.18, the deflecting time-like trajectories have been plotted.

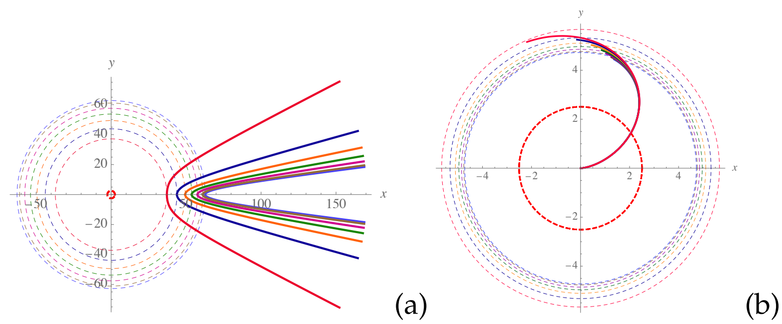

Figure 6.18: The deflecting time-like trajectories, (a) OFK and (b) OSK plotted for the same values of energy as those used in Fig. 6.17. The thin dashed circles indicate r_D for the OFK, and r_F for the OSK. The value of E^2 decreases from the inner to the outer circles in the OFK, and from the outer to the inner circles in the OSK.

Period of the circular orbits

The period of stable and unstable circular orbits at the radial distance r_{CO}, which can be stable or unstable, respectively at r_S or r_C, can be calculated in the same way as in Subsect. 6.2.3, and from Eqs. (6.79) and (6.80). In fact, by solving $V_t'(r) = 0$ for L, one obtains the radial profiles

$$L(r) = r\sqrt{\frac{2M - \gamma r^2}{2(1-\alpha)r - 6M - \gamma r^2}}, \tag{6.113}$$

$$E^2(r) = \frac{2\left[2M - (1-\alpha-\gamma r)r\right]^2}{r\left[2(1-\alpha)r - 6M - \gamma r^2\right]}, \tag{6.114}$$

for the circular orbits. Hence, by means of Eq. (6.79), the proper period for the time-like circular orbits that exist at the distance r_{CO}, becomes

$$T_\tau = 2\pi r_{\text{CO}}\sqrt{\frac{2(1-\alpha)r_{\text{CO}} - 6M - \gamma r_{\text{CO}}^2}{2M - \gamma r_{\text{CO}}^2}}, \tag{6.115}$$

to obtain which, we have let $L_{\text{CO}} \equiv L(r_{\text{CO}})$. Accordingly, at the Schwarzschild limit we have $T_\tau^{\text{Sch}} = 2\pi r_{\text{CO}}\sqrt{\frac{r_{\text{CO}}-3M}{M}}$. The period of the coordinate time, on the other hand, is obtained by using Eq. (6.80) at $r = r_{\text{CO}}$, providing

$$T_t = 2\pi r_{\text{CO}}\sqrt{\frac{r_{\text{CO}}}{r_{\text{CO}} - 2M - \alpha r_{\text{CO}} - \gamma r_{\text{CO}}^2}}, \tag{6.116}$$

with the Schwarzschild limit $T_t^{\text{Sch}} = 2\pi r_{\text{CO}}\sqrt{\frac{r_{\text{CO}}}{r_{\text{CO}}-M}}$. Taking into account the three important cases of $L = L_{\text{IS}}, L_{\text{OS}}$ and L_{C} of the effective potential in Fig. 6.15, we have

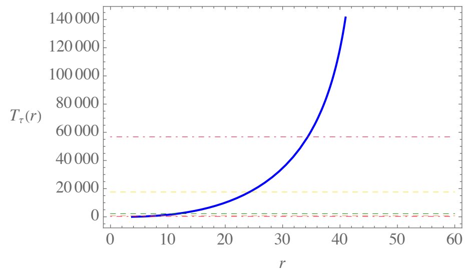

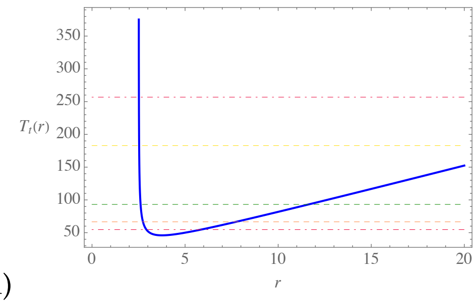

Figure 6.19: The behavior of (a) the proper and (b) the coordinate periods of time-like circular orbits, in accordance with the values of L as in Fig. 6.15. In the diagrams, the red dot-dashed lines correspond to unstable circular orbits at r_{C_1} (lower line) and r_{C_2} (upper line). The dashed lines correspond to the stable circular orbits at r_{IS} (orange), r_{OS} (yellow) and r_S (green).

plotted the proper and coordinate periods in Fig. 6.19, together with their values at the distances r_{IS}, r_{OS}, r_S, and $r_{C_{1,2}}$.

Note that, as they are marginally stable, orbits at the ISCO are sensitive to perturbations along the radial axis, in the sense that the orbiting particles may fall out of the stable orbits under certain circumstances. This way, one can define a limit, beyond which, the orbits become unstable. Such limit may be understood, indirectly, by mean of the radial *epicyclic* frequency v_r, which is related to the formation of accretion disks around black holes (Abramowicz & Fragile, 2013). Therefore, v_r is the frequency of the oscillations of the accreting particles along the radial direction, and is defined as (Abramowicz & Kluźniak, 2005; Rayimbaev et al., 2021)

$$v_r^2 = -\frac{1}{2g_{rr}} V_t''(r), \tag{6.117}$$

given in terms of the effective potential. Taking into account the value of L in Eq. (6.113) in the effective potential (6.97), we obtain

$$v_r^2 = \frac{\left[2M - (1-\alpha)r + \gamma r^2\right]^2 \left[12M^2 - 2M(1-\alpha)r - 12M\gamma r^2 + 3\gamma(1-\alpha)r^3 - \gamma r^4\right]}{r^3 \left[6M - 2(1-\alpha)r + \gamma r^2\right]^2}. \tag{6.118}$$

In Fig. 6.20, the radial profile of v_r^2 has been plotted together with its value at r_{IS}. Recently, the epicyclic frequency for quasi oscillations of massive test particles in circular accretions has been discussed for the same black hole with an associated electric charge (Mustafa et al., 2021).

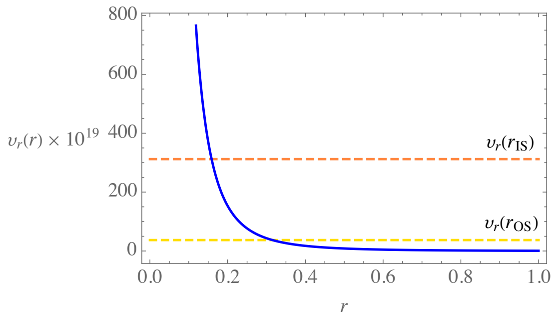

Figure 6.20: The radial profile of the epicyclic frequency together with its values at the two radii of marginally stable orbits ($r_{\rm IS}$ and $r_{\rm OS}$), in accordance with the effective potential in Fig. 6.15.

Critical orbits

Returning to the effective potential in Fig. 6.16, the two double roots r_{C_1} and r_{C_2} can provide a particular form of critical orbits. Once $E^2 = E_C^2$, the characteristic polynomial can be recast as $P_5(r) = r(r - r_{C_1})^2(r - r_{C_2})^2$, for which, the angular equation of motion becomes

$$\phi(r) = L_C \int_{r_j}^{r} \frac{\mathrm{d}r}{|r - r_{C_1}||r - r_{C_2}|\sqrt{r}}, \tag{6.119}$$

for particles approaching from an initial point r_j. After some manipulations, it is found out that the critical orbits can be described in the context of the relation

$$Y(r) = \exp\left[\left(\frac{r_{C_2} - r_{C_1}}{2L_C}\right)\phi - \tilde{\varphi}_j\right], \tag{6.120}$$

in which

$$Y(r) = \left(\frac{1 + \sqrt{\frac{r}{r_{C_2}}}}{1 - \sqrt{\frac{r}{r_{C_2}}}}\right)^{\frac{1}{2\sqrt{r_{C_2}}}} \left(\frac{1 + \sqrt{\frac{r}{r_{C_1}}}}{1 - \sqrt{\frac{r}{r_{C_1}}}}\right)^{-\frac{1}{2\sqrt{r_{C_1}}}}, \tag{6.121}$$

and

$$\tilde{\varphi}_j = \frac{1}{\sqrt{r_{C_2}}}\mathrm{arctanh}\left(\sqrt{\frac{r_j}{r_{C_2}}}\right) - \frac{1}{\sqrt{r_{C_1}}}\mathrm{arctanh}\left(\sqrt{\frac{r_j}{r_{C_1}}}\right). \tag{6.122}$$

Therefore, the simulation of the orbits can be done by means of numerical interpolations. As before, the orbits can be classified in terms of the three cases $r_j > r_{C_2}$, $r_{C_1} < r_j < r_{C_2}$, and $r_+ < r_j < r_{C_1}$. In Fig. 6.21, the domain of the changes in the ϕ-coordinate during the critical orbits has been shown for each of these cases. In Fig. 6.22, the aforementioned three cases have been considered in Eq. (6.120), in order to simulate the possible forms of the critical orbits. As it is observed, the case of

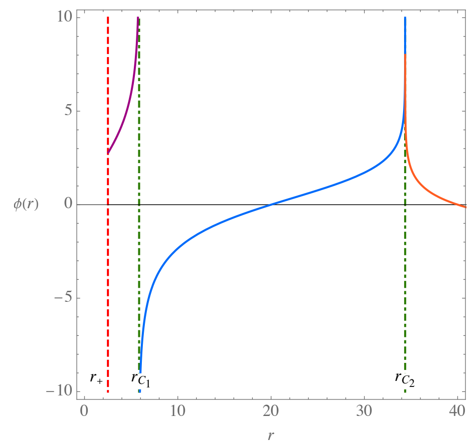

Figure 6.21: The change in the ϕ-coordinate during the time-like critical orbits, classified by colours, in accordance with different ranges of the initial radial distance r_j.

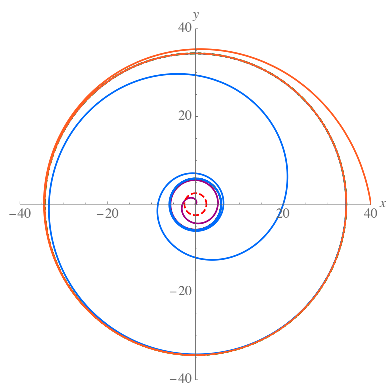

Figure 6.22: The critical orbits of time-like geodesics for $L = L_C$, $E^2 = E_C^2$, and different initial points r_j, in accordance with Fig. 6.21.

$r_j > r_{C_2}$ is indeed a COFK, whereas the orbits are completely confined between the two extremums when $r_{C_1} < r_j < r_{C_2}$. Finally, the case of $r_+ < r_j < r_{C_1}$, is a COSK. Accordingly, distant observers will only be able to detect particles coming from r_{C_2}.

6.3 Summary

In this chapter, we studied the astrophysical implications of a SBH which is associated with cloud of strings and quintessence. This was done by performing standard general relativistic tests in the solar system. The corresponding parameters α and γ are supposed to include the effect of extended sources of gravity, as well as dark matter and dark energy. and the four standard tests could infer the ranges $10^{-9} \leq \alpha \leq 10^{-4}$ and $10^{-21} \leq \gamma M \leq 10^{-11}$. As the smallest values of the parameters appear inside the confidence range for the experiments related to light propagation in the spacetime, it can be inferred that null trajectories are the most sensitive to changes in these parameters. This, in fact, confirms the pretty well-known observational principle, that the impacts of the possible dark components of the universe, would be first noticeable within the optical and spectroscopic astronomical data. The observational constraints we obtained for this black hole could also pave the way for further studies, in the sense that the physical inferences one obtains can be calibrated within the data reported here. We also calculated the QNMs as the black hole's response to gravitational perturbations, based on particular choices for the parameters, as the most reliable ones. For higher degrees of ℓ, each of these modes showed to be of stronger damping, and therefore, of less contribution in the emitted gravitational waves. This feature is in common with other black hole spacetimes, as studied extensively in the literature.

Moreover, aiming at a theoretical study, we considered the null and time-like geodesics that propagate in the exterior geometry of this black hole. As observed in the previous discussions we did, the radial profiles of the proper and coordinate times show two receding branches towards either of these horizons. Although the radial evolution of null and time-like geodesics for this black hole has been formerly studied (Mustafa & Hussain, 2021), here we presented an alternative approach to the analytical solutions reported in that paper, by employing strict elliptic integration methods that resulted in the Weierstraßian expressions for the solutions. Furthermore, we categorized the radial orbits within the corresponding effective potential, and also in accordance with the turning points for which, we found explicit expressions. The radial profiles of the time axes were plotted for the particular cases of frontal scattering and critical motion. The analytical study of the angular trajectories for mass-less particles (photons) were first approached by means of the $\wp$-Weierstraßian elliptic functions which enabled us analyzing the deflecting trajectories from the turning points which were also found explicitly. We continued the study of angular null geodesics by discussing the unstable circular (critical) orbits, which was the only remaining possible motion for mass-less particles. on the other hand, angular motion for massive particles appeared much more diverse in the sense that the effective potential could offer an ISCO and an OSCO, that confine the stable circular orbits. The corresponding angular momentums for these cases were obtained by taking into account the marginality condition $V_t''(r) = 0$. There would be, therefore, some cases of two double roots for the characteristic polynomial. Accordingly, the choice of the angular momentum for the approaching test particles becomes of crucial importance in the analysis of the trajectories. To proceed, we adopted the switching value $L = L_C$, for which the two double extremums (maximums) of the effective potential are equal in the value. This case was analyzed in the context of several types of orbits that it could offer. For the case of planetary orbits, in addition to the periapsis and apoapsis, the characteristic polynomial has two other non-zero real roots that result in a hyper-elliptic integral for the azimuth angle. This integral was solved analytically in terms of the fourth order Lauricella hypergeometric function. To do the plots of the orbits, we obtained the inversion of this integral by means of numerical interpolations. The orbits show larger precession in the periapsis as the particle's energy approaches its critical value. The same method was used to plot the deflecting time-like trajectories. We also determined the proper and coordinate periods of stable circular orbits, and calculated the epicyclic frequency of accreting particles. We closed our discussion by analyzing the critical time-like orbits as they approach from three different initial points to either of the extremums. The simulations indicate that only the particles from the outer critical distance can escape to the infinity.

Chapter 7

Carathéodory thermodynamics and adiabatic analysis of black holes

Ever since their advent, the reconciliation of the laws of thermodynamics with black hole mechanics (Bardeen et al., 1973), the entropy assigned by Bekenstein to the black holes (Bekenstein, 1972, 1973, 1974, 1975) and the possibility of black hole evaporation through the Hawking radiation (Hawking, 1975), have been of great interest among physicists. And although it has not been possible to detect such phenomena from direct observations, nevertheless, strong effort have been being made to mimic similar processes in black hole analogs, such as the experimental Unruh radiation (Unruh, 1981) in stimulated systems, both theoretically and experimentally (Novello et al., 2002; Schützhold & Unruh, 2005; Carusotto et al., 2008; Belgiorno et al., 2010; Weinfurtner et al., 2011; Castelvecchi, 2016; Steinhauer, 2016; Lima et al., 2019; Kolobov et al., 2021). On the other hand, while the famous Bekenstein-Hawking (B-H) entropy formula has been applied widely for the regular black holes, nevertheless, its direct application to the extremal black holes (EBHs) is not that simple. In fact, the special conjecture of zero entropy for EBHs (Teitelboim, 1995; Carroll et al., 2009), leads to overlooking the direct relationship between the entropy and the event horizon's area, as demanded by the B-H formula. In this chapter, we construct the correct foliation of the thermodynamics manifold by using the Carathéodory's approach, for which, the appropriate Pfaffian form $\delta Q_{\rm rev}$, representing the infinitesimal heat exchanged reversibly, is taken into account. We should, however, state that the present study aims at establishing a new method of analyzing black hole thermodynamics and still is not constrained by the experimental data. Although the method does not require a priori knowledge of any of the so-called laws of thermodynamics, we will use the already known results for physical quantities, such as entropy, temperature, ect. Therefore, the adiabatic surfaces are obtained by solving the Cauchy problem associated to the Pfaffian equation $\delta Q_{\rm rev} = 0$.

In this chapter we use the Carathéodory's approach to thermodynamics, to construct the thermodynamic manifold of the Hayward regular black hole, and a rotating SDBTZ black hole. The Pfaffian form representing the infinitesimal heat exchange reversibly is considered to be $\delta Q_{\rm rev} \equiv \mathrm{d}r_s - \mathcal{F}\mathrm{d}X - \cdots$, where r_s is the Schwarzschild radius, X is a property peculiar to the black hole, and $\mathcal{F}$ is a force associated to that property. Note that, other terms may appear in this relation, in accordance with the black hole under consideration. By solving the associated Cauchy problem, the adiabatic paths are confined to the non-extremal manifold, and therefore, the status of the second and third laws are preserved. Consequently, the extremal sub-manifold corresponds to the adiabatically disconnected boundary of the manifold. In addition, the merger of two extremal black holes, for each of he cases, is analyzed.

7.1 The case of the Hayward black hole

In this section, we focus on a particular, non-singular minimal black hole model proposed by Hayward (Hayward, 2006), which constructs a static spherically symmetric and asymptotically flat spacetime. Recently, this solution has been generalized to certain scalar-tensor theories (Babichev et al., 2020), and new regular black holes have been reported, in the context of quasi-topological electromagnetic theories (Cisterna et al., 2020; Cano & Murcia, 2021, 2020). In fact, the non-singular nature of this black hole has made it an interesting topic studying its thermodynamics. Accordingly, the laws of black hole thermodynamics have been investigated for the Hayward black hole (HBH) through studying the relations between its dynamical parameters $\{r_s, l\}$ that define the state of the system (Molina & Villanueva, 2021). The Hayward black hole spacetime, is given by the regular, non-singular, static spherically symmetric metric

$$\mathrm{d}s^2 = -f(r)\,\mathrm{d}(ct)^2 + \frac{\mathrm{d}r^2}{f(r)} + r^2\mathrm{d}\theta^2 + r^2\sin^2\theta\,\mathrm{d}\phi^2, \tag{7.1}$$

in which, the lapse function $f(r)$ is given by (Hayward, 2006)

$$f(r) = 1 - \frac{r_s\, r^2}{r^3 + r_s\, l^2}, \tag{7.2}$$

where $r_s = \frac{2GM}{c^2}$ is the radius of the SBH of mass M, and l is the Hayward's parameter ($0 \leq l < \infty$), so that for $l = 0$, the SBH is regenerated. The spacetime admits an event horizon, which is obtained by solving the cubic equation $f(r) = 0$, and is given by (Molina & Villanueva, 2021)

$$r_+ = r_s \left(\frac{1 + 2\cos\alpha}{3} \right) \equiv r_s R_+, \tag{7.3}$$

where $\alpha(r_s, l) = \frac{1}{3} \arccos\left(1 - 2\frac{l^2}{l_e^2}\right)$, $l_e = \frac{2r_s}{\sqrt{27}}$, and $0 \leq l < l_e$. In the case that $l = l_e$, the roots reduce to the two degenerate positive values, and the EHBH is obtained, representing the thermodynamic limit of the black hole. Hence, l_e is the extremal limit of the Hayward's parameter. In this section, the thermodynamic manifold of this black hole is analyzed in terms of the Carathéodory's thermodynamics (Fathi et al., 2021).

7.1.1 The $\{r_s, l\}$ thermodynamics in the Carathéodory's approach

The most usual way to describe the thermo-geometric (or *geometrothermodynamic*) processes in black hole spacetimes, goes through the second law of black hole thermodynamics, which is postulated as (Bardeen et al., 1973; Bekenstein, 1972, 1973, 1974, 1975; Hawking, 1975):

The area of the black hole event horizon cannot decrease; it increases during most of the physical processes of the black hole.

In fact, the well-known B-H area-entropy formula

$$S = \frac{k_B}{4} \frac{4\pi r_+^2}{\ell_p^2}, \tag{7.4}$$

relates the entropy with the event horizon, where k_B and ℓ_p are, respectively, the Boltzmann constant and the Planck length. Since the event horizon depends on the pair $\{r_s, l\}$, it is useful to define the metric entropy function

$$\mathcal{S}(r_s, l) \equiv \frac{\ell_p^2\, S}{\pi k_B} = r_s^2\, R_+^2(r_s, l). \tag{7.5}$$

On the other hand, the thermodynamics of the system can be approached, geometrically, in the context of the Carathéodory's formulation, which postulates the integrability of the Pfaffian form

$$\delta Q_{\text{rev}} = \mathcal{T} \mathrm{d}\mathcal{S}, \tag{7.6}$$

representing the infinitesimal heat exchanged reversibly (Chandrasekhar, 1939; Belgiorno, 2003b; Belgiorno & Martellini, 2004; Belgiorno, 2003; Belgiorno, 2003a), and this way, it is connected with the Gibbs's thermodynamics (Belgiorno, 2003). Here $\mathcal{T}$ is the integrating factor representing the absolute temperature, defined by

$$\frac{1}{\mathcal{T}} = \left(\frac{\partial \mathcal{S}}{\partial r_s}\right)_l > 0, \tag{7.7}$$

which, by applying Eq. (7.5), yields (Molina & Villanueva, 2021)

$$\mathcal{T} = \frac{\mathcal{T}_s}{R_+(\alpha)\left[R_+(\alpha) + g_*(\alpha)\right]}, \tag{7.8}$$

where $\mathcal{T}_s \equiv (2r_s)^{-1} \equiv (4\mathcal{S}_s)^{-\frac{1}{2}}$ is the SBH temperature, and $g_*(\alpha) = \frac{4}{9}\sin\alpha\,(\csc 3\alpha - \cot 3\alpha)$.

Therefore, considering $\{r_s, l\}$ as independent thermodynamic coordinates, the homogeneity of the system is reflected by the integrable Pfaffian form

$$\delta Q_{\text{rev}} = \mathrm{d}r_s - \mathcal{F}_H \mathrm{d}l. \tag{7.9}$$

Note that, $\mathrm{d}r_s$ and $-\mathcal{F}_H\mathrm{d}l$ represent, respectively, the internal energy and work, and the intensive variable (homogeneous of degree zero)

$$\mathcal{F}_H = \frac{g_*(\alpha)}{R_+(\alpha) + g_*(\alpha)} \frac{r_s}{l}, \tag{7.10}$$

is introduced as the generalized Hayward's force (Molina & Villanueva, 2021). Here, an equilibrium geometrical state is compared with the equilibrium states of standard thermodynamics, by taking the infinitesimal variation of $\mathcal{F}_H$ in Eq. (7.9), along the stationary HBH solution. Then, the open non-extremal manifold $l < l_e$ corresponds to the thermodynamic domain, and is encompassed by the extremal sub-manifold (thermodynamic limit $\mathcal{T} = 0$), formed by $l = l_e$. The foliation of this thermodynamic manifold can be generated by the integrability property $\delta Q_{\text{rev}} \wedge \mathrm{d}(\delta Q_{\text{rev}}) = 0$ (which is trivial in a two-variable case), specifically, on the submanifolds of codimension one, which are solutions of the Pfaffian equation $\delta Q_{\text{rev}} = 0$ (see below).

Before continuing, let us turn our attention to Fig. 7.1, which shows the behaviors of the metric entropy and temperature. The physically accepted segment lies within

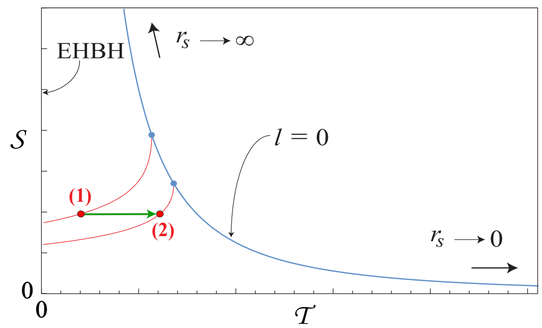

Figure 7.1: The $\mathcal{T}$-$\mathcal{S}$ diagram of the HBH, indicating both the EHBH and the SBH limits.

the domain $0 \leq \mathcal{T} \leq \mathcal{T}_s$ (the blue curve). Note that, if r_s is fixed, then $\Delta\mathcal{S} > 0$ implies $\Delta l < 0$. Therefore, by varying l while keeping r_s fixed (the red curves), the HBH transits to the SBH. It is also straightforward to see that, going from state (1) to state (2) (for which, $\mathcal{T}_1 < \mathcal{T}_2$), the variable r_s decreases. We can therefore infer that, in an adiabatic process (the green arrow), both of the variables (r_s, l) decrease simultaneously.

7.1.2 The adiabatic processes and the extremal limit

Letting $\mathfrak{r}_s \equiv r_s^e = \mathcal{F}_H^e\, l$ to be the extremal limit of r_s, where $\mathcal{F}_H^e = \frac{\sqrt{27}}{2}$ is the Hayward's force for the EHBH, one gets

$$\mathrm{d}\mathfrak{r}_s = \mathcal{F}_H^e\, \mathrm{d}l. \tag{7.11}$$

Then, the area for the extremal states become

$$\mathcal{A}_e = 4\pi\, (r_+^e)^2 = 4\pi\, (r_s^e R_+^e)^2 = \frac{16}{9}\pi\mathfrak{r}_s^2, \tag{7.12}$$

which implies that

$$\mathrm{d}\mathcal{A}_e = 24\pi l \mathrm{d}l. \tag{7.13}$$

Thus, the isoareal condition $\mathrm{d}\mathcal{A}_e = 0$ is satisfied only if $l = \text{const.}$, but these states still satisfy the Pfaffian equation $\delta Q_{\text{rev}} = \mathrm{d}\mathfrak{r}_s - \mathcal{F}_H^e\, \mathrm{d}l = 0$. Consequently, the adiabatic transformations are not isoareal transformations on the extremal submanifold. We will return to this point later, but for now, the EHBH is regarded as an extremal submanifold that resides in the (adiabatic) integral manifold of δQ_{rev} in Eq. (7.9).

For non-extremal states the situation is different, since it is possible to obtain solutions for the isoareal equation $\mathrm{d}\mathcal{A} = 0$, and therefore, one can generate a foliation of the parameter space of the HBH, whose leaves are the surfaces $\mathcal{A} = \text{const.}$ In fact, the

Carathéodory's approach allows for foliating the thermodynamic manifold by means of the solutions to the Pfaffian equation $\delta Q_{\rm rev} = 0$, that provide a smooth and continuous one-form field residing in the non-extremal sub-manifold. Accordingly, the integral manifolds of $\delta Q_{\rm rev}$ are surfaces with constant $\mathcal{S}$, which together with the paths that solve the Pfaffian equation, construct an isentropic surface (i.e. adiabatic and reversible) (Belgiorno & Martellini, 2004). To elaborate on this point, let us apply the changes of variables $x \doteq r_s^2$ and $y \doteq (\mathcal{F}_H^e)^2 l^2$, so that Eq. (7.9) can be recast as

$$\delta Q_{\rm rev} = \frac{{\rm d}x}{2\sqrt{x}} - \frac{\mathcal{F}_H(x,y)}{\mathcal{F}_H^e}\frac{{\rm d}y}{2\sqrt{y}}, \tag{7.14}$$

which holds as long as $y \leq x$. Accordingly, the states which are connected adiabatically with the initial black hole state (x_0, y_0), are solutions to the Cauchy problem

$$\frac{{\rm d}y}{{\rm d}x} = \sqrt{\frac{y}{x}}\frac{\mathcal{F}_H^e}{\mathcal{F}_H(x,y)}, \tag{7.15a}$$

$$y(x_0) = y_0, \tag{7.15b}$$

where $x_0 > y_0$. Applying Eq. (7.10), one can rewrite Eq. (7.15a) as

$$\begin{aligned}\frac{{\rm d}y}{{\rm d}x} &= \frac{y}{x}\left(1 + \frac{R_+(x,y)}{g_*(x,y)}\right),\\ &= \frac{1}{8}\left\{1 + 2\cos\left[\frac{1}{3}\arccos\left(1 - \frac{2y}{x}\right)\right]\right\}^3.\end{aligned} \tag{7.16}$$

The above problem allows for two solutions, say $y_{1,2}$, which are given by (see appendix E.1):

$$y_1(x) = x - y_2(x), \tag{7.17}$$

in which

$$y_2(x) = \frac{27\rho^2}{16}\left(1 - \frac{\rho}{2\sqrt{x}}\right), \tag{7.18}$$

where ρ is a constant determined by the initial condition. For extremal initial states $y(x_0) = x_0$, the Cauchy problem admits the two solutions $\rho = 0$, and $\rho = 2\sqrt{x_0}$. The first one corresponds to the adiabatic transformations between the extremal states, $y(x) = x$. As we have shown, these types of transformations are not isoareal. This statement indicates that the postulate $\mathcal{S} \propto \mathcal{A}$ is not valid for extremal black holes, and in particular, the EHBH. The second solution is more complicated because it connects, adiabatically, the extremal states with non-extremal states. Geometrically, this implies the change in the topology and, due to the reversibility, problems with the second and the third laws of thermodynamics. To prevent any inconsistencies, it is better to eliminate this kind of solution.

For $\rho \neq \{0, 2\sqrt{x_0}\}$ and considering an arbitrary, non-extremal, initial state, the functions given by Eqs. (7.17) and (7.18), yield the following equations for ρ:

$$\rho^3 - 2\sqrt{x_0}\,\rho^2 + \frac{32}{27}\sqrt{x_0}(x_0 - y_0) = 0, \tag{7.19}$$

$$\rho^3 - 2\sqrt{x_0}\,\rho^2 + \frac{32}{27}\sqrt{x_0}\,y_0 = 0, \tag{7.20}$$

whose solutions can be written simply as

$$\rho_k(x_0, y_0) = \frac{2\sqrt{x_0}}{3}\left[1 + 2\cos\left(\omega + \frac{2k\pi}{3}\right)\right], \tag{7.21}$$

where $k = 0, 1, 2$, and

$$\omega \equiv \omega(x_0, y_0) = \frac{1}{3}\arccos\left|1 - \frac{2y_0}{x_0}\right|. \tag{7.22}$$

The above means that, given an initial equilibrium configuration for the HBH, there are six possible curves adiabatically connected with it, say $y_{jk}(x) \equiv y_j(x; \rho_k)$, with $j = 1, 2$ and $k = 0, 1, 2$. Let us designate by ϵ_{jk} and σ_{jk}, the value of the x-coordinate at the intersection of each curve y_{jk} with the EHBH (where $y = x$), and the SBH (where $y = 0$), respectively (green and yellow dots in Fig. 7.2). Then, it is no hard to show that $\epsilon_{1k} = \sigma_{2k}$ and $\epsilon_{2k} = \sigma_{1k}$. In addition, since $\rho_0 > \rho_2 > 0$, one gets $\epsilon_{10} = \sigma_{20} > \epsilon_{12} = \sigma_{22} > 0$, and consequently, $\epsilon_{20} = \sigma_{10} > \epsilon_{22} = \sigma_{12} > 0$. However, because $\rho_1 < 0$, the function $y_2(x)$ is strictly positive and therefore $\epsilon_{21} = \sigma_{11} > 0$ and $\epsilon_{11} = \sigma_{21} \to \infty$.

The above result is crucial to exclude the leaf $\mathcal{T} = 0$ from the adiabatic manifold. In fact, if we delete all the solutions y_{jk}, except y_{11}, then the generated adiabatic surface does not intersect the extremal surface (see Fig. 7.3). Thus, assuming that the relation $\mathcal{S} \propto \mathcal{A}$ is not followed by the extremal black holes (Teitelboim, 1995), we characterize the thermodynamics of the HBH by

$$\mathcal{S}(r_s, l) = \begin{cases} \frac{1}{4}\mathcal{A}, & \text{non-extremal states,} \\ \\ 0, & \text{extremal states.} \end{cases} \tag{7.23}$$

To ensure the correct foliation of the thermodynamic manifold, and based on the processes described above (cf. Fig. 7.1), the following conditions must hold:

1. The slope of the x-y curves is positive,

$$\frac{\mathrm{d}y}{\mathrm{d}x} > 0. \tag{7.24}$$

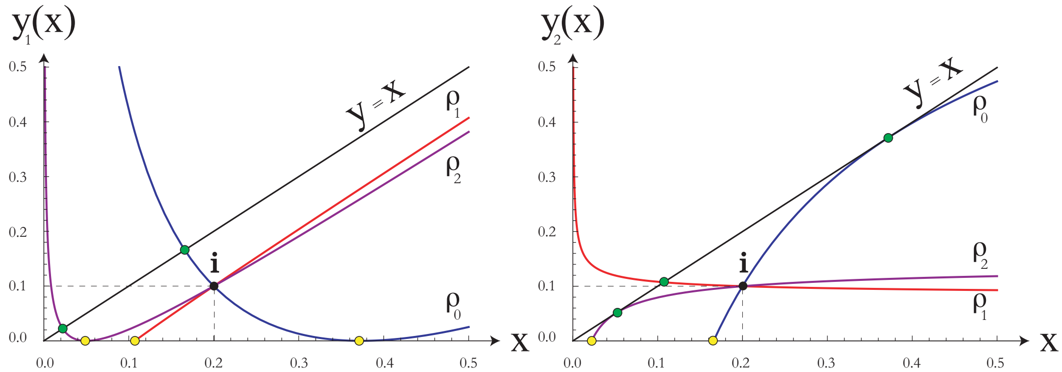

Figure 7.2: Adiabatic solutions for the Cauchy problem given by Eq. (7.16). Top panel: $y_1(x)$ given by Eq. (7.17); Bottom panel: $y_2(x)$ given by Eq. (7.18). In both plots we have used as the initial state $\mathbf{i} = (x_0, y_0) = (0.2, 0.1)$, so that $\rho_0 = 0.815$, $\rho_1 = -0.218$ and $\rho_2 = 0.298$. Green dots represent the intersection of each function with the EHBH, $y(x) = x$, whereas the yellow represent the intersection with the SBH, $y(x) = 0$.

2. As the variables decrease, the system evolves towards the SBH, while when they grow, the EHBH is approached.

3. In the neighborhood of any arbitrary state, $\mathbf{i}$, of a physical system there are neighboring states $\mathbf{i}'$, which are inaccessible from $\mathbf{i}$ along adiabatic paths (Carathéodory's principle (Carathéodory, 1909; Buchdahl, 1949a,b)).

Therefore, the complete solution to the Cauchy problem that satisfies the physical requirements, can be written as

$$y(x) = x - \frac{27\rho_1^2}{16}\left(1 + \frac{|\rho_1|}{2\sqrt{x}}\right), \tag{7.25}$$

whose asymptotic behavior is

$$y(x) \simeq x - \frac{27\rho_1^2}{16}, \tag{7.26}$$

that ensures the condition $x > y$. We will see in the next section, where the adiabatic properties of the SDBTZ black hole is discussed, that the correct thermodynamic foliation is possible by building a piecewise argument with a physically accepted segment, which is the solution (7.25).

7.1.3 Classical scattering of two EHBHs and the second law

Let us assume that the thermodynamic state $(x_a + x_b, y_a + y_b)$, is produced by merging two HBHs of the initial conditions (x_a, y_a) and (x_b, y_b), in a process that no exchange

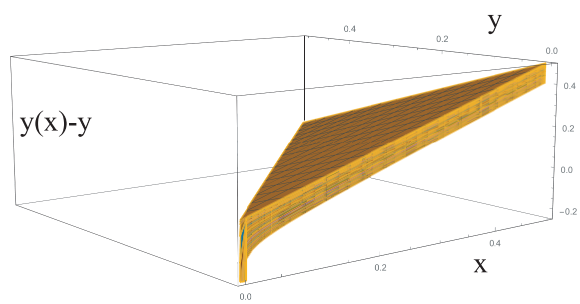

Figure 7.3: Adiabatic volume generated by the physical solution $y(x) = y_{11}(x)$. The construction corresponds to the foliation of the surfaces $y(x) - y$ by fixing $x_0 = 0.2$ and varying y_0 between 0 and 0.198 (with the steps 0.002). The upper limit edge of the surface corresponds to the extremal surface x-y.

of energy is done with the rest of the universe. Defining the quantity

$$\zeta^2(x, y) = x - y, \tag{7.27}$$

the initial state of the process is now characterized by $\zeta_{\text{in}} = \zeta_a + \zeta_b$, with $\zeta_a^2 \equiv \zeta^2(x_a, y_a) \geq 0$ and $\zeta_b^2 \equiv \zeta^2(x_b, y_b) \geq 0$. In the same manner, the final state becomes $\zeta_{\text{fin}} = \zeta_{ab}$, where $\zeta_{ab}^2 \equiv \zeta^2(x_a + x_b, y_a + y_b)$, and Eq. (7.52) yields

$$\zeta_{ab}^2 = \zeta_a^2 + \zeta_b^2 + 2\,(x_a x_b - y_a y_b)\,. \tag{7.28}$$

Exploiting Eq. (7.54), we obtain

$$\zeta_{ab}^2 - (\zeta_a + \zeta_b)^2 = 2\Big[x_a x_b - y_a y_b - \sqrt{(x_a^2 - y_a^2)(x_b^2 - y_b^2)}\,\Big]. \tag{7.29}$$

In the case that the initial states are constituted by extremal black holes (with zero entropy according to Eq. (7.23)), we have $x_a = y_a$ and $x_b = y_b$, giving $\zeta_a = 0 = \zeta_b$ and hence, $\zeta_{ab} = 0$, which implies that the final black hole is as well, extremal and therefore, has zero entropy.

If the merger of the black holes is considered irreversible, then the process would violate the second law of thermodynamics, because they never produce a regular HBH to increase the total entropy of the system. Although this argument holds for systems at non-zero temperature, it puts into question the hypothesis $\mathcal{S} = 0$ for the extremal states. To relax the above, we could consider a small amount of angular momentum so that the final state is a non-extremal state, and thus, the final entropy is greater than the initial one, protecting the second law. This obviously involves a detailed study of such a situation that will not be addressed here. Another way that could alleviate the understanding of the process, consists of abandoning the hypothesis of zero entropy to give rise to a law of the form $\mathcal{S} = f(\mathcal{A})$, where f is a function of the area, which can be proposed in the context of a thin shell for the case of a rotating uncharged SDBTZ black hole (Lemos et al., 2017).

7.2 The case of a rotating SDBTZ black hole

In this section, based on the same method applied in the previous section, we study some thermodynamic aspects of the rotating SDBTZ black hole, in the context of the Carathéodory's postulate of adiabatic inaccessibility, that ensures the integrability of the Pfaffian form $\delta Q_{\rm rev}$. For the case of the (3 + 1)-dimensional black holes, this type of construction has been studied in detail (Belgiorno, 2003; Belgiorno & Martellini, 2004; Belgiorno & Cacciatori, 2011) which gives rise to the isoareal transformations, i.e., the transformations between the black hole states with the same areas. On the other hand, for the (2 + 1)-dimensional black holes, the adiabatic transformations correspond to the isoperimetral transformations between states that reside in the non-extremal manifold. We continue by the study of the geometrothermodynamics of a rotating version of the SDBTZ black hole, in the context of Carathéodory's approach (Fathi et al., 2021).

7.2.1 The rotating SDBTZ black hole and its thermodynamics

As introduced in chapter 4, the (2+1)-dimensional, uncharged, black hole solution with a negative cosmological constant $\Lambda = -\ell^{-2}$, is obtained from the action

$$I = \frac{c}{2\pi G}\int \sqrt{-g}\left[R + 2\,\ell^{-2}\right] \mathrm{d}^2x\,\mathrm{d}t + \mathcal{B}, \tag{7.30}$$

where $\mathcal{B}$ is a surface term (Bañados et al., 1992, 1993). For the stationary circular symmetry, the corresponding spacetime metric is given in terms of the coordinates $-\infty < t < \infty, 0 < r < \infty$, and $0 \leq \phi \leq 2\pi$, and can be written as (Rincón & Koch, 2018b)

$$\mathrm{d}s^2 = -N^2(r)c^2\mathrm{d}t^2 + N^{-2}(r)\mathrm{d}r^2 + r^2\left[N^{\phi}(r)c\,\mathrm{d}t + \mathrm{d}\phi\right]^2, \tag{7.31}$$

in which, the square lapse function and the angular shift are given, respectively, by

$$N^2(r) = -\frac{GM}{c^2} + \frac{r^2}{\ell^2} + \frac{G^2 J^2}{4c^6 r^2}, \tag{7.32a}$$
$$N^\phi(r) = -\frac{GJ}{2c^3 r^2}, \tag{7.32b}$$

where M and J, indicate the mass and the angular momentum of the black hole. This spacetime possesses an inner (r_-), and an event (r_+) horizon, that are located at

$$r_\pm = \frac{c\,\tau_\pm\,(\mathcal{M},\mathcal{J})}{\sqrt{2}}, \tag{7.33}$$

where

$$\tau_\pm\,(\mathcal{M},\mathcal{J}) = \sqrt{\mathcal{M} \pm \sqrt{\mathcal{M}^2 - \mathcal{J}^2}}, \tag{7.34}$$

and

$$\mathcal{M} \equiv \frac{M}{m_p\,\Omega_{\text{ext}}^2}, \tag{7.35a}$$
$$\mathcal{J} \equiv \frac{t_p\,J}{\hbar\,\Omega_{\text{ext}}}. \tag{7.35b}$$

Here the subscript "p" is referred to the Planck quantities in (2+1) dimensions[1], and $\Omega_{\text{ext}} = c\ell^{-1}$ is the angular velocity of the *extremal black hole*. Note that, the physical dimension of $\mathcal{M}$ and $\mathcal{J}$, is [time^2], while the function $\tau_\pm$ has the dimension of [time]. Also, in the extremal case the relation $\mathcal{M} = \mathcal{J}$ is satisfied.

The Bekenstein-Hawking entropy formula, if applied to the SDBTZ black hole, gives the entropy proportional to the event horizon's perimeter $P_{\text{bh}} = 2\pi r_+$ instead of its area A_{bh}, as it is expected from the dimensional ground. Therefore

$$S = \frac{k_B}{4}\frac{P_{\text{bh}}}{\ell_p} = \frac{k_B}{4}\left(\frac{2\pi r_+}{c\,t_p}\right) = a\tau_+, \tag{7.36}$$

where S is the entropy, k_B is the Boltzmann constant, and $a = \frac{\pi}{\sqrt{8}}(k_B\,t_p^{-1}) \approx 1.1(k_B\,t_p^{-1})$. Defining $\mathcal{S} \equiv S\,a^{-1} = \tau_+$, and using Eqs. (7.34) and (7.36), we obtain a Christodoulou-type mass formula, which relates the total mass (energy) $\mathcal{M}$ to the entropy and the angular momentum, in the following form:

$$\mathcal{M}(\mathcal{S},\mathcal{J}) = \frac{1}{2}\,\mathcal{S}^2 + \frac{1}{2}\,\frac{\mathcal{J}^2}{\mathcal{S}^2}. \tag{7.37}$$

[1] In the (2+1)-dimensional gravity, the gravitational constant G has the physical dimension of $\left[\frac{\text{length}^2}{\text{mass}\times\text{time}^2}\right]$ (Cruz & Lepe, 2004). Therefore, the Planck mass, length and time become $m_p = \frac{c^2}{G}$, $l_p = \frac{G\hbar}{c^3}$, and $t_p = \frac{l_p}{c}$.

We base our our study on the framework of Carathéodory's approach to thermodynamics, that postulates the integrability of the Pfaffian form $\delta Q_{\rm rev}$, representing the infinitesimal heat exchanged reversibly (Buchdahl, 1949a,b,c, 1954, 1955; Landsberg, 1964; Marshall, 1978; Boyling, 1968, 1972; Pogliani & Berberan-Santos, 2000; Belgiorno, 2002; Belgiorno, 2003b; Belgiorno & Martellini, 2004; Belgiorno, 2003; Belgiorno, 2003a; Belgiorno & Cacciatori, 2011). In particular, we assume that the so-called metrical entropy $\mathcal{S}$ and absolute temperature $\mathcal{T}$ are as defined in Eq. (7.6), and here,

$$\frac{\partial \mathcal{S}}{\partial \mathcal{M}} \equiv \frac{1}{\mathcal{T}} > 0, \tag{7.38}$$

so that

$$\mathcal{T}(\mathcal{M},\mathcal{J}) = \frac{\left(\mathcal{M}+\sqrt{\mathcal{M}^2-\mathcal{J}^2}\right)^2-\mathcal{J}^2}{\left(\mathcal{M}+\sqrt{\mathcal{M}^2-\mathcal{J}^2}\right)^{3/2}}. \tag{7.39}$$

In fact, if we choose the pair $(\mathcal{M},\mathcal{J})$ as the extensive, independent variables in the equilibrium thermodynamics (i.e. homogeneous functions of degree one), then the homogeneity of the system is reflected in the integrability of the Pfaffian form

$$\delta Q_{\rm rev} = \mathrm{d}\mathcal{M} - \mathcal{W}\,\mathrm{d}\mathcal{J}, \tag{7.40}$$

where $\mathcal{W}$ is the angular velocity of the black hole, given by

$$\mathcal{W}(\mathcal{M},\mathcal{J}) = \frac{\mathcal{J}}{\mathcal{M}+\sqrt{\mathcal{M}^2-\mathcal{J}^2}}. \tag{7.41}$$

Therefore, it is straightforward to show that, under the scaling transformation $(\mathcal{M},\mathcal{J}) \mapsto (\lambda\mathcal{M},\lambda\mathcal{J})$, we get $\delta Q_{\rm rev} \mapsto \lambda\delta Q_{\rm rev}$, which means that the Pfaffian form is homogeneous of degree one. Consequently, we have an Euler vectorial field, or a Liouville operator, as the infinitesimal generator of the homogeneous transformations

$$D = \mathcal{M}\frac{\partial}{\partial\mathcal{M}} + \mathcal{J}\frac{\partial}{\partial\mathcal{J}}, \tag{7.42}$$

using which, we obtain

$$D\mathcal{S} = \frac{1}{2}\mathcal{S}, \tag{7.43}$$

meaning that, $\mathcal{S}$ is homogeneous of degree $\frac{1}{2}$. Similarly, the temperature is also homogeneous of degree $\frac{1}{2}$. Furthermore, it is straightforward to check that the angular velocity is a homogeneous function of degree zero, or $D\mathcal{W} = 0$, and therefore, it is an intensive variable.

It is, naturally, tempting to address a comparison with the natural (3+1)-dimensional counterpart (i.e. the Kerr-(Anti-)de Sitter black hole). In fact, there are some differences between these cases that should be analyzed carefully. Furthermore, we have found a mathematical equivalence of a remarkable theoretical potential. However, for the sake the scope of this study, for now, we strive on presenting some immediate results of the above discussed concepts, and leave the aforementioned mathematical comparison to the future.

7.2.2 The adiabatic-isoperimetral transformations

As discussed in the last section for the case of the HBH, an important result of the Carathéodory's approach is that it allows for the generation of a non-extremal manifold foliation. In fact, the non-extremal thermodynamic space is foliated by those submanifolds of co-dimension one, which are solutions of the Pfaffian equation $\delta Q_{\text{rev}} = 0$.

As stated above, for the non-extremal manifold ($\mathcal{T} > 0$), the Pfaffian form is given by Eq. (7.40). Accordingly, performing the changes of variable $x = \mathcal{M}^2$ and $y = \mathcal{J}^2$, we get

$$\delta Q_{\text{rev}} = \frac{1}{2\sqrt{x}}\mathrm{d}x - \frac{1}{2(\sqrt{x} + \sqrt{x-y})}\mathrm{d}y, \tag{7.44}$$

that respects the condition $x \geq y$. Thus, for the isoperimetral transformation $\delta Q_{\text{rev}} = 0$, that connects, adiabatically, the initial state $\mathbf{i} \equiv (x_i, y_i)$ to the final state $\mathbf{f} \equiv (x_f, y_f)$, the adiabatic trajectories are solutions to the Cauchy problem

$$\frac{\mathrm{d}y}{\mathrm{d}x} = 1 + \sqrt{1 - \frac{y}{x}}, \tag{7.45a}$$

$$y(x_i) = y_i, \tag{7.45b}$$

with $y_i < x_i$. It is then straightforward to show that, the solutions to this problem are

$$y_a(x) = 2\sqrt{\zeta_a}\,\sqrt{x} - \zeta_a, \tag{7.46a}$$

$$y_b(x) = 2\sqrt{\zeta_b}\,\sqrt{x} - \zeta_b, \tag{7.46b}$$

where the constants $\zeta_{a,b} \equiv \zeta_{a,b}(x_i, y_i)$ are given by

$$\zeta_{a,b} = 2x_i - y_i \pm 2\sqrt{x_i(x_i - y_i)}, \tag{7.47}$$

with $x_i > y_i$. Each function vanishes at the point $(x_0, 0)$, with $x_0 = \frac{1}{4}\zeta_{a,b}$, which corresponds to the static SDBTZ black hole. The thermodynamic (extremal) limit, on the other hand, is reached at (x_e, x_e), with $x_e = \zeta_{a,b}$ (see Fig. 7.4, showing both functions intersecting at the initial point $\mathbf{i}$). We will come back to these concepts later in this subsection.

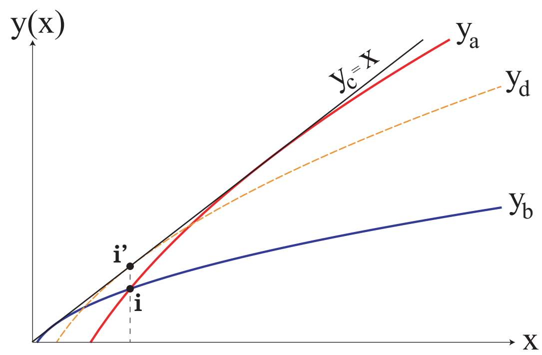

Figure 7.4: The plots of the adiabatic solutions to the Cauchy problem, given in Eqs. (7.46a), (7.46b), (7.49a) and (7.49b). The static black hole limit, for each case, is where the curves hit the x coordinate, whereas, the extremal limit corresponds to the line $y = x$.

Note that, it is important to be cautious about the conditions on the extremal submanifold, on which, the condition $\delta Q_{\rm rev} = 0$ is still satisfied. This implies that the extremal submanifold is an integral submanifold of the Pfaffian form (Belgiorno, 2003; Belgiorno & Martellini, 2004). In fact, considering the extremal point $\mathbf{i}' \equiv (x_i, x_i)$ as the initial state, the Cauchy problem becomes

$$\frac{\mathrm{d}y}{\mathrm{d}x} = 1 + \sqrt{1 - \frac{y}{x}}, \tag{7.48a}$$

$$y(x_i) = x_i, \tag{7.48b}$$

which allows for the two solutions

$$y_c(x) = x, \tag{7.49a}$$

$$y_d(x) = 2\sqrt{x_i}\,\sqrt{x} - x_i. \tag{7.49b}$$

Now that the solutions to the both cases of non-extremal and extremal cases have been given, it is of importance discussing their physical features, regrading the adiabatic processes. In particular, the solution y_a given by Eq. (7.49a), indicates that the extremal states are adiabatically connected to each other. However, the solution y_b in Eq. (7.49b), presents a more complicated situation, because it connects, adiabatically, the non-extremal states with the extremal ones. This, in fact, poses a contradiction to the second law of thermodynamics, since it provides the possibility to construct a Carnot cycle with one hundred percent thermal efficiency, and this, violates the Ostwald's postulate of the second law. Furthermore, it would be possible to transform, completely, the heat into work, that is also in contrast with the second law. To eliminate this singular behavior of the thermodynamic foliation, we assume that the surface $\mathcal{T} = 0$ is a leaf itself, that is, we exclude it from the set of solutions. Accordingly, by introducing a discontinuity in $\mathcal{S}$ between the extremal and non-extremal states, we construct a foliation of the thermodynamic variety, whose leaves are distinguished by

$$\mathcal{S}(\mathcal{M},\mathcal{J}) = \begin{cases} \frac{1}{4}\mathcal{P}, & \text{non-extremal states,} \\ \\ 0, & \text{extremal states.} \end{cases} \tag{7.50}$$

The choice of the value $\mathcal{S} = 0$ for the extremal states, stems in some topological preferences (Hawking et al., 1995; Teitelboim, 1995), and has been explicitly proposed by Carroll (Carroll et al., 2009). Nevertheless, it has been shown that this choice, is a particular case of a well-behaved area-dependent function, that can opt non-zero values (Lemos et al., 2016). In particular, the thin shells (rings) in the (2+1)-dimensional gravity, can change their entropy values during their evolution to a black hole (Lemos & Quinta, 2014; Lemos et al., 2015, 2017).

We can now establish a criteria for the physically acceptable solutions, based on the results obtained above:

1. Due to the homogeneity of the extensive variables $(\mathcal{M},\mathcal{J})$ or (x,y), every adiabatic process must satisfy Eq. (7.24), in the context of the definitions done in this subsection.

2. An initial state belonging to the submanifold $\mathcal{T} > 0$, can only be adiabatically connected to another state, if it neither belongs to the submanifold $\mathcal{T} = 0$, nor it passes through it.

3. In the neighborhood of any equilibrium state of the system, there exists states that are inaccessible by the reversible adiabatic processes (Carathéodory postulate) .

Condition 1, is nothing but the result of expressing the thermodynamic system in terms of the extensive variables, which are, of course, homogeneous of degree one. Condition 2, ensures satisfaction of the second and third laws of thermodynamics. From the geometric point of view, this guarantees that the black hole topology does not change. The above statements have been visualized, qualitatively, in Fig 7.5. There, we have exemplified the allowed processes by o $\leftrightarrow$ p, r $\leftrightarrow$ s, and q $\leftrightarrow$ t, and the

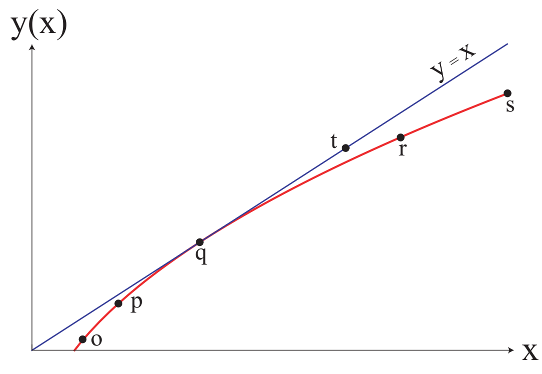

Figure 7.5: The adiabatic solutions to the Cauchy problem and the extremal limit. In order to avoid violation of the second law, the only allowed processes are o $\leftrightarrow$ p; r $\leftrightarrow$ s; q $\leftrightarrow$ t. The processes p $\leftrightarrow$ q; q $\leftrightarrow$ r are, on the other hand, prohibited.

forbidden processes by p $\leftrightarrow$ q, and q $\leftrightarrow$ r. Accordingly, the non-extremal initial state **i**, is connected with the final states, by the adiabatic solution curves

$$y(x) = \begin{cases} y_a(x), & \text{for } x_0 \leq x < x_i, \\ \\ y_b(x), & \text{for } x_i \leq x < \infty. \end{cases} \tag{7.51}$$

In this sense, we can ramify the physically allowed branches of the solutions, as shown in Fig. 7.6. In this diagram, the physically accepted parts of the solution $y(x)$, are

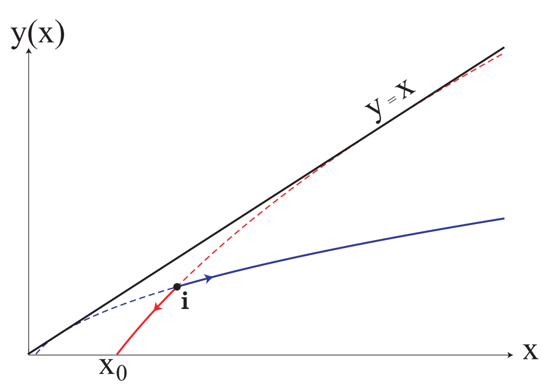

Figure 7.6: The physically allowed solutions to the Cauchy problem for the SDBTZ black hole. The initial state $\mathbf{i} \equiv (x_i, y_i)$, with $y_i < x_i$, can be connected, adiabatically, to the final state $\mathbf{f} \equiv (x_f, y_f)$, with $y_f < x_f$, following the path y_a (red curve), if $x_f < x_i$, and the path y_b (blue curve), if $x_f > x_i$.

those that connect, adiabatically, the initial state $\mathbf{i} \equiv (x_i, y_i)$, with $y_i < x_i$, to another state $\mathbf{f} \equiv (x_f, y_f)$, with $y_f < x_f$, following the y_a branch, if $x_f < x_i$, and the y_b branch, if $x_f > x_i$.

A direct consequence of the condition 3, is that it prevents forming an adiabatic cycle (as desired by engineering). Such cycle has been illustrated in Fig. 7.7. Referring to the triangular path in this diagram, the state $\mathbf{i}$, residing in the submanifold $\mathcal{T} > 0$, is first connected, adiabatically, to the state $\mathbf{i}'$, and then to the state $\mathbf{i}''$, which both reside in the submanifold $\mathcal{T} = 0$, and finally, it is returned to $\mathbf{i}$. Note that, the process $\mathbf{i}' \to \mathbf{i}''$ is adiabatic and isothermal. In fact, since these states are inaccessible by the Carathéodory's postulate, the above adiabatic cycle is not allowed to form. Accord-

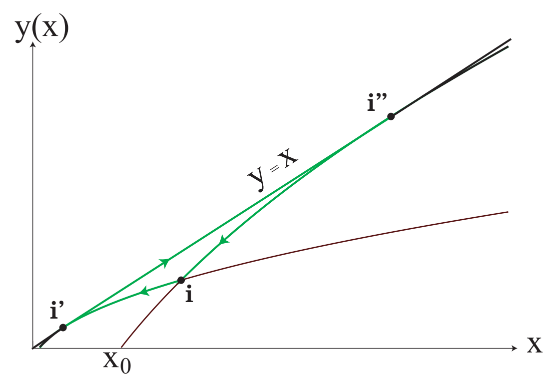

Figure 7.7: The Carathéodory's postulate, prevents the formation of an adiabatic cycle. In such cycle, the equilibrium state $\mathbf{i}$ is adiabatically connected, respectively, to the extremal states $\mathbf{i}'$ and $\mathbf{i}''$, and then, is returned to itself (see the green triangular path). Such cycle is prohibited, because the states $\mathbf{i}'$ and $\mathbf{i}''$ are inaccessible for the state $\mathbf{i}$.

ingly, the extremal limit should be excluded from the adiabatic hypersurface, since there is no adiabatic process that can reach this state. In fact, either of the solutions (7.46a) and (7.46b) can produce an adiabatic surface, that lies between the extremal $(y = x)$ and the static $(y = 0)$ black hole limits (see Fig. 7.8).

Note that, since the conditional solution given by Eq. (7.51) excludes the extremal states (the $\mathcal{T} = 0$ leaf), we can ensure the satisfaction of the third law through all isoperimetral (or adiabatic) processes.

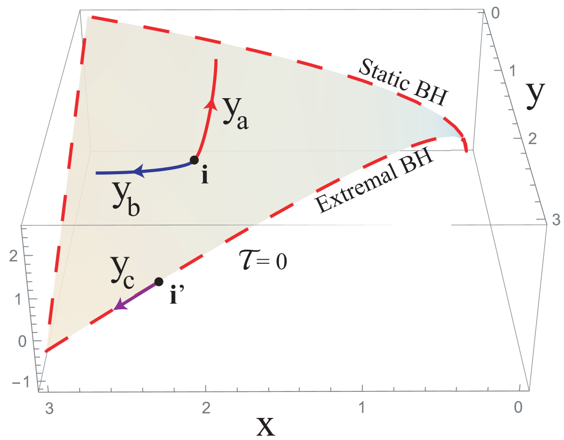

Figure 7.8: The adiabatic surface plotted for $\zeta_a = 1.2$, which is confined by the extremal, and the static black hole (BH) limits. The adiabatic processes y_a and y_b, can connect the initial state **i** to other points on the surface. Same holds for the adiabatic process y_c on the extremal limit, connecting the initial point **i**$'$ to other points on the same line. The transmission **i** $\rightarrow$ **i**$'$ is, however, prohibited by the Carathéodory's postulate.

7.2.3 Scattering of two extremal black holes and the second law

We now explore the possibility of occurring an isolated merger of two extremal rotating SDBTZ black holes with the initial states $(\mathcal{M}_1, \mathcal{J}_1)$ and $(\mathcal{M}_2, \mathcal{J}_2)$, to produce the final state $(\mathcal{M}_1 + \mathcal{M}_2, \mathcal{J}_1 + \mathcal{J}_2)$. Following the same method as applied in the previous section for the HBH, we define the quantity

$$\alpha^2(\mathcal{M}, \mathcal{J}) = \mathcal{M}^2 - \mathcal{J}^2, \tag{7.52}$$

so that, for the initial black holes we have $\alpha_{\rm in} = \alpha_1 + \alpha_2$, where

$$\alpha_1^2(\mathcal{M}_1, \mathcal{J}_1) = \mathcal{M}_1^2 - \mathcal{J}_1^2 \geq 0, \tag{7.53a}$$
$$\alpha_2^2(\mathcal{M}_2, \mathcal{J}_2) = \mathcal{M}_2^2 - \mathcal{J}_2^2 \geq 0, \tag{7.53b}$$

and for the final black hole, $\alpha_{\rm fin} = \alpha_{12}$, with

$$\begin{aligned}\alpha_{12}^2(\mathcal{M}_1 + \mathcal{M}_2, \mathcal{J}_1 + \mathcal{J}_2) &= (\mathcal{M}_1 + \mathcal{M}_2)^2 - (\mathcal{J}_1 + \mathcal{J}_2)^2 \\ &= \alpha_1^2(\mathcal{M}_1, \mathcal{J}_1) + \alpha_1^2(\mathcal{M}_2, \mathcal{J}_2) + 2\,(\mathcal{M}_1\,\mathcal{M}_2 - \mathcal{J}_1\,\mathcal{J}_2)\,.\end{aligned} \tag{7.54}$$

Therefore, for two extremal black holes of the initial states $\alpha_1^2(\mathcal{M}_{\rm ext}^{(1)}, \mathcal{J}_{\rm ext}^{(1)}) = \alpha_2^2(\mathcal{M}_{\rm ext}^{(2)}, \mathcal{J}_{\rm ext}^{(2)}) = 0$, and of the positive masses $\mathcal{M}_{\rm ext} = |\mathcal{J}_{\rm ext}| > 0$, Eq. (7.54) becomes

$$\begin{aligned}
\alpha_{12}^2 \left(\mathcal{M}_{\rm ext}^{(1)} + \mathcal{M}_{\rm ext}^{(2)}, \mathcal{J}_{\rm ext}^{(1)} + \mathcal{J}_{\rm ext}^{(2)}\right) &= 2\left(\mathcal{M}_{\rm ext}^{(1)}\mathcal{M}_{\rm ext}^{(2)} - \mathcal{J}_{\rm ext}^{(1)}\mathcal{J}_{\rm ext}^{(2)}\right) \\
&= 2\left(\left|\mathcal{J}_{\rm ext}^{(1)}\right| \left|\mathcal{J}_{\rm ext}^{(2)}\right| - \mathcal{J}_{\rm ext}^{(1)}\mathcal{J}_{\rm ext}^{(2)}\right) \\
&= 2\left|\mathcal{J}_{\rm ext}^{(1)}\right| \left|\mathcal{J}_{\rm ext}^{(2)}\right| (1-\cos\beta)\,, \qquad (7.55)
\end{aligned}$$

where $\beta = \measuredangle(\mathcal{J}_{\rm ext}^{(1)}, \mathcal{J}_{\rm ext}^{(2)})$. Thus, for extremal black holes rotating in the same direction ($\beta = 0$), the final black hole will be, as well, an extremal one. This is while, for those rotating in opposite directions ($\beta = \pi$), the final black hole will not be extremal.

In the case of having an extremal final state, a possible violation of the second law may occur, since, in fact, the process is irreversible and the entropy of the final state should be greater than that of the initial states (under the assumption that the system is isolated and there is no exchange of energy with the rest of the universe). On the other hand, if the final state is non-extremal, then its entropy is, naturally, greater than that of the initial states. As it was formerly given in Eq. (7.50), the entropy of the SDBTZ black hole is $\mathcal{S} = \frac{1}{4}g\mathcal{P}$, where $\mathcal{P}$ is the perimeter of the event horizon and g is the *genus*, that characterizes the topology of the thermodynamic manifold. In this sense, the extremal and non-extremal black holes are characterized, respectively, by $g = 0$ and $g = 1$. Hence, the latter corresponds to the change of the topology of the black hole.

In fact, passing from one black hole topology to another, we encounter the space-time singularities. And since the above processes accure in the classical environment, these singularities are inevitable. Therefore, to avoid the complexities associated with the change in the topology, it is convenient to infer that the scattering of two initially extremal SDBTZ black holes leads to an extremal SDBTZ black hole, and this, violates the second law. The above statements can be summarized as

$$\beta = \begin{cases} 0 \quad \Rightarrow \quad \text{violation of the second law,} \\ \pi \quad \Rightarrow \quad \text{change of the black hole topology.} \end{cases} \qquad (7.56)$$

7.3 Summary

In this chapter, we constructed the correct foliation of the thermodynamic manifold for the HBH and the rotating SDBTZ black hole, by applying the Carathéodory's axiomatic principle. Accordingly, we solved the Cauchy problem associated with the

Pfaffian equation $\delta Q_{\text{rev}} = 0$, where δQ_{rev} represents the infinitesimal heat exchanged reversibly. It is important to note that, even the procedure of applying the B-H formula, does not demand any priori knowledge of the laws of thermodynamics, in order to construct the submanifold, although of course, they are mathematically connected.

For the case of the HBH, by developing the aforementioned ideas, we found that, given an initial state of equilibrium, one can find twelve isoareal connections with other equilibrium states, through six possible curves, y_{jk} with $j = 1, 2$ and $k = 0, 1, 2$. Five of these curves adiabatically connect the non-extremal states with the extremal ones, which causes contradictions with the second and the third laws; for example, it would be possible to get to the zero temperature in a finite sequence of steps, and therefore, build a heat engine whose efficiency is equal to one. We, however, were able to find a solution that avoids such unwanted behavior; it generates a manifold that does not include the extremal sub-manifold $\mathcal{T} = 0$. This can be better understood in the context of the Carathéodory's principle (cf. condition 3), by assuming such states as being inaccessible. On the extremal sub-manifold, the condition $\delta Q_{\text{rev}} = 0$ is still valid, which gives rise to two kinds of transformations that satisfy the initial extremal condition $y(x_0) = x_0$. One of the solutions, adiabatically connects the extremal states with the non-extremal ones, that have the same areas (isoareal transformations). The other solution connects the extremal states with different areas. This solution, however, can be considered as an adiabatic transformation, by virtue of the null entropy law. This accounts for the disconnection between the leaves $\mathcal{T} = 0$ and $\mathcal{T} > 0$, which is expressed, as well, in the metric entropy (7.23). In fact, as stated above, such disconnection can be provoked by the exclusion of the solutions y_{jk} (except for y_{11}), that allows for eliminating any connections between the above varieties, and respects the second and the third laws. Nevertheless, the scattering process of two static EHBH leads to questioning this issue, even more profoundly, because of the impossibility of the increase in entropy in the final state. As in the other cases, the addition of a new variable seems to be the solution, although the price will be the loss of the homogeneity of the system, which gives rise to quasi-homogeneous potentials that do not allow for fixing the degree of homogeneity of the Pfaffian form, although, a thermodynamic construction is allowed (Belgiorno, 2003b). In fact, all the standard thermodynamic parameters can be connected with each other, in order to obtain different quantities which are of interest. For example, using the Stefan-Boltzmann law together with the corresponding Hayward's quantities, one can calculate the evaporation time of the

HBH, from the differential equation

$$\frac{\mathrm{d}r_s}{\mathrm{d}t} = -br_s^2 R_+^2(r_s,l)\mathcal{T}^4(r_s,l), \tag{7.57}$$

where $b = \frac{1}{120\pi} l_p^2 c$. Expansion of the right hand side of Eq. (7.57) about the Schwarzschild solution (corresponding to $l = 0$) and doing the intergation, yields

$$\Delta t_{\mathrm{evap}} \simeq \frac{16 r_s^3}{3b}\left(1 + 6\frac{l^2}{r_s^2}\right), \tag{7.58}$$

which implies that the lifetime of the HBH is longer than that of the SBH.

We also applied the same approach to study the thermodynamics of the SDBTZ black hole. The natural extensive variables of the uncharged SDBTZ black hole in the equilibrium thermodynamics space (i.e. the homogeneous variables of degree one), are $(\mathcal{M},\mathcal{J})$, that has an associated Pfaffian form $\delta Q_{\mathrm{rev}} = \mathrm{d}\mathcal{M} - \mathcal{W}\mathrm{d}\mathcal{J}$. The symmetry of the homogeneity for δQ_{rev}, can then be inspected by means of the Euler vector field (Liouville operator) in Eq. (7.42), which indicates the consistency of the methods given here, with the thermodynamic definition of the temperature. As the first application of the presented approach, we studied the adiabatic processes, by analyzing the corresponding Cauchy problem. In this sense, the problem is equivalent to the adiabatic processes in the RN black hole spacetime (Belgiorno & Martellini, 2004), since, regarding the adiabatic transformations, the electric charge for the RN black hole plays the same role as the angular momentum for the SDBTZ black hole. Since the obtained adiabatic solutions allow for two definite constants, they can be therefore employed in the correct physical description of the acceptable adiabatic paths. As before, the extremal submanifold must be disconnected from the non-extremal one, and the entropy of the extremal states is considered to be zero. One again, the classical merging of two extremal black holes was discussed, which provided us another tool to inspect the leaf $\mathcal{T} = 0$, and the corresponding property $\mathcal{S} = 0$. The unconformity of the second law with the aforementioned entropy condition, necessitates the inclusion of a net electrical charge for the black hole. In this sense, a new equivalence with the RN black hole could be found, which in that case, relaxes the problem by introducing a definite angular momentum to the system (Belgiorno & Martellini, 2004).

Chapter 8

Outlook for the future studies

As it is well-known, the observation of planetary orbits has had a two-thousand-year history. From the lunar orbits to the motion of the moons on heavy planets like Jupiter, celestial dynamics has appeared as one of the most fascinating field of science to the humans. After the advent of the Newtonian dynamics which were then equipped with the advanced mathematical methods by Euler, Lagrange, Hamilton and Weierstraß , observational astronomers were granted with a powerful tool to do predictions, estimations, and reliable fittings to their observed data. Despite this, there were still some anomalies which remained questionable by the Newtonian celestial mechanics, and were ought to be explained by the fantastic theory of general relativity. Henceforth, the orbits of celestial objects were given a more precise derivation, however, at the expense of more complicated and time-taking computational procedures. Although the advances in the computer hardware and software has helped scientists, significantly, to do rather interesting particle tracings in static and stationary spacetime, the mathematical concepts behind the exact solutions for the orbits continues to rule.

This, mainly, was the aim of this thesis. We have done rigorous investigations on the particle orbits in strongly gravitating systems (black holes) and in appropriate places, applied several standard tests. The summary of the work done for each of the cases has been given at the end of each corresponding chapter, so we skip repeating them in this stage. It is, however, important to derive the attention of the reader to the fact that the discussions given in this thesis are not merely theoretical studies, such that they give no further insights into the observational astrophysics. In fact, even the simplest general relativistic corrections to the Newtonian celestial mechanics have been significantly observed, for example, in the case of precessions in the periapsis of the stellar orbits at the center of our galaxy (GRAVITY Collaboration et al., 2020). This shows that, the more we go deeper into the derivation of analytical expressions for relativistic corrections, the more we can predict unobserved phenomena, as well as being able to explain modern astronomical observations. For example, the recent observation of the polarized photon ring and the relevant magnetic fields observed for M87* (Akiyama et al., 2021a,b), has been given an extensive analytical and numerical study regarding the polarization in the equatorial imaging of a Kerr black hole (Gelles et al., 2021). Same methods hold, for example, in debating the existence of a secondary photon ring (sub-ring) in the confinement of the black hole shadow, which stems in the difference in the number of non-planar orbits that a percentage of infalling photons pursue during their geodesic motion (Johnson et al., 2020). Such phenomena, beside affecting the lensing ring as addressed above, can be also detectable in the accretion lensing (Bisnovatyi-Kogan & Tsupko, 2022). Therefore, we have in our perspective, the following proposals:

1. Derivation of the exact analytical solutions to the strong accretion lensing in stationary spacetimes that go beyond the Kerr solution.

2. Calculation and demonstration of the photon regions for black holes associated with dark energy components. This can be also extended to the determination of the possible sub-rings.

Both of the above proposals are of great astrophysical interest, from both the theoretical and observational points of view. We hope that the experiences and the methods developed in this thesis, together with those that are intended to be developed, will pave the way for the fulfilment of the above research projects.

APPENDIX A

A.1 The relation between the $\wp$-Weierstraß and Jacobi elliptic functions

Let us consider the differential equation for the $\wp$-Weierstraß elliptic function, which is read as

$$\left(\frac{\mathrm{d}y}{\mathrm{d}x}\right)^2 = 4y^3 - g_2 y - g_3. \tag{A.1}$$

Now, applying the transformation

$$y(x) = \alpha s^p(\kappa x) + \beta, \tag{A.2}$$

where $p \in \mathbb{Z}$ $(\neq 0, 1)$ and the constants (α, β, κ) have to be determined. Applying the transformation (A.2), one can recast Eq, (A.1) as

$$\left(\frac{\mathrm{d}s}{\mathrm{d}z}\right)^2 = \frac{4\alpha}{p^2\kappa^2}s^{2+p} + \frac{12\beta}{p^2\kappa^2}s^2 + (12\beta^2 - g_2)\frac{s^{2-p}}{\alpha p^2\kappa^2} + (4\beta^3 - g_2 - g_3)\frac{s^{2-2p}}{\alpha^2 p^2\kappa^2}, \tag{A.3}$$

with $z = \kappa x$. The constants (α, β, κ) and the integer $p \neq 0, 1$ are such that the r.h.s. of Eq. (A.3) has the Jacobi form (1.6). For $p = 2$, this Jacobi form is recovered if we set

$$\beta = -(m+1)\frac{\kappa^2}{3}, \tag{A.4}$$

as a root of the cubic polynomial $4\beta^3 - g_2\beta - g_3$ (i.e. $\beta = e_1, e_2$ or e_3), and

$$\alpha = \kappa^2 = \frac{12\beta^2 - g_2}{4m\kappa^2}. \tag{A.5}$$

Hence, the Jacobi elliptic function $s(z)$ is related to the Weierstraß elliptic function $y(x)$ in the case of $p = \pm 2$. An application of the first transformation ($p = 2$) shows that for $m = \frac{e_2 - e_3}{e_1 - e_3}$ and $\kappa = \sqrt{e_1 - e_3}$, we find $\alpha = e_2 - e_3$ and $\beta = e_3$, and we obtain the relation

$$\wp(x + \omega_2; g_2, g_3) = e_3 + (e_2 - e_3)\mathrm{cn}^2(\kappa x|m), \tag{A.6}$$

or

$$\wp(x + \omega_3; g_2, g_3) = e_3 + (e_2 - e_3)\mathrm{sn}^2(\kappa x|m), \tag{A.7}$$

which oscillates between $e_2 = \wp(\omega_2) = \wp(\omega + \omega_3)$ and $e_3 = \wp(\omega + \omega_2) = \wp(\omega_3)$ (as indicated in Fig. 1.11). The relation (A.7) plays a crucial role in expressing the Weierstraß solution of the planar pendulum in terms of its Jacobian solution in Eq. (1.53). An application of the second transformation ($p = -2$) shows that for the same m and κ as the first transformation, we find $\alpha = e_1 - e_3$ and $\beta = e_3$, and we obtain

$$\wp(x; g_2, g_3) = e_3 + \frac{e_1 - e_3}{\mathrm{sn}^2(\kappa x|m)}, \tag{A.8}$$

which has singularities at $x = 0$ and $\frac{2}{\kappa}K(m) \equiv 2\omega$ and a minimum at $x = \frac{1}{\kappa}K(m) \equiv \omega$ (the upper part of Fig. 1.9). We note that the relation (A.8) is equivalent to the property in Eq. (1.42) of the Weierstraß elliptic function

$$\wp = e_3 + \frac{(e_1 - e_3)(e_2 - e_3)}{\wp(x + \omega_3) - e_3}. \tag{A.9}$$

when substituting Eq. (A.7) into Eq. (A.8).

A.2 Some mathematical details

Assuming $(g_3, \Delta) = (+, +)$, we discuss the relation between the Weierstraß half-periods ω and ω' in Eqs. (1.40), with the quarter periods K and K' of the Jacobi elliptic functions. Introducing the change of variable $s \doteq e_3 + (e_1 - e_3)\csc^2\psi$ (Critchfield, 1989) in the half-period (1.41a), this equation is transformed to

$$\begin{aligned} \omega(g_2, g_3) &= \int_0^{\frac{\pi}{2}} \frac{\mathrm{d}\psi}{\sqrt{(e_1 - e_3) - (e_2 - e_3)\sin^2\psi}} \\ &\equiv \frac{K(m)}{\sqrt{e_1 - e_3}}, \end{aligned} \tag{A.10}$$

where the modulus m of the Jacobian quarter period is defined by the relation $m = \frac{e_2 - e_3}{e_1 - e_3}$. On the other hand, for the case of the half-period in Eq. (1.41b), by introducing the change of variable $s \doteq e_1 - (e_1 - e_3)\csc^2\psi$, we get

$$\begin{aligned}\omega'(g_2, g_3) &= \mathrm{i}\int_0^{\frac{\pi}{2}} \frac{\mathrm{d}\psi}{\sqrt{(e_1 - e_3) - (e_1 - e_2)\sin^2\psi}} \\ &\equiv \frac{\mathrm{i}K(m')}{\sqrt{e_1 - e_3}},\end{aligned} \tag{A.11}$$

where $m' = 1 - m = \frac{e_1 - e_2}{e_1 - e_3}$. Note that, the relations (A.10) and (A.11) between the Weierstraß half-periods (ω, ω') and the Jacobi quarter-periods (K, K') hold because the relation (A.7) between the Weierstraß and Jacobi elliptic functions involves the square of the Jacobi elliptic function, which reduces the latter's period by half (for example, the period of $\sin^2\phi$ is π). These relations played an important role in the Weierstraß solution of the planar pendulum as discussed in subsection. 1.3.1. Under the transformation $\epsilon \to \bar{\epsilon} = 2 - \epsilon$ generated by the transformation $\phi - 0 \to \bar{\phi}_0 \equiv \frac{\pi}{2} - \phi_0$, the Jacobian modulus $m \equiv \frac{\epsilon}{2}$ (in the case (a) in Table 1.2) transforms into the Jacobian modulus $\bar{m} = 1 - \frac{1}{2}\epsilon \equiv m'$ (in the case (b) in Table 1.2), which is the complementary modulus of case (a). According to Eqs. (A.10) and (A.11), since $\omega_1 \equiv \omega = K(m)$ and $\omega_3 \equiv \omega' = \mathrm{i}K'(m) = \mathrm{i}K(m')$, in the cases (a) and (b) we find that

$$\left\{\begin{array}{c} \bar{\omega}_1 = K(\bar{m}) = K'(m) \equiv -\mathrm{i}\omega_3 \\ \bar{\omega}_3 = -\mathrm{i}K'(\bar{m}) = -\mathrm{i}K(m) \equiv -\mathrm{i}\omega_1 \end{array}\right. , \tag{A.12}$$

which is in agreement with the transform nation in Eq. (1.51).

Appendix B

B.1 Switching the values of spacetime coefficients and dynamical quantities between the geometric and SI units

The values of the Newton's gravitational constant and the speed of light are

$$G = 6.67430 \times 10^{-11} \quad (\mathrm{m^3 kg^{-1} s^{-2}}), \tag{B.1}$$

$$c = 299792458 \quad (\mathrm{m\,s^{-1}}). \tag{B.2}$$

The mass of earth is $m_e = 5.97237 \times 10^{24}$ kg (Luzum et al., 2011) which in geometric units becomes

$$\tilde{m}_e = m_e \times \frac{G}{c^2} = 4.4347 \times 10^3 \quad (\mathrm{m}). \tag{B.3}$$

In the geometric units, the value of time is also given in meters by applying $\bar{\tau}\ (\mathrm{m}) = \tau \times c\ (\mathrm{s})$. For example, one year is about 3.1536×10^7 s, which in meters is equivalent to $1\,\mathrm{yr} = 9.45 \times 10^{15}$ m.

The change of units from Coulomb (C) to meters for the electric charge Q, is also done as bellow:

$$[Q\ (\mathrm{m})] = [Q\ (\mathrm{C})] \times \sqrt{\frac{G}{4\pi\varepsilon_0 c^4}}, \tag{B.4}$$

in which $\varepsilon_0 = 8.854 \times 10^{-12}\ \frac{\mathrm{C^2}}{\mathrm{Nm^2}}$ is the vacuum permittivity. This way,

$$[Q\ (\mathrm{C})] = \left(1.15964 \times 10^{17}\right) [Q\ (\mathrm{m})]. \tag{B.5}$$

So, for example, 1 meter electric charge is approximately 10^{17} C, which is equivalent to the charge of 7×10^{35} protons ($Q_{\rm p} = 1.62 \times 10^{-19}$ C).

Furthermore, the factor $\frac{1}{\lambda^2}$ in (3.23a), is a density of dimensions m^{-2}. In fact λ is given by

$$\lambda = \left[3\tilde{\rho}_c + \frac{2}{3}c_1\right]^{-\frac{1}{2}} \quad (\mathrm{m}), \tag{B.6}$$

in which $\tilde{\rho}_w$ is the density of a spherically symmetric charged massive source. Here, we let $c_1 = 2.08 \times 10^{-54}\ \mathrm{m}^{-2}$ (Payandeh & Fathi, 2012) which is comparable to the value of the cosmological constant $\Lambda_0 = 1.1056 \times 10^{-52}\ \mathrm{m}^{-2}$ (**?**).

In geometric units, the dimension of angular momentum is square meters, which is transformed to the SI units [$\mathrm{kg\,m^2\,s^{-1}}$] by applying a $\frac{c^3}{G}$ multiply. However, since we have ignored the mass of the orbiting objects, the value of the constant of motion L, in geometric units, is given in meters which is in conformity with the other dynamical quantities.

Taking into account the above notes and working in the geometric units, the value of precession will be the same as that in the SI units.

B.2 The method of finding L_U in Eq. (3.240)

Equation. (3.236) allows for obtaining an expression for L_U, by solving

$$\mathfrak{a}L_U^4 - \mathfrak{b}L_U^2 + \mathfrak{c} = 0, \tag{B.7}$$

in which

$$\mathfrak{a} = \frac{(Q^2 - 2r_U^2)^2}{r_U^6}, \tag{B.8a}$$

$$\mathfrak{b} = \frac{2Q^2(1+q^2)}{r_U^2} - \frac{Q^4(2+q^2)}{2r_U^4} - \frac{8r_U^2 - 2Q^2(1-q^2)}{\lambda^4}, \tag{B.8b}$$

$$\mathfrak{c} = \frac{Q^4(1+2q^2)}{4r_U^2} - 2q^2Q^2 + \frac{4r_U^6}{\lambda^4} - \frac{2Q^2r_U^2(1-q^2)}{\lambda^2}. \tag{B.8c}$$

Solving Eq. (B.7) for L_U^2, then yields the value in Eq. (3.240).

B.3 Finding the angular equation of motion

Since the closest approach happens at r_S, to deal with the integral in Eq. (3.248), we define the following non-linear change of variable:

$$u \doteq \frac{1}{\frac{r}{r_S} - 1}, \tag{B.9}$$

which reduces Eq. (3.248) to

$$\phi(r) = \kappa_0 \left[\int_u^\infty \frac{\mathrm{d}u}{\sqrt{\mathcal{P}_3(u)}} - u_3 \int_u^\infty \frac{\mathrm{d}u}{(u+u_3)\sqrt{\mathcal{P}_3(u)}} \right], \tag{B.10}$$

where $u_j \doteq \frac{1}{(r_j/r_S)-1}$, with $j = \{2, 3, 5, 6\}$, and

$$\mathcal{P}_3(u) \equiv u^3 + \mathbf{a}u^2 + \mathbf{b}u + \mathbf{c}, \tag{B.11}$$

with

$$\mathbf{a} = u_2 + u_5 + u_6, \tag{B.12a}$$

$$\mathbf{b} = u_2(u_5 + u_6) + u_5 u_6, \tag{B.12b}$$

$$\mathbf{c} = u_2 u_5 u_6. \tag{B.12c}$$

Defining

$$\kappa_0 = \frac{v}{r_S^2} u_3 \sqrt{u_2 u_5 u_6}, \tag{B.13}$$

and applying another change of variable

$$U \doteq \frac{1}{4}\left(u + \frac{\mathbf{a}}{3}\right), \tag{B.14}$$

we can rewrite Eq. (B.10) as

$$\phi(r) = \kappa_0 \left[\int_U^\infty \frac{\mathrm{d}U}{\sqrt{P_3(U)}} - \frac{u_3}{4} \int_U^\infty \frac{\mathrm{d}U}{(U+U_3)\sqrt{P_3(U)}} \right], \tag{B.15}$$

given that $U_3 = \frac{1}{4}\left(u_3 + \frac{\mathbf{a}}{3}\right)$, and

$$P_3(u) \equiv 4U^3 - \mathbf{g}_2 U - \mathbf{g}_3. \tag{B.16}$$

Direct integration of Eq. (B.15), results in the expression in Eq. (3.250).

B.4 Solving depressed quartic equations

The condition $V_r'(r) = 0$, provides the following equation of eighth degree:

$$r^8 + \tilde{a} r^4 + \tilde{b} r^2 + \tilde{c} = 0. \tag{B.17}$$

To solve this equation, we firstly make the change of variable $r^2 \doteq x$. Afterwards, we combine the methods of Ferrari and Cardano to solve a depressed quartic equation of the form (originally studied by Cardano (Cardano, 1993))

$$x^4 + \tilde{a} x^2 + \tilde{b} x + \tilde{c} = 0, \quad (\tilde{a}, \tilde{b}, \tilde{c}) \in \mathbb{R}. \tag{B.18}$$

This equation can be rewritten as the product of two quadratic equations, as follows:

$$x^4 + \tilde{a}x^2 + \tilde{b}x + \tilde{c} = (x^2 - 2\tilde{\alpha}x + \tilde{\beta})(x^2 + 2\tilde{\alpha}x + \tilde{\gamma}) = 0. \tag{B.19}$$

Accordingly, we obtain

$$\tilde{a} = \tilde{\beta} + \tilde{\gamma} - 4\tilde{\alpha}^2, \tag{B.20a}$$

$$\tilde{b} = 2\tilde{\alpha}(\tilde{\beta} - \tilde{\gamma}), \tag{B.20b}$$

$$\tilde{c} = \tilde{\beta}\tilde{\gamma}. \tag{B.20c}$$

Solving the first two equations for $\tilde{\beta}$ and $\tilde{\gamma}$, yields

$$\tilde{\beta} = 2\tilde{\alpha}^2 + \frac{\tilde{a}}{2} + \frac{\tilde{b}}{4\tilde{\alpha}}, \tag{B.21a}$$

$$\tilde{\gamma} = 2\tilde{\alpha}^2 + \frac{\tilde{a}}{2} - \frac{\tilde{b}}{4\tilde{\alpha}}, \tag{B.21b}$$

which together with Eq. (B.20c), results in an equation of sixth degree in $\tilde{\alpha}$:

$$\tilde{\alpha}^6 + \frac{\tilde{a}}{2}\tilde{\alpha}^4 + \left(\frac{\tilde{a}^2}{16} - \frac{\tilde{c}}{4}\right)\tilde{\alpha}^2 - \frac{\tilde{b}^2}{64} = 0. \tag{B.22}$$

Applying the change of variable

$$\tilde{\alpha}^2 = \tilde{U} - \frac{\tilde{a}}{6}, \tag{B.23}$$

we obtain the depressed cubic equation

$$\tilde{U}^3 - \tilde{\eta}_2\tilde{U} - \tilde{\eta}_3 = 0, \tag{B.24}$$

where

$$\tilde{\eta}_2 = \frac{\tilde{a}^2}{48} + \frac{\tilde{c}}{4}, \tag{B.25a}$$

$$\tilde{\eta}_3 = \frac{\tilde{a}^3}{864} + \frac{\tilde{b}^2}{64} - \frac{\tilde{a}\tilde{c}}{24}. \tag{B.25b}$$

The real solution to this cubic equation is obtained as (Nickalls, 2006; Zucker, 2008)

$$\tilde{U} = 2\sqrt{\frac{\tilde{\eta}_2}{3}}\cosh\left(\frac{1}{3}\text{arccosh}\left(\frac{3}{2}\tilde{\eta}_3\sqrt{\frac{3}{\tilde{\eta}_2^3}}\right)\right). \tag{B.26}$$

Therefore, the roots of Eq. (B.41) are

$$x_1 = \tilde{\alpha} + \sqrt{\tilde{\alpha}^2 - \tilde{\beta}}, \tag{B.27a}$$

$$x_2 = \tilde{\alpha} - \sqrt{\tilde{\alpha}^2 - \tilde{\beta}}, \tag{B.27b}$$

$$x_3 = -\tilde{\alpha} + \sqrt{\tilde{\alpha}^2 - \tilde{\gamma}}, \tag{B.27c}$$

$$x_4 = -\tilde{\alpha} - \sqrt{\tilde{\alpha}^2 - \tilde{\gamma}}. \tag{B.27d}$$

B.5 Solving the equation of motion for frontal scattering

Equation (6.58) can be recast as

$$\left(\frac{\mathrm{d}r}{\mathrm{d}\tau}\right)^2 = \frac{m^2\,(r-r_s)\,\mathfrak{p}_3(r)}{\lambda^2 r^2}, \tag{B.28}$$

in which

$$\mathfrak{p}_3(r) \equiv r^3 + r_s r^2 + (r_s^2+\bar{a})r + r_s^3 + r_s\bar{a} + \bar{b}. \tag{B.29}$$

Considering r_s as the initial position, we can rewrite Eq. (B.28) as

$$\tau(r) = \frac{\lambda}{m}\int_{r_s}^{r}\frac{r\mathrm{d}r}{\sqrt{(r-r_s)\mathfrak{p}_3(r)}}, \tag{B.30}$$

which by the linear change of variable

$$z \doteq \frac{r}{r_s} - 1, \tag{B.31}$$

reduces to

$$\tau(z) = \frac{\lambda}{m}\int_0^z \frac{(z+1)\mathrm{d}z}{\sqrt{z\tilde{\mathfrak{p}}_3(z)}}, \tag{B.32}$$

where

$$\tilde{\mathfrak{p}}_3(z) \equiv z^3 + 4z^2 + \gamma_1 z + \gamma_0, \tag{B.33}$$

and

$$\gamma_1 = 6 + \frac{\bar{a}}{r_s^2}, \tag{B.34a}$$

$$\gamma_0 = 4 + \frac{2\bar{a}}{r_s^2} + \frac{\bar{b}}{r_s^3}. \tag{B.34b}$$

Now, letting

$$u \doteq \frac{1}{z}, \tag{B.35}$$

yields the following reduced integral form of Eq. (B.32):

$$\tau(u) = \frac{-\lambda}{m\sqrt{\gamma_0}}\left(\int_\infty^u \frac{\mathrm{d}u}{\sqrt{\bar{\mathfrak{p}}_3(u)}} + \int_\infty^u \frac{\mathrm{d}u}{u\sqrt{\bar{\mathfrak{p}}_3(u)}}\right), \tag{B.36}$$

in which

$$\bar{\mathfrak{p}}_3(u) \equiv u^3 + \frac{\gamma_1}{\gamma_0}u^2 + \frac{4}{\gamma_0}u + \frac{1}{\gamma_0}. \tag{B.37}$$

Applying the last change of variable

$$u \doteq 4\mathrm{U} - \frac{\gamma_1}{3\gamma_0}, \tag{B.38}$$

we get

$$\tau(\mathrm{U}) = \frac{-\lambda}{m\sqrt{\gamma_0}} \left(\int_\infty^{\mathrm{U}} \frac{d\mathrm{U}}{\sqrt{\bar{\mathfrak{P}}_3(\mathrm{U})}} + \frac{1}{4} \int_\infty^{\mathrm{U}} \frac{d\mathrm{U}}{(\mathrm{U} - \frac{\mathfrak{l}_1}{12\mathfrak{l}_0})\sqrt{\bar{\mathfrak{P}}_3(\mathrm{U})}} \right), \tag{B.39}$$

where we have defined

$$\bar{\mathfrak{P}}_3(\mathrm{U}) \equiv 4\mathrm{U}^3 - \bar{g}_2\mathrm{U}^2 - \bar{g}_3. \tag{B.40}$$

The direct integration of the elliptic integral in Eq. (B.39), now results in the expression in Eq. (6.63).

B.6 The method of solving the quartic equation $x^4 - a\,x^2 + b = 0$

We are interest in solving a quartic equations of the form

$$x^4 - a\,x^2 + b = 0, \tag{B.41}$$

where $(a,b) > 0$ and $2\sqrt{b} \leq a$. For this purpose, we make the change of variable $x = Z\sin\vartheta$, and multiply both sides of the equation by a scalar α. This yields

$$\alpha\,Z^4\sin^4\vartheta - \alpha\,a\,Z^2\sin^2\vartheta + \alpha\,b = 0. \tag{B.42}$$

Considering the trigonometric identity

$$4\sin^4\vartheta - 4\sin^2\vartheta + \sin^2(2\vartheta) = 0, \tag{B.43}$$

and comparing Eqs. (B.42) and (B.43), we infer

$$\alpha\,Z^4 = 4, \qquad \alpha\,a\,Z^2 = 4, \qquad \alpha\,b = \sin^2(2\vartheta). \tag{B.44}$$

Solving the above equation for Z and ϑ, we obtain

$$Z = \sqrt{a}, \quad \text{and} \quad \vartheta_n = \frac{1}{2}\arcsin\left(\frac{2\sqrt{b}}{a}\right) + \frac{n\pi}{2}, \tag{B.45}$$

where the period of the trigonometric function is $n\pi$. Therefore, the roots of Eq. (B.43) are obtained by replacing $n = 0, 1$, giving

$$x_0 = \sqrt{a}\sin\left(\frac{1}{2}\arcsin\left(\frac{2\sqrt{b}}{a}\right)\right), \tag{B.46}$$

$$\begin{aligned} x_1 &= \sqrt{a}\sin\left(\frac{1}{2}\arcsin\left(\frac{2\sqrt{b}}{a}\right) + \frac{\pi}{2}\right) \\ &= \sqrt{a}\cos\left(\frac{1}{2}\arcsin\left(\frac{2\sqrt{b}}{a}\right)\right), \end{aligned} \tag{B.47}$$

$$x_2 = -x_0, \tag{B.48}$$

$$x_3 = -x_1. \tag{B.49}$$

The above method enables us to determine the black hole horizons.

APPENDIX C

C.1 Obtaining the analytical radial evolution for the OFK

Applying the method of *synthetic division* to factorize $(r - r_D)$ from the characteristic polynomial $\mathcal{P}(r)$ in Eq. (5.90), we obtain

$$\mathcal{P}(r) = (r - r_D)(r^3 + G_1 r^2 + G_2 r + G_3), \tag{C.1}$$

in which

$$G_1 = r_D, \tag{C.2a}$$

$$G_2 = \mathcal{A} + r_D^2, \tag{C.2b}$$

$$G_3 = r_D^3 + \mathcal{A} r_D + \mathcal{B}. \tag{C.2c}$$

The deflecting trajectory can be then determined by performing, successively, the changes of variables

$$u(r) = \frac{1}{\frac{r}{r_D} - 1}, \tag{C.3}$$

and

$$U(r) = \frac{u(r)}{4} - \frac{6r_D^2 + \mathcal{A}}{12(4r_D^3 + 2\mathcal{A} r_D + \mathcal{B})}. \tag{C.4}$$

C.2 Finding the evolution of the θ-coordinate for the case of $\eta > 0$

In this case, we have from Eq. (5.107) that

$$\gamma = -\frac{M}{\omega_0} \int_{z_{\max}}^{z} \frac{\mathrm{d}z}{\sqrt{\Theta_z(z)}}, \tag{C.5}$$

in which, one can recast $\Theta_z = a^2(z_{\max}^2 - z^2)(z_0^2 + z^2) = a^2(z_{\max} - z)(z + z_{\max})(z_0^2 + z^2) = a^2(z_{\max} - z)\tilde{P}_3(z)$, where $|z_0|$ and $|z_{\max}|$ are the two double zeros of Θ_z, and $\tilde{P}_3(z) = z^3 + z_{\max}z^2 + z_0^2 z + z_{\max}z_0^2$. Therefore

$$\gamma = -\frac{M}{\omega_0} \int_{z_{\max}}^{z} \frac{\mathrm{d}z}{\sqrt{a^2\tilde{P}_3(z)}}. \tag{C.6}$$

Applying the change of variable $y \doteq z_{\max} - z$, the above integral changes to

$$\gamma = \frac{M}{\omega_0 a} \int_0^y \frac{\mathrm{d}y}{\sqrt{y\left[-y^3 + 4z_{\max}y^2 + (-z_0^2 - 5z_{\max}^2)y + 2z_0^2 z_{\max} + 2z_{\max}^3\right]}}. \tag{C.7}$$

The second change of variable $u \doteq \frac{1}{y}$, provides

$$\gamma = \frac{M}{\omega_0 a} \int_u^\infty \frac{\mathrm{d}u}{\sqrt{\delta\left(u^3 - \delta_2 u^2 + \delta_1 u - \delta_0\right)}}, \tag{C.8}$$

where

$$\delta = 2z_{\max}(z_0^2 + z_{\max}^2), \tag{C.9a}$$

$$\delta_0 = \frac{1}{\delta}, \tag{C.9b}$$

$$\delta_1 = \frac{2}{z_0^2 + z_{\max}^2}, \tag{C.9c}$$

$$\delta_2 = \frac{z_0^2 + 5z_{\max}^2}{\delta}. \tag{C.9d}$$

Now, a third change of variable $u \doteq 4U + \frac{\delta_2}{3}$, yields

$$\gamma = \frac{M}{4\omega_0 a\sqrt{\delta}} \int_U^\infty \frac{\mathrm{d}U}{\sqrt{4U^3 - g_2 U - g_3}}, \tag{C.10}$$

in which

$$g_2 = \frac{1}{4}\left(\frac{\delta_2^3}{3} - \delta_1\right), \tag{C.11a}$$

$$g_3 = -\frac{1}{16}\left(\frac{\delta_1\delta_2}{3} - \frac{2\delta_2^3}{27} - \delta_0\right). \tag{C.11b}$$

This way

$$\gamma = \frac{\text{ß}(U)}{\kappa_0}, \tag{C.12}$$

in which $\kappa_0 = \frac{4\omega_0 a\sqrt{\delta}}{M}$. Hence, $U = \wp(\kappa_0\gamma)$, and after reversing the applied changes of variables, we finally obtain

$$\cos\theta = z_{\max} - \frac{3}{12\wp(\kappa_0\gamma) + \delta_2}. \tag{C.13}$$

C.3 Finding the evolution of the θ-coordinate for the case of $\eta < 0$

Let us rewrite Θ_z as

$$\Theta_z = -\left(\frac{a}{2}\mu_0^2\mu_1\right)^2 + a^2\mu_0^2 z^2 - a^2 z^4. \tag{C.14}$$

Applying the method of synthetic division, this can be recast as $\Theta_z = -a^2(z - \bar{\bar{z}}_{\max})\tilde{P}_3(z)$ with $\tilde{P}_3(z) = [z^3 - \bar{\bar{z}}_{\max}z^2 + (\bar{\bar{z}}^2_{\max} - \mu_0^2)z + (\bar{\bar{z}}^2_{\max} - \mu_0^2)\bar{\bar{z}}_{\max}]$. This way, the integral of evolution turns to

$$\gamma = -\frac{M}{\omega_0}\int_{\bar{\bar{z}}_{\max}}^{z} \frac{\mathrm{d}z}{\sqrt{a^2(\bar{\bar{z}}_{\max} - z)\tilde{P}_3(z)}}, \tag{C.15}$$

which after the change of variable $y \doteq \bar{\bar{z}}_{\max} - z$, changes to

$$\gamma = \frac{M}{\omega_0 a}\int_0^y \frac{\mathrm{d}y}{\sqrt{y\left[-y^3 + 4\bar{\bar{z}}_{\max}y^2 + (\mu_0^2 - 6\bar{\bar{z}}^2_{\max})y + \left(2\bar{\bar{z}}^3_{\max} + 2\bar{\bar{z}}_{\max}(\bar{\bar{z}}^2_{\max} - \mu_0^2)\right)\right]}}. \tag{C.16}$$

Now, a second change of variable $u \doteq \frac{1}{y}$, results in

$$\gamma = -\frac{M}{\omega_0}\int_u^\infty \frac{\mathrm{d}u}{\sqrt{\bar{\bar{\delta}}\left(u^3 - \bar{\bar{\delta}}_2 u^2 + \bar{\bar{\delta}}_1 u - \bar{\bar{\delta}}_0\right)}}, \tag{C.17}$$

where

$$\bar{\bar{\delta}} = 2\bar{\bar{z}}_{\max}(2\bar{\bar{z}}^2_{\max} - \mu_0^2), \tag{C.18a}$$

$$\bar{\bar{\delta}}_0 = \frac{1}{\bar{\bar{\delta}}}, \tag{C.18b}$$

$$\bar{\bar{\delta}}_1 = \frac{4\bar{\bar{z}}_{\max}}{\bar{\bar{\delta}}}, \tag{C.18c}$$

$$\bar{\bar{\delta}}_2 = \frac{6\bar{\bar{z}}^2_{\max} - \mu_0^2}{\bar{\bar{\delta}}}. \tag{C.18d}$$

Finally, the third change of variable $u \doteq 4U + \frac{\bar{\bar{\delta}}_2}{3}$, provides

$$\gamma = \frac{M}{4a\omega_0\sqrt{\bar{\bar{\delta}}}} \int_U^\infty \frac{\mathrm{d}U}{\sqrt{4U^3 - \bar{\bar{g}}_2 U - \bar{\bar{g}}_3}}, \tag{C.19}$$

in which

$$\bar{\bar{g}}_2 = \frac{1}{4}\left(\frac{\bar{\bar{\delta}}_2^2}{3} - \bar{\bar{\delta}}_1\right), \tag{C.20a}$$

$$\bar{\bar{g}}_3 = \frac{1}{16}\left(\frac{2\bar{\bar{\delta}}_2^3}{27} + \bar{\bar{\delta}}_0 - \frac{\bar{\bar{\delta}}_1\bar{\bar{\delta}}_2}{3}\right). \tag{C.20b}$$

Now, defining the constant $\kappa_2 = \frac{4a\omega_0\sqrt{\bar{\bar{\delta}}}}{M}$, the above integral results in the solution $U = \wp(\kappa_2\gamma)$, giving

$$z = \bar{\bar{z}}_{\max} - \frac{3}{\bar{\bar{\delta}}_2 + 12\wp(\kappa_2\gamma)}. \tag{C.21}$$

C.4 Calculation of Φ_θ for $\eta > 0$

After the common change of variable $z \doteq \cos\theta$, Eq. (5.125a) can be recast as

$$\begin{aligned}
\Phi_z(\gamma) &= -\frac{L}{\omega_0}\int_{z_{\max}}^{z} \frac{\mathrm{d}z}{(1-z^2)\sqrt{a^2(z_{\max}-z)\tilde{P}_3(z)}} \\
&= -\frac{L}{a\omega_0}\int_{z_{\max}}^{z} \frac{\mathrm{d}z}{(1+z)(1-z)\sqrt{(z_{\max}-z)\tilde{P}_3(z)}},
\end{aligned} \tag{C.22}$$

as introduced in Eq. (C.6). Now applying the change of variable $y \doteq z_{\max} - z$, we get

$$\Phi_y(\gamma) = \frac{L}{a\omega_0}\int_0^y \frac{\mathrm{d}y}{(y_m - y)(y_n + y)\sqrt{y\tilde{P}_3(y)}}, \tag{C.23}$$

where $y_m = 1 + z_{\max}$, $y_n = 1 - z_{\max}$, and $\tilde{P}_3(y) = -y^3 + 4z_{\max}y^2 - (z_0^2 + 5z_{\max}^2)y + 2z_0^2 z_{\max} + 2z_{\max}^3$. The third change of variable $u \doteq \frac{1}{y}$, and doing a proper partial fraction decomposition, we get to the integral equation

$$\begin{aligned}
\Phi_u(\gamma) = \frac{L}{a\omega_0\sqrt{\delta}y_m y_n}\Bigg[\int_u^\infty \frac{\mathrm{d}u}{\sqrt{\tilde{P}_3(u)}} &+ \frac{1+z_{\max}}{8(1-z_{\max})}\int_u^\infty \frac{\mathrm{d}u}{(u+u_n)\sqrt{\tilde{P}_3(u)}} \\
&+ \frac{1-z_{\max}}{8(1+z_{\max})}\int_u^\infty \frac{\mathrm{d}u}{(u-u_m)\sqrt{\tilde{P}_3(u)}}\Bigg],
\end{aligned} \tag{C.24}$$

with $\tilde{P}_3(u) = u^3 - \delta_2 u^2 + \delta_1 u - \delta_0$, in which δ, and $\delta_{0,1,2}$ have been defined in Eqs. (C.9), and $u_{m,n} = \frac{1}{y_{m,n}}$. The only remaining task is to apply the change of variable $u \doteq 4U + \frac{\delta_2}{3}$, and using the identity

$$\begin{aligned}\int_{\wp(\mu)}^{\infty} \frac{\mathrm{d}x}{(x-v)\sqrt{4x^3 - g_2 x - g_3}} &= \int_0^{\mu} \frac{\mathrm{d}\mu}{\wp(\mu) - \wp(v)} \\ &= \frac{1}{\wp'(\mu)}\left[\ln\left(\frac{\sigma(v-\mu)}{\sigma(v+\mu)}\right) + 2\mu\zeta(v)\right], \quad \text{(C.25)}\end{aligned}$$

we can arrive at the solution in Eq. (5.126).

C.5 Calculation of Φ_r

Assuming that the particles approach at the initial point r_i, the r-dependent equation (5.125b) can be recast as

$$\Phi_r(\gamma) = \frac{1}{\omega_0}\int_{r_i}^{r} \frac{a^2 L + 2Ma\omega_0 r}{(r-r_+)(r-r_-)\sqrt{\mathcal{P}(r)}}\mathrm{d}r, \quad \text{(C.26)}$$

in terms of $r_\pm$ as the solutions to the equation $\Delta = 0$, in which $\mathcal{P}(r)$ has the same form as that in Eq. (C.1), considering $r_D \to r_i$. Applying the change of variable $u \doteq \frac{1}{\left(\frac{r}{r_i}\right)-1}$, one obtains

$$\Phi_u(\gamma) = \frac{1}{\omega_0}\int_u^{\infty} \frac{\left[2aMr_i\omega_0 u + a\left(aL + 2Mr_i\omega_0\right)u^2\right]\mathrm{d}u}{\left[r_i + u(r_i - r_+)\right]\left[r_i + u(r_i - r_-)\right]\sqrt{\mathcal{P}_3(u)}}, \quad \text{(C.27)}$$

where $\mathcal{P}_3(u) = \tilde{\alpha}u^3 + \tilde{\beta}u^2 + \tilde{\gamma}u + \tilde{\delta}$, with $\tilde{\alpha} = G_2 + \frac{G_3}{r_i} + G_1 r_i + r_i^2$, $\tilde{\beta} = G_2 + 2G_1 r_i + 3r_i^2$, $\tilde{\gamma} = G_1 r_i + 3r_i^2$, and $\tilde{\delta} = r_i^2$, where $G_{1,2,3}$ are the same as those in Eqs. (C.2), considering $r_D \to r_i$. By doing a partial fractional decomposition the integrand is decomposed to

$$\frac{A_+}{\left[r_i + u(r_i - r_+)\right]\sqrt{\mathcal{P}_3(u)}} + \frac{A_-}{\left[r_i + u(r_i - r_-)\right]\sqrt{\mathcal{P}_3(u)}} + \frac{B}{\sqrt{\mathcal{P}_3(u)}}, \quad \text{(C.28)}$$

in which

$$A_\pm = \mp\frac{ar_i(aL + 2Mr_\pm\omega_0)}{(r_i - r_\pm)(r_+ - r_-)}, \quad \text{(C.29a)}$$

$$B = \frac{a(aL + 2Mr_i\omega_0)}{(r_i - r_+)(r_i - r_-)}. \quad \text{(C.29b)}$$

Therefore, we can decompose Eq. (C.27) as

$$\begin{aligned}\Phi_u(\gamma) = \frac{A_+}{\omega_0}&\int_u^{\infty} \frac{\mathrm{d}u}{\left[r_i + u(r_i - r_+)\right]\sqrt{\mathcal{P}_3(u)}} \\ &+ \frac{A_-}{\omega_0}\int_u^{\infty} \frac{\mathrm{d}u}{\left[r_i + u(r_i - r_-)\right]\sqrt{\mathcal{P}_3(u)}} + \frac{B}{\omega_0}\int_u^{\infty}\frac{\mathrm{d}u}{\sqrt{\mathcal{P}_3(u)}}. \quad \text{(C.30)}\end{aligned}$$

The other change of variable $u \doteq \frac{1}{\tilde{\alpha}}\left(4U - \frac{\tilde{\beta}}{3}\right)$, provides

$$\Phi_U(\gamma) = \frac{A_+}{\omega_0(r_i - r_+)} \int_U^{\infty} \frac{\mathrm{d}U}{\left[U - \left(\frac{4}{\tilde{\alpha}}\right)(r_i - r_+)^{-1}\left(\frac{\tilde{\beta}(r_i - r_+)}{3\tilde{\alpha}} - r_i\right)\right]\sqrt{\mathcal{P}_3(U)}}$$
$$+ \frac{A_-}{\omega_0(r_i - r_-)} \int_U^{\infty} \frac{\mathrm{d}U}{\left[U - \left(\frac{4}{\tilde{\alpha}}\right)(r_i - r_-)^{-1}\left(\frac{\tilde{\beta}(r_i - r_-)}{3\tilde{\alpha}} - r_i\right)\right]\sqrt{\mathcal{P}_3(U)}}$$
$$+ \frac{B}{\omega_0} \int_U^{\infty} \frac{\mathrm{d}U}{\sqrt{\mathcal{P}_3(U)}}, \quad \text{(C.31)}$$

where $\mathcal{P}_3(U) = 4U^3 - \tilde{g}_2 U - \tilde{g}_3$, with $\tilde{g}_{2,3}$ being

$$\tilde{g}_2 = \frac{4}{\tilde{\alpha}}\left(\frac{\tilde{\beta}^2}{3\tilde{\alpha}} - \tilde{\gamma}\right), \quad \text{(C.32a)}$$

$$\tilde{g}_3 = \left(\frac{\tilde{\beta}\tilde{\gamma}}{3\tilde{\alpha}} - \frac{2\tilde{\beta}^3}{27\tilde{\alpha}^2} - \tilde{\delta}\right). \quad \text{(C.32b)}$$

This integral equation (C.31), will then result in the solution (5.137).

C.6 Derivation of the lens equation

Let us Consider the integral in Eq. (5.143) as

$$I(r) = \int_{r_D}^{\infty} \frac{\mathrm{d}r}{\mathfrak{F}(r)} = \frac{1}{\omega_0} \int_{r_D}^{\infty} \underbrace{G(r)}_{\doteq I_2(r)} \times \underbrace{\frac{\mathrm{d}r}{\sqrt{\mathcal{P}(r)}}}_{\doteq I_1(r)}, \quad \text{(C.33)}$$

where $G(r) = \frac{L(r^2-2Mr)-2Ma\omega_0 r}{\Delta} \equiv \frac{\delta(r)}{\Delta}$, and the coefficients of the polynomial $\mathcal{P}(r)$ are the same as those in Eqs. (5.99) and (5.100). The integral $I_1(r)$ can be treated in the same as displayed in appendix C.1. For the case of $I_2(r)$, one can rewrite $\Delta = r_D^2(z + z_+)(z + z_-)$, by applying the successive changes of variables $x \doteq \frac{r}{r_D}$ and $z \doteq x - 1$, and defining $z_\pm \equiv 1 - \frac{r_\pm}{r_D}$. Then the third change of variable $u \doteq \frac{1}{z}$, and having defined $u_\pm = \frac{1}{z_\pm}$, we get

$$\Delta = r_D^2\left(\frac{1}{u} + \frac{1}{u_+}\right)\left(\frac{1}{u} + \frac{1}{u_-}\right) = \frac{r_D^2}{u_+ u_-}\frac{(u + u_+)(u + u_-)}{u^2}. \quad \text{(C.34)}$$

On the other hand, assuming the abbreviation $m \doteq 2M(L + a\omega_0)$, we have $\delta(r) = Lr^2 - mr$. This way, once again, we apply the change of variable in Eq. (C.3), which yields

$$\delta(r) = \frac{Lr_D^2}{u^2} + \frac{2Lr_D^2 - mr_D}{u} + Lr_D^2 - mr_D \equiv \frac{v_0}{u^2}\left[u^2 - u_2 u + u_3\right], \quad \text{(C.35)}$$

in which

$$
\begin{aligned}
v_0 &= r_D(Lr_D - m), && \text{(C.36a)}\\
u_2 &= \frac{2Lr_D - m}{Lr_D - m}, && \text{(C.36b)}\\
u_3 &= Lr_D^2. && \text{(C.36c)}
\end{aligned}
$$

This way, we finally get

$$
I(u) = \mathfrak{K}_0 \int_0^\infty \frac{\tilde{G}(u)}{\sqrt{\mathcal{P}_3(u)}}\mathrm{d}u, \tag{C.37}
$$

where

$$
\begin{aligned}
\mathfrak{K}_0 &= -\frac{v_0 u_+ u_-}{r_D^2 \omega_0 \sqrt{\tilde{\alpha}}}, && \text{(C.38a)}\\
\tilde{G}(u) &= \frac{u^2 + u_2 u + u_3}{(u+u_+)(u+u_-)}, && \text{(C.38b)}
\end{aligned}
$$

in which, $\tilde{\alpha}$ has the same expression as that in Eq. (5.140), by taking into account $r_i \to r_D$. To proceed further, one needs to do a partial fractional decomposition for the integrand of Eq. (C.37), in the form

$$
\tilde{G}(u) = 1 + \frac{\tilde{A}}{u+u_+} + \frac{\tilde{B}}{u+u_-}, \tag{C.39}
$$

for which, the coefficients are derived as

$$
\begin{aligned}
\tilde{A} &= \frac{u_+^2 - u_2 u_+ + u_3}{u_- - u_+}, && \text{(C.40a)}\\
\tilde{B} &= \frac{u_-^2 - u_2 u_- + u_3}{u_- - u_+}. && \text{(C.40b)}
\end{aligned}
$$

Hence, we reach at the integral

$$
I(u) = \mathfrak{K}_0 \left[\tilde{A}\int_0^\infty \frac{\mathrm{d}u}{(u+u_+)\sqrt{\mathcal{P}_3(u)}} + \tilde{B}\int_0^\infty \frac{\mathrm{d}u}{(u+u_-)\sqrt{\mathcal{P}_3(u)}} + \int_0^\infty \frac{\mathrm{d}u}{\sqrt{\mathcal{P}_3(u)}}\right]. \tag{C.41}
$$

The treatment of these integral, will then be the same as before, as done in appendix C.5.

C.7 A guide to the finding the evolution of the t-coordinate

To obtain the analytical solution for the r-dependent integral, we have also exploited the identity (Byrd & Friedman, 1971)

$$\int \frac{\mathrm{d}\mu}{\left[\wp(\mu) - \wp(v)\right]^2} = \frac{\wp''(v)}{\wp'^3(v)} \ln\left(\frac{\sigma(\mu+v)}{\sigma(\mu-v)}\right) - \frac{1}{\wp'^2(v)}\left[\zeta(\mu+v)+\zeta(\mu-v)\right] - \left[\frac{2\wp(v)}{\wp'^2(v)} + \frac{2\wp''(v)\zeta(v)}{\wp'^3(v)}\right]\mu. \quad \text{(C.42)}$$

Appendix D

D.1 Solving quartic equations

The equation of the form

$$x^4 + ax^3 + bx^2 + cx + d = 0, \tag{D.1}$$

can be depressed by applying the change of variable $x \doteq z - \frac{a}{4}$, that yields

$$z^4 + Az^2 + Bz + C = 0, \tag{D.2}$$

where

$$A = b - \frac{3a^2}{8}, \tag{D.3a}$$

$$B = c + \frac{a^3}{8} - \frac{ab}{2}, \tag{D.3b}$$

$$C = d + \frac{a^2 b}{16} - \frac{3a^4}{256} - \frac{ac}{4}. \tag{D.3c}$$

The method of finding the roots of Eq. (D.2) has been given in the appendix B.4.

D.2 The angular solution for planetary orbits

Applying the change of variable $x \doteq \frac{r}{r_A}$, the integral equation (6.108) changes its form to

$$\phi(x) = -\frac{L}{\sqrt{\gamma}} \int_1^x \frac{\mathrm{d}x}{\sqrt{P_5(x)}}, \tag{D.4}$$

where

$$P_5(x) = x(r_D - r_A x)(1-x)(r_A x - r_P)(r_A x - r_F). \tag{D.5}$$

Applying a second change of variable $x \doteq 1-u$, yields

$$\phi(u) = \frac{L}{\sqrt{\gamma}} \int_0^u \frac{\mathrm{d}u}{\sqrt{P_5(u)}}, \tag{D.6}$$

in which

$$\begin{aligned} P_5(u) &= (1-u)\left[r_D - r_A(1-u)\right] u \left[r_A(1-u) - r_P\right]\left[r_A(1-u) - r_F\right] \\ &= u(1-u)(r_D - r_A)(r_A - r_P)(r_A - r_F)\left[1 + \frac{r_A u}{r_D - r_A}\right]\left[1 - \frac{r_A u}{r_A - r_P}\right]\left[1 - \frac{r_A u}{r_A - r_F}\right] \\ &\equiv l^3 u(1-u)(1-c_1 u)(1-c_2 u)(1-c_3 u). \end{aligned} \tag{D.7}$$

Hence, one can recast Eq. (D.6) as

$$\phi(u) = \frac{L}{\sqrt{l^3\gamma}} \int_0^u u^{-\frac{1}{2}}(1-u)^{-\frac{1}{2}}(1-c_1 u)^{-\frac{1}{2}}(1-c_2 u)^{-\frac{1}{2}}(1-c_3 u)^{-\frac{1}{2}}\,\mathrm{d}u. \tag{D.8}$$

The incomplete Lauricella function of order $n+1$, is defined in terms of the integral equation (Akerblom & Flohr, 2005)

$$\begin{aligned} &\int_0^z u^{a-1}(1-u)^{c-a-1}\prod_{i=1}^{n}(1-x_i u)^{-b_i}\,\mathrm{d}u \\ &\qquad = \frac{z^a}{a} F_D^{(n+1)}\left(a, b_1, \ldots, b_n, 1+a-c; a+1; x_1, \ldots, x_n, z\right). \end{aligned} \tag{D.9}$$

By doing a comparison between Eqs. (D.8) and (D.9), it is inferred that $a = \frac{1}{2}$, $c = 1$ and $n = 3$. Accordingly, we get $b_1 = b_2 = b_3 = \frac{1}{2}$, and $x_1 = c_1$, $x_2 = c_2$ and $x_3 = c_3$. This way, the solution in Eq. (6.109) is obtained.

APPENDIX E

E.1 Derivation of the solutions to the Cauchy equation

Applying the change of variable $\mathfrak{z} \doteq x - 2y$ Eq. (7.16) can be rewritten as

$$\frac{\mathrm{d}\mathfrak{z}}{\mathrm{d}x} = -\frac{3}{4}\left[1 + \mathfrak{z}\cos\left(\frac{1}{3}\arccos\left(\frac{\mathfrak{z}}{x}\right)\right)\right]^2 - \frac{\mathfrak{z}}{2x} + \frac{3}{2}. \tag{E.1}$$

Performing another change of variable $u \doteq \frac{\mathfrak{z}}{x}$, then changes the above equation to

$$\frac{\mathrm{d}u}{\mathrm{d}x} = \frac{3}{4x}\left[1 - 2u - 4\cos\left(\frac{1}{3}\arccos u\right) - 4\cos^2\left(\frac{1}{3}\arccos u\right)\right]. \tag{E.2}$$

Defining $\omega \doteq \frac{1}{3}\arccos u$, now gives

$$\frac{\mathrm{d}\omega}{\mathrm{d}x} = -\frac{\mathcal{P}(\omega)}{4x\sin(3\omega)}, \tag{E.3}$$

with

$$\mathcal{P}(\omega) = 1 - 2\cos(3\omega) - 4\cos\omega - 4\cos^2\omega. \tag{E.4}$$

The elements in the numerator and denominator of Eq. (E.4) can then be recast by means of the identities

$$\cos(3\omega) = 4\cos^3\omega - 3\cos\omega, \tag{E.5}$$

$$\sin(3\omega) = 3\sin\omega - 4\sin^3\omega. \tag{E.6}$$

Accordingly, we have

$$\mathcal{P}(\omega) = (1+2\cos\omega)^2(1-2\cos\omega), \tag{E.7a}$$

$$\sin(3\omega) = -\sin\omega\left(1-4\cos^2\omega\right). \tag{E.7b}$$

Substitution of Eqs. (E.7) in Eq. (E.3) results in

$$\frac{\mathrm{d}\omega}{\mathrm{d}x} = \frac{1+2\cos\omega}{4x\sin\omega}, \tag{E.8}$$

which by applying the change of variable $\gamma \doteq 1+2\cos\omega$, changes to

$$\frac{\mathrm{d}\gamma}{\mathrm{d}x} = -\frac{\gamma}{2x}. \tag{E.9}$$

Direct integration of the above equation yields

$$\gamma = \pm\frac{\mathfrak{b}}{\sqrt{x}}, \tag{E.10}$$

where $\mathfrak{b}$ is an integration constant. Taking into account the changes of variables applied above, we get to the solutions

$$y_{1,2}(x) = \frac{x}{2}\left[1 \pm \cos\left(3\arccos\left(\frac{1}{2}\left[\frac{\mathfrak{b}}{\sqrt{x}}-1\right]\right)\right)\right]. \tag{E.11}$$

Defining

$$\varphi(x) = \arccos\left(\frac{1}{2}\left[\frac{\mathfrak{b}}{\sqrt{x}}-1\right]\right), \tag{E.12}$$

the above solutions change their form to

$$y_1(x) = x - \frac{\mathfrak{b}^2}{4}\left(3-\frac{\mathfrak{b}}{\sqrt{x}}\right), \tag{E.13a}$$

$$y_2(x) = \frac{\mathfrak{b}^2}{4}\left(3-\frac{\mathfrak{b}}{\sqrt{x}}\right). \tag{E.13b}$$

Finally, applying the identity (E.5) and defining $\rho \doteq \frac{2\mathfrak{b}}{3}$, we get

$$y_1(x) = x - \frac{27\rho^2}{16}\left(1-\frac{\rho}{2\sqrt{x}}\right), \tag{E.14a}$$

$$y_2(x) = \frac{27\rho^2}{16}\left(1-\frac{\rho}{2\sqrt{x}}\right). \tag{E.14b}$$

Bibliography

Abbott B. P. et al., 2016a, Phys. Rev. Lett., 116, 241103

Abbott B. P. et al., 2016b, Phys. Rev. Lett., 116, 061102

Abdujabbarov A., Amir M., Ahmedov B., Ghosh S. G., 2016, Physical Review D, 93, 104004

Abdujabbarov A., Rayimbaev J., Atamurotov F., Ahmedov B., 2020, Galaxies, 8

Abdujabbarov A., Toshmatov B., Stuchlík Z., Ahmedov B., 2017, International Journal of Modern Physics D, 26, 1750051

Abdujabbarov A. A., Rezzolla L., Ahmedov B. J., 2015, Monthly Notices of the Royal Astronomical Society, 454, 2423

Abramowicz M. A., Fragile P. C., 2013, Living Reviews in Relativity, 16, 1

Abramowicz M. A., Kluźniak W., 2005, Astrophysics and Space Science, 300, 127

Abramowitz M., Stegun I. A., 1964, Handbook of Mathematical Functions with Formulas, Graphs, and Mathematical Tables (ninth Dover printing, tenth GPO printing ed.). Dover, New York

Akerblom N., Flohr M., 2005, Journal of High Energy Physics, 2005, 057

Akiyama K. et al., 2015, The Astrophysical Journal, 807, 150

Akiyama K. et al., 2019a, Astrophys. J., 875, L1

Akiyama K. et al., 2019b, Astrophys. J., 875, L6

Akiyama K. et al., 2021a, Astrophys. J., 910, L12

Akiyama K. et al., 2021b, Astrophys. J., 910, L13

Ali Khan I., Sultan Khan A., Islam S., 2020, International Journal of Modern Physics A, 35, 2050130

Aliev A. N., Özdemir N., 2002, Monthly Notices of the Royal Astronomical Society, 336, 241

Amarilla L., Eiroa E. F., 2012, Phys. Rev., D85, 064019

Amarilla L., Eiroa E. F., 2013, Phys. Rev., D87, 044057

Amarilla L., Eiroa E. F., Giribet G., 2010, Phys. Rev., D81, 124045

Amir M., Singh B. P., Ghosh S. G., 2018, The European Physical Journal C, 78, 399

Anacleto M., Brito F., Campos J., Passos E., 2020, Physics Letters B, 810, 135830

Ashby N., Shahid-Saless B., 1990, Phys. Rev. D, 42, 1118

Astier P., 2012, arXiv e-prints, arXiv:1211.2590

Atamurotov F., Abdujabbarov A., Ahmedov B., 2013, Phys. Rev., D88, 064004

Atamurotov F., Ahmedov B., Abdujabbarov A., 2015, Physical Review D, 92, 084005

Azreg-Aïnou M., 2014, Eur. Phys. J., C74, 2865

Azreg-Aïnou M., 2014, Phys. Rev., D90, 064041

Bañados M., 1999, AIP Conf. Proc., 484, 147

Bañados M., Henneaux M., Teitelboim C., Zanelli J., 1993, Phys. Rev., D48, 1506, [Erratum: Phys. Rev.D88,069902(2013)]

Bañados M., Teitelboim C., Zanelli J., 1992, Phys. Rev. Lett., 69, 1849

Babar G. Z., Babar A. Z., Atamurotov F., 2020, The European Physical Journal C, 80, 761

Babichev E., Charmousis C., Cisterna A., Hassaine M., 2020, J. Cosmol. Astropart. Phys., 06, 049

Bachelot A., Motet-Bachelot A., 1993, Annales de l'I.H.P. Physique théorique, 59, 3

Badía J., Eiroa E. F., 2021, Phys. Rev. D, 104, 084055

Balakin A., van Holten J. W., Kerner R., 2000, Classical and Quantum Gravity, 17, 5009

Bardeen J., 1973, in Les Houches Summer School of Theoretical Physics: Black Holes, p. 215

Bardeen J. M., Carter B., Hawking S., 1973, Commun. Math. Phys., 31, 161

Bardeen J. M., Press W. H., Teukolsky S. A., 1972, ApJ, 178, 347

Barlow N. S., Weinstein S. J., Faber J. A., 2017, Classical and Quantum Gravity, 34, 135017

Barrow J. D., Burd A. B., Lancaster D., 1986, Classical and Quantum Gravity, 3, 551

Batool M., Hussain I., 2017, International Journal of Modern Physics D, 26, 1741005

Bażański S. L., 1989, Journal of Mathematical Physics, 30, 1018

Becker D., Reuter M., 2014, Annals of Physics, 350, 225

Beckwith K., Done C., 2005, Monthly Notices of the Royal Astronomical Society, 359, 1217

Bekenstein J. D., 1972, Lett. Nuovo Cimento, 4, 737

Bekenstein J. D., 1973, Phys. Rev. D, 7, 2333

Bekenstein J. D., 1974, Phys. Rev. D, 9, 3292

Bekenstein J. D., 1975, Phys. Rev. D, 12, 3077

Belgiorno F., 2002, arXiv e-prints, math

Belgiorno F., 2003, Phys. Lett. A, 312, 324

Belgiorno F., 2003, J. Phys. A: Math. Gen., 36, 8165

Belgiorno F., 2003a, J. Phys. A: Math. Gen., 36, 8195

Belgiorno F., 2003b, J. Math. Phys., 44, 1089

Belgiorno F., Cacciatori S. L., 2011, Eur. Phys. J. Plus, 126, 86

Belgiorno F. et al., 2010, Phys. Rev. Lett., 105, 203901

Belgiorno F., Martellini M., 2004, Int. J. Mod. Phys., D13, 739

Belhaj A., Chakhchi L., El Moumni H., Khalloufi J., Masmar K., 2020, Int. J. Mod. Phys. A, 35, 2050170

Bennett C. L. et al., 1994, The Astrophysical Journal, 436, 423

Bicak J., Suchlik Z., Balek V., 1989, Bulletin of the Astronomical Institutes of Czechoslovakia, 40, 65

Bisnovatyi-Kogan G., Tsupko O., 2017a, Universe, 3, 57

Bisnovatyi-Kogan G. S., Tsupko O. Y., 2008, Astrophysics, 51, 99

Bisnovatyi-Kogan G. S., Tsupko O. Y., 2009, Gravitation and Cosmology, 15, 20

Bisnovatyi-Kogan G. S., Tsupko O. Y., 2010, Monthly Notices of the Royal Astronomical Society, 404, 1790

Bisnovatyi-Kogan G. S., Tsupko O. Y., 2015, Plasma Physics Reports, 41, 562

Bisnovatyi-Kogan G. S., Tsupko O. Y., 2017b, Universe, 3

Bisnovatyi-Kogan G. S., Tsupko O. Y., 2018, Phys. Rev., D98, 084020

Bisnovatyi-Kogan G. S., Tsupko O. Y., 2022, arXiv e-prints, arXiv:2201.01716

Blanchet L., Spallicci A., Whiting B., 2011, Mass and Motion in General Relativity, Fundamental Theories of Physics book series. Springer, Dordrecht

Bolejko K., Clarkson C., Maartens R., Bacon D., Meures N., Beynon E., 2013, Phys. Rev. Lett., 110, 021302

Boran S., Desai S., Kahya E., Woodard R., 2018, Physical Review D, 97, 041501

Boyer R. H., Lindquist R. W., 1967, J. Math. Phys., 8, 265

Boyling J., 1968, Commun. Math. Phys., 10, 52–68

Boyling J., 1972, Proc. R. Soc. Lond. A., 329, 35–70

Bozza V., 2010, General Relativity and Gravitation, 42, 2269

Bray I., 1986, Phys. Rev., D34, 367

Breuer R. A., Ehlers J., Penrose R., 1980, Proceedings of the Royal Society of London. A. Mathematical and Physical Sciences, 370, 389

Breuer R. A., Ehlers J., Penrose R., 1981, Proceedings of the Royal Society of London. A. Mathematical and Physical Sciences, 374, 65

Buchdahl H. A., 1949a, Am. J. Phys., 17, 41

Buchdahl H. A., 1949b, Am. J. Phys., 17, 44

Buchdahl H. A., 1949c, Am. J. Phys., 17, 212

Buchdahl H. A., 1954, Am. J. Phys., 22, 182

Buchdahl H. A., 1955, Am. J. Phys., 23, 65

Byrd P. F., Friedman M. D., 1971, Handbook of Elliptic Integrals for Engineers and Scientists. Springer Berlin Heidelberg, Berlin, Heidelberg

Cai X.-C., Miao Y.-G., 2020, Phys. Rev. D, 101, 104023

Cano P. A., Murcia A., 2020, J. High Energy Phys., 10, 125

Cano P. A., Murcia A., 2021, Class. Quant. Grav., 38, 075014

Carathéodory C., 1909, Math. Ann., 67, 355

Cardano G., 1993, Witmer T. R., ed, The Rules of Algebra: (Ars Magna). Dover Publications, Inc.

Cárdenas V. H., Fathi M., Olivares M., Villanueva J. R., 2021, Eur. Phys. J. C, 81, 866

Cardoso V., Lemos J. P. S., 2001, Phys. Rev., D63, 124015

Carlip S., 1995, Class. Quant. Grav., 12, 2853

Carroll S. M., Johnson M. C., Randall L., 2009, J. High Energy Phys., 2009, 109

Carter B., 1968, Communications in Mathematical Physics, 10, 280

Carusotto I., Fagnocchi S., Recati A., Balbinot R., Fabbri A., 2008, New Journal of Physics, 10, 103001

Carvalho G. A., Arbañil J. D. V., Marinho R. M., Malheiro M., 2018, Eur. Phys. J., C78, 411

Castelvecchi D., 2016, Nature, 536, 258

Cataldo M., Cruz N., 2006, Phys. Rev., D73, 104026

Cattaneo C., 1958, Il Nuovo Cimento, 10, 318

Cattaneo C., 1959a, Il Nuovo Cimento, 13, 237

Cattaneo C., 1959b, Atti Accad. Naz. Lincei, VIII. Ser., Rend., Cl. Sci. Fis. Mat. Nat., 27, 54

Cattaneo C., 1959c, Il Nuovo Cimento, 11, 733

Cattaneo C., Caricato G., Roma. U., 1963, Introduzione alla teoria einsteiniana della gravitazione. Eredi Virgilio Veschi, Roma

Cattani C., Scalia M., Laserra E., Bochicchio I., Nandi K. K., 2013, Phys. Rev. D, 87, 047503

Cervero J. M., 1986, American Journal of Physics, 54, 35

Chandrasekhar S., 1939, An Introduction to the Study of Stellar Structure, Astrophysical monographs. University of Chicago Press

Chandrasekhar S., 1998, The mathematical theory of black holes. Clarendon Press Oxford University Press, Oxford England New York

Chatterjee A. K., Flathmann K., Nandan H., Rudra A., 2019, Physical Review D, 100, 024044

Chen B., Kantowski R., 2009a, Phys. Rev. D, 80, 044019

Chen B., Kantowski R., 2009b, Phys. Rev. D, 79, 104007

Chen G.-R., Huang Y.-C., 2019, Physics Letters B, 792, 86

Cisterna A., Giribet G., Oliva J., Pallikaris K., 2020, Phys. Rev. D, 101, 124041

Clifton T., Ferreira P. G., Padilla A., Skordis C., 2012, Physics Reports, 513, 1 , Modified Gravity and Cosmology

Contreras E., Ramirez–Velasquez J. M., Rincón A., Panotopoulos G., Bargueño P., 2019, The European Physical Journal C, 79, 802

Cornbleet S., 1993, American Journal of Physics, 61, 650

Crisostomo J., Lepe S., Saavedra J., 2004, Class. Quant. Grav., 21, 2801

Critchfield C. L., 1989, Journal of Mathematical Physics, 30, 295

Cruz N., Lepe S., 2004, Phys. Lett., B593, 235

Cruz N., Martínez C., Peña L., 1994, Class. Quant. Grav., 11, 2731

Cruz N., Olivares M., Villanueva J. R., 2005, Class. Quant. Grav., 22, 1167

Cruz N., Zanelli J., 1995, Class. Quant. Grav., 12, 975

Cunha P. V. P., Herdeiro C. A. R., 2018, Gen. Relativ. Gravit., 50, 42

Cunningham C. T., Bardeen J. M., 1972, Astrophys. J. Letters, 173, L137

Cunningham C. T., Bardeen J. M., 1973, ApJ, 183, 237

Darwin C. G., 1959, Proceedings of the Royal Society of London. Series A. Mathematical and Physical Sciences, 249, 180

Darwin C. G., 1961, Proceedings of the Royal Society of London. Series A. Mathematical and Physical Sciences, 263, 39

Das A., Saha A., Gangopadhyay S., 2021, Classical and Quantum Gravity, 38, 065015

Das P., Sk R., Ghosh S., 2017, European Physical Journal C, 77, 735

De Falco V., Falanga M., Stella L., 2016, Astronomy & Astrophysics, 595, A38

de Felice F., 1971, General Relativity and Gravitation, 2, 347

de Sitter A. R., W., 1916, Monthly Notices of the Royal Astronomical Society, 77, 155

de Vega H. J., Sanchez N. G., 2013, arXiv e-prints, arXiv:1304.0759

de Vries A., 1999, Classical and Quantum Gravity, 17, 123

Degasperis A., 1998, American Journal of Physics, 66, 486

Deser S., Jackiw R., 1988, Communications in Mathematical Physics, 118, 495

Deser S., Jackiw R., 't Hooft G., 1984, Annals of Physics, 152, 220

Diaferio A., Ostorero L., 2009, Mon. Not. Roy. Astron. Soc., 393, 215

Diaferio A., Ostorero L., Cardone V. F., 2011, J. Cosmol. Astropart. Phys., 1110, 008

Dias e Costa M. M., Toledo J. M., Bezerra V. B., 2019, International Journal of Modern Physics D, 28, 1950074

Dietz J. A., Morris T. R., 2015, Journal of High Energy Physics, 2015, 118

Dymnikova I., Kraav K., 2019, Universe, 5

Eddington A. S., 1920, Space, Time, and Gravitation: An Outline of the General Relativity Theory. Cambridge University Press

Edery A., Methot A. A., Paranjape M. B., 2001, Gen. Rel. Grav., 33, 2075

Edery A., Paranjape M. B., 1998, Phys. Rev., D58, 024011

Ehlers J., 1968, Z. Naturforsch., 22a, 1328

Enolski V., Hackmann E., Kagramanova V., Kunz J., Lämmerzahl C., 2011, Journal of Geometry and Physics, 61, 899

Erdös P., 2000, American Journal of Physics, 68, 888

Everitt C. W. F. et al., 2011, Phys. Rev. Lett., 106, 221101

Everitt C. W. F. et al., 2015, Classical and Quantum Gravity, 32, 224001

Exton H., 1976, Multiple Hypergeometric Functions and Applications, Ellis Horwood series in mathematics and its applications. E. Horwood

Fathi M., 2013, Chinese Physics C, 37, 025101

Fathi M., Kariminezhaddahka M., Olivares M., Villanueva J. R., 2020, The European Physical Journal C, 80, 377

Fathi M., Lepe S., Villanueva J. R., 2021, The European Physical Journal C, 81, 499

Fathi M., Molina M., Villanueva J., 2021, Physics Letters B, 820, 136548

Fathi M., Olivares M., Villanueva J. R., 2020, The European Physical Journal C, 80, 51

Fathi M., Olivares M., Villanueva J. R., 2021a, The European Physical Journal C, 81, 987

Fathi M., Olivares M., Villanueva J. R., 2021b, Galaxies, 9, 43

Fathi M., Olivares M., Villanueva J. R., 2021c, The European Physical Journal Plus, 136, 420

Fathi M., Olivares M., Villanueva J. R., 2022, The European Physical Journal C, 82, 629

Fathi M., Rincón Á., Villanueva J. R., 2020, Classical and Quantum Gravity, 37, 075004

Fathi M., Villanueva J., 2021, Vestnik KRAUNC. Fiz.-mat. nauki., 165

Ferrari V., Gualtieri L., 2008, General Relativity and Gravitation, 40, 945

Ferrari V., Mashhoon B., 1984, Phys. Rev. D, 30, 295

Frankel T., 2011, The Geometry of Physics: An Introduction (3 ed.). Cambridge University Press, Cambridge

Futterman J. A. H., Handler F. A., Matzner R. A., 1988, Scattering from Black Holes, Cambridge Monographs on Mathematical Physics. Cambridge University Press

Gal'tsov D. V., 1982, Journal of Physics A: Mathematical and General, 15, 3737

García A. A., Campuzano C., 2003, Phys. Rev. D, 67, 064014

García A., Hackmann E., Kunz J., Lämmerzahl C., Macías A., 2015, Journal of Mathematical Physics, 56, 032501

Gardner C. S., Greene J. M., Kruskal M. D., Miura R. M., 1967, Phys. Rev. Lett., 19, 1095

Gelles Z., Himwich E., Johnson M. D., Palumbo D. C., 2021, Physical Review D, 104, 044060

Ghaffarnejad H., Amirmojahedi M., Niad H., 2018, Advances in High Energy Physics, 2018, 3067272

Giambó S., Pantano P., Tucci P., 1984, American Journal of Physics, 52, 238

Gibbons G. W., Vyska M., 2012, Classical and Quantum Gravity, 29, 065016

Goebel C. J., 1972, The Astrophysical Journal, 172, L95

Goldstein H., Poole C. P., Safko J., 2011, Classical mechanics. Pearson, United States

González P. A., Olivares M., Papantonopoulos E., Vásquez Y., 2018, Phys. Rev. D, 97, 064034

Gordon W., 1923, Annalen der Physik, 377, 421

Gralla S. E., Lupsasca A., 2020, Physical Review D, 101, 044032

Gratton J., Delellis R., 1989, American Journal of Physics, 57, 683

GRAVITY Collaboration et al., 2020, Astronomy & Astrophysics, 636, L5

Graça J. P. M., Salako G. I., Bezerra V. B., 2017, International Journal of Modern Physics D, 26, 1750113

Gregory R. D., 2006, Classical Mechanics. Cambridge University Press

Grenzebach A., 2016, The Shadow of Black Holes. Springer International Publishing, Cham, p. 55

Grenzebach A., Perlick V., Lämmerzahl C., 2014, Phys. Rev. D, 89, 124004

Grenzebach A., Perlick V., Lämmerzahl C., 2015, Int. J. Mod. Phys., D24, 1542024

Griffiths J. B., Podolský J., 2009, Exact Space-Times in Einstein's General Relativity, Cambridge Monographs on Mathematical Physics. Cambridge University Press

Hackmann E., Hartmann B., Lämmerzahl C., Sirimachan P., 2010a, Physical Review D, 81, 064016

Hackmann E., Lämmerzahl C., 2008a, Physical Review Letters, 100, 171101

Hackmann E., Lämmerzahl C., 2008b, Physical Review D, 78, 024035

Hackmann E., Lämmerzahl C., Kagramanova V., Kunz J., 2010b, Physical Review D, 81, 044020

Hackmann E., Xu H., 2013, Phys. Rev. D, 87, 124030

Hagihara Y., 1930, Japanese Journal of Astronomy and Geophysics, 8, 67

Harko T., Kovács Z., Lobo F. S. N., 2009, Phys. Rev., D80, 044021

Haroon S., Jamil M., Jusufi K., Lin K., Mann R. B., 2019, Physical Review D, 99, 044015

Hassani S., 2013, Mathematical Physics, A Modern Introduction to Its Foundations. Springer International Publishing

Hawking S. W., 1965, Phys. Rev. Lett., 15, 689

Hawking S. W., 1966, Phys. Rev. Lett., 17, 444

Hawking S. W., 1975, Commun. Math. Phys., 43, 199, [,167(1975)]

Hawking S. W., Horowitz G. T., Ross S. F., 1995, Phys. Rev. D, 51, 4302

Hayward S. A., 2006, Phys. Rev. Lett., 96, 031103

Heydari-Fard M., Fakhry S., Hasani S., 2019, Adv. High Energy Phys., 2019, 1879568

Hooft G. T., 2014, arXiv e-prints, arXiv:1410.6675

Horne K., 2016, Mon. Not. Roy. Astron. Soc., 458, 4122

Hsiao Y.-W., Lee D.-S., Lin C.-Y., 2020, Physical Review D, 101, 064070

Hu P.-H., Wang Y.-J., 2006, Chin. Phys. Lett., 23, 2341

Iftikhar, Sehrish , 2018, EPJ Web Conf., 168, 04006

Jackson J., 1999, Classical electrodynamics. Wiley, New York

Jamil M., 2009, Eur. Phys. J. C, 62, 609

Javlon R., Alexandra D., Camci U., Abdujabbarov A., Ahmedov B., 2020, arXiv e-prints, arXiv:2010.04969

Jimenez Madrid J. A., Gonzalez-Diaz P. F., 2008, Grav. Cosmol., 14, 213

Johannsen T. et al., 2016, Phys. Rev. Lett., 116, 031101

Johnson M. D. et al., 2020, Science Advances, 6, eaaz1310

Jonsson R. M., 2007, American Journal of Physics, 75, 463

Junior H. C. D. L., Crispino L. C. B., Cunha P. V. P., Herdeiro C. A. R., 2020, The European Physical Journal C, 80, 1036

Jusufi K., Sarkar N., Rahaman F., Banerjee A., Hansraj S., 2018, The European Physical Journal C, 78, 349

Kagramanova V., Kunz J., Hackmann E., Lämmerzahl C., 2010, Physical Review D, 81, 124044

Kar S., SenGupta S., 2007, Pramana, 69, 49

Karas V., Vokrouhlicky D., 1990, Classical and Quantum Gravity, 7, 391

Kazanas D., Mannheim P. D., 1991, Astrophysical Journal Supplement Series, 76, 431

Khan S. U., Ren J., 2020, Chinese Journal of Physics, 70, 55

Kimpson T., Wu K., Zane S., 2019, Monthly Notices of the Royal Astronomical Society, 484, 2411

Kiselev V. V., 2003, Classical and Quantum Gravity, 20, 1187

Klemm D., 1998, Class. Quant. Grav., 15, 3195

Knox L., Kosowsky A., 1993, Primordial nucleosynthesis in conformal weyl gravity

Koch B., Reyes I. A., Rincón A., 2016, Class. Quant. Grav., 33, 225010

Kokkotas K. D., Schmidt B. G., 1999, Living Reviews in Relativity, 2, 2

Kolobov V. I., Golubkov K., Muñoz de Nova J. R., Steinhauer J., 2021, Nature Physics, 17, 362

Kramer M., Backer D., Cordes J., Lazio T., Stappers B., Johnston S., 2004, New Astronomy Reviews, 48, 993 , Science with the Square Kilometre Array

Kraniotis G. V., 2004, Classical and Quantum Gravity, 21, 4743

Kraniotis G. V., 2005, Classical and Quantum Gravity, 22, 4391

Kraniotis G. V., 2011, Classical and Quantum Gravity, 28, 085021

Kraniotis G. V., 2014, General Relativity and Gravitation, 46, 1818

Kraniotis G. V., 2021, The European Physical Journal C, 81, 147

Kraniotis G. V., Whitehouse S. B., 2003, Classical and Quantum Gravity, 20, 4817

Krisher T. P., 1997, Bulletin of the Astronomical Society of India, 25, 585

Kumar R., Ghosh S. G., 2020, Astrophys. J., 892, 78

Kumar R., Kumar A., Ghosh S. G., 2020, Astrophys. J., 896, 89

Kuniyal R. S., Uniyal R., Nandan H., Purohit K. D., 2016, General Relativity and Gravitation, 48, 46

Labus P., Morris T. R., Slade Z. H., 2016, Physical Review D, 94, 024007

Lämmerzahl C., Everitt C., Hehl F., 2001, Gyros, Clocks, Interferometers...: Testing Relativistic Gravity in Space, Lecture Notes in Physics. Springer Berlin Heidelberg

Lancaster T., Blundell S. J., 2014, Quantum Field Theory for the Gifted Amateur. Oxford University Press

Landau L. D., Lifschits E. M., 1975, Course of Theoretical Physics, Vol. 2, The Classical Theory of Fields. Pergamon Press, Oxford

Landau L. D., Lifshitz E. M., 1976, Mechanics. Elsevier

Landsberg P. T., 1964, Nature, 201, 485

Lemos J. P., Lopes F. J., Minamitsuji M., Rocha J. V., 2015, Phys. Rev. D, 92, 064012

Lemos J. P., Quinta G. M., 2014, Phys. Rev. D, 89, 084051

Lemos J. P., Quinta G. M., Zaslavskii O. B., 2016, Phys. Rev. D, 93, 084008

Lemos J. P. S., Minamitsuji M., Zaslavskii O. B., 2017, Phys. Rev. D, 96, 084068

Lense J., Thirring H., 1918, Phys. Z., 19, 156

Letelier P. S., 1979, Phys. Rev. D, 20, 1294

Li X.-Q., Chen B., Xing L.-l., 2020, Eur. Phys. J. Plus, 135, 175

Lim Y.-K., 2015, Phys. Rev. D, 91, 024048

Lim Y.-K., Wang Q.-h., 2017, Phys. Rev., D95, 024004

Lima C. A. U., Brito F., Hoyos J. A., Vanzella D. A. T., 2019, Nature Communications, 10, 3030

Liu C.-Q., Ding C.-K., Jing J.-L., 2017, Chinese Physics Letters, 34, 090401

Lu H., Pang Y., Pope C. N., Vazquez-Poritz J. F., 2012, Phys. Rev., D86, 044011

Luminet J. P., 1979, A&A, 75, 228

Luzum B. et al., 2011, Celestial Mechanics and Dynamical Astronomy, 110, 293

Mannheim P. D., 2006, Prog. Part. Nucl. Phys., 56, 340

Mannheim P. D., 2012, Phys. Rev., D85, 124008

Mannheim P. D., Kazanas D., 1989, Astrophysical Journal, 342, 635

Marranghello G. F., 2007, International Journal of Modern Physics D, 16, 319

Marshall T. W., 1978, Am. J. Phys., 46, 136

Massey R., Kitching T., Richard J., 2010, Rept. Prog. Phys., 73, 086901

Matos T., Guzmán F. S., Ureña-López L. A., Núñez D., 2002, in Macias A., Cervantes-Cota J. L., Lämmerzahl C., eds, Exact Solutions and Scalar Fields in Gravity. Kluwer Academic Publishers, Boston, p. 165

Mino Y., 2003, Physical Review D, 67, 084027

Mishra A. K., Chakraborty S., Sarkar S., 2019, Phys. Rev., D99, 104080

Misner C. W., Thorne K. S., Wheeler J. A., 2017, Gravitation. Princeton University Press, Princeton, N.J

Mizuno Y. et al., 2018, Nature Astronomy, 2, 585

Mohseni M., Fathi M., 2016, Eur. Phys. J. Plus, 131, 21

Molina M., Villanueva J. R., 2021, Class. Quant. Grav., 38, 105002

Morozova V. S., Ahmedov B. J., Tursunov A. A., 2013, Astrophysics and Space Science, 346, 513

Morris T. R., 2016, Journal of High Energy Physics, 2016, 160

Mustafa G., Hussain I., 2021, The European Physical Journal C, 81, 419

Mustafa G., Hussain I., Liu W.-M., 2021, arXiv e-prints, arXiv:2108.07801

Muñoz G., 2014a, American Journal of Physics, 82, 564

Muñoz G., 2014b, American Journal of Physics, 82, 564

Nakahara M., 2018, Geometry, Topology and Physics (2 ed.). CRC Press

Narzilloev B., Rayimbaev J., Shaymatov S., Abdujabbarov A., Ahmedov B., Bambi C., 2020, Phys. Rev. D, 102, 044013

Navarro J. F., Frenk C. S., White S. D. M., 1995, Monthly Notices of the Royal Astronomical Society, 275, 720

Navarro J. F., Frenk C. S., White S. D. M., 1996, The Astrophysical Journal, 462, 563

Newman E. T., Janis A. I., 1965, J. Math. Phys., 6, 915

Nickalls R. W. D., 2006, The Mathematical Gazette, 90, 203–208

Novello M., Visser M., Volovik G., 2002, Artificial Black Holes. World Scientific

Ohta N., 2017, Progress of Theoretical and Experimental Physics, 2017

Olivares M., Saavedra J., Leiva C., Villanueva J. R., 2011, Modern Physics Letters A, 26, 2923

Olivares M., Villanueva J. R., 2013, Eur. Phys. J. C, 73, 2659

Olver P. J., 1986, Graduate Texts in Mathematics, Vol. 107, Applications of Lie Groups to Differential Equations. Springer US

Panotopoulos G., 2018, Gen. Rel. Grav., 50, 59

Paschalidis V., Stergioulas N., 2017, Living Reviews in Relativity, 20, 7

Payandeh F., Fathi M., 2012, Int. J. Theor. Phys., 51, 2227

Penrose R., 1965, Phys. Rev. Lett., 14, 57

Penrose R., 2002, General Relativity and Gravitation, 7, 1141

Perlick V., 2004, Living Reviews in Relativity, 7, 9

Perlick V., Tsupko O. Y., 2017, Physical Review D, 95, 104003

Perlick V., Tsupko O. Y., Bisnovatyi-Kogan G. S., 2015, Physical Review D, 92, 104031

Perlick V., Tsupko O. Y., Bisnovatyi-Kogan G. S., 2018, Phys. Rev., D97, 104062

Perlmutter S. et al., 1999, Astrophys. J., 517, 565

Phillips K. J. H., 1995, Guide to the Sun. cambridge University Press, Cambridge, UK

Pirani F., 1956, Acta Phys. Polon., 15, 389

Pireaux S., 2004a, Class. Quant. Grav., 21, 4317

Pireaux S., 2004b, Class. Quant. Grav., 21, 1897

Planck Collaboration, et al., 2016, A&A, 594, A13

Plebanski J., 1960, Phys. Rev., 118, 1396

Pogliani L., Berberan-Santos M., 2000, J. Math. Chem., 28, 313–324

Poisson E., 2009, A Relativist's Toolkit: The Mathematics of Black-Hole Mechanics. Cambridge University Press

Poisson E., Pound A., Vega I., 2011, Living Rev. Rel., 14, 7

Press W. H., 1971, The Astrophysical Journal, 170, L105

Psaltis D., 2008, Living Reviews in Relativity, 11, 9

Psaltis D., 2019, Gen. Relativ. Gravit., 51, 137

Psaltis D., Özel F., Chan C.-K., Marrone D. P., 2015, Astrophys. J., 814, 115

Pugliese D., Quevedo H., Ruffini R., 2011, Phys. Rev. D, 83, 104052

Pugliese D., Quevedo H., Ruffini R., 2017, European Physical Journal C, 77, 206

Rauch K. P., Blandford R. D., 1994, The Astrophysical Journal, 421, 46

Raychaudhuri A., 1955, Phys. Rev., 98, 1123

Rayimbaev J., Shaymatov S., Jamil M., 2021, The European Physical Journal C, 81, 699

Reasenberg R. D. et al., 1979, The Astrophysical Journal, 234, L219

Regge T., Wheeler J. A., 1957, Phys. Rev., 108, 1063

Reuter M., Weyer H., 2004, Physical Review D, 69, 104022

Riegert R. J., 1984, Phys. Rev. Lett., 53, 315

Riess A. G. et al., 1998, Astron. J., 116, 1009

Rincón A., Contreras E., Bargueño P., Koch B., Panotopoulos G., 2018, Eur. Phys. J., C78, 641

Rincón A., Koch B., 2018a, J. Phys. Conf. Ser., 1043, 012015

Rincón A., Koch B., 2018b, Eur. Phys. J. C, 78, 1022

Rindler W., 2006, Relativity: Special, general, and cosmological

Rizzi G., Ruggiero M. L., 2003a, Gen. Rel. Grav., 35, 2129

Rizzi G., Ruggiero M. L., 2003b, Gen. Rel. Grav., 35, 1745

Rizzi G., Ruggiero M. L., 2004, Rizzi G., Ruggiero M. L., eds, The Relativistic Sagnac Effect: Two Derivations. Springer Netherlands, Dordrecht, p. 179

Roy R., Yajnik U. A., 2020, Physics Letters B, 803, 135284

Roy S., Sen A. K., 2019, Journal of Physics: Conference Series, 1330, 012002

Rubin V. C., Ford W. K., Jr., Thonnard N., 1980, Astrophys. J, 238, 471

Ruggiero M. L., 2005, Gen. Rel. Grav., 37, 1845

Ruggiero M. L., Tartaglia A., 2014, The European Physical Journal Plus, 129, 126

Ryder L., 2009, Introduction to General Relativity. Cambridge University Press

Saadati R., Shojai F., 2019, Phys. Rev. D, 100, 104041

Sagnac G., 1913, C. R. Acad. Sci., 157, 708

Said J. L., Sultana J., Adami K. Z., 2012, Phys. Rev., D85, 104054

Said J. L., Sultana J., Adami K. Z., 2013, Phys. Rev. D, 88, 087504

Sakurai J. J., 1980, Phys. Rev. D, 21, 2993

Sarkar S., Rahaman F., Radinschi I., Grammenos T., Chakraborty J., 2018, Advances in High Energy Physics, 2018, 5427158

Schee J., Stuchlík Z., 2009, International Journal of Modern Physics D, 18, 983

Schiff L. I., 1960, Proc. Nat. Acad. Sci., 46, 871

Schulze-Koops K., Perlick V., Schwarz D. J., 2017, Classical and Quantum Gravity, 34, 215006

Schutz B. F., 1987, in Carter B., Hartle J. B., eds, Gravitation in Astrophysics, Vol. 156. Springer US, Boston, MA, p. 123

Schutz B. F., Will C. M., 1985, The Astrophysical Journal, 291, L33

Schützhold R., Unruh W. G., 2005, Physical Review Letters, 95, 031301

Shaikh R., 2019, Phys. Rev., D100, 024028

Shapiro I. I., 1964, Physical Review Letters, 13, 789

Shapiro I. I., Pettengill G. H., Ash M. E., Stone M. L., Smith W. B., Ingalls R. P., Brockelman R. A., 1968, Physical Review Letters, 20, 1265

Shaymatov S., Vrba J., Malafarina D., Ahmedov B., Stuchlík Z., 2020, Physics of the Dark Universe, 30, 100648

Shen Z.-Q., Lo K. Y., Liang M.-C., Ho P. T. P., Zhao J.-H., 2005, Nature, 438, 62

Singh B. P., Ghosh S. G., 2018, Annals Phys., 395, 127

Stachel J., 1977, in Abstracts of Contributed Papers, 8th International Conference on General Relativity and Gravitation, University of Waterloo, Ontario, p. 324

Steinhauer J., 2016, Nature Physics, 12, 959

Stevenson P. M., 1981, Physical Review D, 23, 2916

Straumann N., 2013, General Relativity, Graduate Texts in Physics. Springer Netherlands, Dordrecht

Stuchlík Z., 1983, Bulletin of the Astronomical Institutes of Czechoslovakia, 34, 129

Stuchlík Z., Hledík S., 1999, Phys. Rev. D, 60, 044006

Stuchlík, Zdenek , Kolos, Martin , 2016, Eur. Phys. J. C, 76, 32

Stuchlík Z., Hledík S., 1999, Physical Review D, 60, 044006

Stuchlík Z., Kološ M., Kovář J., Slaný P., Tursunov A., 2020, Universe, 6

Sultana J., 2013, Journal of Cosmology and Astroparticle Physics, 2013, 048

Sultana J., Kazanas D., 2010, Phys. Rev., D81, 127502

Synge J. L., 1960, Relativity: The general theory. Series in Physics, Amsterdam: North-Holland Publication Co.

Synge J. L., 1966, Mon. Not. Roy. Astron. Soc., 131, 463

't Hooft G., 1988, Communications in Mathematical Physics, 117, 685

't Hooft G., 2010a, arXiv e-prints, arXiv:1009.0669

't Hooft G., 2010b, arXiv e-prints, arXiv:1011.0061

Tamburini F., Thidé B., Della Valle M., 2019, Monthly Notices of the Royal Astronomical Society: Letters, 492, L22

Tanhayi M. R., Fathi M., Takook M. V., 2011, Mod. Phys. Lett., A26, 2403

Taylor J. R., 2005, Classical Mechanics. Sausalito, CA: University Science Books

Teitelboim C., 1995, Phys. Rev. D, 51, 4315, [Erratum: Phys.Rev.D 52, 6201 (1995)]

Thompson R. T., 2018, Phys. Rev. D, 97, 065001

Toledo J. d. M., Bezerra V. B., 2018, The European Physical Journal C, 78, 534

Toledo J. M., Bezerra V. B., 2019, International Journal of Modern Physics D, 28, 1950023

Toledo J. M., Bezerra V. B., 2020, General Relativity and Gravitation, 52, 34

Toshmatov B., Stuchlík Z., Ahmedov B., 2017, The European Physical Journal Plus, 132, 98

Treu T., Ellis R. S., 2015, Contemporary Physics, 56, 17

Tsukamoto N., 2018, Phys. Rev. D, 97, 064021

Tsupko O. Y., Bisnovatyi-Kogan G. S., 2013, Physical Review D, 87, 124009

Tursunov A., Kološ M., Stuchlík Z., Gal'tsov D. V., 2018, The Astrophysical Journal, 861, 2

Tursunov A., Stuchlík Z., Kološ M., Dadhich N., Ahmedov B., 2020, The Astrophysical Journal, 895, 14

't Hooft G., 2011, Foundations of Physics, 41, 1829

Uniyal R., Nandan H., Purohit K. D., 2018, Classical and Quantum Gravity, 35, 025003

Unruh W. G., 1981, Physical Review Letters, 46, 1351

Vankov K., 2017, HAL Open Science, hal-01571766

Varieschi G. U., 2010, General Relativity and Gravitation, 42, 929

Varieschi G. U., 2014a, Galaxies, 2, 577

Varieschi G. U., 2014b, General Relativity and Gravitation, 46, 1741

Varieschi G. U., Burstein Z., 2013, ISRN Astron. Astrophys., 2013, 482734

Vázquez S. E., Esteban E. P., 2004, Nuovo Cimento B Serie, 119, 489

Vessot R. F. C. et al., 1980, Phys. Rev. Lett., 45, 2081

Villanueva J. R., Olivares M., 2013, J. Cosmol. Astropart. Phys., 1306, 040

Villanueva J. R., Olivares M., 2015, European Physical Journal C, 75, 562

Villanueva J. R., Tapia F., Molina M., Olivares M., 2018, Eur. Phys. J., C78, 10

Villanueva J. R., Vásquez Y., 2013, The European Physical Journal C, 73, 2587

Virbhadra K. S., Ellis G. F. R., 2000, Phys. Rev. D, 62, 084003

Vishveshwara C. V., 1970, Nature, 227, 936

Vrba J., Abdujabbarov A., Kološ M., Ahmedov B., Stuchlík Z. c. v., Rayimbaev J., 2020, Phys. Rev. D, 101, 124039

Wald R. M., 1984, General relativity. Chicago Univ. Press, Chicago, IL

Wei H., Cai R.-G., 2008, Physics Letters B, 660, 113

Weinfurtner S., Tedford E. W., Penrice M. C. J., Unruh W. G., Lawrence G. A., 2011, Phys. Rev. Lett., 106, 021302

Weyl H., 1918, Mathematische Zeitschrift, 2, 384

Whittaker E. T., McCrae S. W., 1988, A Treatise on the Analytical Dynamics of Particles and Rigid Bodies, Cambridge Mathematical Library. Cambridge University Press

Whittaker E. T., Watson G. N., 1996, A Course of Modern Analysis (4 ed.), Cambridge Mathematical Library. Cambridge University Press

Will C. M., 2014, Living Rev. Rel., 17, 4

Witten E., 1988, Nuclear Physics B, 311, 46

Wohlfarth M. N. R., Pfeifer C., 2013, Phys. Rev. D, 87, 024031

Xu Z., Hou X., Gong X., Wang J., 2018, Journal of Cosmology and Astroparticle Physics, 2018, 038

Yi M., Wu X., 2020, Physica Scripta, 95, 085008

Yumoto A., Nitta D., Chiba T., Sugiyama N., 2012, Phys. Rev., D86, 103001

Zerilli F. J., 1970, Phys. Rev. D, 2, 2141

Zhang M., Guo M., 2020, Eur. Phys. J., C80, 790

Zhao F., Tang J., He F., 2016, Phys. Rev. D, 93, 123017

Zhao Q.-Q., Li Y.-Z., Lü H., 2018, Phys. Rev. D, 98, 124001

Zucker I., 2008, The Mathematical Gazette, 92, 264